LA-14036-PR

Los Alamos Neutron Science Center

Activity Report

January – December 2002

2002

LANSCE Overview
- Division Leader's Introduction

Research Highlights
- Accelerator Science and Technology
- Condensed-Matter Science and Engineering
- Neutron Nuclear Science
- Proton Radiography

Special Projects

Facility Upgrades
- Instrumentation
- Infrastructure

Accelerator Operations and User Program
- Operations
- User Program

News and Events

Publications

Experiment Reports
- Instrument Number
- Principal Investigator
- Proposal Number

Search

Los Alamos NATIONAL LABORATORY

LANSCE Los Alamos Neutron Science Center

LA-14036-PR
Progress Report

Issued: August 2003

LANSCE Activity Report 2002

Solving National Problems Using High-Intensity Accelerators and Spallation Neutron Sources

Compiled by

Audrey Archuleta
Grace Hollen
Alan Hurd
Kevin Jones
Frank Merrill
André Michaudon
Sharon Mikkelson
Bruce Takala
Steve Wender

Los Alamos
NATIONAL LABORATORY

LANSCE Activity Report 2002

Solving National Problems
Using High-Intensity Accelerators
and Spallation Neutron Sources

Abstract

The Los Alamos Neutron Science Center (LANSCE) Activity Report describes scientific and technological progress and achievements at LANSCE during calendar year 2002. This report includes a message from the Division Director, an overview of LANSCE, sponsor overviews, research highlights, special projects and facility upgrades achievements, experimental and user program accomplishments, news and events, and a list of publications resulting from research at LANSCE. The research highlights cover the areas of condensed-matter science and engineering, accelerator science, neutron nuclear science, and proton radiography. This report also contains a compact disk that includes an overview, the Activity Report itself, and experiment reports from LANSCE User Program experiments, as well as a search capability.

Table of Contents

LANSCE Overview 1

Research Highlights

Condensed-Matter Science and Engineering 17

Accelerator Science and Technology 45

Neutron Nuclear Science 73

Proton Radiography 93

Special Projects 107

Facility Upgrades 115

Accelerator Operations and User Program 149

News and Events 167

Publications 177

Experiment Reports (on compact disk)

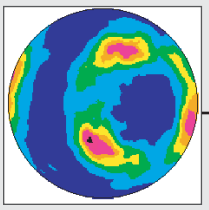

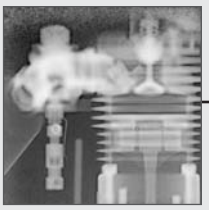

Overview

Division Leader's Introduction 2

Principal Research Sponsors 5
National Nuclear Security Administration 5
Basic Energy Sciences. 6
Laboratory-Directed Research and Development . . 6

Technical and Infrastructure Accomplishments. 8

Particle-Beam Production 10

A National User Facility 11

Programs and Projects 15

Division Leader's Introduction

Thirty years of accelerator operations and the most successful user program to date make 2002 a record-breaking year for LANSCE.

—Paul W. Lisowski

The year 2002 marked the 30th anniversary of achieving an 800-MeV proton beam through the accelerator and was also the best year yet for the Los Alamos Neutron Science Center (LANSCE) user facility. We set a user-facility record, performing 224 experiments and having over 782 user visits. Forty-two dynamic measurements for the weapons program were performed at the Proton Radiography (pRad) facility, also setting a new record. No other user facility in the world is as versatile and broad-based as LANSCE, nor is there one with a more important national mission — serving the science community and performing basic and applied research important to national defense.

The past year was not only a milestone in research and technology at LANSCE but was also an extraordinarily successful time for operational safety and security. No security issues were reported, and a Division safety goal of operating one year without a lost workday was achieved in April 2003.
A considerable effort was needed to begin user operations in 2002. We ended the previous operating cycle with a Lujan Neutron Scattering Center (Lujan Center) neutron-production target-moderator-reflector system (TMRS) that had to be replaced. Consequently, in addition to the usual maintenance needed during the annual outage, we had to accomplish that task. Using project-management techniques to manage the work, LANSCE led a team effort to redesign and rebuild the system before we restarted operations. Removing and replacing the 7-ton TMRS system took only 10% of the time and resulted in only 5% of the personnel radiation exposure of the first TMRS replacement in 1998. Furthermore, the new TMRS met all our expectations, allowing us to set a record for 125 μA of proton beam and an operational availability of over 99%.

Full user operations began this year as scheduled on July 26, 2002, and concluded on January 26, 2003. The facility operated for more than 2,500 hours at 87% overall availability and provided the pRad facility with 100% availability for all dynamic experiments. The Lujan Center operated with an average beam power of 80 kW with more than a 50% increase in the integrated amount of charge over any previous year.

The Lujan Center had an impressive number of world-class instruments operational during the 2002 run cycle; four of these instruments were new to the user program. There were 12 instruments for condensed-matter science and engineering and 2 for nuclear science. New equipment was available for the first time, including sample environments, an 11-T superconducting magnet, an 8-Mbar high-pressure cell, and presses and furnaces that can simultaneously operate with pressures to 30 GPa and temperatures to 2,000 K. Also initiated was the operation of a unique 4-π detector to be used for measuring nuclear cross sections for astrophysics and defense-science studies. Additionally, there was a new record of 375 user visits at the Lujan Center — an increase of 40% over 2001.

The Weapons Neutron Research Facility (WNR) had more than 400 user visits — also a record. With six flight paths at the WNR spallation source, the instrumentation at WNR for nuclear science and technology continues to be unique worldwide. GEANIE, a high-resolution germanium detector array, continues to be a mainstay instrument, allowing scientists to study reactions needed to test nuclear theory and to give the defense community opportunities to improve our understanding of radiochemical diagnostics from past nuclear tests. In support of the Quantification of Margins and Uncertainties initiative within the defense community, LANSCE began a program of measurements on three flight paths to characterize and thus better understand the fission process. Demand for use of the neutron spectrum for accelerated testing of semiconductor devices has continued to grow with our first year operating an improved detector station, the Irradiation of Chips and Electronics House, and selection of WNR as the preferred facility for testing industry-wide.

Forty-two experiments driven by explosives were performed this year at the pRad area, which will be introduced as a new user facility when operations restart in July 2003. We expect the pRad program to grow steadily when academia joins users from other national laboratories and from the Aldermaston Weapons Establishment in the United Kingdom. Studies of dynamic systems are providing important data for our weapons program with impressive new information on energetic materials and material-failure properties. During the 2002 run cycle, the pRad facility tested a new detector system designed to image low-contrast samples. A microscope designed and fabricated for pRad studies gave impressive 15-μm resolution, potentially opening new frontiers for dynamic imaging. During the 2003 operating period, a newly completed pulsed magnet system, known as the "switchyard kicker," will provide a five-fold increase in beam time for pRad.

LANSCE was designed to operate multiple experimental areas simultaneously, and that capability will be expanded with the commissioning of a new Isotope Production Facility (IPF). Funded by the Department of Energy Office of Nuclear Energy, Science and Technology, the IPF will give the nation year-round medical isotope availability, contributing important material needed for more than 10 million medical procedures annually.

Also in 2002, we achieved great progress in understanding and improving the performance of the existing accelerator systems at LANSCE. We have designed a replacement for the ancient 201-MHz radio-frequency (rf) system used in the drift-tube linac (DTL) section of the accelerator. We made progress in understanding and controlling a long-standing Proton Storage Ring beam instability. This strong transverse instability has been a limiting factor on peak intensity and is widely considered a major technical risk to the next generation of high-intensity proton rings. Design of the Advanced Hydrotest Facility, a future pRad facility for three-dimensional studies of dynamic events, continued with improvements to designs, design codes, and technology. Although not in the lead role, LANSCE continues to be a strong supporter of the Laboratory's Spallation Neutron Source Division in controls, rf, and DTL design and fabrication.
With two successive years of reliable neutron and proton beam operation behind us, we have attained an important plateau, but we know that we must do more to reach our goal of world-class status for our user facilities. Over the next few years, we will make a concerted effort to increase our involvement in the science of stockpile stewardship. We have been given an important program element in support of predictive capability for the weapons program, and we will be working hard to bring that effort to maturity. Both of these are challenges for the Division. The good news is that we understand the path ahead and enthusiastically embrace the opportunity to get there.

Paul W. Lisowski

The Los Alamos Neutron Science Center — An Essential Facility for Los Alamos National Laboratory and for Stockpile Stewardship

The Los Alamos Neutron Science Center, or LANSCE, is an accelerator-based multidisciplinary facility that provides extraordinary research opportunities in basic and applied research for civilian and defense applications.

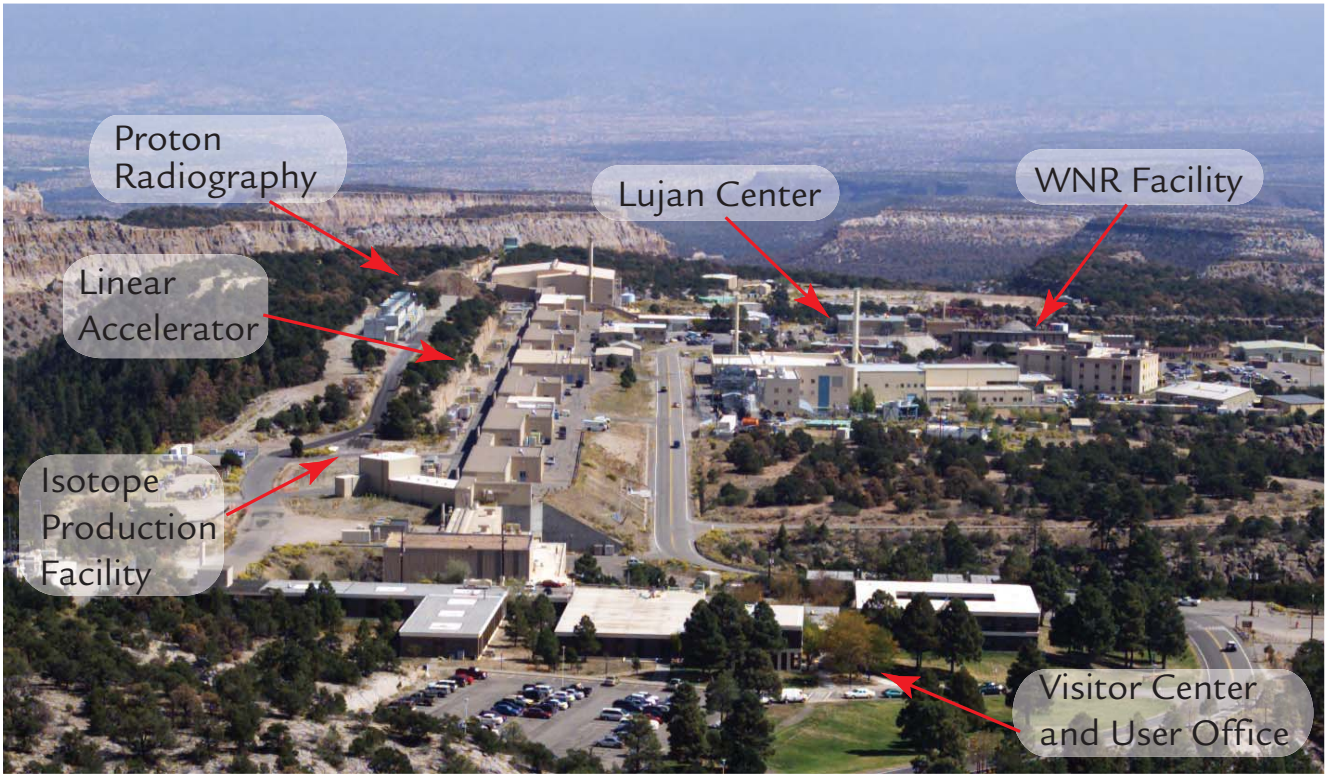

The Los Alamos Neutron Science Center, or LANSCE, is an accelerator-based multidisciplinary facility that provides extraordinary research opportunities in basic and applied science for civilian and defense applications. Central to the LANSCE facility is an 800-MeV proton linear accelerator (linac) that drives three major national user facilities:

- the Lujan Neutron Scattering Center (Lujan Center) for condensed-matter and nuclear-physics research using pulsed beams of moderated cold, thermal, and epithermal neutrons;
- the Weapons Neutron Research Facility (WNR), which uses an unmoderated neutron spallation spectrum for basic and applied nuclear-physics research, neutron radiography, neutron resonance spectroscopy, and irradiation testing of industrial components such as integrated circuits; and
- the Proton Radiography (pRad) facility, which enables high-resolution, time-dependent studies of dynamic events for the study of high-explosive (HE) detonation and burn, hydrodynamics and shock physics, and dynamic materials properties.

Major LANSCE stakeholders include:

- the Department of Energy (DOE) National Nuclear Security Administration (NNSA), which supports accelerator operations, spallation-neutron production, and weapons research in support of stockpile maintenance and certification;
- the DOE Office of Science (SC) Office of Basic Energy Sciences (BES), which supports the Lujan Center National User Program, Lujan Center operations, and condensed-matter and materials research;
- the DOE Office of High Energy and Nuclear Physics, which supports basic-nuclear-physics research;
- Laboratory-Directed Research and Development (LDRD), which supports the development of novel neutron-scattering instruments and research applications; and
- the DOE Office of Nuclear Energy, Science and Technology (NE), which supports the Isotope Production Facility (IPF) project due for completion in FY 2003.

In addition to significant achievements in stockpile stewardship and in basic and applied research, the LANSCE complex has been one of the most important Laboratory "windows" to the academic community and a source of many of the brightest young scientists at the Los Alamos National Laboratory (LANL). It is estimated that LANSCE and its predecessor, the Los Alamos Meson Physics Facility, have served as a gateway to nearly 10% of the workforce at LANL.

Principal Research Sponsors

The scientific vitality of LANSCE Division facilities is strongly coupled to major programs in the DOE NNSA and SC, as well as to significant projects sponsored by LDRD. The NNSA is the principal steward for LANSCE facility operations. NNSA Defense Programs also invest in the scientific capabilities and infrastructure at LANSCE by means of targeted programmatic research in support of stockpile stewardship. Data from this research are tied to both near- and long-term milestones for developing a scientific understanding of nuclear weapons.

The DOE/SC/BES supports the Lujan Center at LANSCE as one of its major national user facilities in neutron scattering. BES requires the Lujan Center to offer reliable, world-class capabilities for basic and applied research to users from universities, national laboratories, and industry. Areas of supported research include condensed-matter physics, polymer science, chemistry, earth sciences, structural biology, and neutron nuclear science. Scientists apply for facility time through a competitive peer-review proposal process.

The LDRD program funds basic and applied research and development focusing on early exploration of scientific ideas and concepts. LDRD has been an important part of LANSCE strategic investments in new instruments and neutron-research applications.

National Nuclear Security Administration. LANSCE-based research and capabilities are strongly tied to the requirements for maintaining and certifying the U.S. nuclear deterrent. LANSCE facilities are engaged in nuclear, materials, and hydrodynamics research necessary for accurately assessing and modeling weapons performance. LANSCE researchers and users are also defining research to meet weapons certification and maintenance milestones. A schematic of how LANSCE facilities support principal areas of scientific research of relevance to nuclear-weapons issues is shown in Fig. 1. Specific areas of focus include:

- measuring neutron-capture cross sections important to (1) interpreting radiochemical measurements of previous nuclear weapons tests and (2) modeling actinide inventories to infer device yield;
- measuring principal fission and fusion cross sections of nuclear fuels and cross sections of fission products to the required accuracy to accurately predict nuclear weapons yield;
- determining the hydrodynamic and shock behavior of weapons materials under the extreme physical conditions of relevance to weapons operation;
- measuring the properties, including the equation of state, of

Weapons Issues	Performance Drivers	HE Science	Materials Science	Actinide Materials Science	Hydro, Mix Turbulence, Shock Physics	Nuclear Science
Primary Performance	HE Performance	In Progress	In Progress	N/A	In Progress	N/A
	Implosion Performance	In Progress	In Progress	In Progress	In Progress	N/A
	Criticality	N/A	Potential	In Progress	In Progress	In Progress
	Burn	N/A	N/A	In Progress	In Progress	In Progress
	Yield Assessment	N/A	N/A	Potential	N/A	In Progress
Secondary Performance	Energy Flow	N/A	In Progress	N/A	In Progress	N/A
	Explosion Performance	N/A	In Progress	Potential	Potential	In Progress
	Yield Assessment	N/A	N/A	In Progress	N/A	In Progress
Engineered Systems	Initiator Performance	Potential	In Progress	N/A	N/A	N/A
	Other Mech. Systems	Potential	In Progress	N/A	In Progress	N/A
Manufacturing	Aging	In Progress	In Progress	In Progress	Potential	Potential
	Stockpile Life Extension Program	Potential	In Progress	Potential	Potential	Potential

Legend

N/A

In Progress

Potential

Fig. 1. LANSCE support of research relevant to nuclear weapons issues.

actinides and other weapons materials over a relevant range of pressures and temperatures;

- using the unique, high-resolution and temporal capabilities of pRad to study HE burn, hydrodynamics, and dynamic material properties;
- assessing the change in strength, texture, and compressibility of weapons-relevant materials with age;
- understanding the properties of energetic materials (HEs) with a view to predicting the performance of weapons and the response of weapons systems in both normal and abnormal environments; and
- developing enhanced neutron tomography for the advanced surveillance of stockpile systems and components.

NNSA-supported activities featured in this report are listed in Table 1. However, a significantly more comprehensive overview of LANSCE weapons research will be forthcoming in a classified report due to be released in early fall of 2003.

Basic Energy Sciences. The DOE/SC/BES has a major responsibility for planning, designing, constructing, and operating national user facilities. These user facilities offer world-class capabilities for basic and applied research to researchers from academia, national laboratories, and industry. Acquiring new knowledge that cannot be obtained by other means enables the determination of behavior of matter. The experiments at these user facilities embrace the full range of scientific and technological endeavors, including chemistry, physics, materials science, geology, biology, and engineering science. The Lujan Center contributes to this objective through the development of world-class spectrometers and by supporting forefront research. Some current activities in support of these goals featured in this report are listed in Table 2.

Laboratory-Directed Research and Development. LANL's LDRD program supports innovative research

Table 1. DOE/NNSA/DP research or projects featured in the 2002 LANSCE Activity Report.

Plutonium-Phonon Measurements on Pharos	24
New Findings in Texture Development and Phase Transformation in Shocked Zirconium Shed Light on Models for Shock-Induced Phase Transformations	26
In Situ Neutron-Diffraction Study of Lithium-Ion Batteries	40
Control of the e-p Instability at the Proton Storage Ring	46
H^- Injector Development for the Short-Pulse Spallation Source Enhancement Project	68
Neutron Capture on Unstable Nuclides	74
Frontiers in Neutron-Induced Fission	82
Improving Radiochemical Diagnostics: Studying Iridium and Europium with the Germanium Array for Neutron-Induced Excitations	86
2002 Proton Radiography Overview	94
A Cerenkov Radiation Detector for Proton Radiography at LANSCE	96
Proton Radiography Microscope	100
Proton Radiography Capabilities Illuminate Studies of Explosively Driven Fragmentation	102
Advanced Hydrotest Facility	110
The LANSCE Switchyard-Kicker Project Nears Installation	112
Pharos — A Chopper Spectrometer for Inelastic-Neutron-Scattering Studies of Excitations in Materials	120
FIGARO: A Neutron- and γ-Ray-Detector Array for Studying Fast-Neutron-Induced Reactions	122
An Advanced Detector for Studying Neutron Capture at LANSCE	130
Accelerator Development Activities in 2002	138
Replacement of the LANSCE 1L Target-Moderator-Reflector System	140
Upgrade of the Fiber-Optic-Cable Plant at LANSCE	141
A Multiwire-Proportional-Chamber System Used to Monitor Off-Momentum Beam in Accelerators	142
Magnet-Power-Supply Upgrades for 2002	143
LANSCE Accelerator-Control-System Upgrade	144
EPACS and Shutter Controls Installed at Lujan Center in 2002	145
Accelerator Operations	149

Table 2. DOE/SC/BES research or projects featured in the 2002 LANSCE Activity Report.

Electric-Field-Driven Transformations of a Supported Model Biological Membrane	18
The Response of Cemented-Carbide Composites to Compressive Load	20
Proton Dynamics in Very Short, Strong Hydrogen Bonds	28
Electrical Anomalies in α-Glycine	32
Thermal Neutron Protein Crystallography — Enzyme-Mechanism Investigations with D-xylose Isomerase	34
Texture Changes During the Quartz α-β Phase Transition Studied by Neutron Diffraction	36
In Situ Neutron-Diffraction Study of Lithium-Ion Batteries	40
Magnetic Exchange Coupling in Metal/Native-Oxide Multilayers Studied by Polarized Neutron Reflectometry	42
Development and Testing of High-Power Vacuum Windows for the Spallation Neutron Source	54
Design of a Radio-Frequency System for the Spallation Neutron Source	58
Development of a Polyphase-Resonant-Converter Modulator for the Spallation Neutron Source	62
Scientists Perform First Neutron-Scattering Experiment Using the 11-T Superconducting Magnet at the Lujan Neutron Scattering Center	116
Pharos — A Chopper Spectrometer for Inelastic-Neutron-Scattering Studies of Excitations in Materials	120
Timing-Reference Generators and Chopper Controllers Designed for Neutron Sources	124
NPDF: A New High-Resolution Total-Scattering Powder Diffractometer	126
Enhanced-Beam-Extraction System Implemented in IN500	128
A Sharper SPEAR	132
The LQD Upgrade: Challenges and Opportunities of Brighter Neutron Sources	134
EPACS and Shutter Controls Installed at Lujan Center in 2002	145
User Program	157

and development work that extends LANL's science and technology capabilities. The selection process is highly competitive, with a comprehensive review by peers or LANL managers and selection based on innovation and scientific merit in a mission context. The LDRD program has two major components: (1) directed research, which provides funds to make larger strategic investments in research and development projects, and (2) exploratory research, which provides funds to conduct staff-initiated research and development that is highly innovative in scope and often at the forefront of their disciplines. LANSCE has many projects that owe much of their success to LDRD support, including

- synthesis and characterization of superhard materials;
- test of "Big Bang" nucleosynthesis model predictions by measurement of the n+p → d+γ cross section;
- measurement of neutron cross sections for unstable nuclei of interest to s-process nucleosynthesis;
- exploration of nanoscale dynamics in soft matter;
- short-range order in materials;
- high-pressure crystal chemistry and acoustic elasticity of clathrates;
- stroboscopic studies of polymer dynamic response to stress;
- synthesis, characterization, and modeling of nanoporous hybrid materials;
- studies aimed at understanding lung-surfactant properties;
- development of high-performance cold-neutron spectroscopy;
- development of advanced-neutron-detection technology for nuclear science; and
- partial research and upgrade support for Lujan Center instruments Asterix, SPEAR, and LQD.

In addition to these LDRD projects within LANSCE, there is also substantial LANSCE involvement in projects within other LANL divisions, including neutron- and accelerator-based science, advanced-neutron-detection technology for nuclear science, and nuclear-isomer physics.

Technical and Infrastructure Accomplishments

The LANSCE linac accelerated the first protons in 1972, making 2002 the 30th anniversary of the year the accelerator reached its design energy of 800 MeV. Since that time, the mission has evolved, but investment in the physical infrastructure has not kept pace with that required for long-term sustainable operation at high reliability. During 2002, LANSCE used a peer-reviewed cost estimate completed in 2001 to address this critical issue and developed a business plan for the next six years. The plan, when implemented, will upgrade accelerator infrastructure to enable the reliable delivery of protons and neutrons to all LANSCE user facilities well into the future. The business plan was approved by all members of the LANSCE executive council (NNSA, DOE/SC/BES, DOE/NE) at the December 2002 meeting. Furthermore, several major infrastructure investments were completed in 2002, including the installation of two new cooling towers.

For the 2002-2003 run cycle, LANSCE employed a targeted operations and maintenance methodology to achieve operations at reliability levels that exceeded the expectations of the user community.

Selected accomplishments for 2002. A number of significant accomplishments in both science and technology were achieved in 2002, including the following.

- The upgraded Neutron Powder Diffractometer (NPDF) opened its shutter for the first time on September 27, 2002, and produced over 300 experimental data sets during the 2002 run cycle (Fig. 2). Funded by the National Science Foundation, LANL, the University of Pennsylvania, and other academic institutions, the NPDF project started in September 2000, and in only nine months, the old neutron powder diffractometer was removed from FP1, and the new instrument, NPDF, was built. Promising results obtained during the 2002 run cycle not only put

Fig. 2. The NPDF instrument in Lujan Center Experimental Room 2 was upgraded in record time.

NPDF at the cutting edge of local-structure determination but also served as a development platform for this new structure-analysis tool for disordered and nanostructured materials.

- *In situ* neutron diffraction measurements at high temperature made on the High-Pressure-Preferred Orientation (HIPPO) diffractometer revealed texture changes in quartzite during the α to β phase transition that establish this rock as a shape-memory system where the orientation selection is controlled by internal stresses. Shape memory is a desirable attribute in metal alloys for applications like eyeglass frames — if bent, only modest heating is required to return the frames to the original condition. The revelation that earth materials have a similar attribute could have profound implications about the plasticity of the Earth's crust.
- Researchers used the newly upgraded Pharos (Fig. 3) to perform inelastic-neutron scattering from a plutonium-aluminum alloy and extracted the first-ever phonon density of states. Combining this information with specific heat measurements on the same sample allowed researchers to extract the electronic contribution to the specific heat between 15 K and 300 K. Accurate measurements of the electronic, phonon, and quasi-harmonic contributions to the thermodynamics of plutonium is fundamental in obtaining the equations of state needed for models of weapons performance.
- The new 11-T superconducting magnet (Fig. 4) provided Lujan Center users with the first results of an intensity image of neutron data collected from an antiferromagnetic material on the new Asterix instrument. Significantly, the mass of material contributing to the reflection is only about 100 μg. Moreover, exceedingly good thermal stability was achieved during the measurements.

Fig. 4. The new 11-T Oxford superconducting magnet hosted its first user experiment in 2002.

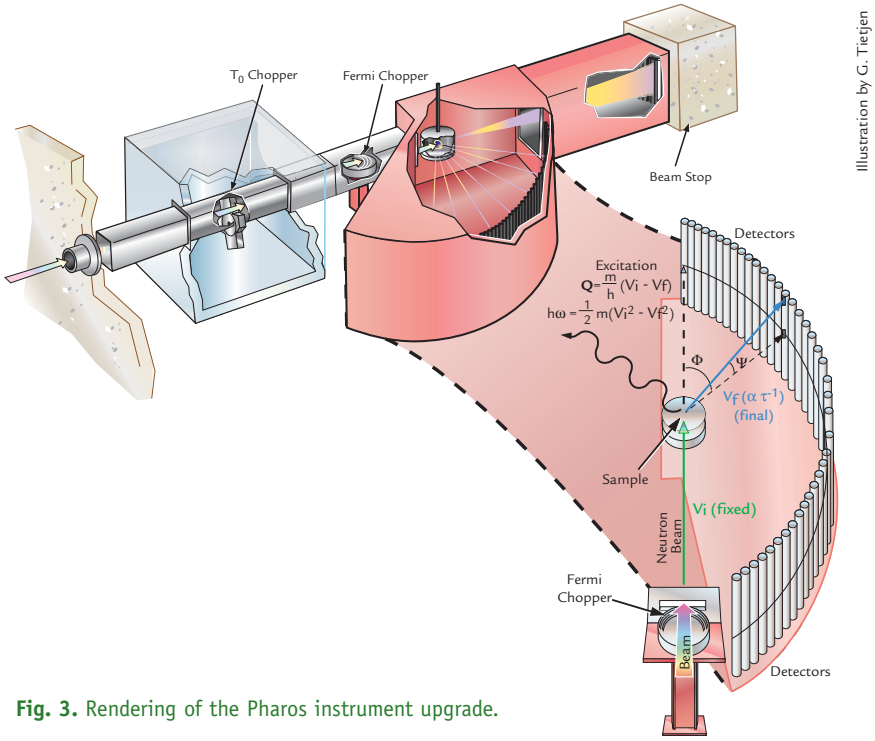

Fig. 3. Rendering of the Pharos instrument upgrade.

- During the 2002 run cycle, 42 dynamic pRad experiments — a pRad shot record — were performed at LANSCE in support of weapons-physics research efforts (Fig. 5). In addition, a new microscope radiography system that established an order of magnitude improvement in resolution and a novel detection scheme for radiography of thin systems were commissioned.
- Scientists and engineers from LANL and Hewlett Packard (HP) used WNR to measure neutron-induced failure rates in one of the most powerful supercomputers in the world, the ASCI Q-machine. The ASCI Q-machine has experienced a number of failures possibly from single-event upsets caused by neutrons produced by cosmic-ray bombardment of nuclei in the upper atmosphere. The WNR beam has a spectral shape that is similar to the cosmic-ray-induced neutron spectrum but 5 orders of magnitude more intense. This large intensity allowed the LANL/HP team to

Fig. 5. Researchers prepare for a dynamic pRad experiment.

test many operational configurations of the Q-machine during the 2002 run cycle while also monitoring the intensity of the cosmic-ray-induced neutron flux within the ASCI Q-machine room.

- The intense beam from the LANSCE Proton Storage Ring (PSR) was used to measure the effects of pulsed beams on the liquid-mercury targets for the Spallation Neutron Source (SNS) project (Fig. 6). As a result, scientists discovered that pitting in the container surfaces caused by the intense PSR beam pulse may be a lifetime-limiting problem for the SNS targets. Studying this problem at WNR before the SNS targets are installed has led to the development of mitigation techniques.
- The commissioning of the Detector for Advanced Neutron Capture Experiments (DANCE) has allowed scientists to measure neutron-capture rates (cross sections) of importance to the interpretation of radiochemical measurements of previous nuclear weapons tests. DANCE enables, for the first time, studies of reactions on radioactive isotopes.
- A new robust target-moderator system, the Mark 2, was designed and installed at Lujan Center. The new target has improved cooling compared to the Mark 1 (Fig. 7) moderator and upper target. A beryllium reflector replaced the lead reflector, cooling was simplified, and cadmium decoupling in the reflector was removed for more robust operation. The target received first beam on July 8, 2002.

Fig. 7. The cask used to remove the old (Mark 1) irradiated target (the old target is inside the cask). The cask is being moved into Area A East where the target will be stored.

- The Basis for Interim Operation for actinide experiments was completed. This new authorization basis enabled over a dozen plutonium and uranium studies to be completed and restores an important capability to the DOE science complex.
- The PSR "e-p instability" was tamed. A series of successful PSR development tests confirmed that the instability could be controlled at accumulated charge levels approaching 10 μC, well above the goal of 6.7 μC (Fig. 8).

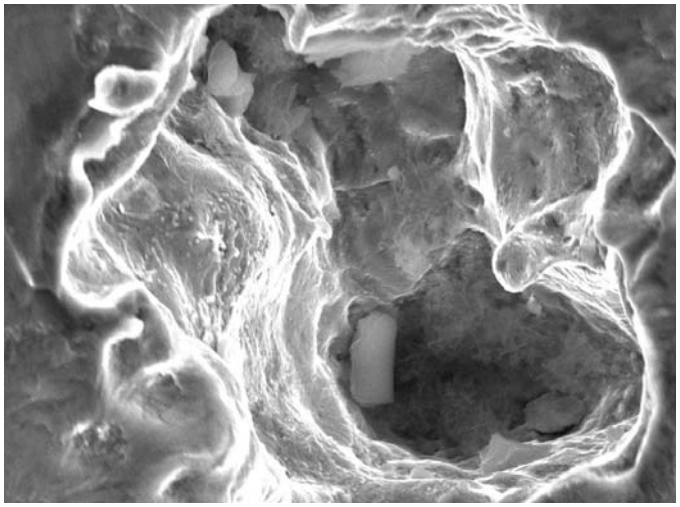

Fig. 6. A scanning-electron-microscope image of a large pit caused by the collapse of a bubble in a mercury target used in the SNS mercury-target tests conducted at WNR during the 2002 run cycle.

Particle-Beam Production

High-intensity proton linear accelerator. LANSCE is the world's most versatile spallation neutron source. Its high-intensity, 1-MW capable proton linac is the heart of many LANSCE activities. The LANSCE high-intensity linac can simultaneously produce and accelerate protons (H^+) and H^- ions

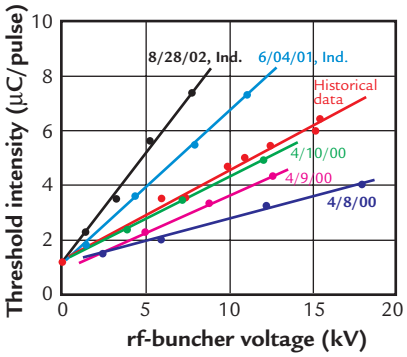

Fig. 8. The e-p instability-threshold curve measured at the PSR at various times during the 2000 to 2002 beam operations. These data show considerable improvement in the instability-threshold intensity over time.

(which have two electrons orbiting each proton) to energies of 800 MeV. The three-stage, half-mile-long linac can provide H^+ beam with an average current of up to 1 mA at a repetition rate of up to 120 Hz and a peak current of up to 17 mA. The H^- beam to Lujan Center has an average current of up to 125 μA at a repetition rate of 20 Hz and a peak current of 20 A and up to 5 μA at 100 Hz at WNR.

The first stage of the accelerator contains injector systems for each kind of particle (H^+ and H^-). Each injector system has a 750-keV Cockroft-Walton generator and an ion source. The two ion sources produce H^+ and H^- particles inside high-voltage domes. After they leave the injector, the two ion beams are merged, bunched, and matched into a 201.25-MHz drift-tube linac for further acceleration to 100 MeV. The third and longest stage of the accelerator (800 m) is the side-coupled-cavity linac, where particles are accelerated to their final energy of 800 MeV.

The particle beams from the linac are separated and directed down three main beam lines leading to several experimental areas, including pRad, Lujan Center, and WNR. Operators can control the H^+ and H^- beams separately, allowing most experiments to run simultaneously.

Proton Storage Ring. The PSR converts H^- linac macropulses of approximately 750-μs duration into short (0.13-μs, full-width at half maximum), intense H^+ bursts, which are sent to the Lujan Center neutron-production target 20 times a second. These short and intense bursts provide the capability for precise neutron time-of-flight measurements for a variety of experiments.

Neutron production. The nuclear-reaction process that occurs when protons strike targets, such as tungsten, is known as spallation, which expels many neutrons from target nuclei. For 800-MeV incident protons, about 20 neutrons per proton are ejected. The short and intense bursts of spallation neutrons are directly used for nuclear-physics experiments at WNR. Spallation neutrons are also slowed down in moderators before they are used at the Lujan Center.

Moderators. For most neutron-scattering research at the Lujan Center, the initial spallation-neutron energies are too high, and, correspondingly, their wavelengths are too short, for investigating condensed matter. For this reason, the neutrons must be "cooled down" before being used for scattering experiments. This process is accomplished by allowing the neutrons to interact with a moderator — a light material with a large scattering cross section such as water or liquid hydrogen. Neutrons enter the moderator (close to the neutron source), and in a series of collisions, lose energy to moderator atoms. After a few tens of collisions, the neutron energies are similar to the thermal energy of atoms in the moderator. Thus neutrons are emitted from the moderator with an average energy determined by the moderator temperature. The average energy of the neutrons from a water moderator at room temperature is approximately 25 meV, whereas the average energy from the liquid-hydrogen moderator at 20 K is approximately 5 meV. The energies and wavelengths (around 1.8 Å for 25 meV) of these neutrons match excitation energies and interatomic spacings of matter, respectively, and are thus very useful for neutron-scattering experiments that probe material structure and excitations.

A National User Facility

As a National User Facility for defense and civilian research in radiography, nuclear science, and condensed-matter science, LANSCE hosts scientists and engineers from academia, industry, national laboratories, and other research facilities around the world. Scientists apply for beam time by completing a proposal, which undergoes peer review before beam time can be allocated. Information about accessing the user facilities at LANSCE is available at http://lansce.lanl.gov/users/index_users.htm.

Lujan Center. The Lujan Center uses the 800-MeV proton beam from LANSCE to produce low-energy neutrons for basic and applied research. A unique split target and flux-trap and backscattering moderator system together with the PSR yields a higher peak neutron flux than any other spallation source currently available. The pulsed neutron source of the Lujan Center will remain the most intense in the United States until the SNS is in operation in 2006.

The Lujan Center also compares very favorably with the best pulsed-spallation-neutron source outside the U.S., ISIS in the United Kingdom, which has a higher average but a lower peak neutron intensity. A significant strength of the Lujan Center is its high-peak cold-neutron flux capability and its low pulse-repetition rate. At 20 Hz, the Lujan Center is unique relative to existing or proposed facilities (the SNS at 60 Hz and ISIS at 50 Hz).

Lujan Neutron Scattering Center Instrument Suite

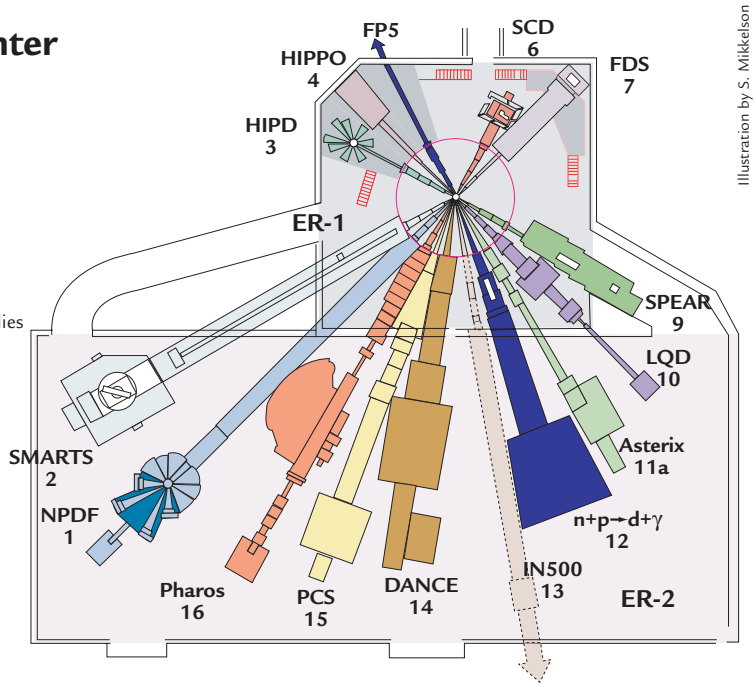

Illustration by S. Mikkelson

FP1: Neutron Powder Diffractometer (NPDF)
NPDF is a high-resolution, total-scattering powder diffractometer designed for pair-distribution-function studies of disordered and nanocrystalline materials and for high-resolution crystallographic studies.
Thomas Proffen, 505-665-6573, proffen@lanl.gov

FP2: Spectrometer for Materials Research at Temperature and Stress (SMARTS)
SMARTS allows measurements of spatially resolved strain fields, phase deformation, and load transfer in composites; the evolution of stress during temperature (or pressure) fabrication; and the development of strain during reaction (such as reduction oxidation or other phase transformations).
Mark Bourke, 505-665-1386, bourke@lanl.gov

FP3: High-Intensity Powder Diffractomer (HIPD)
HIPD is designed to study the atomic structure of materials that are available only in polycrystalline or noncrystalline forms.
Pete Encinias, 505-665-5718, encinias@lanl.gov

FP4: High-Pressure-Preferred Orientation (HIPPO)
HIPPO is a high-intensity powder diffractometer for high-pressure and texture measurements.
Sven Vogel, 505-667-7016, sven@lanl.gov

FP5: Transmission Spectroscopy (FP5)
FP5 is used to study the Doppler shift and broadening of low-energy nuclear resonances in materials under extreme conditions and for structural studies using transmission Bragg diffraction.
Walter Trela, 505-667-3939, trela@lanl.gov

FP6: Single-Crystal Diffractometer (SCD)
SCD has been used to study the structure of organometallic molecules, unique binding within H_2 crystal structural changes at solid-solid phase transitions, magnetic spin structures, twinned or multiple crystals, and texture.
Yusheng Zhao, 505-667-3886, yzhao@lanl.gov

FP7: Filter Difference Spectrometer (FDS)
FDS is designed to determine energy transferred to vibrational modes in a sample by measuring the changes in energy of the scattered neutrons.
Luc Daemen, 505-667-9695, lld@lanl.gov

FP8: Vacant

FP9: Surface Profile Analysis Reflectometer (SPEAR)
SPEAR is used with an unpolarized neutron beam to study solid/solid, solid/liquid, solid/gas, and liquid/gas interfaces.
Jaroslaw Majewski, 505-667-8840, jarek@lanl.gov

FP10: Low-Q Diffractometer (LQD)
LQD is designed to study structures with dimensions in the range from 10 to 1000 Å. It measures a broad Q-range in a single experiment without physical changes to the instrument.
Rex Hjelm, 505-665-2372, hjelm@lanl.gov

FP11a: Asterix
Asterix provides a polarized neutron beam for studies of magnetic materials using reflectometry and diffraction and includes the application of high magnetic fields.
Mike Fitzsimmons, 505-665-4045, fitz@lanl.gov

FP11b: Vacant

FP12: Basic Nuclear Physics
FP12 is used for a fundamental nuclear-physics experiment to precisely measure the asymmetry of the emission of γ-rays from the capture of polarized neutrons by protons.
Seppo Penttila, 505-665-0641, penttila@lanl.gov

FP13: IN500
IN500 is a prototype instrument employing novel techniques to enhance inelastic cold-neutron spectroscopy at spallation neutron sources.
Margarita Russina, 505-667-8841, russina@lanl.gov
Ferenc Mezei, 505-667-7633, mezei@lanl.gov

FP14: Detector for Advanced Neutron Capture Experiments (DANCE)
This flight path is used for the study of neutron capture on radioactive nuclei in support of the Stockpile Stewardship Program and for nuclear astrophysics.
John Ullmann, 505-667-2517, ullmann@lanl.gov

FP15: Protein Crystallography Station (PCS)
The PCS is a single-crystal diffractometer designed for structure determinations of large biological molecules.
Paul Langan, 505-665-8125, langan_paul@lanl.gov
Benno Schoenborn, 505-665-2033, shoenborn@lanl.gov

FP16: High-Resolution Chopper Spectrometer (Pharos)
Pharos is a high-resolution chopper spectrometer designed for studies of Brillouin scattering, magnetic excitations, phonon density of states, crystal-field levels, chemical spectroscopy, and measurements of $S(Q,\omega)$.
Robert McQueeney, 505-665-0841, mcqueeney@lanl.gov

Weapons Neutron Research Facility

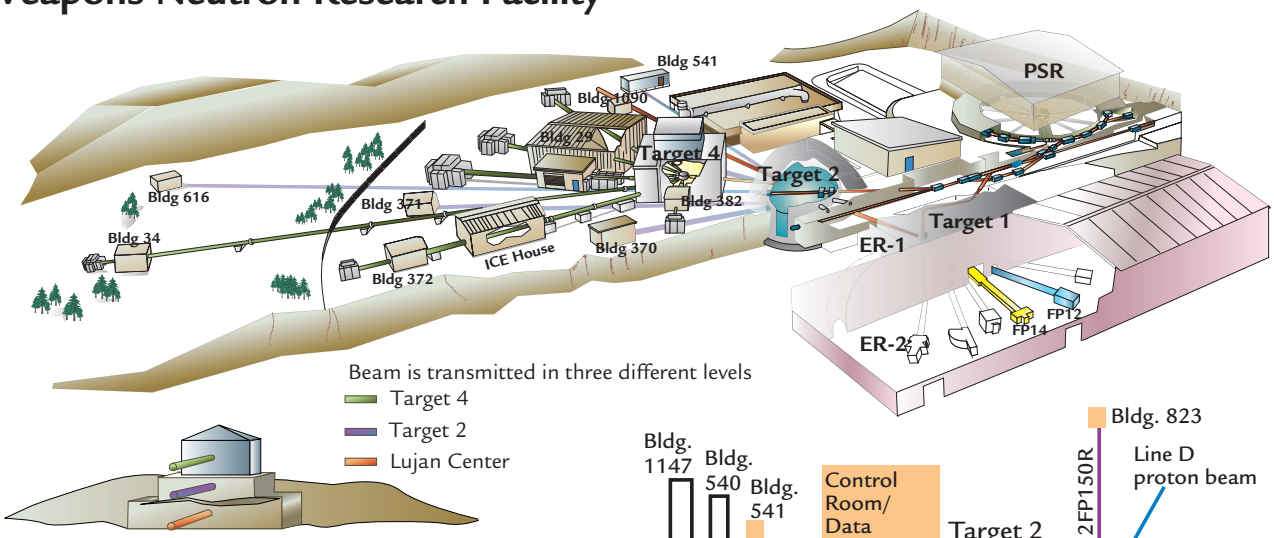

Illustration by S. Mikkelson

Beam is transmitted in three different levels

- Target 4
- Target 2
- Lujan Center

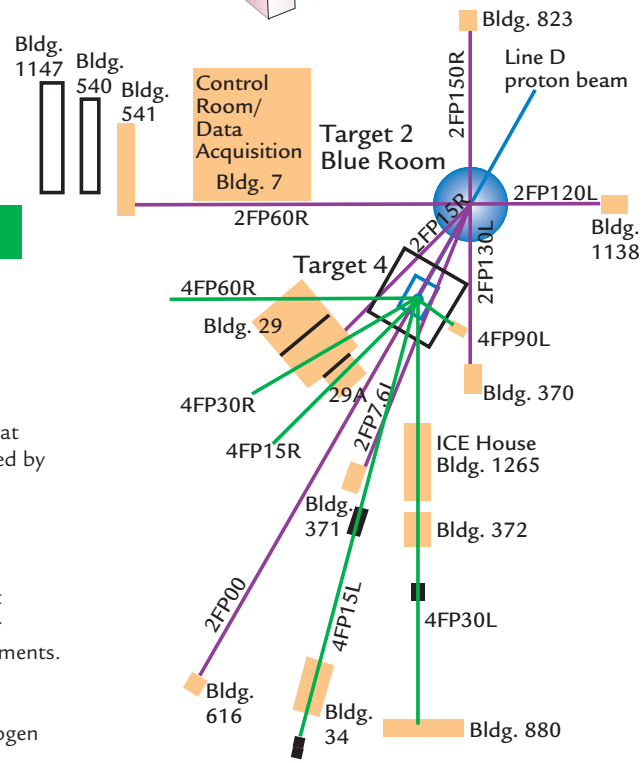

Target 4 Flight Paths (FPs)

4FP90L This FP is used to measure neutron-proton-capture cross sections important for understanding "Big Bang" nucleosynthesis.
Steve Wender, 505-667-1344, wender@lanl.gov

4FP30L This FP has two experimental stations. The first station is at approximately 20 m from the production target and is used by industry, universities, and other national labs to measure neutron-induced failures in semiconductor devices.
Bruce Takala, 505-665-2029, takala@lanl.gov

4FP15L This FP provides the highest neutron-energy resolution. At present, the approximately 90-m-long FP is being used for dosimetry, neutron transport, and neutron-spectra experiments.
John Ullmann, 505-667-2517, ullmann@lanl.gov

4FP15R The (n,d) scattering experiments, which use a liquid-hydrogen target, are located on this approximately 18-m-long FP.
Steve Wender, 505-667-1344, wender@lanl.gov

4FP30R Most recently, experiments on this approximately 20-m-long FP studied neutron-induced reactions for nuclear-level-density studies and neutron-induced fission and gas production in structured materials.
Robert Haight, 505-667-2829, haight@lanl.gov

4FP60R The GEANIE spectrometer consists of approximately 26 Compton-suppressed, high-resolution germanium γ-ray detectors and is located on this approximately 20-m-long FP. The GEANIE instrument is used to address issues of nuclear structure, spectroscopy, and cross-section measurements for both stockpile stewardship and basic science.
Ron Nelson, 505-667-7107, nelson@lanl.gov

Target 2 (Blue Room) Experiments

In neutron resonance spectroscopy, the PSR beam is used to produce an intense single pulse of neutrons for measuring the temperature and particle velocities of dynamic systems at different times during their evolution. The temperature is obtained by measuring the Doppler broadening of low-energy neutron resonances.

Single pulses from the PSR beam are used to study the shock induced by the incident beam on a liquid-mercury target for the SNS.

Overview

As a National User Facility, the Lujan Center provides instrumentation and support for scientists, engineers, and students to study materials science and engineering, condensed-matter physics, polymer science, chemistry, earth sciences, structural biology, and neutron-nuclear-science research. During the 2002 run cycle, Lujan Center hosted 375 user visits from academia, industry, national laboratories, and other research facilities around the world.

Lujan Center users now have access to an 11-T superconducting magnet; a CryoFurnace from the Institute Laue-Langevin (ILL); and new fluid-driven, high-pressure cells that exceed 8 Mbar. TAP-98, a new 5-MN toroidal anvil press that enables experiments at simultaneous high pressures and temperatures up to 30 GPa and 2,000 K, is also available.

Moreover, four new neutron-scattering instruments entered the user program [HIPPO, SMARTS (Fig. 9), PCS, and Asterix] along with Pharos, a newly rebuilt inelastic chopper spectrometer. In addition, the venerable NPD was completely upgraded to become the NPDF by adding substantial new detector coverage and an improved data-acquisition system. NPDF will enter the user program in 2003.

Of the 16 beam ports and 17 FPs, 2 are currently vacant; 12 are instrumented for condensed-matter science and engineering, including 1 under development; 1 is used for transmission spectroscopy; and 2 are used for neutron nuclear science (1 of which is under development). A brief description of each FP at Lujan Center is shown on page 12.

WNR Facility. At the WNR Facility, high-energy neutrons and protons are used for basic and applied research in neutron nuclear science and weapons-related measurements. WNR consists of two target areas: Target 2 and Target 4 and their associated FPs. Each FP's name identifies the target and the direction of the FP with respect to the proton beam. For example, 4FP15R is a FP that starts at Target 4 and is 15° to the right (15R) of the incoming proton beam.

Fig. 9. Adrian DeWald, a University of California at Davis graduate student, holds a large S-FAP single crystal used as a laser amplification medium in second-generation fusion devices. The laser properties of this new crystal are superior to all other types of crystals for high-power lasers, but it tends to fracture during the cutting operation required to fabricate amplifier slabs. DeWald obtained measurements on SMARTS during the 2002 run cycle to determine where the residual stress in the crystal resides.

At Target 2, also known as the Blue Room, proton-induced reactions can be studied using the linac or the PSR proton beam. In addition, Target 2 is used for a variety of proton-irradiation experiments. This target consists of a low-background room with seven FPs. Experiments in the Blue Room can exploit the variable-energy feature of the linac using proton beams from 250 to 800 MeV. Target 4 is the most intense high-energy neutron source in the world. Target 4 consists of a "bare" (unmoderated) neutron production target and six FPs with distances ranging from 10 to 90 m and at angles of 15° to 90° with respect to the proton beam. The shape of the neutron spectrum ranges from a hard (high average energy) spectrum at 15° to a softer (lower average energy) spectrum at 90°. The time structure of the proton beam can be modified to produce neutron pulses with different spacings for particular experiments.

The WNR neutron beams from Target 4 complement those produced at the Lujan Center because the WNR beams have much higher energy and shorter pulse duration. With both capabilities, LANSCE is able to deliver neutrons with energies ranging from small fractions of an eV to 800 MeV. Fig. 10 shows experimenters examining the position of their sample at the WNR Irradiation of Chips and Electronics (ICE) House. A description of the FPs and capabilities at WNR are shown on page 13.

Proton Radiography Facility. In Area C, scientists use H^- beam from the linac as a radiographic probe for creating multiple high-spatial-resolution images (Fig. 11) with submicrosecond time resolution. Protons interact through both the strong and the electromagnetic forces, allowing the simultaneous measurement of different material properties, such as material density and composition distributions. Protons have several properties that are advantageous for these types of experiments, including high penetrating power, high detection efficiency, very low scattered background, and inherent multi-pulse capability. In addition, large distances are possible from the test object and the containment vessel for the incoming and transmitted beams, thereby reducing the background contribution from scattered particles. LANL scientists have developed magnetic optics; fast, integrating, large-area detectors; and containment vessels to solve important weapons-physics problems.

Fig. 10. Experimenters view the multiple memory modules positioned for testing at the WNR ICE House.

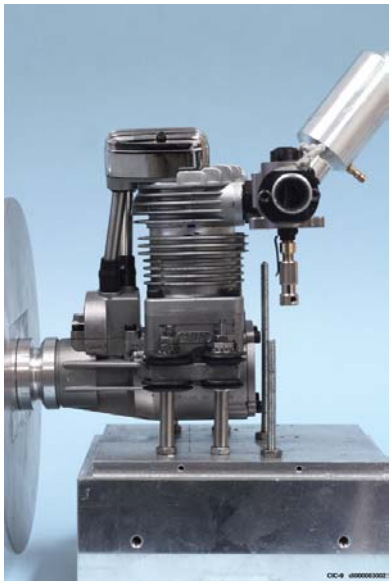

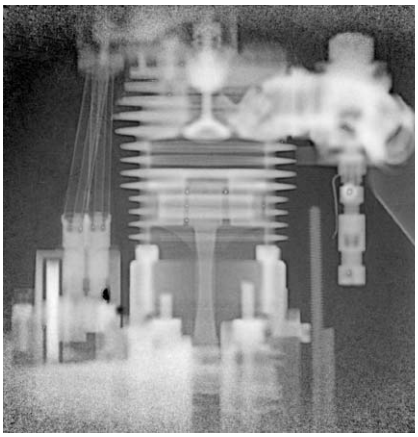

Photo by J. Flower

Fig. 11. A 150-cm^3 model airplane engine (left) and a radiograph of the engine produced by 800-MeV protons from the LANSCE linac (right). (Photo courtesy of Brian Fishbine, LANL.)

Ultra-Cold Neutron Facility. In Area B, the H^- beam will be directed onto a small tungsten target to produce neutrons. These neutrons will be moderated to very low energies by layers of polyethylene at liquid-nitrogen temperature (77 K) and liquid-helium temperature (5 K) surrounding solid deuterium to produce ultra-cold neutrons (UCNs). UCNs have sufficiently low energy that they cannot penetrate materials; thus, they undergo total reflection at all angles. As a result, the UCNs produced by this target/moderator configuration will be trapped in bottles and directed along guide tubes. The UCN team achieved the current world's record for the density of UCNs stored in a bottle: 100 UCNs/cm^3. The predicted steady-state UCN density for this facility under operational conditions is 300 UCNs/cm^3, which is approximately 8 times the highest existing UCN production source capability of 41 UCNs/cm^3 measured at the ILL research reactor in France. Construction of the full-scale UCN source at LANSCE was initiated in 2002. When completed in 2003, this new source will be the most intense source of UCNs in the world. The first experiment will allow scientists to measure neutron-decay asymmetry with previously unattainable precision.

Programs and Projects

Spallation Neutron Source. The SNS project, under construction at Oak Ridge National Laboratory (ORNL), is a major DOE initiative designed to develop the world's most intense pulsed neutron source for neutron-scattering experiments. The design and construction of the SNS is being carried out by a collaboration of six DOE laboratories: ORNL, LANL, Argonne National Laboratory, Brookhaven National Laboratory (BNL), Lawrence Berkeley National Laboratory, and Jefferson National Laboratory. LANL's main responsibilities are to (1) design,

construct, deliver, and help install and commission a normal-conducting linac that consists of 87-MeV-drift-tube and 186-MeV-coupled-cavity accelerating systems; (2) provide beam-physics analyses for the entire linac; (3) provide more than 100 MW of radio-frequency (rf) power for the entire linac; and (4) develop the experimental physics and industrial control system for the linac.

Isotope Production Facility. To ensure a steady supply of medical isotopes, DOE/NE is funding the construction of a new IPF to replace the deactivated facility at LANSCE. Construction of the new $20M IPF began in February 2000 with expected completion in 2003. Combining the new IPF output with similar isotope production capabilities at BNL will supply adequate, year-round, accelerator-produced medical isotopes. These isotopes are needed to perform 36,000 diagnostic procedures daily and 50,000 therapies annually, along with 100 million laboratory tests annually. The DOE Office of Isotopes for Medicine and Sciences estimates the annual value of these procedures to the medical industry at between $7-$10B. The Chemistry Division at LANL has produced some of these medical isotopes, such as strontium-82 and germanium-68, at LANSCE for more than 20 years. Using a portion (~100 MeV) of the 800-MeV LANSCE proton beam, the new IPF will irradiate a wide range of materials underground, including rubidium chloride, gallium, and other targets. Irradiated targets will then be shipped to LANL's Chemistry Division for processing. Fig. 12 shows the last two quadrupole magnets in the IPF beam line.

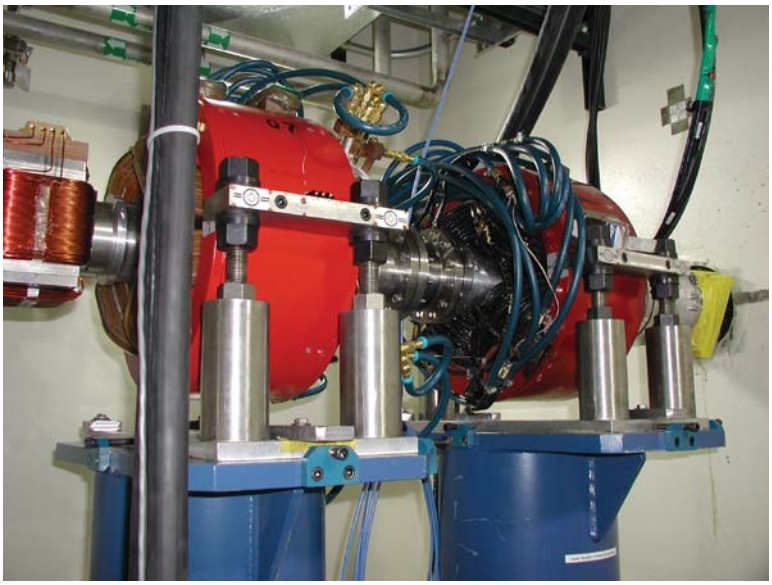

Fig. 12. Quadrupole magnets in the IPF beam tunnel.

Advanced Hydrotest Facility. An Advanced Hydrotest Facility (AHF) is an important potential future capability of the NNSA Defense Programs Stockpile Stewardship Program for three-dimensional studies of fast dynamic events. As presently envisioned and if sited at LANSCE, the AHF would consist of a 50-GeV proton synchrotron constructed in a tunnel some 100 m below the LANSCE linac and an array of transport lines that would deliver proton pulses at user-specified intervals to illuminate a dynamic test object. A set of large-aperture magnetic lenses would image the protons passing through the test object, creating a radiographic movie. Those images would give LANL and Lawrence Livermore National Laboratory (LLNL) scientists critical information necessary to assess the safety, performance, and reliability of our aging nuclear-weapons stockpile. LANL has led the planning for this future National User Facility that would provide unique data crucial to nuclear-weapons certification in the coming decades. During the past two years, the LANSCE AHF project team, in collaboration with LLNL, other DOE laboratories, industry, and university partners, developed options and performed design trade-off studies for a facility that would meet all future requirements of the weapons community. During 2002, the project made significant progress in the engineering development of key system components — a fast-rise, anharmonic, kicker-magnet modulator; large field-of-view superconducting quadrupole lenses; and the composite inner vessel. The project is pursuing preconceptual studies in anticipation of entering the conceptual design phase.

Research Highlights

Condensed-Matter Science and Engineering

Electric-Field-Driven Transformations of a Supported Model Biological Membrane 18

The Response of Cemented-Carbide Composites to Compressive Load 20

Plutonium-Phonon Measurements on Pharos 24

New Findings in Texture Development and Phase Transformation in Shocked Zirconium Shed Light on Models for Shock-Induced Phase Transformations 26

Proton Dynamics in Very Short, Strong Hydrogen Bonds 28

Electrical Anomalies in α-Glycine 32

Thermal Neutron Protein Crystallography — Enzyme-Mechanism Investigations with D-xylose Isomerase 34

Texture Changes During the Quartz α-β Phase Transition Studied by Neutron Diffraction 36

In Situ Neutron-Diffraction Study of Lithium-Ion Batteries 40

Magnetic Exchange Coupling in Metal/Native-Oxide Multilayers Studied by Polarized Neutron Reflectometry 42

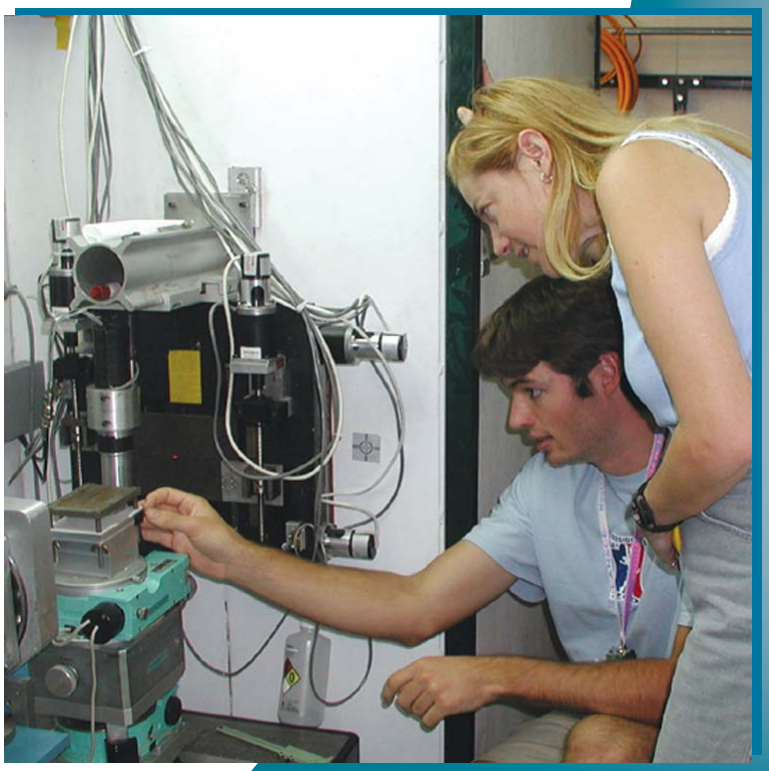

Electric-Field-Driven Transformations of a Supported Model Biological Membrane

I. Burgess, G. Szymanski, M. Li, S. Horswell, J. Lipkowski (University of Guelph, Ontario),
J. Majewski, E. Watkins (LANSCE Division)

Phospholipid bilayers (films), formed by fusing small unilamellar vesicles (SUVs) onto surfaces, constitute an attractive model of a biological membrane used to study cell-membrane processes.[1] These membranes can also be used to study the influence of an electric field on voltage-gated membrane proteins, lipid-lipid interactions, and lipid-protein interactions.[2] In addition, films of phospholipids with incorporated proteins deposited on a metal or metal-oxide electrode have important applications in the development of novel electrochemical sensors.[3] At an electrode surface, phospholipid films are exposed to high electric fields on the order of 10^9 V/m. A field of this magnitude affects the membrane properties, and the knowledge of this effect is needed for both scientific and practical applications of supported phospholipid bilayers.

Surface Profile Analysis Reflectometer Experiment

As a model biological membrane, we used a mixed dimyristoylphosphatidylcholine (DMPC)/cholesterol bilayer (70:30 mol % ratio) deposited on a gold electrode surface by vesicle fusion. Because DMPC is a neutral (zwitterionic) lipid, the field acting on this membrane is solely due to the charge on the metal. Our electrochemical studies show that the membrane is stable at the electrode surface in the charge-density range of ±8 $\mu C\ cm^{-2}$ (from -450 mV to +350 mV versus Ag/AgCl, which is the standard reference used by electrochemists for measuring potentials). Above or below these values, the charge-density curve for the membrane-covered electrode merges with the curve for the film-free interface. The merging of these two curves indicates that the membrane has become detached from the gold surface.

We have performed neutron-scattering experiments using the time-of-flight Surface Profile Analysis Reflectometer (SPEAR) at LANSCE to investigate electric-field-driven changes of the membrane structure. Due to scattering-length-density (SLD) differences between gold, CH_2-chains, and D_2O, the thickness of the membrane and its water content (D_2O) can be determined from SLD curves.

Results

We have demonstrated that a model biological membrane is stable when the charge on the metal is less than -8 μC cm^{-2} or when the field acting at the membrane is less than 5 x 10^9 V/m. At zero charge on the metal, the DMPC chains are tilted, and the membrane contains defects.

By charging the metal and increasing the field, the chains become more porous and less tilted. At a potential of -750 mV versus Ag/AgCl (i.e., corresponding to a surface charge of -23 μC cm^{-2} and a field exceeding 5 x 10^9 V/m), the membrane becomes detached from the electrode. We have shown for the first time that this membrane remains in close proximity to the metal electrode and is suspended on a thin cushion of the electrolyte (Fig. 1). This membrane is essentially defect free. Additionally, the charge-driven changes in the membrane structure are fully reversible. By turning a knob on a control instrument, one can inject or withdraw the charge from the metal surface. The membrane responds to these changes either by being lifted up or by being directly deposited onto the metal. This ability to use the electric field to control the membrane structure opens new opportunities for biomimetic research.

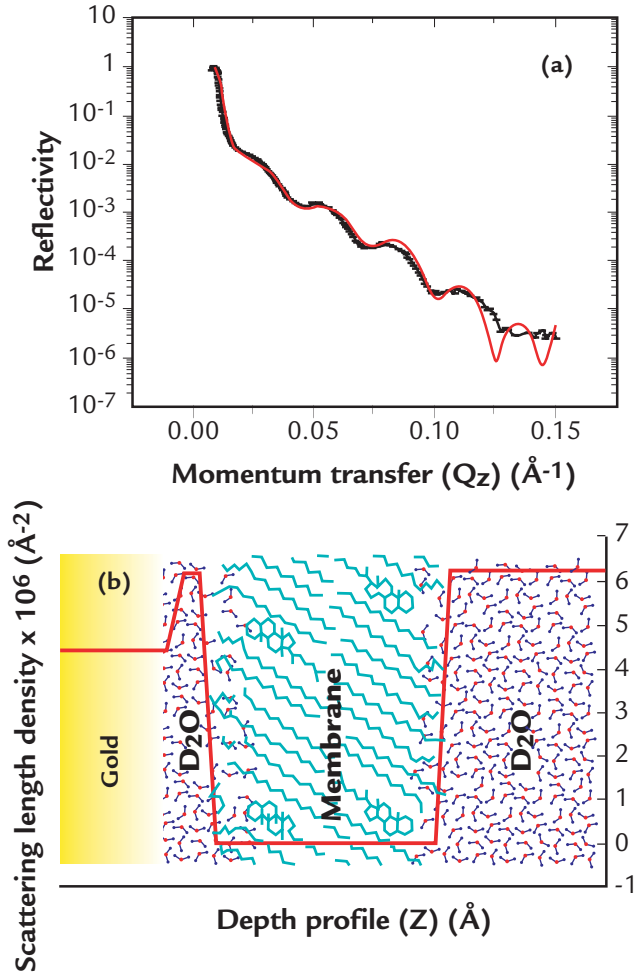

Fig. 1. (a) Neutron-reflectivity data as a function of the momentum transfer vector Q_z (in $Å^{-1}$) obtained for a mixed cholesterol/DMPC bilayer spread at the electrode surface when the surface charge density of the gold is highly negative (i.e., -23 μC cm^{-2} corresponding to -750 mV versus Ag/AgCl). The red line is the fit resulting from a one-layer model used to represent the biomimetic film. It is important to note that even though the film is now no longer directly attached to the gold electrode, neutron reflectivity still detects its presence in close vicinity to the support. This is a unique ability of the neutron-reflectivity technique. (b) Profile of the biomimetic film/gold interface in the direction perpendicular to the electrode. The red line is the SLD profile, determined from the neutron-reflectivity curve given above in (a). The model shows a defect-free biological film with no solvent penetration cushioned by a thin film of solvent.

Acknowledgements

The researchers would like to acknowledge the U.S. Department of Energy Office of Science and Office of Basic Energy Sciences for access to SPEAR at LANSCE. This research was supported by a grant from the Natural Sciences and Engineering Research Council (NSERC) of Canada. Ian Burgess, in particular, would like to thank the NSERC for a post-graduate scholarship.

References

1. E. Sackmann, *Science* **271**, 43 (1996).
2. S.W. Jones, *Journal of Bioenergetics and Biomembranes* **30**, 299 (1998).
3. W. Knoll et al., *Reviews in Molecular Biotechnology* **74**, 137 (2000).

The Response of Cemented-Carbide Composites to Compressive Load

A.D. Krawitz, J.W. Paggett (University of Missouri), E.F. Drake (ReedHycalog/Grant Prideco, Inc.), M.A.M. Bourke (MST Division)

Cemented-carbide composites are used in the extraction of oil and gas and in mining and machining applications because of their strength, toughness, wear resistance, and high-temperature performance. They consist of micrometer-sized particles of a hard ceramic reinforcement (often tungsten carbide, WC) that is embedded in a metal binder. Despite 80 years of use, the detailed response of these materials under load is not fully understood. When a load is applied, how do the two components in the composite (i.e., the particles and the metal binder) respond to the load? Does the response differ when the WC content is sufficient to form a continuous skeleton? Do the large thermal residual stresses (TRS) that are initially present in such systems change with the applied load?

The Spectrometer for MAterials Research at Temperature and Stress (SMARTS) at LANSCE was specifically designed to measure the strain response in individual phases of multiphase materials under load. SMARTS uses the diffraction of thermal neutrons from the nuclei in the phases and the penetrating power of neutrons to study engineering materials. During the LANSCE 2002 run cycle, SMARTS was used to measure the individual response of samples made of WC particles in a nickel (Ni) binder subjected to uniaxial compressive stress (pressure) up to 2,000 MPa (about 300,000 lb per square inch). The d-spacings of atomic planes, which were used as internal strain gauges, were determined from peaks obtained in the diffraction of thermal neutrons.[1] SMARTS, with its two sets of detector banks, is able to measure strains both axially and transversely to the loading direction. Our study also exploits the widths of these diffraction peaks. We initially used samples of WC-Ni because Ni stays in one phase and is a strong neutron scatterer. Preliminary measurements on WC-Co indicate that an interesting reversible phase change occurs during load-unload cycles. Future work will pursue the more commercial WC-Co material.

In Situ Response to Compressive Load

In our studies, we used WC-Ni samples with Ni contents of 8, 16, and 31 vol % and WC particle sizes of 2 to 4 µm. The sample microstructures ranged from a continuous WC skeleton (8 vol % of Ni) to WC *floating* in Ni (31 vol % of Ni). The samples were cylinders 12 mm in diameter and 28.8 mm in length. The overall composite strain (ε) curves were mechanically measured with an extensometer (an instrument designed to measure deformations of small objects subjected to stress) at the same time that the WC and Ni phases were measured with neutrons. Each sample underwent three load-unload cycles at stress levels of -500, -1,000, and -2,000 MPa successively (i.e., three 0 to -500 MPa to 0 cycles, then three 0 to -1,000 to 0 cycles, and so on).

The mechanical stress-strain curve for the first -2,000 MPa cycle for the composite with 8 vol % of Ni is bracketed by the Ni and WC curves (Fig. 1). The strain in the WC is less than the total strain of the composite so that rigid skeleton behavior is not exhibited. The total strain is initially elastic and shared by both phases. Clear plasticity in the Ni is present at 1,000 MPa.

The transverse strain response for the Ni begins to reverse at about 1,400 MPa. This suggests a net conversion of strain in the Ni from elastic to plastic. The strain values in each phase are determined from changes in the positions of the diffraction peaks. The fact that the peak positions essentially return to their initial positions upon unloading indicates that the TRS present in the composite has not yet changed.

The corresponding peak width behavior is shown in Fig. 2 for three crystallographic directions in the Ni: (111), (200), and (311). The peak widths for each direction are reversible with the applied load,

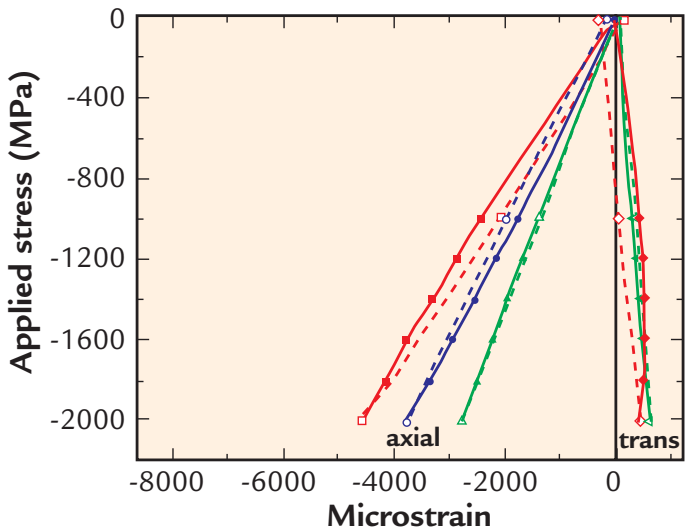

Fig. 1. Mechanical (blue) and diffraction (Ni is red, and WC is green) strain response for the first -2,000-MPa load cycle for the 8 vol % Ni sample. Solid and dashed lines are loading and unloading, respectively. Both axial and transverse directions are shown.

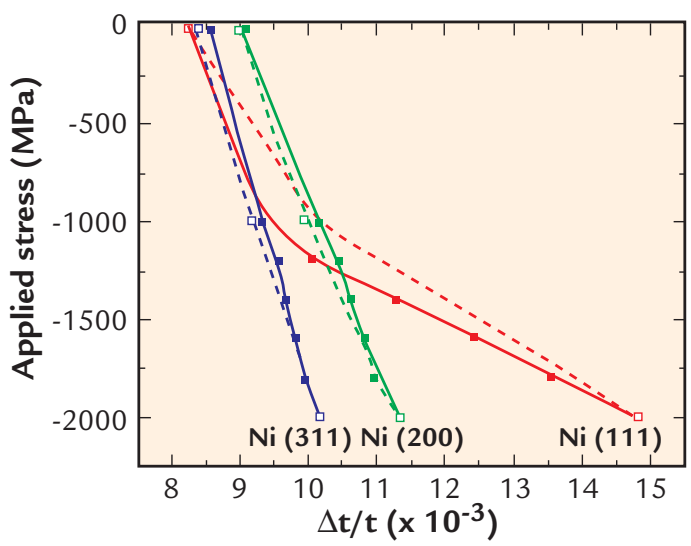

Fig. 2. The peak breadth response for the Ni (111), (200), and (311) peaks for the 8 vol % Ni sample. Solid and dashed lines are loading and unloading, respectively. Only the axial direction is shown. The parameter Δt/t is the width in time of the peaks relative to the time of flight of the neutrons for the peak. The reversibility indicates that the breadths are due mainly to the point-to-point variation of strain in the Ni binder phase, which is a function of the applied stress.

which means there are changes in the variance or distribution of elastic strain (the positional strain variation within the Ni regions) during the loading cycle.[2] The fact that they return to their starting values means they are not due to plasticity (i.e., dislocations). The plastic strains are too low to cause measurable peak broadening in these experiments.

The reversibility also suggests that the TRS is not decreasing substantially during the loading cycle. The width for the (111) planes is strikingly different, and this is not understood at present. WC peak widths show a smaller, reversible increase on loading in the axial direction and little change in the transverse direction.

The first -2,000-MPa cycle for the sample with 31 vol % of Ni (Fig. 3) shows that the composite stress-strain curve bends because of plastic deformation at 1,000 MPa. Below this stress, the strains in the Ni and in the composite are the same, as predicted by the shear lag model.

The deviation occurs because the diffraction data is a measure of only the elastic strain in the Ni, whereas the extensometer records total (elastic and plastic) strain. (The Ni phase is elastic to -1,000 MPa because of the previous cycles to this level.) The plastic flow of the Ni phase creates a large hysteresis that narrows on subsequent cycles. The second cycle is shown, and the third cycle almost coincides with the second.

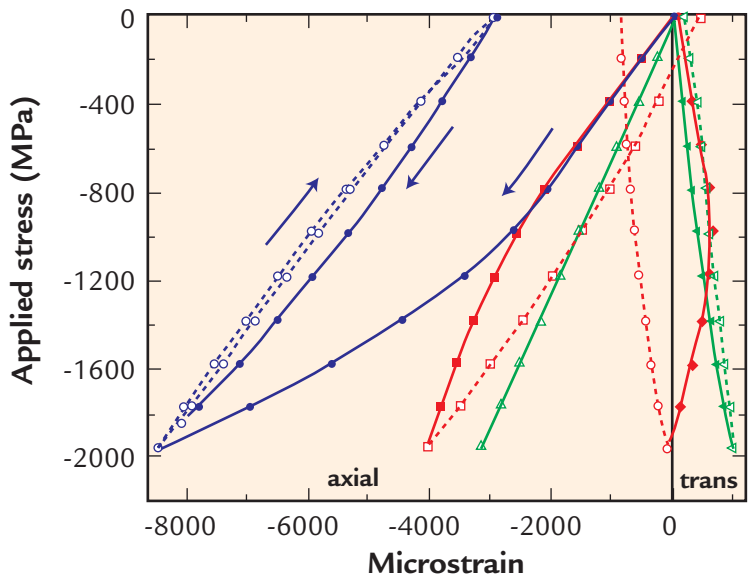

Fig. 3. One load cycle (0 to -2,000 MPa to 0) for the 31 vol % Ni sample. Solid and dashed lines are loading and unloading, respectively. Both axial and transverse directions are shown. The mechanical strain is blue, the Ni is red, and the WC is green. The second load cycle shows that the hysteresis loop closes up substantially.

The decrease in elastic-strain accumulation in the Ni phase is taken up by the WC. However, the high Young's modulus (700 GPa) and WC content (69 vol % in Ni) lead to an effect too small to be observed.

In the transverse direction, the Ni phase yields at which time the strain-accumulation rate not only slows down but also reverses sign back to zero. Apparently the elastic component of the strain is converted to plastic strain in the unconstrained transverse direction.[3]

Ongoing Work

We intend to more fully understand the observed composite responses in cemented-carbide composites, including the load sharing between the phases of the composite. A comprehensive set of compressive load data using WC-Co, a widely used, but more complex, cemented carbide, is planned. In WC-Co, we recently observed a reversible stress-induced transformation of the Co phase between face-centered-cubic and hexagonal-close-packed structures during load/unload cycling.

Acknowledgements

We acknowledge the support of the Reed Hycalog division of Grant Prideco and the U.S. Department of Energy Office of Basic Energy Sciences. The assistance of B. Claussen, S. Vogel, and T. Sisneros was invaluable.

References

1. A.D. Krawitz, in *Research Society Symposium Proceedings* (1990).
2. A.D. Krawitz et al., *Materials Science and Engineering A* **105/106**, 275-281 (1988).
3. D.H Carter and M.A.M. Bourke, *Acta Materialia* **48**, 2885-2900 (2002).

Plutonium-Phonon Measurements on Pharos

R.J. McQueeney (LANSCE Division), A.C. Lawson (MST Division), M. Ramos,
B. Martinez (NMT Division), T.M. Kelley, B.T. Fultz (California Institute of Technology)

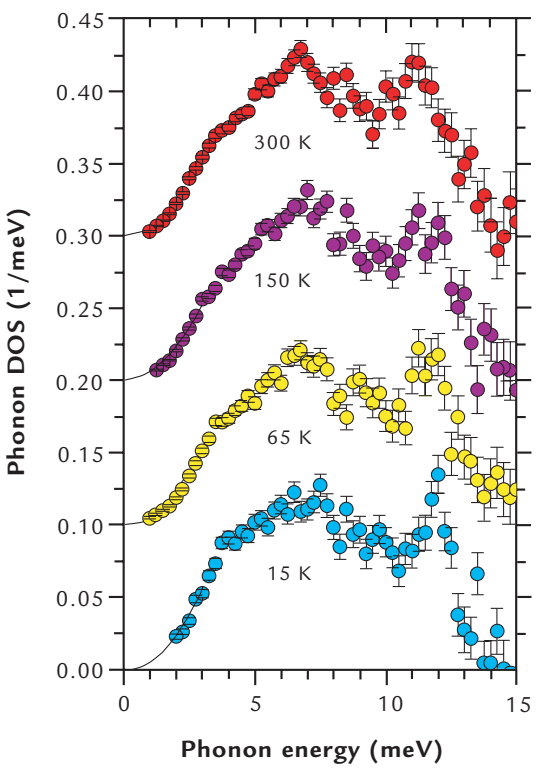

Fig. 1. The phonon DOS of δ-phase $Pu_{0.95}Al_{0.05}$ at four different temperatures.

Developing a fundamental understanding of plutonium material properties is one of the most critical issues in stockpile stewardship. The solid-state properties of plutonium (Pu) are significantly more complicated than most other metals. Pu has six crystallographic phases at ambient pressure with large density variations and an anomalously low melting point.[1] These complex physical properties arise from the role of the 5f electrons in the chemical bonding between atoms. The 5f electrons in Pu sometimes participate in bonding (similar to the 3d orbitals in the transition metals) and sometimes do not (like the 4f orbitals in the rare-earth metals). Through the light-actinide series, there is a changeover from itinerant (bonding) to localized (nonbonding) 5f behavior with the crossover occurring at Pu. Even within the Pu phase diagram alone, there is a varied degree of 5f bonding for each crystallographic phase. The fluctuations of the electron in and out of the narrow 5f band fall generally into the physics of correlated electrons, which makes the electronic-structure problem a difficult one to solve. One possible way to verify the accuracy of electronic-structure calculations is through the measurement of the phonon dispersion in the different phases of Pu. Phonons are the normal modes of atomic vibration on a crystal lattice. The frequency of a particular phonon depends on the wavelength and displacement pattern of the atom's motion and the forces acting between atoms. These forces arise entirely from the bonding properties and are a stringent test of first-principles electronic-band-structure calculations. A poorly understood Pu phase is the face-centered-cubic (fcc) δ-phase, although it is very important.

Experiment

Inelastic-neutron-scattering (INS) measurements from single crystals of Pu directly give the phonon dispersion. However, single-crystal samples of sufficient size (~ 1 cm^3) for this technique are not presently available. From polycrystalline samples, we can obtain the phonon density of state (DOS), which contains a complete description of the lattice thermodynamics and some information about the interatomic forces. We were able to obtain ~ 35 grams of $Pu_{0.95}Al_{0.05}$ enriched to 95% ^{242}Pu (the ^{242}Pu isotope is necessary to reduce absorption). The DOS for $Pu_{0.95}Al_{0.05}$ (Fig. 1) was measured at several temperatures using the Pharos spectrometer at LANSCE.

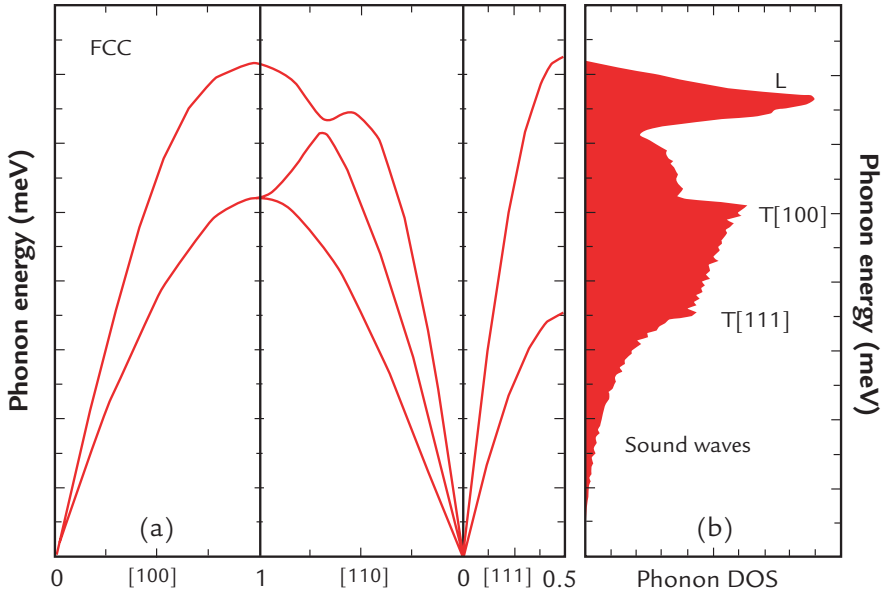

Fig. 2. (a) The three panels show the typical phonon dispersion curves expected for an fcc metal along certain symmetry directions. Panel b shows the phonon DOS calculated from the same model.

Results

The phonon DOS is the distribution of all phonon-mode frequencies in a crystal. For simple crystal structures (such as fcc), the phonon DOS can be characterized by several prominent features that are directly related to the phonon-dispersion relation. Fig. 2 shows the phonon dispersion along certain symmetry directions in the crystal and also the DOS of nickel as calculated from a lattice-dynamical model. Peaks or discontinuities in the DOS occur at the maxima, minima, or saddlepoints of the dispersion surface (called van Hove singularities, or vHs). Most vHs occur at the Brillouin zone boundaries where the slope of the dispersion surface must be zero due to lattice periodicity. At the longest wavelengths, all phonon dispersions have three modes that approach zero-frequency linearly (i.e., sound waves), giving a quadratic-energy dependence to the DOS related to the elastic constants.[2] In Fig. 1, the first vHs appearing at ~ 3.5 meV is the zone-boundary transverse-phonon energy along [111]. The second vHs at ~ 7 meV is the transverse zone-boundary mode along [100]. Finally, the large peak at ~ 12 meV corresponds to the zone-boundary longitudinal phonons, which are the highest-energy phonons in the system.

From the analysis of the Pu-phonon DOS data, we have already learned a great deal. The Pu phonon energies are very low but have a similar energy scale to those of cerium and lead. Because the mass of Pu is nearly twice that of cerium, the interatomic forces are stronger in Pu. Thus, the Pu 5f electrons may play some role in bonding (i.e., in cerium the 4f electron is localized and contributes very weakly to the bonding). The temperature dependence of the phonon frequencies between 15 K and 300 K is weak with the largest effect being a broader, lower-energy longitudinal band. This low-energy band comes from a fairly typical softening of the lattice due to the ~ 1% thermal expansion in this temperature range.

Conclusion

The measured DOS can also be used to calculate and compare to other experimental quantities such as Debye-Waller factors, elastic constants, and specific heat. After integrating all of these experimental data sets, we hope to have a very complete understanding of the lattice dynamics of this system.

Acknowledgements

The researchers would like to acknowledge the U.S. Department of Energy Office of Basic Energy Sciences and the National Nuclear Security Administration.

References

1. "Challenges in Plutonium Science," in *Los Alamos Science,* No. 26, Volume 1 (2000), Los Alamos National Laboratory report LA-UR-00-4100.
2. H.M. Ledbetter et al., *Acta Metallurgica* **24,** 891 (1976).

New Findings in Texture Development and Phase Transformation in Shocked Zirconium Shed Light on Models for Shock-Induced Phase Transformations

G.T. Gray, D.W. Brown (MST Division), R.S. Hixson, P.A. Rigg (DX Division)

A detailed understanding of the stress-induced texture evolution and phase transformations that occur during shock loading of weapons materials is central to understanding and accurately modeling the underlying implosion physics in nuclear weapons. Transitions of importance include solid-solid phase transformations, dissociation transitions, and shock-induced melting. Phase transitions in weapons materials, especially if associated with a large volumetric change, can profoundly affect material states and constitutive, damage, and fracture properties during implosion. During the 2002 run cycle at LANSCE, we examined shock-induced changes in a sample of high-purity zirconium using neutron diffraction with the High-Intensity Powder Diffractometer (HIPD). Zirconium exhibits a subset of the extremely complex dynamics and phase-stability behavior exhibited by materials relevant to the Stockpile Stewardship Program, the Stockpile Life Extension Program (a Defense Program thrust to extend the service life of existing weapons systems), and core elements of the Nuclear Weapons Technology Program. The goals for the zirconium studies were to develop models of the equation of state and strength of weapons materials and to improve our understanding of the fundamental physics and materials science of nuclear weapons.

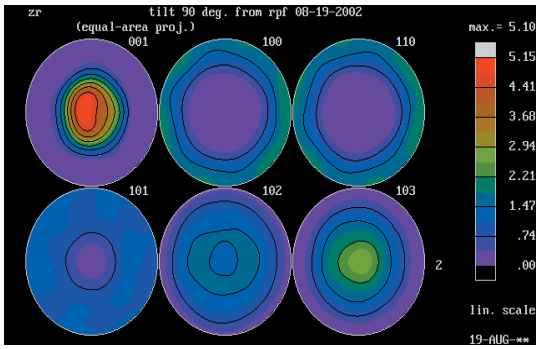

Fig. 1. Strong basal texture in the annealed zirconium.

Quantifying Texture Evolution and Phase Transformations in Shocked Zirconium

The recent experiment on HIPD quantified the texture evolution and phase transformations in zirconium before and after the sample had been shocked below and above the shock-induced transition from the hexagonal α phase at room temperature and atmospheric pressure and the cubic ω phase that occurs above a pressure of ~ 74 kbar. The sample was subjected to high-pressure shocks at 65 and 80 kbar (below and above the phase-transition pressure, respectively) with the 80-mm gas-gun launcher in MST Division at LANL. The shocked sample was then recovered intact for a metallurgical evaluation of the effects of the shock on the microstructure of the sample. Because of the difficulties involved in studying the physical properties of materials during a shock, shock-recovery experiments like the one that we performed on HIPD offer researchers an opportunity to study the mechanisms involved in the generation and storage of defects in materials subjected to impulse-loading histories.

The α-ω shock-induced phase transition in zirconium was quantified using velocity interferometric wave-profile measurements in DX Division at LANL to occur at ~ 74 kbar. Obtaining a bulk measurement of the volume fraction and lattice parameters of the metastable ω phase retained in the soft recovered sample following a shock above 74 kbar was critical to the success of this experiment.

X-ray measurements can only provide surface information, which is almost certainly not representative of the bulk, leaving neutron diffraction as the sole experimental method with access to the quantitative volume-fraction information that we are seeking to support validation of phase equilibrium modeling. The combination of HIPD's multiple-detector banks at high scattering angles and the high neutron intensity at the Lujan Center made HIPD the ideal instrument with which to perform these measurements.

Results

We measured the texture of the zirconium sample as a control to quantify the starting orientation of the material before it was shocked. The texture of the starting material exhibits strong basal texture (Fig. 1). After the sample was shocked below the phase-transition pressure, analysis of the crystallographic texture showed essentially no change (Fig. 2). However, shocking the sample above the phase transition decreased the basal texture significantly (Fig. 3).

Rietveld analysis of the neutron-diffraction data showed that 39% of the zirconium sample shocked at 80 kbar retained the metastable ω phase, whereas there was no evidence of the presence of the ω phase in the sample that was shocked below the α-ω phase transition. The substantial amount of retained metastable ω phase in the sample shocked above 74 kbar is consistent with wave-profile results from DX Division, which note the absence of a rarefaction shock upon shock release when the sample was loaded above the phase-transition pressure. The retained metastable ω phase also exhibited a strong basal component to its texture in the sample shocked above the phase-transition pressure (Fig. 4). This observation is consistent with the strong orientation relationship between the α and ω phases, which accommodates the c-axis collapse during the phase transition.

Conclusion

We will use the initial results of this study to quantify the texture evolution in zirconium as a function of imposed shock pressure and will contribute to fundamental modeling studies of the kinetics of the α-ω phase transition.

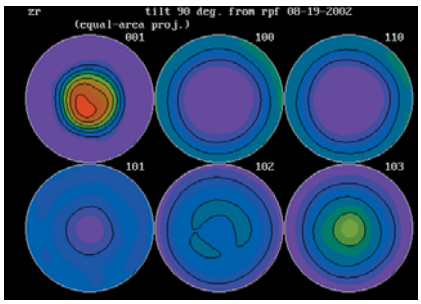

Fig. 2. Texture of zirconium following shock below the α-ω phase transition (at ~ 6.5 GPa).

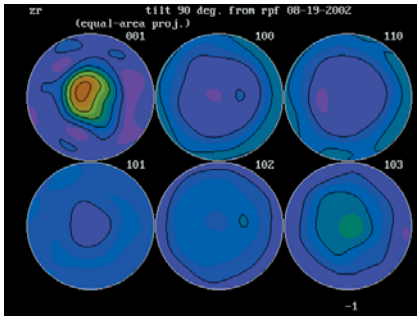

Fig. 3. Texture of zirconium following shock above the α-ω phase transition (at 8.0 GPa).

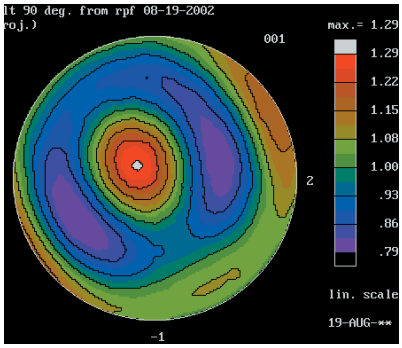

Fig. 4. Texture of the retained ω phase in the zirconium shocked to 8.0 GPa.

Acknowledgements

The researchers would like to acknowledge the U.S. Department of Energy Office of Science, Office of Basic Energy Sciences, and the National Nuclear Security Administration for financial support. A portion of this work is supported by the core nuclear weapons Stockpile Stewardship Program under Campaign II, MTE 2.2.

Proton Dynamics in Very Short, Strong Hydrogen Bonds

D. Hadži, J. Stare (National Institute of Chemistry, Slovenia), J. Eckert (University of California at Santa Barbara and LANSCE Division), L.L. Daemen (LANSCE Division)

Hydrogen (H) bonds are ubiquitous in nature, and their importance in a governing structure and reactivity in biological and chemical systems can hardly be overstated.[1] For example, H-bonds determine the secondary structure of biomolecules (including DNA) and the structure and properties of water and ice. They also control the self-assembly of macromolecules and are a crucial ingredient in crystal engineering. Proton transfer along H-bonds plays a dominant role in many chemical and biological reactions. Very short, strong H-bonds[2] are particularly interesting because proton dynamics in these H-bonds play a key role in diverse processes such as ferroelectricity and enzyme catalysis.

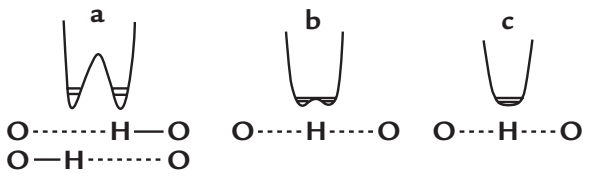

Fig. 1. Schematics of one-dimensional, potential-energy surfaces for O-H…O H-bonds. (a) Symmetric double-minimum potential with a high barrier in between. The H-bond proton can transfer by tunneling. (b,c) Short, strong H-bonds with a low barrier (b) or no barrier (c).

Spectroscopic Studies of Short H-Bonds

An H-bond is an attractive interaction between an H donor A-H and an H acceptor B. A and B are usually highly electronegative atoms, such as N, O, and F, with large dipole moments. H-bonding is commonly understood as the electrostatic interaction between the positive end of the bond dipole of A-H and the negative end of the dipole associated with B, but the contribution of covalent interactions across the H-bond increases as the H-bond becomes shorter.

Our study concerns H-bonds where both A and B are O atoms. The

motion of an H atom in such an H-bond can be understood in terms of the double-well potential between the two O donors.

When the barrier between the two wells is high (Fig. 1a), the H-bond proton can be transferred from one well to the other by tunneling. In cases where the two O atoms are close to each other (less than about 2.5 Å), the barrier to proton transfer is dramatically lowered, and the system is said to exhibit a low-barrier hydrogen bond (LBHB). These H-bonds are very strong because of the short separation between O atoms or, in terms of the dynamics, because of the large amount of energy that is required to stretch the O-H bond from its normal value of about 1 Å (Fig. 1a) to nearly a centered position of about 1.2 Å (Fig. 1b,c).

Cleland and Kreevoy[3] have proposed that LBHBs play an important role in enzymatic catalysis. Their proposal has not only triggered a new wave of investigations into the properties of such bonds but has also demonstrated that these are still poorly understood despite intense research spanning several decades. Although recent progress in understanding strong, intramolecular H-bonds has been considerable,[4] it has covered mainly the static aspects. Despite these extensive structural studies, questions about the proton dynamics and the effect of the environment upon these dynamics in LBHBs remain unanswered. A precise description of the proton dynamics in LBHBs combined with theoretical modeling of the underlying potential surface is the focus of current H-bond research.

Experimental information on the dynamics of the H-bond proton can be obtained by a variety of methods, most notably through infrared vibrational spectroscopy. The primary aim of spectroscopy in this application is to identify the vibrational modes of the H-bond, principally O-H stretching and in- and out-of-plane O-H bending.

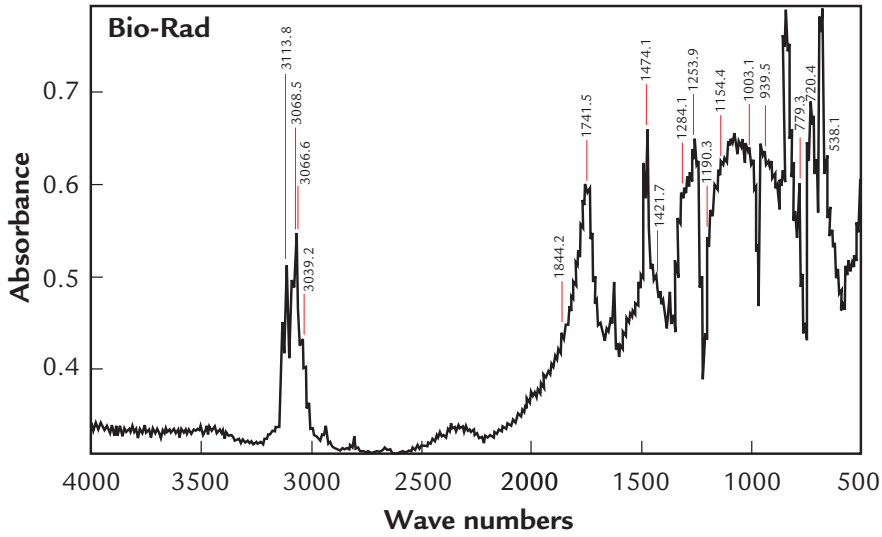

Fig. 2. Infrared spectrum of the crystalline trichloroacetic acid/pyridine-N-oxide (TCA-PyO). The very broad feature below 2,000 cm^{-1}, which peaks around 1,000 cm^{-1}, is the signature of the O-H stretching vibration of the H-bond.

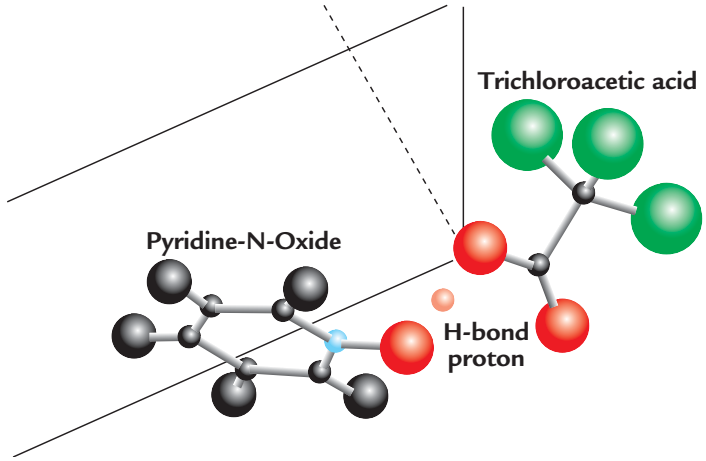

Fig. 3. PyO complex with TCA. The H-bond proton is located between the O atoms on PyO and TCA.

Although infrared spectroscopy is the most commonly used spectroscopic technique for investigations of H-bonding in general, its application to the study of very short hydrogen bonds (VSHBs), as those found in some LBHBs, is seriously hampered by the problem that the O-H stretching mode and, in some cases, the deformation modes can be very difficult to locate. The difficulty arises from the enormous broadening (and low intensity) of this band (Fig. 2) in most systems with VSHBs and from mixing with the various skeletal modes in the case of intramolecular H-bonds.

Vibrational spectra obtained by inelastic-neutron scattering (INS), on the other hand, do not reflect these broadening mechanisms because the

neutron interacts with atomic nuclei and not with electrons, in contrast to infrared spectroscopy.

One example of our extended series of studies on VSHBs is the complexes of PyO with trihaloacetic acids (Fig. 3). These were chosen because of their short O...O distances (2.42 to 2.45 Å) and the availability of extensive characterization by related methods (e.g., crystallography, infrared and Raman spectra, ^{1}H-nuclear-magnetic-resonance and ^{17}O-nuclear-quadrupole-resonance parameters, and theoretical calculations).[5]

The systematic changes (i.e., varying the relative acidities of donor and acceptor groups) of such a series gives a broader view of the H-bond potential in these systems. The infrared spectrum of one member of this family, TCA-PyO, is shown in Fig. 2. It exhibits the very broad O-H stretching band centered at approximately 1,000 cm^{-1}, which is characteristic of VSHBs.

INS spectra, collected on the Filter Difference Spectrometer (FDS) at LANSCE, of three such complexes with ring-deuterated PyO are shown in Fig. 4. We expect to be able to identify vibrational modes related to the H-bond because INS vibrational spectra principally reflect the motions of H atoms, and the only H in this system is that in the H-bond. However, the richness of the spectra (Fig. 4) clearly indicates that the motions of the H-bond proton are extensively coupled to vibrations of the two molecules that form the complex.

Nonetheless, we can readily identify the principal modes involving the H-bond and observe systematic shifts in these modes between the different complexes caused by changes in H-bond geometry from one compound to another. The in- and out-of-plane bends are the strong bands at around 1,600 and 1,100 cm^{-1}, respectively, whereas O-H stretching appears in at least two modes around 900 cm^{-1}.

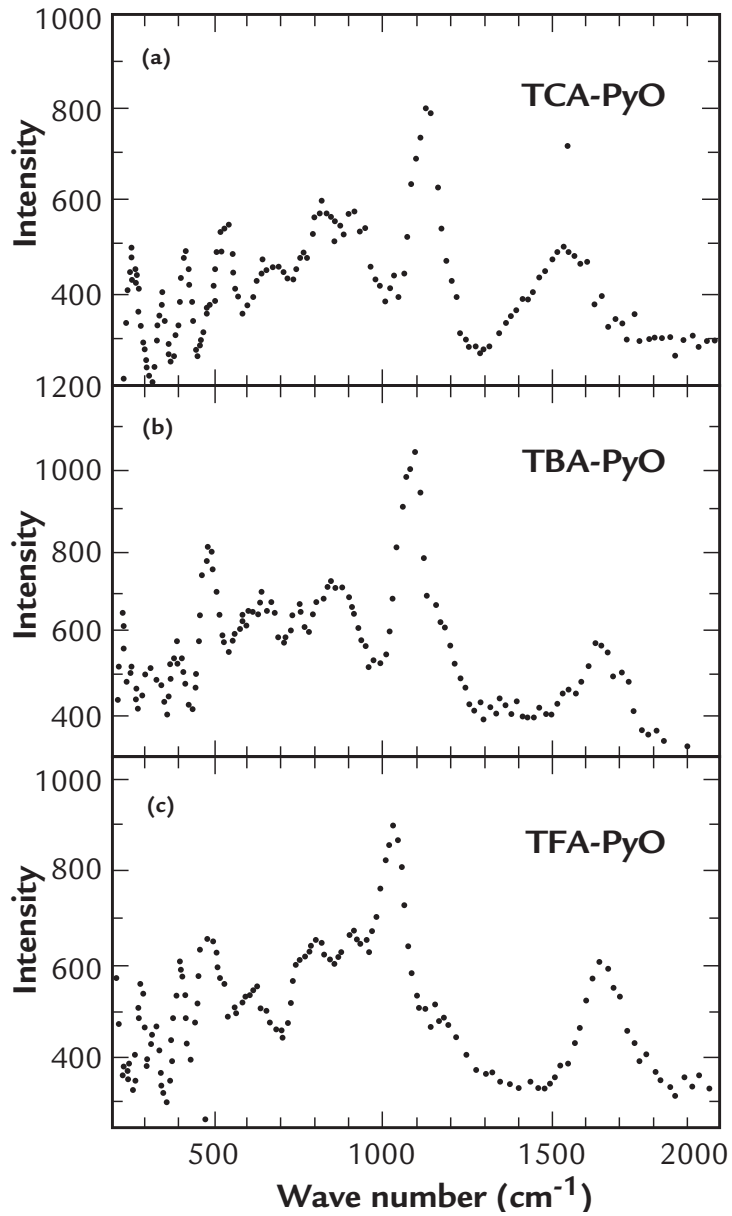

Fig. 4. INS vibrational spectra of crystalline complexes of PyO with (a) trichloro-, (b) tribromo-, and (c) trifluoroacetic acid.

The identifications are in part derived from our extensive theoretical studies, which use chemical *ab initio* methods. This approach is particularly challenging in the present case because the isolated TCA-PyO complex (as used in our calculation) has a rather different geometry than that of a solid, including considerably weaker H-bonds. This is the result of strong interactions between complexes in the solid, which is being taken into account in our ongoing theoretical studies.

Conclusion

These studies help determine the H-bond proton-potential-energy surface, which in turn governs H-bond proton dynamics. From information garnered from these and other studies, it appears that the one-dimensional potential-energy surface for the proton (as seen in Fig. 1) requires an investigation of more dimensions. Although the latter is a real challenge for theory, experimental studies that use techniques like INS must provide the necessary framework for the development of realistic theories.

Acknowledgements

This work was supported in part by the U.S. Department of Energy Office of Basic Energy Sciences and has benefited from the use of facilities at the Lujan Center at LANSCE.

References

1. G. Jeffrey, *An Introduction to Hydrogen Bonding* (Oxford University Press, New York, 1997).
2. C.L. Perrin and J.B. Nielsen, *Annual Review of Physical Chemistry* **48,** 511 (1997).
3. W.W. Cleland et al., *Science* **264,** 1887 (1994).
4. F. Hibbert et al., *Advances in Physical Organic Chemistry* **26,** 255 (1990).
5. V. Balevičius et al. (in preparation).

Electrical Anomalies in α-Glycine

P.A. Langan, B. Schoenborn (B Division), S. Mason (Institut Laue-Langevin)

Glycine, the smallest of the amino acids, is one of the principle components of structural proteins, enzymes, and hormones. Glycine exhibits complex chemical behavior, crystallizing into three polymorphic zwitterionic (neutral) crystal structures (α, β, and γ) and converting to its nonionic form when vaporized. Depending on pH levels, glycine can adopt cationic (positive charge), zwitterionic, and anionic (negative charge) forms. A structural understanding of the mechanism behind an electrical anomaly observed in single crystals of glycine at the atomic level, described below, could lead to the identification and design of new materials with enhanced electrical properties.

Anomalous Electrical Properties Discovered in Single-Crystal Samples

Past measurements of the electrical conductance (the ability to conduct electrical charge) and capacitance (the ability to store electrical charge) of a single crystal of α-glycine revealed anomalous electrical properties that were dependent on temperature.[1] Cooling the crystal from 50°C slowly decreased its electrical conductance down to 31°C. Further cooling caused a dramatic increase in the crystal's conductance! A similar anomaly occurred in the electrical capacitance of the crystal — capacitance is essentially temperature independent above 31°C but decreases precipitously below this temperature. The usual mechanisms used to explain insulating single crystals could not adequately describe these observations. Instead, it was suggested that perhaps a phase transition of the α-glycine crystal causes a pyroelectric occurrence — the property of certain crystals to produce a state of electrical polarity by a change in temperature.

In 2001, researchers from LANL in collaboration with the Institut Laue-Langevin (ILL) carried out a variable-temperature neutron-diffraction study of α-glycine at the ILL high-flux nuclear reactor.[2] Neutron diffraction was used instead of x-ray diffraction, the standard technique for determining crystal structures, because it

can provide more accurate information on hydrogen-atom positions. Hydrogen atoms are expected to play an important role in the phenomenon under investigation. The results from the analyses of six complete data sets collected over a temperature range of 288 K to 427 K proved that pyroelectricity could not explain the anomalous electrical properties observed in the single-crystal samples. In these experiments, the unit cell expanded anisotropically with increasing temperature. The unique b axis, which corresponds to the stacking direction of molecular layers, showed the most change. The increasing separation of antiferroelectric molecular layers with increasing temperature is driven by oscillations about the axis perpendicular to the b axis (Fig. 1). The interlayer hydrogen bonds also weakened with temperature, but there was little evidence of any change in the polarization of the bonds.

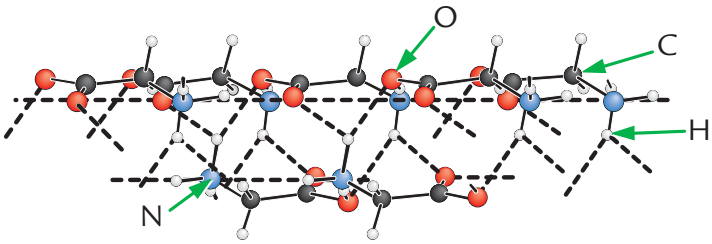

Fig. 1. A view perpendicular to the b axis of α-glycine showing a hydrogen-bonded anti-parallel double layer. The bifurcated hydrogen bonds between single layers are represented by dashed lines.

Neutron-Diffraction Studies of Electric-Field-Induced Structural Changes in a Single Crystal

Although the results of the experiment at the ILL dismissed the possibility of pyroelectricity or a phase transition as the cause of the anomalous electrical behavior of α-glycine, they did suggest another possible mechanism. Glycine molecules in their zwitterionic form have a large associate electric dipole moment. The increasing separation of the molecular layers would change the ability of these dipoles to reorient in an applied electric field and therefore change the electrical properties of the crystal. To investigate this possibility, we carried out new experiments on the Protein Crystallography Station (PCS) at LANSCE during the 2002 run cycle (Fig. 2). These experiments were the *first ever* neutron-diffraction studies of electric-field-induced structural changes in an organic single crystal. As such, our goal was to determine the reorientation of the molecular dipoles in the applied electric field and how this reorientation relates not only to the observed increase in oscillation of the axis that is perpendicular to the b axis, but also to the separation of molecular layers. We also wanted to determine whether the molecular reorientation had significant effects on the interlayer hydrogen bonding and therefore on the hydrogen-bond and molecular polarizations as well.

Results

Using a neutron time-of-flight technique with the large-area detector on the PCS allowed us to collect all of our data at the same time without moving the crystal or detector. Data can be collected in a parametric fashion as a function of temperature or electric field, and very subtle changes can be detected in the diffraction data. In preliminary measurements, a clear change in the diffraction data of α-glycine has been observed at ambient temperature when an electric field of 100 mV is applied across the crystal. The data are currently being analyzed to relate these changes to changes in crystal structure.

Acknowledgements

The researchers would like to acknowledge the U.S. Department of Energy Office of Science, Office of Basic Energy Sciences, and Office of Biological and Environmental Research for financial support and for access to the Protein Crystallography Station at LANSCE.

References

1. T.C. Chilcott et al., *Philosophical Magazine B* **79**, 1695-1901 (1999).
2. P. Langan et al., *Acta Crystallographica B* **58**, 728-733 (2002).

Fig. 2. Paul Langan of the Bioscience Division points out the single-crystal sample (shown in the inset) of α-glycine used in the current experiments on the PCS.

Thermal Neutron Protein Crystallography — Enzyme-Mechanism Investigations with D-xylose Isomerase

B.L. Hanson, G.J. Bunick (Oak Ridge National Laboratory), A. Katz, J.P. Glusker (Fox Chase Cancer Center), X. Li, B.P. Schoenborn, P.A. Langan (B Division)

The protein D-xylose isomerase is an enzyme that catalyzes the conversion of D-xylose to D-xylulose and D-glucose to D-fructose by hydrogen-atom transfer. The catalytic mechanism of hydrogen-atom transfer is currently believed to involve a metal ion-bound water molecule. To understand this mechanism, scientists must first find a way to locate the hydrogen atoms within D-xylose isomerase, not just the heavier atoms found by x-ray diffraction. Neutrons are a unique tool for such studies because, in contrast to x-ray diffraction, light atoms (hydrogen atoms) diffract neutrons as strongly as do the other atoms commonly found in macromolecules (carbon, nitrogen, oxygen, and phosphorus).

Researchers from Oak Ridge National Laboratory (ORNL), Fox Chase Cancer Center, and LANSCE are participating in a long-running National Institutes of Health (NIH) structural biology project to determine the hydrogen-atom positions of D-xylose isomerase by high-resolution x-ray crystallography and neutron diffraction (Fig. 1). Because about 50% of the atoms in this protein are hydrogen atoms, knowing the exact atomic positions of the hydrogen atoms is critical to understanding its structure and function. Neutrons can be used to locate hydrogen atoms even at moderate resolutions (around 2.2 Å), thus providing a strong scientific justification for using neutron diffraction in biological studies. Another major advantage of using neutron diffraction is that neutrons do not cause extensive radiation damage to the crystal.

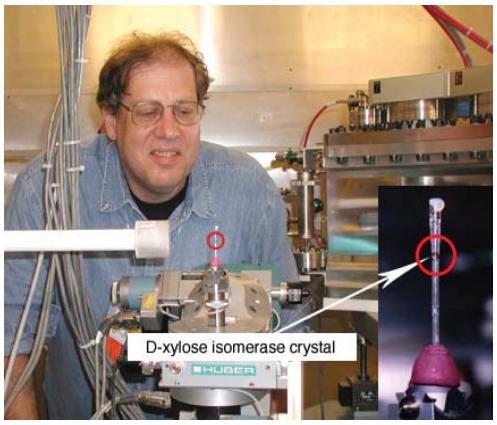

Fig. 1. Leif Hanson of ORNL examines the crystal sample of the D-xylose isomerase protein used in recent experiments on the Protein Crystallography Station (PCS) at Lujan Center at LANSCE. To the right of Hanson is the PCS detector array. This sample of D-xylose isomerase is the largest biological molecule ever studied at high resolution using time-of-flight (TOF) neutron diffraction.

Determining the Mechanism for Hydrogen Transfer in Biological Systems

D-xylose isomerase is the largest biological molecule (with unit-cell lengths around 100 Å) ever studied at high resolution using neutron diffraction and one of the first proteins to be studied using TOF techniques (Fig. 2). The primary goal of the experiments on the PCS, however, was to collect neutron-diffraction data on a crystal sample of D-xylose isomerase to compare the structural information obtained by this technique with that derived from x-ray data taken at the Advanced Photon Source at Argonne National Laboratory. The study is also being done in response to a request by the Department of Energy Office of Biological and Environmental Research to provide clear evidence for neutron diffraction as a tool for macromolecular structure/function research. In a broader perspective, these studies demonstrate that protein crystallography at a spallation neutron source will greatly increase the number of proteins for which hydrogen positions, especially partially mobile hydrogen atoms, can be resolved. PCS is the pioneer instrument of what will be multiple neutron beam lines for macromolecular crystallography at the future Spallation Neutron Source.

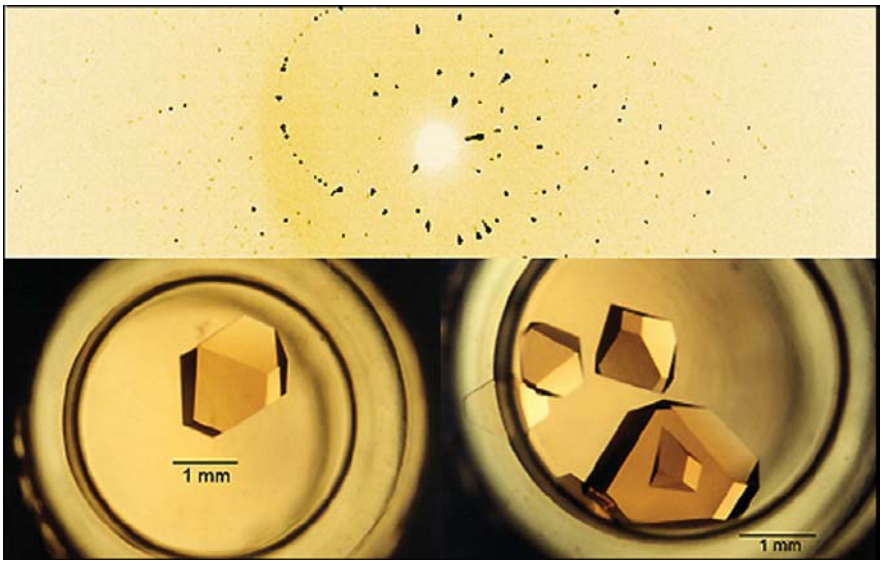

Fig. 2. The top image is the neutron-diffraction data taken on the PCS of one of the D-xylose isomerase protein crystals shown in the bottom right image. This sample was provided by Genencor International, Inc., a worldwide supplier of enzymes and other biochemicals for industrial use. These crystals were grown at ORNL in a counter diffusion cell, which is a National Aeronautics and Space Administration (NASA) device originally developed for microgravity protein crystallization.

D-xylose isomerase has significant commercial impact in the production of high-fructose corn syrup, but, more importantly, it serves as a model for biochemical structure and function studies of metalloenzymes. These enzymes comprise nearly one-third of all known proteins. They have significant implications in all cellular functions and in disease states such as cancer. Scientists at Fox Chase Cancer Center are interested in what they believe is the metal ion-mediated ionization of water as the enzymatic mechanism of D-xylose isomerase. The result is a transfer of a proton from one part of the substrate of the enzyme to another part. The overall aim is to discover how this magnesium-utilizing enzyme works. The key to this discovery lies in locating the atomic positions of hydrogen via neutron diffraction.

Conclusion

With the end of the 2002 LANSCE run cycle, data collection from the crystal shown in Fig. 1 is now complete. We made diffraction measurements from 20 different crystal positions to ensure that all possible crystal reflections were collected. The 2002 run cycle at LANSCE marks the first year of PCS operations for outside users. The performance of the instrumentation is still being explored with challenging structural problems like that encountered in the experiments with D-xylose isomerase. We now know that this is one of the best neutron-diffraction data sets ever measured for a protein. The data are complete to a resolution of approximately 1.7 Å. Our plan is to finish the structural analysis before summer 2003 in order to present our findings at the American Crystallographic Association national meeting as part of a special Transactions Symposium on Neutron Protein Crystallography.

Acknowledgements

The researchers would like to acknowledge the U.S. Department of Energy Office of Science, Office of Basic Energy Sciences, and Office of Biological and Environmental Research for financial support and for access to the PCS at LANSCE. The researchers at ORNL are also supported by grants NAG8-1568 and NAG8-1826 from NASA and GM-29818 from NIH. The researchers at Fox Chase Cancer Center are supported by grant CA-10925 from NIH and by an appropriation from the Commonwealth of Pennsylvania.

Texture Changes During the Quartz α-β Phase Transition Studied by Neutron Diffraction

H.-R. Wenk, S. Grigull, J. Pehl (University of California at Berkeley), D.J. Williams (LANSCE Division)

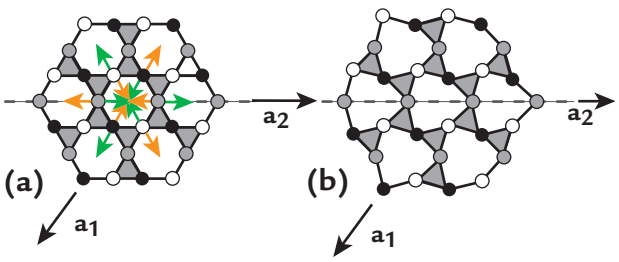

Fig. 1. A c-axis projection of the structure of quartz (a_1 and a_2 axes are indicated). Only silicon atoms are shown with patterns indicating different z-levels (the white, gray, and black circles). (a) Hexagonal β-phase quartz with potential distortions to trigonal α-phase quartz indicated by orange and green arrows. (b) Trigonal α-phase quartz representing one orientation variant produced by green-arrow distortions. The second variant, produced by orange-arrow distortions, would be related by a 180° rotation.

Phase transitions in polycrystals have a profound impact on physical properties of materials, in particular, on the anisotropy pattern, which is due to preferred orientation (or texture) of crystals. In general, textures are measured at room temperature, and high-temperature texture is implied by modeling. Time-of-flight neutron diffractometers, such as the High-Pressure-Preferred Orientation (HIPPO) instrument at LANSCE, have made *in situ* investigations of texture changes during phase transformations possible. We report here on texture changes for the displacive trigonal-hexagonal phase transition of quartz, which occurs at 573°C.

Exploring Texture Changes in Bulk Quartzite During α-β Phase Transitions

The α-β phase transition of quartz has long been of interest in crystallography.[1] Through slight atomic displacements, the high-temperature hexagonal structure (Fig. 1a) of quartz distorts to a trigonal structure upon cooling (Fig. 1b) without changing the orientation of the c-axis or the a-axes (a_1 and a_2). There are two orientation variants for trigonal quartz, related geometrically through a 180° rotation about the c-axis and requiring only slight distortions of the crystal structure as indicated by the colored arrows in Fig. 1a. The β-phase quartz can be viewed as an average of two orientation variants of trigonal α-phase quartz. Upon cooling, crystals could assume either of these two orientations. Internal strains are critical for the variant selection, and this requires characterization of *bulk* materials where each grain is influenced by its surrounding neighbors. Many aspects of the α-β phase transformation in quartz remained enigmatic because traditional investigations, such as x-ray diffraction and electron microscopy, relied on surface characterization. Thus neutron diffraction with minimal absorption offers unique opportunities. During the 2002 run cycle at LANSCE, we used the texture/temperature capabilities of HIPPO to explore the texture changes of bulk quartzite during the α-β phase transition and to resolve the question as to which trigonal orientation variant the material selects during subsequent cooling.

The unique features of HIPPO are high count rates, a large array of detectors, and a wide range of ancillary instruments for *in situ* low- and high-temperature and -pressure studies. With HIPPO, diffracted neutrons are detected by an array of 50 detector panels with 1,400 ^{3}He detector tubes located at different directions and diffraction angles. Only 30 detectors from the 40°, 90°, and 150° banks were used in our experiment because of limitations in resolution that decrease with diffraction angle (Fig. 2). It is possible to have 6 orientation angles about the vertical axis, resulting in 6 x 30 = 180 orientations (Fig. 3a). The size of each circle corresponds to the intensity for the 201 reflection and is proportional to the number of crystallites in that orientation. Fig. 3b is an averaged pole-density distribution for diffraction peak 201. HIPPO is equipped with a 300- to 2,000-K vacuum furnace for conducting *in situ* texture measurements as a function of temperature.

The sample used in our experiment was a naturally deformed fine-grained quartz mylonite with a simple texture that resembles a single crystal with a pronounced trigonal symmetry (i.e., a single c-axis maximum and three maxima for positive rhombs). The sample was mounted on a vanadium holder. Diffraction spectra were recorded for 500 s. The Rietveld analysis technique[2] could not be used because the diffraction spectra were contaminated by parasitic peaks originating from diffraction by the metal surface of the vacuum furnace. Instead, an automatic-intensity-extraction procedure for recording individual diffraction peaks was developed. The 180 corrected intensities at different pole-figure coordinates for 4 quartz diffraction peaks (100, 101, 201, and 112) were then used to calculate the orientation distribution.[3] Diffraction peak 101 is a superposition of the 2 non-equivalent diffractions 101 and 011 with scattering

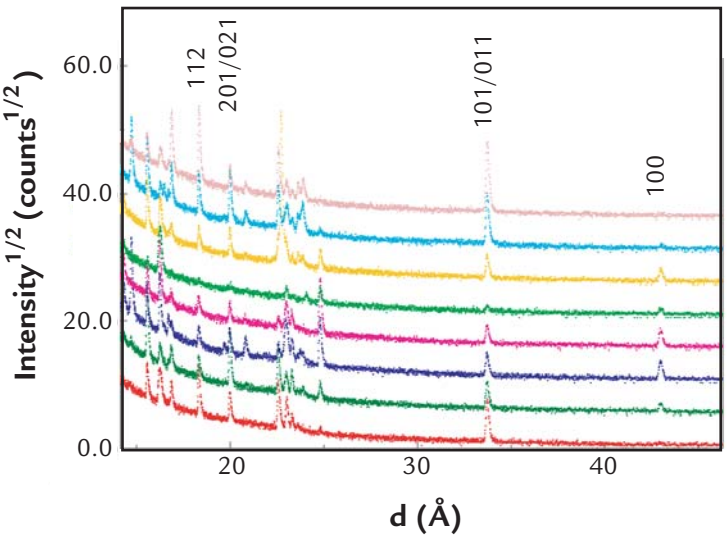

Fig. 2. Typical diffraction spectra for one rotation setting of the 150° bank. Diffraction peaks of quartz used in the texture analysis are indicated. Notice relative intensity variations between spectra that are due to texture. In addition to quartz peaks, there are numerous diffraction peaks from the furnace metal, which made the analysis difficult.

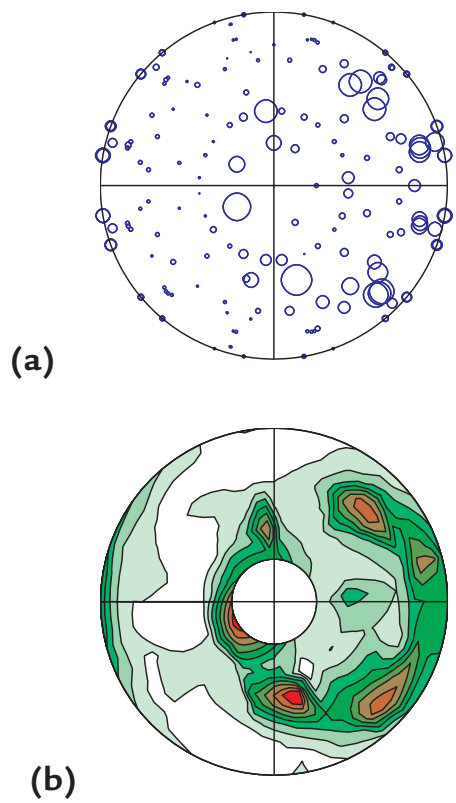

Fig. 3. Pole-figure coverage with 30 detectors on 150°, 90°, and 40° banks of HIPPO and 6 sample rotations. (a) The discrete circles represent detectors. The size of the circle is proportional to the intensity of the 201 crystal-plane reflection and thus the pole density in that direction. (b) Averaging of the discrete pole density produces a continuous coverage. Such incomplete pole figures were used for determining the orientation distribution.

contributions for neutrons of 70% and 30%, respectively. Peak 201 is a superposition of 201 and 021 with contributions of 20% and 80%, respectively. This intensity difference was used to resolve the trigonal texture symmetry.

From the orientation distribution, individual pole figures for 001 (c-axis), 100 (prism), 101, and 011 were recalculated (Fig. 4). Before the phase transition (Fig. 4a), we observed a strong texture with a single c-axis maximum — 100 poles are distributed on a great circle with 6 concentrations at 60° intervals, and 101 and 011 poles each show 3 slightly asymmetric concentrations related by a 120° rotation about the c-axis. Heating to 625°C did not change the 001 and 100 patterns, but texture intensities for rhombohedral (101 and 011) poles were distributed over a small circle with 6 concentrations consistent with hexagonal crystal symmetry (Fig. 4b). Upon cooling, the texture became trigonal again (Fig. 4c) and was identical with the starting texture — even for minor details. We obtained the same results upon repeating the heating-cooling cycle.

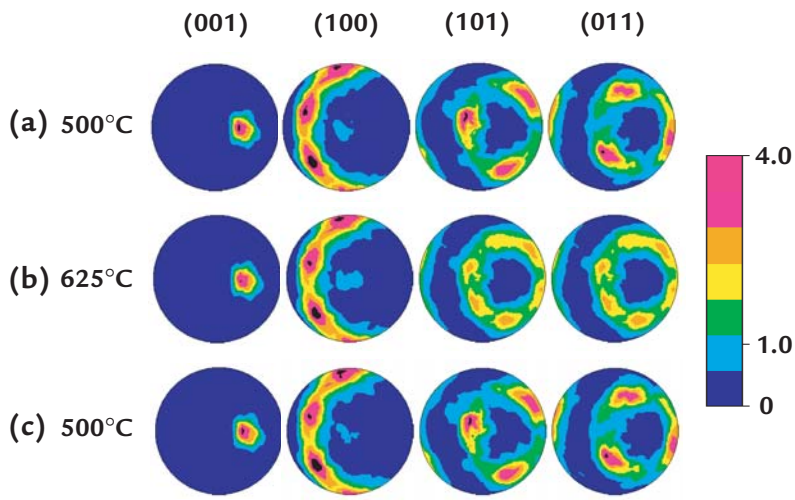

Fig. 4. Pole figures 001, 100, 101, and 011 for a metamorphic quartzite recalculated from the orientation distribution: (a) 500°C (before heating), (b) 625°C, (c) 500°C (after heating). Equal-area projection, linear-pole-density scale in multiples of a random distribution. The scale for the 001 pole figure needs to be multiplied by a factor of 5 relative to the others. The trigonal low-temperature texture becomes hexagonal upon heating and returns to exactly the same pattern upon cooling.

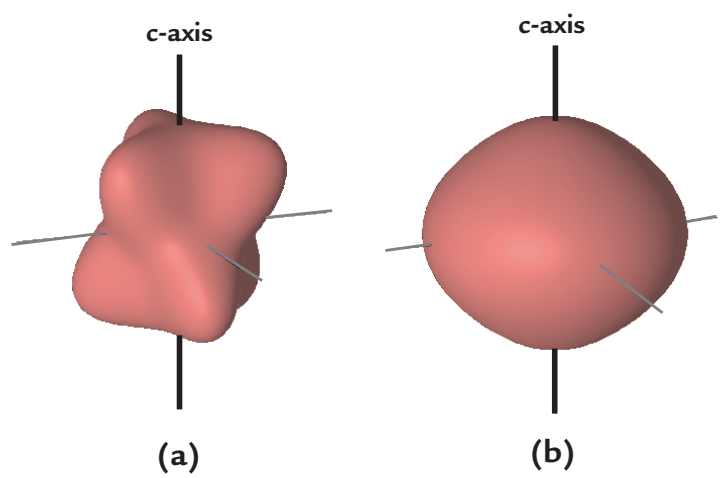

Fig. 5. Young's modulus for (a) trigonal α-phase quartz and (b) hexagonal β-phase quartz, illustrating the elastic anisotropy. The surfaces are normalized so that the maximum values are equal.

HIPPO Experiment Paves the Way for Studying Texture Changes During Heating

To our knowledge, this is the first *in situ* determination of texture changes during phase transformations by neutron diffraction. As such, the experiment opens a new field to investigate texture changes during heating. The 50-minute time period used to record data for one temperature interval allowed us to follow texture changes in real time. The results for quartzite clearly show that the aggregate retains its "shape memory" (the shape-memory effect refers to a phenomenon whereby a material, when mechanically deformed and then heated, returns to its original shape). Quartzite thus emerges as a shape-memory system similar to those previously observed in some metals.[4] When quartz becomes hexagonal upon heating, the orientation distribution also becomes hexagonal. Upon cooling, crystals could choose at random between the two possible trigonal orientation variants. Yet the memory is retained, presumably by elastic strains imposed by neighboring grains, and crystals revert to their initial orientation. Contrary to β-phase quartz with a very weak elastic anisotropy[5] and axial symmetry about the c-axis (Fig. 5a), α-phase quartz is elastically strongly anisotropic[6] with a direction near 011 almost twice stiffer than one

near 101 (Fig. 5b). If the initial low-temperature microstructure is without internal strains, the phase transformation will thus impose large elastic stresses through compatibility requirements of neighboring grains. Those stresses will determine the orientation variant upon cooling. Because the preferred-orientation pattern depends on interaction between neighbors, polycrystalline bulk samples need to be characterized via neutron diffraction.

Conclusion

In this context, the issue of the stress field becomes relevant.[7] Deformation experiments at low temperature documented texture changes owing to imposed stress with minimal macroscopic strain.[8] If a stress is imposed during the phase transformation and the quartzite does not undergo significant plastic deformation at lower temperature, the active stress field will influence the variant selection, and the "trigonality" of the quartz texture could therefore be used as a piezometer of the ancient stress field in metamorphic rocks.[9] (A piezometer is an instrument for measuring pressure, particularly high pressures.)

The investigation of preferred orientation in many naturally deformed quartzites revealed that the orientation distribution of positive and negative rhombs is different. The texture has a trigonal symmetry with a great variety of natural quartz textures that form under different temperature, pressure, and strain conditions.[10] Systematic transition experiments on different texture types and imposing stresses during the phase transitions can shed some light on the deformation behavior of this mineral, which is so important for plasticity in the Earth's crust.

Acknowledgements

The researchers would like to acknowledge the U.S. Department of Energy Office of Basic Energy Sciences and the National Nuclear Security Administration.

References

1. W.H. Bragg et al., *Proceedings of the Royal Society of London A* **109**, 405 (1925); M.A. Carpenter et al., *American Mineralogist* **83**, 2 (1998); U.T. Höchli and J.F. Scott, *Physical Review Letters* **26**, 1627 (1971).
2. L. Lutterotti et al., *Journal of Applied Physics* **81**, 594 (1997); R.B. Von Dreele, *Journal of Applied Crystallography* **30**, 577 (1997).
3. H.-R. Wenk et al., *Journal of Applied Crystallography* **31**, 262 (1998).
4. C. Jourdan et al., *Journal of Materials Science* **26**, 4355 (1991); K. Otsuka et al., Shape Memory Materials (Cambridge University Press, 1998); R. Vaidyanathan et al., *Acta Materialia* **47**, 3353 (1999).
5. H.B. Huntington, *Solid State Physics* **7**, 213 (1958).
6. R.F.S. Hearmon, *Advances in Physics* **5**, 323 (1956).
7. A. Schubnikov et al., *Zeitschrift fuer Kristallographie* **83**, 243 (1932).
8. J. Tullis, *Science* **168**, 1342 (1970); J. Tullis and T.E. Tullis, *American Geophysical Union Monogram* **16**, 67-82 (1972).
9. T.E. Tullis, *Journal of Geophysical Research* **85**, 6263 (1980).
10. D.W. Baker et al., *Journal of Geology* **80**, 81 (1972); D.W. Baker et al., *Journal of Geology* **77**, 143 (1969); S.M. Schmid et al., *American Geophysical Union Monogram* **36**, 263 (1986); S.M. Schmid et al., *Tectonophysics* **78**, 101 (1981); H.-R. Wenk, in *Reviews in Mineralogy* **29**, Silica Minerals (Mineralogical Society of America, Washington D.C., 1994).

In Situ Neutron-Diffraction Study of Lithium-Ion Batteries

M.A. Rodriguez, D. Ingersoll, D.H. Doughty (Sandia National Laboratories)

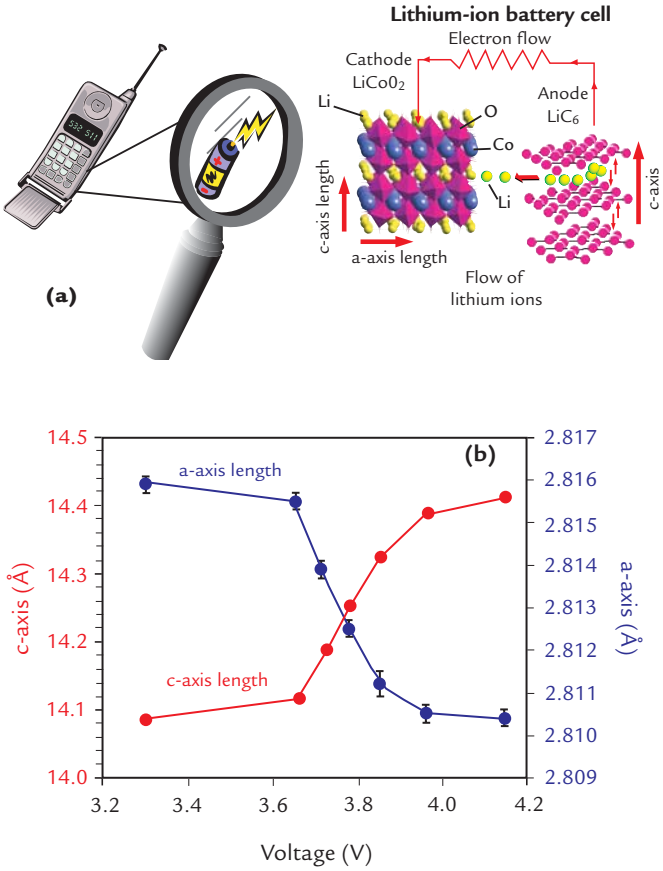

Fig. 1. (a) A schematic diagram of a lithium-ion cell illustrates the $LiCoO_2$ and LiC_6 (lithium-intercalated graphite) along with the external circuit. During charging, the lithium is removed from the cathode ($LiCoO_2$), passes through a cell separator, and intercalates into the graphite anode. During discharge, the lithium ions are shuttled back into the $LiCoO_2$. (b) $LiCoO_2$ lattice parameters (a and c axes) as a function of voltage.

Long-lived, compact power sources are required for many national security applications, including nuclear weapons. Lithium-ion batteries are a leading technology in these applications, and their lifetime and efficiency are limited by fundamental electrochemistry. *In situ* measurements yield the best information about the way battery cells work because the data are collected on functioning cells as they charge and discharge. Our first attempt at using *in situ* neutron diffraction to analyze lithium-ion batteries allowed us to observe changes in only two states of charge (separately): charged and uncharged. Conducted on the High-Intensity Powder Diffractometer (HIPD) at LANSCE, this proof-of-principle experiment did not yield a large count rate and involved long data-collection times (it took 12 hours to obtain one data set per charge state). Our goal for the 2002 run cycle was to drastically improve the count rate by making changes in the configuration of the cell and by using the new High-Pressure-Preferred Orientation (HIPPO) spectrometer at LANSCE. HIPPO's high neutron flux and large detector array allowed us to measure structural changes occurring in the anode/cathode. We also successfully located the position and occupancy of hard-to-detect lithium ions in near real time. Using HIPPO allowed us to achieve a factor-of-40 improvement in data-collection rates over that obtained on HIPD.

We collected neutron-scattering data on HIPPO using a commercial lithium-ion battery cell from Saehan Enertech, Inc., in its uncharged state. A schematic diagram of a typical lithium-ion-battery system is shown in Fig. 1a. Our initial neutron-diffraction scans on this commercial cell indicated that we could obtain useful data in as short as 15 minutes. This demonstrated that *in situ* measurements in near real time were feasible. Next we fully charged the cell to ~ 4.1 V and collected data in 15-minute increments at 7 different states of charge in the battery (i.e., 100%, 80%, etc., charge states). The entire experiment took five hours to complete, which included equilibration time for the cell.

We performed Rietveld analysis, a data-refinement technique for structural studies, on the observed data to obtain information from the $LiCoO_2$ cathode. A useful range of neutron wavelengths from 1.3 Å – 1.75 Å contains five reflection planes from $LiCoO_2$ — namely the (113), (110), (108), (107), and (009) reflection planes — and a single aluminum (220) reflection plane from the current collector within the battery. By using the aluminum peak as an internal standard, we were able to obtain accurate lattice parameters from the 140°, 90°, and 40° HIPPO diffraction spectra. Fig. 1b shows a plot of lattice parameters for the a- and c-axes as a function of voltage. The contraction of the $LiCoO_2$ c-axis and the expansion of the a-axis upon discharge of the cell (decreasing voltage) are clearly evident. This finding is consistent with other experimental observations.[1] The trends in the data are smooth. The small errors represent three standard deviations of the output of refined values obtained from the Generalized Structure Analysis System (GSAS) (a powder-diffraction, data-analysis package used to refine and determine crystal structure). Additionally, we were successful in obtaining lithium-site occupancy information for the $LiCoO_2$ even though there was strong correlation of the lithium-site occupancy to the March-Dollase orientation vector. Both the $LiCoO_2$ and graphite displayed some degree of preferred orientation (a preference for the granules of material to orient in a specific, nonrandom fashion). We were able to model this nonrandom orientation with the use of the March-Dollase vector within GSAS. To study the lithium content, we refined a site occupancy of lithium in $LiCoO_2$ for the various states of charge by first assigning reasonable values to the lithium occupancy based on estimates from the electrochemical data. Then refinement of the preferred orientation, followed by simultaneous refinement of the lithium-site occupancy, converged and resulted in the observed plot in Fig. 2. The refined values, as shown in Fig. 2, track well with the calculated lithium content based on electrochemical data.

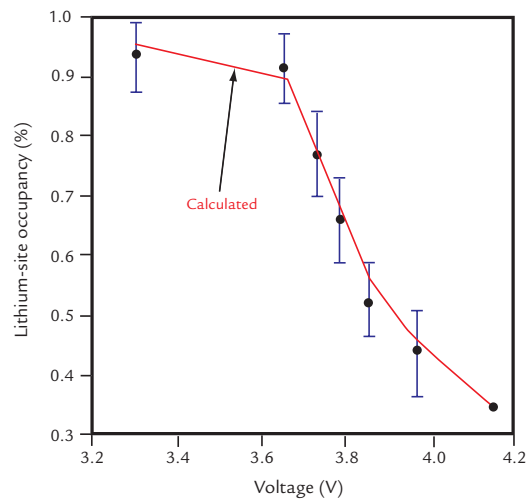

Fig. 2. Lithium-site occupancy of $LiCoO_2$.

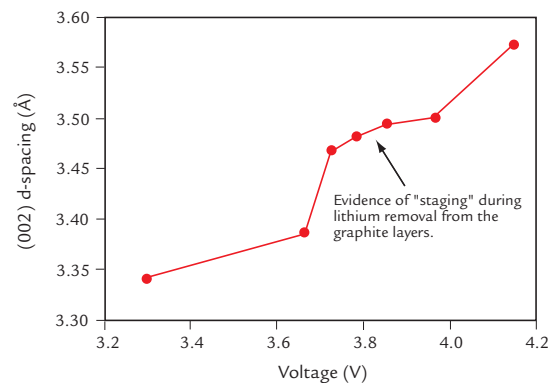

Fig. 3. (002) d-spacing for the graphite (LiC_6) anode during a lithium-ion-cell discharge cycle (decreasing voltage from 4.2 to 3.3 V). "Staging" occurs at a given point of lithium "fill," whereby the graphite planes expand as lithium ions fill the interlayer spaces and then contract upon discharge (see Fig. 1a).

Finally, we were able to obtain simultaneous structural information regarding the graphite anode as well. A quick plot of the (002) d-spacing as a function of voltage showed evidence of staging of the lithium-carbon alloys during cell discharge (Fig. 3). Hence, the anode and cathode of the lithium-ion cell can be diagnosed simultaneously in a nondestructive fashion to obtain valuable information about the inner workings of the battery system. Directly correlating this information to simultaneously collected electrochemical data provides a highly detailed picture of the cell performance.

Acknowledgements

The researchers would like to acknowledge the U.S. Department of Energy (DOE) Office of Science and Office of Basic Energy Sciences for financial support. A very special thanks is also given to Darrick Williams, Dave Bish, and Sven Vogel of Los Alamos National Laboratory for help with HIPPO data acquisition. Sandia is a multiprogram laboratory operated by Sandia Corporation, a Lockheed Martin Company, for the U.S. DOE under contract DE-AC04-94AL85000.

References

1. M.A. Rodriguez et al., *Powder Diffraction* **18** (2003), in press.

Magnetic Exchange Coupling in Metal/Native-Oxide Multilayers Studied by Polarized Neutron Reflectometry

G.S.D. Beach, S.K. Sinha, A.E. Berkowitz (University of California at San Diego), M.R. Fitzsimmons, S. Park (LANSCE Division)

There is a strong demand in industry for new high-permeability magnetic thin films with operating frequencies in the GHz regime. Applications range from magnetic recording (magnetic shielding in read heads) to telecommunications (high-frequency thin-film inductor cores). In these applications, the magnetization must respond to rapidly varying magnetic fields. However, at high frequencies, conventional (metallic) materials are limited by eddy currents, or electrical currents generated in response to a varying magnetic field. Eddy currents screen the interior of a material from changes in the external magnetic field, in effect, decreasing the active volume of the material.

A CoFe metal/native-oxide multilayer (MNOM)[1] was developed at the University of California at San Diego as a solution to the eddy-current problem. This system is composed of nanolayers (~ 2 nm thick) of strongly magnetic CoFe separated by thin (~ 1 nm thick) native-oxide layers. The oxide layers, which are formed by oxidizing the metal surface, provide a high electrical resistance barrier to eddy currents, thus permitting magnetic response to occur at several GHz.[2] In addition, because the native-oxide layers are magnetic,[3] they augment the total magnetization of the MNOM while allowing magnetic coupling to occur across the layers. This magnetic coupling is vital because it leads to the desirable magnetically soft behavior — the ability to easily change the magnetization direction with a modest magnetic field.

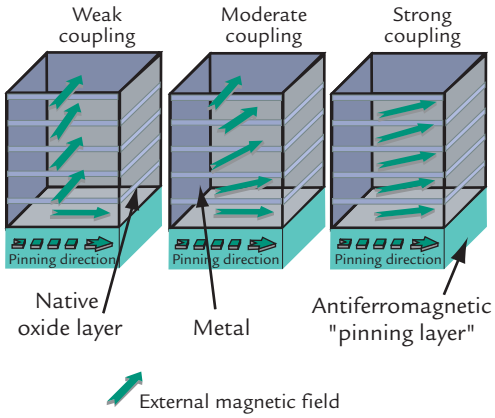

Fig. 1. Schematic of metal/native-oxide multilayer grown on an antiferromagnetic "pinning" layer. The pinning direction is indicated by the dashed arrow, and an external magnetic field is applied perpendicular to that direction. The magnetization increasingly rotates towards the applied field direction with distance from the pinning layer. The change in rotation angle from layer to layer is related to the magnetic coupling strength. If the layers are weakly coupled, only the bottom layer is pinned. If all layers are strongly coupled, their magnetization rotates together.

Neutron Reflectometry

Because of the key roles played by the native-oxide layers in the MNOM, understanding the oxide properties is essential. Few techniques permit the direct study of buried layers of these dimensions; one of the most powerful is spin-polarized neutron reflectometry (PNR). PNR can provide *depth-dependent* magnetic and chemical information with nanometer resolution and is therefore ideal for studying the native oxide and its interactions with the metal in the MNOM system. We conducted an experiment using this technique on Asterix in 2002 at LANSCE to study magnetic coupling in the MNOM. In PNR, a beam of spin-polarized neutrons is directed towards the sample at a glancing angle. The intensity and polarization of the reflected neutrons are then measured as they exit the sample. These measurements are performed as a function of the angle θ of the incident beam with respect to the sample surface.

There are two contributions to the neutron scattering (reflection) by the sample: nuclear and magnetic. Neutrons are scattered by the nuclei (nuclear scattering) with an element-specific probability. Because neutrons have spin (a magnetic moment), they also interact magnetically with the sample. There are four possible magnetic-scattering events. In non-spin-flip (NSF) scattering, the incident neutron spin direction ("up" or "down") is the same as the reflected spin direction. These *reflectivities* are denoted (+ +) and (- -), where the symbols indicate the spin directions of the incoming and outgoing neutrons. If the sample magnetization is not along the neutron polarization axis — neither "up" nor "down" but instead at some angle — spin-flip (SF) scattering can occur. Here the incident neutron spin is rotated so that an "up" neutron becomes a "down" and vice versa, leading to (+ -) and (- +) scattering. The SF and NSF reflectivities measured versus θ provide the magnetization profile (magnitude and direction) across the layers.

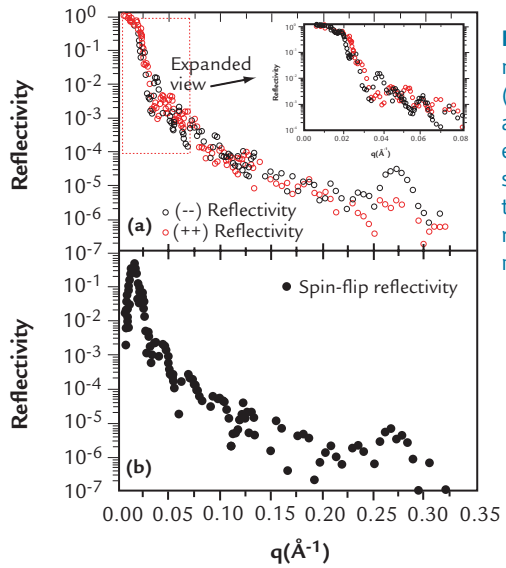

Fig. 2. (a) NSF and (b) SF polarized-neutron reflectivity versus $q = 4\pi\sin(\theta)/\lambda$ (where λ is the neutron wavelength) from a pinned MNOM sample that was subjected to an applied magnetic field. The strong SF scattering indicates magnetization rotation due to the applied field. The rotation profile depends on interlayer magnetic-coupling strength.

Experiments and Data

To determine the strength of the magnetic coupling across the oxide layers, we designed an experiment shown in Fig. 1. Application of an external magnetic field perpendicular to the equilibrium magnetization direction ("easy magnetization axis") causes coherent rotation of the magnetization. However, if the magnetization were somehow "pinned," or fixed (see Fig. 1), at the bottom of the film, the angle of rotation will vary from layer to layer. With no magnetic coupling across the native oxide, the magnetization of the bottom layer would remain pinned, while the layers above would rotate freely with the applied field. On the other hand, very strong coupling between layers would require the magnetization of all layers to rotate together (to the extent that the external field can overcome the pinning at the bottom of the film). Between these extremes, a spiral structure will form with the angle of magnetization slowly increasing with distance from the pinning layer. The change in angle from one layer to the next is related to the strength of the magnetic coupling between layers — the smaller the angle change, the stronger the coupling.

An antiferromagnet can act as a pinning layer for a ferromagnet, a phenomenon known as exchange bias.[4] In our experiments, an MNOM sample with 10 metal/oxide repeats was grown on an antiferromagnetic NiCoO film, and a magnetic field was applied perpendicular to the pinning direction (Fig. 1). By comparing the PNR spectrum of this sample (Fig. 2) to that of an identical unpinned sample (i.e., with uniform magnetization rotation), extraction of the coupling strength is possible.

Conclusion

A full analysis of the reflectivity spectra is currently under way. In addition to the oxide composition and magnetization, these experiments will lead to the layer-dependent magnetization profile of the MNOM. From this, magnetic coupling strength between the layers will be extracted, providing a basis for quantitative models of the magnetic behavior of the MNOM system.

Acknowledgements

The researchers would like to acknowledge the U.S. Department of Energy Office of Science and Office of Basic Energy Sciences for access to Asterix at LANSCE. This work is supported in part by the Nanotechnology Initiative of the National Institute of Standards and Technology.

References

1. G.S.D. Beach et al., *Applied Physics Letters* **79**, 224 (2001).
2. G.S.D. Beach et al., submitted (2003).
3. G.S.D. Beach et al., *Journal of Applied Physics* **91**, 7526 (2002).
4. W.H. Meiklejohn et al., *Physical Review* **102**, 1413 (1956).

Accelerator Science and Technology

Research Highlights

Control of the e-p Instability at the Proton Storage Ring 46

Superconducting Spoke Cavities Demonstrate Excellent Performance 48

Beam-Halo Experiment in the High-Current Proton Beam of the Low-Energy Demonstration Accelerator 50

Development and Testing of High-Power Vacuum Windows for the Spallation Neutron Source 54

Design of a Radio-Frequency System for the Spallation Neutron Source 58

Development of a Polyphase-Resonant-Converter Modulator for the Spallation Neutron Source 62

Development of a New 201.25-MHz Power Amplifier 64

H^- Injector Development for the Short-Pulse Spallation Source Enhancement Project 68

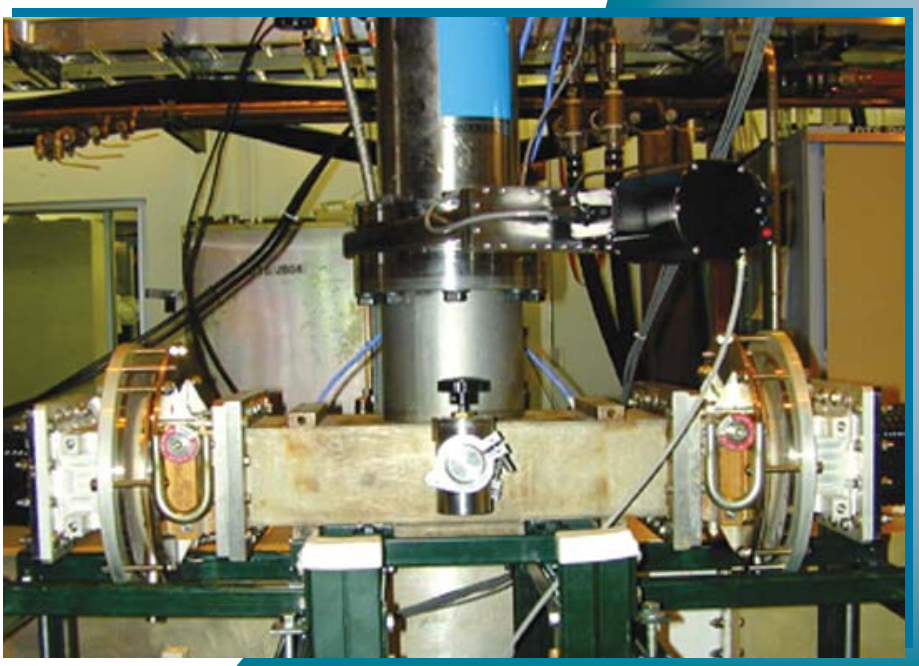

Control of the e-p Instability at the Proton Storage Ring

R.J. Macek, A.A. Browman, D.H. Fitzgerald, R.C. McCrady, T. Spickermann, T.S. Wang, T.J. Zaugg (LANSCE Division)

The strong transverse instability long observed at the LANSCE Proton Storage Ring (PSR) has been a limiting factor on peak intensity and is widely considered a major technical risk to the next generation of high-intensity proton rings. It has been the subject of much recent research that has led to a deeper understanding of its mechanism and several methods of control. The evidence is now compelling that this is a two-stream, electron-proton (e-p) instability caused by coupled oscillations of a low-energy electron cloud with the intense PSR beam. Experiments at PSR and various simulations have shown that a form of beam-induced multipacting (electron avalanche caused by multiple collisions with the PSR wall) on the trailing edge of the long PSR pulse generates a strong electron cloud. Furthermore, sufficient electrons survive the passage of beam-free gaps to cause an e-p instability with the characteristics observed at PSR.

A number of potential cures have been tested at PSR and found to be useful in significantly raising the instability threshold. Various measures to increase the spread of the betatron-wave frequency (and thereby increasing Landau damping) have been effective and are now implemented in PSR as part of the Short-Pulse Spallation Source (SPSS) Enhancement Project. Control of the instability by suppressing the generation of electron clouds has also been studied experimentally at PSR. As a result of these studies, global conditioning, or beam scrubbing, of the vacuum-chamber surfaces in the PSR has raised the instability threshold. (Beam scrubbing refers to the bombardment of the chamber surfaces with an intense electron cloud created by beam-induced multipacting.) Other methods of electron suppression (i.e., TiN coatings, use of weak magnetic solenoid fields) have been effective in reducing the electrons in short test sections but have not been tried over a large fraction of the ring circumferences. The measures that have been implemented at PSR have been sufficient to raise the instability threshold to 10 μC/pulse (6×10^{13} proton/pulse).

Instability Characteristics

Measurement of the instability threshold is typically done by accumulating a given number of protons and storing them for 400 to 500 μs after the end of accumulation. The radio-frequency (rf) buncher voltage is lowered until (1) the high-frequency, unstable motion appears on the vertical-difference signal of a beam-position monitor (BPM) near the end of the beam storage, and (2) a significant amount of beam is lost, as shown in the oscilloscope traces of Fig. 1. The growth time for the unstable motion is in the 50- to 100-μs range. Compelling evidence for e-p instability includes the observation that (1) the frequency content of the unstable motion is predominately at the bounce frequency of electrons captured in the potential well of the beam, and (2) the center frequency at threshold varied with the square root of the beam intensity as predicted for the e-p instability.

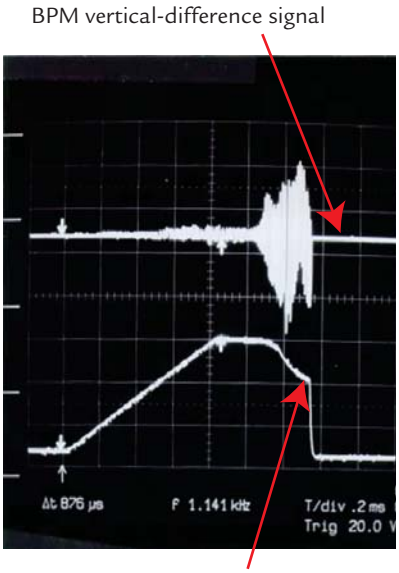

Fig. 1. Oscilloscope traces of diagnostic signals from the e-p instability at PSR.

Control by Landau Damping

Early models of the e-p instability predicted that Landau damping would be an important process because an increase in the spread of betatron-wave frequencies (caused by the spread of the momentum of the particle beam) results in more damping of the instability. The damping was observed in the strong linear dependence of the instability threshold on rf-buncher voltage (which increased the proton-beam momentum spread) shown in the curve labeled *historical data* in Fig. 2. An upgrade of the rf buncher to raise the maximum reliable voltage from 12 kV to 18 kV was part of the SPSS Enhancement Project and was important for control of the instability at higher-peak intensities. Other methods of increasing the betatron frequency spread to create additional Landau damping include the use of higher-order multipole fields (i.e., sextupole and octupole magnets), coupling of the betatron oscillations with a skew-quadrupole magnet (i.e., magnet rotated 45° about the beam axis), and inductive inserts. The inductive inserts are a passive means of compensating for the effects of longitudinal-space-charge fields and are equivalent to adding additional rf voltage, which further increases the momentum spread and damping of the instability. In addition, the inductors are effective in keeping beam from leaking into the gap between bunch passages under the influence of longitudinal-space-charge forces. A small amount of beam in the gap can trap additional electrons, which will contribute to the instability.

Suppressing the Generation of the Electron Cloud

Our studies in 2002 focused on testing measures to reduce the electron cloud and the hypothesis that reduction of the electron-cloud generation will raise the instability threshold. To this end, two additional sections were coated with TiN, which is effective in reducing the prompt multipactor electrons. The new tests with the additional TiN coatings showed an immediate factor-of-10 reduction of electrons in section 9 of the PSR. Although there was no initial reduction of the electron cloud in section 4, it did improve over time during beam operations. After 10 weeks of production-beam operations at 100 to 110 μA, the prompt-electron signal was reduced about a factor of 20, and the electrons remaining in the pipe at the end of the gap were down a factor of 5 — another indication of the benefit of surface conditioning by the beam.

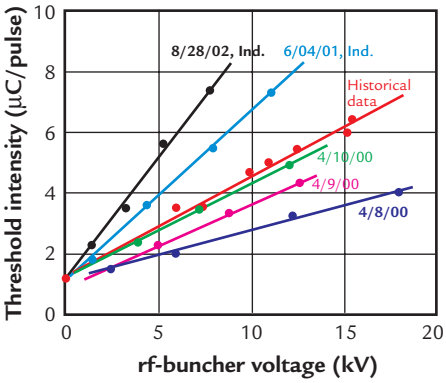

Fig. 2. e-p instability threshold-intensity curves taken at various dates during the 2000 to 2002 beam operations. The data for 2001 and 2002 also include the effect of inductive inserts.

Electron bombardment of vacuum-chamber surfaces has been shown to reduce the secondary emission yield in bench experiments at other laboratories. We therefore expected beam scrubbing to reduce the electron-cloud generation and the resulting e-p instability over time. Fig. 2 shows the instability-threshold curve that we measured at PSR at various times during the 2000 to 2002 beam operations. These data show considerable improvement in the instability threshold intensity over time. A systematic reduction in the prompt-electron-cloud signal (as measured by electron detectors in the PSR) by about a factor of 10 was also measured during the 2002 run cycle.

Conclusion

As a result of extensive beam-physics research, the strong transverse instability at PSR is reasonably well understood in terms of a two-stream, e-p instability caused by the coupled oscillations of a low-energy electron cloud with the intense proton beam in PSR. The intense electron cloud is produced from beam-induced multipacting on the trailing edge of the long beam pulse and from the high reflectivity of low-energy electrons. The high reflectivity allows significant numbers to survive the 80- to 100-ns gap between bunch passages. Reduction of the electron cloud by beam scrubbing over time and by using several measures to enhance Landau damping have permitted us to stably store peak proton intensities up to 10 μC/pulse (6×10^{13} protons/pulse), which is a factor-of-2 improvement compared to the value achieved before these improvements.

References

1. R.J. Macek et al., Los Alamos National Laboratory report LALP-02-142.
2. R.J. Macek, in *Proceedings of ECLOUD'02: Mini-Workshop on Electron-Cloud Simulations for Proton and Positron Beams* (CERN, 2002), 259-268.
3. D. Neuffer et al., *Nuclear Instruments and Methods A* **321**, 1 (1992).

Superconducting Spoke Cavities Demonstrate Excellent Performance

T. Tajima, F.L. Krawczyk, J.E. Ledford, J.-F. Liu, R.J. Roybal, D.L. Schrage, A.H. Shapiro (LANSCE Division), R.C. Gentzlinger, D.I. Montoya (ESA Division), R.L. Edwards (MST Division)

Superconducting radio-frequency (SCRF) cavities have been successfully used in electron accelerators and for high-velocity ($\beta = v/c = 1$) particles and low-velocity heavy ions. However, a recent trend is to apply SCRF technology to intermediate velocity particles by shortening the accelerating gap (which is proportional to β) in successful $\beta = 1$ elliptical cavities. However, shortening the gap does not work well for $\beta < 0.4$ because of mechanical weakness and multipacting within the cavity. A more promising approach is to use a structure called a spoke cavity (also known as a spoke resonator). In tests on a spoke cavity from Argonne National Laboratory, where this technology was originally developed,[1,2] we confirmed that it exhibits good performance. In addition, we designed, procured from industry, and tested two other $\beta = 0.175$ two-gap spoke cavities in 2002 in support of the Advanced Accelerator Applications (AAA) program at LANL.[3-5] These cavities have also shown excellent results.

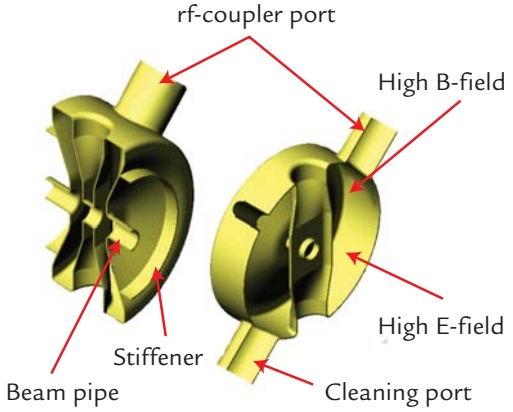

Fig. 1. Cut-away views of the inside of the spoke cavity.

Testing Spoke Cavities for Advanced Accelerator Applications

Figs. 1 and 2 show cut-away views of the inside of the cavity and a photograph of the cavity. It consists of a spoke in a 40-cm-diam barrel. The particle acceleration occurs in the two gaps between the spoke and the end walls. The 5-cm beam aperture is large enough for the cavity not to be activated by the proton beam.

The major radio-frequency (rf) design parameters are shown in Table 1. The ratios of peak-surface-electric and -magnetic fields to accelerating gradient were well optimized. This has helped our cavities achieve the highest accelerating gradient among other existing cavities in the world.

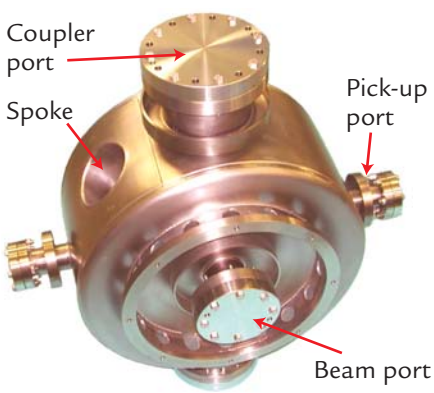

Fig. 2. A photograph of the spoke cavity, which is made of 3.5-mm-thick niobium sheets. Two cavities were fabricated on schedule by E. Zanon, an Italian manufacturer of pressure vessels.

Test Results

We tested the mechanical properties at room temperature and measured the cavity quality factor (Q_0) as a function of accelerating gradient (E_{acc}).[4] Fig. 3 shows the Q-E curve of one of the cavities. This cavity (EZ01) reached an E_{acc} of 13.5 MV/m, and the second cavity (EZ02) reached an E_{acc} of 12.9 MV/m. The design goal of the AAA project is 7.5 MV/m with a Q_0 of 5 x 10^8 (i.e., a loss of ~ 10 W). Our excellent results ensure the highly reliable operation required for transmutation of waste projects.

Table 1. rf design parameters.[3]

Q_0 (4 K)	1.05 x 10^9 (for 61 nΩ)
T (βg)	0.7765 (βg = 0.175)
T_{max}(β)	0.8063 (at β = 0.21)
G	64.1 Ω
E_{pk} /E_{acc}	2.82
B_{pk} /E_{acc}	73.8 G/MV/m
P_{cav} (4 K)	4.63 W at 7.5 MV/m
R/Q	124 Ω

Future Prospects

Because of increased interest in spoke cavities, we held an international workshop on this subject at LANL in October 2002.[6] It is likely that spoke cavities will be developed and used for future proton and heavy-ion accelerators designed for studies in neutron science, nuclear waste transmutation, rare-isotope physics, and other related areas.

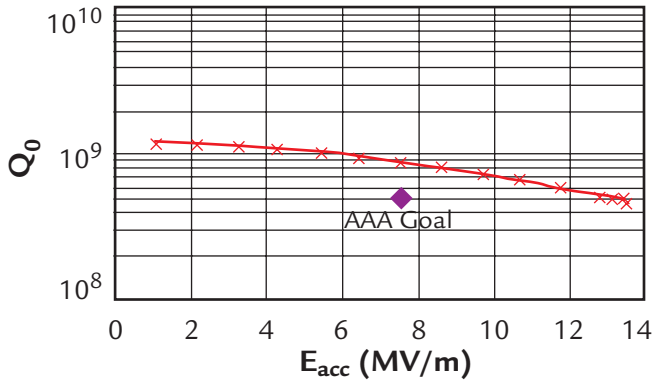

Fig. 3. The cavity quality factor Q_0 as a function of accelerating gradient E_{acc}. These data are of the first cavity (EZ01). The second cavity (EZ02) exhibited a similar curve and reached an E_{acc} of 12.9 MV/m.

Acknowledgements

We would like to thank Bill Clark and the LANSCE-1 Machine Shop personnel for helping us prepare for the spoke-cavity tests. We also would like to acknowledge the continuous support and encouragement of Mike Cappiello, Dominic Chan, Andy Jason, and Rich Sheffield.

References

1. F.L. Krawczyk et al., Los Alamos National Laboratory report LALP-13943-PR (2001).
2. T. Tajima et al., in *Proceedings of the 2001 Particle Accelerator Conference,* 18-22 (2001).
3. F.L. Krawczyk et al., in *Proceedings of the European Particle Accelerator Conference* (2002).
4. T. Tajima et al., in *Proceedings of the International Linear Accelerator Conference* (2002).
5. See http://laacg1.lanl.gov/scrflab/spoke.html.
6. See http://laacg1.lanl.gov/spokewk/.

Beam-Halo Experiment in the High-Current Proton Beam of the Low-Energy Demonstration Accelerator

R.W. Garnett, J.D. Gilpatrick, W. Lysenko, R.L. Sheffield, T.P. Wangler (LANSCE Division), K.C.D. Chan, P.L. Colestock, J.D. Schneider (NIS Division), C.K. Allen (SNS Division), H.V. Smith (DX Division), M.E. Schulze (General Atomics), K.R. Crandall (TechSource), J. Qiang (Lawrence Berkeley National Laboratory)

A unique and systematic experimental study of beam-halo formation in a high-current proton beam was carried out using the 6.7-MeV proton beam propagating in a 52-quadrupole periodic-focusing channel at the Low-Energy Demonstration Accelerator (LEDA) facility.[1] Emittances and beam widths were obtained from measured profiles for comparisons with maximum-emittance-growth predictions of a free-energy model and maximum-halo-amplitude predictions of a particle-core model. The experimental results support both models and the present theoretical picture of beam-halo formation.

Beam halo can be a major source of beam loss and induced radioactivity, which limits the beam intensity in high-beam-power proton linear accelerators (linacs). Understanding the mechanisms of halo formation is important for a new generation of high-intensity linacs with future applications in spallation-neutron sources; neutrino factories; and accelerator-driven, subcritical reactors for nuclear-waste transmutation. Theoretically, emittance growth relates to the conversion of *beam free energy* caused by mismatch oscillations into the *thermal energy* of the beam. For a given mismatch strength, the free-energy model determines the maximum growth in emittance resulting from the complete transfer of free energy into emittance.[2] The particle-core model provides a physical mechanism of halo formation.[3-5] In this model, beam mismatch produces an imbalance between beam focusing, space charge, and emittance. This imbalance excites an oscillation of the beam core. The space-charge field of the oscillating core modulates the net focusing force acting on individual particles and drives particles in a nonlinear parametric resonance.[4] The model predicts a maximum-resonant-particle amplitude as a function of the mismatch strength.[5] The objective of the halo experiment was to test these two halo-formation models — the free-energy model and the particle-core model.

Description of the Experiment

To test these two theoretical models, we installed a 52-quadrupole, periodic-focusing, 6.7-MeV beam-transport channel (see Fig. 1) at LEDA.[6] An 11-m channel length was sufficient for developing about 10 mismatched oscillations.

The most important diagnostic elements were the transverse beam-profile scanners and pairs of graphite scraper plates.[7] Each scanner contains a 33-μm-diam carbon wire for measuring the beam profile of the dense beam core. The graphite scraper plates were used to measure the outer beam profiles. The magnitudes of the charges detected from the wires and the plates are combined in the software to produce a single beam-profile distribution. Scanners at nine stations, each located midway between pairs of quadrupoles, measured the horizontal and vertical beam distributions. The beam was matched by adjusting the first four quadrupoles to produce equal root-mean-square (rms) sizes at the last eight scanner locations. The mismatch strength for mismatched beams was measured by a parameter μ, which is defined as the ratio of the rms size of the initial beam to that of the matched beam. For a perfect match, μ = 1.

Fig. 1. The 52-quadrupole-magnet beam line for the halo experiment.

Experimental Results and Comparison with Theory

Fig. 2 shows the matched and mismatched 75-mA beam profiles at the last scanner. For the matched beam, we observed a low-density halo that extended as far as 9 rms. This matched-beam halo was observed at all scanners and was most easily explained as a halo that has formed before the periodic quadrupole channel. However, halo caused by beam mismatch was our main interest because the mismatch mechanism is expected to involve more particles and can form a halo even at high energy where collimation becomes more difficult. A mismatch beam profile for μ = 1.5, as seen in Fig. 2, shows the growth of shoulders, which indicates substantial halo formation.

The free-energy model can be tested by comparing the measured emittance growths, obtained from the rms-size measurements, with the emittance-growth upper limits from that model. Fig. 3 shows the x-y averaged rms-emittance-growth results (points with error bars) versus μ for a 75-mA mismatch. The maximum-emittance-growth curves from the free-energy model are shown for the two tune-depression values (i.e., particle frequencies reduced by space charge) that bracket the values for the debunching beam. The theoretical maximum is insensitive to the tune depression over this range. The data in Fig. 3 are consistent at all μ values with the maximum emittance growth predicted by the free-energy model.

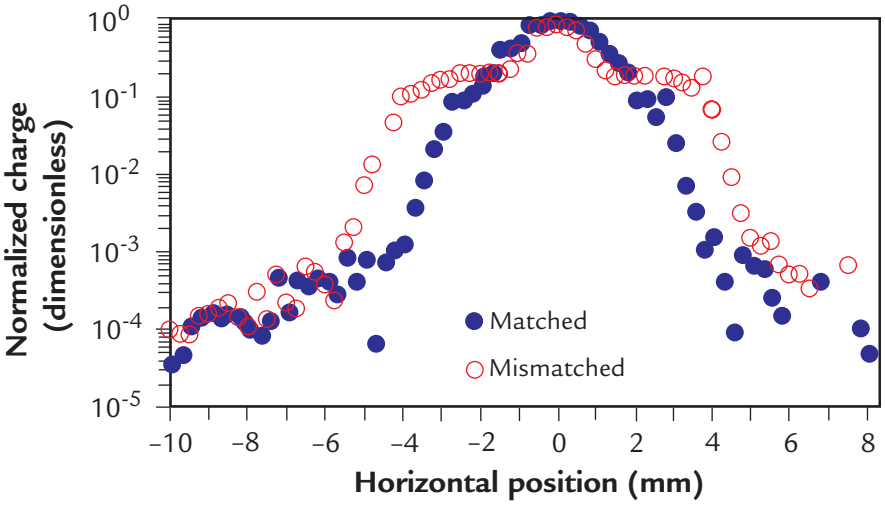

Fig. 2. Horizontal beam profiles at the last scanner for a current of 75 mA. These results show a μ = 1 matched beam (blue solid circles) and a μ = 1.5 mismatched beam (red open circles).

The particle-core model predicts the maximum-resonant-particle amplitude as a function of mismatch parameter μ.[5] We compared the measured 75-mA-beam half widths at three different fractional beam-profile intensity levels (10%, 1%, and 0.1% of the peak) with the maximum amplitude predicted by the particle-core model (Fig. 4). The shapes of all three measured half-width curves are consistent with the shape of the maximum-amplitude curve from the particle-core model, and all three measured curves lie below the maximum-amplitude curve from the particle-core model.

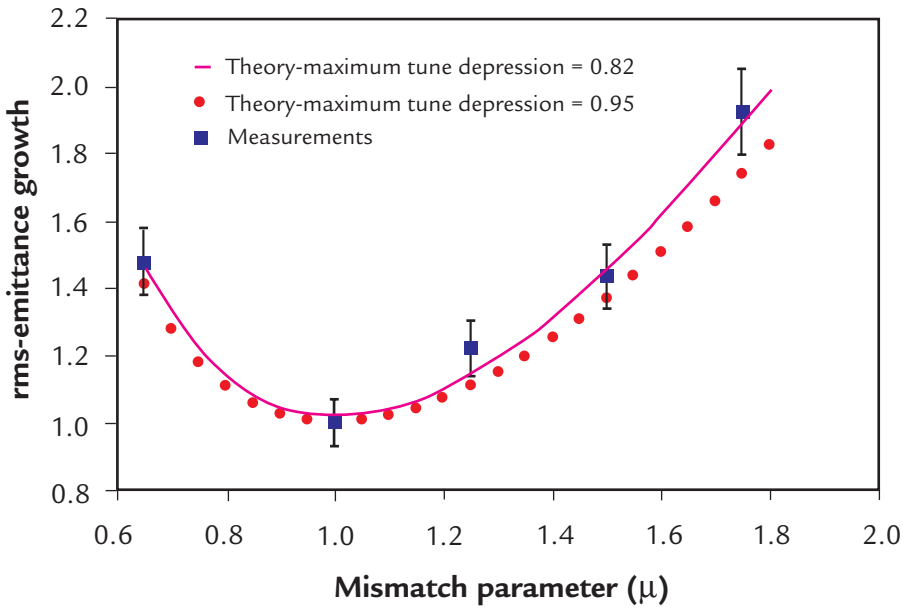

Fig. 3. Measured rms-emittance growth averaged over x and y for a current of 75 mA. The curves show maximum growth from the free-energy model.

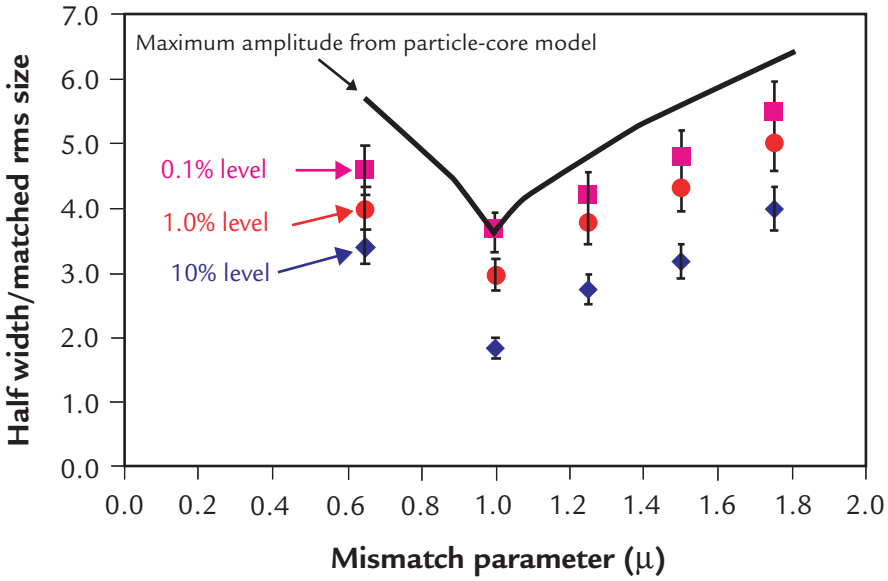

Fig. 4. Measured 75-mA beam half widths at different fractional-intensity levels versus mismatch strength μ for comparison with the maximum-resonant-particle amplitude of the particle-core model.

Conclusion

Our experiment strongly supports both models and the present theoretical picture of halo formation in mismatched beams. This result is important because these models predict upper limits to emittance and halo-amplitude growth in high-current transport channels and linacs. These models also allow for the estimation of focusing strength and aperture requirements in future designs.

References

1. C.K. Allen et al., *Physical Review Letters* **89** (21) 214802 (2002).
2. M. Reiser, *Theory and Design of Charged Particle Beams* (John Wiley & Sons, Inc., New York, 1994), p. 477; M. Reiser, *Journal Applied Physics* **70**, 1919 (1991).
3. J.S. O'Connell et al., in *Proceedings of the 1993 Particle Accelerator Conference* (IEEE Catalog No. CH3279-7, 3657-3659).
4. R.L. Gluckstern, *Physical Review Letters* **73**, 1247 (1994).
5. T.P. Wangler et al., *Physical Review ST-AB* **1**, 084201 (1998).
6. P.L. Colestock et al., in *Proceedings of the 2001 Particle Accelerator Conference* (IEEE Catalog No. 01CH37268, 170-172).
7. J.D. Gilpatrick et al., in *Proceedings of the 2001 Particle Accelerator Conference* (IEEE Catalog No. 01CH37268, 525-527).

Development and Testing of High-Power Vacuum Windows for the Spallation Neutron Source

K.A. Cummings, J.M. De Baca, J.S. Harrison, M. Rodriguez, P.A. Torrez (LANSCE Division), D.K. Warner (SNS Division)

Historically, radio-frequency (rf) windows are a common point of failure in power couplers used to couple the rf power into the accelerator; therefore, reliable rf windows are critical to the success of the Spallation Neutron Source (SNS) project. The normal-conducting SNS linac requires six rf windows at 402.5 MHz and eight at 805 MHz. Each window transmits up to 180 kW of average power and 2.5 MW of peak power at 60 Hz with 1.2-ms pulses. Thales — a French company that manufactures rf windows and klystrons — was selected as the vendor for both the 402.5- and 805-MHz windows based on a technical and cost evaluation. Windows must pass low-power acceptance tests at the vendor's facility and high-power tests at LANL. The high-power tests involve both average-power and peak-power tests. The high-average-power test conditions the windows for typical operating conditions on the accelerator, whereas the high-peak-power test conditions the windows for the cavity-fill transient. All windows have passed low-power tests. Two 402.5-MHz and two 805-MHz windows have been high power tested. This article describes the high-power test runs and results to date.

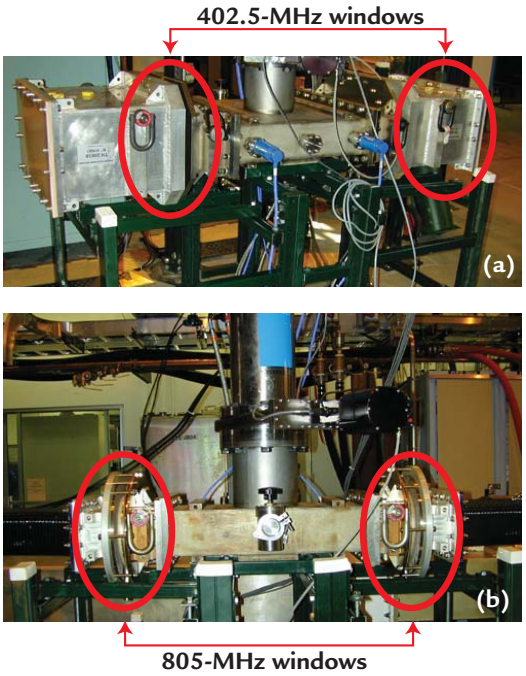

Fig. 1. (a) 402.5-MHz and (b) 805-MHz windows and vacuum waveguides.

Experimental Setup

Window geometry. The geometry of the 402.5- and 805-MHz windows that we used in these test runs is a planar configuration (Fig. 1). The vacuum side of both windows is a copper-plated stainless-steel waveguide, and the air side is an aluminum waveguide. The 402.5-MHz windows consist of one half-height WR 2100 waveguide on the vacuum side and one full-height WR 2100 waveguide on the air side. The 805-MHz windows consist of a full-height WR 975 waveguide on both the air and the vacuum side. The ceramic in both windows is a high-purity alumina ceramic.

Test-Stand Configuration and Diagnostics

Our high-average-power and high-peak-power tests required different test configurations. In the high-average-power test, the forward power was transmitted through the windows into a matched load, as shown in Fig. 2. The peak-power setup was the same, but instead of using a load, we employed a sliding short (a metal plate that reflects all power). Windows were subjected to full average power and duty factor (the effective time that the rf power is on) for 4 hours. They were then subjected to an effective 10-MW forward power by transmitting 2.5-MW of forward power into a short and varying the phase of the standing wave. The sliding short was moved from 0° to 180° to ensure that no arcing or breakdown problems would occur in any part of the window.

We measured the rf power with four directional couplers (Fig. 2) and the vacuum pressure with two interlocked ion gauges that turn off the rf power if the pressure rises above 1×10^{-7} torr. The water inlet, outlet, and surface temperatures were also measured. Fiber-optic arc detectors were used on both the air and vacuum sides of the ceramic. If an arc was detected, an interlock turned off the rf power for 1.6 s. A LabVIEW data-acquisition system was used to record, monitor, and display the rf power, pressure, water inlet, and outlet temperatures, as well as the number of arcs detected.

Experimental Results

High-temperature bakeout results. A high-temperature vacuum bakeout was done to release particles and water vapor embedded in the ceramic- and vacuum-waveguide surfaces. The bakeout is essential to conditioning the windows successfully and expediently. The windows are held between 150°C to 200°C until the pressure drops below 5×10^{-7} torr, as shown in Fig. 3.

High-power test results. The conditioning procedure consists of beginning with a low duty factor and gradually increasing the power. Then power is lowered, the duty factor is increased, and the power is gradually raised at the new duty factor. Peak power versus time is shown in Fig. 4 for the 805-MHz windows. Once the windows are conditioned, the 4-hour heat run is done at full power and duty factor, which is also illustrated in Fig. 4. It took about 10 hours to condition the 805-MHz windows to the full power and duty factor. There were only a few arcs and the conditioning rate was limited by the pressure, as expected.

It took 5 hours to condition the 402.5-MHz windows to 500 kW. The available power-supply voltage was limited, thus we ran at 500 kW for 7 more hours. Once the full power-supply capacity was available, we conditioned quickly up to the full power. We did not finish the average-power testing or begin the peak-power testing on the 402.5-MHz windows because of problems with the power supply.

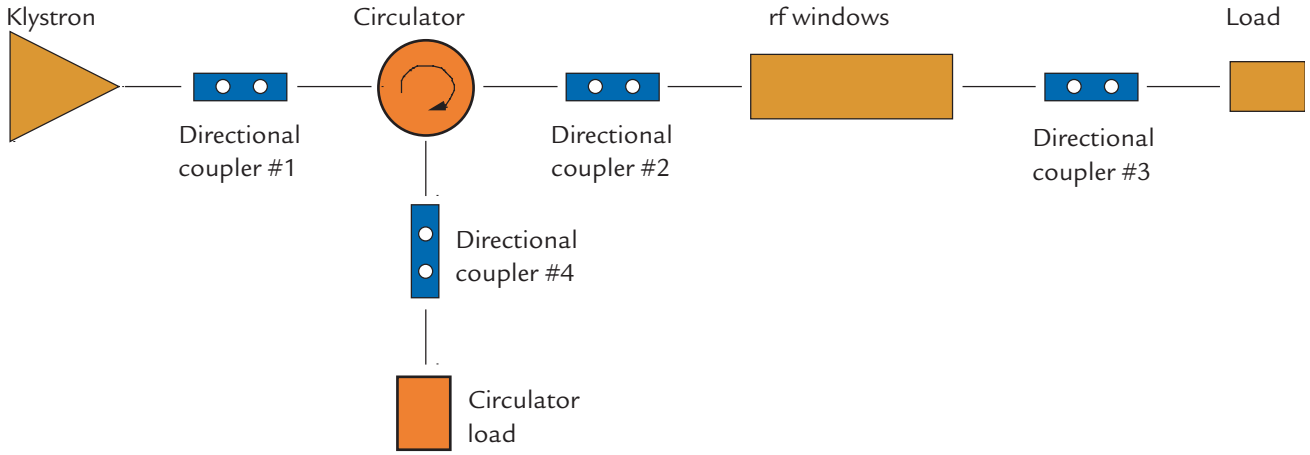

Fig. 2. Test schematic for the average-power tests.

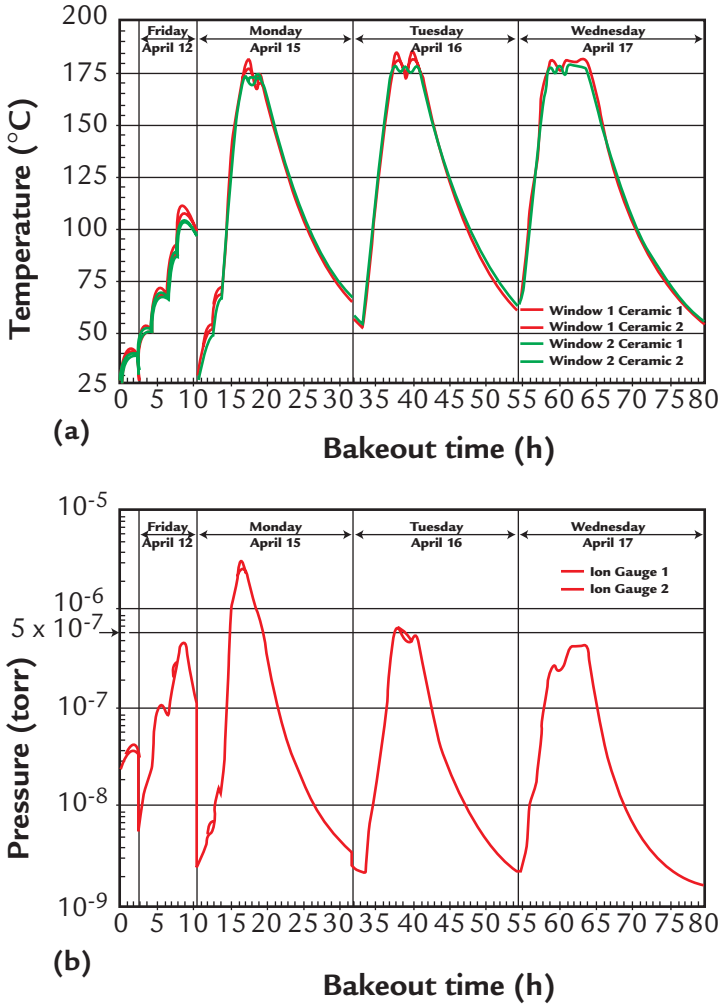

Fig. 3. Temperatures and pressure versus time. (a) 805-MHz window temperatures during bakeout. (b) Vacuum pressure during bakeout.

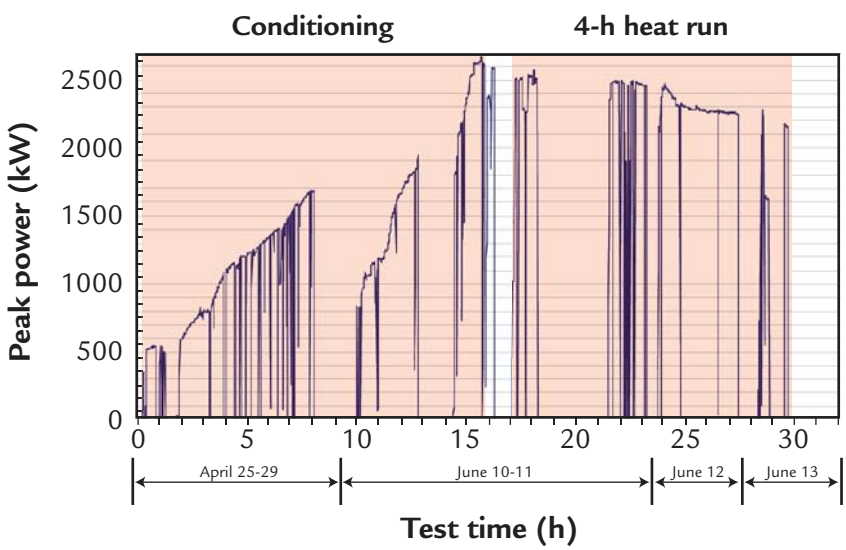

Fig. 4. Peak forward rf power versus test time for the 805-MHz windows.

Conclusion

Two of the eight 805-MHz windows have been successfully tested, and two of the six 402.5-MHz windows have been successfully baked out and conditioned. When the test stand is available, we will finish testing the 402.5-MHz windows. The test results so far are very encouraging because they prove the design concept of the windows. Once all the windows are tested, we will discuss the variation between individual windows.

Design of a Radio-Frequency System for the Spallation Neutron Source

D.E. Rees, M.T. Lynch, W.T. Roybal, K.A. Cummings (LANSCE Division), P.J. Tallerico, T.W. Hardek, J.T. Bradley (SNS Division)

The Spallation Neutron Source (SNS) includes a nominally 1,000-MeV, 1.4-mA, average-current proton linear accelerator (linac) consisting of a radio-frequency quadrupole (RFQ), a drift-tube linac (DTL), a coupled-cavity linac (CCL), a medium- and high-beta superconducting (SC) linac, and two buncher cavities for beam transport to the proton storage ring. LANSCE-5 is responsible for the high-power radio-frequency (rf) systems for all sections of the pulsed SNS linac. These rf systems must support a 1-ms beam pulse up to a 60-Hz repetition rate. All of the rf hardware for the SNS linac is currently in production (Fig. 1). Achieving a reasonable cost with the large number of high-power klystrons needed for the SNS linac was a challenge.

Fig. 1. View of two SNS 805-MHz klystrons. On the left is the CPI 550-kW klystron and on the right is the Thales 5-MW klystron.

Design of the Radio-Frequency System

The partitioning of the rf system for the SNS linac is illustrated in Fig. 2. The RFQ and DTLs are driven by pulsed, 2.5-MW, 402.5-MHz klystrons. These accelerating structures are followed by four CCL cavities. A single pulsed, 5-MW, 805-MHz klystron provides power to each CCL cavity. The power from each klystron is split, and the cavity is driven through two rf windows. The CCL cavities are followed by 81 SC cavities, each of which is driven by a pulsed, 550-kW klystron.

The klystrons are sized to allow at least 25% power overhead in the room-temperature portion and as much as 40% in the high-beta SC linac for fast-cavity-field control and transmission and reflection loss. Two variations of a similar power-supply design are used for the linac rf systems. The RFQ, DTL, and CCL klystrons use a 140-kV, 90-A, pulsed power supply capable of an average power of 1 MW and a peak power of 11 MW. The SC linac uses an 80-kV, 140-A, pulsed power supply capable of 1 MW of average power and 11 MW of peak power. Because rf-station requirements are well below the tube rating for the RFQ and first two DTL cavities, one power supply is used to run these three systems. For the remainder of the DTL rf stations, two 2.5-MW klystrons share a single power supply. For the CCL rf stations, one 140-kV power supply is required for each klystron. The first 48 klystrons (rated at 550 kW) are run at less than maximum power and are fed in 12 groups from 4 power supplies. The next 33 klystrons (rated at 550 kW) are run at close to maximum power and are fed in 11 groups from 3 power supplies due to the 11-MW peak power.

SNS klystrons do not have a modulating anode. The klystron gun is a diode gun, and the cathode voltage from the pulsed power supply determines the klystron beam current. Table 1 lists the klystron parameters. Because the cathode voltage determines the klystron beam current, the system design must accommodate variations in the klystron perveance and end-of-life klystron operation. When operating 12 klystrons from a common power supply, the tube with the lowest perveance will set the operating voltage for the entire group of klystrons. Eliminating the modulating anode was motivated by experience at other laboratories, the reduction in cost of the klystron and associated electronics, and the improvement of rf-system availability.

Radio-Frequency Equipment for the Spallation Neutron Source

Klystrons. The SNS klystrons are supplied by four manufacturers. The specifications of the SNS klystrons are included in Table 1. The 2.5-MW, 402.5-MHz klystrons (Fig. 2a) were supplied by E2V Technologies; the 5.0-MW, 805-MHz klystrons were supplied by Thales; and the 550-kW, 805-MHz klystrons were supplied by CPI and Thales. The klystrons operate in a vertical orientation with localized shielding and are mounted to a socket

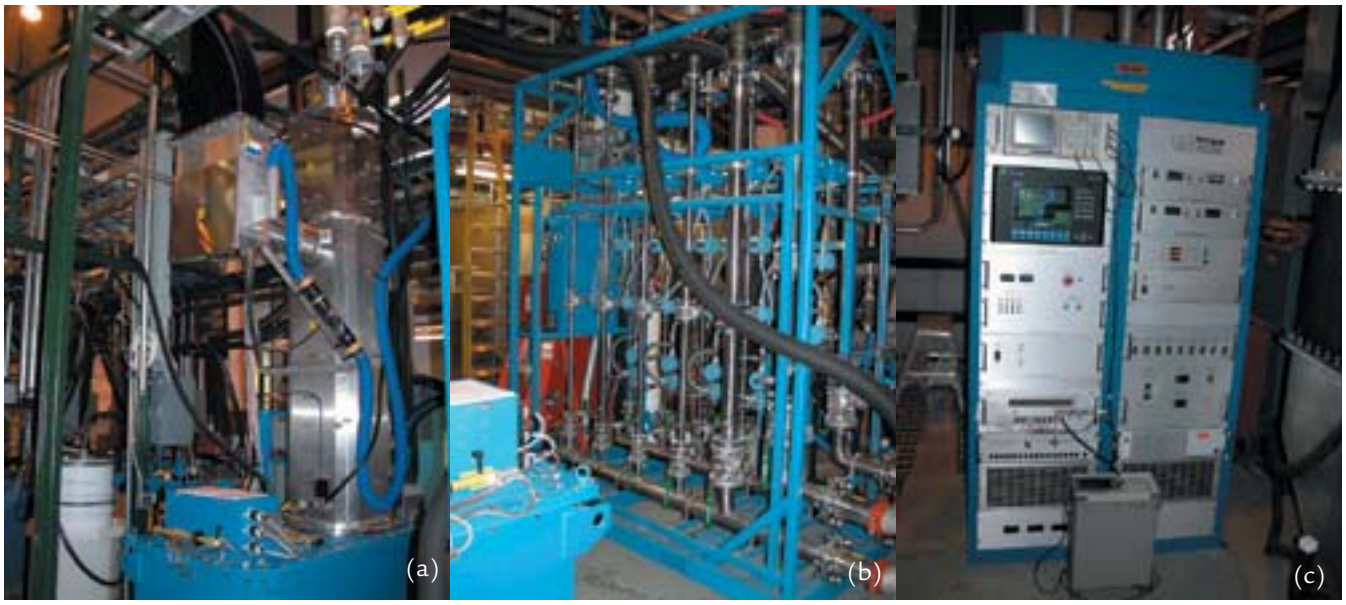

Fig. 2. Each transmitter in the room-temperature portion of the SNS linac supports a single 2.5-MW or 5-MW klystron. (a) A 402.5-MHz klystron mounted on a transmitter oil tank. (b) The transmitter subsystem for the water-cooling flow control and diagnostics for the klystron. (c) The transmitter control rack.

Table 1. SNS-klystron-operating parameters.

Minimum peak power	2,500 kW	5,000 kW	550 kW
Test power	2,750 kW	5,500 kW	605 kW
Frequency	402.5 MHz	805 MHz	805 MHz
Duty factor	8%	8%	9%
Minimum efficiency	58%	55%	65%
Maximum beam voltage	125 kV	140 kV	75 kV
Bandwidth (at 1dB)	1.0 MHz	2.6 MHz	2.6 MHz
Height	13 ft	13 ft	9 ft

attached to the lid of the tank of dielectric oil. They are protected from high reflected power by a circulator. The 805-MHz klystrons have a separate magnet, and the 402.5-MHz klystron has an integral magnet. As of the end of CY 2002, seven 402.5-MHz klystrons have been delivered. CPI delivered six 550-kW, 805-MHz klystrons, and Thales delivered one 5-MW, 805-MHz klystron.

Transmitters. The transmitters in the SNS rf systems comprise the support systems for the klystrons. They are being provided by Pulsed Sciences Division of the Titan Systems Corporation. Transmitter subsystems include the following:

- water-cooling flow control and diagnostics,
- a filament power supply for each klystron,
- magnet power supplies for each klystron,
- a solid-state preamplifier for each klystron,
- a vacuum-ion-pump power supply,
- an oil-filled tank(s) for high-voltage connections to the klystrons,
- safety interlocks and equipment interlocks,
- a programmable-logic-controller interface, and
- klystron-overcurrent diagnostics.

Each of the transmitters for the RFQ, DTL, CCL, and high-energy beam transport (HEBT) is designed to support a single 2.5-MW or 5-MW klystron. These transmitters consist of a control rack, a cooling diagnostics cart, and a klystron high-voltage tank, as shown in Fig. 2.

The transmitters for the SC portion of the linac are significantly different. The SC-linac design requires many smaller klystrons. Cost and floor-space constraints forced us to develop a transmitter design capable of supporting six 550-kW klystrons per transmitter. These transmitters consist of a four-cabinet control rack, a cooling diagnostics cart, and two klystron high-voltage tanks capable of supporting three klystrons each, as shown in Fig. 3.

Each of the six klystron sockets have an individual filament transformer, but all six sockets are connected to a single high-voltage connection input. Energy stored in stray capacitance can damage a klystron during an arc. To prevent damage from occurring, the six filament transformers are designed to have a total stray capacitance of less than 1,000 pF.

Compared to the transmitters in the room-temperature portions of the linac, the floor space of the control rack in the SC portion of the linac is only doubled, the floor space of the cooling cart is the same, and the floor space of the klystron high-voltage tanks is less than five times as large. Significantly reducing the number and sophistication of the diagnostics and interlocks within the transmitters allowed us to increase the number of klystrons supported per unit of floor space and per unit of cost.

For example, transmitters in the SC portion of the linac will monitor only a threshold value of water flow in each cooling circuit, whereas transmitters in the room-temperature portions of the linac will measure

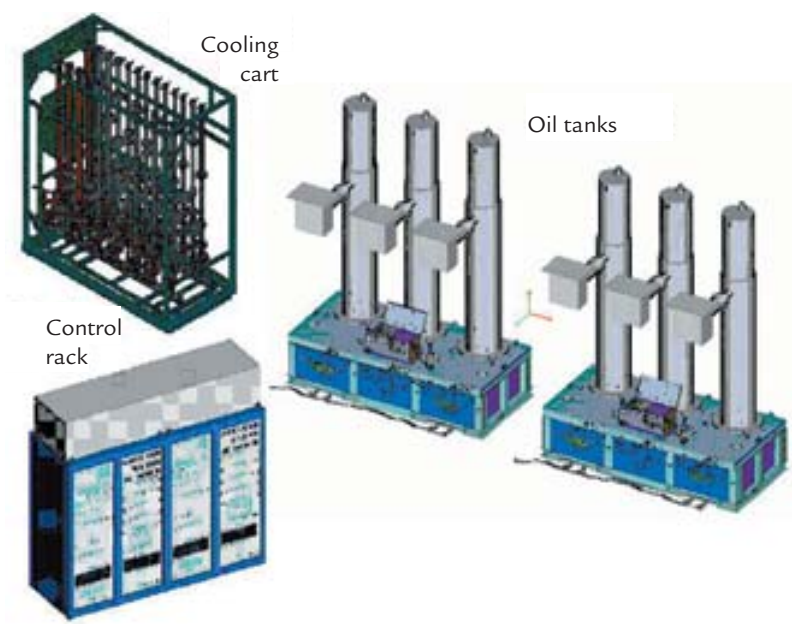

Fig. 3. Each transmitter in the SC portion of the linac can support up to six 550-kW klystrons.

and display flow rates and inlet and outlet temperatures and calculate dissipated power in each cooling circuit. We made further reduction in cost and space by providing power to the six klystron ion pumps from a single power supply with a single overcurrent interlock. These changes will reduce the initial cost required to diagnose a faulty klystron.

Conclusion

As of the end of CY 2002, all 19 transmitters for the room-temperature portion of the SNS linac have been delivered, 5 have been installed, and 3 have been commissioned. Final assembly of the first transmitter for the SC portion of the SNS linac was completed, and integration testing at the vendor's facility has begun.

Development of a Polyphase-Resonant-Converter Modulator for the Spallation Neutron Source

W.A. Reass, S.E. Apgar, D.M. Baca, J.M. Gonzales, R.F. Gribble, P.G. Trujillo (SNS Division), J.D. Doss (NIS Division)

We have developed new methodologies and techniques to generate high voltages [i.e., pulsed or direct current (dc)] with a high average power from a low-voltage input source (e.g., ±1.2 kV). This technology, as presently developed, is being used with the radio-frequency (rf) klystron amplifiers for the Spallation Neutron Source (SNS) accelerator at Oak Ridge National Laboratory (ORNL). The SNS klystron systems will operate up to 140-kV and 1.1-MW average power. The polyphase-resonant-converter modulator borrows many components from the traction-motor industry, such as insulated-gate bipolar transistors (IGBTs) and self-clearing metallized hazy-polypropylene traction capacitors. Hazy polypropylene is a polypropylene plastic with a rough surface; this plastic is important in facilitating the wicking of insulating oil between capacitor layers. An aluminum vapor is deposited onto the surface of the plastic in vacuum (i.e., metallized). In addition, the use of an amorphous nanocrystalline transformer alloy, which was also developed for the SNS effort, permits high-frequency power-conversion techniques with low loss and small size.

Other new techniques engineered for the converter-modulator topology are polyphase-resonant-voltage multiplication and resonant rectification. These techniques offer a reduced size (~ 10 times) and improve electrical efficiency as compared to previous technologies. Because of the resonant-conversion techniques, crowbars and other load-protective networks are not required. A shorted load de-tunes the resonance, which results in little power transfer. This technique provides for a high-power and high-voltage system that is inherently self-protective. To provide regulated voltages, pulse-width modulation (PWM) of the individual IGBT pulses is used to regulate the output voltage. A digital signal processor (DSP) is used to control the IGBTs with adaptive feedforward and feedback control algorithms that improve pulse fidelity. The converter modulator (Fig. 1) has many attributes that make it attractive for various pulsed- and high-power applications, such as high-power rf sources, neutral-beam modulators, high-voltage process systems (e.g., flue gas scrubbers), and high-voltage dc power supplies.

Fig. 1. Converter-modulator assembly.

Converter-Modulator Development

The SNS is a new 1-GeV accelerator with a 1.4-MW average-power proton beam. The accelerator requires 15 converter-modulator stations, each typically providing 10-MW pulses with up to 1,100-kW average power. Two variants of the converter modulator include an 80-kV and a 140-kV design that share a common topology with many interchangeable parts. Each converter modulator derives its buss voltage from a standard 13.8-kV to 2,100-Y (1.5-MVA) cast-core-transformer substation, which is also typically used in traction applications. The SNS substations also include harmonic traps and filters to improve power factor and minimize utility-line disturbances. Each substation is followed by a silicon-controlled-rectifier regulator that accommodates system voltage changes from no load to full load.

Energy storage and filtering is provided by specially developed low-inductance self-clearing metallized hazy-polypropylene traction capacitors. These capacitors do not short but instead clear any internal anomaly, thus providing a lifetime of over 300,000 hours. Three H-bridge IGBT-switching networks are used to generate the polyphase 20-kHz boost-transformer primary drive waveforms, which are chirped for the appropriate duration to generate the desired klystron pulse width. The PWM of individual 20-kHz pulses is used to provide regulated output waveforms with DSP-based adaptive feedforward and feedback techniques. Capacitive tuning is used on the boost transformer secondary to resonate the leakage inductance. The resonant condition of the boost transformer and the three phase interconnections result in the effect of polyphase-resonant-voltage multiplication.

Even though the transformers are wound with a 1:19 turns ratio, the output is over 1:60. This added benefit results in additional size reduction and increased electrical efficiency. The important design feature of this transformer is that it is wound for leakage inductance, not turns ratio. The resonant topology has the added benefit of being self-protective in a klystron fault (i.e., shorted output). The resonant conditions are spoiled, and little energy transfer can occur. This design feature obviates the need for crowbars and other related protective networks.

The IGBT-switch-plate assemblies (Fig. 2) are designed for easy removal, maintenance, and repair and can be accommodated off-line. Each switch plate contains four (3,300-V, 1,200-A) IGBTs, in an H-bridge configuration.

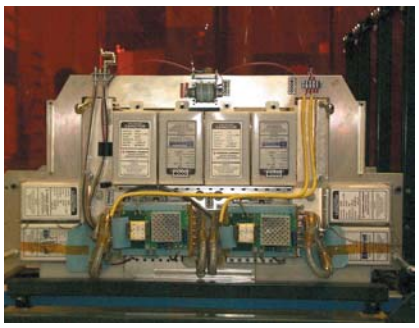

Fig. 2. IGBT-switch-plate assembly.

The amorphous nanocrystalline boost transformer (Fig. 3) has exceptional performance as a function of frequency and flux density with the added benefit of having zero magnetostriction. The transformer does not vibrate or make significant noise when excited. The windings on the core are wound as two single-layer solenoids with a 1:19 turns ratio for the 140-kV-output configuration.

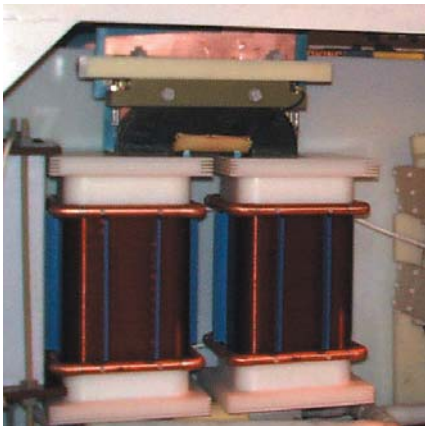

Fig. 3. The 330-kW, 140-kV amorphous nanocrystalline boost transformer.

Conclusion

The polyphase-resonant-converter modulator has demonstrated several new design methodologies that are expected to revolutionize high-power, long-pulse modulators and high-voltage dc power supplies. These new technologies include special low-inductance, self-clearing capacitors; large, amorphous nanocrystalline cut-core transformers; high-voltage and high-power polyphase-resonant-conversion techniques; and adaptive DSP methods for high-power supplies. Design economies are achieved by using industrial traction components such as cast power transformers, IGBTs, and self-clearing capacitors. The compact and modular design minimizes on-site construction, and a simplified scheme for interconnecting utilities further reduces installation costs. The design does not require high-voltage capacitor rooms and related crowbars. By generating high voltage when needed, reliability and personnel safety are greatly enhanced.

Acknowledgements

The authors would like to thank John Sullard, Adam Martinez, and Diego Jaramillo for their assistance.

Development of a New 201.25-MHz Power Amplifier

J.T.M. Lyles, S.F. Archuletta, D.C. Clark, J.L. Davis, G.R. Roybal (LANSCE Division)

The radio-frequency (rf) team at LANSCE is developing replacement systems for the 201.25-MHz rf plant for the drift-tube linear accelerator (DTL), which was commissioned over 30 years ago. The DTL consists of four large cavities, or tanks, which accelerate protons from 0.75 to 100 MeV before they are injected into the coupled-cavity linear accelerator (CCL) and boosted to 800 MeV for neutron research and proton radiography. Also at the 100-MeV energy, protons can be diverted to the new Isotope Production Facility for medical radioisotope production. Each tank is driven by a source of high-power rf from four nearly identical systems. These systems are made of a chain of successively more powerful rf amplifiers, starting with hundreds of milliwatts of power from a master oscillator and ending with as much as 3 MW of peak pulsed power for the largest tank. The larger two power amplifiers in each chain use gridded vacuum tubes as their active devices to convert direct current (dc) into rf at 201.25 MHz. This rf power creates extremely high rf voltages in the gaps between the drift tubes of the DTL where the protons are given their energy gain during each voltage alternation. This article describes our efforts to replace the intermediate amplifier with a new design, which also can be used as a high-power amplifier to drive the first DTL tank alone.

Continued Requirement to Use Vacuum Tubes

The lowest-level amplifiers have used silicon transistors for many years. This technology was installed up to the 5-kW level as a reliability improvement in 1994.[1] Transistors have the advantage of a long mean time to failure when properly rated and cooled in power amplifiers. However, vacuum tubes are still used in high-powered amplifiers, especially at the higher frequencies needed for proton, electron, and heavy-ion accelerators. They have finite life expectancies because they depend on the thermionic emission of electrons from a cathode or filament, which is consumed over time.

Modern gridded vacuum tubes are still based on the technology developed by DeForest, Langmuir, and others as early as 1907. Advances in ceramics and high-purity metals, manufacturing techniques, vacuum technology, and rf-circuit engineering have made them the primary choice for very high-power levels. At LANSCE, they are used in the intermediate and final amplification stages for each rf amplifier chain at the DTL.

A critical upgrade component is the intermediate-power-amplifier (IPA) stage, which generates 120-kW peak power at up to a 12% duty factor. Currently each IPA uses a Burle Industries, Inc., 4616 tetrode vacuum tube in an RCA Y1065 cavity amplifier. This unit is used to drive the final power amplifier (FPA), which uses a Burle Industries, Inc., 7835V4 triode vacuum tube in a larger cavity amplifier.

The long-term commercial viability of Burle Industries, Inc., has been of critical concern because the company has repeatedly been for sale. A gradual reduction in the size of their technical staff has occurred through attrition since the company was purchased from RCA in 1987. Another problem has been the variable life expectancy of the 4616 tetrodes because of manufacturing changes and the ambient operating conditions in the amplifiers at LANSCE over the years. Lifetimes have varied from hundreds of hours to over 20,000 hours. A mean lifetime of 10,290 hours was calculated from 15 inoperative 4616 tetrodes in the past 4 years of operation. By comparison, the mean lifetime of 88 of these tetrodes recorded from 1972 to 1998 was 5,498 hours. Thus, it would appear that improvements are already under way. However, this trend can easily reverse as evident by a particularly bad period around 1995.

The first goal of the replacement program is to develop an alternate source that can operate at the same power gain and output power as the 4616 tetrodes, but with a long predictable life. This source should come from a reputable manufacturer with a long-term focus on the high-power vacuum-tube market. Many companies have been bought out or have closed their doors already as many rf components have become miniaturized on chips for today's tiny wireless devices. A new tube would be useful as a replacement for the IPA stage at DTL modules 2, 3, and 4 at LANSCE, driving the FPA in each.

Module 1 Situation

The first DTL tank accelerates protons to 5 MeV and requires approximately 12% of the peak power needed by each of the other three tanks. Early in LANSCE's history, various schemes were tried to implement a simple tetrode-based rf amplifier for this system. For various reasons all were unsuccessful, and a duplicate of the system for the other three higher-powered modules was installed in module 1. This wasted power, cooling capacity, and space led to a complex control system with many interlocks for the various components. These disadvantages have been overlooked when considered in the scope of the overall plant size, energy consumption, and complexity. In many ways, having a common module design has been a benefit for maintenance and operator training. However, a fundamental problem has remained because of the lack of adequate control of this large amplifier system when operating at such a reduced power level.

The magnitude of this problem can be understood by first explaining the need for rf-field stability. The accelerating rf field in the first DTL tank must remain absolutely stable as it acts on the relatively slow-moving protons (i.e., 10% of the speed of light). Any instability, including that which may be caused by overshoot or ringing of the rf voltages in the tank, can impart undesirable longitudinal motion to the protons or impart the wrong energy to them. These wayward protons are either lost in the machine or subsequently accelerated through the remaining length of the half-mile-long linear accelerator, causing additional problems. To prevent this loss of beam and degradation of beam quality, control systems monitor the rf-field stability and prevent the injection of protons into the linac if the fields are not kept within acceptable limits.

For module 1, these systems are often operated within a very narrow range of acceptance because of a suboptimal control system. The gain-bandwidth product of the FPA modulator and the performance of the *throttled-back* vacuum tubes themselves have affected the response of the system. Therefore, the second goal of this project is to replace the complex, oversized rf system driving DTL tank 1. The peak-power output would need to be 350 to 400 kW with some margin for tuning and higher power for a future high-peak-current beam of 21 mA. The new amplifier also would have application as a compact power source for other loads such as a 201.25-MHz rf quadrupole, a potential upgrade that could improve the performance of the LANSCE beam for many applications.

Development of a New Amplifier

To respond to these two needs, we have developed an rf-amplifier system at LANSCE that is based on a different tetrode vacuum tube from Thales Electron Devices, a worldwide manufacturer of electronic tubes. This company has invested in modern manufacturing equipment and continues to hire new engineers and scientists to develop improved products. LANSCE already has good experience with their tubes in other amplifiers.

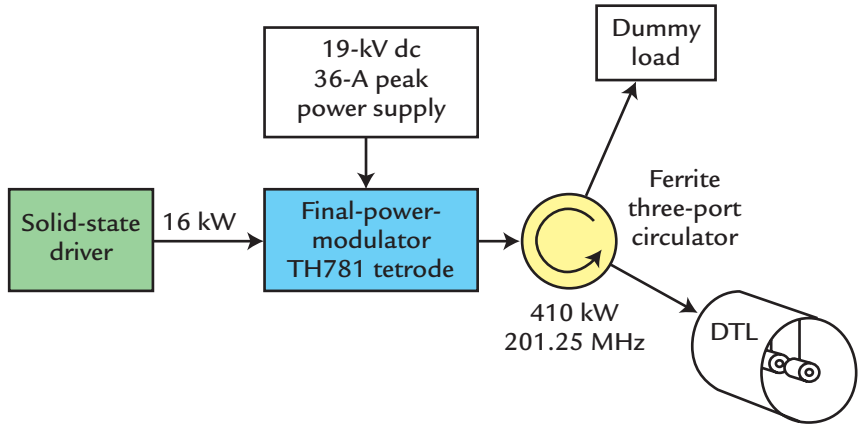

Fig. 1. Diagram of the amplifier layout for module 1. The IPA is shown in green, and the ferrite three-port circulator is shown in yellow.

The new amplifier uses a Thales Electron Devices TH781 tetrode in a Thales-designed cavity amplifier. The new tetrode uses pyrolytic graphite grids and an improved anode cooler, which both contribute to higher power capability and longer life expectancy. At these rf-power levels and frequencies, there are very few identical (drop-in) replacement vacuum tubes, which is the situation for the 4616-based amplifier. The new amplifier subsystem has been packaged as a standalone assembly to be tested with high peak power and high duty factor. After thoroughly testing this subsystem off-line, we will install this new component at module 1 (Fig. 1). The ferrite three-port circulator — a standard coaxial-transmission-line component from a commercial television supplier — will prevent reflected power from the tank from reaching the tetrode amplifier. Instead, it sends the power to a water-cooled dummy-load resistor.

Ancillary Systems

As the IPA in modules 2 through 4, the new amplifier will replace the existing 4616 stage, using the same power supplies, solid-state driver amplifier, and cooling connections. For the module 1 standalone application, the existing high-voltage capacitor bank, transformer rectifier, and heat-removal system will be used after reconfiguration. The elimination of the modulator and large FPA of the present system will reduce the plant-cooling demand. A new programmable logic controller is being developed to provide start-up and interlock functions for the amplifier to replace the existing panel with over 60 mechanical relays in module 1. The new tetrode stage needs approximately 16 to18 kW of drive at module 1, which is beyond the capability of the existing 5-kW solid-state driver amplifier. The new amplifier assembly is shown in Fig. 2.

Fig. 2. The new amplifier assembly.

Band II television transmitters are capable of this performance but with the penalty of high cost, large size, excess bandwidth, and complexity. Magnetic-resonance-imaging (MRI) systems have demonstrated linear solid-state amplifiers with 10 kW at 10% duty factor.[2] We are investigating these MRI systems from several manufacturers to drive the tetrode at tank 1. We are also considering retrofitting the existing 5-kW driver amplifiers with more powerful solid-state modules to reach our goal. Table 1 shows the operating parameters expected for our two goals with the TH781 tetrode. These parameters were generated from analysis of the operating curves of the tube and are in reasonable agreement with the manufacturer's actual test data.

With these new power amplifiers, LANSCE DTL operations will improve by having a viable source of intermediate-power vacuum tubes. The new power amplifiers will simplify the first rf module and enhance beam performance with better field control. Development of the new high-power rf system for the DTL is the first step in modernizing the remaining higher-power rf modules for tanks 2, 3, and 4.[3]

Table 1. Expected operating values for both applications of the new amplifier.

Parameter (Peak Values During Pulse)	Modules 2-4 IPA	Module 1 FPA
Power output (kW)	136.7	507.7
Anode current (A)	14.06	36.25
Anode voltage (V)	13,000	19,000
Screen voltage (V) and current (A)	1,000 and 0.29	1,500 and 0.88
Control grid bias (V) and current (A)	-275 and 0.43	-350 and 1.73
Power input (kW)	4.3	18.2

References

1. J.T.M. Lyles and C. Friedrichs, in *Proceedings of International Linear Accelerator Conference*, Geneva (1996).
2. Communications Power Corporation, *Microwave Journal* **42** (2), 168-172 (1999).
3. J.T.M. Lyles et al., in *Proceedings of the European Particle Accelerator Conference*, Paris (2002).

H^- Injector Development for the Short-Pulse Spallation Source Enhancement Project

E. Chacon-Golcher, S. Cohen, E.G. Geros, E.G. Jacobson, B.J. Meyer, G. Rouleau, S. Schaller, F.E. Shelley, J.D. Sherman, J.E. Stelzer, J.C. Sturrock, T.J. Zaugg (LANSCE Division), D.S. Warren (SNS Division)

The development of a new H^- injector is being pursued as an element of an effort funded by the National Nuclear Security Administration to achieve reliable and sustainable LANSCE operations. Specifically, electronics in the present 750-keV injector dome (injector B) are not compatible with planned upgrades to the control system at LANSCE. In addition, higher-current H^- sources previously developed for LANSCE were accompanied by an undesired emittance growth.[1] Sources with larger emittance were studied in the 80-keV and 750-keV injector beam lines with the conclusion that significant changes in these beam lines would have to be made to accommodate larger emittance beams.[2] We have established an intermediate goal of a 25-mA H^- source with smaller emittance growth compatible with operations of the linear accelerator (linac). To this end, we have completed design studies that indicate that this H^- current goal can be achieved with minimal (20%) emittance growth.

Upgraded Injector Electronics and Control System

The upgraded H^- electronics and control system can accommodate both the six-filament sources developed at Lawrence Berkeley National Laboratory (LBNL) for LANSCE and the present two-filament LANSCE production source. Most of the recent H^- source development has been directed at bringing the new injector electronics and control system into operation. The injector is a complex electromechanical device in which about half of the equipment resides in an 80-kV isolated power rack, and the remaining equipment sits in local ground racks. The electrical system can be compromised by the environment of electromagnetic interference (EMI) generated by the ion source. It is necessary to control EMI for reliable injector operations. Table 1 summarizes the description, specification, and function of the principal equipment located in the 80-kV racks.

The filament power supplies heat the tungsten filaments to electron-emissive temperatures, and the arc modulator then provides these electrons with sufficient energy (100 eV) to create a hydrogen-cesium plasma in the vicinity of the surface converter electrode. With proper cesium balance, the negatively biased converter electrode converts incident positive hydrogen ions and neutrals to the desired H^- species. Further details on the H^- source operation are found in Reference 3. The 80-kV system is controlled by local ground fiber-optic links by distribution through the 80-kV computer-aided measurement and control (CAMAC) crate. CAMAC distributes commands through a 12-bit-resolution data-acquisition board integrated into each power-supply system.[4] Table 2 summarizes the principal equipment located at the local ground potential. The beam-energy supply provides the extracted H^- ions with 80-keV energy for subsequent transport through the

Table 1. Summary of the 80-kV isolated power equipment required to operate the ion source at 80 kV.

Description	Specification	Function
Filament power supplies (6)	20 V, 150 A	Emissive tungsten filaments
Converter power supply (1)	600 V, 16 A	Converter bias voltage
Repeller power supply (1)	33 V, 33 A	Improve e/H^- ratio
Arc modulator	300 V, 200 A	Discharge current
Extractor electrode HVPS*	45 kV, 6 mA	Beam-extraction potential
Focus electrode HVPS	15 kV, 10 mA	Beam-dynamics control
Analog light links from Dymec (4)	1-MHz bandwidth	Communication to ground
Hydrogen-gas flow	0 to 5 sccm**	Ion-source gas throughput
Cesium oven	20 to 260°C	Cesium throughput
CAMAC crate	1- to 2-Hz scan, 16-bit resolution	Controls and diagnostics
Analog control modules (14)	12-bit resolution	Power-supply set point
Binary control modules (14)	--	Power-supply on/off

*High-voltage power supply
**Standard cubic centimeters per minute

Table 2. Summary of the ground-level equipment and controls for the 80-keV injector.

Description	Specification	Function
Beam-energy supply (regulator plus power supply)	± 2 V/mA, peak to peak, at 80 kV	Provides nearly monoenergetic beam energy
Solenoid-magnet power supplies (2)	20 V, 500 A	Beam focus and transport
Steering-magnet power supplies (5)	± -20 V, ± -20A	Beam centroid control
Bending-magnet power supply (1)	20 V, 30 A	Suppresses residual electrons before 670-kV column
Ion-trap power supply	15 kV, 10 mA	Traps LEBT positive ions
Turbo-pump controller	Balzers AG 2,000 l/s	Pumps source gas, P_{LEBT} < 2 x 10^{-5} torr
Cryo-pump controller	CTI CryoTorr 1,000 l/s	Maintains P_{LEBT} < 1 x 10^{-5} torr
Ion-pump controller	Varian	Maintains $P_{670\ kV}$ < 5 X 10^{-6} torr
CAMAC crate	1- to 2-Hz scan, 16-bit resolution	Controls and diagnostics
Analog-control modules (10)	12-bit resolution	Power-supply set point
Binary-control modules (30)	--	Power-supply on/off and device activation (in/out, open/closed)
Fiber optics from FiberPlex, Inc. (5)	Timing distribution	670-kV dome communication

low-energy beam transport (LEBT) system and injection into the 670-kV injector B column. Two solenoid magnets provide beam focusing, and five steering magnets give beam centroid control. This system provides efficient transport of H^- ions to the 670-kV column and simultaneous suppression of the co-extracted electrons. This local ground-level equipment will be controlled by fiber-optic links as for the 80-kV racks. An additional function of the local ground-level equipment is device activation, such as the insertion of beam-line devices and the control of vacuum pumps and valves.

25-mA H^- Source for 2004

We are pursuing two approaches for achieving an operational 25-mA H^- source for linac operations. The first approach involved testing the six-filament axial prototype source, which was extensively characterized in the Short-Pulse Spallation Source (SPSS) Enhancement Project.[1] This source gave a 23-mA H^- beam current at the upper limit of the emittance specification, but its lifetime, while providing this performance, is unknown.

The second approach to achieve a 25-mA H^- beam current with acceptable emittance is to use a modified production source. To this end, fabrication and assembly of a fourth production source is in progress. This work includes modified repeller and emission-aperture (i.e., the Pierce electrode) assemblies to allow H^- beam formed on the converter surface to reach the extraction region of the source. The first series of simulations for expected performance has been completed using the PBGUNS code.[5] The simulations have modeled the geometry of the production source using Pierce apertures of 0.50-, 0.55-, and 0.60-cm radii. Also included is the effect of increasing the repeller aperture from a 0.64-cm to a 0.86-cm radius. The LANSCE production column is used in the model for forming the beam. A condition imposed on the simulations is that discharge power is maintained at the level of the LANSCE operations source, thus, in theory, preserving its 28-day lifetime.

The simulations indicate extracted H^- current is sensitive to the H^- sputter energy at the converter surface. For example, Fig. 1 shows simulation results for a sputter energy of 12 eV and a repeller radius of 0.86 cm. The figure shows the H^--converter current density versus the accelerated (80-keV) H^- current for the three Pierce aperture radii. The horizontal bar intersecting the H^--converter current-density axis at 1.95 mA/cm^2 corresponds to usual linac-source-operation conditions (28-day lifetime). By reading the intersections of the 1.95-mA/cm^2 line with the simulations parametric in the Pierce radii, one finds 18-, 23-, and 26-mA-predicted H^- currents for the three apertures. The simulations predict an emittance growth from 0.14 (πmm-mrad) for 18 mA to 0.17 (πmm-mrad) for 26 mA, which is a 20% effect. By redoing the simulations of Fig. 1 with a 6-eV sputter energy, one arrives at the results shown in Fig. 2. Two items are

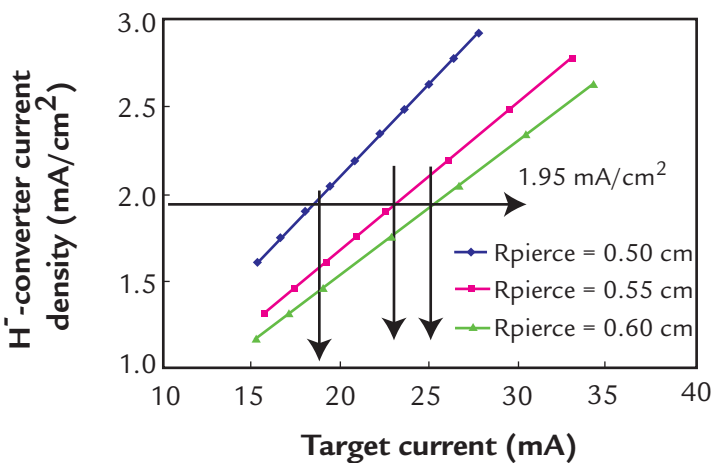

Fig. 1. Predictions for accelerated H^- current (horizontal axis) at 12-eV H^- sputter energy. ("Rpierce" is the radius of the emission aperture.)

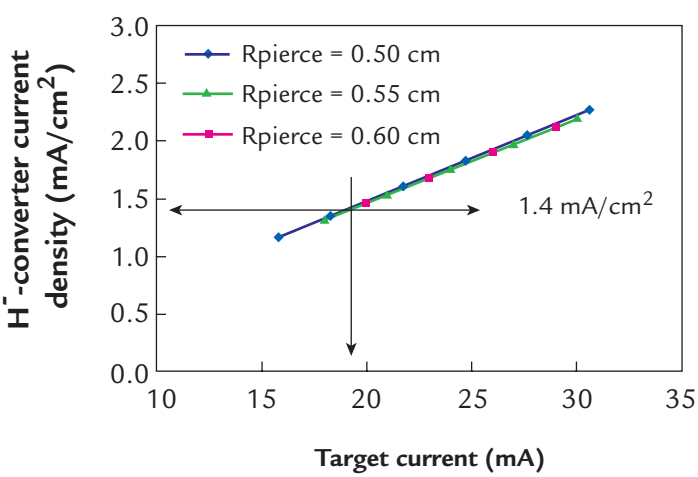

Fig. 2. Predictions for accelerated H^- current (horizontal axis) at 6-eV H^- sputter energy.

immediately apparent. First, only 1.4-mA/cm^2 H^--converter current density is required to reproduce the 18-mA H^- operations current. Second, there is little increase of target current as the Pierce aperture radius is increased. Thus, the simulations predict that at the lower-H^- sputter energy nearly all of the converter current can pass through a 0.5-cm-radius aperture, whereas higher-H^- sputter energies spread the beam enough so that an increase in aperture size allows for the extraction of a higher-H^- current. The only way to differentiate these predictions is by experimental testing.

Conclusion

Earlier work[2] showed that beams with 250% emittance growth as compared to the production source were problematic to linac operations. The 20% emittance growth simulated for the 12-eV sputter case is likely to be acceptable to linac operations if the 12-eV sputter simulations are appropriate to the operations (production) source.

References

1. B.A. Prichard, Jr., and R.R. Stevens, Jr., Los Alamos National Laboratory report LA-UR-02-547.
2. R.C. McCrady et al., Los Alamos National Laboratory report LA-13943-PR.
3. R.R. Stevens, Jr., et al., in *Proceedings of the Linear Accelerator Conference* 226 (1984).
4. S. Cohen et al., Los Alamos National Laboratory report LA-13943-PR.
5. J.E. Boers, PBGUNS Users Manual (Version 5.04), available from Thunderbird Simulations, 626 Bradfield Drive, Garland, Texas.

Research Highlights
Neutron Nuclear Science

Neutron Capture on Unstable Nuclides 74

Inclusive (n,xn) Double-Differential Cross-Section Measurement (II) 76

Neutron-Deuteron Elastic Scattering: Three-Nucleon Forces or Δ(1232) Excitation? 78

Measurements of Cross Sections for Gas Production in Neutron-Induced Reactions at LANSCE 80

Frontiers in Neutron-Induced Fission 82

Production of ^{148}Gd by 600- and 800-MeV Protons on Tungsten, Tantalum, and Gold 84

Improving Radiochemical Diagnostics: Studying Iridium and Europium with the Germanium Array for Neutron-Induced Excitations 86

Demand Grows for Single-Event-Effects Measurements at the LANSCE Irradiation of Chips and Electronics House 88

Neutron Particle Effects on a Redundant Flight-Control Computer 90

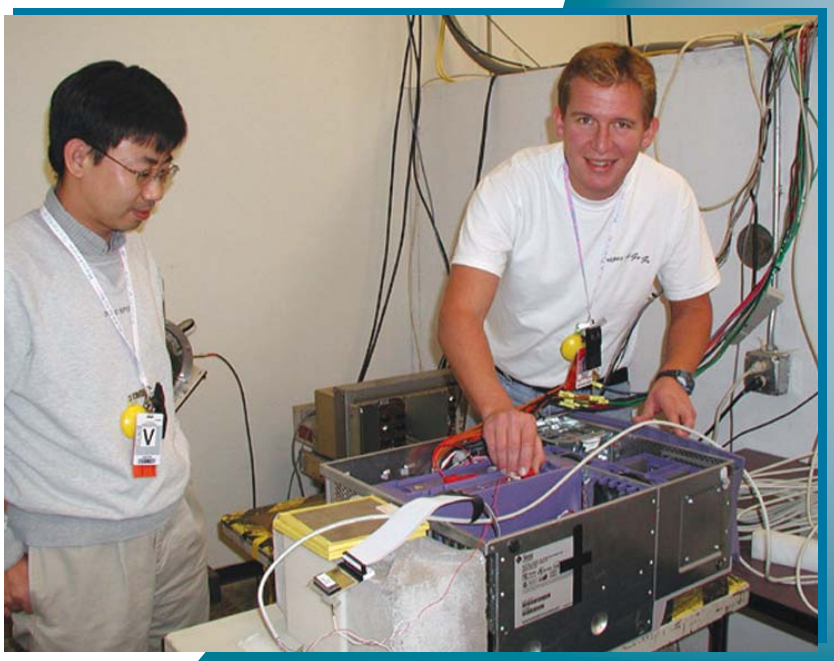

Neutron Capture on Unstable Nuclides

T.A. Bredeweg, P.D. Palmer, R.S. Rundberg, D.J. Vieira, J.B. Wilhelmy (C Division), R.C. Haight, J.M. O'Donnell, R. Reifarth, J.L. Ullmann (LANSCE Division), J.M. Wouters (IM Division)

The abundance of isotopes produced in nuclear explosions and asymptotic-giant-branch stars are affected by neutron capture on unstable nuclides (radioactive isotopes). The thermonuclear neutron fluences produced in nuclear detonations in past underground-nuclear-weapons tests were determined by placing radiochemical (radchem) detectors in components of the device and measuring the radioactive isotopes produced in the post-shot debris. The neutron capture in the 1- to 30-keV energy range affects the isotopic distribution of these elements. The Detector for Advanced Neutron Capture Experiments (DANCE) on flight path (FP) 14 at Lujan Center is designed to measure neutron-capture cross sections with neutron energies from thermal (0.0253 eV) to 100 keV on radioactive targets with masses as low as 0.5 mg. Because DANCE discriminates backgrounds on the basis of γ-ray multiplicity (the number of γ-rays emitted in the decay of a compound nucleus) and neutron-binding energy (which determines the total energy of the γ-rays emitted in the cascade), it provides superior performance over other γ-ray detectors like deuterated-benzene scintillators. During the 2002 run cycle at LANSCE, we made the first measurement of the neutron-capture cross section of ^{234}U with DANCE.

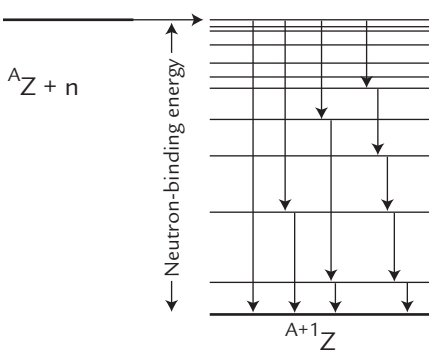

Fig. 1. A target nucleus with atomic number Z and mass A captures a neutron to form an excited state in the compound nucleus, $^{A+1}$Z. The γ-ray decay of this compound nucleus can proceed with different γ-ray multiplicities. This illustration has a reduced level density for visual clarity. A 4-π detector will sum the γ-rays to yield the neutron-binding energy, which is characteristic of the compound nucleus.

Measuring Neutron Capture on Unstable Nuclides with DANCE

Neutron-capture cross sections are measured with DANCE using the neutron time-of-flight (TOF) method. A neutron-capture event is registered when γ-rays are detected in the DANCE scintillator array. The neutron energy is determined by TOF (the time that γ-rays are emitted from the target relative to the time protons from the Proton Storage Ring strike the tungsten target producing a burst of neutrons used in experiments). The neutrons emitted from the tungsten target are slowed down in a water moderator to give an intense epithermal (> ~ 0.5 eV) neutron flux. These moderated neutrons travel along a

20.3-m vacuum pipe lined with neutron collimators to produce a well-defined 0.89-cm-diam neutron beam at the center of DANCE. DANCE consists of 159 barium-fluoride scintillators in a soccer-ball configuration. Barium fluoride has a high efficiency for detecting γ-rays with energies above 1 MeV. The thickness of the barium-fluoride shell is 15 cm. Barium fluoride has a relatively low sensitivity to neutrons scattered from the target. A 6-cm-thick ^{6}LiH absorber surrounding the target position further reduces the sensitivity of the array to scattered neutrons. Fig. 1 illustrates a cascade of γ-rays following neutron capture by a target nucleus. A γ-ray cascade can have large γ-ray multiplicities. The sum of the energies of γ-rays that are detected within a time window of several nanoseconds is equal to the neutron-binding energy of the compound nucleus. Summed γ-ray energies following neutron capture in barium fluoride have different neutron-binding energies from the natural isotopes of barium. The summed γ-ray energies from barium are different from the target and can be discriminated against.

A target consisting of 1 mg of ^{234}U electro-deposited on two 2.5-μm-thick titanium foils was bombarded in the DANCE target chamber. The only previous ^{234}U neutron-cross-section measurements made in the 1-eV to 100-keV energy range were total cross sections (i.e., capture plus scattering) and preliminary neutron-capture measurements using deuterated-benzene scintillators at FP14 with 10-mg samples. In these FP14 measurements, the neutron resonances were broadened by neutron scattering in the quartz vials used to hold the ^{234}U oxide.

The advantage of using a 4-π detector is illustrated in Fig. 2, which shows the neutron-capture rate in ^{234}U at neutron energies near the 5.16-eV resonance. The first curve shows the neutron-capture rate obtained when a window was set for summed γ-ray energies around the 5.29-MeV sum peak corresponding to the neutron-binding energy in the ^{234}U compound nucleus. The second curve shows the neutron-capture rate after subtracting captures in the barium-fluoride crystals. After subtraction, the off-resonance background is reduced by more than 2 orders of magnitude.

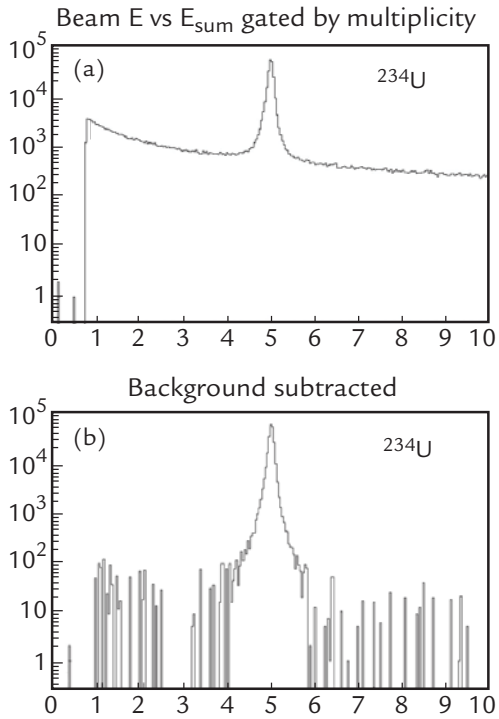

Fig. 2. Neutron-capture rates near the 5.16-eV resonance of ^{234}U before (a) and after (b) subtraction of γ-rays from neutron capture in the barium-fluoride scintillators.

Conclusion

The γ-ray-detection efficiency of DANCE enabled us to measure neutron-capture cross sections on 1-mg targets with good statistics. Most unstable nuclides require this level of detection efficiency. The 4-π geometry of the DANCE array allows the measurement of the total γ-ray energy emitted per neutron capture. This geometry greatly reduces the background caused by neutrons scattered from the target into the barium-fluoride array. As such, DANCE allows for the measurement of neutron capture on many isotopes of importance to both nuclear astrophysics and the interpretation of radchem weapons diagnostics. With the intense neutron flux available at Lujan Center, DANCE is presently the most sensitive instrument for neutron-capture experiments.

Inclusive (n,xn) Double-Differential Cross-Section Measurement (II)

K. Ishibashi, Y. Iwamoto, S. Kunieda, D. Satoh, N. Shigyo (Kyushu University), R.C. Haight (LANSCE Division), T. Nakamura (Tohoku University)

Calculating radiation transport with protons and neutrons requires a description of nucleon-induced reactions. These processes are especially important for incident energies above 20 MeV for the development of accelerator-driven systems (ADSs). The quantity that describes the probability of a nucleon being emitted at a given angle with a given energy is called the double-differential cross section (DDX). For proton-induced reactions, DDXs have been measured for many years. But DDX data for neutron-induced reactions where neutrons are emitted have never been obtained above 100 MeV. This article describes the measurements that we obtained at WNR of inclusive (n,xn) cross sections (i.e., one neutron is detected, but no other reaction product *x*) for incident-neutron energies ranging from 20 to 400 MeV. These cross sections will be compared to calculations from the intra-nuclear-cascade-evaporation (INCE) code,[1] the quantum-molecular-dynamics (QMD) code,[2] and the GNASH code.[3]

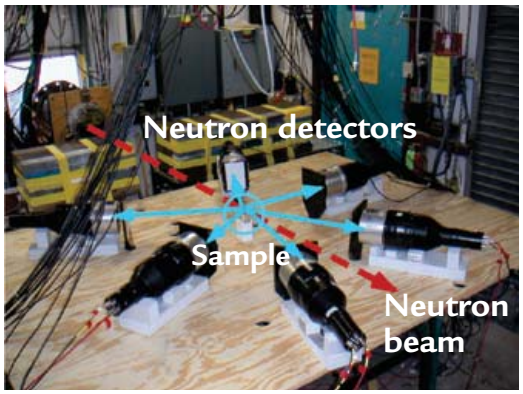

Fig. 1. Detector arrangement showing the direction of the incident neutron beam, the Pb sample, and the liquid-organic-scintillation detectors.

DDX Data — Needs and Challenges

Intermediate-energy proton accelerators are used in conceptual ADSs. To design these facilities, DDX measurements of proton-induced reactions were performed after 1988. These data contributed to improvements to the INCE, QMD, and GNASH codes.[1-3] For instance, predictions from recent INCE calculations have greatly improved since the early 1970s. Adjustments to parameters, such as the effective nucleon-nucleon-collision cross sections at medium energies, were made in INCE and QMD codes.

The present state of data suggests that the nuclear-model codes might have trouble predicting DDXs. For example, it is well known that there are relatively important changes in the nuclear-optical potential[4] in the 50- to 300-MeV energy region. The optical-model parameters are important input to the calculations. Secondly, DDX data for proton-induced reactions barely cover this energy range, and therefore they do not constrain the calculations as much as needed. Then there are the thick-target-neutron yields[5] that we measured for incident-proton energies around 1 GeV; these have some disagreement with the results of the LAHET code[6] in the energy region of 20 to 100 MeV. Thus, even proton-induced data leave much to be desired in the development of reaction-model codes to predict neutron-induced DDXs.

Measurement of (n,xn) Cross Sections

WNR provides short, intense neutron pulses over a wide continuous-energy range that covers the nuclear-optical-potential changing region. Data at these energies can supplement those for proton-induced reactions for improving the INCE model and thus provide advances in intermediate-energy nuclear physics and neutron-transport calculations.

The purpose of our study was to measure inclusive Fe(n,xn) and Pb(n,xn) DDXs for incident neutrons with energies from 20 to 400 MeV. The measurement required an experimental method that had both an acceptable detection efficiency and a good energy resolution.

The experiment shown in Fig. 1 was performed on WNR flight path 4FP15L. With a continuous-energy-neutron beam, the time between neutron production from the spallation target and the detector signal gives the sum of the flight times for the incident and emitted neutrons. The time of flight (TOF) of emitted neutrons can be obtained from their energy measured in the detector. The TOF of incident neutrons is obtained by difference. To detect the emitted neutrons, we used the recoil-proton method in 2001.[7] However, the detection efficiency of the method was very low. To improve the efficiency, we used liquid-organic scintillators as neutron detectors and the recoil-proton method in 2002.

The distance between the sample and the liquid-organic-scintillation detectors was about 50 cm, and the detection angles were 15°, 30°, 60°, 90°, 120°, and 150°. The samples used were a 4-cm-thick, 5-cm-diam Fe disk and a 2-cm-thick, 5-cm-diam Pb disk. To subtract background events, we also made measurements without the samples. To eliminate charged-particle events from the sample, a plastic scintillator was set in front of each scintillation detector.

Conclusion

The data obtained at WNR cover the neutron energies from 20 to 400 MeV. Data analysis is in progress.

References

1. H. Takada et al., Japan Atomic Energy Research Institute report JAERI-Data/Code 98-005 (1998).
2. K. Niita et al., *Physical Review C* **52**, 2620 (1995).
3. P.G. Young et al., Los Alamos National Laboratory report LA-12343-MS (1992).
4. F.S. Dietrich et al., in *Proceedings of the International Conference on Nuclear Data for Science and Technology* **402** (1997).
5. S. Meigo et al., *Nuclear Instruments and Methods A* **431**, 521 (1999).
6. R.E. Prael and H. Lichtenstein, Los Alamos National Laboratory report LA-UR-89-3014 (1989).
7. K. Ishibashi et al., Los Alamos National Laboratory report LA-13943-PR (2001).

Neutron-Deuteron Elastic Scattering: Three-Nucleon Forces or Δ(1232) Excitation?

J.L. Matthews, T. Akdogan, M. Chtangeev, W.A. Franklin (Massachusetts Institute of Technology), R. DeYoung, B. King, S. Marthai, M. Yuly (Houghton College), M.A. Kovash (University of Kentucky), S.A. Wender (LANSCE Division)

A measurement of the differential cross section for neutron-deuteron elastic scattering has been performed using the fast-neutron beam at WNR. Theoretical calculations[1] have shown this cross section to be sensitive to three-nucleon forces — forces that depend on the simultaneous interaction among three nucleons. Other calculations[2] reproduce the existing data by invoking virtual excitation of the Δ(1232) isobar — the *first excited state* of the nucleon. Our measurement over the broad range of neutron energies available at WNR should allow us to determine which, if either, explanation is correct.

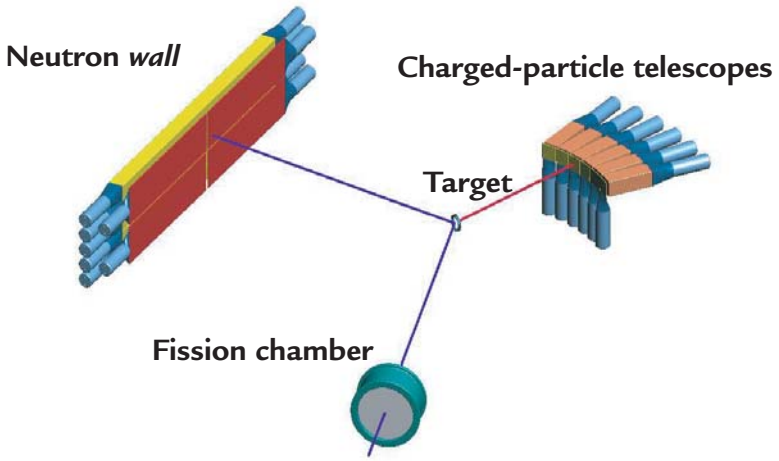

Fig. 1. Schematic illustration of experimental setup.

Measuring the Differential Cross Section

A schematic illustration of our experimental setup is shown in Fig. 1. The incident neutron beam passes through a fission chamber, which provides a monitor of the neutron flux, and impinges on a cryogenic target filled with either liquid hydrogen or liquid deuterium. Scattered neutrons and recoil charged particles were observed in coincidence on the left and right sides, respectively, of the beam line, as shown. Neutrons were detected by a *wall* consisting of five bars of plastic scintillator preceded by veto detectors to eliminate charged particles. Neutron angles, in the range between 40° and 100°, were determined by measuring the difference in arrival times of the signals at each end of the bars. Charged particles were observed at angles between 24° and 54° in an array of six detector telescopes consisting of CsI crystals preceded by thin plastic scintillators. This combination of detectors allows the identification and separation of protons and deuterons.

Results

Some preliminary results are displayed in Figs. 2 and 3. Fig. 2 shows the cross section for neutron-proton scattering at 150 MeV. The agreement achieved with existing data gives us confidence that we understand the parameters of our experiment. Fig. 3 shows the cross section for neutron-deuteron scattering at 140 MeV. Our data (the red circles) agree with previous measurements and with the theoretical calculation[1] that includes three-nucleon forces. The calculation based on Δ(1232) excitation yields very similar results. Again, the agreement with previous data gives us confidence in the accuracy of our results.

Our next task will be to analyze data taken at higher neutron energies where there are no previous neutron-deuteron scattering data and where the two theoretical explanations are expected to diverge.

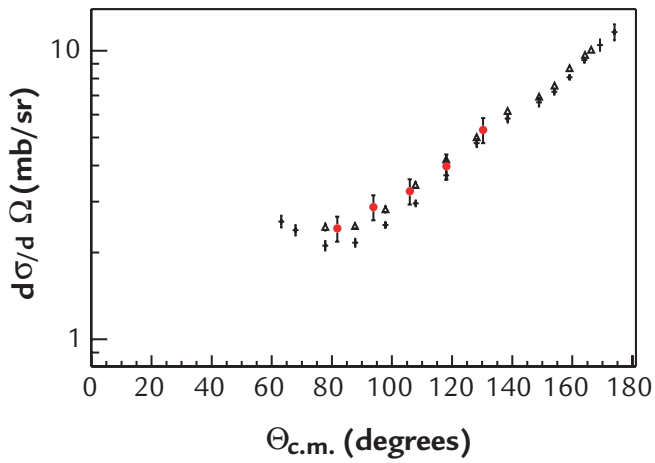

Fig. 2. Preliminary results for the differential cross section for neutron-proton scattering at 150 MeV. The present data are shown as the red circles. The statistical uncertainty is smaller than the size of the symbols; a systematic error of 10% has been included. Previous data (crosses and triangles) have been taken from the SAID database.[3]

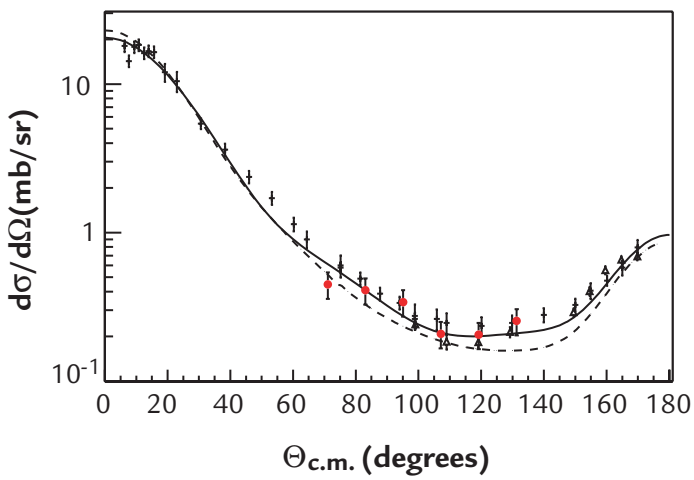

Fig. 3. Preliminary results for the differential cross section for neutron-deuteron scattering at 140 MeV. The present data are shown as the red circles. The crosses are proton-deuteron scattering data[4] at 146 MeV, and the triangles are neutron-deuteron scattering data[5] at 152 MeV. The curves are from Reference 1 and represent the theoretical calculation without (dashed curve) and with (solid curve) the inclusion of three-nucleon forces.

Acknowledgements

This work was supported in part by the U.S. Department of Energy and the National Science Foundation.

References

1. H. Witala et al., *Physical Review Letters* **81**, 1183 (1998).
2. S. Nemoto et al., *Physical Review C* **58**, 2599 (1998).
3. D.F. Measday, *Physical Review* **142**, 584 (1966); J.N. Palmieri and J.P. Wolfe, *Physical Review C* **3**, 144 (1971).
4. R. Postma and R. Wilson, *Physical Review* **121**, 1229 (1961).
5. J.N. Palmieri, *Nuclear Physics A* **188**, 72 (1972).

Measurements of Cross Sections for Gas Production in Neutron-Induced Reactions at LANSCE

R.C. Haight, D. Rochman, J.K. Gallegos (LANSCE Division)

During the 2002 run cycle at LANSCE, we began measurements of the cross sections for hydrogen and helium production in neutron-induced reactions from threshold to 100 MeV on structural materials important to the Advanced Fuel Cycle Initiative (AFCI) program at LANL. Our approach is to directly measure hydrogen and helium isotopes as they were emitted in nuclear reactions such as (n,xp), (n,xd), and (n,xα). The data include not only the gas-production cross sections corresponding to the emission of these hydrogen and helium isotopes but also the angular distributions and energy spectra of the emitted particles. These benchmark data further serve as tests of nuclear-reaction model calculations. Materials under study include iron and the two principal isotopes of nickel (^{58}Ni and ^{60}Ni).

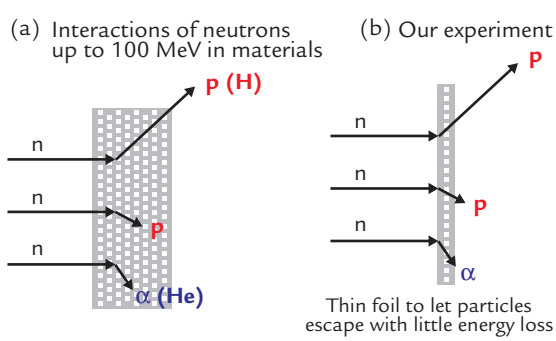

Fig. 1. Gas production by neutrons in materials. (a) Charged particles stop in the material or neighboring materials, depending on the range. Protons have millimeter to centimeter ranges. They capture an electron when they stop in the material and become hydrogen. The α-particles have millimeter ranges. They capture two electrons when they stop and become helium. (b) We detect outgoing charged particles and measure their energy and angular distributions. Then hydrogen and helium production can be calculated with confidence.

Comprehensive Program Aimed at Studying Elemental Constituents of Structural Materials

Hydrogen and helium are known to contribute significantly to radiation damage and alteration of the mechanical properties of materials subjected to neutron irradiation. At present, there are few data for such important elements as iron, chromium, nickel, and molybdenum. New evaluations that extend to higher neutron energies[1] are based to a great extent on nuclear model calculations. The data in these new evaluations, especially for the structural materials, invite tests and validation. We have therefore begun a program to measure these cross sections on the elemental constituents of structural materials. This work is a continuation of our measurements made up to 60 MeV on other materials such as silicon[2] and cobalt.[3]

Our method is to detect protons, α-particles, and other isotopes of hydrogen and helium emitted in reactions induced by neutrons at the WNR spallation-neutron source at LANSCE. Schematically, our measurement approach is shown in Fig. 1, where the correspondence of these microscopic measurements is made to the realm of structural materials.

Protons, deuterons, tritons, ^{3}He, and α-particles are emitted in reactions of neutrons with the constituent elements of the material. In a thick sample (i.e., more than a few millimeters), most of these light, charged particles stop in the material itself, although a few with high enough energy will exit the component and stop in neighboring materials. For our experiments, we select thin foils of the material of interest so that all of the light charged particles could escape with little energy loss. We were thereby able to measure not only the gas-production cross sections corresponding to hydrogen and helium isotopes but also the energies of the emitted particles and their angular distributions. These latter two quantities do not affect the hydrogen and helium production, but they are important for validating nuclear model calculations because they serve as further constraints on the models. With improved models, we will have greater confidence in calculations of gas-production cross sections for materials that are difficult to study in the laboratory. The reaction chamber and collimation for the neutron beam, target position, and array of detectors that identify charged particles and their energies are shown in Fig. 2.

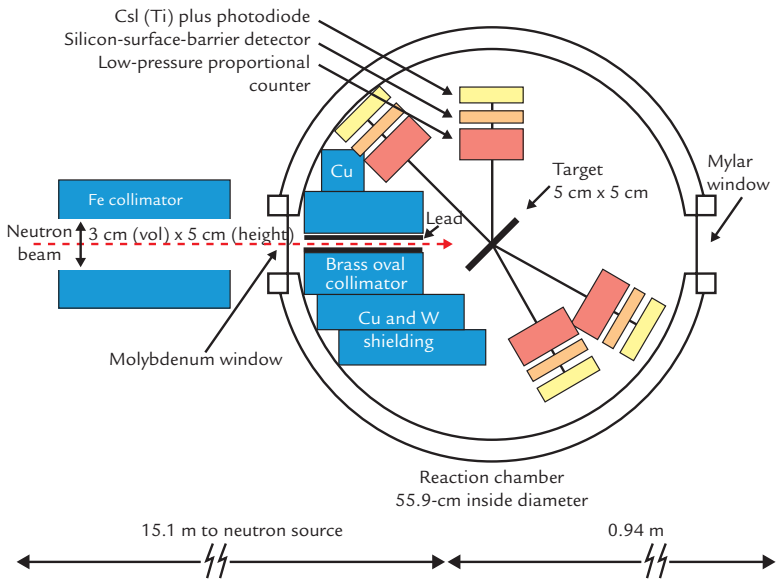

Fig. 2. Layout of apparatus for measuring neutron-induced hydrogen and helium production showing collimation for the neutron beam, target position, and array of detectors that identify charged particles and their energies.

Progress to Date

We obtained preliminary data in late 2001 in an effort to commission the detector station, shielding, detectors, and the data-acquisition system. We used an iron sample in this experimental run and concentrated on proton emission at several angles. Detection of protons from the sample was challenging because protons are easily produced by neutron interactions with shielding materials. Typical data are shown in Fig. 3. A measure of the quality of data is the signal-to-background ratio, which we found to be 6:1 in the forward angles and 3.5:1 at 90° at an incident-neutron energy E_n = 100 MeV. At lower neutron energies, the signal-to-background ratio was significantly better. We began taking production data on iron and two isotopically enriched nickel isotopes (^{58}Ni and ^{60}Ni) in July 2002. Preliminary analysis of the data shows that the signal-to-background ratios are significantly higher with the upgraded collimation and shielding.

Acknowledgements

This work, supported by the Advanced Fuel Cycle Initiative at LANL, has benefited from the use of LANSCE. LANL is funded by the U.S. Department of Energy and operated by the University of California under Contract W-7405-ENG-36.

References

1. M.B. Chadwick et al., *Nuclear Science and Engineering* **13**, 293 (1999).
2. F.B. Bateman et al., *Physical Review C* **60**, 064609-1 (1999).
3. S.M. Grimes et al., *Nuclear Science and Engineering* **124**, 271 (1996).

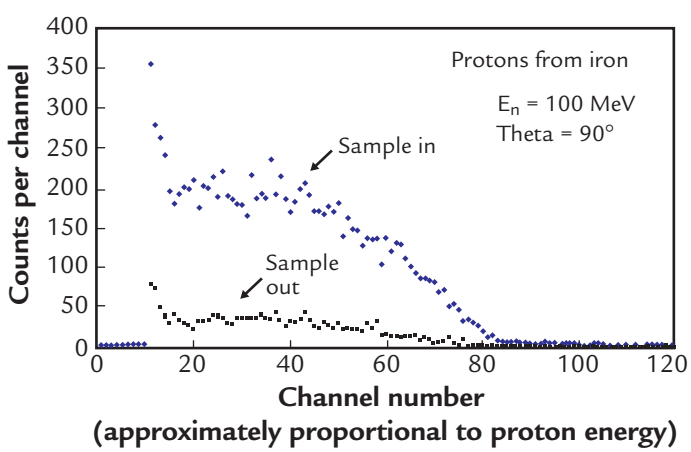

Fig. 3. Sample-in and sample-out measurements of proton production from an iron sample at a neutron energy of 100 MeV. The signal-to-background ratio is good at this neutron energy and significantly better at lower incident-neutron energies.

Frontiers in Neutron-Induced Fission

R.O. Nelson, M.J. Devlin, N. Fotiadis, R.C. Haight, J.M. O'Donnell, D. Rochman (LANSCE Division), R. Drosg (University of Vienna), P. Casoli, T. Ethvignot, T. Granier (CEA, Bruyéres-le-Châtel), J.A. Becker, P.E. Garrett, W. Younes (Lawrence Livermore National Laboratory)

Understanding the nuclear reactions that occur in a nuclear weapon is critical both for calculating weapon performance and for understanding data from underground tests. The intense neutron flux present in a nuclear explosion drives fission of the primary fuel. However, many other reactions occur that affect the weapon yield. Fission is a process whereby a nucleus splits (at scission) into neutron-rich primary fragments. These fragments rapidly emit prompt neutrons after which they become secondary fragments, which further decay by prompt γ-ray emission to finally become fission products. Some fission products are stable, but most of them undergo beta decay on a time scale from hundreds of seconds to milliseconds. In our experiments, we studied prompt γ-rays emitted within less than a few nanoseconds after scission. From these prompt-γ-ray yields, we can infer many fission-product yields, including stable products that are not usually observed in radiochemical measurements of fission yields. In addition, measured $K_{\alpha\text{-}\beta}$ x-ray fission-fragment yields allow us to deduce charge distributions (i.e., yields summed over isotopes for a given atomic number) and complement the data obtained from the observed γ-rays. New measurements of the energy spectra of the prompt neutrons emitted and of the prompt-γ-ray energy spectra are also in progress. Some phenomena of interest include the transition from asymmetric to symmetric fission as a function of excitation energy, the competition between neutron and γ-ray emission, nuclear-structure effects in fission, and the angular momentum imparted to the fission products.

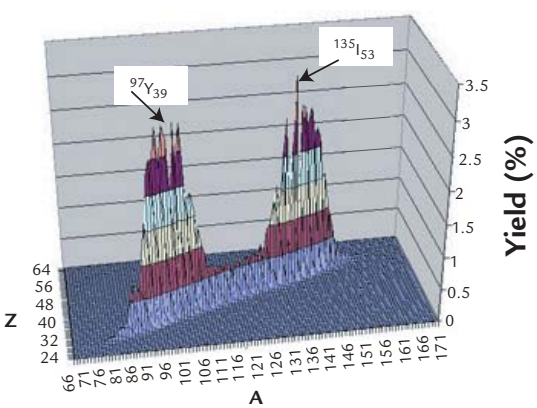

Fig. 1. Fission-product yields as a function of charge and mass for 14-MeV neutron-induced fission of ^{235}U.[1]

New Fission Experiments with GEANIE and FIGARO

Data are acquired using the GEANIE high-resolution γ-ray spectrometer at WNR, which provides neutrons with energies from below 1 MeV to over 200 MeV. The time-of-flight (TOF) technique is used to determine the incident neutron energies. GEANIE consists of 11 low-energy γ-ray and x-ray detectors and 15 higher-energy γ-ray high-resolution, high-purity germanium detectors. For γ-ray measurements, samples consisted of ~ 400 mg/cm^2 metal disks of ^{238}U and ^{235}U. Of the many hundreds of fission fragments that are created in the fission of actinides, ~ 100 of the most strongly produced fragments were observed in our γ-ray spectra. Each fragment can emit several γ-rays, thus producing a very complicated overall spectrum. The fragment yields range over many orders of magnitude with the maximum yield being about 4% of the total fission yield. Fig. 1 shows the fission yields for the 14-MeV neutron-induced

fission of ^{235}U as an example.[1] The peak yields for one light (^{97}Y) and one heavy (^{135}I) product are indicated for orientation purposes. At high incident-neutron energies, the region between the light- and heavy-mass products fills in as more symmetric fission dominates.

For the x-ray measurements, it is necessary to detect the fission fragments in coincidence with the x-rays to get a clean spectrum in which the x-rays are observable above background. For these measurements, solar cells are used as fission-fragment detectors with very thin (400 to 1,000 μg/cm^2) deposits of uranium so that the fission fragments escape from the uranium and are detected.[2] A total of eight solar cells were used to increase the count rate. Very thin (~ 75 μm) silicon solar cells were used to reduce attenuation of x-rays in the target. The transmission averaged over the eight cells ranged from about 20% for 10-keV x-rays (light fragments) to 70% for 35-keV x-rays (heavy fragments). Detailed fitting of the K_α and K_β x-rays was carried out to extract the total x-ray yields for a given element.

The x-rays following fission are produced primarily by electrons filling orbitals of the fragments after internal conversion (the process whereby a nucleus ejects an atomic electron rather than emitting a low-energy γ-ray). Because of the properties of the internal-conversion process, greater x-ray yields (up to ~ one x-ray per product nuclide) are observed for the higher-Z fragments. Also, the x-ray yields depend strongly on the structure of the low-lying nuclear levels and the energy and multipolarity of the transitions. Strong odd-even mass effects are observed. We use the Reisdorf prescription[3] obtained from detailed measurements to relate measured x-ray yields to charge yields. Preliminary charge yields obtained for two different neutron-energy ranges from ^{238}U(n,fx-ray) data are shown in Fig. 2.

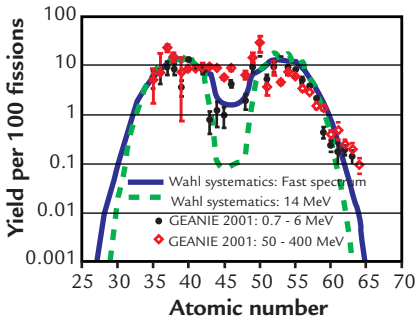

Fig. 2. Fission charge yields for ~ 2-MeV and ~ 100-MeV neutron-induced fission of ^{238}U. Wahl systematics for a fast-reactor spectrum (~ 2 MeV) and for 14-MeV incident neutrons are shown for comparison.[4]

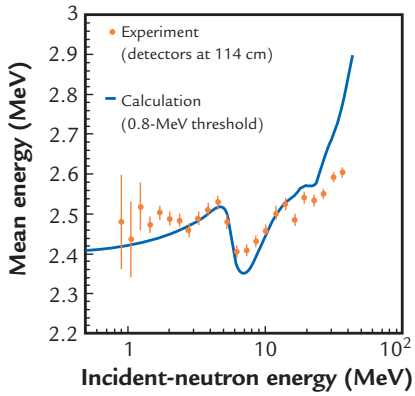

Fig. 3. Average fission-neutron energies plotted versus incident-neutron energy for the fission of ^{235}U from the FIGARO data. The line is from a calculation using the Los Alamos Model.[5] A decrease in the mean energy was observed and calculated to occur at the onset of pre-fission neutron emission at about 6 MeV.

Work on FIGARO to measure prompt-fission-neutron and γ-ray spectra began in late 2001 and has demonstrated the feasibility of the technique (Fig. 3). Prompt-fission-neutron spectra were measured using 6 liquid-scintillator neutron detectors and special fission-ionization chambers consisting of approximately 200 thin uranium deposits. The fission chamber provides a timing signal that allows two separate TOF measurements to be made to determine the energy of the incident neutron and the energy of a fission neutron. The neutron detectors are located about 1 to 2 m from the fission chamber as a compromise between detector acceptance and adequate neutron-energy resolution. In 2002, large BGO and BaF_2 detectors were added to measure the fission spectra up to high γ-ray energies in an effort to determine the total energy emitted as γ-rays and the properties of the γ-ray energy distribution. We are making these measurements relative to ^{252}Cf spontaneous fission from which we can more easily make an absolute determination of the production rates.

Conclusion

Data were taken on FIGARO and GEANIE in 2001 with ^{238}U samples. The experiments permitted extraction of mass and charge yields and prompt-neutron spectra for neutron-induced fission from 1 to 200 MeV. These results are being prepared for publication. In 2002, similar data with ^{235}U were taken, and a novel measurement of the total γ-ray energy spectrum was performed. Plans for future work include fission measurements on the more difficult cases of ^{239}Pu and ^{237}Np and extending the results to other actinide and sub-actinide nuclei.

Acknowledgements

This work was supported in part by the U.S. Department of Energy under contracts W-7405-ENG-36 (LANL) and W-7405-ENG-48 (Lawrence Livermore National Laboratory) and by the CEA, Bruyères-le-Châtel, France.

References

1. B.F. Rider and T.R. England, LANL report LA-UR-94-3106 (1994).
2. T. Ethvignot et al., *Nuclear Instruments and Methods A* **490**, 559 (2002).
3. W. Reisdorf et al., *Nuclear Physics A* **177**, 337 (1971).
4. A. Wahl, Los Alamos National Laboratory report LA-13298 (2002).
5. D.G. Madland, *Acta Physica Hungarica* **10**, 231 (1999).

Production of ^{148}Gd by 600- and 800-MeV Protons on Tungsten, Tantalum, and Gold

R.K. Corzine (LANSCE Divison and Georgia Institute of Technology), M.J. Devlin, E.J. Pitcher (LANSCE Division), N.E. Hertel (Georgia Institute of Technology), S.G. Mashnik (X and T Divisions)

At LANSCE, protons are accelerated to 800 MeV and directed to two tungsten targets — Target 4 at the WNR and the Mark 2 Target at the Lujan Center. A cascade of radioisotopes are produced by spallation reactions in these targets. The Department of Energy (DOE) requires hazard classification analyses performed on these targets and places limits on certain radionuclide inventories that are produced. These analyses help the facilities to be kept below the threshold that characterizes nuclear facilities.

^{148}Gd is one such radioisotope created from spallation reactions in a tungsten target. Allowed isotopic inventories are particularly low for this radioisotope because it is an α-particle emitter with a 75-year half-life. The activity level of ^{148}Gd is low; however, based on present yield estimates, it amounts to almost two-thirds of the total dose burden for the two tungsten targets at LANSCE. From a hazard-classification standpoint, this severely limits the time these tungsten targets can be used. The production cross section for ^{148}Gd is not well known, hence, the motivation for measuring it.

A Need for Better Knowledge of the ^{148}Gd Production Rates in Tungsten Targets in the 600- to 800-MeV Energy Range

The 800-MeV protons lose about 200 MeV when passing through the tungsten target at WNR and the tungsten target at the Lujan Center. They therefore exit the targets with an energy of 600 MeV. Because DOE limits the inventory of ^{148}Gd, a better estimate of the ^{148}Gd production rate in tungsten targets is needed for proton energies between 600 MeV and 800 MeV. From a basic nuclear-physics standpoint, the ideal strategy would be to measure the production cross sections for each tungsten isotope in this energy range. However, obtaining isotopically pure tungsten foils is cost prohibitive. An alternative is to perform measurements with a mono-isotopic element close to that of tungsten (Z = 74) in atomic number. Tantalum (Z = 73), which is 99.988% ^{181}Ta, provides a good alternative for testing the physics models used to estimate spallation products at these energies. Furthermore, tantalum is used as target cladding at two spallation-neutron-source (SNS) facilities — KENS (Japan) and ISIS (Rutherford-Appleton Laboratory Neutron Facility, United Kingdom) — which operate at 500 MeV and 800 MeV, respectively. By measuring ^{148}Gd production from tantalum, we can use nuclear-physics models with measured production cross sections from elemental tungsten to gain a better understanding of production rates for individual tungsten isotopes. These models will then help in evaluating dose burdens at other SNS facilities.

Several other measurements of spallation-product yields exist for intermediate-energy proton interactions with tungsten, tantalum, and gold. Gold, a mono-isotopic element (Z = 79), is of interest to the new Spallation Neutron Source located at Oak Ridge National Laboratory because of its atomic-number proximity to that of mercury (Z = 80), the candidate target material. Previous measurements[1,2,3] used γ-ray spectroscopy, radiochemical analysis, or a fragment separator to determine independent and cumulative (which includes decay from radioactive parents) spallation-product yields.

The ^{148}Gd inventory is difficult to deduce in a thick target because it decays only by α-particle emission (with a short range) with no associated γ-ray emission. To date, only one measurement of the number of ^{148}Gd atoms produced from tungsten has been made. A radiochemistry analysis, which was done as part of the decay-heat experiment for the Accelerator Production of Tritium (APT) project, measured the number of ^{148}Gd atoms in the center of three tungsten foils irradiated with 800-MeV protons.[1] Assuming that this radioisotope is only produced within the confines of the beam spot, a ^{148}Gd production cross section of 16.40 ± 0.41 mb can be inferred from this measurement. A current theoretical estimate obtained with the CEM2k+GEM2 code[4] for the cumulative production of ^{148}Gd from ^{184}W is 24.24 ± 0.19 mb. For purposes of hazard classification, conservative efforts require that this theoretical estimate be multiplied by a factor of 2, which further limits the time that the target can be irradiated.

To assess the production of ^{148}Gd in a thick target, we performed a series of thin-foil irradiations. The foils had to be thin enough for the α-particles from ^{148}Gd decay to exit the foils and be detected. The acceptable foil thickness was 3 μm for tungsten, tantalum, and gold. Aluminum foils (10 μm) were used to determine an absolute proton flux on the foils using the well-known ^{27}Al(p,x)^{22}Na cross section. Stacks of three foils were used to investigate any possible loss of ^{148}Gd and ^{22}Na recoils in the material of interest. ^{148}Gd cross sections were determined by directly counting decay α-particles with the appropriate energy in a dedicated detector system.

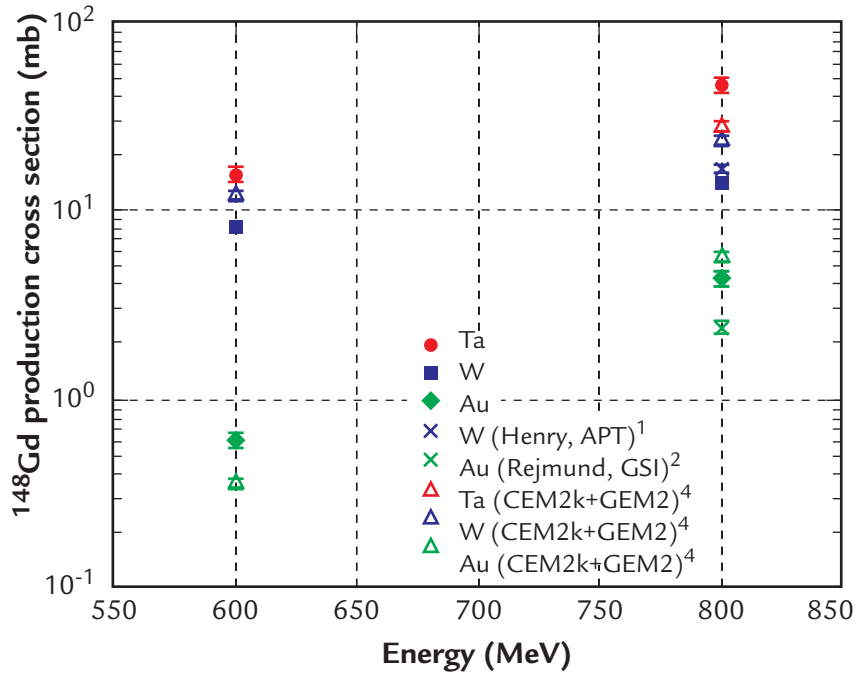

Fig. 1. Preliminary ^{148}Gd-cumulative-production-cross-section measurements for tungsten, tantalum, and gold interactions with 600- and 800-MeV protons at WNR compared to previous measurements and predictions.

During the 2002 run cycle at LANSCE, we irradiated thin samples of tungsten, tantalum, gold, and aluminum with 600- and 800-MeV protons at WNR to obtain cross-section measurements and compare them to previous measurements and theoretical estimates from the CEM2k+GEM2 code (Fig. 1). Preliminary analyses indicate that our measurements for tungsten are within 40% of CEM2k+GEM2 predictions and within 14% of the APT decay-heat measurement. Another set of irradiations at 800 MeV is planned for January 2003 in the WNR Blue Room. Measurements for other isotope-production cross sections are also being investigated via γ-ray spectroscopy and compared to previous measurements and predictions.

Acknowledgements

The authors would like to acknowledge the operators in the Central Control Room (LANSCE-6) and the support of Gregg Chaparro (LANSCE-3) in the WNR Blue Room. This study is supported by the U.S. Department of Energy.

References

1. E.A. Henry and K.J. Moody, APT internal report, Lawrence Livermore National Laboratory (1999).
2. F. Rejmund et al., *Nuclear Physics A* **683**, 540-565 (2001).
3. R. Michel et al., *Nuclear Instruments and Methods B* **129**, 153-193 (1997) and references therein.
4. S.G. Mashnik et al., Los Alamos National Laboratory report LA-UR-02-0608 (2002).

Improving Radiochemical Diagnostics: Studying Iridium and Europium with the Germanium Array for Neutron-Induced Excitations

R.O. Nelson, M.J. Devlin, N. Fotiadis, A. Michaudon (LANSCE Division), J.A. Becker, J. Cooper, P.E. Garrett, W. Younes (Lawrence Livermore National Laboratory), T. Ethvignot (CEA, Bruyères-le-Châtel)

Radiochemical (radchem) diagnostics play an important role in understanding the detonation of a nuclear device. Some elements or isotopes were at times inserted as radchem detectors at various locations in a nuclear device. During detonation, these detectors are subjected to a short and intense flux of fission and possibly fusion neutrons. After the detonation, the radchem detectors and their long-lived activation products are retrieved from the underground-explosion site and subsequently analyzed. These radchem detectors are sensitive only to neutrons with energies above the energy threshold of the reaction responsible for the formation of the activation products. A large amount of such radchem data exists from past underground nuclear tests.

The neutron-energy spectrum and the location of the detector are time-dependent quantities, which can only be determined from computer simulation. A basic ingredient in the analysis of data from radchem detectors is an accurate knowledge of the activation cross sections of these detectors.

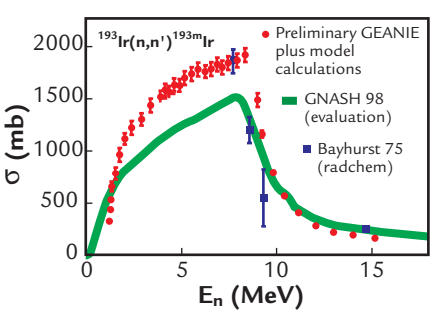

Fig. 1. Activation cross section for the ^{193}Ir(n,n')^{193m}Ir reaction.

Measurement of Cross Sections

A LANL/Lawrence Livermore National Laboratory (LLNL) collaboration is studying the use of iridium and europium (and other isotopes) as radchem detectors. Each isotope has a specific activation cross section as a function of incident-neutron energy. These cross sections are often difficult to measure by conventional means. The collaboration has developed a technique for determining activation cross sections over a wide incident-neutron energy range using the Germanium Array for Neutron-Induced Excitations (GEANIE), a large γ-ray detector array at LANSCE's WNR facility. GEANIE is well suited to resolve the complex and specific γ-ray cascades emitted in neutron-induced reactions and to subsequently help identify the radioactive products of interest. Measurements with GEANIE can detect the most intense γ-ray cascades, and theory is used to calculate the contribution from undetected γ-rays. By combining the two approaches, we obtain the needed activation cross sections.

Iridium Isotopes

Natural iridium consists of ^{191}Ir (37.3%) and ^{193}Ir (62.7%), both of which can serve as radchem detectors. A long-lived state in ^{193}Ir (called ^{193m}Ir, where "m" stands for metastable) at an excitation energy of 80.22 keV and with a half-life of 10.53 days can be formed by inelastic scattering on ^{193}Ir and serve as a neutron-fluence detector most sensitive to low-energy neutrons (i.e., with energies above the threshold energy of 80.6 keV). Little relevant data existed, in part, because of the lack of intense monoenergetic fast-neutron sources. The previous data and an evaluation are shown in Fig. 1. The recent γ-ray cascade data obtained with GEANIE and supplemented by model calculations are also shown in Fig. 1. These results substantially differ from the GNASH 98 evaluation over most of the energy range.

The previous experimental data point at 7.57 MeV is in agreement with our results but far above the cross-section evaluation. Measurements on ^{191}Ir, similar to those done on ^{193}Ir, have also been started. As seen from the results above, better nuclear-reaction modeling of activation cross sections is needed.

Europium Isotopes

Natural europium consists of ^{151}Eu (47.3%) and ^{153}Eu (52.2%), both of which can serve as radchem detectors. With a threshold of 7.98 MeV, the ^{151}Eu(n,2n)^{150}Eu reaction can produce ^{150}Eu in an isomeric state (called ^{150m}Eu) at an excitation energy of E_x = 42.1 keV and with a half-life of 12.8 hours, which is compatible with commonly used radiochemical techniques.

There are, however, uncertainties in the activation cross section for the production of this isomer (Fig. 2). The ^{151}Eu(n,2n)^{150}Eu cross section has been measured by directly counting the two neutrons emitted in the reaction. This measurement can only give the sum of the cross sections for the reactions ending with the ^{150}Eu ground state (called ^{150g}Eu, where "g" stands for ground state) and ^{150m}Eu.

Cross sections for the ^{151}Eu(n,2n)^{150g}Eu and the ^{151}Eu(n,2n)^{150m}Eu reactions have been measured by radiochemical methods. The sum of these cross sections is also shown in Fig. 2. Reducing the uncertainties in these cross sections will improve the sensitivity of the diagnostics. Knowing the formation by neutron-inelastic scattering of ^{151}Eu in its ground state and its main isomeric state at 196.245 keV, with a half-life of 58.9 μs, will allow a full computer simulation of the production of the isomeric state of ^{150}Eu.

Such a calculation will include the effect of the ^{151}Eu isomeric state for the first time. The team has collected data on the reactions described above and are currently in the process of analyzing these data.

Conclusion

Combining γ-ray cascade measurements obtained on GEANIE with nuclear-reaction model calculations allows scientists to determine activation cross sections, including those for ^{193}Ir(n,n')^{193m}Ir and ^{151}Eu(n,2n)^{150m}Eu reactions, useful for radchem diagnostics. These activation cross sections, which are difficult to obtain by other means, could be used to better understand the detonation of nuclear devices and in other applications for which radchem-fluence measurements are needed. Data obtained with GEANIE extend to high incident-neutron energies (up to ~ 200 MeV) such as those found in systems for transmutation of nuclear waste or other high-energy systems that use neutrons.

References

1. Data retrieved from the CSISRS database, ^{151}Eu(n,2n) EXFOR files, and references therein are available from the National Nuclear Data Center at http://www.nndc.bnl.gov/.

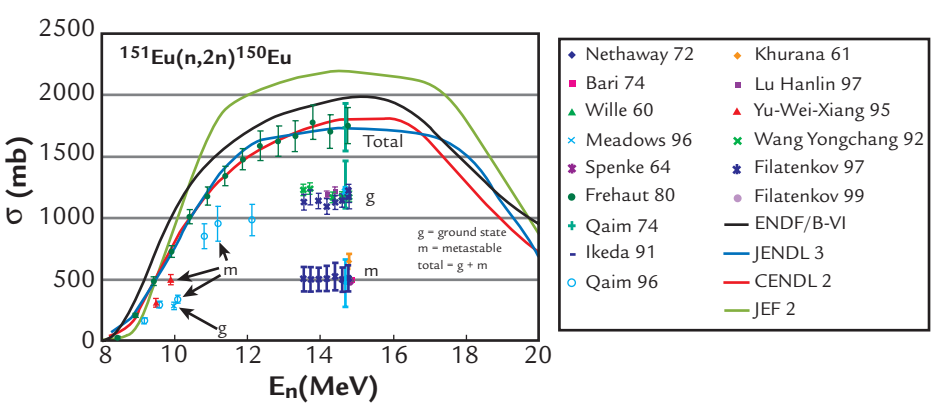

Fig. 2. Plots of ^{151}Eu(n,2n) cross sections for neutron energies between 8 and 20 MeV. Experimental data points are given for the ^{151}Eu(n,2n)^{150g}Eu cross section (g) and for the ^{151}Eu(n,2n)^{150m}Eu cross section (m). Data points and evaluated data (solid lines) are also given for the sum of these two cross sections (total = g + m).[1]

Demand Grows for Single-Event-Effects Measurements at the LANSCE Irradiation of Chips and Electronics House

B.E. Takala (LANSCE Division)

The Irradiation of Chips and Electronics (ICE) House is located on the 30° left flight path (FP) of the high-energy-neutron source at LANSCE. The shape of the neutron spectrum on this FP is very similar to the spectrum of neutrons produced in the atmosphere by cosmic rays but with a flux more than 5 orders of magnitude higher (Fig. 1). This large neutron flux allows testing of semiconductor devices at greatly accelerated rates.

Testing neutron-induced single-event effects (SEEs) is important because neutrons have been recognized as a significant threat to semiconductor devices at aircraft altitudes and below. Since WNR was first demonstrated as an effective SEE testing tool in 1992, a growing number of companies from around the world are using the WNR high-energy-neutron source to characterize components and study various failure modes caused by neutron radiation.

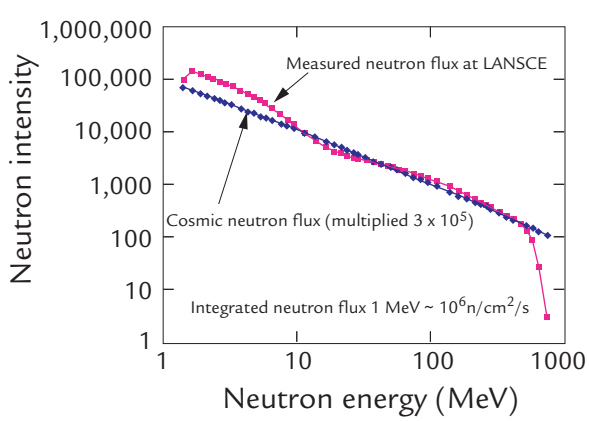

Fig. 1. The LANSCE neutron spectrum is very similar to the cosmic-ray-induced neutron spectrum but with a flux more than 5 orders of magnitude higher.

Effects of Neutrons Produced in the Upper Atmosphere

Galactic and solar cosmic rays collide with nuclei in the upper atmosphere creating a shower of subatomic particles. The charged-particle components of the cosmic-ray shower are strongly absorbed by the atmosphere, but the uncharged neutrons are able to reach aircraft altitudes and below. These energetic incoming neutrons penetrate semiconductor devices and collide with the atoms in the material, causing charged recoils (from neutron and atom collisions) and the production of secondary particles (e.g., protons, electrons) that deposit charge and energy in the devices (Fig. 2). This charge deposition can initiate so-called SEEs in semiconductor devices that can seriously affect their performance.

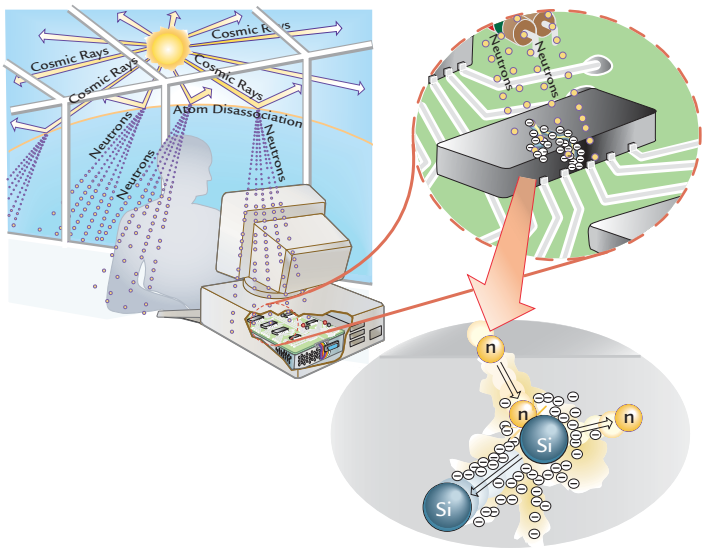

Illustration by G. Tietjen

Fig. 2. Incoming neutrons are produced by cosmic rays in the upper atmosphere. These neutrons penetrate semiconductor devices where they collide with atoms, causing recoils that deposit charge and thus initiating SEEs.

Single-event upsets occur when a memory location changes its state because of charge deposited by an energetic particle. Failures such as latchup in which a device ceases to function are more serious because they usually require turning the device off and then on to eliminate the latchup. Other more serious failure modes occur in high-power devices in which a neutron can initiate a cascade of charged particles that causes these devices to draw large currents that can permanently damage them.

ICE House Capabilities Make It the "Preferred Facility" for SEE Testing

The ICE House provides experimenters with several advantages over other testing methods. Unlike heavy-ion tests where a device must have its case material removed and then be placed in vacuum to permit particles to reach the sensitive regions of the chip, testing in the ICE House beam permits normal operation of the device in the open air. In fact, because neutrons are not strongly absorbed by the device, several devices may be placed in the neutron beam at once, one behind the other.

The integrated neutron flux at the ICE House is approximately 10^6 neutrons/cm^2/s for energies above 1 MeV. No other facility in the world can offer this intensity with a spectrum matching the natural atmospheric spectrum so closely. The Joint Electron Device Engineering Council (JEDEC), which represents about 300 manufacturers and users of electronics, recognized the ICE House in its published memory-testing standard, JESD89, stating, "The WNR at Los Alamos is the preferred facility."

Growth of the SEE Research Program Continued During 2002

Efforts to publicize the new ICE House facility and the emergence of JESD89 have increased the demand for beam time. The number of proposals and industrial participants were both at record levels during the LANSCE 2002 run cycle. In 2001, 8 experiments were conducted, whereas 21 experiments were run in 2002. Also notable was having six new first-time industrial user companies. The early arrival of proposals for the 2003 run cycle is a good indicator that user growth will continue.

Recent Developments in Neutron-Induced SEE Research at LANSCE

New issues continue to emerge from recent experiments. Effects on logic nodes in field-programmable gate arrays are being widely studied. The relationship between failure rates and feature size is hotly debated. Wide variations in latchup susceptibility have been observed. Variations depending on geometric orientation, socket type, and even circuit layout have been demonstrated. Research opportunities in the field are abundant at this time.

New tests have also been undertaken this year. The National Aeronautics and Space Administration (NASA), the Federal Aviation Administration, and Honeywell have placed a running flight-control system in the beam with the output fed to a flight simulator to observe effects. (See *Neutron Particle Effects on a Redundant Flight-Control Computer,* p. 90.) The goal is to eventually provide real-time output to a high-fidelity simulator at the NASA Langley Research Center. Also new this year was the first test of high-power insulated-gate bipolar transistors.

The industrial community has recognized the increased involvement of LANSCE in the SEE field. We have been invited to participate in developing a JEDEC test method to complement JESD89 or to be incorporated into another appropriate JEDEC standard.

Conclusion

LANSCE, through the new ICE House, is uniquely positioned to address the SEE problem for the electronics industry and the nation. Valuable research at the forefront of the field is being conducted at the ICE House where new research opportunities are being uncovered. Demand for time at the facility has grown dramatically and evidence suggests that the growth will continue.

Neutron Particle Effects on a Redundant Flight-Control Computer

C.M. Belcastro, K. Eure, D. Koppen (National Aeronautics and Space Administration Langley Research Center), O. Gonzalez, W.S. Gray (Old Dominion University), R. Hess (Honeywell International, Inc.), J. Dimtroff, A. Wilson (Federal Aviation Administration), S.A. Wender, B.E. Takala (LANSCE Division)

Although the atmospheric neutron environment is relatively well understood by scientists, the effects of this environment on aircraft electrical/electronic systems are not. By and large, system effects have only been anecdotally reported. Thus, there is an urgent need for characterizing aircraft-systems-level effects.

Single-event-upset (SEU) phenomena have been documented at the chip level since 1979. In 1992, atmospheric neutrons were found to be the cause of SEUs in avionics. A survey of SEU phenomena and research was developed for an industry Avionics Working Group in 2000. A new research partnership was established in 2002 to study the effects of neutrons on flight-critical systems. Participants in this research partnership are the Federal Aviation Administration (FAA), the National Aeronautics and Space Administration (NASA) Langley Research Center, LANSCE, Honeywell International, Inc., and Old Dominion University.

The research objectives of this FAA/NASA-funded research are to (1) investigate the effects of SEUs on closed-loop systems, (2) develop methods and a capability for testing SEU closed-loop systems, (3) develop design and analysis methods to mitigate and assess SEU closed-loop-system effects, and (4) investigate the applicability of recoverable computing techniques to mitigating SEU effects. The expected benefit of this research will be the development of design and validation guidelines for achieving cost-effective aircraft-system performance in the atmospheric neutron environment, thus providing the degree of safety needed for aircraft functions.

SEU Research at the Irradiation of Chips and Electronics House

The SEU research to be performed under this partnership involves a series of experiments that will be conducted at the Irradiation of Chips and Electronics (ICE) House at LANSCE during this multi-year effort. The experiments will use NASA-owned flight systems: (1) older electronic-device technology used in a redundant Flight Control Computer (FCC) with four separate processors calculating the control laws; (2) newer electronic-device technology (1-μm, or less, feature size) used in a recoverable FCC; and (3) the latest electronic-device technology used in a Flight Management and Electronic Instrument System implemented in an integrated modular architecture with independent application partitions. A closed-loop, system-level experiment was conducted at LANSCE during the 2002 run cycle (Fig. 1).

Fig. 1. The redundant FCC experimental setup at the ICE House before exposure to the LANSCE neutron beam. (a) The ICE House, and (b) the redundant FCC aligned in the neutron beam.

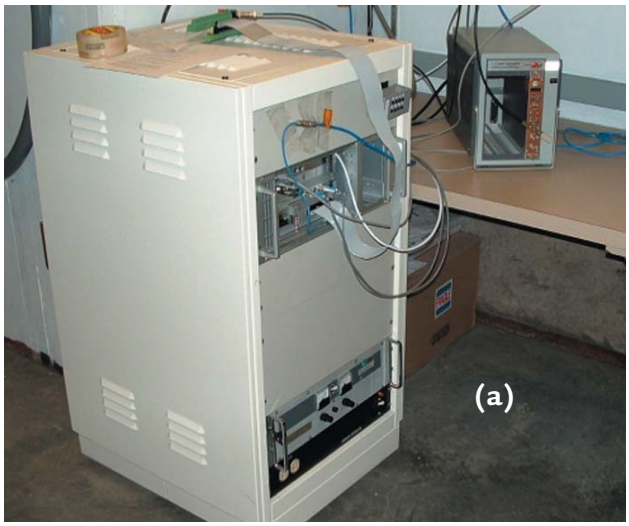

Fig. 2. (a) Aircraft-emulation computer interfaced to the redundant FCC, and (b) data-collection computer and monitor displays for each FCC command.

In this experiment, a redundant FCC representing 20-year-old digital computer technology with relatively large feature sizes was subjected to the neutron beam to investigate system effects and the associated impact on the aircraft. During the exposure, the redundant FCC was executing B737 control laws and was interfaced to a virtual-memory-extension (VME)-based, real-time computer emulation of the B737 aircraft (which was not exposed to the neutron beam). Simulated aircraft parameters from this emulation software were input to each of the four processing channels of the FCC. Each of the four processors calculated all four aircraft commands: (1) throttle command for controlling thrust; (2) elevator command for controlling pitch angle; (3) aileron command for controlling rolling moment; and (4) rudder command for controlling yaw angle. Each of these commands from each processor was output from the FCC and input into the aircraft emulation computer. A combined, or voted, value for each command was determined by discarding the high and low values from the four processors and averaging the remaining two command calculations. These voted commands were then input to the aircraft simulation. The control commands calculated by each processor were monitored in real time during neutron exposure on an independent data-collection computer. This computer displayed information in strip-chart format on four displays — one for each command. Data were collected and compared at each 50-ms calculation frame. The B737 emulation computer and monitor displays are shown in Fig. 2.

Conclusion

This is the first closed-loop-system experiment to be conducted at LANSCE. Data from this experiment are currently being analyzed for publication in a NASA technical paper.

Research Highlights
Proton Radiography

2002 Proton Radiography Overview 94

A Cerenkov Radiation Detector for Proton Radiography at LANSCE 96

Proton Radiography Microscope 100

Proton Radiography Capabilities Illuminate Studies of Explosively Driven Fragmentation 102

2002 Proton Radiography Overview

F.E. Merrill (P Division), Proton Radiography Team

The Proton Radiography (pRad) program at LANSCE is investigating weapons-physics issues related to the detonation of high explosives (HE) along with the equation of state of the burned HE products, the dynamic failure processes of explosively driven metals such as spall and shear banding, and the hydrodynamics of implosions. This program provides the unique capability of studying the evolution of explosive processes with high spatial and temporal resolution. With this technique, 800-MeV protons provided by the LANSCE linear accelerator penetrate directly through the dynamic system (Fig. 1). The protons, delivered in 50- to 100-ns-long pulses, interact with the material of the dynamic system in a containment vessel (Fig. 2) and undergo scattering that is proportional to the product of the density and thickness of the material. The configuration of the materials, which are moving with typical velocities of ~ 1 mm/μs, is effectively frozen during the short duration of the proton pulses. These protons are then transported from the object through a magnetic lens to a Fourier point where protons are intercepted if they are scattered to angles larger than some maximum cutoff. This cutoff angle provides the image contrast whereby the proton density is lowered for protons passing through thicker materials. The protons surviving the cutoff angle are then magnetically transported to a scintillator located at an image location where the proton positions are identical to their initial positions at the object location. The scintillator converts the proton flux to light, which is collected by a series of fast-gated cameras. The multiple images are separated in time by typically 1 μs for up to 21 pulses per dynamic event. These images can then be combined to produce a motion picture of the dynamic event in which materials travel ~ 1 mm between frames.

Fig. 1. Panoramic view of the pRad facility.[1]

In 2002, 42 dynamic pRad experiments — a pRad-shot record — were performed at LANSCE in support of the weapons-physics efforts at LANL, Sandia National Laboratories (SNL), Lawrence Livermore National Laboratory (LLNL), and the Aldermaston Weapons Establishment (AWE), bringing the total number of dynamic pRad experiments performed at LANSCE to 156. For these shots, the LANSCE accelerator and beam-delivery complex provided protons

Fig. 2. Peter Pazuchanics (LANL) inspects a 3-ton steel vessel used to confine the explosions involved in many pRad experiments.[1]

with 100% reliability. In addition to these dynamic experiments, beam time was used for detector and concept development and for the radiography of static mockups to determine shot configurations and the design of future experiments.

The 42 pRad shots in 2002 fell into three categories: (1) outside-user experiments, (2) studies of HE burn characteristics, and (3) the study of material failure mechanisms such as spall and shear banding. Two experiments were fired for SNL to continue investigations on the dynamics of explosively driven voltage bars used for neutron generators. Three experiments were performed with LLNL to study the material-failure characteristics of steel under various shear- and stress-dynamic-loading scenarios. A sixth dynamic experiment was performed with AWE to investigate the bonding strength of a thin lead layer bonded to an aluminum disk. Of the 42 dynamic experiments, 18 were devoted to the study of HE burn characteristics. Three of these experiments were designed to study the equation of state of HE burn products, two measured the width of the HE detonation zone in PBX-9501 and PBX-9502 high explosives, and the remaining experiments were designed to study the characteristics of detonating HE (Fig. 3). An experimental series named AFX-221 was performed for the U.S. Air Force to study the HE burn characteristics around objects embedded within the HE. Nine dynamic experiments were performed to study the spall-formation process in aluminum, copper, tin, and 316L stainless steel (Fig. 4). Two experiments were performed to study the fracture mechanisms of thin cylinders of titanium (see *Proton Radiography Capabilities Illuminate Studies of Explosively Driven Fragmentation*, p. 102). The third experiment was a classified configuration containing the largest HE load (~10 lb) ever fired at LANSCE. This experiment is being carefully simulated to provide model data for comparison to the data collected at pRad.

In addition to the experiments performed in 2002, two new radiography systems were commissioned. The first was installed in the spring to study the possibility of using Cerenkov light, rather than scintillation light, to image the proton distribution. The accelerator was tuned to provide ~ 500-MeV protons, which is the threshold energy for protons to emit Cerenkov light in water, to the standard pRad magnetic imaging system. A new radiator and imaging system was built and installed to collect the Cerenkov light. This system successfully imaged very thin systems with a factor of ~ 40 improvement in contrast over the standard radiography system (see *A Cerenkov Radiation Detector for Proton Radiography at LANSCE*, p. 96). The second new capability, a pRad microscope, was commissioned in the fall of 2002. This microscope system was designed to improve the radiographic resolution to study the mesoscale properties of dynamic systems. The commissioning effort was very successful in improving the resolution from the 200 μm achieved with the standard radiography system to 18 μm (see *Proton Radiography Microscope*, p. 100).

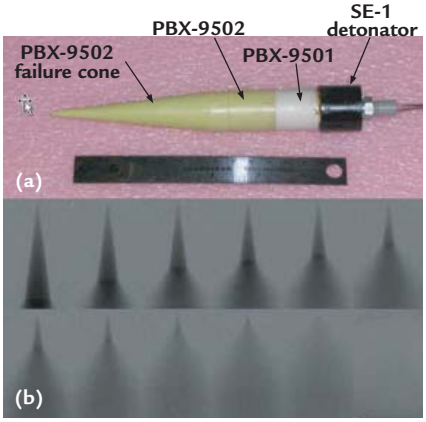

Fig. 3. (a) Failure cone designed to study the detonation characteristics of PBX-9502. (b) Proton radiographs at various times throughout the detonation of the failure cone showing characteristics of the detonation front as it propogates to the end of the failure cone.

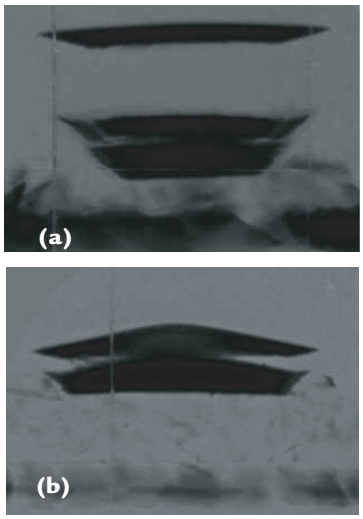

Fig. 4. Late-time (80 μs after the shock entered the steel) proton radiograph from the two 316L stainless-steel failure experiments fired in November 2002. (a) 1/2-in.-thick sample. (b) 1/4-in.-thick sample.

References

1. B. Fishbine, Los Alamos National Laboratory report LALP-03-003, p. 14.

A Cerenkov Radiation Detector for Proton Radiography at LANSCE

A. Saunders (P Division)

A new radiographic imaging system was installed in 2002 to study the use of Cerenkov light, rather than scintillation light, to image proton distribution in pRad experiments. This Cerenkov radiation detector (Fig. 1) has successfully imaged very thin systems with an order of magnitude higher contrast than could have been achieved with the standard radiography system. We have demonstrated the enhanced contrast possible with this new detector for pRad studies. It uses the energy loss of the protons in a radiographic object — a source of information that is ignored in conventional multiple scattering radiography. Contrast with our Cerenkov radiation detector is much better than that in multiple-scattering radiography.

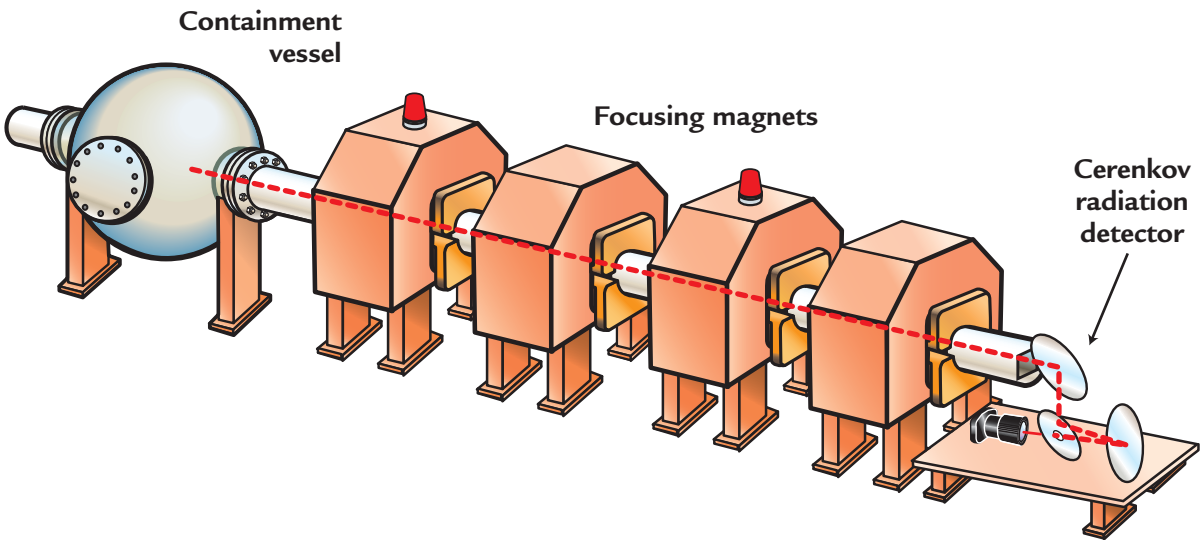

Fig. 1. A Cerenkov radiation detector can improve the ability of 800-MeV proton radiography (shown here) to image very thin systems with minimal radiation doses.

Measuring Different Types of Proton Interactions with Test Objects Using the pRad Technique

The pRad technique uses the transmission of a proton beam through an object to make quantitative measurements of the interactions of protons with this object. For the 800-MeV protons delivered by LANSCE to the pRad facility in Line C, these interactions fall into three categories. The first is the nuclear, or hadronic, interaction between the protons and the nuclei of the material in the object. This interaction can be characterized as a *loss cross section* because any proton that undergoes this type of interaction is likely to be lost from the incident beam either by scattering through an angle larger than the angular acceptance of the pRad system or by losing so much energy that it no longer falls within the momentum acceptance of the system.

The second type of interaction seen in 800-MeV pRad studies is Coulomb multiple scattering. This scattering causes small random angular deviations along each proton's path because of many weak, long-range Coulomb interactions with the nuclei in the object. Because the average angular deviation depends on the thickness of the object measured in radiation lengths, obtaining the average scattering angle for the protons passing through each pixel of the object results in a measurement of the thickness along that pixel. This method is used in pRad to measure the thickness of dynamic objects, such as high-explosive-driven shock waves in metal.

In the third interaction, the protons interact via the Coulomb force with the electrons in the object. Because the electron mass is only about 1/2,000 that of the proton, these interactions do not significantly change the proton's trajectory, but instead they slightly decrease the proton's kinetic energy at each collision, causing the proton to steadily lose energy as it passes through the object. The thicker the object along the proton trajectory, the greater the energy loss. Because the magnetic-lens system used to focus the protons at the image plane can only have optimum resolution at one proton energy, the variation in proton energies across the object blurs parts of the object that are not at the focus energy setting.

We have developed a new Cerenkov detector that takes advantage of the variation in proton-energy loss in the object by making an energy-dependent measurement of the number of protons reaching the image plane. The pRad detectors now used at the image plane are nearly energy independent. As such, information present in the distribution of proton energies is lost. By building an energy-dependent detector, we can use this information to distinguish fine variations in the density of the object.

New Detector Makes Use of Cerenkov Radiation

The new detector makes an energy-dependent measurement of the protons by using Cerenkov radiation, which is light emitted by charged particles moving through a medium faster than the local speed of light (which, in a material, is less than the speed of light in vacuum). This radiation is caused by the particle — protons in our case — moving faster than the subsequent spreading electric field can keep up with; it is directly analogous to the sonic boom caused by objects moving faster than the speed of sound in air. The Cerenkov light is emitted at a characteristic angle, θ_c, that is dependent on the speed of the particle, βc, and the index of refraction of the detector medium, n:

$$\theta_c = \cos^{-1}(1/n\beta).$$

The number of photons emitted, N, per unit path length and per unit photon energy is also dependent on the same two variables via the characteristic angle:

$$\frac{d^2N}{dxdE} = \frac{\alpha z^2}{\hbar c} \sin^2 \theta_c,$$

where x is the path over which the particle passes, E is the emitted photon-energy distribution, $\hbar$ is the Planck constant divided by 2π, z is the charge of the incident particle in units of the electron charge, and α is the fine structure constant. The threshold speed above which Cerenkov light is emitted is $\beta = 1/n$.

By tuning the index of refraction of the detector material to the speed of the protons (or vice versa), a threshold Cerenkov radiation detector can be built whereby the faster protons that pass through the thinner parts of the radiographic object will emit light but not the slower protons that pass through the thicker parts of the object. This technique, however, is very limited in statistics for an object with small density variations because the light emitted from protons just above the speed threshold is very small (because of the $\sin^2 \theta$ dependence above). A better approach is to design a detector that can measure the angle of the emitted Cerenkov light from the radiator. From this angle the proton speed is known, and energy-dependent measurements can be

made at larger light angles that correspond to speeds higher above threshold for the medium and to greater numbers of emitted photons.

Our detector, which achieves the goal of measuring the light emitted from the Cerenkov radiator as a function of angle, is shown schematically in Fig. 2. The incident protons create Cerenkov light in the radiator medium, shown in green. The light emerges at different angles depending on the speed of the protons, which in turn depends on the thickness of the object along their respective paths. The light is focused by a spherical mirror and then it passes through a Fourier plane where it is sorted by the angle (rather than position) with which it emerged from the radiator. Note that the rays in Fig. 2 are sorted by color at the Fourier plane, and the colors correspond to different angles of light emerging from the radiator. Finally, the light is detected by a charge-coupled-device (CCD) camera focused on an image plane, which is downstream of the Fourier plane. A cut can be made on the light at the Fourier plane, to allow only light emerging at larger angles to reach the camera. Because larger angles correspond to faster, higher-energy protons, this cut ensures that only light from protons that passed through thinner parts of the object will reach the camera and produce a high-contrast image of the object.

The ideal tuning of the proton-beam speed relative to the Cerenkov radiator medium changes when the angle-dependent measurement system is used instead of a threshold detector. In the case of the threshold detector, the ideal incident-proton energy has

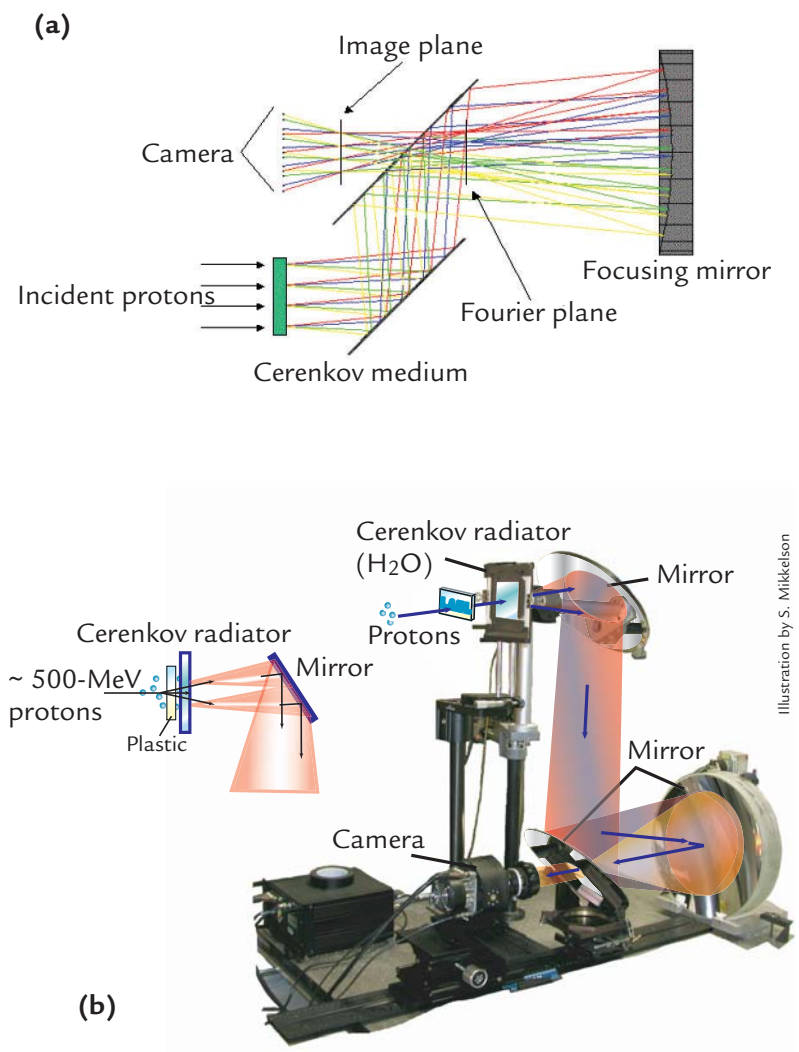

Fig. 2. (a) Schematic representation of an angle-dependent Cerenkov radiation detector. (b) Rendering of the Cerenkov detector.

protons that pass through the thick part of the object moving at a speed below the Cerenkov threshold and those that pass through thin parts of the object moving at a speed above the threshold. In the case of the angle-dependent device, however, the ideal tuning has the incident protons at a higher energy relative to the threshold. Thus, the protons that pass through the thick parts of the object still create Cerenkov radiation in the detector but at a smaller angle than their higher-energy counterparts. Therefore, their light is blocked at the Fourier plane and does not reach the camera.

Prototype of the Cerenkov Radiation Detector

We have built a prototype Cerenkov detector and tested it using the proton beam in Line C. For simplicity, we chose water for the Cerenkov radiator medium with a corresponding tuned proton energy of 500 MeV. We made energy-dependent radiographs of several thin objects. The object shown in Fig. 3 consisted of an 1/8-in.-thick piece of plastic with letters machined through it. The contrast in this Cerenkov-enhanced picture is about 20%; using conventional 800-MeV pRad, the best achievable contrast would have been about 0.5%, or a factor of 40 worse. Therefore, we have demonstrated the capability of making high-contrast-enhanced radiographs using the pRad system with a Cerenkov radiation detector.

As we continue to improve the technology of the Cerenkov detector, our work will be focused in two directions. First, we need to better understand the quantitative dependence of the detected light level in the CCD camera on the object thickness, the accelerator emittance, and the energy loss and spread in the other beam-line elements. Second, we intend to build a Cerenkov radiator that is tuned to 800-MeV protons so that we can do further tests without retuning the accelerator to 500 MeV. The index of refraction that corresponds to the speed of 800-MeV protons is about 1.2. A possible Cerenkov radiator with this index is liquid nitrogen.

Conclusion

We have made an initial demonstration of the enhanced contrast possible using a Cerenkov radiation detector for pRad studies. This type of detector uses the energy loss of the protons in a radiographic object — a source of information that is ignored in conventional multiple-scattering radiography. Contrast with our system is much better than that in multiple-scattering radiography.

We will continue to improve our understanding of the operation of our prototype detector through further tests, either with the present water radiator or one tuned to 800-MeV protons.

Fig. 3. A radiograph made with a water-based Cerenkov detector and 500-MeV protons.

Proton Radiography Microscope

D.B. Barlow, B. Blind, A. Jason, C.T. Mottershead, R. Valdiviez (LANSCE Division), G.E. Hogan, F.E. Merrill, C. Morris (P Division)

During the 2002 run cycle, LANSCE-1 (Accelerator Physics and Engineering) designed and built a new high-gradient permanent-magnet microscope, which was successfully tested by members of the pRad team. The design of this new permanent-magnet-quadrupole (PMQ) microscope system was part of a larger Laboratory-Directed Research and Development project to develop a pRad capability to study dynamic phenomena on a 10-μm scale. The PMQ microscope further enhances the application of pRad to understanding dynamic material properties at grain scales.

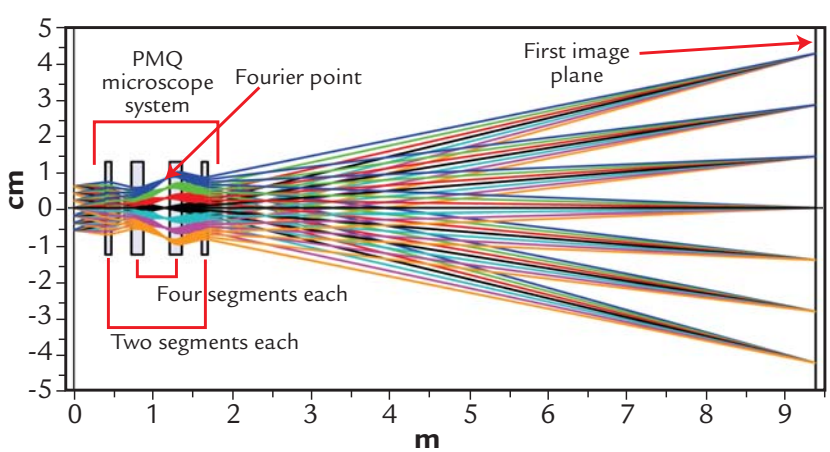

Fig. 1. Russian-quadruplet configuration showing the proton trajectories from the object to the first image plane.

Design of a Microscope for pRad Experiments

The pRad facility in Area C consists of a diffuser to spread the beam, an illuminator-matching section to tailor the phase-space distribution of the beam, a monitor lens to copy this distribution onto the object, and two sequential imaging lenses. The imaging lenses focus the scattered protons onto scintillator screens in two locations, thereby forming visible-light images that are recorded by a set of gated charged-couple-device TV cameras. The lenses and illuminator-matching section are made of magnetic quadrupoles.

The new PMQ microscope system had to fit smoothly into the operations at Area C, using as much of the existing equipment (e.g., the camera systems) as possible. In our initial studies, we explored the possibility of achieving high magnification by using alternative power settings for the eight existing quadrupoles, the new PMQ microscope system, or some combination of the two. Very high magnifications (i.e., over 100x) were achieved by combining the two types of quadrupoles into a hybrid system but with correspondingly high chromatic aberrations. The real measure of performance requires dividing the aberration coefficient by magnification to express the resulting chromatic aberration in object coordinates. Magnification must be sufficient enough to allow the digital-imaging system to somewhat oversample the chromatic-aberration function. By this measure, we achieved the best performance with a microscope system made up of the new high-gradient PMQs in the *Russian-quadruplet* configuration shown in Fig. 1.

The new radiographic imaging system is composed of 12 PMQ segments that are 1.5 in. thick, each containing 16 permanent magnets (Fig. 2). The inner pair of PMQs was assembled from four segments each, and the outer pair was assembled from two segments each. The PMQ microscope system is mounted in the Area C beam line in the location normally occupied by the first two large quadrupoles, which have been mounted on rails to facilitate the configuration change (Fig. 3).

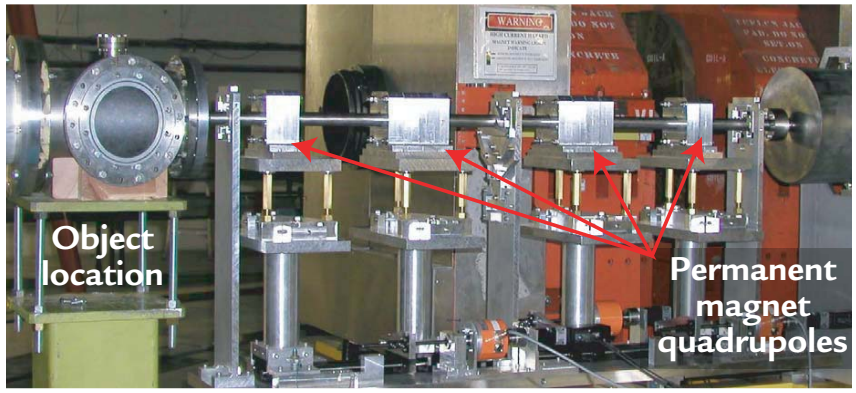

Fig. 3. The PMQ microscope installed in the pRad facility at LANSCE.

The position of the PMQs may be adjusted from the control room by actuators to focus the lens on either the first image location with a magnification of 7.2x or the second image location with a magnification of 15.8x. The rays in Fig. 1 are color coded by scattering angle in 2-mrad increments. The location near the center of the lens where the rays are completely sorted by scattering angle is called the Fourier point. A small aperture collimator at the Fourier point attenuates the scattered rays. This collimator provides image contrast by darkening the pixels that come from the locations containing the material that causes the scattering. We adjusted the illuminator-matching section to place the Fourier point at the location calculated to cancel the energy dependence of the magnification. The first test object used was a small stainless-steel plate with the acronym LANL milled in it in about 7-mm-high letters. At first beam, we obtained a good picture with the nominal settings. But after some tuning, we obtained a resolution better than 15 μm as seen in Fig. 4. A finer test object is needed to fully characterize the resolution limits of the system.

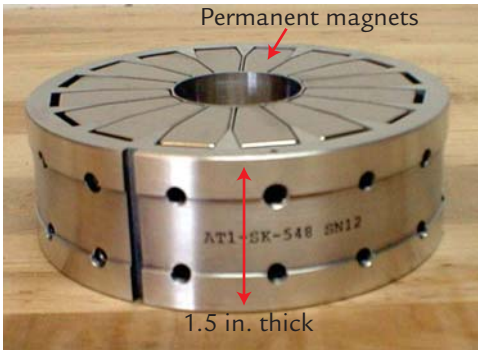

Fig. 2. One of 12 segments that comprise the new radiographic imaging system. These segments, which exceeded specifications, were manufactured by Aster Corporation.

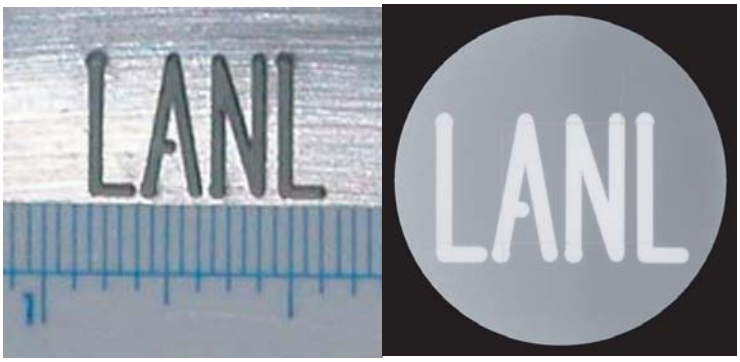

Fig. 4. LANL logo used as the first test object — a small stainless-steel plate with the acronym LANL milled in it in about 7-mm-high letters. The finest tick marks on the ruler are 1/32 in.

Proton Radiography Capabilities Illuminate Studies of Explosively Driven Fragmentation

P.M. Rightley, K.P. Prestridge (DX Division)

The central mission of the Dynamic Experimentation Division at LANL is the experimental study of the behavior of materials under extreme conditions. Accomplishing this mission requires a comprehensive understanding of the energetic materials (explosives) themselves and of the interaction of detonating explosives with the materials around them. LANL is acknowledged as a world-leading institution in understanding how materials are driven by explosives. Such knowledge is necessary in working with both conventional and nuclear explosives. The pRad facility at LANSCE provides a unique capability to study the properties of energetic materials and the effects of explosively driven shocks on materials in general.

Understanding the Shear-Banding Process in Explosively Driven Material

As a detonation wave passes through an explosive, the pressure immediately behind the wave is on the order of 100,000 atm (100 kbar). A phenomenon known as the Taylor wave immediately begins to reduce this extremely high pressure — but the damage has already been done. This extremely high pressure sends a shock wave into materials adjacent to the explosive, which usually modifies the properties of the material from their initially well-understood values. For instance, the shock wave could harden the material and thereby make it more brittle even before the material has had a chance to move in response to the pressure. This dynamic modification of the materials make explosively driven systems very hard to understand because the properties of the material under dynamic loading are unique to that situation. Thus, it is difficult to reproduce those conditions in the laboratory without actually destroying the laboratory. After the material has been dynamically modified, the Taylor wave will reduce the pressure of the detonation products, but these products are still at a very high pressure. It is this latent pressure that then drives (or pushes) the materials near the explosives.

The yield strength of some of the strongest steel (i.e., Vascomax 300) is around 15 kbar, which is only about 15% of the pressure immediately behind the detonation wave of an explosive. Therefore, even as the Taylor wave reduces the pressure of the detonation products, the pressure is still near or higher than the strength of the materials in the vicinity. Because these materials are driven by pressures well above their strength, they behave like fluids, including supporting instabilities like many fluid flows. For example, commercially pure titanium (CP Ti) exhibits a shear-banding instability where, as the material is strained at high rates, shear is localized into very thin shear bands. Therefore, as the overall strain in the system increases, the majority of the material is not strained at all; rather, all the strain is concentrated into these regions. Eventually, as these shear-band regions experience significant heating (caused by the strain) and then soften, they will fail and form cracks. This phenomenon can lead an expanding metal driven by explosives to fall apart. Knowledge of such failure mechanisms is important in understanding fragmentation in general (e.g., hand grenades are a case where fragmentation is a desired outcome).

To understand the shear-banding process, we therefore need to explosively drive a shear-banding material (i.e., CP Ti) and watch the temporal evolution of features that appear. However, shear banding is not the only failure mechanism that needs to be understood. Some materials like copper can behave with great ductility even under extreme loading, but they will eventually fail through mechanisms not related to shear banding. Our samples also need to be subjected to a wide variety of stress states, including uniaxial and biaxial stress, because stress will alter the nucleation and development of features. In any failure mechanism, we presume that small perturbations in the material will grow under dynamic loading and eventually form large-scale cracks. Therefore, watching the temporal and spatial evolution of small features allows us to study the failure mechanisms of a material for a given stress state. The pRad capability at LANSCE can accomplish this task with unprecedented temporal and spatial resolution.

The Half-Cylinder Test

The *half cylinder* is a test that we designed to help us understand the fragmentation and failure of an expanding metal cylinder driven by explosives. Fig. 1 describes the arrangement of this test. The outside diameter of the PBX9501 high explosive is 1 in., and its inside diameter is 0.75 in. This explosive system was designed for a series of complementary tests that required the appropriate shock modification of the materials (hence, we use a high-energy explosive, PBX9501). We used a hollow cylinder instead of a full cylinder to eliminate excess energy that could breach the pRad vessel. The explosive is detonated on one end. The detonation wave then travels down the length of the cylinder. The cylindrical geometry provides a stress state in the CP Ti that is principally uniaxial (i.e., hoop stress). This uniaxial stress state would be expected to produce shear bands along the axis of the cylinder. This is fundamentally different from a spherically expanding material, which is subjected to a biaxial stress state. We look at half of a CP Ti cylinder (cut lengthwise) instead of a full cylinder because we want the pRad beam to pass through only one evolving surface. Because pRad is a penetrating diagnostic, if we used a full cylinder, our post-shot analysis would have to disentangle the features from the front and the back sides of the cylinder — a nearly impossible task.

At the pRad facility at LANSCE, we have fired two such shots with two different CP Ti wall thicknesses: 2 mm for the first shot and 1 mm

Fig. 1. Arrangement of the half-cylinder test.

for the second shot. Although pRad diagnostics produced a detailed time history of these events with approximately 21 images for each shot, we show only 2 images from the first test and 1 image from the second test (Fig. 2). Interestingly, each of the approximately 21 images produced by pRad includes time-history information of the evolution of the cylinder. In the time that it takes for the detonation wave to pass down the length of the cylinder, the portion of the cylinder near the detonator has evolved further (i.e., because of the work done by the gaseous products from the detonation) than has the portion of the cylinder that is at the opposite end of the detonator.

In Fig. 2, the lower portion of the cylinders exhibits no apparent features, but the upper portion of the cylinders exhibits noticeable cracks. We are now focusing our post-shot analysis effort on three avenues. First, we will examine the progressing front between the uncracked and cracked regions to understand the smallest spatial dimension of the features obtained from pRad. Are we actually seeing shear bands, or is the smallest feature that pRad discerns already a crack after the failure of the shear band? Our second approach is to try to understand the nature of the shear-banding instability resulting from geometric changes. For example, more cracks appear in the thinner cylinder (Fig. 2c) than they do in the thicker cylinder (Fig. 2b). This could simply be due to the fact that the instability is related to the interaction of the inner and outer surfaces in the thinner cylinder. Alternatively, because the amount of material being pushed by the explosives has been reduced in the case of the thinner cylinder, the strain rate has been increased. The number of cracks formed may be due to strain-rate effects. We are currently working with modelers in T and X Divisions at LANL to try to more completely understand these influences. Our third approach is to compare these dynamic data produced by pRad with another suite of similarly configured experiments aimed at understanding the same phenomenon. Fig. 3a is a photograph of the two halves of a CP Ti cylinder that was expanded and then stopped at about a 65% overall strain. In the process of stopping the expansion, the outer layer of the CP Ti was melted, and presumably the cracks that are seen have been somewhat modified. To understand how this recovered sample compares to the dynamic situation, we have begun quantitatively comparing the nature of the cracks seen in the dynamic pRad data with an x-ray (Fig. 3a) and a proton radiograph (Fig. 3c) of the recovered sample (Fig. 3b).

The Dynamic Bulge Test

The *dynamic bulge* is a test to study the hemispherical expansion of a copper shell at the pRad facility. This challenging test is the largest one done to date with pRad in terms of the high-explosive load and of the amount of driven materials. A great deal of fragment and blast mitigation was needed to prevent damage to the 6-ft pRad vessel. Good pRad data of the event were difficult to obtain because the test was designed with the detonator in the center of the hemispherical charge — right in the middle of the pRad-diagnostic field of view. Therefore, to see around the detonation system, we arranged the shot at an angle whereby the diagnostics could view the detonation system through only one layer of the shell (like in the half-cylinder test).

After overcoming all of these challenges, the data have been initially examined, and we can see the formation of cracks caused by the biaxial stress state induced by the hemispherical geometry. Other tests with

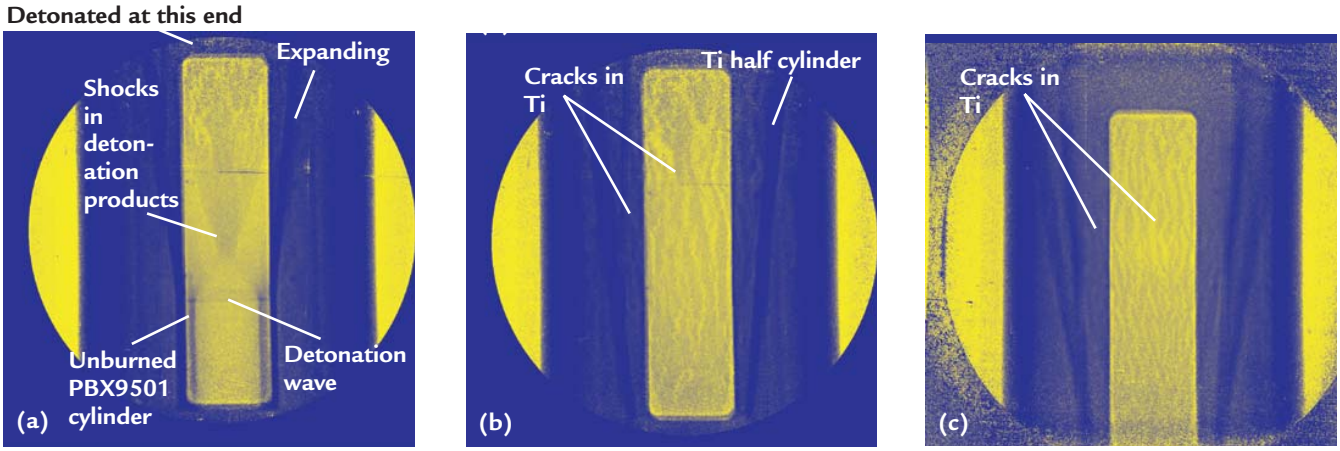

Fig. 2. (a) pRad image of 2-mm half cylinder at 13.6 μs after the detonator was fired. (b) pRad image of 2-mm half cylinder at 20.8 μs after the detonator was fired. (c) pRad image of 1-mm half cylinder at 20.8 μs after the detonator was fired.

Fig. 3. (a) Static x-ray of a piece of the cylinder on the left-hand side of Fig. 3b. (b) Photographs of two halves of the CP Ti cylinder that was expanded and then stopped at about a 65% overall strain. (c) Static proton radiograph of the half cylinder shown on the right-hand side of Fig 3b.

this hemispherical geometry are being designed to use smaller charges, to generate more optimized fragment mitigation, and to view experiments using both ductile (copper) and shear-banding (CP Ti) materials. These tests will allow us to study biaxial stress states using a variety of material, sample wall thicknesses, and radii of curvature in a cost-effective manner.

Conclusion

Failure in materials starts with small regions that nucleate damage (i.e., initiation of a shear band). Although the damage in these regions can grow rapidly like a crack or can stay quite small like the thickness of a shear band, it eventually leads to failure of the material. Models developed to treat the huge disparity between the largest and smallest scales involved in failure tend to be extremely complex because they need to simulate unresolved small scales onto the resolved large scales actually being computed. The complexity of these models requires a significant amount of experimental data to both generate and validate the model.

The unprecedented temporal and spatial radiographic ability of the pRad facility to document dynamic events is being used to understand the basic phenomena of failure of expanding materials under the influence of a high-explosive drive. We have developed and fired tests that examine the failure of CP Ti in uniaxial stress and of copper in biaxial stress states. We are beginning to perform detailed analyses of the data obtained from pRad and other tests to understand the influence of material properties, explosive-shock modification, stress state, and geometrical variations involved in the shear-banding instability of CP Ti. Finally, these data will be used to generate and validate modern Advanced Strategic Computing Initiative models of failure.

Special Projects

Completion and Initial Use of the 100-MeV Isotope Production Facility. 108

Advanced Hydrotest Facility 110

The LANSCE Switchyard-Kicker Project Nears Installation 112

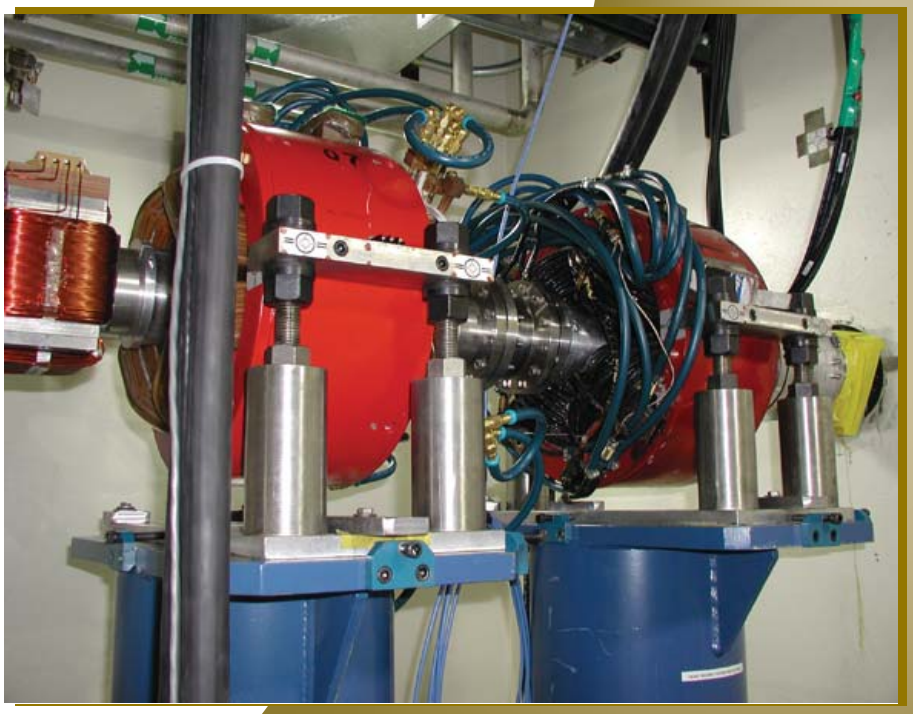

Completion and Initial Use of the 100-MeV Isotope Production Facility

R.C. Heaton, F.M. Nortier, E.J. Peterson (C Division), K.F. Johnson (LANSCE Division)

The design and construction of the 100-MeV Isotope Production Facility (IPF)[1] at LANSCE began in November 1998. The project is currently 90% complete. During 2002, modifications were made to the existing H^+ main accelerator beam line in the transition region between the drift-tube linear accelerator (DTL) and the side-coupled cavity linac (SCL). The proton beam used to produce the radioisotopes is extracted from this transition region. Also, three distinct systems comprising a new facility under construction were assembled: (1) building structures above and below ground to house the special facility equipment; (2) a new accelerator beam line; and (3) target-insertion and -retrieval hardware and a hot cell to handle the irradiated targets.

Remaining work includes installation of the target-insertion and -retrieval hardware, installation of the target controls, and installation of the beam-line instrumentation and control. A Laboratory Readiness Assessment will be completed before the facility is authorized for operations. We expect that these efforts will be concluded in FY 2003, at which time the facility will be ready to accept H^+ beam for isotope production.

Isotope Production

The new IPF target assemblies will consist of three targets arranged in a stacked configuration in the target holder. They will be thick enough to stop the beam within the last target in the assembly. The individual target thickness will be determined by the energy range to be deposited in each target in the stack. Water will flow between the subassemblies in the stack to cool the targets. The thickness of the water channels is important not only in achieving effective heat transfer but also in obtaining the desired amount of beam-energy degradations for subsequent targets.

We have developed a model for the target box and for specific target subassemblies, and we are modeling the performance and survivability of targets in this environment. The results of these calculations will help with the design of initial target irradiations and minimize the potential for target failures during early operations.

We are also investigating the types of target materials and the yields that may be expected for typical production irradiations. Several proposed target stacks are given in Fig. 1 with yield data and other information. Our initial efforts are directed at isotopes with commercial applications and revenue potential (i.e., strontium-82 and germanium-68) and at isotopes that have been selected for production as a result of the Nuclear Energy Protocol for Research Isotopes (NEPRI) process. The strontium-82 and germanium-68 isotopes are essential for the clinical application of positron-emission tomography, and most of the research isotopes have potential applications in nuclear-medicine diagnosis and therapy. As the NEPRI process matures, we expect that more research isotopes will be added to the portfolio of products produced at the LANSCE 100-MeV IPF.

4-week period

	Target Stack #1			Target Stack #2			Target Stack #3			Target Stack #4		
Beam current (μA)	125	125	125	125	125	125	125	125	125	125	125	125
Bombardment time (days)	4.00	4.00	4.00	20.00	20.00	20.00	2.00	2.00	2.00	2.00	2.00	2.00
Target	RbCl	RbCl	Ga	NaCl	Mg	Ga	Cr	Zn	W-186	Nb	Zn	W-186
Isotope	**Sr-82**	**Sr-82**	**Ge-68**	**Si-32**	**Na-22**	**Ge-68**	**V-48**	**Cu-67**	**Re-186**	**Zr-88**	**Cu-67**	**Re-186**
Half-life (days)	25.5	25.5	25.5	62823	950.7	270.82	15.97	2.6	3.72	83.4	2.6	3.72
Production rate (mCi/μAh)	0.130	0.230	0.032	0.000	0.024	0.032	1.100	0.115	0.050	0.235	0.115	0.050
Yield at EOB* (mCi)	1478	2615	382	0.0180	1436	1872	6322	534	250	1398	534	250
Decay time (days)	12.00	12.00	12.00	14.00	14.00	14.00						

*End of bombardment

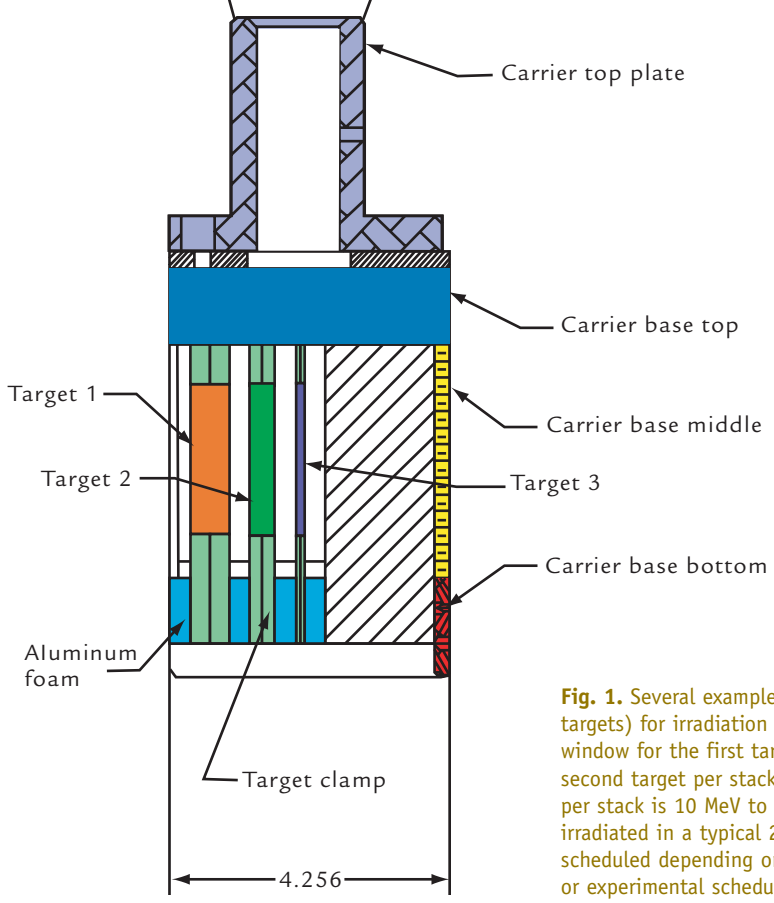

Fig. 1. Several example target stacks (each stack having three targets) for irradiation in the 100-MeV IPF. The nominal energy window for the first target per stack is 70 MeV to 90 MeV, the second target per stack is 45 MeV to 65 MeV, and the third target per stack is 10 MeV to 30 MeV. These four target stacks can be irradiated in a typical 28-day irradiation cycle with irradiations scheduled depending on delivery dates for major revenue isotopes or experimental schedules of NEPRI research customers.

Acknowledgements

The researchers would like to acknowledge the U.S. Department of Energy Office of Nuclear Energy, Science, and Technology and Office of Isotopes for Medicine and Science for financial support both for the line-item construction project and for operating funds for isotope-production infrastructure support.

References

1. R.C. Heaton and E.J. Peterson, Los Alamos National Laboratory report LALP-01-258; http://lansce.lanl.gov/research/pdf/IPF.pdf.

Advanced Hydrotest Facility

A. Jason, J.A. Paisner (LANSCE Division)

The Advanced Hydrotest Facility (AHF) may provide an important future capability for the Department of Energy (DOE)/National Nuclear Security Administration (NNSA) Stockpile Stewardship Program. The AHF will use pulses of protons traveling at almost the speed of light to penetrate dense, fast-moving objects at many angles simultaneously, providing three-dimensional, very high-resolution radiographic motion pictures. Those images will give LANL and Lawrence Livermore National Laboratory (LLNL) critical information necessary to assess the safety, performance, and reliability of our aging nuclear-weapons stockpile. LANL has been given the lead role by the NNSA to develop this critical national capability.

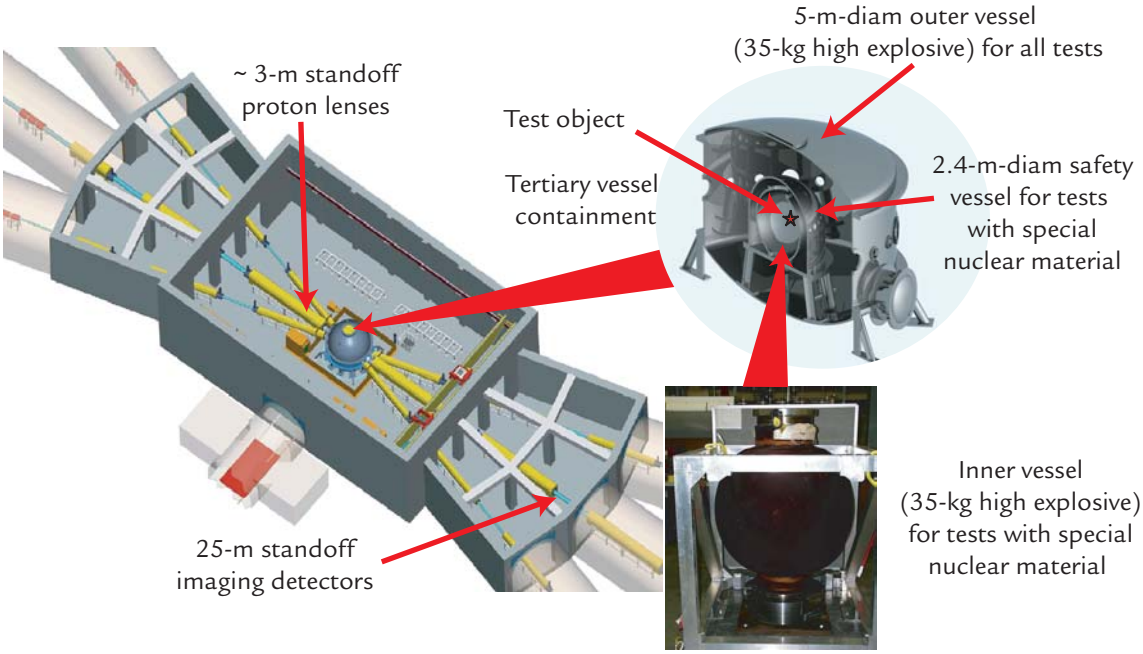

Fig. 1. Concept for an initial-phase AHF firing site with three axes.

Project Accomplishments and Expectations

The AHF concept has undergone considerable development since it was first conceived in 1994. Experimental verification of the idea has been promoted by pRad tests at LANL. In addition, detailed scenarios have been conceived within the past three years for implementing the AHF concept using preliminary specifications obtained from LANL and LLNL weapons designers. These scenarios have been documented in an extensive technical memorandum library and in the proceedings of technical reviews. Two of these reviews, in FY 2002 and FY 2003, were by an external expert committee known as the Beam Technical Advisory Group. An overview of the concept and its scenarios may be found in the 1999-2000 and 2001 LANSCE Activity Reports[1] and in a LANL technical report and a future conference proceeding.[2]

The AHF will be designed to measure important quantities directly related to weapons certification. Measurements of criticality, cavity shape, and mix can ostensibly be made and compared with weapons-design codes. As such, the time history of fast dynamic implosions can be tracked at many angles with better than 50-ns resolution and up to 20 frames each separated by 200 ns or more over the event time of about 100 μs. This technique would replace previously used experimental methods, such as pin shots and core punches, with a higher accuracy of results.

The three-dimensional photos obtained will use up to 12 axes for tomographic reconstruction of events. As far as we know to date, results will be of sufficient accuracy for stockpile certification with a spatial resolution of 0.5 to 1 mm and an ability to find edges to better than 50 μm. The criticality α-parameter, which is a measure of reactivity, can be determined to within several generations/μs, and the mix within the cavity can be determined with sufficient accuracy. Many other events relating to the implosion, such as spall or instability, can be viewed as a process in great detail.

The firing site under consideration can contain explosive events up to a 35-kg TNT equivalent while handling beryllium and special nuclear materials. Further mission justification by the weapons-design community, including a set of radiographic requirements, is expected over the next year to enable the project to start by 2007. A basic system, which is planned for the initial phase, could be completed in the 2013 to 2015 time frame. This system will include the high-energy synchrotron driver and a small number of axes included in a firing site. In a later time frame, a booster will be added with a more sophisticated multi-axis firing site for accurate tomographic reconstruction.

During 2002, the design detail on generic and specific concepts has substantially improved. Several accelerator concepts were explored in detail and have resulted in a favored design that is less expensive and has higher performance than previous ones. This design features a synchrotron with transition energy that is less than the injection energy and uses a minimal number of elements to attain higher intensity.

The beam transport and lens design have been further analyzed, and their realistic performance is better understood. Substantial engineering developments include the fabrication of a sensitive real-time beryllium monitor that will benefit the hydrotest program and progress in the design and costing of superconducting lens magnets. Additional work was done on firing-site concepts, including lens-to-vessel interfaces and plant layout. A drawing of a possible first-phase, firing-site concept is shown in Fig 1.

References

1. *1999-2000 LANSCE Activity Report*, Los Alamos National Laboratory report LA-13865-PR; http://lansce.lanl.gov/news/ARpdfs/special_projects.pdf; *2001 LANSCE Activity Report*, Los Alamos National Laboratory report LA-13943-PR; http://lansce.lanl.gov/libraries/AR2001/pdf/projects.pdf.
2. J.A. Paisner, Los Alamos National Laboratory report LA-UR-03-0170; to be published in *Proceedings of the Second LANSCE Workshop on Defense, Basic, and Applied Science* (2003).

The LANSCE Switchyard-Kicker Project Nears Installation

D.H. Fitzgerald, M.S. Gulley (LANSCE Division)

Simultaneous delivery of the H^- beam to Lines D and X at LANSCE is presently not possible. Line D feeds the Lujan Center and WNR, whereas Line X feeds pRad in Area C and ultra-cold-neutron (UCN) research in Area B. The switchyard-kicker system, which will soon be installed at the end of the LANSCE accelerator, will enable simultaneous, uninterrupted beam delivery to Line D and, on request, a tailored H^- beam pulse to Line X. The switchyard-kicker system will thus increase beam availability by 25% to the experimental programs at the Lujan Center and WNR, and beam availability to the pRad experimental programs will increase five-fold. The switchyard-kicker system eliminates the need to retune the accelerator to accommodate varying beam intensities and time structures. This stable-accelerator operation at fixed-beam intensity yields more reliable beam delivery for all programs and reduces time and resources needed for beam retuning.

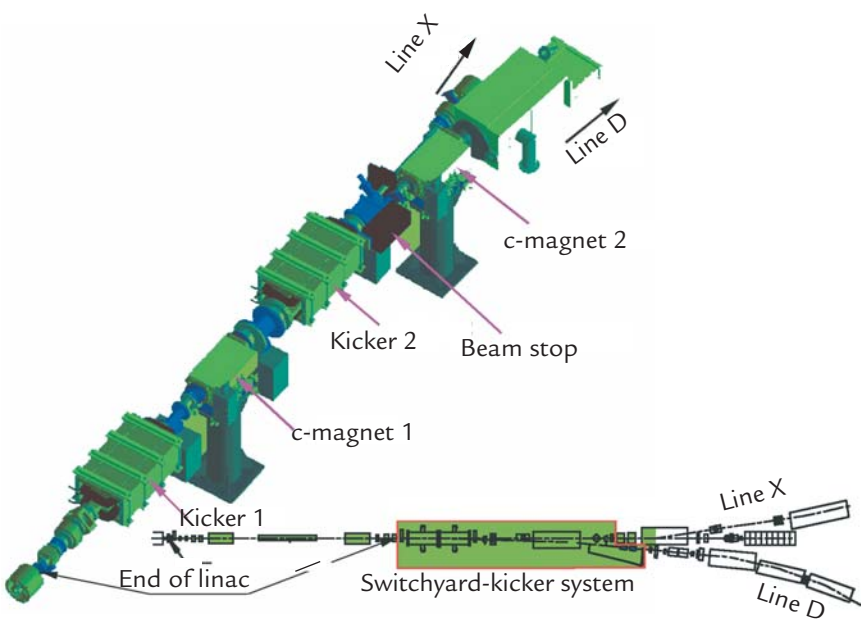

Fig. 1. Three-dimensional layout of the switchyard-kicker system.

2002 Progress on the Switchyard-Kicker System

Fig. 1 is a three-dimensional layout of the system, which includes two pulsed magnets, two direct-current c-magnets, beam-position monitors and other beam diagnostics, a revised vacuum system, and controls enhancements. The c-magnets deflect the beam into Line D. When fired, the two kicker magnets counteract the bend of the first c-magnet, sending the beam straight ahead into Line X. The kicker system has the capability of delivering a single macropulse on request with a micropulse structure tailored to the experimenter's requirements, and it preserves the capability to operate in all the other existing modes.

In 2002, design, procurement, and fabrication were completed for all major components of the switchyard-kicker system. Extensive testing of the pulsed magnets and their modulators was also successfully completed, as well as magnetic-field measurements for all magnets. As a risk-reduction measure, the installation of all major components was staged. Fig. 2 shows the upstream c-magnet and its vacuum chamber on its support and alignment stand during staging.

Fig. 2. The c-magnet and vacuum chamber mounted on a stand during staging.

Conclusion

The fabrication, procurement, and testing phases of the switchyard-kicker project have been completed on budget. The project is on schedule for installation beginning in late January 2003. Commissioning the switchyard-kicker system with beam is expected to be completed during May 2003, and beam delivery to research programs is scheduled for July 2003.

Facility Upgrades
Instrumentation

Scientists Perform First Neutron-Scattering Experiment Using the 11-T Superconducting Magnet at the Lujan Neutron Scattering Center 116

Pharos — A Chopper Spectrometer for Inelastic-Neutron-Scattering Studies of Excitations in Materials 120

FIGARO: A Neutron- and γ-Ray-Detector Array for Studying Fast-Neutron-Induced Reactions 122

Timing-Reference Generators and Chopper Controllers Designed for Neutron Sources 124

NPDF: A New High-Resolution Total-Scattering Powder Diffractometer 126

Enhanced-Beam-Extraction System Implemented in IN500 128

An Advanced Detector for Studying Neutron Capture at LANSCE 130

A Sharper SPEAR 132

The LQD Upgrade: Challenges and Opportunities of Brighter Neutron Sources 134

Scientists Perform First Neutron-Scattering Experiment Using the 11-T Superconducting Magnet at the Lujan Neutron Scattering Center

D. Lederman (West Virginia University), D. Belanger, L.J. Shelton, F. Ye (University of California at Santa Cruz), M.R. Fitzsimmons, S. Park (LANSCE Division)

During the 2002 run cycle at LANSCE, scientists successfully completed the first neutron-scattering experiment using the 11-T Oxford superconducting magnet on the Asterix spectrometer — an instrument designed for studies of magnetic materials. As a consequence of a special October 2002 call for proposals for experiments requiring high magnetic fields, an experiment involving the order-parameter measurement of a three-dimensional, random-field Ising model, as realized in a dilute antiferromagnet, was selected. The intent of the experiment was to measure how the sublattice magnetization of the dilute antiferromagnet changes with temperature near the phase transformation. Magnetic ordering in this system results within the formulism of the Ising model when the magnetic moments align themselves in one of two anti-parallel directions.

Our experiment was noteworthy for several reasons. First, neutron beams in bulk single crystals have often confounded order-parameter measurements of these systems with neutron scattering. To overcome this problem, the researchers used a 1-cm- by 1-cm- by 250-nm-thick $Fe_xZn_{1-x}F_2$ (where $x > 0.754$) single crystal as their sample. Because the sample was so thin, extinction of the neutron beam was minimized. Secondly, a 10-T (or more) magnetic field was needed to cause a crossover to the critical behavior (i.e., the behavior of magnetic spin near a phase transition as predicted by theory and computer models and measured experimentally) observed in the random-field Ising model. Thirdly, precise and accurate control of the thermal environment to better than 5 mK was needed in the 63.8-K thermal transition region. With this experiment, we demonstrated the capability of Asterix to obtain high-quality data from exceedingly small samples at high fields under extremely stable thermal conditions.

Achieving Thermal Stability in an Unstable Temperature Region

Our most challenging technical problem was to obtain thermal stability in a temperature region where the Oxford cryostat is most unstable. Near 60 K, the measured temperature stability of the Oxford cryostat is on the order of 50 mK when better than 5 mK is needed. We solved this problem by connecting a spare calibrated carbon-glass thermometer (with the fiber axis parallel to the field axis of the magnet) at the sample location to a Lakeshore temperature controller. We then used the Lakeshore controller to regulate the sample temperature with a second heater wired to the sample stage (Fig. 1). With this arrangement we could change the temperature of the sample in a completely monotonic fashion. During subsequent neutron measurements, which typically lasted between 30 and 120 minutes, we measured the sample temperature to acquire a thermal distribution. The standard deviation of the distribution was typically less than 0.3 mK — much less than the 5-mK requirement.

During the two-week experimental run, we used Asterix to measure the intensity of the (100) Bragg reflection from the antiferromagnetic order in the $Fe_xZn_{1-x}F_2$ crystal sample. Because the d-spacing of the (100) Bragg reflection is large, we used ~ 6-Å neutrons to measure this reflection with the Asterix spectrometer in the unpolarized mode. This setup minimized background scattering from the aluminum in the magnet cryostat (Fig. 2), the variable temperature insert, and the sample holder. To further reduce background scattering, we inserted borated polyethylene neutron shields between the magnet and the two-dimensional, position-sensitive-detector (PSD) array (Fig. 2). The stepper-motor-controlled goniometer and sample stick allowed us to align the sample within about one minute after it was inserted in the magnet. (Prealignment of the sample with a Laue camera was not performed.)

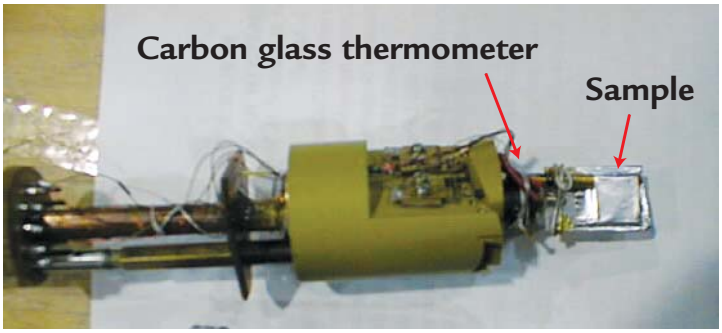

Fig. 1. View of the end of the sample stick for the 11-T Oxford superconducting magnet. The gold-colored object is a stepper-motor-controlled goniometer used to quickly align the sample. To achieve 0.3-mK thermal stability, we attached a carbon glass thermometer and heater wire to the sample holder and used a Lakeshore temperature controller to control them.

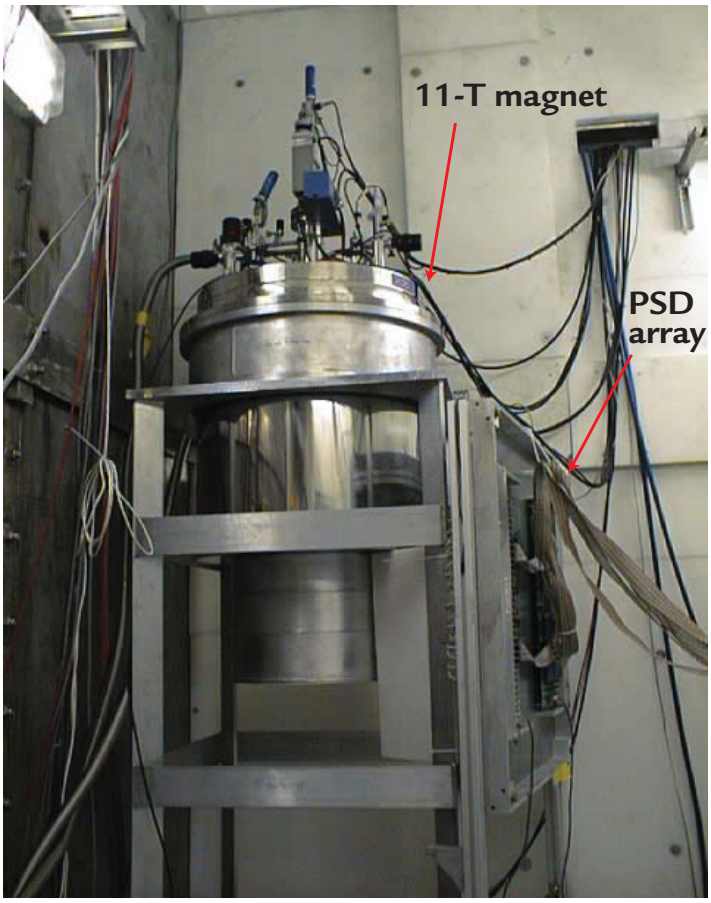

Fig. 2. View of the 11-T Oxford superconducting magnet during the neutron-scattering measurement. To the right of the magnet is the Asterix two-dimensional PSD array. Between the magnet and the detector, we installed borated polyethylene shields, which helped reduce the neutron background by one order of magnitude.

Instrumentation

Fig. 3 shows an image of the intensity of neutron scattering as a function of scattering angle (in the equatorial plane of the magnet) and wavelength taken with a magnetic field of 10.000 ± 0.001 T and a sample temperature of 50.0000 ± 0.00003 K in 30 minutes (with a 120-µA target current). The arrow points to the (100) Bragg reflection that resulted from antiferromagnetic ordering in the sample.

The mass of the sample material contributing to this reflection is about 100 µg (its volume is about 0.025 mm^3). The intensity of the reflection is plotted in Fig. 4 as a function of temperature for two of the six measurement conditions investigated. The first measurement is of the sample after it was cooled in a zero magnetic field and then warmed up through the transition (in zero field). The second measurement is of the sample as it was warmed up in a 10-T magnetic field after first being cooled in a zero magnetic field.

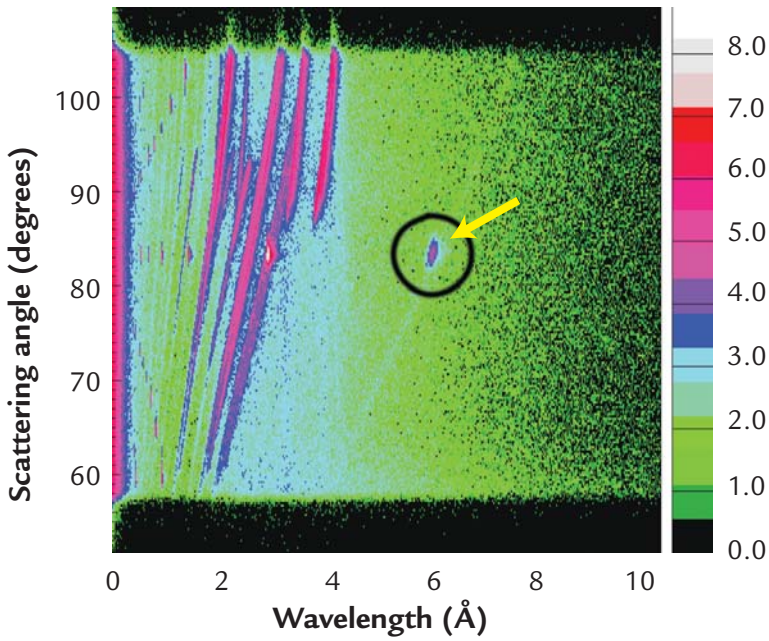

Fig. 3. An intensity image of neutron-scattering data plotted versus scattering angle and wavelength. The arrow points to the (100) Bragg reflection that resulted from antiferromagnetic ordering in the sample.

Conclusion

We have succeeded in obtaining data that provides insight into critical behavior predicted by the random-field Ising model. We have also demonstrated that Asterix can obtain wide-angle diffraction data from a single-crystal, thin-film sample in a timely manner; can obtain measurements from a sample in the presence of high magnetic fields; and can maintain an extremely stable thermal environment.

Interestingly as well is the juxtaposition of the roles for magnetic scattering using x-rays and neutrons. Extinction of the neutron beam would confound order-parameter measurements for some bulk single crystals, whereas the problem was successfully studied with neutron scattering using a thin-film single crystal. Magnetic scattering of x-rays

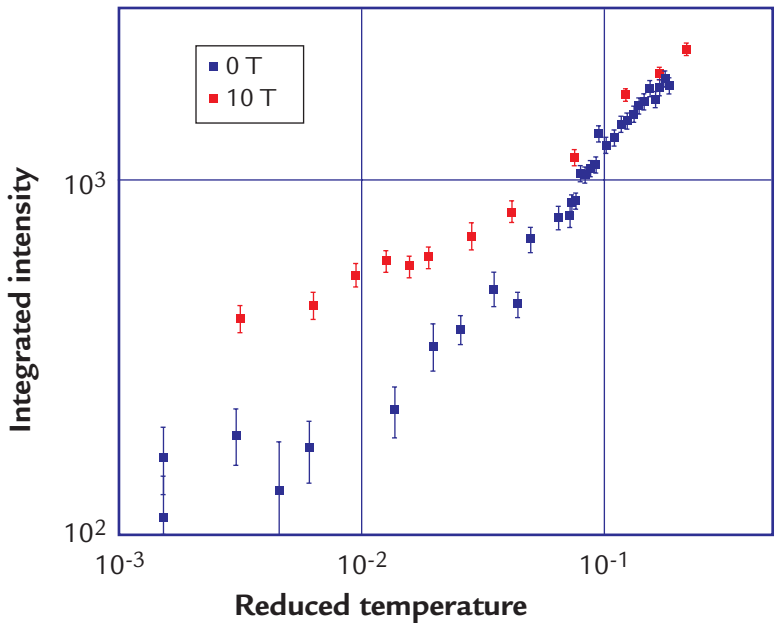

Fig. 4. The intensity of the (100) Bragg reflection from $Fe_xZn_{1-x}F_2$ after the sample was cooled in a zero magnetic field. The intensity was then measured as the sample was warmed up through the Néel transition in a zero magnetic field (■) and in a 10-T magnetic field (■). The latter condition is one that promotes detection of critical behavior in the random-field Ising model.

was successful at solving a similar problem using a bulk single crystal.[1] However, this technique failed in a thin-film-crystal study because the charge scattering from the forbidden Bragg reflection from the surface of the non-magnetically ordered MgF_2 single-crystal substrate (on which the $Fe_xZn_{1-x}F_2$ crystal is grown) is superimposed on and overwhelms the x-ray measurement of the (100) Bragg reflection from anti-ferromagnetic order in $Fe_xZn_{1-x}F_2$.

Acknowledgements

The magnet and construction of Asterix were supported by Laboratory-Directed Research and Development funding and the U.S. Department of Energy Office of Basic Energy Sciences.

References

1. F. Ye et al., *Physical Review Letters* **8915** (15), 7202 (2002).

Pharos — A Chopper Spectrometer for Inelastic-Neutron-Scattering Studies of Excitations in Materials

R.J. McQueeney (LANSCE Division), R.A. Robinson (Australian Nuclear Science and Technology Organisation)

The Pharos spectrometer (Fig. 1) has been a part of the LANSCE user program for nearly a decade. Originally, the instrument possessed only a small-scattering-angle flight path used primarily for neutron Brillouin scattering studies.[1] However, in the last year, a major upgrade of Pharos was completed, adding 317 new position-sensitive detectors (PSDs) at large scattering angles (for a total of 392), new data-acquisition system hardware and software, a more reliable Fermi chopper system, a new time-zero (T_0) chopper control system, and a new vacuum system. These upgrades have expanded the scope of scientific problems that Pharos can address and have improved the reliability and efficiency of the instrument. In addition, the suite of Pharos sample-environment devices are presently being expanded to provide high temperatures (up to 1500°C), large magnetic fields (up to 11 T), and high pressures (up to 10 kbar) and include a three-axis, single-crystal rotation stage. Pharos can now perform a full range of inelastic-neutron-scattering measurements, including those of phonon and spin-wave dispersions in single crystals; phonon and spin-wave densities of states; crystal-field, spin-orbit, and other electronic excitations; and neutron Brillouin scattering.

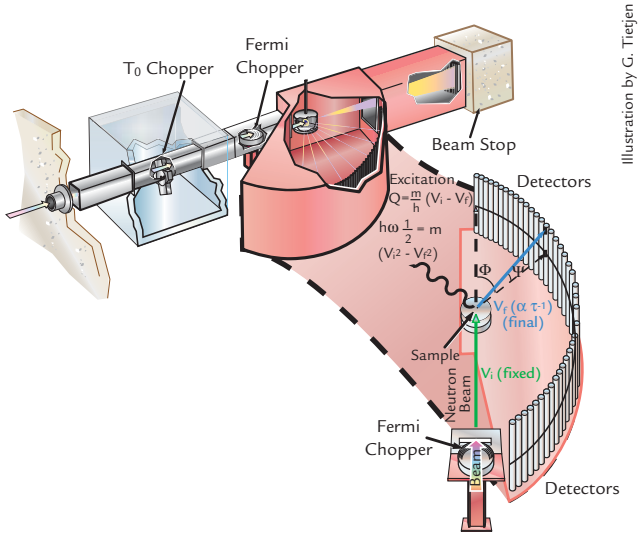

Fig. 1. Rendering of the Pharos instrument.

Pharos Specifications

Moderator and beam transport. Pharos is viewed at a 15° angle by a 12- x 12-cm^2 ambient high-resolution water moderator poisoned with gadolinium at a depth of 1.5 cm. The beam is reduced down to a 5- x 7.5-cm^2 area at the sample position (at 20 m from the moderator) by continuous beam scraping.

Fermi choppers. A Fermi chopper is used to obtain a monochromated incident beam. The efficiency of transmitting neutrons through the Fermi chopper depends on its rotational frequency, body radius, and slit radius and on the neutron incident energy. Pharos has three different Fermi choppers to provide different incident energies from ~ 10 to 1,000 meV (see Table 1).

Detector and data-acquisition systems. Pharos is outfitted with 392 ^{3}He-filled PSDs that are 1 in. in diameter. This detector bank contains 376 tubes that are 1 m long at a distance of 4 m from the sample. These tubes continuously cover horizontal scattering angles from -10° to -1.5° and 1.5° to 145° and vertical angles from -7° to +7°. The other 16 detectors are 16-in.-long PSDs (above and below the direct beam). All of these detectors have a position sensitivity better than 1 cm, but they are typically divided into 1-in. elements for data collection. (There are ~ 15,000 detector pixel elements of 1 x 1 in^2.) We typically work with several thousands time-of-flight channels of 1 to 3 μs in duration over a range of several milliseconds. Thus, the instrument contains an astounding 50 million individual elements in each histogram.

Background suppression. Due to the monochromatic beam and the intrinsic weakness of neutron inelastic scattering (which is several orders of magnitude less than elastic Bragg scattering), the suppression of external sources of neutron and γ-ray background is extremely important. The T_0 chopper attenuates fast neutrons and γ-rays from the prompt pulse by rotating a large Inconel chopper into the beam precisely at the time T_0. These fast neutrons and γ-rays are emitted from the target. Without the T_0 chopper, fast neutrons would thermalize in the shielding and leak out over time, contributing to a significant background signal. The Pharos T_0 chopper can rotate up to 60 Hz in multiples of 20 Hz. To minimize air scattering in the secondary flight path, the entire secondary spectrometer vessel (1,100 m^3) is evacuated down to 10^{-3} torr. A separate smaller sample chamber can reach cryogenic vacuum levels (10^{-8} torr). In the near future, we plan to install a radial collimation system in the secondary flight path to reduce the scattering from bulky sample-environment devices (e.g., the 11-T cryomagnet and gas-pressure cells).

Table 1. Pharos specifications.

Energy transfer resolution	ΔE/Ei = 1% to 4%
Moderator	Chilled water at 283 K (1.5-cm Gd-poisoning depth)
Beam size	5 cm x 7.5 cm
Sample distance from moderator	20 m
Fermi chopper	
- Distance from moderator	18 m
- Frequency	60 Hz to 600 Hz
- Diameter	10 cm
- Optimal energy at 600 Hz	100, 300, and 1,000 meV
- Slit spacing	3.6 mm, 2.1 mm, and 1.0 mm
- Slit curvature	0.58 m, 1.0 m, and 1.83 m
- Phasing error to alternating-current line (FWHM)	~ 1.5 μs
- Manufacturer	Revolve Magnetic Bearings, Inc.
T_0 chopper	
- Distance from moderator	14 m
- Material	Inconel (341 kg)
- Frequency	10 to 60 Hz
Detectors	
- Distance from moderator	24 m (low angle movable to 30 m)
- 376 position-sensitive detectors	1 in. diam., 1 m long
- 16 position-sensitive detectors	1 in. diam., 16 in. long, above and below direct beam
- Scattering-angle coverage	1.5° to 145°
- Solid-angle coverage	0.7 sr
- Positional resolution (FWHM)	< 1 cm
- Manufacturer	Reuter-Stokes, Inc.

Acknowledgements

The researchers would like to acknowledge the U.S. Department of Energy Office of Basic Energy Sciences and the National Nuclear Security Administration.

References

1. R.A. Robinson et al., in *Proceedings of the 10th Meeting of the International Collaboration on Advanced Neutron Sources, Institute of Physics Conference Series* **97**, 403 (1989).

FIGARO: A Neutron- and γ-Ray-Detector Array for Studying Fast-Neutron-Induced Reactions

M. Devlin, R.C. Haight, R.O. Nelson, J.M. O'Donnell, D. Rochman, L. Zanini (LANSCE Division)

Neutron emission from reactions induced by fast neutrons is a subject of much interest for two reasons: (1) the fundamental nature of the interactions, which are free from the complications of the Coulomb interaction, makes it simpler to interpret the results, and (2) these reactions have many applications in defense, nuclear energy, waste transmutation, accelerator shielding, medical therapy, and geological studies. Nevertheless, the experimental database for these processes is very meager simply because the reactions are difficult to measure. At LANSCE, we are developing the FIGARO (Fast neutron-Induced GAmma-Ray Observer) array for carrying out these measurements with the pulsed spallation neutron source of WNR. The neutron and γ-ray detectors that comprise this unique instrument are being developed for studies involving neutron-induced reactions such as neutron-inelastic scattering, fission-neutron and fission-γ-ray spectra, and neutron-emission spectra from general reactions.

(a) FIGARO (now)

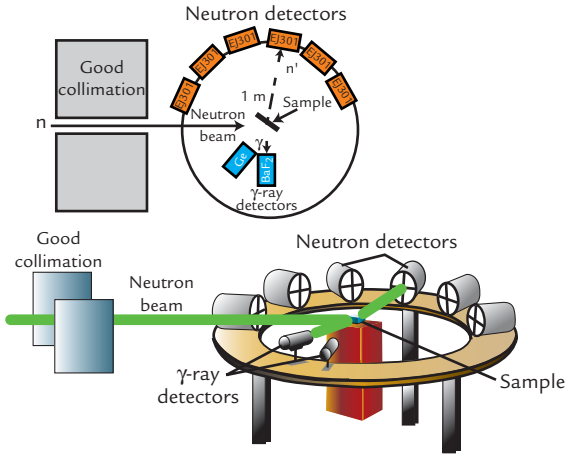

(b) Future larger neutron-detector array for FIGARO

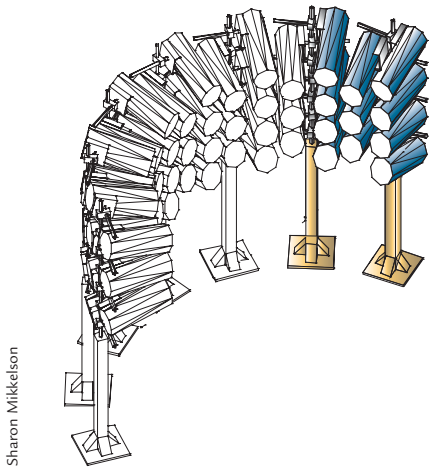

Sharon Mikkelson

Fig. 1. FIGARO detector array showing (a) the present Ge and BaF_2 γ-ray and neutron detectors and (b) the future array of neutron detectors. The energy of neutrons emitted from the sample is determined by TOF over a 1-m flight path.

The FIGARO array (Fig. 1) consists of neutron and γ-ray detectors arranged around a sample, which is placed 22 m from the WNR pulsed source of fast neutrons. Both high-resolution, high-purity germanium detectors (HPGe) and very fast BaF_2 detectors are used to detect the γ-rays. A detected γ-ray gives several important pieces of information:

(1) it indicates that a reaction has taken place;
(2) it identifies the residual nucleus and therefore the type of reaction by the characteristic γ-ray energy;
(3) it *stops* the clock that had been started by the WNR neutron source for measuring the time of flight (TOF) and therefore the energy of the incident neutron; and
(4) it *starts* the clock for measuring the TOF (and therefore the energy) of the emitted neutron between the sample and the neutron detector, which is a liquid scintillator that can differentiate neutrons from γ-rays.

Our first experiments with the neutron detectors were measurements of fission-neutron spectra as a function of incident-neutron energy up to at least 100 MeV. These studies were made with a fission chamber in the sample position and provided new data on the fission-neutron spectra from neutron-induced fission of ^{235}U and ^{238}U.

To test the capabilities of γ-ray-neutron coincidences, we have studied samples of carbon, silicon, and iron. Each of these elements has a dominant isotope and a strongly populated first-excited state, which decays to the ground state with the emission of an easily detected γ-ray. Fig. 2 shows an example of the data. The energy imparted to the nucleus, the *excitation energy*, is plotted against the incident-neutron energy.

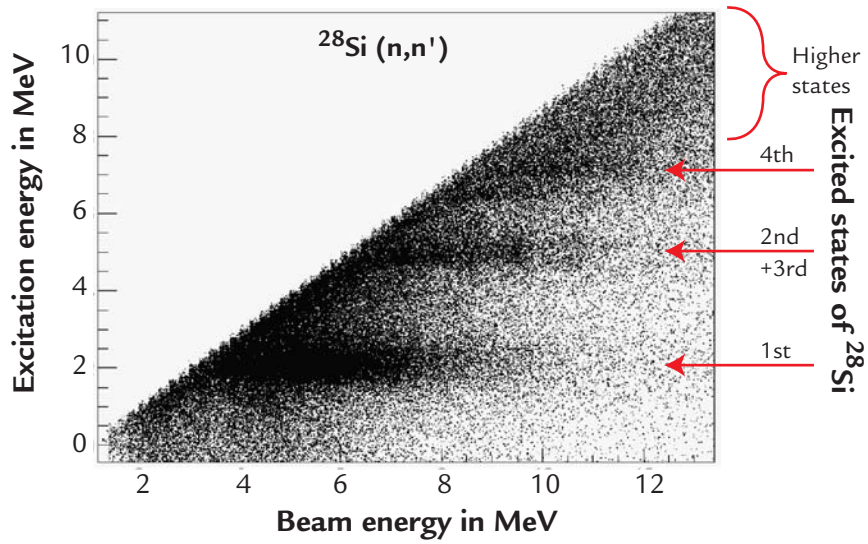

Fig. 2. Energy imparted to the ^{28}Si nucleus versus beam energy. This excitation energy is calculated from the difference between the incident and outgoing neutron energies in inelastic-scattering interactions (n,n'). Each event is represented by a dot. Distinct regions for exciting the first, second, third, fourth, and higher-excited states of ^{28}Si are clearly seen.

FIGARO's present small array of detectors is being enhanced by adding more neutron detectors and a few more γ-ray detectors. Up to 49 neutron detectors will eventually be installed in modules of 7 detectors each. The plan for the neutron-detector array is shown in Fig. 1b. With these additional detectors, the efficiency for neutron detection will be increased by nearly an order of magnitude. We plan to pursue a wide range of measurements with this new capability.

Acknowledgements

This work has benefited from the use of LANSCE at LANL. LANL is funded by the U.S. Department of Energy and operated by the University of California under Contract W-7405-ENG-36.

Timing-Reference Generators and Chopper Controllers Designed for Neutron Sources

R.O. Nelson, R.B. Merl, C. Rose (LANSCE Division)

Because of power-grid frequency fluctuations, pulsed-spallation-neutron facilities equipped with choppers like LANSCE must optimize the conflicting demands of accelerator and neutron-chopper performance. Powerful new simulation techniques have enabled the modeling of the timing systems that integrate chopper controllers and chopper hardware. Thus for the first time, the tradeoffs between accelerator and neutron-chopper performance can be quantitatively assessed, allowing for a facility design or upgrade that optimizes total system performance. As such, we now operate the multiple chopper systems and the accelerator at LANSCE as simple slaves to a single master-timing-reference generator. The Spallation Neutron Source (SNS) is also following this design.

Development of Master-Slave Architecture for Total System Performance

Although designers for targets and moderators at spallation sources can tailor the neutron-energy spectrum for the requirements of the neutron-scattering instruments, there are limits to what they can accomplish. It is often necessary to further *filter* the neutron beam.

Neutron choppers are rotating electromechanical devices that remove undesired energy components from the neutron beam. The time-zero (T_0) choppers rotate a large mass through the beam to effectively place a beam stop in the path of the beam to block unwanted high-energy neutrons. When scientists want neutrons blocked except those in a narrow energy band, an energy-selector (E_0) chopper is placed downstream from a T_0 chopper. These choppers must operate in phase with the production of the neutron pulses and in phase with one another.

Unfortunately, accelerators typically are coupled to an alternating-current (ac) power grid and therefore have phase fluctuations that preclude the delivery of proton pulses to the target in a precise periodic manner. The radio-frequency (rf) power modulators in the accelerator operate best when they are able to follow the phase of the power grid. In contrast, the choppers with their massive rotating blades and lethargic motors perform best when rotating with a constant period. Although previous schemes enabled a single chopper to operate well with the accelerator, no system provided excellent operation for all choppers in a facility.

Thanks to better analysis tools and to new technologies available for high-performance implementations, we have developed a master-slave architecture (Fig. 1) that enables excellent performance for the accelerator and all choppers. We modeled all subsystems beginning with the ac power grid and ending with the rotating chopper blade to predict and analyze neutron-chopper performance. The timing-reference generator takes the phase information from the grid and smoothes it. By varying the smoothing parameters, we can effectively limit the phase acceleration passed along to the choppers. We selected a family of choppers (20-Hz T_0, 60-Hz T_0, and 600-Hz E_0) that span the range of performance to realistically model a neutron-scattering facility. Each chopper is paired with its own controller.

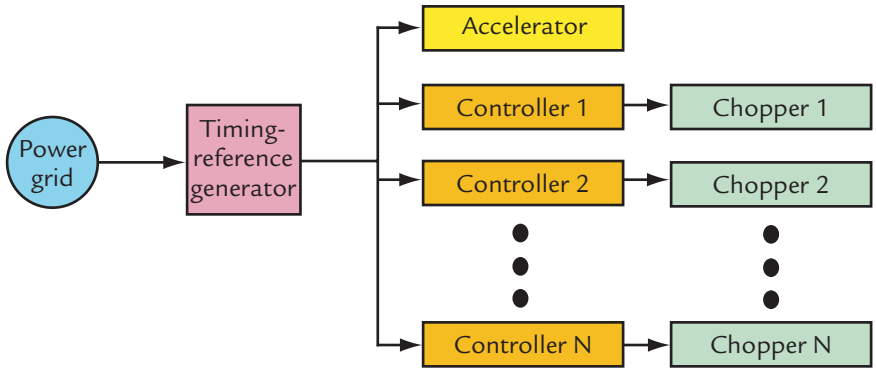

Fig. 1. Master-slave architecture for timing control of accelerator and neutron choppers.

Because the performance of the various choppers and the accelerator is linked to the amount of coupling to the ac power grid, we wanted to quantify this coupling. Hence, we measured the standard deviation of the timing-reference phase with respect to the raw-grid phase. We defined this metric as the grid-tracking sigma and varied the grid-tracking sigma by changing the smoothing parameters in the timing-reference generator. Traditionally, accelerators prefer a low grid-tracking sigma (tight-grid coupling), whereas choppers prefer a large grid-tracking sigma (loose-grid coupling). We also quantified chopper performance by measuring the standard deviation of the chopper arrival at *top dead center* with respect to the timing-reference pulse. Analogously, we define this metric as the chopper-tracking sigma.

Fig. 2 presents simulated and measured performance. The simulations use measured grid-phase-drift data and models of the timing-reference generator, controllers, and chopper hardware. The timing-reference generator in both the simulation and hardware has a knob that parameterizes the smoothing over the range 0 to 125 µs for the grid-tracking sigma. Data were taken with production systems for the 20-Hz and 600-Hz choppers, whereas the 60-Hz chopper was optimized well beyond requirements.

Conclusion

The data from the simulations (Fig. 2) reproduced the expected trends. What we found is that the choppers follow a smoothed-phase drift better when the timing-reference generator smoothes out variations in the grid. Greater smoothing produces still smaller chopper-tracking sigmas. However, there are diminishing returns as the timing-reference generator increases the smoothing — chopper-tracking sigmas asymptotically approach a value near zero. The sigmas will not approach zero because of system noise, errors in quantification, and internal timing jitters in the control circuits. The knee in the measured data and simulations indicates that the accelerator and choppers at LANSCE will run best with a grid-tracking sigma of 15 µs or more. Values larger than 15 µs offer little improvement in chopper performance while values smaller than 15 µs severely degrade chopper performance. The accelerator operates well within a window of ±100 µs of the grid, whereas the T_0 and E_0 choppers typically require ±10 and ±1 µs, respectively. All requirements can therefore be met simultaneously with a grid-tracking sigma of 25 µs while adhering to the simple master-slave architecture.

The successful architecture developed and used at LANSCE is directly applicable to the SNS. Indeed the requirements for SNS have been amended to reflect the technological innovations demonstrated at LANSCE.

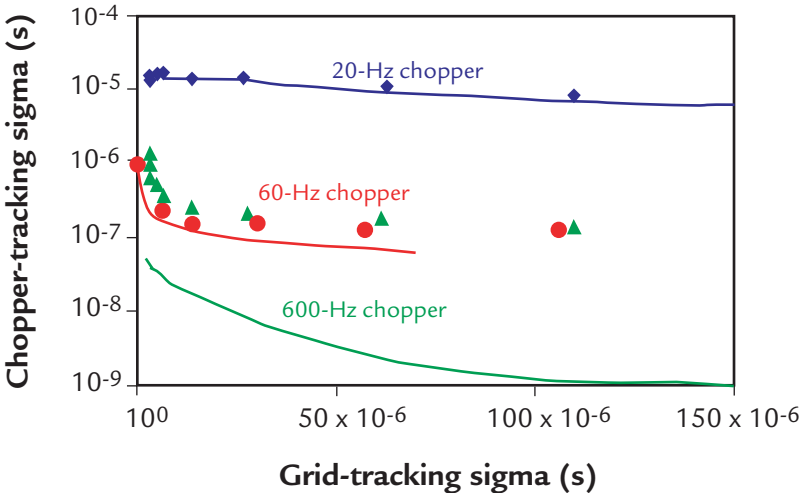

Fig. 2. The results of the simulations and measurements. The smooth lines show predictions for the chopper suite as a function of coupling to the power grid.

NPDF: A New High-Resolution Total-Scattering Powder Diffractometer

Th. Proffen (LANSCE Division), T. Egami (University of Pennsylvania), S.J.L. Billinge (Michigan State University), A.K. Cheetham (University of California at Santa Barbara), D.A. Louca (University of Virginia), J. Parise (State University of New York at Stony Brook)

Knowing the atomic structure of materials usually means determining their crystal structure. However, many modern materials are complex, and their real structure often is deviated locally from the average crystal structure in significant ways. It is thus necessary to know the structure on various length scales because properties are more directly governed by local atomic arrangements. But the conventional crystallographic approach cannot provide a complete picture — it has to be complemented by local probes such as the Pair Distribution Function (PDF) method. These studies can be carried out with the Neutron Powder Diffractometer (NPD), which has recently been upgraded to the NPDF.

January 2002

October 2002

Fig. 1. Images from the NPDF construction.

Instrument Upgrade

The NPD upgrade to NPDF is funded by the National Science Foundation, LANL, University of Pennsylvania, and other academic institutions. The project started in September 2000, and in only nine months between January and September 2002, the old instrument (NPD) was removed from flight path 1, and the new instrument (NPDF) was built (Fig. 1). The upgrade added 160 position-sensitive ^{3}He detector tubes to the backscattering area.

First Data

On September 27, 2002, the NPDF shutter opened for the first time. During the rest of the 2002 run cycle, NPDF produced over 300 experimental data sets. An example of a PDF of nickel extending out to a distance of r = 100 Å is shown in Fig. 2. A standard data set suitable for PDF analysis can be obtained in only two hours. These promising results not only put NPDF at the cutting edge of local-structure determination but also serve as a development platform for this new structure-analysis tool for disordered and nanostructured materials. The instrument will be available to general users during the 2003 run cycle (Fig. 3).

Acknowledgements

The researchers would like to acknowledge the National Science Foundation, the University of Virginia, the University of Pennsylvania, Michigan State University, and the Laboratory-Directed Research and Development Program.

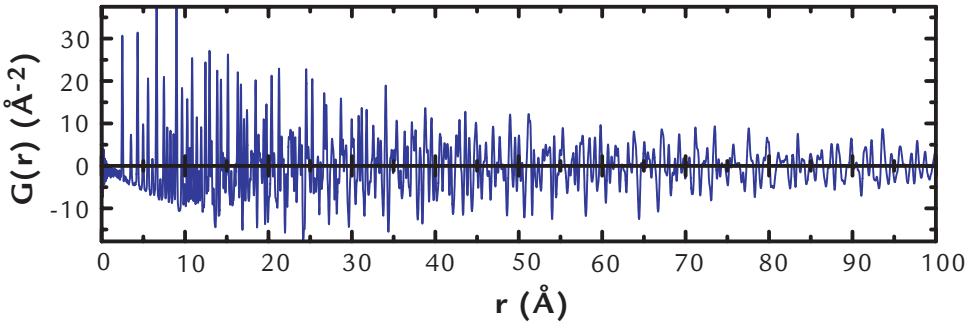

Fig. 2. PDF of nickel measured at T = 10 K with NPDF.

Fig. 3. Thomas Proffen (Lujan Center) stands with sponsors — Takeshi Egami of the University of Pennsylvania (top *left*), Despina Louca of the University of Virginia (top *right*), and Simon Billinge of Michigan State University (bottom *right*) — on top of the NPDF sample area.

Enhanced-Beam-Extraction System Implemented in IN500

F. Mezei, M. Russina, M.P. Hehlen (LANSCE Division)

Neutron scattering is widely used for condensed-matter research. The most powerful neutron-scattering facilities today use reactors as neutron sources, but this technology has reached its technical limits. Progress in neutron-scattering research now depends on our ability to develop spallation neutron sources that are competitive and ultimately superior to nuclear reactors for core applications (e.g., cold-neutron spectroscopy). Developing this technology will be a challenge of the next decade.

Development and Testing of the Enhanced-Beam-Extraction System

LANSCE made a major step in meeting this challenge by installing the first coupled moderators at the Lujan Center. These moderators can produce six to eight times more useful neutrons for the same proton-beam power than those used at other leading spallation sources, such as ISIS (Rutherford-Appleton Laboratory Neutron Facility, United Kingdom). This high neutron intensity comes in 3- to 4-ms pulses. All future spallation sources earmarked for commissioning in 7 to 10 years will use these moderators. The IN500, a Laboratory-Directed Research and Development project at LANSCE, is developing a series of novel approaches specifically conceived to use these long pulses (i.e., mechanical pulse shaping; repetition-rate multiplication; enhanced-neutron, optical-beam extraction and delivery system). IN500, which will use cold neutrons from a coupled H_2 moderator, will pave the way for spallation neutron sources to surpass the most advanced reactor facilities in cold-neutron spectroscopy — one of their core capabilities. IN500 will be a crucial research tool for the study of soft and complex matter, including collective phenomena in polymers, biological matter, soft metals like plutonium, liquids, and nanostructured matter.

The first experimental test of the coupled cold moderator at Lujan Center took place in January 2003 (Fig. 1). The neutron-flux performance of moderators on pulsed

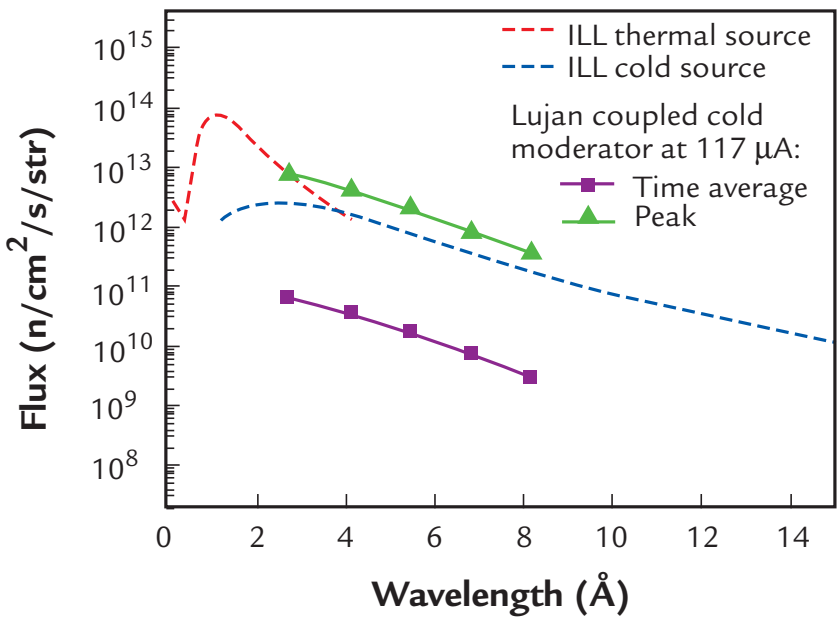

Fig. 1. Brightness of the Lujan Center coupled cold moderator as a function of neutron wavelength compared to the neutron sources at the Institute Laue-Langevin (i.e., preliminary evaluation from the January 2003 tests).

sources is characterized at a given position over the moderator surface by the instantaneous flux as a function of time and neutron wavelength (energy), $\Phi(t,\lambda)$, emitted close to perpendicular to the surface. We have implemented a novel method based on two-dimensional, time-of-flight analysis to determine both the shape and the absolute value of this function.

The key of the setup is a mechanical chopper with a small diaphragm placed about half way between the moderator and a detector in the beam axis. The chopper runs asynchronously to the source, and neutron counts are stored in a two-dimensional histogram, $I(t_o,t_{ch})$, where t_o and t_{ch} are the times elapsed since the last firing of the source and the last opening of the chopper, respectively. The function $\Phi(t,\lambda)$ can readily be computed from this histogram with a resolution broadening primarily defined by the length of the chopper pulse and by obvious geometrical factors. Our method functions with full efficiency without phasing the chopper to the source, and, in this sense, it is a precursor example for the event-recording data-collection approach, which will enable us to fully eliminate the effects of jitter in chopper phasing on pulsed-source spectra. Using this new method, we have successfully determined, in the wavelength range 1 to 10 Å, the absolute instantaneous flux of the coupled cold moderator at Lujan Center. We found the peak flux to surpass all existing cold-neutron beams by about a factor of 2 to 3.

Another source of gain in neutron-beam intensity in the IN500 project is the innovative beam-extraction system, which transports cold neutrons from the source to the surface of the bulk shielding more efficiently than conventional beam holes. We achieved this higher flux by using a supermirror-coated neutron guide with a special geometry starting at 1.3 m from the source.

Conclusion

The full-beam-extraction system on the IN500 beam line was successfully installed from February to May 2002. We also tested the performance of the beam-extraction system in January 2003 by using a time-resolved, neutron-imaging camera system. The analysis of the relative brightness of the moderator and of its images mirrored by the neutron guide walls confirmed the expected high performance of this beam-extraction system. It also showed that the supermirror walls maintained the originally specified > 80% reflectivity after irradiation deep within the bulk shielding for the complete 2002 run cycle.

Acknowledgements

This work benefited from Laboratory-Directed Research and Development funding.

An Advanced Detector for Studying Neutron Capture at LANSCE

R.C. Haight, L.F. Hunt, J.M. O'Donnell, R. Reifarth, J.L. Ullmann (LANSCE Division),
T.A. Bredeweg, R.S. Rundberg, D.J. Vieira, J.B. Wilhelmy (C Division), J.M. Wouters (IM Division)

Measurements of neutron-capture reactions on unstable nuclides are of fundamental importance to understanding nuclear-weapons performance and to understanding the astrophysics of slow- and rapid-process nucleosynthesis in stars. A state-of-the-art γ-ray detector, the Detector for Advanced Neutron Capture Experiments (DANCE), has been built on flight path 14 at the Lujan Center at LANSCE to make these measurements (Fig. 1). Calibration and commissioning experiments and preliminary measurements on radioactive targets have been completed.

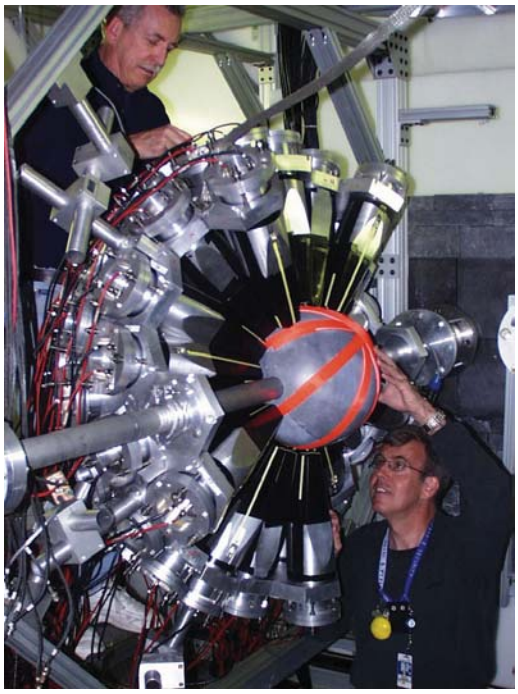

Fig. 1. A portion of the DANCE detector, which is used to detect γ-rays from neutron-induced reactions. The individual crystal detectors (wrapped in black to keep out light) point to the center of the ^{6}LiH sphere, which absorbs scattered neutrons. The neutron beam travels through the vacuum pipe in the center. Lloyd Hunt of LANSCE (upper left) and Bob Rundberg of the Chemistry Division make adjustments to the detectors.

Commissioning DANCE

Neutron capture is a reaction in which a neutron strikes a target nucleus to form a product nucleus that de-excites by the emission of γ-rays. The probability (or cross section) for this reaction depends on neutron energy. The reaction probability is very difficult to calculate accurately because it depends on precise details of nuclear structure — theoretical models can only predict cross sections to within a factor of 2. For this reason, experimental measurements are required. The neutron energies of greatest interest are from about 1 keV to about 500 keV, which are readily available from the water moderators at the Lujan Center.

DANCE was designed to measure the total energy released in a neutron-capture reaction and must therefore be very efficient at detecting γ-rays. It consists of 159 BaF_2 crystals, each 15 cm deep, arranged to cover nearly the entire surface of a sphere with an inner radius of 17 cm. Full coverage of the sphere would require 162 crystals, but 2 crystals were removed to allow the beam to enter and exit the array, and 1 crystal was also removed for target insertion. For the commissioning experiments on DANCE, only 140 crystals were installed.

The data rates that we acquired in the DANCE commissioning experiments were quite high. We used state-of-the-art data-acquisition electronics consisting of fast transient digitizers. Two 8-bit digitizers are required for each crystal, plus additional digitizers for the neutron-flux monitors. The digitizers have a 500-MHz sampling rate and a 150-MHz bandwidth that allows a minimum rise time of 2.3 ns. Time-of-flight (TOF) and pulse-height information from the crystals must be extracted in the 50 ms between beam bursts. To do this, the digitizers are arranged in 14 crates, each with its own distributed analysis computer, which are networked to a central computer.

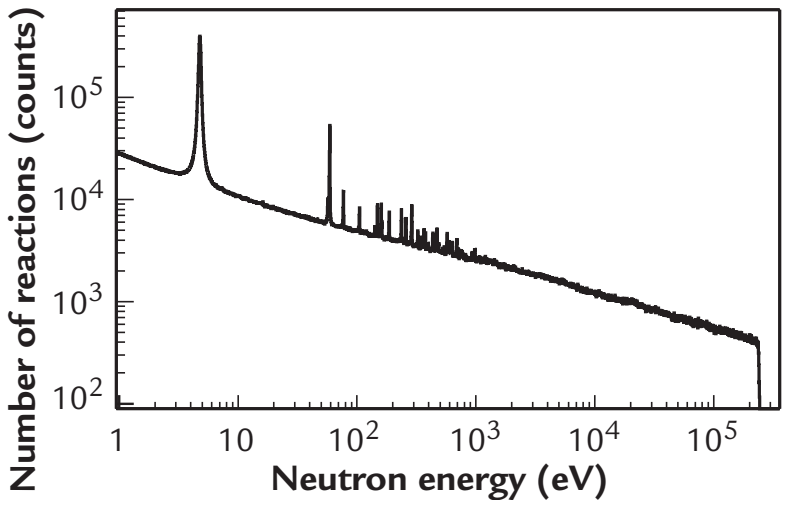

Fig. 2. Neutron-energy spectrum obtained from TOF data for neutron capture on a 3.9-mg/cm^2 Au target, measured with the DANCE array. Au is a well-studied calibration target. The neutron energy (eV) is on the horizontal axis, and the number of reactions (counts) is on the vertical axis. Neutron resonances are obvious in the 1- to 1,000-eV range.

Fig. 2 shows a neutron capture TOF spectrum taken for calibration using a 3.9-mg/cm^2 Au target. The large resonances at low energies are obvious. The combination of the DANCE detector, the intense neutron source at the Lujan Center, and the radioactive-target fabrication and handling facilities in C Division provide a means for measuring neutron capture reactions on small quantities of rare or radioactive nuclides that are unique in the world. An experimental program of targets of interest for studying stellar nucleosynthesis and archived nuclear-test data will be pursued during the 2003 run cycle at LANSCE.

A Sharper SPEAR

E.B. Watkins, J. Majewski (LANSCE Division)

Neutron reflectometry is a powerful tool for the study of nanostructures and thin layered films. The Surface Profile Analysis Reflectometer (SPEAR), located on flight path 9 in the Lujan Center, is ideally suited to study thin organic and inorganic layers (5 Å - 3,000 Å) in a variety of different environments (Fig. 1). SPEAR is a time-of-flight (TOF) neutron reflectometer using two choppers to define a typical neutron wavelength range of 1 Å to 16 Å (Fig. 2). With this polychromatic beam, a range of momentum transfer vectors (Q_z) can be measured without altering the angle of the incident beam. A position-sensitive detector records the TOF and reflected positions of individual neutrons. This arrangement allows scientists to obtain good statistics for a minimum reflectivity of about 5×10^{-7} in 3 to 4 hours.

In 2002, SPEAR's capabilities and performance were sharpened by the addition of a new detector gantry, a PC-based data-acquisition system, and an automated sample changer. These upgrades simplify the operation of the instrument and provide more precise and reproducible reflectivity measurements.

Fig. 1. From left to right, Professor Jacek Lipkowski (University of Guelph), Grzegorz Szymanski (Research Associate, University of Guelph), and Ian Burgess (Professor Lipkowski's Ph.D. student) discuss a sample embedded in a electrochemical cell (inset) from which they obtained neutron-reflectivity data using SPEAR. The experiments on SPEAR were aimed at understanding the influence of electric potential on the phase transitions in ultrathin films of phospholipids deposited onto the surface of a gold electrode. These important experiments will provide fundamental information about the stability of the model biomembranes in the presence of large electric fields.

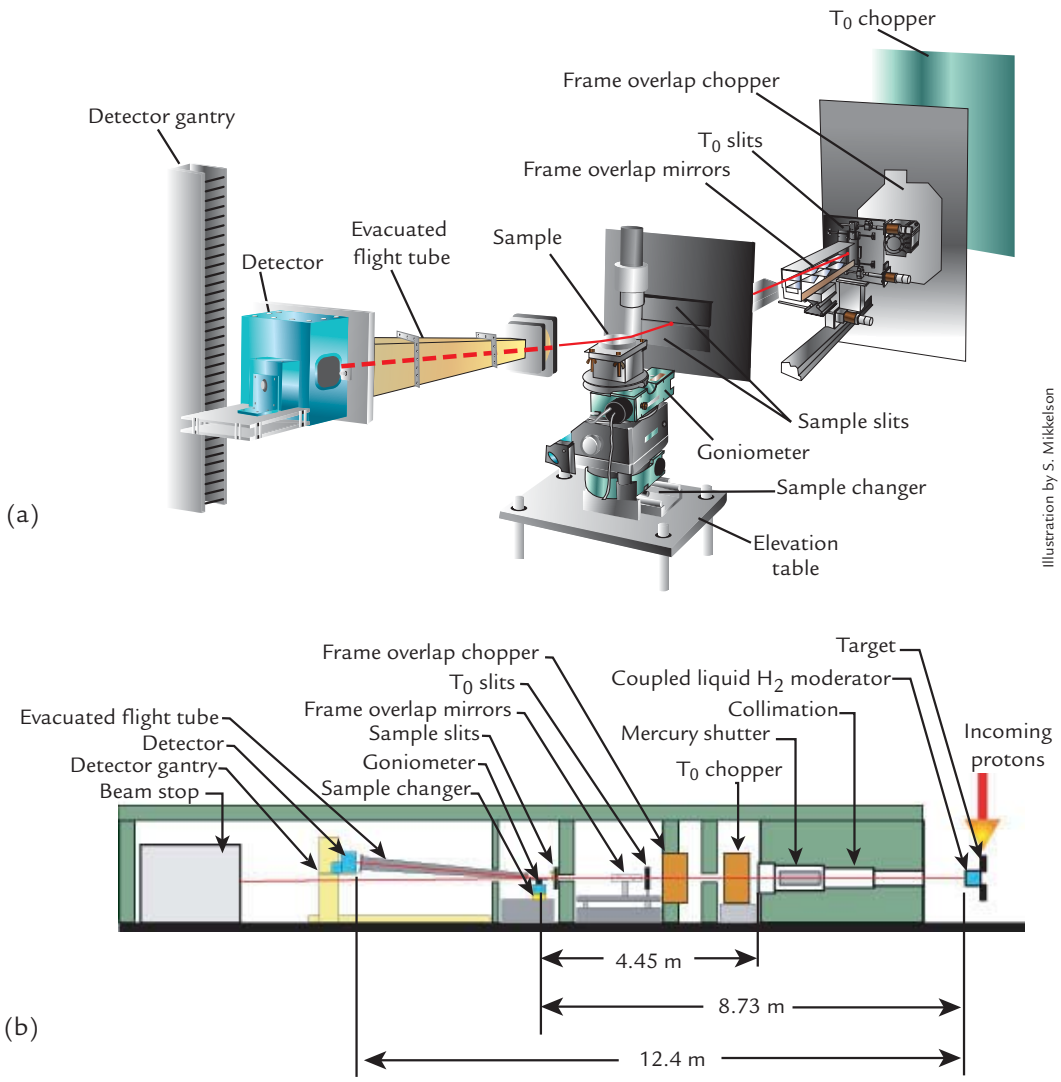

Fig. 2. A three-dimensional (a) and schematic (b) view of SPEAR. The yellow items in Fig. 2b indicate components that were upgraded in 2002.

New Detector Gantry

Replacing the cumbersome and unreliable ceiling-mounted detector gantry was a priority for the 2002 run cycle at LANSCE. The new detector gantry, mounted on the floor, incorporates a linear optical encoder that enables precise and reproducible detector movements.

PC-Based Data-Acquisition System

SPEAR, along with other instruments at the Lujan Center, was upgraded from an older virtual-address-extension (VAX)-based data-acquisition (DAQ) system to a PC-based system. With the PC-based system, the standardized NeXus file format is used, and the raw data are easily transported to other machines. In addition to the new DAQ system, the control of SPEAR's stepper motors was transferred to a LabView-based system, which has dramatically reduced the communication time between the user interface and the motors.

Sample Changer

Before the addition of a new sample changer on SPEAR, operating the instrument required frequent user input and incessant monitoring. Now the measurement of two or three samples at multiple angles can be accommodated, thus allowing the continuous, automated operation of the instrument for up to 12 hours.

Future Upgrades

Enhancing SPEAR's performance and adapting it to a wider variety of experiments is a continuing process. Several major future upgrades include a precisely controlled mirror used to alter the beam trajectory and extend the momentum transfer range when studying liquid/air interfaces, precise and robust slit packages, and a more integrated sample environment.

The LQD Upgrade: Challenges and Opportunities of Brighter Neutron Sources

R.P. Hjelm, G. Muhrer, R.O. Nelson, G. Russell, K.M. Kupcho (LANSCE Division)

Small-angle, neutron-scattering (SANS) measurements are designed to probe large length-scale structures. As will any instrument that uses elastic scattering, information on structure is obtained by measuring the scattering intensity, I(Q), as a function of the momentum transferred to the neutron, Q. For elastic scattering, Q is related to the neutron wavelength, λ, and the scattering angle, 2θ, as $Q = 4\pi/\lambda \sin\theta$. Given that the length scale probed goes as Q^{-1}, a SANS instrument must reach the smallest possible scattering angle and the longest wavelength to attain its design objective to probe large length scales. Modern SANS instruments use neutrons from cold moderators to achieve these requirements. The term cold implies that the neutron energy, E_n , is quite small; thus, the wavelength for a neutron with mass, m, given by the deBroglie relationship, $l = h/\sqrt{(2mE)}$, is large. A scattered-neutron detector is placed directly in the neutron beam to measure as small a scattering angle as possible. To protect the detector from exposure to the direct beam, a beam stop is located in front of the detector. The width of the beam stop, which is determined by the width of the unscattered beam at the detector, determines the minimum scattering angle.

The Low-Q Diffractometer at Lujan Center

The design of most SANS instruments, such as the Low-Q Diffractometer (LQD) at Lujan Center (Fig. 1), includes a source of moderated neutrons, a collimator usually consisting of two pinholes to define the direction of the incident beam, and a detector to measure the direction of the scattered beam. The LQD detector records both the incident neutron energy and the momentum transfer of neutron-scattering events. This detector reports momentum transfer in two dimensions; therefore, it is highly efficient in measuring isotropic scatter, and it enables the measurement of non-isotropic scattering.

Lujan Center uses a pulsed-spallation neutron source obtained by bombarding a tungsten target with an 800-MeV proton beam. The source is designed to feed the fast neutrons from the tungsten target into the moderators and hence into the instrument collimators. The neutrons are produced over a very short period of time determined by the duration of the proton pulse and the design of the moderator. LQD, like other neutron-scattering instruments at Lujan Center, relies on the pulsed characteristics of the source for obtaining time-of-flight (TOF) measurements of the scattered neutrons. The neutron wavelength is calculated using the deBroglie relationship. The Q-domain and the frequency of the pulse determine the TOF frame over which useful data are obtained.

Advanced spallation-neutron-source concepts and moderator designs have significantly increased the neutron flux available to scattering instruments. The latest partially coupled cold moderator at Lujan Center has a cold neutron output of 2.5 times that of its predecessor, and the proton power delivered to the tungsten target has increased from 52 to 96 kW. The neutron flux available to LQD has therefore been increased by about a factor of 5.

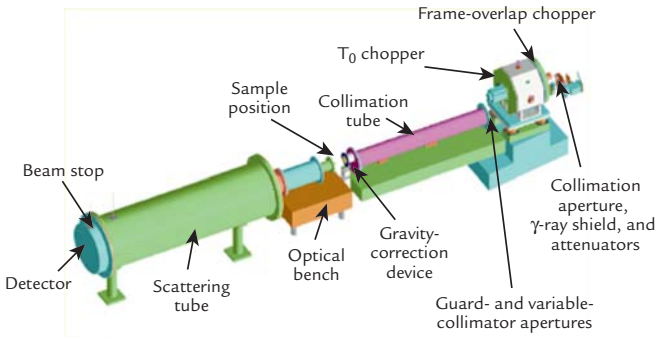

Fig. 1. A schematic of the LQD showing instrument elements described in the text. The neutron beam enters the instrument through the collimator on the right and is scattered by the sample into the detector on the left.

An increase in neutron flux means better opportunities. For example, more measurements can be performed, the data will be of higher quality, and more sophisticated experiments can be carried out. Facilities need to be built into LQD to take advantage of these opportunities. However, the level of background increases with source power and moderator output. Also, we must design data-acquisition systems that can handle higher data rates. The LQD instrument upgrade is designed to meet these challenges and to exploit these opportunities.

Background Mitigation

Background mitigation is perhaps the greatest challenge facing the design of instruments at pulsed-spallation sources, particularly for instruments close to the neutron source such as LQD. There are several types of background, including neutron background from the general facility, beam-induced neutron background, and γ-ray background. Each type has its own particular characteristics and sources, and there are strategies for dealing with each.

General-facility neutron background. This type of background, which includes instrument crosstalk from nearby flight paths, is reduced by strategically placed shielding between the flight paths and around the detector. We have come up with new shielding designs that are 100 times more effective than past concepts and far more compact.

Beam background. This type of background partly comes from high- and very-low-energy neutrons that enter the instrument and are assigned incorrect TOF values. Additional background comes from beam spill around the beam stop. We control this background with choppers and neutron-beam optic improvements. A time-zero (T_0) chopper, which closes at early times in the TOF frame, largely eliminates high-energy neutrons, whereas a frame-overlap chopper, which closes late in the TOF frame, eliminates very-low-energy neutrons. The successful implementation of a frame-overlap chopper in the current upgrade has made significant reductions in the beam background. Beam spill limits the minimum measurable value of the scattering angle. We have installed guard apertures in the collimator to clean up scattering from the chopper and defining-aperture elements. Neutrons fall under gravity. With a fixed collimation aperture, a significant part of the low-energy neutrons falls below the beam stop. To counter this, we moved the downstream aperture of the collimation upward during the TOF frame to select those neutrons that will hit the center of the beam stop. Although this concept is not new to LQD, we have implemented a new gravity-correction device based on a rotating cam system that is far more accurate and reliable than the older hydraulic system.

Background from γ-rays. We have found that the most important source of γ-rays is from neutron-capture reactions of ^{27}Al and ^{24}Na from the cold-moderator canister. The flux from this source is extremely high — 10^5 γ-rays for every neutron! Every γ-ray event takes up detector-signal processing time, during which the arrival of a neutron cannot be properly processed. We have installed a γ-ray collimator, which restricts the number of γ-rays that can enter the detector. We are also experimenting with lead and bismuth filters to reduce the γ-ray background contribution further.

Controlling Count Rate and Instrument Resolution

We have developed strategies to optimize the count rate at the detector by changing collimator aperture sizes and introducing neutron filters. For collimators, the count rate and the instrument resolution, δQ, are both affected. We installed apertures with variable diameters from 8 to 2 mm in addition to the standard 9.3-mm size. This action reduced count rates by a factor of 0.002 while, at the same time, decreasing δQ/Q from about 0.1 to 0.02, allowing greater flexibility in configuring LQD to meet experimental needs. Beryllium filters have also been installed to reduce the neutron count rate, particularly in the short wavelength part of the spectrum where the instantaneous count rate on the detector is highest.

Toward Counting at Higher Rates: A New Detector

We are installing a new two-dimensional detector that promises an improvement in count rate by a factor of 10^3. This development, along with the other upgrades, will give users the full power of the beam, allowing more measurements and more sophisticated experiments.

Acknowledgements

This work was supported by the U.S. Department of Energy Office of Basic Energy Sciences and has benefited from the use of the LQD located in Lujan Center at LANSCE.

Infrastructure Improvements

Facility Upgrades

Accelerator Development Activities in 2002 138

Replacement of the LANSCE 1L Target-Moderator-Reflector System 140

Upgrade of the Fiber-Optic-Cable Plant at LANSCE 141

A Multiwire-Proportional-Chamber System Used to Monitor Off-Momentum Beam in Accelerators 142

Magnet-Power-Supply Upgrades for 2002 143

LANSCE Accelerator-Control-System Upgrade 144

EPACS and Shutter Controls Installed at Lujan Center in 2002 145

New Access to the WNR Target-2 Detector Shed 147

Accelerator Development Activities in 2002

There is a continuous effort to better understand the performance of the linear accelerator (linac) at LANSCE to improve its performance and deliver optimum beams to the experimental areas. The following development activity was undertaken during the 2002 run cycle, specifically to understand the properties of the WNR beam in the low-energy beam transport (LEBT). The normal production current to WNR Target 4 is about 4.5 mA compared to the possible 10 mA that the target can handle. Measuring the beam parameters for the WNR beam in the linac during the 2001 run cycle revealed that the transverse beam size in the linac was consistently larger than that of the Proton Storage Ring (PSR) beam by about 25%. In addition, low-capture efficiency and higher beam losses may have occurred because the measured beam emittance at the end of the linac was about 50% larger for the WNR beam than that for the PSR beam.

Measuring Beam Emittance

We measured the beam emittance for both PSR (long-bunch enable gate) (Fig. 1) and WNR (micropulse enable gate) (Fig. 2) beams at the

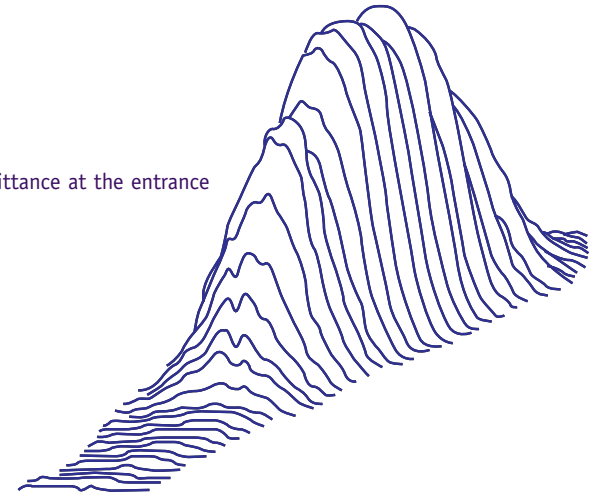

Fig. 1. PSR beam emittance at the entrance to the LANSCE linac.

Run: 14229/STN: TDEM1-H/12-17-02/21:03:21

Beam: H-	Measurement	Norm
Emittance (total)	4.140	0.166 pi
Emittance (edge)	3.949 pi	
Emittance (rms)	0.460	0.018 pi
Emittance (total/rms)	9.01	
Alpha	-1.963	
Beta	0.171	
4 x emittance (rms)	1.839 pi	
C	0.110 cm	
CP	0.043 mr	
X Sigma	0.2808 cm	
XP Sigma	3.6076 mr	
Threshold	2.0%	
Threshold	21 CNTS	
Maximum counts	1081	
Beam through threshold	250668	
Total beam	275142	
Charge-collector position	1340	1930
Jaw position	1339	1931

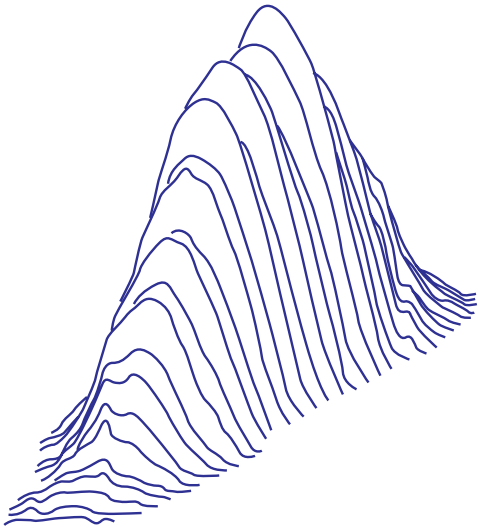

Run: 14228/STN: TDEM1-V/12-17-02/20:59:00

Beam: H-	Measurement	Norm
Emittance (total)	3.551	0.142
Emittance (edge)	3.409 pi	
Emittance (rms)	0.441	0.018
Emittance (total/rms)	8.04	
Alpha	-1.499	
Beta	0.119	
4 x emittance (rms)	1.766 pi	
C	0.046 cm	
CP	-1.013 mr	
X Sigma	0.2295 cm	
XP Sigma	3.4670 mr	
Threshold	2.0%	
Threshold	29 CNTS	
Maximum counts	14	
Beam through threshold	3484	
Total beam	3665	
Charge-collector position	1364	1946
Jaw Position	1349	1938

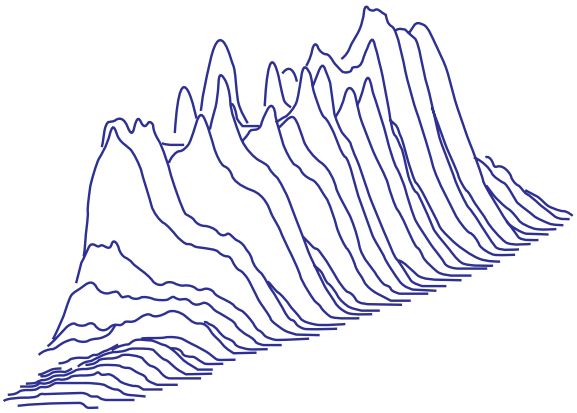

Run: 14230/STN: TDEM1-H/12-17-02/21:09:18

Beam: H-	Measurement	Norm
Emittance (total)	6.399	0.256 pi
Emittance (edge)	6.132 pi	
Emittance (rms)	0.900	0.036 pi
Emittance (total/rms)	7.11	
Alpha	-1.700	
Beta	0.208	
4 x Emittance (rms)	3.600 pi	
C	0.071 cm	
CP	-0.782 mr	
X Sigma	0.4327 cm	
XP Sigma	4.1037 mr	
Threshold	2.0%	
Threshold	18 CNTS	
Maximum counts	936	
Beam through threshold	364596	
Total beam	375201	
Charge-collector position	1340	1930
Jaw position	1340	1931

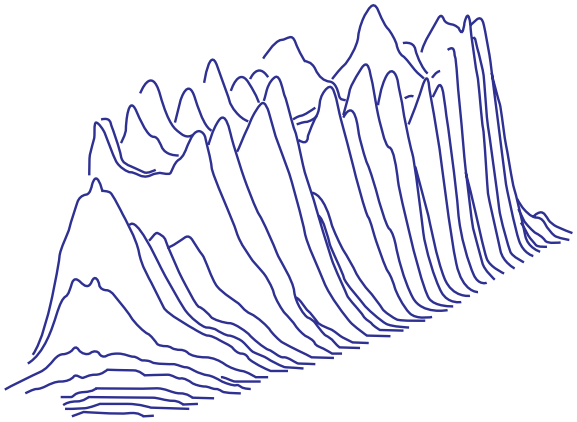

Run: 14231/STN: TDEM1-V/12-17-02/21:13:28

Beam: H-	Measurement	Norm
Emittance (total)	6.010	0.240 pi
Emittance (edge)	5.788 pi	
Emittance (rms)	0.940	0.038 pi
Emittance (total/rms)	6.39	
Alpha	-1.409	
Beta	0.188	
4 x Emittance (rms)	3.761 pi	
C	0.022 cm	
CP	-1.248 mr	
X Sigma	0.4200 cm	
XP Sigma	3.8675 mr	
Threshold	2.0%	
Threshold	18 CNTS	
Maximum counts	928	
Beam through threshold	448075	
Total beam	454842	
Charge-collector position	1358	1943
Jaw position	1348	1938

Fig. 2. WNR beam emittance at the entrance to the LANSCE linac.

entrance to the 201.25-MHz drift-tube linac. The horizontal emittance for the WNR beam was about 50% larger than that of the PSR beam, and the vertical emittance for the WNR beam was about 70% larger than that of the PSR beam. (Remember that the beam is chopped in the vertical direction for both beams.) The micropulse width for the PSR beam is 250 ns, whereas the micropulse width for the WNR beam is 20 ns. The rise and fall time of the pulse is about 7 ns. The capture efficiency of the PSR beam was 80% and that of the WNR beam was 50%. The beam loss in the machine for the WNR beam was about 30% of that of the PSR beam even though the average beam current for the WNR beam was only 4% of that of the PSR beam. Emittance of the WNR beam was reduced closer to that of the PSR beam by inserting beam-limiting jaws in the transport. The capture efficiency of this WNR beam then increased to 70%, and the beam loss went down to 10%. Theoretical calculations predict that fast chopping, narrow pulse width, and bunching affects beam emittance substantially.

C. Pillai, R.C. McCrady, M.S. Gulley
(LANSCE Division)

Replacement of the LANSCE 1L Target-Moderator-Reflector System

We successfully replaced the LANSCE 1L Target (called Mark 1) at the Lujan Center during the 2002 maintenance outage. The Mark 1 Target ran with excellent availability (99.2%) in calendar year 2001 but was limited to 55 mA of proton beam current because of cooling problems that developed in the lower lead reflector. Our operations-trending analysis and subsequent engineering analysis led us to redesign several components for the new Mark 2 Target.

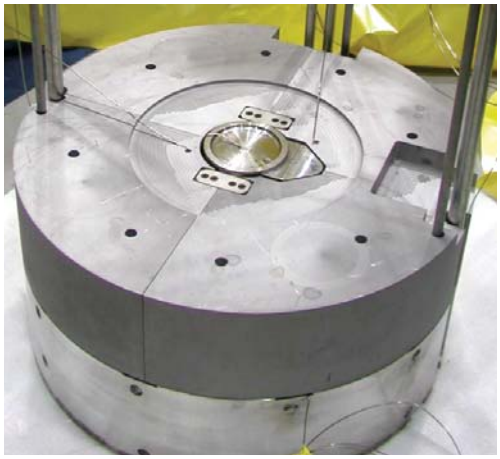

Fig. 1. Composite lower reflector for the 1L Mark 2 Target insert. The lower tungsten target is shown at the center. The assembly is 60 cm in diameter and 30 cm high.

This new target was installed in May 2002, and we were ready for operation at the end of June 2002. The new target ran successfully through calendar year 2002 with 99.2% availability and an average production beam current of 104.5 mA. We also established a new record high current of 125 mA. The overall beam availability, including all beam delivery systems, was 86.4%

Design Improvements

Our engineering analysis and operations-trending analysis of the Mark 1 Target led to several design improvements for the Mark 2 Target. We believe that the lower lead reflector failed because the stainless-steel cooling tubes that had been cast into the lead separated from the lead due to thermal cycling. We also saw a change in the coolant flow resistance of the upper target that we attributed to bypass flow in the cooling manifold.

We began design modifications and concurrent construction of the Mark 2 Target in October 2001. Most of the components were identical to those of the Mark 1 except for the upper and lower lead reflectors and the cooling manifold on the upper tungsten target. We replaced the lower lead reflector with a composite of beryllium and water-cooled stainless steel. Fig. 1 shows the new lower reflector.

Although the upper lead reflector had not failed, it was showing signs of deterioration so we replaced it with water-cooled stainless steel. The steel is directly cooled using drilled water passages and the beryllium is cooled on the edge. The upper-target-cooling-manifold design was modified to eliminate the possibility of an internal shunt and to improve the quality of the electron-beam weld.

Installation

The removal and replacement scheme was devised in 1997 when the target system was upgraded during the LANSCE Reliability Improvement Project. The new change procedure uses the concept of a chimney cask that is open at both ends. The overhead crane hook reaches through the chimney and pulls the insert inside. Although we tested this plan during dry runs, an actual removal operation with activated components had never been attempted.

The Mark 1 Target required 12 **months** to change and exposed the workers to 12 man-rem of radiation. The new scheme required 37 **working days** and 0.56 man-rem of radiation exposure. We have identified further improvements that can reduce the time to about 30 working days.

Conclusion

We have successfully replaced the Mark 1 Target with an improved system. The new Mark 2 Target is operating at over 100 μA with greater than 99% availability.

Acknowledgements

This work was supported by the U.S. Department of Energy. Engineering design and analysis for the new reflectors were performed by Rick Wood (LANSCE-1). Target-physics design and Monte Carlo calculations were performed by Gary Russell, Eric Pitcher, and Guenter Muhrer (LANSCE-12).

J.B. Donahue, M.J. Baumgartner
(LANSCE Division)

Upgrade of the Fiber-Optic-Cable Plant at LANSCE

The linear accelerator at LANSCE uses a fiber-optic-cable plant to connect control-system-network nodes and to transfer timing signals to various points around the facility. The original implementation provided a limited number of signal paths that were not susceptible to noise, grounding, and lightning issues associated with running cables between buildings. As the control- and timing-distribution systems have expanded, resources for the limited-signal path have been depleted to the point where installation of additional cabling is required. We developed and implemented a comprehensive plan to manage the growth of the fiber-optic-cable plant and completed a large portion of the upgrade plan during CY 2002.

General Upgrade Path

The upgrade plan required multi-fiber cables be run between various centralized locations at LANSCE. These locations act as junction points where signals can be routed through to different areas of the facility. The junction points are categorized by the installation of cable-termination boxes. In the boxes, jumper cables are used to connect the trunk cables together or to allow fiber-optic transmitter/receiver sets access to the trunk cable. The junction locations, the number of fiber-optic-signal paths in the trunk cables, and progress to date are depicted in Fig. 1. The majority of the plan has been implemented. The remaining installations are scheduled for the 2003 maintenance outage.

As part of the upgrade, we tested several commercial fiber-optic-transmitter/receiver sets and selected those from FiberPlex, Inc., as the standard for timing, voice, and video signals. Dymac instrumentation analog fiber-optic-data links were chosen for analog signals with bandwidths from direct current (dc) to 1 MHz. Links with bandwidths greater than 1 MHz were selected on a case-by-case basis.

Cable Selection

In selecting cables, we wanted to ensure compatibility with existing transmission electronics. As such, we chose a graded-index, multi-mode fiber cable. Graded index implies that the index of refraction of the glass core of the cable varies from the center to the outer edges. This refocuses the signal, reduces dispersion, and allows operation at higher data rates. Multi-mode refers to the transmission mode of the signal and implies that several modes are possible. We selected a high-quality, fiber-optic cable with an attenuation that ranges from 3.0 dB/km at a wavelength λ = 800 nm to 0.3 dB/km at λ = 1,550 nm. One single-mode cable with twelve fibers was installed between the equipment building of the Proton Storage Ring and the Central Control Room for use with longer wavelength laser-based transmitter/receiver systems.

V.S.A. Gonzales, D.J. Hayden, M.D. Lusk, R.B. Merl, J.M. Potter, J.A. Reynolds, D.B. Romero, F.E. Shelley, M.A. Thome (LANSCE Division)

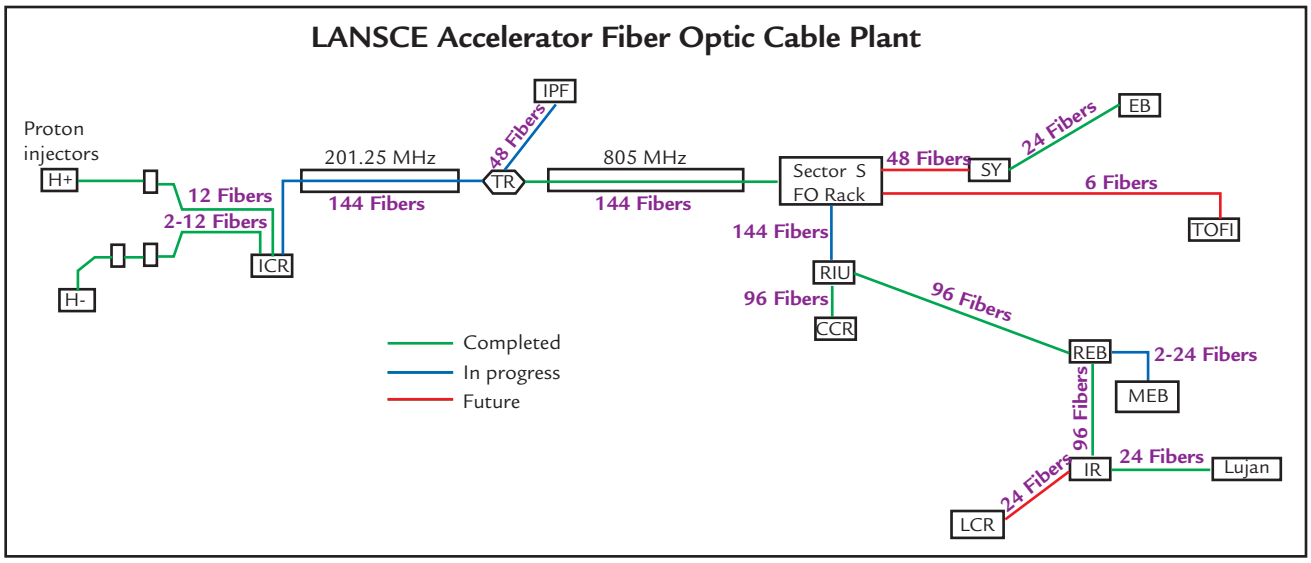

Fig. 1. Fiber-optic-cable plant upgrade.

A Multiwire-Proportional-Chamber System Used to Monitor Off-Momentum Beam in Accelerators

Identifying and eliminating unwanted off-momentum components in an accelerator beam is critical for maintaining the transverse and longitudinal parameters of the beam to within the specifications of the accelerator. The off-momentum components in an accelerator beam appear when the beam goes through a dispersive element such as a bending magnet. At the exit of this bending magnet, the different energy (i.e., momentum) beam components are separated [e.g., analogous to the way the various color (wavelength) components of a beam of light are separated when crossing a prism]. This type of bending magnet is located at the end of the LANSCE proton linear accelerator (linac). Normally, a phosphor screen illuminated by the low-energy beam at the exit of the magnet is monitored by a camera.

This phosphor screen has been superseded by a proportional chamber that detects and eliminates the low-momentum components of the linac beam.

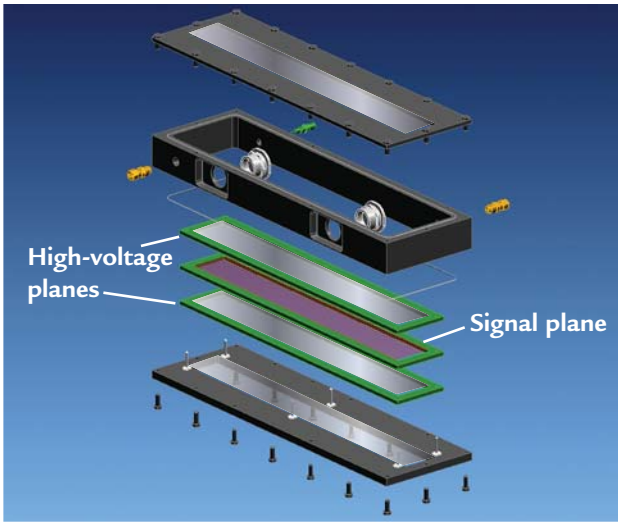

Fig. 1. Schematic of the MWPC.

Multiwire Proportional Chamber Replaces Phosphor Screen

We have developed a multiwire proportional chamber (MWPC) to replace the phosphor-camera system. This MWPC is positioned to detect protons with an energy smaller than that of the full 800-MeV beam, which is deflected outside the chamber. This new chamber gives a much better position resolution (~ 2 mm) than that of the phosphor-camera system (~ 1 cm). The phosphor does not respond well when the intensity of a low-momentum beam is less than a few nA, whereas the MWPC is sensitive even at a few pA. The MWPC is thus more efficient at detecting weak off-energy components of the beam than a phosphor detector. Moreover, the gain (multiplication factor) of the MWPC can very easily be changed by adjusting its high voltage, making it possible to change the sensitivity of the device to off-energy components.

The chamber includes three frames made of G-10 fiberglass with an active area of 300 cm^2 (50 cm x 6 cm). There is 1 frame, called a signal frame, with 64 gold-plated tungsten wires (20 µm in diameter) that have a 2-mm spacing between adjacent wires (Fig. 1). Only wires close to the beam particle trajectory are activated. There are two other frames, each covered with an aluminum foil, on either side of the signal frame to handle the high voltage. The whole assembly is enclosed in an aluminum box with 6-µm aluminum windows covering the active area of the detector and flushed with a gas mixture of argon and methane (90% and 10% in volume, respectively).

The signal from each wire is digitized by a custom-made digitizer and can be displayed on any computer terminal. This signal indicates the presence of a particular low-energy beam component, which has to be eliminated or minimized to achieve optimum tuning of the accelerator. The signals from the wires are also fast enough to identify beam losses arising from low-energy components across the entire macropulse of the beam. If necessary, high-energy components of the linac beam could also be detected by locating the MWPC on the other side of the main beam.

Acknowledgements

This work was supported by the U.S. Department of Energy. The engineering drawing of the detector box was rendered by James Witt (LANSCE-2).

C. Pillai, R.B. Merl, C.A. Burns, A.I. Steck (LANSCE Division)

Magnet-Power-Supply Upgrades for 2002

One of our greatest challenges with the LANSCE 675-magnet-power-supply subsystem is maintaining the original eighteen 400-W to 500-kW power supplies used for the quadrupole magnets in the Proton Storage Ring (PSR). These power supplies provide a precise source of current that excites the magnetic beam optics (i.e., electromagnets) for the linear accelerator. Each of the 18 power supplies must regulate its current output to about 100 ppm. To accomplish this, we use motor-driven variable-voltage transformers (VVT) to maintain a constant voltage across a set of 20 to 100 transistors that provide the precise regulation required by the quadrupole magnets. When these VVTs fail, they fail catastrophically via a process known as "thermal runaway." Thermal runaway occurs when carbon brushes, which carry the current, fail to make good contact with the VVT coils (windings). The brushes and coils subsequently heat up, reducing their current-carrying capacity. As the brushes continue to heat up, eventually all of the electric current at the brush-coil connections is converted to heat, and the VVT assembly melts and destroys itself (Fig. 1). Replacing the VVTs is mechanically challenging and usually takes 6 to 8 hours to complete, which implies losing a good part of a beam-production shift. By adding cooling fans and a preventive maintenance program, we have reduced the VVT failure rate. From 1998 to 2001, we had an average of three VVT failures per run cycle. During the 2002 run cycle, we had no failures. Replacement parts for these 20-year-old transformers are expensive and difficult to obtain.

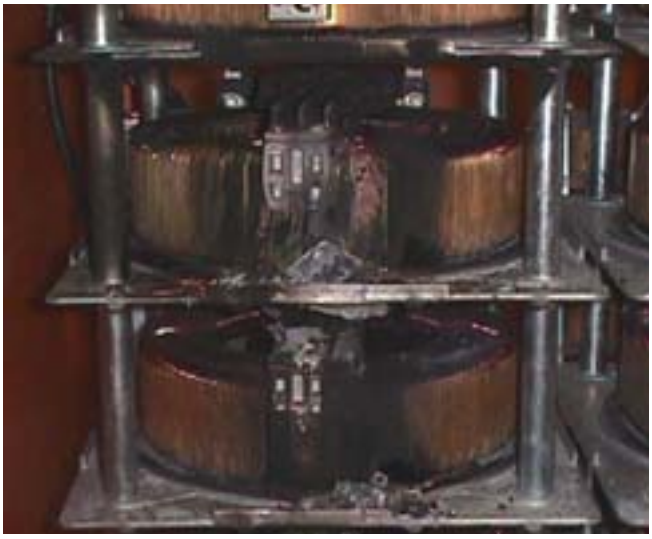

Fig. 1. VVT failure due to thermal runaway.

Line-D Replacement Quadrupole Power Supply

The LANSCE-6 Magnet Power Supply Team worked with Alpha Scientific Electronics, a leading company in the design and manufacturing of high-current precision power supplies, to develop a replacement power supply for Line D that would use modern power electronics and a flexible control-system interface. The new interface emulates the control characteristics of the older power supplies (Fig. 2). Its modular geometry requires the design and replacement of only one circuit board to be compatible with future control-system upgrades. The first two replacement power supplies have been in place since July 2002. Over the next several years, all 18 VVT-regulated power supplies will be upgraded.

Fig. 2. New (yellow) and old (orange) VVT quadrupole power supplies.

Power-Supply Upgrade of the Proton Radiography Magnetic Lenses

The primary magnetic lenses used for proton radiography (pRad) consist of four, large quadrupole magnets connected in series. These lenses require a current of almost 2,000 A with a voltage of about 150 V, which amounts to a power of 300,000 W! The first of three new lens power supplies was installed before the start of

the 2002 run cycle. This new power supply (Fig. 3) has better stability (by a factor of 10) compared to the 30-year-old unit it replaces. Inside the power supply are many easily replaceable commercial components common to other recently installed power supplies. This makes repair simpler and reduces the size and complexity of the spares inventory.

As with other new power supplies that are being installed, the modern controllers eliminate 4 interconnect cables containing 200 conductors.

Safety Enhancements

All of the new power supplies are now being delivered with an additional contactor and a low-impedance bleeder resistor across the output buss of the power supply. When the bleeder resistor is switched into the system, the contactor time for the capacitor bank to discharge is reduced to 15 s. This safety measure not only reduced the time for the output filter capacitors to discharge but also lessened the chances of hazardous shock from a charged capacitor bank, which could store upwards of 25,000 J.

Fig. 3. LCMP10, the new power supply for pRad lenses.

S. Cohen, M. Fresquez, E.A. Morgan, T.D. Pence, J.B. Sandoval (LANSCE Division)

LANSCE Accelerator-Control-System Upgrade

The LANSCE Accelerator Control System (LCS) uses hardware and software originally developed in the 1960s through the 1980s for the half of the facility that has not been upgraded to the Experimental Physics and Industrial Control System (EPICS). EPICS contains a set of tools for building applications, a run-time environment, and a high-performance, flexible architecture — all of which provide a foundation for building software to control experimental physics facilities. Vendor support for LCS hardware and software is withering or gone, and spare parts are becoming difficult to obtain. An effort is under way to upgrade the LCS software and hardware to modern, maintainable standards. Approximately half of the 25,000 command and read-back channels in the LCS have been upgraded to EPICS, but progress has been slow due to limited resources. The upgrade strategy[1] is to first replace those things that are most likely to fail and cause accelerator downtime. During 2002, progress was made on hardware and software upgrades.

Computer Hardware Upgrades

The LCS uses VAX (virtual address extension) computers in remote locations along the beam line to command and read devices in those locations. Operators use other VAXs in the control room (Fig. 1) to monitor and control the accelerator. By today's standards, these VAXs are very slow and extremely expensive. Maintenance is also expensive, and repair times are becoming longer.

Fig. 1. LANSCE Central Control Room.

Approximately $1 million (original cost) of VAXs and VAX-disc server hardware were decommissioned before the startup of the 2002 run cycle. Their functions were moved to EPICS systems or to less-expensive, more-maintainable VAX systems. Because vendor maintenance for some of the decommissioned hardware was terminated in early 2002, a large risk to operational reliability was avoided.

Computer Software Upgrades

The software in the LCS is heavily dependent on the VAX/VMS (virtual memory system) operating system. The control-system programs must be rewritten to move their functionality to EPICS. Of the approximately 250 programs in the LCS, 73 have been identified as necessary in the new EPICS system. Some of these programs are fairly simple and required only a few man months to write the original code, but others are very complicated and required several man years for original code. Fortunately, with modern software tools (such as the EPICS Display Manager and Java), the programs can be rewritten with much less effort and cost. During 2002, software programs for current-monitor-data archiving, data-strip charting, the generation of data histograms, status-message logging, and the display of web data were converted to EPICS. Also a generic facility was implemented to allow experimenters access to all accelerator data from EPICS applications.

Work is in progress to convert VAX programs for accelerator status, wire-scanner control and display, accelerator longitudinal tuning, facility logs, and harp control and display.

Remote Instrumentation and Control Equipment Replacement Test

The Remote Instrumentation and Control Equipment (RICE) system is the hardware interface to approximately 9,000 input and 2,100 command channels for the linear accelerator and experimental-area beam lines. The system was designed and built in-house in the late 1960s. As the system aged, the majority of its hardware components became unavailable. Replacement of this old custom-made system with a new single system is very difficult — hence only minor improvements have been made over the years.

Tests in the previous year indicated that about 80% of the channels in RICE could be replaced by a commercial programmable logic controller (PLC) system using software developed by LANSCE-8 in support of the Spallation Neutron Source project. During 2002, we selected and tested specific PLC modules; developed and tested PLC-ladder-logic templates; made system-loading and update-rate tests; developed and implemented a junction-box wiring scheme; and designed (and ordered the components for) a communication architecture. We plan to test modules 47 and 48 in preparation for operation in 2003. A proposal for replacing all of these RICE channels with PLC hardware is being prepared.

The remaining 20% of RICE channels require special timing and gating capabilities that are not available in a PLC. However, a virtual-memory-extension module under development for the low-momentum switchyard detector shows promise for this application. After we have gained experience with the module, we will evaluate its applicability.

References

1. LANSCE Control System Upgrade Progress and Plan, Los Alamos National Laboratory report LA-UR-02-7632 (2002); http://lansceops2.lanl.gov/controls/Upgrades/20021001PlanProgress.pdf.

E.A. Bjorklund, M.J. Burns, G.P. Carr, J.A. Faucett, D.J. Hayden, M.D. Lusk, R.B. Merl, M.A. Oothoudt, J.M. Potter, J.A. Reynolds, D.B. Romero, S.C. Schaller, F.E. Shelley, Jr. (LANSCE Division)

EPACS and Shutter Controls Installed at Lujan Center in 2002

During 2002, a total of 12 flight paths (FPs) were involved in new Experimental Personnel Access Control System (EPACS) and shutter-control installations at the Lujan Center at LANSCE.

Upgrades of Existing Shutters

Eight shutters were upgraded to a new sealed mercury system that eliminated the need for bottled helium as a pressure source and the need to vent that helium to the atmosphere. The new system uses a sealed system containing helium and a pump to pressurize the gas to move the mercury out of the shutter. The helium is returned to the mercury reservoir when the shutters are refilled with mercury. The controls for these new-styled shutters are

integrated with the EPACS controls to form an integrated system. FPs 10 through 13 have mechanical shutters. FP10 has its shutter controls integrated with EPACS, whereas FP11 uses a new stand-alone system, but it should be integrated into EPACS next year. FP12 and FP13 have new mechanical shutters but no beam lines as of yet. The controls for these new mechanical shutters are also integrated into the EPACS.

The shutter controls are also available to the Experimental Physics and Industrial Control System (EPICS) to allow remote operation of the shutters. Interface to the Central Control Room for both the shutters and EPACS is also done through EPICS. The EPACS Radiation Security System has its hard relay logic contained in panels in Experimental Room 2 (ER2) at the Lujan Center (Fig. 1). The system is fault tolerant and has battery backup to help prevent the need for sweeping the FPs after a power failure.

EPACSs were installed on nine FPs, including two FPs with mechanical shutters. This leaves FP8, FP12, and FP13 without EPACS. The operation of the shutters for these three FPs is controlled by lock-out-tag-out devices placed on the shutter infrastructure panels located towards the north end of ER2. FP8 is an inactive FP with a shield block covering its shutter.

The EPACSs range in complexity from a simple sample hatch to complex multi-zone systems that exclude people from various areas of the FPs. All the systems use the same operator interface that simplifies the use of these FPs. All data reporting and interface between the EPACS and shutters is done in ER2. This moves most of the active controls out of Experimental Room 1 (ER1) into the more benign environment of ER2. The system is modular and includes extensive self-checking and diagnostics.

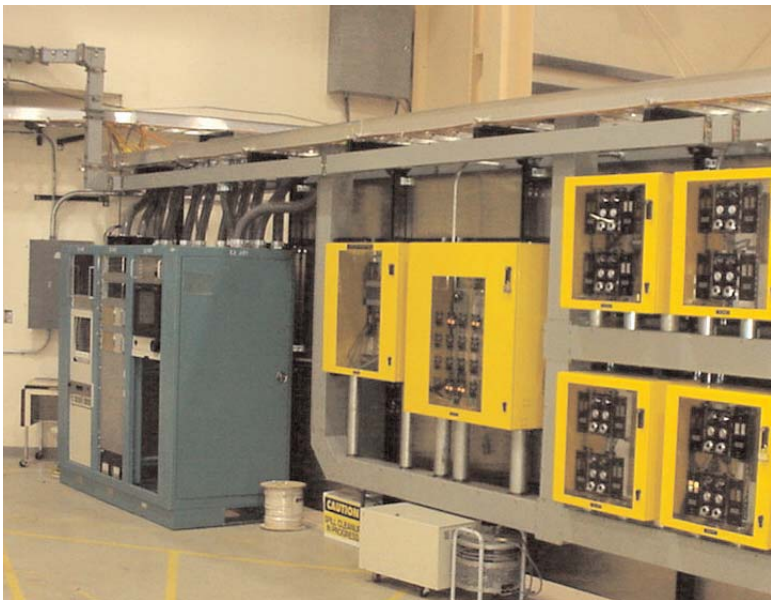

Fig. 1. New EPACS and shutter-control installation in ER-2 at the Lujan Center.

Conclusion

All the older open-mercury shutters have been replaced with a new sealed design. All of the old Personnel Safety System has been removed and replaced with EPACS. All the old shutter controls have been removed from ER1, replaced with new ones located in ER2, and fully integrated with the EPACS (except for FP11, which will be integrated in 2003). Remote shutter control and data collection are being handled through EPICS.

J.C. Sturrock (LANSCE Division)

New Access to the WNR Target-2 Detector Shed

Experimenters using the 120° flight path on WNR Target 2 previously had to trek across hillsides and through mud to get their equipment to MPF-1138, which is the flight-path detector shed. This was particularly hazardous during the winter and at night. As part of the LANSCE-3 (Neutron Nuclear Science Group) experimental-area improvement plan, the access to this flight path underwent significant upgrades during 2002.

Experimental Area Improvement

During the construction of the Irradiation of Chips and Electronics (ICE) House, an access road was also constructed in this area. Using this road and parking area as a starting point, LANSCE constructed a walkway to replace the "goat path" regularly used to get to MPF-1138. (These paths worn by years of use have been referred to as goat paths for as long as anyone can remember.) A design goal for the project was to provide a smooth access such that hand carts could be used to move heavy material to the flight-path access gate. The design was complicated because the path traversed an old beam-line berm and crossed major area drainage and utility structures.

The completed project provides a dramatic improvement in both safety and utility on the flight path. Figs. 1 through 6 show before and after photos of the sites.

B. Takala (LANSCE Division)

Fig. 1. Previous access route to the east side of Target 4.

Fig. 3. "Goat path" from above to MPF-1138.

Fig. 5. "Goat path" to MPF-1138.

Fig. 2. New access route to the east side of Target 4.

Fig. 4. New access from above to MPF-1138.

Fig. 6. New access to MPF-1138.

2002 Run Cycle Planning and Outage Execution 150

2002 Operations and Beam Delivery 151

2003 Outage Planning. 155

Accelerator Operations and User Program

Accelerator Operations

Accelerator Operations

K.W. Jones (LANSCE Deputy Division Director)

Maintenance and enhancement activities were performed during the LANSCE user facility scheduled outage from January through April 2002. This outage was followed by accelerator turn-on and contingency time that culminated in the start of full user-facility operations on July 26, 2002. Operations continued through December 24, 2002, and were then suspended for the annual Laboratory holiday closure. Operations resumed on January 2, 2003, and the 2002 run cycle concluded on January 26, 2003.

2002 Run Cycle Planning and Outage Execution

A detailed 2002 outage was planned beginning in the last quarter of 2001 to both coordinate and level personnel resources across major tasks selected for the outage. A representative overview schedule during the outage is shown in Fig. 1. This detailed planning allowed the accelerator turn-on to begin as scheduled on May 1, 2002. The pRad facility in Area C began operations on May 28, whereas Proton Storage Ring (PSR) development activities began on June 9, and WNR operations began on June 22. The new Mark 2 Target-Moderator-Reflector System (TMRS) for the Lujan Center received beam for the first time on July 8 and full user-facility operation began on schedule on July 26. Key tasks that were completed included:

- fabrication, assembly, installation, and testing of the Mark 2 1L TMRS;
- relocation of the Mark 1 TMRS unit to storage for use as a low-current spare, including preparation of necessary authorization-basis documentation;
- installation of the remaining beam-line components for the Isotope Production Facility (IPF) in the main accelerator tunnel, including the kicker magnet;

Activity ID	Activity Description	Orig Dur	Early Start	Early Finish	% Comp	Total Float
1.2.1.15.01 1L Water Systems						
TO-H2O-110	Pressure test target H2O/calibrate transducers	3	18JUN02	20JUN02	0	-15
TO-H2O-115	Pressure test reflector H2O/calibrate transducers	3	21JUN02	25JUN02	0	-11
TO-H2O-120	Pressure test moderator H2O/calibrate transducers	3	25JUN02	26JUN02	0	-11
TO-H2O-140	Perform water-pump preventive maintenance	0	01JUL02	28JUN02	0	-11
TO-H2O-130	Fill water system(s)	2	01JUL02	02JUL02	0	-11
TO-H2O-155	RSS flow switch checks (LANSCE-7-OP-3-12)	1	03JUL02	03JUL02	0	-11
TO-H2O-160	RP flow switch checks (LANSCE-7-OP-3-14)	0	05JUL02	03JUL02	0	-11
1.2.1.15.03 1L Instrumentation and Controls						
TO-I&C-060	Run permit checks (LANSCE-7-OP-3-13)	1	05JUL02	05JUL02	0	-11
1.2.3.05 TMRS Replacement						
TM-000-051	Mark 2 ready for beam	0		05JUL02	0	-11
1.2.3.05.03 TMRS- 1L Instrumentation and Controls						
TM-CCC-040	Fabricate water moderators	45	09NOV01A	12APR02	98	-11
1.2.3.05.04 TMRS- MARK II Assembly						
TM-CCC-210	Radiograph upper target	5	03APR02A	12APR02	80	-11
TM-DDD-090	Assemble lower-tier moderators	3	15APR02	17APR02	0	-10
TM-DDD-200	Assemble upper-tier moderators	3	18APR02	22APR02	0	-11
TM-DDD-100	Weld cooling lines to lower TMRS subassembly	3	23APR02	25APR02	0	-10
TM-DDD-210	Radiograph cooling line welds	2	25APR02	29APR02	0	-11
TM-DDD-110	Mate upper and lower TMRD subassembly	2	30APR02	29APR02	0	-10
TM-DDD-120	Seal and route thermocouples	3	02MAY02	07MAY02	0	-10
TM-DDD-130	Seal weld cooling lines at upper plate	5	08MAY02	14MAY02	0	-10
TM-DDD-140	TMRS final QA checks	4	15MAY02	21MAY02	0	-10
TM-DDD-150	TMRS final alignment check	2	22MAY02	23MAY02	0	-10
1.2.3.05.05 TMRS- Mark II Installations						
TM-FFF-030	Install Mark 2 TMRS	1	24MAY02	24MAY02	0	-10
TM-FFF-050	Check TMRS alignment	1	25MAY02	25MAY02	0	-10
TM-FFF-060	Install top bellows assembly	1	29MAY02	29MAY02	0	-10
TM-FFF-070	Check crypt vacuum	1	30MAY02	30MAY02	0	-10
TM-FFF-080	Replace target service connections	5	03JUN02	07JUN02	0	-10
YM-FFF-090	Replace bending magnets	1	10JUN02	10JUN02	0	-10
TM-FFF-120	1LTC final alignment check	1	11JUN02	11JUN02	0	-10
TM-FFF-140	Replace magnet platforms	1	12JUN02	12JUN02	0	-11
TM-FFF-100	Replace beam-line connections	1	13JUN02	13JUN02	0	-10
TM-FFF-110	Check beam-line vacuum	1	17JUN02	17JUN02	0	-10

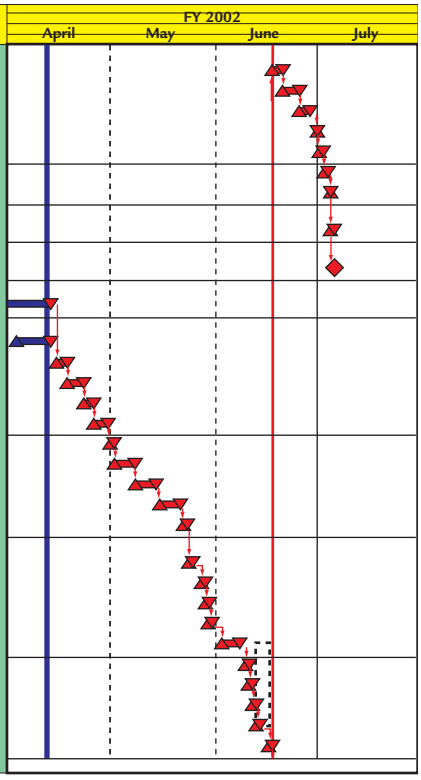

Fig. 1. A portion of the 2002 outage schedule, including activity descriptions and duration.

- procurement, fabrication, and testing of components for the Switchyard Kicker System;
- connection and commissioning of the new experimental-area cooling tower, together with demolition and site clean-up of the three old cooling towers;
- continued development of planned Documented Safety Analysis (DSA) documentation for the nuclear facilities and activities at LANSCE;
- essential, high-priority accelerator and facility maintenance; and
- successful turn-on of the accelerator and beam-delivery systems.

The outage was once again managed as a project subject to change control, and over 2,000 activities were scheduled and completed. The most substantial effort was devoted to fabrication, assembly, installation, testing, and commissioning of the Mark 2 TMRS for the Lujan Center. A three-week cumulative delay in this project occurred because of slippage in the delivery schedules of key components from off-site vendors, causing the delay in turn-on of the Lujan Center user program, which was originally scheduled for July 1. Despite this short delay, this project was completed without incident, and the new target operated successfully at incident-beam currents of up to 125 μA during the 2002 operating period (see *Replacement of the LANSCE 1L Target-Moderator-Reflector System*, p. 140.)

Integrated efforts to formalize long-range planning continued, and a predictable operating schedule for the 2002 operating period was developed. Several changes were made to the operating schedule in response to input received from the user community from the 2001 run cycle. First, the maintenance weeks were reduced in length from five to four days (with one exception). This reduction permitted restart of the user program before the weekend. Second, the single contingency days that followed each sole-use period in the middle of the 28-day cycle were changed to 2 blocks of 9 and 7 days each, the first place at the halfway point of the operating period. This arrangement better addressed reclamation of lost time for some experiments and also allowed the prompt scheduling of new, urgent experiments. These changes resulted in 2 more days of scheduled beam for the user programs at Lujan Center and WNR in each 28-day cycle and removed the necessity to restart these programs on weekends. Sole-use activities, defined as any research and development use of the LANSCE accelerator that precludes or interferes with beam delivery to the Lujan Center or WNR, were scheduled for 6 days within each 28-day cycle. Two days were scheduled in parallel with necessary maintenance of the Lujan Center target, and 4 days were scheduled in the middle of each 28-day cycle. The details of the operating schedule are shown in Fig. 2.

2002 Operations and Beam Delivery

The successful on-time completion of all outage work (other than the Mark 2 TMRS) and efficient accelerator restart combined to allow certain key sole-use programs to be executed prior to the start-up of the full user facility. In June 2002, the pRad program conducted a very successful campaign, which formed the foundation for the most successful year in the history of that program. The LANSCE accelerator once again delivered 100% beam availability for dynamic experiments conducted at pRad. The second key program conducted during June and early July 2002 was the irradiation of target-test assemblies for the Spallation Neutron Source (SNS) at the WNR Target 2 facility using intense beam pulses extracted from the PSR. These experiments were used to study techniques developed to mitigate shock-induced pitting of containment vessels for liquid-mercury targets.

The LANSCE user facility continued to achieve strong beam reliability in 2002. Our commitment was to deliver beam to all four active target areas for at least six months from July 1 to December 24, 2002. This commitment was met for all but the Lujan Center in CY 2002, and the operating period was extended into January 2003 to fulfill this obligation for the Lujan Center. Operational achievements are summarized in Figs. 3-7. Overall beam reliability during the 2002 run cycle for all areas is summarized in Table 1.

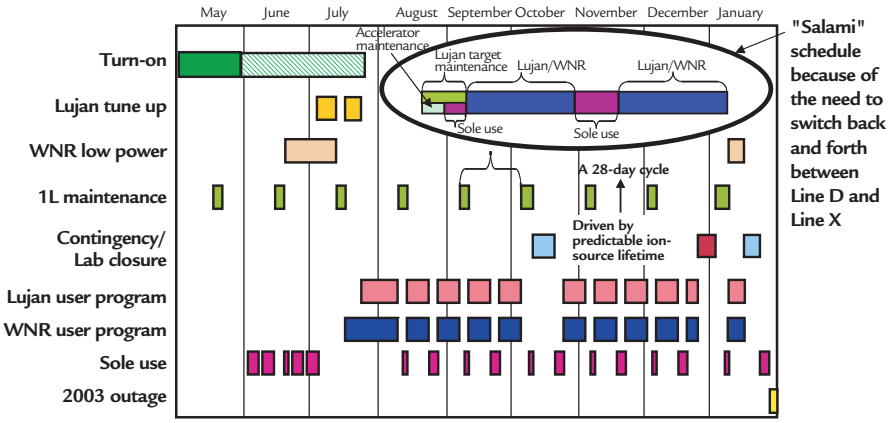

Fig. 2. LANSCE operating schedule for CY 2002.

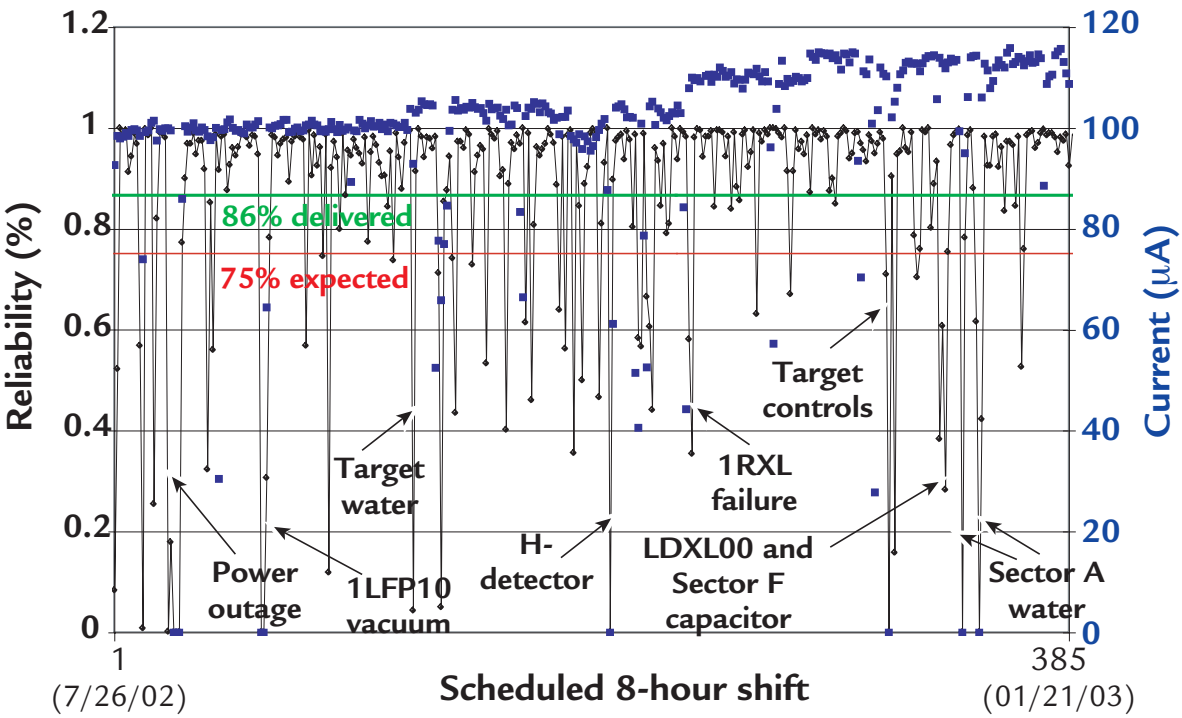

Fig. 3. Lujan Center performance for 2002.

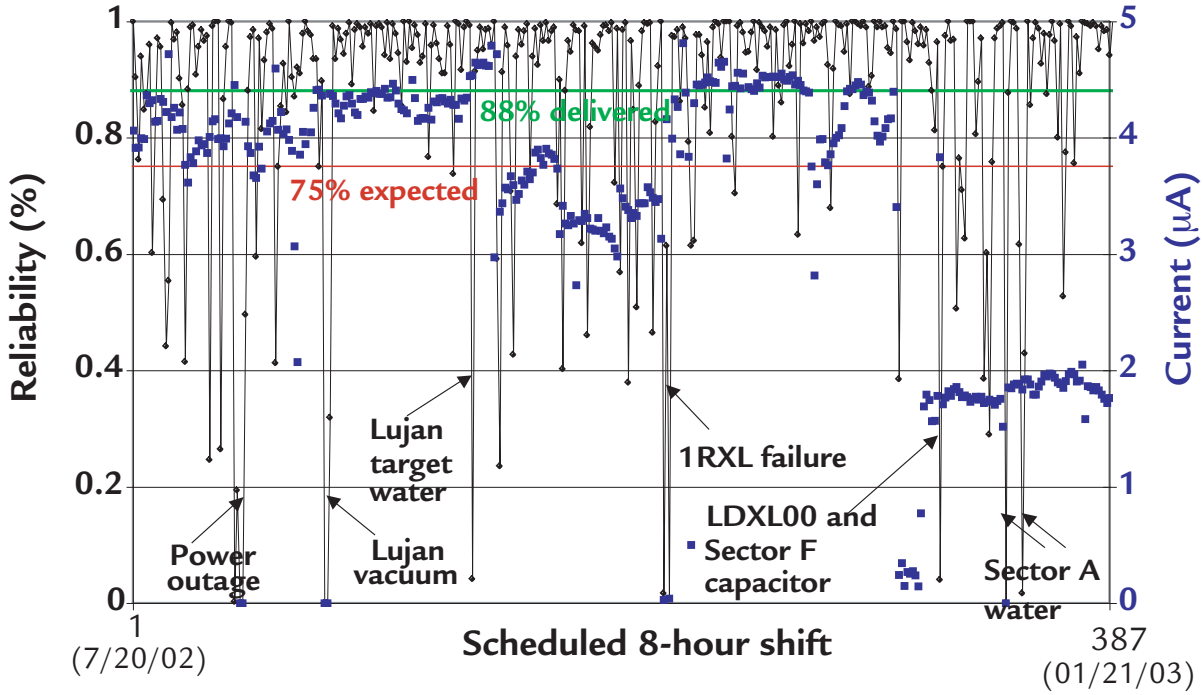

Fig. 4. WNR performance for 2002.

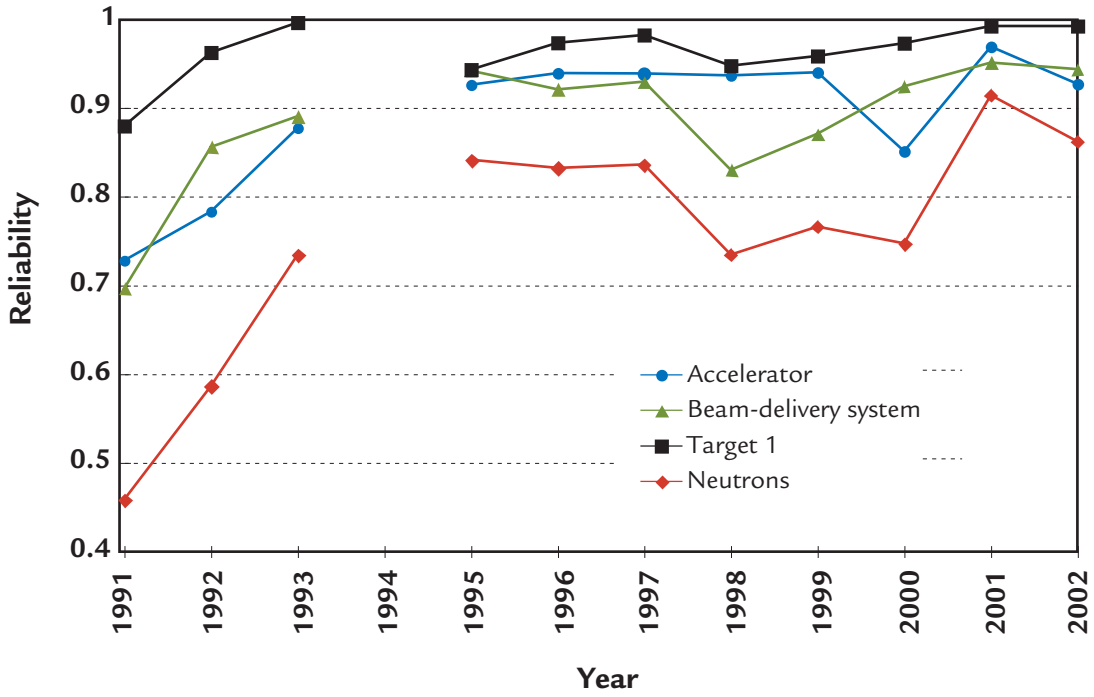

Fig. 5. Subsystem reliability for Lujan Center beam delivery.

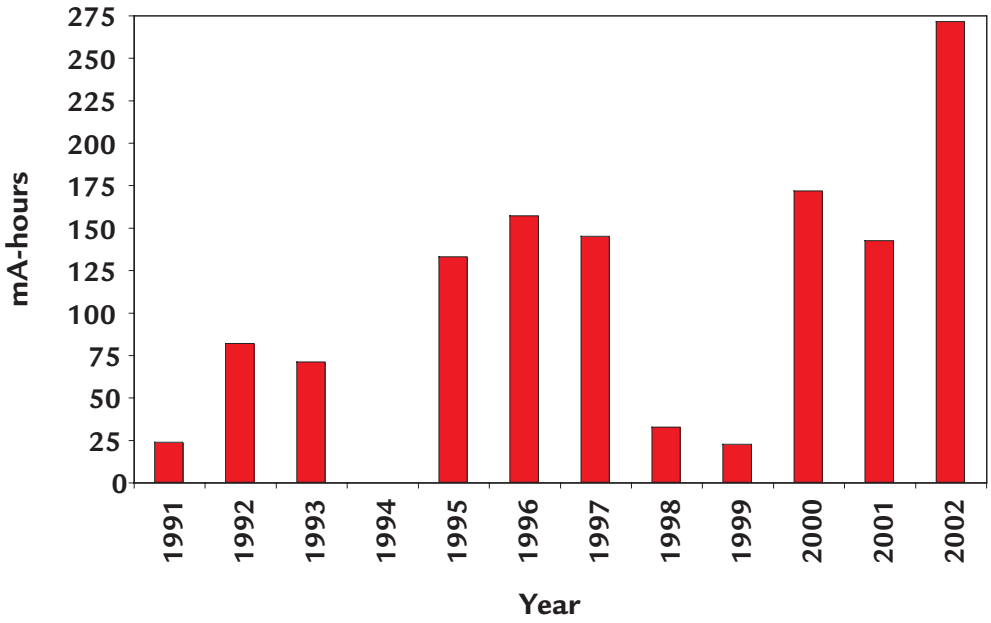

Fig. 6. Integrated beam charge delivered to the Lujan Center.

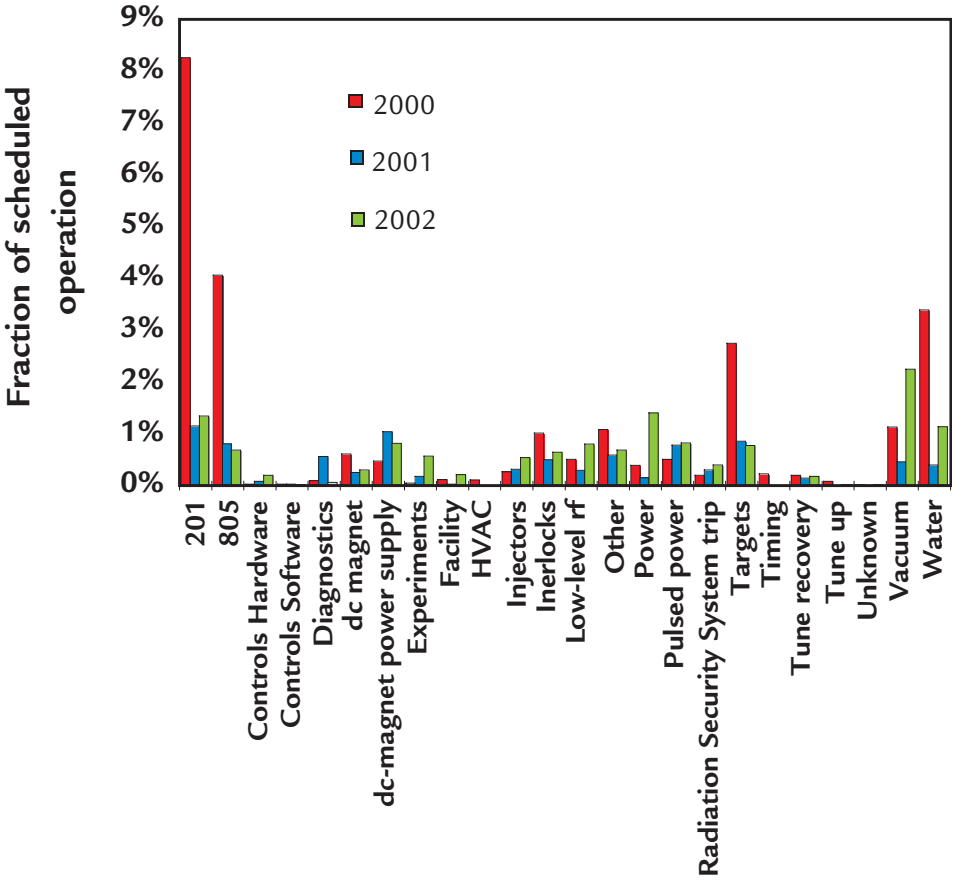

Fig. 7. Lujan Center beam downtime by system.

Table 1. LANSCE beam delivery for the 2002 run cycle.

Area	Scheduled	Delivered	Reliability
Lujan Center	2,972.4 hours	2,567.9 hours	86.4%
WNR Target 4	3,032.8 hours	2,672.2 hours	88.1%
WNR Target 2	361.3 hours	323.4 hours	89.5%
Lines X, B, and C	502.0 hours	434.0 hours	86.4%

This performance allowed the user facility to host 224 experiments at the Lujan Center and WNR, serving 782 user visits. For the pRad program, a total of 42 dynamic experiments were performed during the 2002 run cycle, bringing the total number of pRad experiments for which beam had been delivered when requested to 156.

Another important metric for LANSCE operations is the fraction of scheduled time lost for downtimes greater than eight hours. Performance in prior years led management to establish a goal of 10% for this metric in 2002. The fraction of scheduled time lost for downtimes of greater than 8 hours was ~ 3.3% for both Lujan Center and WNR Target 4. This metric remains substantially better than the goal but was somewhat worse than our performance in 2001 of 1.7% and 1.1%, respectively.

2003 Outage Planning

Planning for the 2003 outage began in October 2002. Key tasks included in the schedule are:

- perform essential user-facility maintenance,
- install the Switchyard Kicker System,
- install and test instrumentation and controls for the IPF,
- develop planned Authorization Basis Documentation,
- continue installation of the Ultra-Cold Neutron facility, and
- perform lower-priority user-facility maintenance.

Several other activities will be considered for inclusion in the outage schedule subject to resource availability during the outage. These tasks include:

- replacement of the 1L target beam-profile harp,
- refurbishment and commissioning of Injector A/Transport A for the IPF,
- installation of the mercury-shutter-switch upgrade at Lujan Center,
- flight-path construction and other upgrades at Lujan Center,
- pRad/Line C activities,
- H^--ion-source development,
- implementation of the Maintenance Implementation Plan,
- Occurrence Reporting System corrective actions, and
- installation of the Experimental Personnel Access Control System on the WNR flight paths.

As in previous years, the schedule will be managed according to a formal management plan and change-control process. One of the most important items planned during this outage is the installation of the Switchyard Kicker System. This system will remove the necessity for sole-use operation when delivering beam to Areas B and C. The Switchyard Kicker System (Fig. 8) will result in a 5-fold increase in beam time available for pRad and a 25% increase in beam time available to Lujan Center and WNR Target 4 in a given operating period.

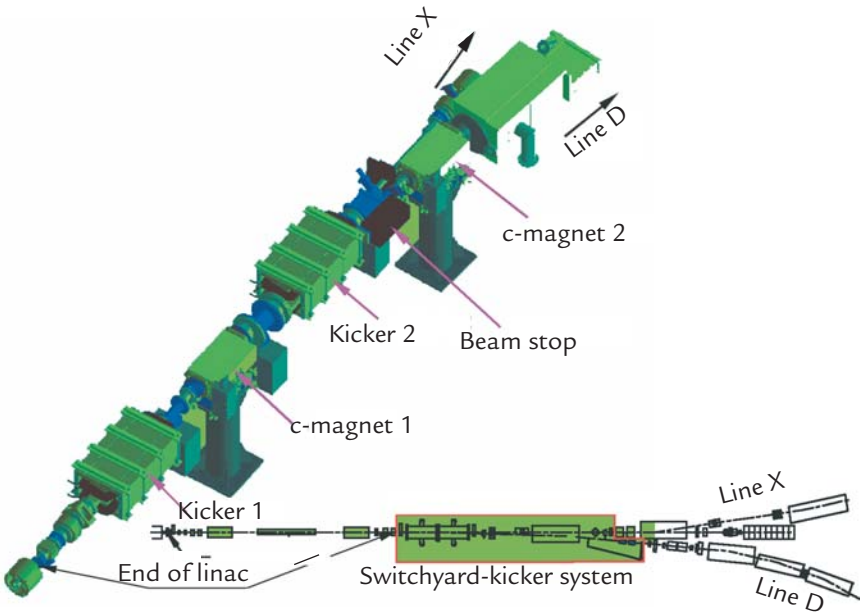

Fig. 8. Three-dimensional layout of the switchyard-kicker system.

Accelerator Operations and User Program

User Program

Supporting Student Research at LANSCE 160

Experiment Reports 161

The LANSCE User Office 161

The LANSCE User Population Continues Substantial Growth 162

Communicating With Our Users 162

A Message from the Chair 165

User Program

A.L. Archuleta (LANSCE User Program Coordinator)

The major portion of funding for LANSCE is provided by the Department of Energy (DOE) National Nuclear Security Administration (NNSA), which uses LANSCE in support of its mission to ensure the safety and reliability of the U.S. nuclear deterrent. The obvious synergy between the weapons-science uses of LANSCE and the areas of basic research, particularly in the area of condensed-matter science, has led to a cooperative agreement between the NNSA and the DOE Office of Science Basic Energy Sciences (BES) to support and use LANSCE. BES provides funding for a National User Program at the Lujan Center, which serves scientists in many disciplines who use neutron scattering in support of their research. The WNR Facility, supported primarily by the NNSA, serves the nuclear neutron science community. This allows scientists from various institutions to perform defense, basic, and industrial research at LANSCE (Fig. 1).

Experiments at the Lujan Center and WNR are selected on the basis of proposals that are peer reviewed by the appropriate subcommittee of the Program Advisory Committee (PAC). Members of the PAC (see Table 1) are selected for three-year terms and are chosen from recommendations from the LANSCE User Group (LUG) through its Executive Committee and LANSCE management. Starting with the 2002 proposal cycle, the Materials (Lujan Center) PAC subcommittees moved from an instrument- to materials-based organization. In addition, proposals were also rated based on discipline, including defense science, geosciences, engineering, biology and nanoscience, and general research. Fig. 2 shows selected proposal and user statistics at both the Lujan Center and WNR for the 2002 run cycle (July 26, 2002 – January 26, 2003).

Experiments at LANSCE that involve publishable results in the open literature or support the DOE's national-defense missions receive beam time at no cost to the user. Beam time for proprietary work can be purchased by a special user agreement under DOE's full-cost recovery rules.

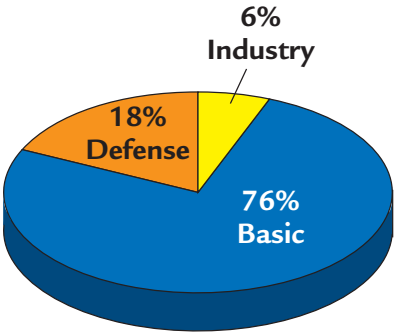

Fig. 1. Distribution of experiments run during 2002. Frequently, basic-research experiments have both defense and/or industrial applications as well.

Table. 1. 2002 LANSCE Program Advisory Committee (PAC)

Materials Program Advisory Subcommittees (MPAC)		
Hard Materials		**Soft Materials**
Kathi Alexander **(2)** Los Alamos National Laboratory	Dimitri Argyriou **(3)** Argonne National Laboratory	Shenda Baker, **Chair (3)** Harvey Mudd College
David Bish **(1)** Los Alamos National Laboratory	Gian Felcher **(3)** Argonne National Laboratory	Seth Fraden **(2)** Brandeis University
Mike Fitzsimmons **(3)** Los Alamos National Laboratory	George (Rusty) Gray **(1)** Los Alamos National Laboratory	William Hamilton **(3)** Oak Ridge National Laboratory
Wil Gauster **(2)** Sandia National Laboratories	Tom Holden **(1)** Chalk River Laboratories	Gabriel Lopez **(1)** University of New Mexico
Michael Janicke **(1)** Los Alamos National Laboratory	Thomas Koetzle **(3)** (retired) Brookhaven National Laboratory	Thomas Rieker **(3)** Corning, Inc.
Despo Louca **(3)** University of Virginia	Christian Mailhiot **(2)** Lawrence Livermore National Laboratory	Bob Stroud **(1)** University of California at San Francisco
Jonathan Phillips **(1)** Los Alamos National Laboratory	Thomas Proffen, **Chair (2)** Los Alamos National Laboratory	
James Richardson **(3)** Argonne National Laboratory	Andy Winholtz **(3)** University of Missouri	
Dynamics of Materials Subcommittee		**Structural Biology Subcommittee**
Meigan Aronson **(3)** University of Michigan	Brad Clements **(2)** Los Alamos National Laboratory	Kent Blaisie **(1)** University of Pennsylvania
Brent Fultz **(3)** California Institute of Technology	Kenneth Herwig **(3)** Argonne National Laboratory	Kenn Gardner **(1)** Dupont
Dan Neumann **(3)** National Institute of Standards and Technology	Marie-Louise Saboungi, **Chair (3)** Argonne National Laboratory	Jim Sacchettini **(1)** Texas A&M University
Frans Trouw **(2)** Los Alamos National Laboratory		Bob Stroud **(1)** University of California at San Francisco
		Mark Yeager **(1)** Scripps University
Nuclear Science Program Advisory Subcommittees (NPAC)		
Defense-Related Nuclear Science		
Grant Bazan **(1)** Lawrence Livermore National Laboratory	Steve Becker **(1)** Los Alamos National Laboratory	Jolie Cizewski **(1)** Rutgers University
John Sarracino **(2)** Los Alamos National Laboratory	Anna Hayes-Sterbenz, **Chair (3)** Los Alamos National Laboratory	Mark Stoyer **(2)** Lawrence Livermore National Laboratory
W. Scott Wilburn **(2)** Los Alamos National Laboratory		
Basic Nuclear and Particle Physics		
Ani Aprahamian **(1)** University of Notre Dame	Gerald Hale **(substitute)** Los Alamos National Laboratory	Chris Gould, **Chair (3)** North Carolina State University
Anna Hayes-Sterbenz **(3)** Los Alamos National Laboratory	Scott Wissink **(2)** Indiana University	Steve Yates **(2)** University of Kentucky
Mark Stoyer **(2)** Lawrence Livermore National Laboratory		
Nuclear Technology		
Rick Anderson **(3)** Los Alamos National Laboratory	Mark Chadwick, **Chair (3)** Los Alamos National Laboratory	Steve Yates **(substitute)** University of Kentucky
Chris Gould **(3)** North Carolina State University	Eric Pitcher **(1)** Los Alamos National Laboratory	Mark Stoyer **(2)** Lawrence Livermore National Laboratory

The numbers in parentheses indicate the number of years on the committee; members typically serve three-year terms with chair-personship rotating annually.

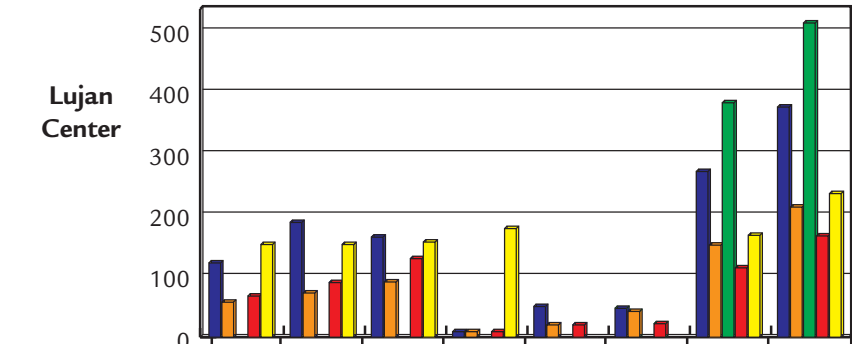

	1995	1996	1997	1998	1999	2000	2001	2002
User Visits	121	187	163	9	50	47	270	375
Unique User Visits	57	72	90	9	20	42	150	212
Research Participants	*	*	*	*	*	*	382	512
Experiments Run	67	89	128	9	20	22	113	165
Proposals Received	151	151	155	177	N/A	N/A	166	234

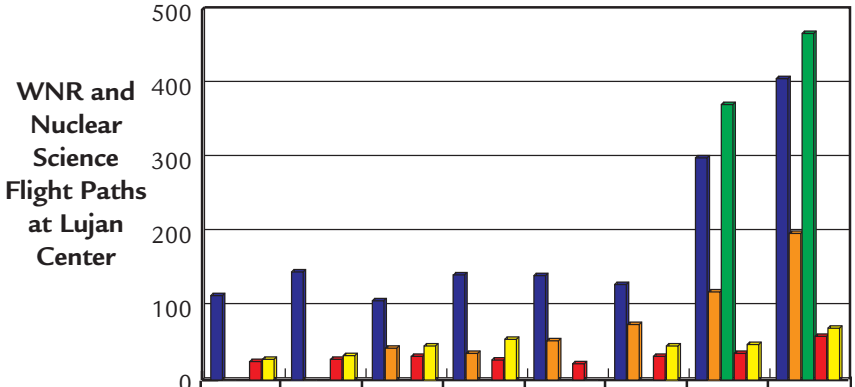

	1995	1996	1997	1998	1999	2000	2001	2002
User Visits	114	146	107	142	141	129	300	407
Unique User Visits	*	*	43	36	53	75	119	198
Research Participants	*	*	*	*	*	*	372	468
Experiments Run	25	28	32	27	22	32	36	59
Proposals Received	28	33	46	55	N/A	46	48	70

Fig. 2. Run-cycle user and proposal statistics. Users include all users on the experimental team coming to LANSCE or sending in samples to be run by a local contact. Unique user visits counts each user only once, regardless of the number of visits or experiments conducted during the run cycle. Research participants (not tracked until 2001) include all researchers included on the proposal as part of the experimental team along with those that participated in the experiment (each individual is counted only once).

Supporting Student Research at LANSCE

LANSCE takes great pride in serving as a training ground for undergraduate and graduate students in the use of neutron-scattering techniques (Fig. 3). During the 2002 run cycle, the user facility continued to see a substantial growth in the number of student users coming to participate in experimental work. Sixty-one percent of our users were under the age of 40 — 22% graduate or undergraduate students and 10% postdoctoral associates (Fig. 4).

Additionally, many students spend summer months as LANL employees working in the LANSCE user facility groups, usually at the recommendation of their thesis advisor. WNR employed approximately 10 technical students in 2002; 24 were employed at the Lujan Center. Students are paid a salary during their tenure. More

Fig. 3. Lujan Center postdocs and graduate students learn about the operation of the NPDF instrument.

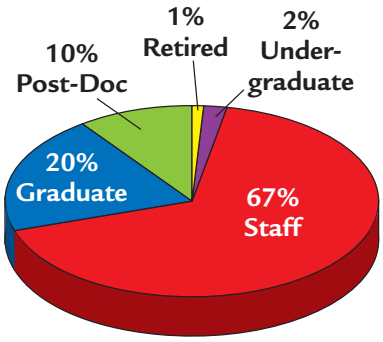

Fig. 4. Distribution of 2002 run-cycle users by position type.

information on student employment programs can be obtained from LANL's Human Resources Division web site at http://www.lanl.gov/education.

The STONE Program (Student Travel Opportunities for Neutron Experiments) is aimed at broadening the user community, increasing instrument access to students and faculty, and providing training to new student users in neutron-scattering techniques. These program goals are accomplished by providing travel funds for students to participate in research experiments during the run cycle, and training on the use of the spectrometers and assistance in experimental setup and data analysis. This level of technical support often allows professors to send students to conduct experiments without a high impact on their research budget or on their own time. STONE is funded by LANL's University of California Directed Research and Development Office and LANSCE. Over 16 experiments representing many academic institutions benefited from this program in 2002 (Table 2).

Experiment Reports

Reports describing research conducted at LANSCE are required for all experiments performed at the Lujan Center or WNR three months following collection of data. Experiment Reports received from 2002 are included on the CD in the inside back cover of this report. Past reports can be obtained by contacting the LANSCE User Office, 505-665-1010 or lansce_users@lanl.gov.

The LANSCE User Office

The LANSCE User Office has the central role for administering the user program and for user reception. Building on the record 2001 run cycle, 2002 continued to see an increase in proposals, user visits, and first-time users.

User visits (those users that come to LANSCE to conduct an experiment, or the Principal Investigator of a team sending in samples for local staff to run) grew by 142% over the 1997 run cycle! From 2001 to 2002, user visits increased overall (both Lujan Center and WNR combined) by 37%.

Staff processed just under 300 proposals, a 42% growth over 2001, and provided support for over 780 user visits (Fig. 5). Almost exactly one-half of the unique users coming to LANSCE in 2002 were first-time users.

The User Office staff (Fig. 6) continue to provide users with a wide variety of support, including travel arrangements, training schedules, and providing tourist and a multitude of other information. In addition, they are responsible for administering the proposal, review, and scheduling processes; improving processes for user access, orientation, training, and services; communicating the beam schedules and changes; supporting conferences and workshops; supporting the LUG and other committees integral to the user program; collecting statistical information; reporting user satisfaction survey results; arranging student funding support; accommodating all visitors and users; and arranging facility tours.

Table 2. Institutions served by the STONE program in 2002.
Carnegie Institute
Christian Albrechts Universitaet
Cornell University
Houghton College
Michigan State University
University of British Colombia
University of California-Berkeley
University of California-Davis
University of California-San Diego
University of Minnesota
University of Southern California
University of Virginia

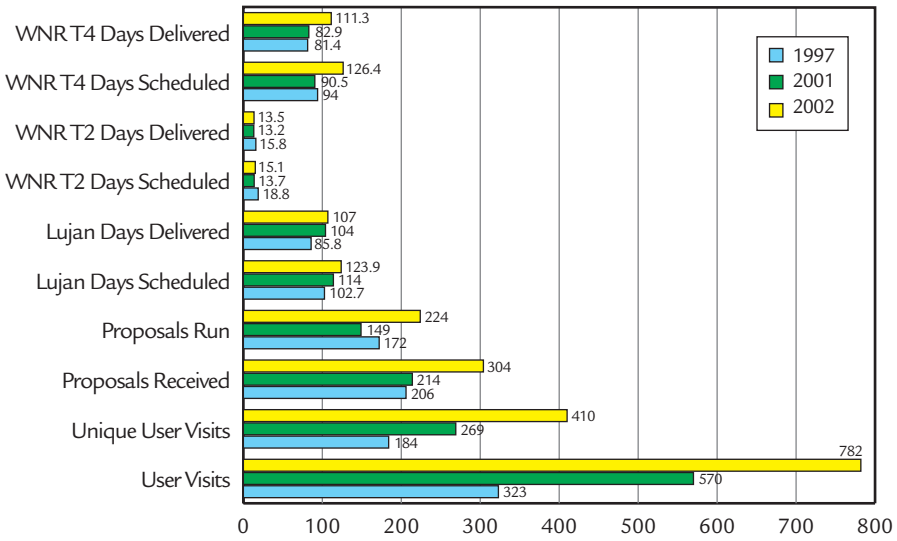

Fig. 5. Statistical comparison of the 1997, 2001, and 2002 run cycles for WNR and Lujan Center.

Fig. 6. The LANSCE User Office staff includes (from left to right) Rebecca Garcia, Undergraduate Student, Sandy Chance (formerly Booth), Database Administrator; Lynn Varoz and Evan Sanchez, Direct User Support; and Elizabeth Vigil, Reception and User Processing (part-time). Varoz is a recent addition to the staff who joins the User Office to provide some welcome assistance in accommodating the extensive growth in the user program.

In addition to continuing to provide quality user support to all 782 user visits, the staff in the User Office also underwent some personal milestones as well in 2002. On September 21, Sandy Booth, Database and Proposal Administrator, married and became Sandy Chance. Evan Sanchez, probably the name most familiar to users, made it through the run cycle (just barely) and gave birth to an almost 10 lb (4.5 kg) baby boy, Isaiah Jude, on February 18, 2003.

The LANSCE User Population Continues Substantial Growth

The 2002 run cycle saw a continued growth in the user program, not only in the number of experiments but in the number of users as well. Figs. 7 and 8 show affiliation and age distribution by unique user of those users visiting the Lujan Center and WNR during the 2002 run cycle. At Lujan Center, just under 50% were first-time users; 30% were under age 30, with 76% coming from outside LANL. The WNR Facility also saw a growth in the number of user visits and unique users with exactly one-half being first-time users and 78% coming from outside LANL. The largest growth at WNR was the industrial component (Fig. 9) who came in record numbers (comprising 40% of the 2002 unique user population) to take advantage of the new ICE House Facility for single-event-effects studies (see *Demand Grows for Single-Event-Effects Measurements at the LANSCE Irradiation of Chips and Electronics House,* p. 88).

Communicating With Our Users

The LANSCE User Satisfaction Survey (an 18-question on-line survey covering all aspects of the user program, including administrative and technical support, beam reliability, instrument and equipment, data collection

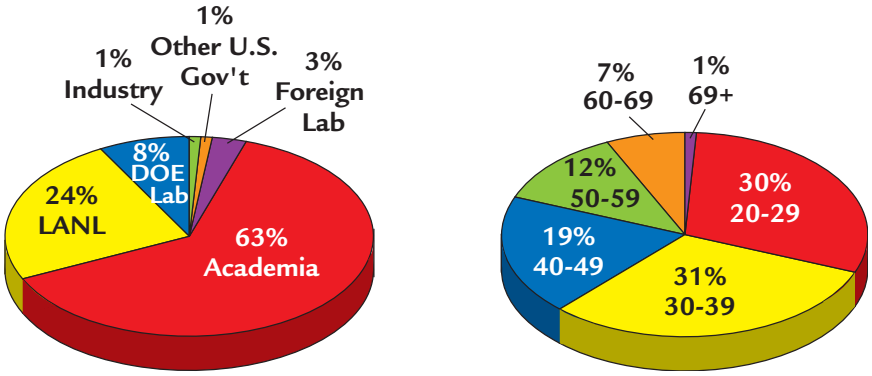

Fig. 7. 2002 Lujan Center unique user distribution by affiliation and age. A unique user means that each user is counted only once, regardless of the number of visits and/or experiments conducted during the run cycle.

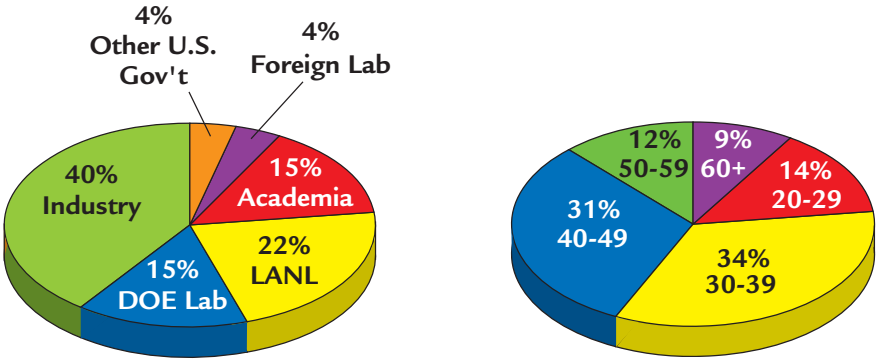

Fig. 8. 2002 WNR unique user distribution by affiliation and age. A unique user means that each user is counted only once, regardless of the number of visits and/or experiments conducted during the run cycle.

and analysis, and user amenities) is given to all users during the check-in process. Collecting information on user satisfaction is very helpful to the facility for identifying issues and trends, for giving recognition to staff, and especially for prioritizing and allocating resources for the user program. Survey results from 2002 are shown in Fig. 10. The free-form comments provide even more detailed information that can be used to improve the user program in future run cycles.

Another mechanism for providing direct user feedback to LANSCE management is the LANSCE User Group (LUG). The LUG was established in 1996 and actively provides users and potential users the opportunity to influence the way in

Fig. 9. Experimenters from CEA, Bruyéres-le-Châtel, France, at the ICE House enjoy a lunch break outside the new facility.

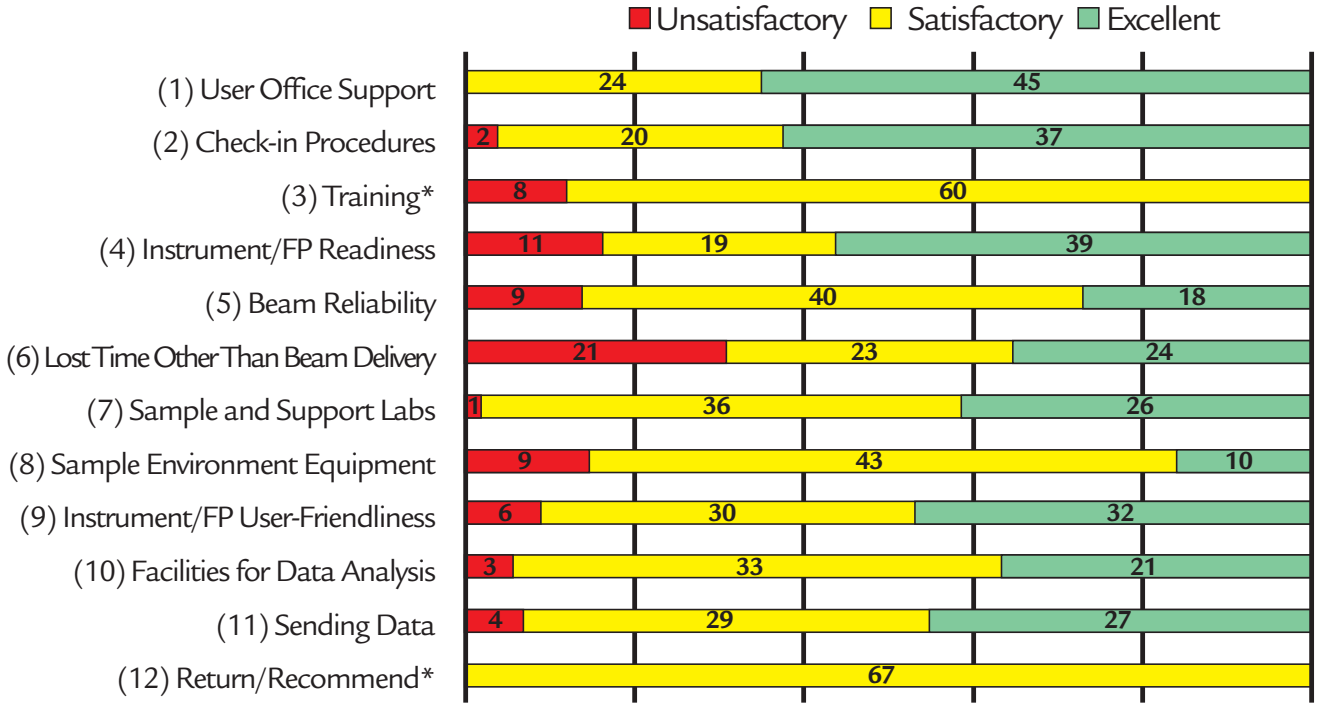

Fig. 10. User Satisfaction Survey results from the 2002 run cycle from both Lujan Center and WNR users. (Questions marked with an asterisk allow only a negative or positive response.) Free-form comments indicate overall satisfaction with the beam conditions, new instrumentation, and staff support. Area accommodations, transportation, and dining options continue to be a major point of dissatisfaction, as well as an identified need to upgrade and coordinate sample environments and ancillary equipment.

which the facility is managed and improved. Unlike other national user facilities, biennial renewal of membership is required to maintain active status to ensure that we hear primarily from active users. LUG membership stands at 447 as of December 2002 with users from across a diverse spectrum (Fig. 11).

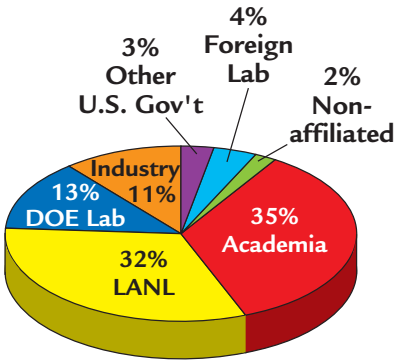

Fig. 11. LUG membership (over 440 individuals) distribution by affiliation as of December 2002. Biennial renewal of membership is required to maintain active status in the LUG to ensure feedback from active users.

The LUG is represented by an 11-member Executive Committee (ExecCom). ExecCom (Fig. 12) membership represents the principal activities at LANSCE: neutron scattering, defense-related research, industry, and nuclear physics and technology, plus one graduate student or postdoctoral fellow in any of these disciplines holding a one-year term. Starting with the 2003 election held in October 2002, a position representing the biosciences community was added to reflect this new user base. The ExecCom holds monthly conference calls and meets at LANSCE on a quarterly basis to work on a variety of issues, including communicating with LANSCE's sponsors, discussing funding and scheduling issues, and organizing the biennial user meeting. The next LANSCE User Group Meeting is scheduled for October 20-21, 2003.

Fig. 12. The LUG ExecCom is elected by the LUG each October, with members holding two-year terms. The 2002 ExecCom is shown from

Back, left to right:
- Mike Kent, Sandia National Laboratories
- Michel Gerspacher, Sid Richardson Carbon Company
- Brent Fultz, California Institute of Technology
- William Hamilton, Oak Ridge National Laboratory (Vice Chair)
- Paul Koehler, Oak Ridge National Laboratory

Front, left to right:
- Thomas Bowles, Los Alamos National Laboratory
- Christopher Morris, Los Alamos National Laboratory
- Ward Beyermann, University of California at Riverside
- Shenda Baker, Harvey Mudd College (Chair)

Not pictured:
- Shannon McDaniel, University of Washington
- Laurie Waters, Los Alamos National Laboratory

A Message from the Chair

Shenda Baker, Harvey Mudd College
2002 LANSCE User Group Executive Committee Chair

The LANSCE facility delivers neutrons and protons to a variety of users. From supporting interrogation of materials for defense programs, industrial analysis of single-event effects simulating cosmic radiation, and stockpile stewardship to examining the structure of bio-membranes (for example, in the 2002 run cycle), a broad user base takes advantage of the particular pulse structures available from the accelerator. Because of the diversity of activities on the mesa in three major programs — proton radiography, weapons and nuclear research, and neutron scattering — many users may not be aware of the other experiments occurring nearby. However, this activity report reflects the interesting breadth of science and research taking place at LANSCE.

In 2002, the LANSCE facility provided experimental opportunities for over 400 unique experimenters from academia, industry, and the national laboratories with reliability of the accelerator at its highest since 1992 (98%) and with Lujan Center running at 86.4% (the major contributors to the losses being two LANL-wide power outages). The new instruments at Lujan Center — HIPPO, a high-pressure powder texture diffractometer; SMARTS, a diffraction instrument specifically designed to address engineering applications; Asterix, a reflectometer with magnetic capabilities; and the Protein Crystallography Station — were brought into the user program for the first time. In addition, the Detector for Advanced Neutron Capture Experiments (DANCE) has been completed, and the largest number of users and proposals to the Lujan Center and WNR ever were received. The pRad team developed a magnifying technique that produces 7.8x images while all 42 planned pRad shots occurred as requested. Experiments using the pRad technique are expected to join the user program in the next run cycle as well. And progress was made on building an ultra-cold-neutron experimental area that will take beam in 2003.

As we look to the next run cycle, I would like to highlight some current activities. Work is now under way on installation of a kicker magnet that will provide transparent operation of pRad, WNR, and Lujan Center experiments. Strategic hires, including two instrument assistants and a experimental floor coordinator at Lujan Center, will help users in the upcoming year. Also note that the Sixth LANSCE User Group meeting will be held on October 20-21, 2003. In addition, two proposal review cycles will begin starting in 2003 with the goal being to run eight months per year. My hope is that the two-year trend in reliability will be a predictor of the future. Of course, this success will not come without the continued support from the sponsors to bring funding levels up to those established in last year's cost estimate.

LANSCE personnel at all levels have shown me that they are committed to scientific, engineering, and operational excellence. I am optimistic about the future of LANSCE and look forward to the increased synergy that LANSCE facilities will have for all its basic science and defense- and weapons-research users. I would like to thank the LANSCE management and staff and the other members of the LUG Executive Committee for their insightful assistance and dedication throughout the year. It has been a honor to represent the users of LANSCE.

Shenda M. Baker

News and Events

A 30-Year Milestone Anniversary for the LAMPF/LANSCE Accelerator 169

LANL Family Day Comes to LANSCE 170

LANSCE Hosts Several Student Events 171

LANSCE Continues in the Holiday Spirit 172

Some Much Needed Help for Users on the Lujan Center Experimental Floor 172

Hats Off to 172

Tour and Visits 175

News and Events

A.L. Archuleta, S.E. Harper (LANSCE Division)

- A 30-Year Milestone Anniversary for the LAMPF/LANSCE Accelerator
- LANL Family Day Comes to LANSCE
- LANSCE Hosts Several Student Events
- LANSCE Continues the Holiday Spirit
- Some Much Needed Help for Users on the Lujan Center Experimental Floor
- Hats Off to . . .
- Tours and Visits

Fig. 1. Several notable pioneers of LAMPF/LANSCE were present at the 30-year celebration, including: (left to right) Lew Agnew, Jim Bradbury, Darragh Nagle, John Browne (LANSCE Director 1993-1997), Ed Knapp, Don Hagerman, Roger Pynn (LANSCE Director 1997-2000), Paul Lisowski (LANSCE Director 2001-present), Louis Rosen (LAMPF Director 1965-1986), and Peter Barnes (LAMPF Director 1991-1993).

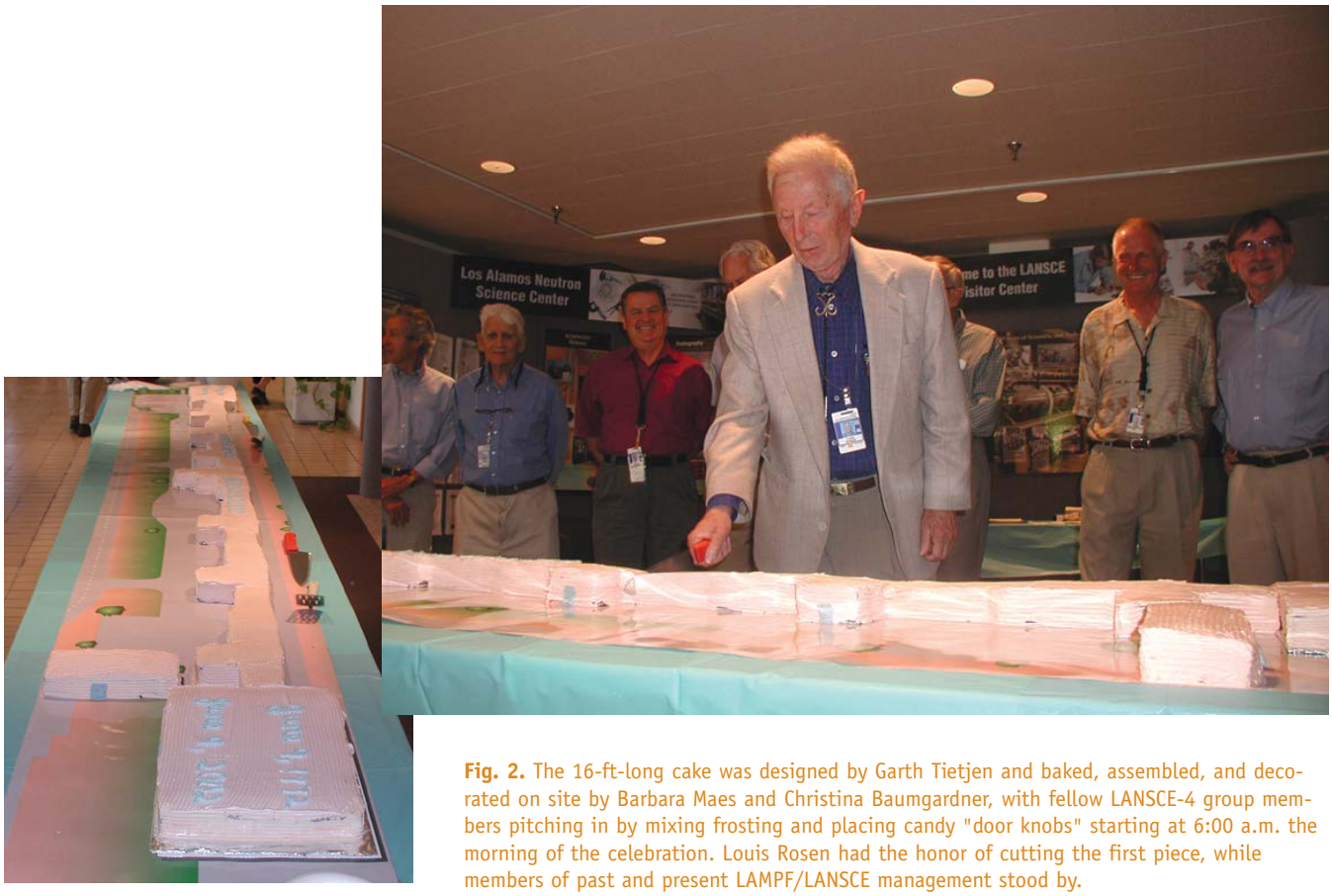

Fig. 2. The 16-ft-long cake was designed by Garth Tietjen and baked, assembled, and decorated on site by Barbara Maes and Christina Baumgardner, with fellow LANSCE-4 group members pitching in by mixing frosting and placing candy "door knobs" starting at 6:00 a.m. the morning of the celebration. Louis Rosen had the honor of cutting the first piece, while members of past and present LAMPF/LANSCE management stood by.

A 30-Year Milestone Anniversary for the LAMPF/LANSCE Accelerator

How do you celebrate the 30th anniversary of the LAMPF/LANSCE accelerator reaching its full design energy of 800,000,000 electron volts? By throwing an anniversary party, complete with a 16-ft-long cake that is a scaled replica of the original accelerator buildings, of course! On June 20, 2002, LANSCE celebrated this technological milestone, which occurred on June 9, 1972.

It was an impressive event, complete with dignitaries in attendance (Fig. 1) at LANSCE's Louis Rosen Auditorium. Kevin Jones, LANSCE Deputy Director, opened with a talk on safety, noting that the 1987 LAMPF Safety Manual was so thorough it could apply to LANSCE activities today. John Browne, LANL Director from 1993-1997, followed with his own reminiscences of the days when he worked on the mesa and what remarkable achievements have been made at LANSCE. Next on the agenda was Ray Juzaitis, LANL Associate Director for Weapons Physics, who stressed how important LANSCE is to the Weapons Physics directorate and how it is a portal to the international scientific community. Paul Lisowski, LANSCE Division Director, then spoke of past and present accomplishments of LANSCE and about future plans for the facility.

Last, but certainly not least, came the keynote speaker of the day: Dr. Louis Rosen, director of LAMPF (LANSCE's predecessor) from construction until 1986. His speech invoked laughter and applause from the standing-room-only audience on numerous occasions. At the end of Dr. Rosen's talk, people in the audience showed their deep respect and appreciation for the man who was so integral to the realization and success of this facility by giving him a standing ovation that lasted several minutes.

After the presentations, Kevin Jones presented a historical slide show of people and events of the LAMPF/LANSCE era with many rare photos found in old drawers and filing cabinets. The slide show is available at http://lansce.lanl.gov/news/30annivs.htm. Outside the auditorium, there was a display of past and present publications and photos that portray the important history and achievements of the accelerator facility.

LANL Family Day Comes to LANSCE

LANSCE has always been a popular tourist spot, and LANL's Family Day, held on Saturday, April 13, 2002, was no exception. This event provided a rare opportunity for LANSCE to open up the infamous gate to families of LANSCE and LANL employees interested in touring the half-mile-long accelerator (Fig. 3) and various experimental areas. Interestingly enough, the majority of visiting families were not TA-53 residents – 80% were from families of employees from divisions outside the facility.

Fig. 3. Visiting family members and fellow LANL employees were impressed by the size of the linear accelerator, which most had previously only viewed as a long line of buildings from the distant Jemez Road.

Guided tours of the accelerator's injection room, the Central Control Room, and the Lujan Center were held throughout the day. About 170 people took advantage of the opportunity to participate in these guided tours while about 200 others received private tours by their resident family member. All the originally scheduled tours were completely booked by 10:00 a.m., and additional tour openings and transportation were arranged at the last minute so as not to necessitate turning people away.

Guided tours started with a stop at the building housing the 750,000-V, three-story-high injector power supply. Next stop was the Central Control Room, the heart of LANSCE operations, which is staffed 24 hours a day, 7 days a week, during the run cycle. Operators responsible for the successful operation of the LANSCE beam delivery systems were on hand to show the myriad of computer screens detailing the status of all major operations systems for beam delivery. A few anecdotes of interesting events occurring at late hours were also entertaining.

At the Lujan Center, visitors were able to walk through the main Experimental Floor, called ER-2, where the majority of the neutron spectrometers are located. The tour groups were also allowed inside the cave of the SMARTS spectrometer (Fig. 4). This instrument allows components of dimensions up to or greater than 1 m and masses up to 1,500 kg to be mounted in the beam, thus each tour group of approximately 35 people fit in the cave quite easily.

Fig. 4. Darrick Williams, Lujan Center graduate student, briefs guests on the uses of the SMARTS instrument before they are led into the cave to view an experimental setup (inset).

Among the most popular giveaways for the approximately 260 adults and 150 children at LANSCE that day was a coloring book (Fig. 5) detailing each of the major experimental areas and information on the accelerator with text aimed at ages 6-10. This book was conceived by Audrey Archuleta (LANSCE-4); written by Sue Harper (LANSCE-4/IM-1); edited by Joyce Roberts (LANSCE-DO) and Audrey Archuleta; and illustrated by Garth Tietjen (IM-1, formerly of LANSCE-4). The coloring book has proved to be extremely popular with children and adults alike. We received many requests from adults, not only to send to other children outside the Los Alamos area but also to send to physics professors at academic institutions. We are not too sure why we had so many of those requests, but perhaps the future physics curriculum will include Neutron Man!

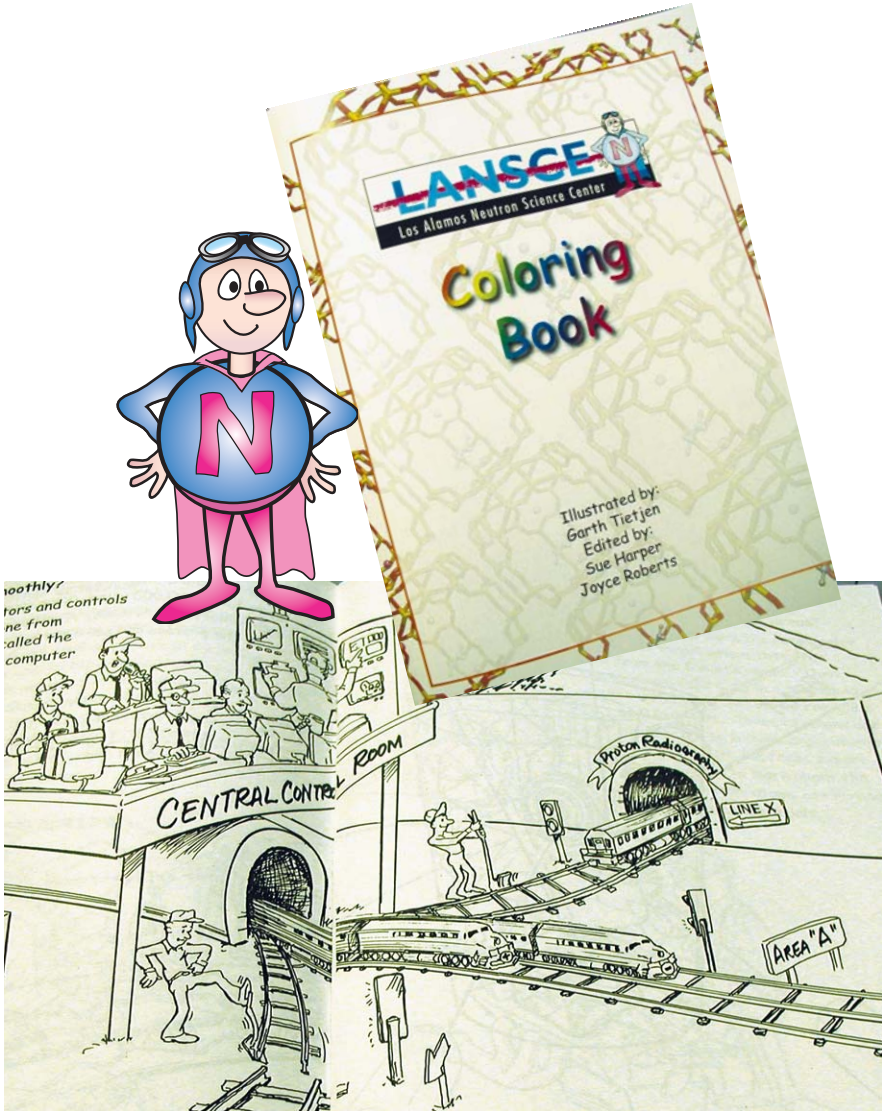

Fig. 5. The LANSCE Coloring Book, featuring Neutron Man, might go down in history as one of LANSCE's most popular "publications."

LANSCE Hosts Several Student Events

Throughout the summer of 2002, LANSCE organized several events for its undergraduate and graduate employees (and those from other LANL divisions) to provide mechanisms for students to broaden their view of LANSCE activities, to meet managers and fellow students they do not work with on a daily basis, and to provide an excuse for some cool summer treats. LANSCE Division employs about 85 students during the summer, with approximately 60 working year-round.

New and returning students attended student orientation on June 10. Students were informed about where to go if they needed help on any issue and about the rules and regulations of using government property, including telephones, computers, and vehicles. But the stress was on safety and the importance of getting the training and information they need to perform their jobs safely. The session ended with an encouragement from Deputy Division Director, Kevin Jones, to ask questions, to work safely, and most of all, to enjoy their jobs.

On July 25, a Laboratory-wide student breakfast was held to educate other LANL students about work performed at LANSCE. Paul Lisowski, Division Director, provided an overview and answered a number of questions from students. Group Leaders Alan Hurd (Lujan Center), Andy Jason (Accelerator Physics and Engineering), Mike Lynch (Radio-Frequency Accelerator Technology), Hamid Shoaee (Accelerator Controls and Automation), and Steve Wender (WNR) presented information about the work performed in those groups and available career opportunities. Following the presentations, students toured the accelerator complex and experimental areas.

As the summer season wound to a close, LANSCE Division honored students and their mentors by hosting an ice cream social on August 8. In spite of a rainy start, the skies cleared and students played volleyball (Fig. 6) and enjoyed testing their skill at throwing water balloons at staff (but mostly at each other, the chickens!).

Fig. 6. Once the rain cleared, students took to the Building 1 lawn for some impromptu volleyball games.

LANSCE Continues in the Holiday Spirit

Thanks to the generosity of LANSCE employees, over 105 children from the Española and Santa Fe communities received a brand-new toy, outfit, and shoes for the 2002 holiday season (Fig. 7). Each year for the past five years, Ginger Grant, LANSCE Division Executive Administrator, has organized this special holiday drive. By contacting different agencies throughout the northern New Mexico area, she manages to spread LANSCE's generosity to the various communities surrounding the Laboratory. The agencies provide a list of children along with clothing and shoe sizes and a short wish list. Grant then calls upon the resident employees of TA-53 (LANSCE and other resident groups) who continue to respond overwhelmingly by selecting a child or children and providing all the items on his or her wish list. During this two-week period, the Division Office is transformed into a delightful, magical place in which presents are gathered and wrapped, and there always seems to be smiles on everyone's faces as the pile of gifts grows.

Fig. 7. The holiday spirit at LANSCE in 2002 was as high as this mountain of toys — and this photo doesn't even begin to show all the packages lined up and down the corridors of the LANSCE Division Office suite!

Some Much Needed Help for Users on the Lujan Center Experimental Floor

Lujan Center users were greeted by a new face when they came to conduct experiments in 2002. Responding to numerous comments from past User Satisfaction Surveys, the User Office and the Lujan Center created the position of Lujan Center Floor Coordinator just in time for the 2002 run cycle. **Leilani Conradson** (Fig. 8) joined the Lujan Center in May 2002 to provide much needed technical and administrative support for users. She is responsible for a myriad of tasks — all aimed at enabling users to perform their experiments as efficiently as possible. Although the first run cycle was consumed by learning exactly what it is users need, she is already hard at work with the User Office and technical staff implementing several improvements to make upcoming run cycles even smoother for Lujan Center users.

Fig. 8. Leilani Conradson, Lujan Center Floor Coordinator.

Hats Off to . . .

Although we all know the LANSCE staff and our users are some of the best in their fields, it is also nice to know that they are recognized by their peers and by prestigious organizations for their many accomplishments. Following are some of those receiving formal recognition for their efforts and contributions in various ways in 2002.

Rajan Vaidyanathan (Fig. 9), assistant professor in the Advanced Materials Processing and Analysis Center and the Department of Mechanical, Materials, and Aerospace Engineering at the University of Central Florida, received a **Faculty Early Career Development (CAREER) Award from the National Science Foundation**. The award will provide funding for his project *Neutron, Synchrotron X-ray Diffraction, and Instrumented Indentation Studies of Deformation in Shape-Memory Alloys* from February 1, 2003, through January 31, 2008. A significant portion of this research will be conducted at LANSCE on the *Spectrometer for Materials Research at Temperature and Stress (SMARTS)* with Mark Bourke, SMARTS Instrument Scientist. Previously, Vaidyanathan and Bourke used the LANSCE Neutron Powder Diffractometer for measurements on shape-memory alloys (for which Vaidyanathan received the 17th Louis Rosen Prize from the LANSCE User Group for best doctoral thesis while at the Massachusetts Institute of Technology).

The CAREER Program offers the National Science Foundation's most prestigious award for new faculty members by recognizing and supporting the early career-development activities of those teacher-scholars who are most likely to become the academic leaders of the 21st century. CAREER awardees are selected on the basis of creative career-development plans that effectively integrate research and education within the context of the mission of their organization.

Carol F. Kirchhoff, a graduate student at the University of Illinois at Chicago's College of Pharmacy, received the **Pharmaceutical Research and Manufacturers of America (PhRMA) Foundation Pre-doctoral Fellowship Award for 2002-2003**. Kirchhoff is a user of the Low-Q Diffractometer at Lujan Center. She received this award for the project titled *Physical Stabilization of Model Proteins Through Interaction with PEGylated Phospholipids*.

Fig. 9. Rajan Vaidyanathan.

Preliminary data suggest that this project will provide a useful formulation approach enabling safe and effective delivery for protein drugs. The overall hypothesis being tested is that PEGylated phospholipids stabilize therapeutic proteins and increase their shelf life without reducing the bioactivity of the drug. Kirchhoff is currently working on her dissertation, which is based in part on the research conducted at LANSCE.

PhRMA was established in 1965 to promote public health through scientific and medical research and provides funding for research and education and training of scientists and physicians who have selected pharmacology, pharmaceutics, toxicology, informatics, or health outcomes as a career choice.

The **LANSCE Director's Award for Scientific Excellence**, established by former Director Roger Pynn in 1999, recognizes the scientific excellence and leadership of a LANSCE staff scientist through his/her own research program or in collaboration with users. The recipient of the third LANSCE Director's Award is **Stephen M. Sterbenz**. Sterbenz, formally the Senior Advisor for the LANSCE Stockpile Stewardship Program, is now a staff member in the Primary Design and Assessment group of the Applied Physics Division at LANL. The award, which includes a $2,000 prize, was presented (Fig. 10) during the Second LANSCE Workshop on Defense, Basic, and Applied Science on January 13, 2003. Following tradition, Sterbenz presented a technical overview of his research interests and the programs he supported titled, *Stockpile Stewardship at LANSCE: Yesterday, Today, and Tomorrow.* Sterbenz was nominated by Michael Kreisler, Lawrence Livermore National Laboratory (LLNL), with support from Bharat Agrawal, National Nuclear Security Administration (NNSA), and John Becker, LLNL. Some quotes from the nomination package include:

"Steve Sterbenz did a truly remarkable job in being an advocate for the science and technology efforts at LANSCE."

Fig. 10. LANSCE Director Paul Lisowski presents Stephen Sterbenz the Third LANSCE Director's Award for Scientific Excellence.

"Dr. Sterbenz served with distinction in a field that was highly technical, broad in its disciplines, and extremely challenging."

"Steve Sterbenz is one of the unsung heroes of the ^{239}Pu(n,2n) cross-section measurement."

Sterbenz joined LANSCE in 1994 at the initiation of the efforts in stockpile stewardship and worked for seven years to nurture technical initiatives and research teams. He served as the link between the weapons community and LANSCE. His accomplishments cover a broad range of experiments in hydrodynamics — proton radiography and neutron resonance spectroscopy, materials science, and nuclear science.

The LANSCE User Group (LUG) Executive Committee and a member of the LANSCE staff reviewed all nominations and made their recommendation to the LANSCE Director, Paul Lisowski, who made the final decision. Beginning in 2003, the focus and intent of the award will change from a user focus to a broader community and will be administered out of LANSCE Division rather than the LUG.

The annual **Defense Program Awards of Excellence** recognize significant achievements in quality, productivity, cost savings, safety, or creativity in support of the NNSA's defense programs. Everet Beckner, deputy administrator for NNSA Defense Programs, traveled to Los Alamos to present the 2001 awards, which included several LANSCE teams or other LANL staff using LANSCE facilities in their research program. These include: *Aging of HE Binders Using Small Angle Neutron Scattering at LANSCE* (team led by **Rex Hjelm**, Lujan Center); *Beryllium Stress Measurements* (research conducted in part at LANSCE/Lujan Center; team led by Donald Brown, MST-8); *LANSCE Accelerator Operations* (team led by **Kevin Jones**, LANSCE-DO); and *Neutron Resonance Spectroscopy* (research conducted at LANSCE/WNR Blue Room; team led by Vincent Yuan, P-23).

Once again, several members of LANSCE Division were recipients of a **2001 LANL Distinguished Performance Award**. These awards are highly competitive and are the highest award a LANL employee can receive in any discipline/profession. The awards are designed to recognize individuals and teams that have made outstanding and unique contributions that have a positive impact on LANL's programmatic, scientific, operational, or administrative activities.

***Michael Fitzsimmons**, Lujan Center.* Michael Fitzsimmons single-handedly designed and built the polarized neutron reflectometer/diffractometer Asterix at the Lujan Center (Fig. 11). Asterix incorporates novel neutron optical concepts to polarize a large, pulsed neutron beam, something the neutron-scattering community had considered difficult to accomplish. Fitzsimmons built Asterix from the ground up, using surplus equipment from LANL and other facilities. He developed partnerships abroad to help develop and test components. Because he had to base his instrument on whatever equipment he could find, Fitzsimmons performed much of the work with minimal assistance. For more information on the Asterix spectrometer, see *Scientists Perform First Neutron-Scattering Experiment Using the 11-T Superconducting Magnet at the Lujan Neutron Scattering Center,* p. 116.

Fig. 11. Mike Fitzsimmons examines data recently obtained on Asterix.

The Lujan Center Mechanical Team (**Melvin Borrego, Jonathan Ferris, Michael Geelan, Tim Medina, Ross Sanchez,** and **Thomas Sisneros**) (Fig. 12) is responsible for the Lujan Center's operation and maintenance and has helped make it a Laboratory

Fig. 12. The Lujan Center Mechanical Team includes (left to right) Tim Medina, Michael Geelan, Melvin Borrego, Ross Sanchez, Jonathan Ferris, and Thomas Sisneros.

flagship facility. During a two-year shutdown, the team participated actively in months-long cleanup and afterward worked heroically to restart the Lujan Center. The team provided an extraordinary level of support during the construction and commissioning of several new spectrometers while continuing to handle operation and maintenance of existing instruments — all with extremely limited resources. Applying a combination of talent, hard work, dedication, and professional workmanship, the team raised the Lujan Center's level of operation to the most exacting professional standards. The team always deals successfully with a broad range of safety issues, demands for technical expertise, and customer requests. In support of their nomination for the award, a satisfied user wrote,

"The outstanding quality of the services offered goes well beyond anything I have ever seen at other facilities, both in England and in the United States."

Members of the Biosciences Division were also recognized for the design, installation, and commissioning of the new Protein Crystallography Station (PCS) constructed at the Lujan Center. The only facility of its kind, PCS enables the use of neutron diffraction for studying the three-dimensional structure of proteins. The members of the PCS team, **Gayle C. Greene, Paul A. Langan,** and **Benno P. Scheonborn**, were lauded for bringing distinction to the Laboratory by establishing a major new capability for cutting-edge research. Recent research conducted on PCS is described in *Electrical Anomalies in α-Glycine*, p. 32.

Former NNSA Administrator, John Gordon, commissioned a coin to recognize employees at NNSA sites for exceptional service, hard work, and dedication to the organization. About 200 coins were distributed among the NNSA work force of approximately 42,000 federal,

Fig. 13. Danny Olivas, NNSA coin recipient.

military, and contractor employees. **Danny Olivas,** LANSCE-7, received a coin (Fig. 13) in recognition for his superior technical support to the pRad program.

Tours and Visits

Dr. Everet H. Beckner, who at the time was just recently sworn in as the Deputy Administrator for Defense Programs for the NNSA, visited the Lujan Center on March 28, 2002, as part of a day-long visit to LANL. He was accompanied by (former) Laboratory Director John C. Browne on a tour of LANSCE. Dr. Beckner was first briefed by Kevin Jones, LANSCE Deputy Division Director, who gave an overview of the facility and its capabilities (Fig. 14). Next Jeff Paisner, Project Director for the Advanced Hydrotest Facility Project, discussed LANSCE's important role in the viability of that program. Finally, Alan Hurd, Lujan Center Director, along with instrument scientists Greg Smith and John Ullmann, discussed neutron-scattering instrumentation and the research being conducted at the Lujan Center. Dr. Beckner, who was visiting LANL for the first time since his new appointment, directs the programs responsible for maintaining the safety, security, and reliability of the nation's nuclear weapons stockpile.

Fig. 14. Kevin Jones (left) briefs Dr. Beckner (middle) on the accelerator complex and beam-delivery systems as John C. Browne (right) looks on.

On October 16-18, 2002, LANSCE hosted a review of the Lujan Center by a special committee (Fig. 15) convened by the DOE Office of Basic Energy Sciences. The purpose of the review was to follow up on progress expected from the Basic Energy Sciences Advisory Committee review

Fig. 15. Committee members participating in the October 2002 review of the Lujan Center included (from left to right) Roger Eccleston (ISIS, Rutherford Appleton Laboratory), Ian Anderson (Spallation Neutron Source), Jim Rhyne (University of Missouri), Hajo Heyck (Paul Scherrer Institute), Brent Fultz (California Institute of Technology), Christian Vettier (Institut Laue-Langevin), and Pedro Montano and Helen Kirsch (DOE/BES). Not shown is John Tranquada (Brookhaven National Laboratory).

held two years prior. During the 2.5-day review, this special committee reviewed all aspects of operations, instrumentation, research, and the user program for the Lujan Center. They also held special feedback sessions with a small group of external LANSCE users and with Lujan Center scientific, technical, and administrative staff. The final report on the review was received in February 2003. Overall, the review indicated that considerable progress had been made from the previous two years in getting institution support for LANSCE, increasing the instrument suite, growing the user program, and improving beam reliability.

Fig. 16. Matthew Murray conducted a tour for the Chimayo Youth Conservation Group on August 13, 2002.

Currently, LANSCE is the only LANL technical area that offers public tours (Figs. 16 and 17). The size, complexity, and scientific diversity of this facility make it a very popular tour itinerary for visiting dignitaries, public-interest groups, and, most frequently, school groups. Students and faculty alike appreciate the information imparted by our "volunteer" tour guides, who must adjust their tour format frequently depending upon the tour audience. A recent letter of appreciation from a Casper College (Wyoming) physics and engineering professor stated:

"[tour guide] did an awesome job. I have worked on accelerators before and I learned a lot from him but what really impressed me was that the two elementary education students who were on the tour remarked on how well he talked to them at their level . . . This was a great experience for all of us and the students really got a feel for the kinds of activities that are out there for them."

Following are some photos of just a couple of the over 50 public tours conducted during 2002. Tours are arranged by the LANSCE User Office, lansce_users@lanl.gov, or 505-665-1010.

Fig. 17. Jim Amann (in the striped shirt) explains the workings of the proton accelerator.

Publications

Materials Science, Instrumentation, and Spallation Science and Technology 178

Neutron Nuclear Science 183

Accelerator Science and Technology 186

Theses 189

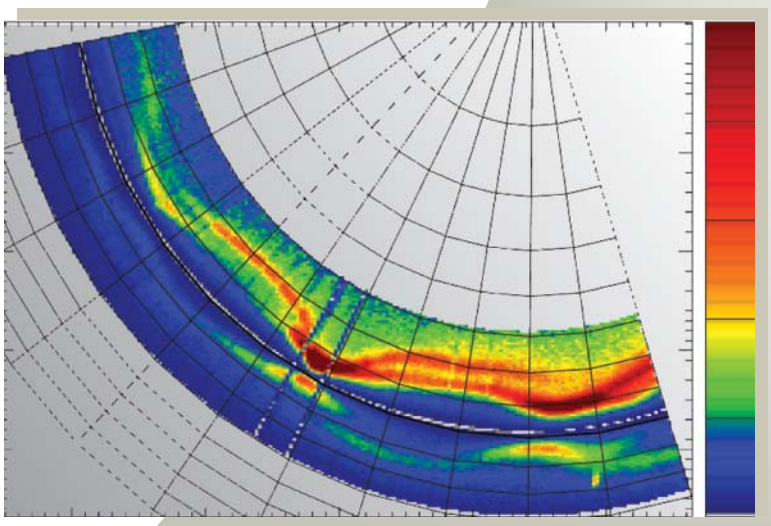

Publications

The following publications (196 papers plus 7 theses) relate to all work carried out at LANSCE and reported since the 2000-2001 LANSCE Activity Report (LA-13943-PR) was published. Work performed elsewhere by LANSCE staff is included where relevant. **This list does not include publications submitted or in press as of December 2002.**

Publications are an important "product" of LANSCE and a valuable metric to our sponsors and review boards. All facility users are requested to send complete references of all publications resulting from experimental work conducted utilizing LANSCE resources, in whole or in part, to the User Office.

Authors should bear in mind that LANSCE is funded by the U.S. Department of Energy, and an appropriate acknowledgement is required. A recommended acknowledgement citation is the following:

> *This work has benefited from the use of the Los Alamos Neutron Science Center at Los Alamos National Laboratory. This facility is funded by the U.S. Department of Energy under Contract W-7405-ENG-36.*

Materials Science, Instrumentation, and Spallation Science and Technology

AGNEW, S. R., BROWN, D. W., VOGEL, S., and HOLDEN, T. M., *"In situ* Measurement of Internal Strain Evolution During Deformation Dominated by Mechanical Twinning," *Materials Science Forum* **404-407**, 747-754 (2002).

AGNEW, S. R., TOME, C. N., BROWN, D. W., HOLDEN, T. M., and VOGEL, S. C., "Study of Slip Mechanisms in a Magnesium Alloy by Neutron Diffraction and Modeling," *Scripta Materialia* **48** (8), 1003-1008 (2003).

ALSMADI, A.M., CHANG, S., JUNG, M. H., LACERDA, A. H., BRUCK, E., PROKES, K., SECHOVSKY, V., KAMARAD, J., MIHALIK, M., and NAKOTTE, H., "Resistance and Magnetoresistance of UIrGe Under High Pressure," in *Proceedings of the NATO Advanced Research Workshop* (Kluwer Academic, 2001) 463-472.

ASAY, B. W., PETERSON, P., and MANG, J. T., "Propogation Studies of Metastable Intermolecular Composites," in *Proceedings of the 29th International Pyrotechnics Seminar*, (United Kingdom, 2002).

BARTHES, M., VIK, A. F., SPIRE, A., BORDALLO, H. N., and ECKERT, J., "Breathers or Structural Instability in Solid L-Alanine: A New IR and Inelastic Neutron Scattering Vibrational Spectroscopic Study," *Journal of Physical Chemistry A* **106** (21), 5230-5241 (2002).

BENNETT, K. A., "Uncool Callisto," *Nature* **412,** 395-396 (2001).

BOURKE, M. A. M., DUNAND, D. C., and USTUNDAG, E., "SMARTS — A Spectrometer for Strain Measurement in Engineering Materials," *Applied Physics A* **74** (2), S1707-S1709 (2002).

CHEN, J., ROMANZETTI, S., SOMMER, W. F., and UMAIER, H., "Helium Bubble Formation in 800-MeV Proton-Irradiated 304L Stainless Steel and Alloy 718 During Post-Irradiation Annealing," *Journal of Nuclear Materials* **304** (1), 1-7 (2002).

CHINTA, S., CHOUDHARY, T., DAEMEN, L. L., ECKERT, J., and GOODMAN, D. W., "Characterization of C_2 (C_xH_y) Intermediates from Adsorption and Decomposition of Methane on Supported Metal Catalysts by *In Situ* Inelastic Neutron Scattering Vibrational Spectroscopy," *Angewandte Chemie* **41** (1), 144-146 (2002).

CHOO, H., RANGASWAMY, P., BOURKE, M. A. M., and LARSEN, J. M., "Thermal Expansion Anisotrophy in Ti-6Al-4V/SiC Composite," *Materials Science and Engineering A* **325** (1-2), 236-241 (2002).

CHRISTIANSON, A. D., LACERDA, A. H., HUNDLEY, M. F., and SARRAO, J. L., "High-Field Magnetotransport Heavy Electron in $Ce_{1-x}La_xRhIn_5$ Alloys," *Physica B* **312**, 241-243 (2002).

CHRISTIANSON, A. D., LACERDA, A. H., HUNDLEY, M. F., PAGLIUSO, P. G., and SARRAO, J. L., "Magnetotransport of $CeRhIn_5$, *Physical Review B* **66** (5), 054410-054410 (2002).

CHRISTIANSON, A. D., LACERDA, A. H., PAGLIUSO, P. G., MORENO, N. O., HUNDLEY, M. F., and SARRAO, J. L., "High-Field Magnetotransport in $CeRh_{1-x}Ir_xIn_5$ Heavy Electron Alloys," *International Journal of Modern Physics B* **16** (20-22), 3045-3048 (2002).

CHUNG, J., EGAMI, T., MCQUEENEY, R. J., YETHIRAJ, M., ARAI, M., YOKOO, T., MOOK, H. A., ENDOH, Y., TAJIMA, S., FROST, C. D., et al., "Phonon Dispersion Measurements of $YBa_2Cu_3O_{6.15}$ and $YBa_2Cu_3O_{6.95}$ by Time-of-Flight Neutron Spectroscopy," *Journal of Superconductivity* **15** (5), 327-330 (2002).

CHUNG, J., EGAMI, T., MCQUEENEY, R. J., YETHIRAJ, M., ARAI, M., YOKOO, T., PETROV, Y. V., MOOK, H. A., ENDOH, Y., TAJIMA, S., et al., "In-plane Anisotropy and Temperature Dependence of Oxygen Phonon Modes in $YBa_2Cu_3O_{6.95}$," *Physical Review B* **6701** (1), 4517 (2003).

CLAUSEN, B., LEE, S., USTUNDAG, E., BROWN, D. W., and BOURKE, M. A. M., "Deformation of *In Situ*-Reinforced Bulk Metallic Glass Matrix Composites," in *Proceedings of the 6th European Conference on Residual Stress* **404**, 553-558 (2002).

CLAUSEN, B., USTUNDAG, E., and BOURKE, M. A. M., "Investigation of the Reduction of $NiAl_2O_4$, *Advances in X-Ray Analysis* **44**, 32-37 (2001).

DAYMOND, M. R., TOME, C. N., and BOURKE, M. A. M., "Intergranular Strains in Textured Steel," *Materials Science Forum* **347-349**, 54-59 (2000).

DAYMOND, M. R., TOME, C. N., and BOURKE, M. A. M., "Measured and Predicted Intergranular Strains in Textured Austenitic Steel," *Acta Materialia* **48** (2), 553-564 (2000).

DRAGOI, D., USTUNDAG, E., CLAUSEN, B., and BOURKE, M. A. M., "Residual Stresses in Tungsten/Bulk Metallic Glass Composites," *Advances in X-Ray Analysis* **44**, 168-173 (2001).

ECKERT, J., DRAZNIEKS, C. M., and CHEETHAM, A. K., "Direct Observation of Host-Guest Hydrogen Bonding in the Zeolite NaY/Chloroform System by Neutron Scattering," *Journal of the American Chemical Society* **124** (2), 170-171 (2002).

ECKERT, J., WEBSTER, C. E., HALL, M., ALBINATI, A., and VENANZI, L. M., "The Vibrational Spectrum of TP(3,5-Me)RhH(2)(H-2): A Computational and Inelastic Neutron-Scattering Study," *Inorganica Chimica Acta* **330**, 240-249 (2002).

EGAMI, T., CHUNG, J., MCQUEENEY, R. J., YETHIRAJ, M., MOOK, H. A., FROST, C. D., PETROV, Y. V., DOGAN, F., INAMURA, Y., ARAI, M., TAJIMA, S., and ENDOH, Y., "Electron-Phonon Interactions in HTSC Cuprates," *Physica B* **316**, 62-68 (2002).

EGAMI, T., MCQUEENEY, R. J., CHUNG, J., YETHIRAJ, M., MOOK, H. A., ARAI, M., INAMURA, Y., ENDOH, Y., TAJIMA, S., FROST, C. D., et al., "Lattice and Charge Effects in High-Temperature Superconductors," *Applied Physics A* **74** (2), S1635-S1637 (2002).

FITZSIMMONS, M. R., FRITZSCHE, H., MAJOR, J., PYNN, R., and REKVELD, M. T., "Enhancing the Resolution and Intensity of Neutron-Scattering Experiments Using Neutron Spin Echo, Advances in Neutron-Scattering Instrumentation," in *Proceedings of Advances in Neutron-Scattering Instrumentation* **4785**, 143 (2002).

FITZSIMMONS, M. R., LEIGHTON, C., NOGUES, J., HOFFMANN, A. F., LIU, K., MAJKRZAK, C. F., DURA, J. A., GROVES, J. R., SPRINGER, R. W., ARENDT, P. N., LEINER, V., LAUTER, H., and SCHULLER, I., "Influence of In-plane Crystalline Quality of an Antiferromagnet on Perpendicular Exchange Coupling and Exchange Bias," *Physical Review B* **65** (13), 134436/1-8 (2002).

FORSTER, P. M., ECKERT, J., CHANG, J. S., PARK, S. E., FEREY, G., and CHEETHAM, A. K., "Hydrogen Adsorption in Nanoporous Nickel(II) Phosphates," *Journal of the American Chemical Society* **125** (5), 1309-1312 (2003).

GROVES, J. R., YASHAR, P. C., ARENDT, P. N., DEPAULA, R. F., PETERSON, E. J., and FITZSIMMONS, M. R., "Ultra-Thin Bi-Axially Textured IBAD MgO Template Layers Resolved by Grazing Incidence X-ray Diffraction," *Physica C* **355** (3-4), 293-298 (2001).

HAINES, J. R., RIERNER, B. W., TSAI, C. C., HUNN, J. D., WENDER, S. A., TAKALA, B. E., and TCHARNOTSKAIA, V., "'Pitting' in Mercury Targets — Crucial Test Experiments at LANSCE," *Neutron News* **14** (1), 19-22 (2003).

HAMILTON, M. L., GARNER, F. A., TOLOCZKO, M. B., MALOY, S. A., SOMMER, W. F., JAMES, M. R., and FERGUSON, P. D., "Shear Punch and Tensile Measurements of Mechanical Property Changes Induced in Various Austenitic Alloys by High-Energy Mixed Proton and Neutron Irradiation at Low Temperatures," *Journal of Nuclear Materials* **283-287** (1), 418-422 (2000).

HANAN, J. C., USTUNDAG, E., CLAUSEN, B., SIVASAMBU, M., BEYERLEIN, I. J., and BROWN, D. W., "Residual Strain Evolution During the Deformation of Single Fiber Metal Matrix Composites," *Materials Science Forum* **404**, 907-911 (2002).

HANSON, B. L., BUNICK, G. J., HARP, J. M., and EDMUNDSON, A. B., "Mcg in 2030: New Techniques for Atomic Position Determination of Immune Complexes," *Journal of Molecular Biology* **15** (5), 297-305 (2002).

HE, D., ZHAO, Y., DAEMEN, L. L., QIAN, J., SHEN, T. D., and ZERDA, T. W., "Boron Suboxide: As Hard As Cubic Boron Nitride," *Applied Physics Letters* **81**, 643-645 (2002).

HENSON, N. J., HAY, P. J., DAEMEN, L. L., KOERMER, G., and ECKERT, J., "Probing Adsorbate Structure in Catalytic Materials Using Inelastic Neutron Scattering," *Neutron News* **14** (1), 19-22 (2003).

HJELM, R. P., "Carbon Black Structure and Associations in Filled Rubber," invited chapter for *Polymer Nanocomposites*, R. Viai and R. Kristamoort, Eds. (American Chemical Society, 2002).

HJELM, R. P., GERSPACHER, M., YANG, H., HAWLEY, M. E., and LINDNER, P., "Carbon Black Structure and Associations in Filled Rubber: A Small-Angle Neutron Scattering Study," in *Proceedings of the World Wide Amazon Rubber Conference*, (Germany, 1999), 125-128.

HOFFMANN, A. F., FITZSIMMONS, M. R., DURA, J. A., and MAJKRZAK, C. F., "Investigating Magnetic Proximity Effects in NiO/Pd with Polarized Neutron Reflectometry," *Physical Review B* **65** (2), 024428/1-7 (2002).

HOLDEN, T. M., HOLT, R. A., and PANG, J. W., "Intergranular Stresses in Zircaloy-2," *Metallurgical Transactions A* **33** (3/SISI), 749-755 (2002).

HUFNAGLE, T. C., and HELLMAN, F., "Structural and Magnetic Length Scales in Amorphous $TbFe_2$," *Journal of Magnetism and Magnetic Materials* **256** (1-3), 322-327 (2003).

HURD, A. J., "Lujan Center: Condensed-Matter Science with Neutrons," *Neutron News* **14** (1), 16-18 (2003).

IOFFE, A., and MEZEI, F., "4p-Symmetry of the Neutron Wave Function Under Space Rotation," *Physica B* **297**, 303-306 (2001).

JEONG, I., GRAF, M. J., HEFFNER, R. H., and BILLINGE, S. J. L., "Lattice Dynamics and Correlated Atomic Motion From the Atomic Pair Distribution Function," *Physical Review B* **67**, 104301 (2003).

JUNG, M. H., INOUE, I. H., NAKOTTE, H., and LACERDA, A. H., "High-Field Properties of Single-Crystal $CaVO_3$," *Philosophical Magazine B: Physics of Condensed Matter* **82**, 801 (2002).

KENT, M. S., YIM, H., SASAKI, D. Y., MAJEWSKI, J. P., SMITH, G. S., SHIN, K., and SATIJA, S. K., "Segment Concentration Profile of Myoglobin Adsorbed on Metal Ion-Chelating Lipid Monolayers at the Air-Liquid Interface by Neutron Reflection," *Langmuir* **18** (9), 3754-3757 (2002).

KUBAS, G. J., *Metal-Dihydrogen and Sigma-Bond Complexes: Structure, Bonding, and Reactivity* (Kluwer Academic/Plenum Publishers, New York, 2001).

KUHL, T. L., SMITH, G. S., MAJEWSKI, J., HAMILTON, W., and ALCANTAR, N., "Investigating Confined Complex Fluids with Neutron Reflectivity," *Neutron News* **14** (1), 19-22 (2003).

LAWSON, A. C., ROBERTS, J. A., VON DREELE, R. B., MARTINEZ, B., and SHELDON, R. I., "Diffuse Scattering in Powder Dirrfaction from the Delta Phase of Plutonium," *Neutron News* **14** (1), 19-22 (2003).

LEE, D. R., SRAJER, G., FITZSIMMONS, M. R., METLUSHKO, V., and SINHA, S. K., "Polarized Neutron Scattering from Ordered Magnetic Domains on a Mesoscopic Permalloy Antidot Array," *Applied Physics Letters* **82** (1), 82-84 (2003).

LEE, K. Y. C., GOPAL, A., VON NAHMEN, A., ZASADZINSKI, J. A., MAJEWSKI, J. P., SMITH, G. S., HOWES, P. B., and KJAER, K., "Influence of Palmitic Acid and Hexadecanol on the Phase Transition Temperature and Molecular Packing of Dipalmitoylphosphatidylcholine Monolayers at the Air-Water Interface," *Journal of Chemical Physics* **116** (2), 774-783 (2002).

LEIGHTON, C., FITZSIMMONS, M. R., HOFFMANN, A. F., DURA, J. A., and MAJKRZAK, C. F., "Thickness Dependent Coercive Mechanisms in Exchange Biased Bilayers," *Physical Review B* **65** (6), 064403/1-7 (2002).

LEIGHTON, C., FITZSIMMONS, M. R., HOFFMANN, A. F., DURA, J. A., MAJKRZAK, C. F., and SCHULLER, I., "Thickness Dependent Coercive Mechanisms in Exchange Biased Bilayers," *Bulletin of the American Physical Society* **47**, 788 (2002).

LEIGHTON, C., SCHULLER, I., FITZSIMMONS, M. R., YASHAR, P. C., HOFFMANN, A. F., NOGUES, J., DURA, J. A., and MAJKRZAK, C. F., "Two-Stage Magnetization Reversal in Exchange Biased Bilayers," *Bulletin of the American Physical Society* **46**, 261 (2001).

LILLARD, R. S., KANNER, G. S., and DAEMEN, L. L., "The Influence of a Mixed Radiation Environment on the Properties of the Passive Film on Tungsten," *Electrochimica Acta* **47** (15), 2473-2482 (2002).

MADDOX, S. A., GOMEZ, P., MCCALL, K. R., and ECKERT, J., "Water Mobility in Calico Hill Tuff Measured by Quasi-Elastic Neutron Scattering," *Geophysical Research Letters* **29** (8), 100-104 (2002).

MANG, J. T., PETERSON, P. D., ORLER, E. B., WROBLESKI, D. A., LANGLOIS, D. A., ESPADA, L. I., and HJELM, R. P., "Small-Angle Neutron Scattering Study of a Thermally Aged, Segmented Poly(ester urethane) Binder," *Neutron News* **14** (1), 19-22 (2003).

MANG, J. T., SKIDMORE, C. B., HJELM, R. P., and RIEKER, T. P., "An Optical Microscopy and Small-Angle Scattering Study of Porosity in Thermally Treated PBX 9501," in *Proceedings of the 12th American Physical Society Topical Group on Shock Compression of Condensed Matter* (American Institute Physics CD, 2002).

MANLEY, M. E., FULTZ, B. T., COOLEY, J. C., HULTS, W. L., and SMITH, J. L., "Microstructural Strain and Strain Energy of Alpha-Uranium Determined by Neutron Diffraction and Calorimetry," *Physical Review B* **66**, 024117 (2002).

MANLEY, M. E., FULTZ, B. T., COOLEY, J. C., HULTS, W. L., and SMITH, J. L., "Vibrational and Electronic Entropy of Gamma-Cerium and Beta-Cerium Measured by Inelastic Neutron Scattering," *Physical Review B* **65**, 144111 (2002).

MCQUEENEY, R. J., and ROBINSON, R. A., "Pharos — A Chopper Spectrometer for Inelastic-Neutron-Scattering Studies of Excitations in Materials," *Neutron News* **14** (1), 19-22 (2003).

MEZEI, F., DRABKIN, G. M., and IOFFE, A., "Polarimetric Neutron Spin Echo," *Physica B* **297**, 9-13 (2001).

MOJET, B. L., ECKERT, J., VAN SANTEN, R. A., ALBINATI, A., and LECHNER, R. E., "Evidence for Chemisorbed Molecular Hydrogen in Fe-ZSM5 from Inelastic Neutron Scattering," *Journal of the American Chemical Society* **123** (33), 8147-8148 (2001).

NELSON, R. O., BOURKE, M. A. M., BOWLING, P. S., COOPER, G. M., KOZLOWSKI, T., LARA, P. D., ROSE, C. R., ROSS, J. J., SEAL, J. R., and WILLIAMS, B. C., "The LANSCE Data Acquisition System and SMARTS," in *Proceedings of the 11th IEEE NPSS Real Time Conference* (IEEE, 2000).

ORLER, E. B., LANGLOIS, D. A., COOKE, D. W., MANG, J. T., ESPADA, L. I., WROBLESKI, D. A., BENNETT, B. L., PETERSON, P., and HJELM, R. P., "Thermal Aging of Nitroplasticized Estane 5703," in *Proceedings of the 24th Aging, Compatibility and Stockpile Stewardship Conference* (Los Alamos National Laboratory, 2002).

PAINTER, T., WALSH, R., WILLIAMS, V., TOPLOSKY, V., and MAIER, S., "Conductor and Reinforcement Materials for the Los Alamos Neutron Science Center 30-T Split-Pair and Future Pulse Coils," in *Proceedings of the IEEE Transactions on Applied Superconductivity* **10** (1), 1770-1772 (2002).

Proceedings of the Filled and Nanocomposite Polymer Materials Conference, Nakatani, A. I., Hjelm, R. P., Gerspacher, M., and Krishnamoorti, R., Eds. (Materials Research Society, 2001).

PROFFEN, T., EGAMI, T., BILLINGE, S. J. L., CHEETHAM, A. K., LOUCA, D. A., and PARISE, J. B., "Building a High-Resolution Total Scattering Powder Diffractometer — Upgrade of NPD at MLNSC," *Applied Physics A: Materials Science and Processing* **74** (01), 1770-1772 (2002).

PROFFEN, T., PETKOV, V. G., BILLINGE, S. J. L., and VOGT, T., "Chemical Short Range Order Obtained from the Atomic Pair Distribution Function," *Zeitschrift fur Kristallographie* **217**(2), 47-50 (2002).

PROKES, K., DE CHATEL, P. F., BRUCK, E., DE BOER, F. R., NAKOTTE, H., and SECHOVSK, V., "Canted Ferromagnetic Structure of UNiGe in High Magnetic Fields," *Physical Review B* **6514**, 4429 (2002).

PYNN, R., FITZSIMMONS, M. R., REKVELDT, M. T., MAJOR, J., FRITZSCHE, H., WELLER, D., and JOHNS, E. C., "Optimization of Neutron-Scattering Instrumentation Using Neutron Spin Echo: Application to the Discrimination of Diffuse Scattering in Neutron Reflectivity Experiments," *Review of Scientific Instruments* **73** (8), 2948-2957 (2002).

QIAN, J., VORONIN, G., ZERDA, T. W., and ZHAO, Y., "High-Pressure/High-Temperature Siatoring of Diamond-Sic Composites by Ball Milled Diamond-Si Mixtures," *Journal of Material Research* **17** (8), 2153-2160 (2002).

RANGASWAMY, P., BOURKE, M. A. M., BROWN, D. W., KASCHNER, G. C., ROGGE, R. B., STOUT, M. G., and TOME, C. N., "A Study of Twinning in Zirconium Using Neutron Diffraction and Polycrystalline Modeling," *Metallurgical and Materials Transactions A* **33** (3A), 757-763 (2002).

RANGASWAMY, P., DAYMOND, M. R., BOURKE, M. A. M., VON DREELE, R. B., BENNETT, K. A., and JAYARAMAN, N., "Texture and Residual Strain in Two SiC/Ti-6-2-4-2 Titanium Composites," *Metallurgical and Materials Transactions A* **31** (3A), 889-898 (2000).

RETSOS, H., TERZIS, A. F., ANASTASIADIS, S. H., ANASTASSOPOULOS, D., TOPRAKCIOGLU, C., THEODOROU, D. N., SMITH, G. S., MENELLE, A., GILL, R., HADZIIOANNOU, G., and GALLOT, Y., "Mushrooms and Brushes in Thin Films of Diblock Copolymer/Homopolymer Mixtures," *Macromolecules* **35** (3), 1116-1132 (2002).

RICH, D. R., BOWMAN, J. D., CRAWFORD, B. E., DEL-HEIJ, P. P. J., ESPY, M. A., HASEYAMA, T., KEITH, C. D., KNUDSON, J. N., LEUSCHNER, M. B., MASAIKE, A., MASUDA, Y., MATSUDA, Y., PENTTILA, S. I., POMEROY, V. R., SMITH, D. A., SNOW, W. M., STEPHENSON, S. L., THOMPSON, A. K., and YUAN, V. W., "A Measurement of the Absolute Neutron Beam Polarization Produced by an Optically Pumped ^{3}He Neutron Spin Filter," *Nuclear Instruments and Methods A* **481** (1-3), 145-154 (2001).

SEEGER, P. A., and DAEMEN, L. L., "Mosaic Crystal Algorithm for Monte Carlo Simulations," *Applied Physics A* **74** (2), 1458-1461 (2002).

SENCER, B. H., BOND, G. M., GARNER, F. A., HAMILTON, M. L., OLIVER, B. M., THOMAS, L. E., MALOY, S. A., SOMMER, W. F., JAMES, M. R., and FERGUSON, P. D., "Microstructural Evolution of Alloy 718 at High Helium and Hydrogen Generation Rates During Irradiation with 600- to 800-MeV Protons," *Journal of Nuclear Materials* **283-287**, 324-328 (2000).

SENCER, B. H., BOND, G. M., GARNER, F. A., HAMILTON, M. L., MALOY, S. A., and SOMMER, W. F., "Correlation of Radiation-induced Changes in Mechanical Properties and Microstructural Development of Alloy 718 Irradiated with Mixed Spectra of High-Energy Protons and Spallation Neutrons," *Journal of Nuclear Materials* **296** (1-3), 145-154 (2001).

SITEPU, H., SCHMAHL, W. W., and VON DREELE, R. B., "Quantitative Texture Analysis in Polycrystalline NiTi Shape Memory Alloys by Rietveld Refinement with the Generalized Spherical Harmonic Description," *Materials Research Forum* **394-395**, 233-236 (2002).

SITEPU, H., SCHMAHL, W. W., and VON DREELE, R. B., "Use of Rietveld Refinement with the Generalized Spherical-Harmonic Model for Describing Crystallographic Texture in Polycrystalline NiTi Shape Memory Alloys with Time-of-Flight Neutron Powder Diffraction Data," *Applied Physics A* **75** (1-3), (2002).

SKIDMORE, C. B., PHILLIPS, D. S., HOWE, P. M., and MANG, J. T., "The Evolution of Microstructural Changes in Pressed HMX Explosives," in *Proceedings of the 11th International Detonation Symposium* (2000), 556.

SNOW, W. M., HUSSEY, D., BAILEY, C., BELOV, A., SMITH, T. B., GENTILE, T. R., RICH, D. R., THOMPSON, A. K., and JONES, G. L., "Development of Polarized ^{3}He-Based Neutron Spin Filters at IUCF," in *Proceedings of the 9th International Workshop on Polarized Sources and Targets* (World Scientific, 2002), 248.

SWIFT, G. A., USTUNDAG, E., CLAUSEN, B., BOURKE, M. A. M., and LIN, H.-T., "High-Temperature Elastic Properties of *In situ*-Reinforced Si_3N_4," *Applied Physics Letters* **82** (7), 1039 (2003).

TOME, C. N., AGNEW, S. R., BLUMENTHAL, W. R., BOURKE, M. A. M., BROWN, D. W., KASCHNER, G. C., and RANGASWAMY, P., "The Relation Between Texture, Twinning, and Mechanical Properties in Hexagonal Aggregates," *Materials Science Forum* **408,** 263-268 (2002).

VAIDYANATHAN, R., BOURKE, M. A. M., and DUNAND, D. C., "Investigating Shape-Memory Alloys and Composites with Neutron-Diffraction Techniques," *Neutron News* **14** (1), 19-22 (2003).

VAIDYANATHAN, R., BOURKE, M. A. M., and DUNAND, D. C., "Texture, Strain and Phase Fraction Measurements During Mechanical Cycling in Superelastic NiTi," *Metallurgical and Materials Transactions A* **32** (3), 777-786 (2001).

VOGEL, S., and PRIESMEYER, H. G., "Automated Analysis of Large Numbers of Datasets," *Advances in X-ray Analysis* **44**, 91-95 (2001).

VOGEL, S., BOURKE, M. A. M., HANAN, J. C., PRIES-MEYER, H. G., and USTUNDAG, E., "Non-Destructive *In Situ* Real-Time Measurements of Structural Phase Transitions Using Neutron Transmission," *Advances in X-ray Analysis* **44**, 75-84 (2001).

VOGEL, S., BOURKE, M. A. M., HANAN, J. C., USTUNDAG, E., and YUAN, V. W., "*In Situ* Investigation of the Reduction of NiO by a Neutron Transmission Method," *Materials Science and Engineering A* **333**, 1-9 (2002).

WEHRMANN. F., ALBRECHT, J., GEDAT, E., KUBAS, G. J., ECKERT, J., LIMBACH, H.-H., and BUNTKOWSKY, D. G., "Hydrogen Deuterium Isotope Effect on Exchange Rates in 2 Bond Transition Metal Dihydrogen Complexes Revealed by ^{2}H Solid State NMR Spectroscopy," *Journal of Physical Chemistry A* **106** (12), 2855-2861 (2002).

YIM, H., KENT, M. S., HALL, J. S., BENKOSKI, J. J., and KRAMER, E. J., "Probing the Structure of Organosilane Films by Solvent Swelling and Neutron and X-ray Reflection," *Journal of Physical Chemistry B*, **106** (10), 2474 -2481 (2002).

YIM, H., KENT, M. S., HALL, J., BENKOSKI, J. J., and KRAMER, E. J., "Probing the Structure and Chemistry of GPS Films by Solvent Swelling and Neutron Reflection," in *Proceedings of the 24th Annual Meeting of the Adhesion Society* (2001), 371.

YIM, H., KENT, M. S., J. S. HYUN, and SMITH, G. S., "Study of Interfacial Structure in Epoxy Bilayer Films Using Neutron Reflection," *Journal of Polymer Science and Polymer Physics* **40**, 1710 (2002).

YU, B., ZOJCESKI, Z., HARDER, J. A., HRISOHO, A., RADEKA, V., and SMITH, G. C., "Front-End Electronics for High Rate, Position Sensitive Neutron Detectors," *Nuclear Instruments and Methods in Physics Research A* **485** (3), 645-652 (2002).

ZHAO, Y., HE, D., DAEMEN, L. L., SHEN, T. D., SCHWARZ, R. B., ZHU, Y., BISH, D. L., HUANG, J. Y., ZHANG, J., SHEN, G., QIAN, J., and ZERDA, T. W., "Superhard B-C-N Materials Synthesized in Nanostructured Bulks," *Journal of Materials Research* **17** (12), 3139-3145 (2002).

Neutron Nuclear Science

ANDERSON, J. D., BAUER, R. W., DIETRICH, F. S., GRIMES, S. M., FINLAY, R. W., ABFALTERER, W. P., BATEMAN, F. B., HAIGHT, R. C., MORGAN, G. L., BAUGE, E., DELAROCHE, J., and ROMAIN, P., "Failure of Standard Optical Models to Reproduce Neutron Total Cross Section Differences in the W Isotopes," *Journal of Nuclear Science and Technology* **1** (2), 822-825 (2002).

BADHWAR, G. D., SINGLETERRY, J. R., ROBERT, C., WILKINS, R., HUFF, H., MOORE, J., ZHOU, J., WENDER, S. A., and FOGARTY, T. N., "Observation of Changes in the Single-Event-Upset Rate in 4MB SRAM Due to Intervening Materials in a Neutron Environment," in *Proceedings of the 6th European Conference on Radiation and its Effects on Components and Systems* **1** (2), 469-473 (2002).

BADHWAR, G., HUFF, H., and WILKINS, R., "Alterations in Dose and Lineal Energy Spectra Under Different Shieldings in the Los Alamos High-Energy Neutron Field," *Radiation Research* **154**, 697 (2000).

BADHWAR, G., HUFF, H., WILKINS, R., and THIBEAULT, S., "Comparison of Graphite, Aluminum, and Transhab Shielding Material Characteristics in a High-Energy Neutron Field," *Radiation Measurements* **35**, 545 (2002).

BECKER, J. A., BERNSTEIN, L. A., YOUNES, W., MCNABB, D. P, GARRETT, P. E., ARCHER, D., MCGRATH, C. A., STOYER, M. A., CHEN, H., ORMAND, W. E., et al., "Partial Gamma-Ray Cross Sections for the Reaction ^{239}Pu(n,2nγ_i) and the ^{239}Pu Cross Sections" *American Chemical Society* **222** (2), U25 (2001).

BERNSTEIN, L. A., ARCHER, D. E., BECKER, J. A., GARRETT, P. E., HAUSCHILD, K., MCGRATH, C. A., MCNABB, D. P., YOUNES, W., DEVLIN, M., DRAKE, D. M., et al., "Studying the Role of Nuclear Structure Effects in Neutron-Induced Reactions Using GEANIE at LANSCE," *Nuclear Physics A* **682**, 404C-414C (2001).

BERNSTEIN, L. A., BECKER, J. A., GARRETT, P. E., YOUNES, W., MCNABB, P. D., ARCHER, D. E., MCGRATH, C., CHEN, H., ORMAND, W. E., STOYER, M. A., NELSON, R. O., CHADWICK, M. B., JOHNS, G. D., WILBURN, W. S., DEVLIN, M., DRAKE, D. M., and YOUNG, P. G., "^{239}Pu(n,2n)^{238}Pu Cross Section Deduced Using a Combination of Experiment and Theory," *Physical Review C* **65** (2), 021601/1-5 (2002).

BOUKHAROUBA, N., BATEMAN, F. B., BRIENT, C. E., CARLSON, A. D., GRIMES, S.M., HAIGHT, R. C., MASSEY, T. N., and WASSON, O. A., "Measurement of the n-p Elastic Scattering Angular Distribution at E-n = 10 MeV," *Physical Review C* **65**, (1), 014004 (2002).

CIZEWSKI, J., BECKER, J. A., MCNABB, P. D., CLARK, R. M., LEE, I. Y., BERNSTEIN, L. A., YOUNES, W., FALLON, P., MACCHIAVELLI, A. O., HOLT, A. E., and HJORTH-JENSEN, M., "High-Spin Excitations in $^{92, 93, 94, 95}$Zr," *Physical Review C* **65**, 044303-044309 (2002).

CORZINE, K., PITCHER, E., DEVLIN, M., and HERTEL, N., "^{148}Gd Production Cross-Section Measurements for Accelerator Target Facilities," in *Transactions of the American Nuclear Society* **87**, 542-543 (2002).

DEVLIN, M., FOTIADES, N., NELSON, R. O., HAIGHT, R. C., ZANINI, L., BECKER, J. A., BERNSTEIN, L. A., GARRETT, P. E., MCGRATH, C., YOUNES, W., SALADIN, J. X., and APRAHAMIAN, A., "Nuclear Physics with Fast Neutrons at LANSCE/WNR: GEANIE and FIGARO," in *Proceedings of the 16th International Conference on the Application of Accelerators in Research and Industry*, **576**, 309-12 (2002).

DODD, P. E., SHANEYFELT, M., SCHWANK, J., and HASH, G., "Neutron-Induced Soft Errors, Latchup, and Comparison of SER Test Methods for SRAM Technologies," *IEDM Technical Digest* **333-336** (2002).

FOTIADES, N., CIZEWSKI, J. A., BECKER, J. A., BERNSTEIN, L. A., MCNABB, D. P., YOUNES, W., CLARK, R. M., FALLON, P., LEE, I. Y., MACCHIAVELLI, A. O., et al., "High-Spin Excitations in ^{92}Zr, ^{93}Zr, ^{94}Zr, ^{95}Zr," *Physical Review C* **65** (4), 044303-4303 (2002).

FOTIADES, N., CIZEWSKI, J., CLARK, R. M., LEE, I. Y., BECKER, J. A., YOUNES, W., FALLON, P., MACCHIAVELLI, A. O., MCNABB, P. D., BERNSTEIN, L. A., and KRUCKEN, R., "High-Spin States in Neutron-Rich Rh Isotopes," in *Proceedings of the International Conference on Nuclear Structure* **638**, 237-238 (2002).

GARRETT, P. E., BECKER, J. A., BERNSTEIN, L. A., YOUNES, W., NELSON, R. O., DEVLIN, M., and FOTIADES, N., "Measurements of Neutron-Induced Reactions on Y-89 and Zr-90," *American Chemical Society* **222** (2), U25 (2001).

HAIGHT, R. C., DEVLIN, M., ZANINI, L., O'DONNELL, J. M., APRAHAMIAN, A., and SALADIN, J. X., "The FIGARO Facility at Los Alamos: Capabilities and First Results," *Journal of Nuclear Science and Technology* **1** (2), 634-637 (2002).

HAIGHT, R. C., WERMER, J. R., and FIKANI, M. M., "Tritium Production by Fast Neutrons on Oxygen: An Integral Experiment," *Journal of Nuclear Science and Technology* **2** (2), 1232-1235 (2002).

HARTLEY, D. J., RIEDINGER, L. L., DANCHEV, M., REVIOL, W., ZEIDAN, O., GALINDO-URIBARRI, A., GROSS, C. J., BAKTASH, C., LIPOGLAVSEK, M., PAUL, S. D., RADFORD, D. C., YU, C. H., SARANTITES, D. G., CARPENTER, M. P., JANSSENS, R. V., SEWERYNIAK, D., PADILLA, E., and ZHANG, J., "Towards Complete Spectroscopy of ^{128}Pr and Rotational Structures in ^{126}Pr," *Physical Review C* **6504** (4), 4329 (2002).

HASEYAMA, T., ASAHI, K., BOWMAN, J. D., DELHEIJ, P. P. J., FUNAHASHI, H., ISHIMOTO, S., MASAIKE, A., MASUDA, Y., MATSUDA, Y., MORIMOTO, K., MUTO, S., PENTTILA, S. I., POMEROY, V. R., SAKAI, K., SHARAPOV, E. I., SMITH, D. A., and YUAN, V. W., "Measurement of Parity-Nonconserving Rotation of Neutron Spin in the 0.734-eV p-Wave Resonance of ^{139}La," *Physics Letters B* **534**, 39 (2002).

HENLEY, E. M., HWANG, W. P., and KISSLINGER, L. S., "Nonleptonic Hyperon Decays with QCD Sum Rules," *Nuclear Physics A* **706**, 153 (2002).

KINNISON, J. D., MAURER, R. H., ROTH, D. R., and HAIGHT, R. C., "High-Energy Neutron Spectroscopy with Thick Silicon Detectors," *Radiation Research* **159** (2), 154-160 (2003).

KIRCH, K., BOWLES, T. J., FILLIPONE, B., GELTENBORT, P., HILL, R., HINO, M., HOEDL, S., HOGAN, G., ITO, T. M., KAWAI, T., et al., "Status of the New Los Alamos UCN Source," in *Proceedings of the Sixteenth International Conference on the Application of Accelerators in Research and Industry* **576**, 289-92 (2001).

LAIRD, R. W., RILEY, M., KONDEV, F. G., ARCHER, D. E., BROWN, T., CLARK, R. M., FALLON, P., HARTLEY, D. J., LAFOSSE, D. R., SARANTITES, D. G., SIMPSON, J. E., DOBACZEWSKI, J., DEVLIN, M., HIBBERT, I. M., JOSS, D. T., NOLAN, P. J., O'BRIEN, N. J., PAUL, E. S., PFOHL, J., SHELINE, R. K., SHEPHERD, S. L., WADSWORTH, R., MATEV, M. T., AFANASJEV, A. V., LALAZISSIS, G. A., NAZAREWICZ, W., and SATULA, W., "Quadrupole Moments of Highly Deformed Structures in the A ~ 135 Region: Probing the Single-Particle Motion in a Rotating Potential," *Physical Review Letters* **88**, 152501 (2002).

LAMOREAUX, S. K., ARCHIBALD, G., BARNES, P. D., BUTTLER, W. T., CLARK, D. J., COOPER, M. D., ESPY, M. A., GREENE, G. L., GOLUB, R., LEI, C. M., MAREK, L. J., PENG, J.-C., and PENTTILA, S. I., "Measurement of the ^{3}He Diffusion Coefficient in Superfluid ^{4}He in the 0.45-0.95 K Temperature Range," *Europhysics Letters* **58**, 718 (2002).

MORRIS, C. L., ANAYA, J. M., BOWLES, T. J., FILIPPONE, B. W., GELTENBORT, P., HILL, R. E., HINO, M., HOEDL, S., HOGAN, G. E., ITO, T. M., KAWAI, T., KIRCH, K., LAMOREAUX, S. K., LIU, C.-Y., MAKELA, M., MAREK, L. J., MARTIN, J. W., MORTENSEN, R. N., PICHLMAIER, A., SAUNDERS, A., SEESTROM, S. J., SMITH, D., TEASDALE, W., TIPTON, B., UTSURO, M., YOUNG, A. R., and YUAN, J., "Measurements of Ultracold-Neutron Lifetimes in Solid Deuterium," *Physical Review Letters* **89** (27), 272501/1-4 (2002).

NELSON, R. O., and MICHAUDON, A. F., "High-Resolution Cross-Section Measurements for Production of the 0.478-MeV Gamma Ray from the ^{9}Be(n,$x\gamma$)^{7}Li Reaction for Neutron Energies Between 12 and 200 MeV with Insight into the ^{10}Be Level Scheme," *Nuclear Science and Engineering* **140** (3), 195-204 (2002).

PADMINI, P., PULIKKATHARA, M., WILKINS, R., and PANDEY, R. K., "Neutron Radiation Effects on the Nonlinear Current-Voltage Characteristics of Ilmenite-Hematite Ceramics," *Applied Physics Letters* **82** (4), 586-588 (2003).

RUNDBERG, R. S., FOWLER, M. M., HAIGHT, R. C., MILLER, G. G., PALMER, P. D., SEABURY, E. H., ULLMANN, J. L., WILHELMY, J. B., KOEHLER, P., and KAPPELER, F., "Neutron Capture Cross Section Measurements for the Analysis of the s-Process," in *Origin of Elements in the Solar System: Implications of Post-1957 Observations* (Kluwer/Plenum, 2001).

SISTERSON, J. M., et al., "Production of ^{22}Na and Other Radionuclides by Neutrons in Al, SiO_2, Si, Ti, Fe, and Ni Targets: Implications for Cosmic Ray Studies," in *Lunar and Planetary Science XXXII*, Abstract No. 1302, Lunar and Planetary Institute, Houston (CD-ROM), 2001.

SISTERSON, J. M., et al., "Production of Short-Lived Radionuclides by Protons and Neutrons in Fe and Ni Targets: Cross Sections Needed for Cosmic Ray Studies," in *Lunar and Planetary Science XXXI*, Abstract No. 1432, Lunar and Planetary Institute, Houston (CD-ROM), 2000.

SISTERSON, J. M., et al., "Revised Calculations of the Production Rates for Co Isotopes in Meteorites Using New Cross Sections for Neutron-Induced Reactions," in *Lunar and Planetary Science XXXIII*, Abstract No. 1541, Lunar and Planetary Institute, Houston (CD-ROM), 2002.

SISTERSON, J. M., et al., "The Status of Cross-Section Measurements for Neutron-Induced Reactions Needed for Cosmic Ray Studies," in *Lunar and Planetary Science XXXIV*, Abstract No. 1326, Lunar and Planetary Science Institute, Houston, (CD-ROM), 2003.

SMITH, D. A., BOWMAN, J. D., CRAWFORD, B. E., CROSSMAN, C. A., HASEYAMA, T., MASAIKE, A., MATSUDA, Y., MITCHELL, G. E., PENTTILA, S. I., ROBERSON, N. R., SEESTROM, S. J., SHARAPOV, E. I., STEPHENSON, S. L., and YUAN, V. W., "Parity Violation in Neutron Resonances of Palladium," *Physical Review C* **65**, 035503 (2002).

SMITH, D. A., BOWMAN, J. D., CRAWFORD, B. E., HASEYAMA, T., MASAIKE, A., MATSUDA, Y., MITCHELL, G. E., PENTTILA, S. I., ROBERSON, N. R., SEESTROM, S. J., SHARAPOV, E. I., STEPHENSON, S. L., YUAN, V. W., and CROSSMAN, C. A., "Neutron Resonance Spectroscopy of ^{104}Pd, ^{105}Pd and ^{110}Pd," *Physical Review C* **65**, 024607 (2002).

SMITH, J. F., CHIARA, C. J., FOSSAN, D. B., LAFOSSE, D. R., LANE, G. J., SEARS, J. M., STAROSTA, K., DEVLIN, M., LERMA, F., SARANTITES, D. G., et al., "Excited States and Deformation of ^{112}Xe," *Physics Letters B* **523** (1-2), 13-21 (2001).

TAKEDA, E., MURAKAMI, E., TORII, K., OKUYAMA, Y., EBE, E., HINODE, K., and KIMURA, S., "Reliability Issues of Silicon LSIs Facing 100-nm Technology Node," *Microelectronics Reliability* **42**, 493-506 (2002).

TAVUKCU, E., BERNSTEIN, L. A., HAUSCHILD, K., BECKER, J. A., GARRETT, P. E., MCGRATH, C., MCNABB, P. D., YOUNES, W., NELSON, R. O., JOHNS, G. D., MITCHELL, G. E., and CIZEWSKI, J., "States in ^{196}Pt Observed with the (n,n'γ) Reaction with Spallation Neutrons," *Physical Review C* **65** (6), 064309/1-8 (2002).

THOMPSON, J. R., OSSANDON, J. G., KRUSIN-ELBAUM, L., KIM, H. J., SONG, K. J., CHRISTEN, D. K., and ULLMANN, J. L., "Vortex Pinning in High-T_c Materials Via Randomly Oriented Columnar Defects, Created by GeV Proton-Induced Fission Fragments," *Physica C* **378** (1), 409-415 (2002).

WILHELMY, J. B., CHAMBERLIN, E. P., DRAGOWSKY, M. R., FOWLER, M. M., HAIGHT, R. C., HEIL, M., KAEPPELER, F., MILLER, G. G., PALMER, P. D., PANGAULT, L. N., REIFARTH, R., RUNDBERG, R. S., SEABURY, E. H., STROTTMAN, D. D., ULLMANN, J. L., and WISSHAK, D. K., "DANCE: Device for Measurement of (n,γ) Reactions on Radioactive Species," *Journal of Nuclear Science and Technology* **1** (2), 614-619 (2002).

WILLIS, J. O., COULTER, J. Y., MALEY, M. P., ULLMANN, J. L., FLESHLER, S., and RILEY, G. N., "Enhanced Critical Currents in Bi-2223/Ag Sheathed Tapes by High-Energy Proton Irradiation," in *Proceedings of the 2001 Joint Cryogenic Engineering Conference and International Cryogenic Materials Conference* **614B**, 1201-1208 (2002).

YAHAGI, Y., et al., *2002 IEEE Integrated Reliability Workshop Final Report* (2002), 143-146.

YOUNES, W., BECKER, J. A., BERNSTEIN, L. A., GARRETT, P. E., MCGRATH, C., MCNABB, P. D., NELSON, R. O., JOHNS, G. D., WILBURN, W. S., and DRAKE, D. M., "Transition from Asymmetric to Symmetric Fission in the ^{235}U(n,f) Reaction," *Physical Review C* **64**, 054613 (2001).

YOUNES, W., BECKER, J. A., BERNSTEIN, L. A., GARRETT, P. E., MCGRATH, C., MCNABB, P. D., NELSON, R. O., JOHNS, G. D., WILBURN, W. S., and DRAKE, D. M., "Transition from Asymmetric to Symmetric Fission in the ^{235}U(n,f) Reaction," in *Proceedings of the 2001 International Nuclear Physics Conference* **610**, 673-677 (2002).

ZANINI, L., APRAHAMIAN, A., CHADWICK, M. B., DEVLIN, M., HAIGHT, R. C., SALADIN, J. X., and YOUNG, P. G., "Study of Reactons of Fast Neutrons with Nuclei with FIGARO at LANSCE," in *Proceedings of the 16th International Conference on Applications of Accelerators in Research and Industry* **576**, 346-349 (2001).

ZEIDAN, O., HARTLEY, D. J., RIEDINGER, L. L., DANCHEV, M., REVIOL, W., ZHANG, J., GALINDO-URIBARRI, A., GROSS, C. J., PAUL, S. D., BAKTASH, C., LIPOGLAVSEK, M., RADFORD, D. C., YU, C. H., SARANTITES, D. G., CARPENTER, M. P., JANSSENS, R. V., SEWERYNIAK, D., PADILLA, E., and DEVLIN, M., "Rotational Structures in ^{129}Nd and Signature Splitting Systematics of $\nu h_{11/2}$ Bands in A ~ 130 Nuclei," *Physical Review C* **65** (2), 024303/1-15 (2002).

ZEIDAN, O., HARTLEY, D. J., RIEDINGER, L. L., REVIOL, W., ZHANG, J., GALINDO-URIBARRI, A., PAUL, S. D., SARANTITES, D. G., DEVLIN, M., CARPENTER, M. P., JANSSENS, R. V., and SEWERYNIAK, D., "Yrast Spectroscopy of $_{60}{}^{128}$Nd$_{68}$ and Systematics of the $\nu h_{11/2}$ Crossing in A ~ 130 Nuclei," *Physical Review C* **66** (4), 044311 (2002).

ZHOU, J., MOORE, J., HUFF, H. SHOJAH-ARDALAN, S., WILKINS, R., FOGARTY, T. N., and ZHONG, Y., "Study of Regolith Material for Structural and Space Radiation Shielding Applications," in *Proceedings of the 34th International Society for the Advancement of Material and Process Engineering Technical Conference* (2002), 358-364.

Accelerator Science and Technology

ALLEN, C. K., and WANGLER, T. P., "Parameters for Quantifying Beam Halo," in *Proceedings of the 2001 Particle Accelerator Conference* **3**, 1732-1734 (2001).

ALLEN, C. K., CHAN, K. C. D., COLESTOCK, P. L., CRANDALL, K. R., GARNETT, R. W., GILPATRICK, J. D., LYSENKO, W., QIANG, J., SCHNEIDER, J. D., SCHULZE, M. E., et al., "Beam-Halo Measurements in High-Current Proton Beams," *Physical Review Letters* **89** (21), 214802/1-4 (2002).

ALLEN, C. K., CHAN, K. C. D., COLESTOCK, P. L., CRANDALL, K. R., GARNETT, R. W., GILPATRICK, J. D., LYSENKO, W., QIANG, J., SCHNEIDER, J. D., SCHULZE, M. E., et al, "Beam-Halo Measurements in High-Current Proton Beams," *Physical Review Special Topics - Accelerators and Beams* **5**, 11 (2002).

BARR, D. S., DAY, L. A., GILPATRICK, J. D., GRUCHALLA, M. E., MARTINEZ, D. G., O'HARA, J. F., SHURTER, R. B., STETTLER, M. W., and VALDIVIEZ, R., "Design and Experience with the WS/HS Assembly Movement Using LabVIEW VIs, National Instrument Motion Controllers, and Compumotor Electronic Drive Units and Motors," in *Proceedings of the 2001 Particle Accelerator Conference* **2**, 794-796 (2001).

BARR, D. S., GILPATRICK, J. D., and SHURTER, R. B., "Upgrade to Initial BPM Electronics Module and Beamline Components for Calibration of the LEDA Beam Position Measurements," in *Proceedings of the 2001 Particle Accelerator Conference* **2**, 1369-1371 (2001).

BENCK, S., D'ERRICO, F., DENIS, J., MEULDERS, J. P., NATH, R., and PITCHER, E. J., "In-Phantom Spectra and Dose Distributions from a High-Energy Neutron Therapy Beam," *Nuclear Instruments and Methods A - Accelerators, Spectrometers, Detectors, and Associated Equipment* **476** (1-2), 127-131 (2002).

CHANNELL, P. J., "Phenomenological Two-Stream Instability Model in the Nonlinear Electron Regime," *Physical Review Special Topics - Accelerators and Beams* **5**, 11 (2002).

COLESTOCK, P. L., ALLEN, C. K., CHAN, K. C. D., CRANDALL, K. R., GARNETT, R. W., GILPATRICK, D., LYSENKO, W., SCHNEIDER, J. D., SCHULZE, M. E., SHEFFIELD, R. L., SMITH, H. V., and WANGLER, T. P., "Measurements of Halo Generation for a Proton Beam in a FODO Channel," in *Proceedings of the 2001 Particle Accelerator Conference* **1**, 170-172 (2001).

DAY, L. A., BARR, D. S., GILPATRICK, J. D., KERSTIENS, D. M., STETTLER, M. W., KAMPERSCHROER, J., GRUCHALLA, M. E., and O'HARA, J. F., "Automated Control and Real-Time Data Processing of Wire Scanner/Halo Scraper Measurements," in *Proceedings of the 2001 Particle Accelerator Conference* **2**, 1309-1311 (2001).

GARNETT, R. W., WANGLER, T. P., KRAWCZYK, F. L., KELLEY, J. P., and CRANDALL, K. R., "Conceptual Design of a Low-Beta Superconducting Proton Linac," in *Proceedings of the 2001 Particle Accelerator Conference* **5**, 3293-3295 (2001).

GILPATRICK, J. D., BARR, D. S., COLESTOCK, P. L., DAY, L. A., SELLYEY, W. C., SHURTER, R. B., STETTLER, M. W., VALDIVIEZ, R., GRUCHALLA, M. E., O'HARA, J. F., and KAMPERSCHROER, J., "Experience with the Low-Energy Demonstration Accelerator (LEDA) Halo Experiment Beam Instrumentation," in *Proceedings of the 2001 Particle Accelerator Conference* **2**, 2311-2313 (2001).

GILPATRICK, J. D., BARR, D. S., DAY, L. A., KERSTIENS, D. M., O'HARA, J. F., STETTLER, M. W., VALDIVIEZ, R., GRUCHALLA, M. E., and KAMPERSCHROER, J., "Wide Dynamic-Range Beam-Profile Instumentation for a Beam-Halo Measurement: Description and Operation," in *Proceedings of the 20th ICFA International Beam Dynamics Workshop on High Intensity and High Brightness Hadron Beams* **642**, 108-110 (2002).

GILPATRICK, J. D., BARR, D. S., DAY, L. A., KERSTIENS, D. M., STETTLER, M. W., VALDIVIEZ, R., GRUCHALLA, M. E., and O'HARA, J. F., "Beam-Profile Instrumentation for Beam-Halo Measurement: Overall Description and Operation," in *Proceedings of the 2001 Particle Accelerator Conference* **1**, 525-527 (2001).

GILPATRICK, J. D., GRUCHALLA, M. E., KAMPER-SCHROER, J., and O'HARA, J. F., "Biasing Wire Scanners and Halo Scrapers for Measuring 6.7-MeV Proton-Beam Halo," in *Proceedings of the 2002 Beam Instrumentation Workshop* **648**, 297-304 (2002).

HARKAY, K. C., ROSENBERG, R. A., MACEK, R. J., BROWMAN, A., and WANG, T.-S., "Electron Cloud Effects at Positron/Electron (e^+/e^-) Machines and Electron Cloud Diagnostics," in *Proceedings of the 20th ICFA International Beam Dynamics Workshop on High Intensity and High Brightness Hadron Beams* **642**, 354-356 (2002).

JASON, A. J., BARLOW, D. B., BLIND, B., KELLEY, J. P., LYSENKO, W. P., MOTTERSHEAD, C. T., NERI, F., WALSTROM, P. L., and WAYNERT, J. A., "Beam-Distribution System for Multi-Axis Imaging at the Advanced Hydrotest Facility," in *Proceedings of the 2001 Particle Accelerator Conference* **5**, 3374-3376 (2001).

KAMPERSCHROER, J., O'HARA, J. F., DAY, L. A., GILPATRICK, J. D., and KERSTIENS, D. M., "Analysis of Data from the LEDA Wire Scanner/Halo Scraper," in *Proceedings of the 2001 Particle Accelerator Conference* **2**, 1306-1308 (2001).

KELLEY, J. P., ROYBAL, P. L., LAFAVE, R. P., GENTZLINGER, R. C., WAYNERT, J. A., SCHRAGE, D. L., SCHMIERER, E. N., KRAWCZYK, F. L., GARNETT, R. W., and TAJIMA, T., "ADTF Spoke Cavity Cryomodule Concept," in *Proceedings of the 2001 Joint Cryogenic Engineering Conference and International Cryogenic Materials Conference* **613A**, 507-514 (2002).

KELLEY, J. P., and MULHOLLAND, G. T., "AHF Magnetic Lens Cryosystems," in *Proceedings of the 2001 Joint Cryogenic Engineering Conference and International Cryogenic Materials Conference* **613A**, 60-67 (2002).

KELLEY, J. P., and MULHOLLAND, G. T., "AHF Beam Transport Lattice Cryosystems," in *Proceedings of the 2001 Joint Cryogenic Engineering Conference and International Cryogenic Materials Conference* **613A**, 68-75 (2002).

KRAWCZYK, F. L., GARNETT, R. W., LAFAVE, R. P., KELLEY, J. P., SCHRAGE, D. L., TAJIMA, T., and ROYBAL, P. L., "Design of a Low-Beta 2-Gap Spoke Resonator for the AAA Project," in *Proceedings of the 2001 Particle Accelerator Conference* **2**, 906-908 (2001).

KURENNOY, S. S., "Effects of Transverse Beam Size in Beam Position Monitors," in *Proceedings of the 2001 Particle Accelerator Conference* **2**, 1372-1374 (2001).

KURENNOY, S. S., POWER, J. F., ROYBAL, R. J., and SCHRAGE, D. L., "Progress with SNS Fast Beam Chopper," in *Proceedings of the 2001 Particle Accelerator Conference* **2**, 1435-1437 (2001).

LYSENKO, W. P., GILPATRICK, J. D., QIANG, J., RYBARCYK, L. J., RYNE, R. D., SCHNEIDER, J. D., SMITH, H. V., YOUNG, L. M., and SCHULZE, M. E., "Characterizing Proton Beam of 6.7-MeV LEDA RFQ by Fitting Wire-Scanner Profiles to 3-D Nonlinear Simulations," in *Proceedings of the Particle Accelerator Conference* **4**, 3051-3053 (2001).

MACEK, R. J., BROWMAN, A., FITZGERALD, D. H., MCCRADY, R., PLUM, M., and SPICKERMANN, T., "New Developments on the e-p Instability at the Los Alamos Proton Storage Ring," in *Fifteenth Meeting of the International Collaboration on Advanced Neutron Sources* **1**, 229-239 (2001).

MACEK, R. J., BROWMAN, A., FITZGERALD, D., MCCRADY, R., MERRILL, F., PLUM, M., SPICKERMANN, T., WANG, T. S., GRIFFIN, J., NG, K. Y., WILDMAN, D., HARKAY, K., KUSTOM, R., and ROSENBERG, R., "Electron Proton Two-Stream Instability at the PSR," in *Proceedings of the 2001 Particle Accelerator Conference* **1**, 688-692 (2001).

MACEK, R. J., "Possible Cures for Electron Cloud Problems," in *Proceedings of the Mini-Workshop on Electron-Cloud Simulations for Proton and Positron Beams* (CERN, 2002) 259-268.

MALOY, S. A., JAMES, M. R., SOMMER, W., Jr., WILLCUTT, G. J., Jr., LOPEZ, M., and ROMERO, T.J., "The Effect of 800-MeV Proton Irradiation on the Mechanical Properties of Tungsten," *Materials Transactions* **43** (4), 633-637 (2002).

O'HARA, J. F., GILPATRICK, J. D., LEDFORD, J. E., SHURTER, R. B., and ROYBAL, R. J., "The Mechanical Design and Preliminary Testing Results of Beam Position Monitors for the LANSCE Isotope Production Facility and Switchyard Kicker Projects," in *Proceedings of the 10th Beam Instrumentation Workshop* **648**, 305-12 (2002).

PLUM, M. A., GARNETT, R. W., MEYER, R., SR., and SHAFER, R. E., "Diagnostics Plate for SNS Linac Commissioning," in *Proceedings of the 2001 Particle Accelerator Conference* **3**, 2374-2376 (2001).

POWER, J. F., O'HARA, J. F., KURENNOY, S. S., PLUM, M. A., and STETTLER, M. W., "Beam Position Monitors for the SNS Linac," in *Proceedings of the 2001 Particle Accelerator Conference* **2**, 1375-7 (2001).

QIANG, J., and GARNETT, R. W., "Smooth Approximation with Acceleration in an Alternating Phase Focusing Superconducting Linac," *Nuclear Instruments and Methods in Physics Research A* **496** (1), 33-43 (2003).

QIANG, J., COLESTOCK, P. L., GILPATRICK, J. D., SMITH, H. V., and WANGLER, T. P., "Macroparticle Simulation Studies of a Proton Beam Halo Experiment," *Physical Review Special Topics - Accelerators and Beams* **512** (12), 4201-4201 (2002).

QIANG, J., GARNETT, R. W., and RYNE, R. D., "A Systematic Comparison of Position and Time Dependent Macro-Particle Simulation in Beam Dynamics Studies," *Physical Review Special Topics - Accelerators and Beams* **5**, 6 (2002).

SCHMIERER, E. N., HAYNES, W. B., KRAWCZYK, F. L., GAUTIER, D. C., GIOIA, J. G., MADRID, M. A., LUJAN, R. E., CHAN, K. C. D., SCHRAGE, D., SMITH, B. G., et al., "Results of the APT RF Power Coupler Development for Superconducting Linacs," in *Proceedings of the 2001 Particle Accelerator Conference* **2**, 1110-12 (2001).

SCHRIBER, S. O., "One-Step Tuning Algorithm for pi-Mode Cavities," *Physical Review Special Topics - Accelerator and Beams* **4**, 122002 (2001).

SCHULTHEISS, T., COLE, M., RATHKE, J., WOOD, R., KRAWCZYK, F., LESLIE, P., and SCHRAGE, D., "RF/Thermal/Structural Analysis of the APT LEDA Hot Model Cavity Assembly," in *Proceedings of the 2001 Particle Accelerator Conference* **2**, 969-71 (2001).

SCHULZE, M. E., ALLEN, C. K., COLESTOCK, P. L., GILPATRICK, J. D., LYSENKO, W. P., RYBARCYK, L. J., SCHNEIDER, J. D., SHEFFIELD, R. L., SMITH, H. V., WANGLER, T. P., and CRANDALL, K. R., "Characterization of the Proton Beam from the 6.7-MeV LEDA RFQ," in *Proceedings of the 2001 Particle Accelerator Conference* **1**, 591-593 (2001).

SELLYEY, W. C., GILPATRICK, J. D., and SENIOR, R., "Bench Test of a Residual Gas Ionization Profile Monitor (RGIPM)," in *Proceedings of the 2001 Particle Accelerator Conference* **2**, 1318-1320 (2001).

SELLYEY, W. C., GILPATRICK, J. D., MARROQUIN, P. S., and GRUCHALLA, M. E., "Experience with Photomultiplier Base Beam Loss Monitors (PMBLM) at the Low-Energy Demonstration Accelerator (LEDA)," in *Proceedings of the 2001 Particle Accelerator Conference* **2**, 1315-1317 (2001).

SHURTER, R. B., COTE, T. J., and GILPATRICK, J. D., "Analog Front-End Electronics for Beam Position Measurement on the Beam Halo Measurement," in *Proceedings of the 2001 Particle Accelerator Conference* **2**, 1378-1380 (2001).

STISHOV, S. M., and SADKOV, Y. A., "A Compact Hydraulic Press to Use with High-Pressure Devices for Neutron Scattering Studies," *Instruments and Experimental Techniques* **45** (4), 573-575 (2002).

STISHOV, S. M., "A Reliable Valve for Application in High-Pressure Hydrostatic Installations," *Instruments and Experimental Techniques* **45** (6), 846-847 (2002).

SUGAI, I., TAKEDA, Y., OYAIZU, M., KAWAKAMI, H., OHMORI, C., HATTORI, T., KAWASAKI, K., BORDEN, M. J., and MACEK, R. J., "Development of Long-Lived Cluster and Hybrid Carbon Stripper Foils for High-Energy, High-Intensity Ion Beams," in *Proceedings of the Fifteenth Meeting of the International Collaboration on Advanced Neutron Sources* **1**, 257-68 (2001).

TAJIMA, T., CHAN, K. C. D., GENTZLINGER, R. C., HAYNES, W. B., KELLEY, J. P., KRAWCZYK, F. L., LAFAVE, R. P., MADRID, M. A., MONTOYA, D. I., SCHRAGE, D. L., and SHAPIRO, A. H., "Evaluation and Testing of a Low-Beta Spoke Resonator," in *Proceedings of the 2001 Particle Accelerator Conference* **2**, 903-905 (2001).

TAJIMA, T., CHAN, K. C. D., GENTZLINGER, R. C., HAYNES, W. B., KELLEY, J. P., KRAWCZYK, F. L., MADRID, M. A., MONTOYA, D. I., SCHRAGE, D. L., SHAPIRO, A. H., and MAMMOSSER, J., "Developments of 700-MHz 5-Cell Superconducting Cavities for APT," in *Proceedings of the 2001 Particle Accelerator Conference* **2**, 1119-21 (2001).

VALDIVIEZ, R., MARTINEZ, F. A., RENDON, A. M., WRIGHT, T. O., LEDFORD, J. E., PATTERSON, N. K., BRUHN, D. C., HAAGENSTAD, H., and GILPATRICK, J. D., "The Final Mechanical Design, Fabrication, and Commissioning of a Wire Scanner and Scraper Assembly for Halo-Formation Measurements in a Proton Beam," in *Proceedings of the 2001 Particle Accelerator Conference* **2**, 1324-1326 (2001).

WALSTROM, P. L., and COOK, E. G., "Extraction Kickers and Modulators for the Advanced Hydrotest Facility," in *Proceedings of the 2001 Particle Accelerator Conference* **3**, 2311-2313 (2001).

WANG, T.-S. F., CHANNELL, P. J., MACEK, R. J., and DAVIDSON, R. C., "Transverse Electron-Proton Two-Stream Instability in a Bunched Beam," in *Proceedings of the 2001 Particle Accelerator Conference* **1**, 704-706 (2001).

WANGLER, T. P., and QIANG, J., "Los Alamos Beam Halo Experiment: Comparing Theory, Simulation, and Experiment," in *Proceedings of the Advanced Accelerator Concepts Tenth Workshop* **647**, 878-883 (2002).

WANGLER, T. P., ALLEN, C. K., CHAN, K. C. D., COLE-STOCK, P. L., CRANDALL, K. R., GARNETT, R. W., GILPATRICK, J. D., LYSENKO, W. P., SCHNEIDER, J. D., SCHULZE, M. E., SHEFFIELD, R. L., and SMITH, H. V., "Experimental Study of Proton-Beam Halo Induced by Beam Mismatch in LEDA," in *Proceedings of the 2001 Particle Accelerator Conference* **4**, 2923-2925 (2001).

WANGLER, T. P., "Linac-Based Proton Drivers," in *20th ICFA International Beam Dynamics Workshop on High Intensity and High Brightness Hadron Beams* **642**, 43-47 (2002).

WAYNERT, J. A., BLUMENFELD, P. E., PRENGER, F. C., KELLEY, J. P., CURRIE, S. A., and STEWART, J. A., "Experimental Heat Leak Measurements on the APT 210-kW CW RF Power Coupler," in *Proceedings of the 2001 Joint Cryogenic Engineering Conference and International Cryogenic Materials Conference* **613A**, 540-547 (2002).

WEI, J., and MACEK, R. J., "Electron-Cloud Effects in High-Intensity Proton Accelerators," in *Proceedings of the Mini-Workshop on Electron-Cloud Simulations for Proton and Positron Beams* (CERN, 2002), 29-40.

Theses

BALCH, D. K., "X-Ray and Neutron Diffraction Studies of Syntactic Metal Foams and Metal Matrix Composites," Northwestern University, U.S.A. (December 2002).

CHANG, S. C., "Magnetic Transitions in Some Correlated-Electron Systems," New Mexico State University, U.S.A. (December 2002).

CHRISTIANSON, A., "Heavy Fermion Behavior in Selected Ce-Based Heavy Fermion Systems: Magnetism and Superconductivity," Colorado State University, U.S.A. (May 2003).

KELLEY, T., "Neutron Scattering from Uranium-Based Non-Fermi Liquid Systems," University of California at Riverside, U.S.A. (March 2002).

LIU, C.-Y., "A Superthermal Ultra-Cold Neutron Source," Princeton University, U.S.A. (June 2002).

MARONE, S., "Measurements of Neutron Capture Cross Sections at the n_TOF Facility at CERN," University of Bari, Italy (March 2003).

SUTTON, M. R., "High-Energy Neutron Dosimetry," Georgia Institute of Technology, U.S.A. (May 2001).

Prop ID	Title	PI Last Name	PI First Name	Instrument	Report Availability
2002539	Neutron Capture on Off-stable Nuclides	Rundberg	Robert	1FP14	Not available
2002553	Neutron Capture Measurements on (sup147)Pm and (sup151)Sm Using DANCE	Ullmann	John	1FP14	available
2002554	DANCE Development	Ullmann	John	1FP14	available
2002567	Neutron Induced Soft Error Rates in Microprocessors	Vrijen	Rutger	1FP4	Not Available
2002514	Improving Reaction Rates for Explosive Nucleosynthesis Studies via (n,a) Cross Section Measurements; Proof-of-Principle Experiment at LANSCE	Koehler	Paul	1FP5	available
2002516	Test of Gd Plasma Coatings as a Neutron Absorber for the NPDgamma Experiment	Penttila	Seppo	1FP5	Not Available
2002005	Investigation of Austenite Phase Transformation and Carbon Concentration Changes in Steel in the Intercritical Annealing Process	Vogel	Sven	1FP5	Not Available
2002081	Investigation of Pressure Dependence of Nuclear Resonances	Vogel	Sven	1FP5	Not Available
2002535	Sample Characterization for Dynamic Temperature Measurements Using Neutron Resonance Spectroscopy (NRS) on FP5	Yuan	Vincent	1FP5	available
2002524	High Energy Neutron Health Physics Survey Measurements at the Weapons Neutron Research Facility	Duran	Michael	4FP15L	Not Available
2002538	Inclusive (n,xn) Double-Differential Cross Section Measurement (II)	Ishibashi	Kenji	4FP15L	available
2002570	Identification of Neutron-induced Light Ion Spallation Products in CsI Using Pulse Shape Discrimination	McLean	Thomas	4FP15L	Not Available
2002522	Response of a High-Energy Neutron Dosimeter [see also 2002541 on FP30L-A]	Miles	Leslie	4FP15L	Not Available
2002518	Evaluation of Passive and Active Neutron Personnel Dosimeters	Olsher	Richard	4FP15L	available
2002551	The Response of Radiochromic Film to High Energy Neutrons	Walker	L. Scott	4FP15L	Not Available
2002550	Feasibility Studies for N-D Radiative Capture	Kovash	Michael	4FP15R	Not Available
2002525	Neutron-Deuteron Elastic Scattering and the Three-Nucleon Force	Matthews	June	4FP15R	Not Available
2002505	Cross Section Measurements for Cosmic Ray Studies Using Neutrons	Sisterson	Janet	4FP15R	available
2002513	Neutron-Induced Soft Errors in SRAM Devices	Abusaidi	Armin	4FP30L-A	available
2002564	Neutron-Induced Failures in Avionic Systems	Belcastro	Celeste	4FP30L-A	Not available
2002507	Neutron-Induced Single Event Characterization of 0.8-, 0.35- and 0.18-Micron CMOS Technology Integrated Circuits	Browning	John	4FP30L-A	available
2002503	Investigation into the Cosmic Ray Sensitivity of High Power Semiconductor Devices for Use in Aerospace and Terrestrial Applications	Coulbeck	Lee	4FP30L-A	Not Available
2002542	Neutron-induced Single-event Upsets and Transients in High-speed Digital Logic Integrated Circuits	Dodd	Paul	4FP30L-A	available
2002566	Neutron Soft Error Sensitivity Investigation of SRAM based programmable logic devices with embedded user memory.	Euzent	Bruce	4FP30L-A	Not available
2002540	Atmospheric Neutron Sensitivity Measurements of Advanced Silicon Sub-micron CMOS Technologies	Fabula	Joseph	4FP30L-A	available
2002561	Study of SOI and Bulk Technologies - Influence of Integration	Ferlet-Cavr	Veronique	4FP30L-A	Not Available
2002543	Neutron Accelerator Soft-error Test of Deep Sub-micron Semiconductor Electron Device	Fujii	Tatsuya	4FP30L-A	available
2002509	Accelerated Neutron Testing of Single Event Upsets in Semiconductor Devices	Hareland	Scott	4FP30L-A	Not Available
2002568	Experiments on the Effects of High Energy Neutrons on SRAM Components in HP AlphaServer ES45 Computer Systems Similar to Those Deployed in ASCI-Q Systems in Los Alamos	Harris	Kevin	4FP30L-A	Not Available
2002501	Single Event Effects Studies on Commercial Electronic Memories and Field Programmable Gate Arrays	King	Douglas	4FP30L-A	available

2002502	Neutron SEU and SEL Testing of Commercial SRAMs and Logic Devices	Kravetz	John	4FP30L-A	available
2002565	Single Event Upset in High End Memories SRAM (.13 mu m)	Lauzeral	Olivier	4FP30L-A	available
2002512	Neutron Accelerated Soft Error Rate for Different Memory Technologies	Ma	Manny	4FP30L-A	available
2002541	Response of a High-Energy Neutron Dosimeter [see also 2002522 on FP15L]	Miles	Leslie	4FP30L-A	Not Available
2002506	Neutron-Induced Failure Tests of IGBT Devices	Reass	William	4FP30L-A	Not Available
2002510	Accelerated Tests of the Cosmic Component of Soft Errors in Logical ICs with Embedded DRAM and SRAM Arrays	Schindlbeck	Guenter	4FP30L-A	available
2002521	Development of SEU Cross Sections and Proportional Dose Effects Measurements in an Incrementally Hardened Neutron Beam [see also 2002530 on FP90L]	Wilkins	Richard	4FP30L-A	Not Available
2002523	Development of Comparative Effect Curves Due to Varying Thickness of Intervening Materials	Wilkins	Richard	4FP30L-A	Not Available
2002528	Prompt Fission Neutron Measurements from 235U at WNR Energies	Ethvignot	Thierry	4FP30R	Not Available
2002544	(n,z) Reactions from Threshold to 50 MeV	Haight	Robert	4FP30R	available
2002546	Nuclear Level Densities Studied Through (nxgamma) Reactions at FIGARO	Haight	Robert	4FP30R	available
2002556	Measurement of Prompt Gamma Rays from Neutron-Induced Fission of Uranium and Other Actinides	Nelson	Ronald	4FP30R	available
2002557	Study of (sup18)O(n,2ngamma) with GEANIE	Becker	John	4FP60R	Not available
2002562	Preliminary Study of (sup151)Eu(n,2ngamma) with GEANIE	Becker	John	4FP60R	Not Available
2002558	Measurement of the (sup150)Sm(n,2n)(sup149)Sm Cross Section	Cooper	Jeff	4FP60R	available
2002548	Measurement of the 233U(n,2n) Cross Section with gammagamma Coincidences	Devlin	Matthew	4FP60R	Not Available
2002527	Intermediate Energy Neutron Induced Fission: Fragment Yields & New Isomers	Ethvignot	Thierry	4FP60R	Not Available
2002569	Measurement of (n, xngamma) Cross Sections of Natural Fe	Fotiadis	Nikolaos	4FP60R	Not Available
2002549	Investigation of (sup232)Th via the (n,n'gamma) Reaction and Neutron-Induced Fission Studies	Garrett	Paul	4FP60R	available
2002563	Classified Proposal #2002563	Hill	Tony	4FP60R	available
2002555	Measurement of (sup191)Ir(n,n'gamma), (n,2ngamma), (n,3ngamma), and (n,4ngamma) Cross	Nelson	Ronald	4FP60R	available
2002559	Test of Big Bang Nucleosynthesis Mode Predictions by Precision Measurement of the (n+p)->(d+gamma) Cross Section	Esch	Ernst	4FP90L	Not Available
2002519	The Development of a Database of Neutron-induced Gamma-ray Yields for Elements of Interest in General PGNAA Measurements	McGrath	Christophe	4FP90L	Not Available
2002530	Development of SEU Cross Sections and Proportional Dose Effects Measurements in an Incrementally Hardened Neutron Beam [see also 2002521 on 4FP30L-A]	Wilkins	Richard	4FP90L	Not Available
2002074	Magnetic Structure Determination of the Heavy-Fermion Antiferrmagnet Ce2RhIn8 Using Polarized Neutrons	Bao	Wei	ASTERIX	Not Available
2002099	Magnetic Coupling in Metal/Native Oxide Multilayers	Beach	Geoffrey	ASTERIX	Not Available
2002045	Understanding Exchange Bias Through Control of Uncompensated Moments in Dilute Antiferromagnets	Fitzsimmon	Michael	ASTERIX	available
2002046	How is Frozen Magnetization Correlated with Exchange Bias?	Fitzsimmon	Michael	ASTERIX	available
2002049	Quantifying Spatial Distribution of Magnetization in Spintronic Materials	Fitzsimmon	Michael	ASTERIX	available
2002014	Magnetization Depth Profiling in Modulation Doped Colossal Magnetoresistive Manganites	Hoffmann	Axel	ASTERIX	available
2002230	Order Parameter Measurement of d=3 Random-Field Ising Antiferromagnet Fe(sub0.8)Zn(sub0.2)F(sub2) Thin Films	Lederman	David	ASTERIX	available
2002007	Thickness Dependent Magnetization Reversal Asymmetry in Exchange Biased Bilayers	Leighton	Christophe	ASTERIX	Not Available

2002008	Coercive Mechanisms in NiMn/ferromagnet Bilayers and Epitaxial Superlattices	Leighton	Christophe	ASTERIX	Not Available
2002010	Probing Depth Dependent Magnetism in Ferromagnet/GaAs Epitaxial Heterostructures	Palmstrom	Chris	ASTERIX	available
2002150	Strain Driven Spin Reorientation Transitions in Co Thin Films	Park	Sungkyun	ASTERIX	available
2002545	Production of (sup148)Gd by 800-MeV Protons on Tungsten	Corzine	R. Karen	Blue Room	Not Available
2002504	Mercury Target Thermal Shock Tests	Haines	John	Blue Room	available
2002511	Oxide Film Dielectric Properties: The Influence Proton Irradiation on the Corrosion Kinetics of Structural Materials in LBE Coolant Systems	Lillard	R. Scott	Blue Room	Not Available
2002517	Neutron Spallation Target Experiments in Support of the Advanced Accelerator Applications (AAA) Programs	Morgan	George	Blue Room	Not Available
2002547	Lujan Center Mark-III Target System Experiments	Russell	Gary	Blue Room	Not Available
2002560	Effects of a Pulsed Proton Beam on Liquid Lead-Bismuth Eutectic Target	Tcharnotsk	Valentina	Blue Room	Not Available
2002532	Neutron Resonance Spectroscopy (NRS) Measurement of Temperature Rise at a Sliding Interface at high Pressure and Velocities.	Yuan	Vincent	Blue Room	available
2002534	Measurement of Metal Jet Temperatures Using Neutron Resonance Spectroscopy (NRS)	Yuan	Vincent	Blue Room	available
2002160	Hydrogenation of Acetylene by Metal Catalysts	Chinta	Sivadinara	FDS	Not Available
2002163	Proton Dynamics in Very Short Hydrogen Bonds	Eckert	Juergen	FDS	Not Available
2002168	Hydrogen Dynamics in the New Hydrogen Storage Material Ti-doped Sodium Aluminium Hydride	Jensen	Craig	FDS	Not Available
2002165	Hydroxylation of MgO Surfaces	Larese	John	FDS	Not Available
2002032	Using Inelastic Neutron Scattering for Structural Characterization of Synthetic Binary and Ternary Metal Cyanides	Williams	Darrick	FDS	Not Available
2002033	Using Inelastic Neutron Scattering for Structural Characterization of Synthetic Binary and Ternary Metal Cyanates	Williams	Darrick	FDS	Not Available
2002022	Effect of Texture Randomization Processing on the Deformation Mode Activity in Magnesium Alloys	Agnew	Sean	HIPD	available
2002229	Phase Equilibria and Kinetics of Carbon Doixide and Natural Gas Clathrates	Bobev	Svilen	HIPD	Not Available
2002051	High Pressure and Temperature Investigations in the Mn(subx)Fe(sub1-x)S Solid Solution	Ehm	Lars	HIPD	Not Available
2002087	Texture Development and Phase Transformation in Shock Loaded Zirconium	Gray	George	HIPD	Not Available
2002158	High Pressure Induced Phase Transformations in the Alkaline Earth Dihydrides MgD2, CaD2 and SrD2	Kohlmann	Holger	HIPD	Not Available
2002164	Deformation Behavior of Superalloys: Micro-strain Measurements, Dislocation Mechanisms, and Modeling [See also 2002118 on SMARTS]	Majumdar	Bhaskar	HIPD	Not Available
2002148	Water in Constituents of Yucca Mountain Tuff	McCall	Katherine	HIPD	Not Available
2002060	Study of the Atomic Structure of Nanocrystals Using Large-Q Diffraction and RDF Analysis	Palosz	Witold	HIPD	Not Available
2002006	Investigation of Texture in Equal-Channel Angular Pressed (ECAP) Materials	Vogel	Sven	HIPD	Not Available
2002037	Study of P-T Diagrams of Si, Ge, SiGe Alloys and Kinetics of Their Reaction with Diamond at High Pressures and Temperatures	Zerda	T. Waldek	HIPD	Not Available
2002095	Texture Evolution During ECAP'ing of Beryllium	Alexander	David	HIPPO	Not Available
2002094	Microstructural Evolution of Metals During ECAPing	Beyerlein	Irene	HIPPO	Not Available
2002052	Phase Separation and Superconductivity in Mg(sub1-x)Al(subx)B(sub2)	Billinge	Simon J.	HIPPO	available
2002053	Average and Local Structure of the Intermediate and High-Temperature Phases of Rb(sub3)D(SeO(sub4))sub2	Billinge	Simon J.	HIPPO	available
2002025	High-Pressure Crystal Chemistry of Clathrates	Bish	David	HIPPO	Not Available
2002096	Texture Evolution in Beryllium as a Function of Deformation [see also 2002102 on HIPD]	Blumenthal	William	HIPPO	Not Available

2002098	Investigation of the Nature of Doped Charge Distribution and the Possibility of Local Stripe Correlations in Underdoped La{sub2-x}Sr{subx}CuO{sub4}	Bozin	Emil	HIPPO	Not Available
2002038	Deformation Texture of Plutonium (see also 2002041 on HIPD)	Brown	Donald	HIPPO	Not Available
2002068	A Neutron Diffraction Study On (K, Na, H3O) Jarosite Solid Solutions	Drouet	Christophe	HIPPO	Not Available
2002146	Coordination Environments That Accommodate Be: The Crictical Role of Ca for Be Occupancy in Crystalline Materials	Evensen	Joseph	HIPPO	Not Available
2002091	Texture in U6Nb in High Temperature Beta Phase	Field	Robert	HIPPO	Not Available
2002013	Neutron Powder Diffraction Determination of the Laumontite Crystal Structure Under Elevated Temperature and Pressure Conditions	Fridriksson	Thrainn	HIPPO	Not Available
2002086	Texture in HE-driven Shock-loaded 316 SS and U-6Nb	Gray	George	HIPPO	Not Available
2002039	Atomic Structure of CsC(sub60) by the Rietveld and Pair Distribution Function (PDF) Analysis	Jeong	Il-Kyoung	HIPPO	available
2002140	In-Situ Investigation of the Local Phase Transition of Pb(Mg(sub1/3)Nb(sub2/3))O(sub3) Near Burns Temperature Using Neutron Pair Distribution Function (PDF) Analysis	Jeong	Il-Kyoung	HIPPO	available
2002123	Experimental Analysis of the Evolution of Radiogenically Produced Helium in Erbium Dihydride Films	Mangan	Michael	HIPPO	available
2002147	Phase Transition in U-6Nb Under Hydrostatic Pressure?	Manley	Michael	HIPPO	Not Available
2002126	Structure Determinations of New Hydrogen Clathrates	Mao	Wendy	HIPPO	available
2002031	Internal Strains in Co-deformed Two Phase Compounds	Mecking	Heinrich	HIPPO	available
2002097	Critical Experiments for the Assessment of Elastic Moduli in a Multiphase Metallic Alloy Using In Situ Neutron Diffraction	Miller	Matthew	HIPPO	Not Available
2002154	Kinetics, Texture, and Decomposition of Ettringite	Monteiro	Paulo	HIPPO	Not Available
2002111	Structure and Local Ordering of Metal Sites in Zeolites and Nanoporous Materials	Ott	Kevin	HIPPO	Not Available
2002107	Flow-related Microlite Preferred Orientation in Lavas	Pehl	Jenny	HIPPO	available
2002036	Local Structure of Zeolite Beta	Peral	Immaculad	HIPPO	Not Available
2002054	Rare-Earth Substituted PZT	Rodriguez	Mark	HIPPO	available
2002057	In-Situ Neutron Diffraction Study of Sony LI-ion Batteries	Rodriguez	Mark	HIPPO	available
2002131	Structure and Texture Investigation of Phases Ni(sub 53) Ti(sub 47) and in IrTi	Schmahl	Wolfgang	HIPPO	Not Available
2002122	Texture of Rocks from the Santa Rosa Mylonite Zone	Shomglin	Kome	HIPPO	Not Available
2002162	Search for the Atomic-Level/Microscopic Source of "Slow Dynamical" Recovery Processes in Geomaterials	Tencate	James	HIPPO	available
2002104	Texture and Internal Strain development in Uranium Alloy Samples [see also 2002092 on SMARTS]	Teter	David	HIPPO	Not Available
2002089	Texture Changes During the alpha-beta Phase Transformation in Quartz	Wenk	Hans-Rud	HIPPO	available
2002066	High-Temperature Neutron Diffraction Studies on NaTixNb1-xO3-0.5x Perovskites	Xu	Hongwu	HIPPO	Not Available
2002016	Thermoelastic Equation of State of b.c.c. Refractory Metal and U-238	Zhao	Yusheng	HIPPO	available
2002017	High Pressure Crystal Chemistry of Hydrous Minerals	Zhao	Yusheng	HIPPO	Not Available
2002019	Development of High P-T Capability for Neutron Powder Diffraction Studies with HIPPO and TAP-98	Zhao	Yusheng	HIPPO	Not Available
2002183	Investigation of Radiogenically Produced (sup3)He in Erbium Dihydride Systems: Depth Profiling using Neutron Reflectometry	Browning	James	LQD	available
2002210	Investigation of Carbon Black Flocculation in Rubber Composites	Gerspache	Michel	LQD	Not Available
2002209	SANS Investigation of Hydride Formation Mechanisms in Uranium Alloys	Hanrahan	Robert	LQD	Not Available
2002187	Characterization of Protein/Phospholipid Complexes by SANS	Kirchhoff	Carol	LQD	Not Available

2002193	The Ultra-structural Arrangement of Chitin and Protein in the Pen from a Giant Squid	Langan	Paul	LQD	Not Available
2002194	SANS Study of Internal Void Structures in HMX and RDX	Mang	Joseph	LQD	available
2002195	SANS Studies of the Microstructure of HMX-based Composite Energetic Materials	Mang	Joseph	LQD	Not Available
2002178	Pressure Effects on Block Copolymer Order/Disorder Transition	Mayes	Anne	LQD	Not Available
2002186	Structural Analysis of Nanoarchitectures in Porous and Block Copolymer	Mercer-Sm	Janet	LQD	available
2002189	Characterization of Micellar Drug Delivery Systems by Small-Angle Neutron Scattering	Onyuksel	Hayat	LQD	Not Available
2002191	SANS Study of the Structure of Estane	Orler	E. Bruce	LQD	Not Available
2002192	Experiments on the Structure of Polyester Polyurethanes	Orler	E. Bruce	LQD	Not Available
2002190	Interactions in Charge-Stabilized Colloidal Dispersions	Wu	Jianzhong	LQD	Not Available
2002215	Phase Separation and Superconductivity in Mg(sub 1-x)A1(sub x)B(sub 2)	Billinge	Simon J.	NPDF	Not Available
2002216	Average and Local Structure of the Intermediate and High-temperature Phases of Rb(sub 3)D(SeO(sub 4))(sub 2)	Billinge	Simon J.	NPDF	Not Available
2002217	High Resolution Atomic Pair Distribution Function Round Robin	Billinge	Simon J.	NPDF	Not Available
2002225	Preliminary Search for Amorphous Constituents of Rocks Using PDF Analysis	Darling	Tim	NPDF	Not Available
2002226	Structure of Mixed Valence Perovskites and Ceria-Zirconia Nonopowders	Dmowski	Wojtek	NPDF	Not Available
2002221	Local Structure of Superconducting Cuprates with Stripes	Egami	Takeshi	NPDF	Not Available
2002222	Local Structure of Frustrated Magnet, LiNiO(sub2)	Egami	Takeshi	NPDF	Not Available
2002223	Local Structure of CMR Manganites	Egami	Takeshi	NPDF	Not Available
2002201	In-Situ Investigation of the Local Phase Transition of Pb(Mg(sub1/3)Nb(sub 2/3)O(sub 3) Near Burns Temperature Using Neutron Pair Distribution Function (PDF) Analysis	Jeong	Il-Kyoung	NPDF	available
2002202	Neutron Pair Distribution Function (PDF) Study on the Role of Local Structural Change in the Parraelectric-to-Ferroelectric-to Relaxor Phase Transition of the Sr(sub 1-x)Ca(sub x)Ca(sub x)TiO(sub 3)	Jeong	Il-Kyoung	NPDF	available
2002204	Local Lattice Distortions Induced by Frustration in ZrCr(sub 2)O(sub 4)	Louca	Despo	NPDF	Not Available
2002235	Structure of Amorphous Metallic Glasses	Louca	Despo	NPDF	Not Available
2002206	Local Structure of Nano Crystalline Clay Particles	Neder	Reinhard	NPDF	Not Available
2002205	Local Structure of Nano-crystalline (li,D)(sub x)MnO(sub 2) Battery Material from Analysis of PDF Data	Parise	John	NPDF	Not Available
2002207	The Local Structure of "Amorphous" FeS	Parise	John	NPDF	Not Available
2002208	Origin of Ionic Conductivity in Cs(sub 14) (super 6)Li(sub 24)[Si(sub 72) (super 7)Li(sub 18)O(sub 172)]: Exchange between (super 7)Li and (super 6)Li in Channel and Framework Sites, Respectively at High Temperature Using PDF	Parise	John	NPDF	Not Available
2002228	Local Structure in Semiconductor Alloys	Peterson	Peter	NPDF	Not Available
2002218	High Resolution, Hi-Q Study of the Structure of Potassium Niobate Tellurite Glass Ceramic	Zwanziger	Joe	NPDF	Not Available
2002067	Comparative Hydrogen Position Studies Using X-rays and Neutrons	Bunick	Gerard	PCS	available
2002015	Investigation of Catalysis of E. Coli DHFR and Yeast PGK by Neutron Diffraction	Dealwis	Chris	PCS	Not Available
2002077	Binding Studies with Immune Protein Fragments	Edmundso	Allen	PCS	available
2002063	Structural Characterisation of Crystals of Alpha-glycine During Anomalous Electrical Behaviour	Langan	Paul	PCS	Not Available
2002167	Neutron Diffraction Studies of the Hydration of Z-DNA Duplex d(CGCGCG)	Langan	Paul	PCS	Not Available
2002064	Charge States in the Active Site of Orotidine 5'monophosphate Decarboxylase	Pai	Emil	PCS	available

2002093	Rubredoxin Crystallography in TOF Neutron Measurement	Tanaka	Ichiro	PCS	available
2002065	Determination of Hydrogens and Bound Water Molecules in Photosynthetic Reaction Center Complex by Neutron Diffraction	Thiyagaraja	Pappanna	PCS	Not Available
2002138	Phonons in High-Temperature Superconductors	Egami	Takeshi	PHAROS	available
2002143	Phonons in Ni at Elevated Temperature - Analysis of Coherent Scattering	Fultz	Brent	PHAROS	available
2002213	Crystal Field Levels in (U, Th)O2	Lander	Gerard	PHAROS	Not Available
2002001	Quasielastic Scattering in CeRhin(sub5)	Lawrence	Jon	PHAROS	available
2002042	Deep Inelastic Scattering from Helium Fluid Under Pressure	McQueene	Robert	PHAROS	Not Available
2002040	Sound Waves in Highly Viscous Liquids	Russina	Margarita	PHAROS	Not Available
2002009	Neutron Brillouin Scattering on a Polymeric Glass Former	Zorn	Reiner	PHAROS	Not Available
2002211	Search of the Structure and Magnetic Structure of UNi1-xRux and UNi1-xRhxAl Systems	Alsmadi	Abdel	SCD	Not Available
2002083	Crystal Structure of RPtSn Compounds (R=Ce,Pr,Nd)	Janousova	Blanka	SCD	Not Available
2002137	Neutron Diffraction of Single-Crystal FeO at High Pressures and Low Temperatures - Investigation of Paramagnetic - Antiferromagnetic Transitions	Mao	Ho-Kwang	SCD	Not Available
2002212	Pressure Dependence of Structure and Magnetic Structure in Single Crystalline LaSrFe04	Takabatake	Toshiro	SCD	Not Available
2002170	In-Situ Neutron Single-Crystal Diffraction Study on Methane-Hydrogen Clathrates at High Pressures	Xu	Jian	SCD	available
2002106	Effect of Texture Randomization Processing on the Deformation Mode Activity in Magnesium Alloys	Agnew	Sean	SMARTS	available
2002103	Texture Evolution During ECAP'ing of Beryllium	Alexander	David	SMARTS	Not Available
2002145	Investigation of Elastic/Plastic Behavior of Pure Uranium	Balzar	Davor	SMARTS	Not Available
2002085	High Temperature Deformation of Beryllium	Brown	Donald	SMARTS	available
2002088	Residual Strains in Welded Stainless Steel Parts	Brown	Donald	SMARTS	Not Available
2002153	Load Partitioning in a Ti-6A1-4V/SiC Composite During Uniaxial Tensile Loading at Elevated Temperature	Choo	Hahn	SMARTS	Not Available
2002012	Deformation Mechanisms of Titanium as a Function of Temperature	Daymond	Mark	SMARTS	available
2002180	Determination of Residual Stresses in Green Bodies of Steel Powder After High Speed Compaction	Ericsson	Torsten	SMARTS	Not Available
2002108	Residual Stress Mapping in Single Crystal S-FAP Boules Used for Laser Amplification	Hill	Michael	SMARTS	available
2002082	Neutron Diffraction Measurements of Bulk Internal Strains in TiAl-Based Low Symmetry Composite Materials	Kad	Bimal	SMARTS	Not Available
2002011	Load Sharing in Cemented Carbide Composites	Krawitz	Aaron	SMARTS	available
2002179	Determination of Strain Pole Figures From Compressed Steel Samples	Larsson	Cecilia	SMARTS	Not Available
2002118	Deformation Behavior of Superalloys: Micro-strain Measurements, Dislocation Mechanisms, and Modeling [See also 2002164 on HIPPO]	Majumdar	Bhaskar	SMARTS	available
2002136	Critical Experiments for the Assessment of Elastic Moduli in a Multiphase Metallic Alloy Using In-Situ Neutron Diffraction	Miller	Matthew	SMARTS	Not Available
2002130	Deformation of Calcium Hydroxide Crystal Lattice in Hydrated Cement Paste	Monteiro	Paulo	SMARTS	Not Available
2002177	Validation of Residual Stress Predictions in Heat Treated Components and Correlation to Distortion Effects	Nash	Philip	SMARTS	Not Available
2002127	Residual Stress Mapping in Two Stainless Steel Pipe Welds Fabricated from Electron Beam Welding	Rangaswai	Partha	SMARTS	Not Available
2002028	Residual Stresses in Zircaloy-4 Weldments	Ripley	Maurice	SMARTS	available
2002029	Measurements of the Strain Response to Applied Stress in Zircaloy-4	Ripley	Maurice	SMARTS	available
2002152	Primary Creep Behavior of a Precipitation Strengthened Titanium Aluminide	Seo	Dongyi	SMARTS	Not Available

2002161	Investigation of Stress-Strain During the Elastic and Plastic Deformation of Marble, Limestone, and Sandstone	Tencate	James	SMARTS	available
2002092	Texture and Internal Strain Development in Uranium Alloy Samples [see also 2002104 on HIPPO]	Teter	David	SMARTS	available
2002084	Aging in Uranium Niobium Alloys	Thoma	Dan	SMARTS	available
2002155	Shape Memory Behavior in U-Nb Alloys	Thoma	Dan	SMARTS	available
2002169	Effect of Beam Divergence on Strain Data from SMARTS	Ustundag	Ersan	SMARTS	Not Available
2002173	In-Situ Deformation of Bulk-Metallic Glass-Matrix Composites	Ustundag	Ersan	SMARTS	Not Available
2002056	In Situ Neutron Diffraction Study of Shape-Memory Alloys at Cryogenic Temperatures	Vaidyanath	Rajan	SMARTS	Not Available
2002059	In-Situ Neutron Diffraction Study of the Linear-Superelastic-Effect in Shape-Memory Alloys	Vaidyanath	Rajan	SMARTS	Not Available
2002004	Investigation of Strain in Equal-Channel Angular Pressed (ECAP) Materials	Vogel	Sven	SMARTS	Not Available
2002113	Structure of Freely Suspended Lipid Multilayer Films Over Nanoporous Polymer Films	Baker	Shenda	SPEAR	Not Available
2002002	Neutron Reflectivity from Langmuir Monolayers of a Synthetic Electron Transfer Protein	Blasie	J. Kent	SPEAR	available
2002100	Investigation of Radiogenically Produced {sup3}He in Erbium Dihydride Systems: Depth Profiling Using Neutron Reflectometry	Browning	James	SPEAR	available
2002182	Neutron Reflectivity Studies on the Interface Between Water and Biocompatible, Rigid Organic Monolayer Films	Grunze	Michael	SPEAR	available
2002233	Neutron Reflectivity Studies on the Interface Between Water and Biocompatible, Rigid Organic Monolayer Films	Grunze	Michael	SPEAR	Not Available
2002129	Electrical Double Layer Formation Near Electrified Surfaces	Hamilton	William	SPEAR	Not Available
2002125	Probing the Interphase Structure in the Oxidation of Glucose at a Platinum Electrode	Ingersoll	David	SPEAR	Not Available
2002115	Probing the Structure of Organosilane Films and Silane/Resin Interphases by X-ray and Neutron Reflection	Kent	Michael	SPEAR	available
2002116	Probing Crosslink Density Gradients in Thin Epoxy Films on Aluminum Using Neutron Reflection	Kent	Michael	SPEAR	available
2002120	Molecular Density and Orientation in Confined Polymer Layers Under Static and Dynamic (flow) Conditions	Kuhl	Tonya	SPEAR	Not Available
2002121	Neutron Reflectometry Studies of Binding and Penetration of Lipid Membranes by Cholera Toxin	Kuhl	Tonya	SPEAR	Not Available
2002139	The Structure of Charged Polymer Brushes Created via the Adsorption of Polymeric Surfactants	Li	Feng	SPEAR	Not Available
2002142	The Segment Density Profile and Counterion Cloud of Polyelectrolyte Brushes	Li	Feng	SPEAR	Not Available
2002003	Field Driven Phase Transitions in Monolayers and Bilayers of Amphiphiles at Electrode Surfaces	Lipkowski	Jacek	SPEAR	Not Available
2002124	Experimental Observation of Hydrogen Diffusion in Scandium Dideuteride Thin Films Using Neutron Reflectometry	Mangan	Michael	SPEAR	available
2002172	Structure of Synthesized Non-Linear Optical Films	Robinson	Jeanne	SPEAR	available
2002135	Neutron Time Distribution and Absolute Neutron Spectrum [see also 2002133 on HIPD and 2002134 on HIPPO]	Russell	Gary	SPEAR	Not Available
2002109	Morphology of Toughened Anti-Corrosion Films	Schaefer	Dale	SPEAR	available
2002114	Structure of Nanoporous Polymer Supported Lipid Bilayers	Smith	Gregory	SPEAR	Not Available
2002128	Electrosorption of Common Surfactant and Ionic Liquid Molecules from Aqueous Solutions	Tsouris	Costas	SPEAR	available
2002055	Polymer Processing in Supercritical CO(sub2): Block Copolymer Phase Ordering and Diffusion and Reaction in Interfaces	Watkins	James	SPEAR	Not Available

Prop ID	Title	PI Last Name	PI First Name	Instrument	Report Availability
2002513	Neutron-Induced Soft Errors in SRAM Devices	Abusaidi	Armin	4FP30L-A	available
2002022	Effect of Texture Randomization Processing on the Deformation Mode Activity in Magnesium Alloys	Agnew	Sean	HIPD	available
2002106	Effect of Texture Randomization Processing on the Deformation Mode Activity in Magnesium Alloys	Agnew	Sean	SMARTS	available
2002095	Texture Evolution During ECAP'ing of Beryllium	Alexander	David	HIPPO	Not Available
2002103	Texture Evolution During ECAP'ing of Beryllium	Alexander	David	SMARTS	Not Available
2002211	Search of the Structure and Magnetic Structure of UNi1-xRux and UNi1-xRhxAl Systems	Alsmadi	Abdel	SCD	Not Available
2002113	Structure of Freely Suspended Lipid Multilayer Films Over Nanoporous Polymer Films	Baker	Shenda	SPEAR	Not Available
2002145	Investigation of Elastic/Plastic Behavior of Pure Uranium	Balzar	Davor	SMARTS	Not Available
2002074	Magnetic Structure Determination of the Heavy-Fermion Antiferrmagnet Ce2RhIn8 Using Polarized Neutrons	Bao	Wei	ASTERIX	Not Available
2002099	Magnetic Coupling in Metal/Native Oxide Multilayers	Beach	Geoffrey	ASTERIX	Not Available
2002557	Study of (sup18)O(n,2ngamma) with GEANIE	Becker	John	4FP60R	Not available
2002562	Preliminary Study of (sup151)Eu(n,2ngamma) with GEANIE	Becker	John	4FP60R	Not Available
2002564	Neutron-Induced Failures in Avionic Systems	Belcastro	Celeste	4FP30L-A	Not available
2002094	Microstructural Evolution of Metals During ECAPing	Beyerlein	Irene	HIPPO	Not Available
2002052	Phase Separation and Superconductivity in Mg(sub1-x)Al(subx)B(sub2)	Billinge	Simon J.	HIPPO	available
2002053	Average and Local Structure of the Intermediate and High-Temperature Phases of Rb(sub3)D(SeO(sub4))sub2	Billinge	Simon J.	HIPPO	available
2002215	Phase Separation and Superconductivity in Mg(sub 1-x)A1(sub x)B(sub 2)	Billinge	Simon J.	NPDF	Not Available
2002216	Average and Local Structure of the Intermediate and High-temperature Phases of Rb(sub 3)D(SeO(sub 4))(sub 2)	Billinge	Simon J.	NPDF	Not Available
2002217	High Resolution Atomic Pair Distribution Function Round Robin	Billinge	Simon J.	NPDF	Not Available
2002025	High-Pressure Crystal Chemistry of Clathrates	Bish	David	HIPPO	Not Available
2002002	Neutron Reflectivity from Langmuir Monolayers of a Synthetic Electron Transfer Protein	Blasie	J. Kent	SPEAR	available
2002096	Texture Evolution in Beryllium as a Function of Deformation [see also 2002102 on HIPD]	Blumenthal	William	HIPPO	Not Available
2002229	Phase Equilibria and Kinetics of Carbon Doixide and Natural Gas Clathrates	Bobev	Svilen	HIPD	Not Available
2002098	Investigation of the Nature of Doped Charge Distribution and the Possibility of Local Stripe Correlations in Underdoped La{sub2-x}Sr{subx}CuO{sub4}	Bozin	Emil	HIPPO	Not Available
2002038	Deformation Texture of Plutonium (see also 2002041 on HIPD)	Brown	Donald	HIPPO	Not Available
2002085	High Temperature Deformation of Beryllium	Brown	Donald	SMARTS	available
2002088	Residual Strains in Welded Stainless Steel Parts	Brown	Donald	SMARTS	Not Available
2002100	Investigation of Radiogenically Produced {sup3}He in Erbium Dihydride Systems: Depth Profiling Using Neutron Reflectometry	Browning	James	SPEAR	available
2002183	Investigation of Radiogenically Produced (sup3)He in Erbium Dihydride Systems: Depth Profiling using Neutron Reflectometry	Browning	James	LQD	available
2002507	Neutron-Induced Single Event Characterization of 0.8-, 0.35- and 0.18-Micron CMOS Technology Integrated Circuits	Browning	John	4FP30L-A	available
2002067	Comparative Hydrogen Position Studies Using X-rays and Neutrons	Bunick	Gerard	PCS	available
2002160	Hydrogenation of Acetylene by Metal Catalysts	Chinta	Sivadinara	FDS	Not Available
2002153	Load Partitioning in a Ti-6A1-4V/SiC Composite During Uniaxial Tensile Loading at Elevated Temperature	Choo	Hahn	SMARTS	Not Available

2002558	Measurement of the (sup150)Sm(n,2n)(sup149)Sm Cross Section	Cooper	Jeff	4FP60R	available
2002545	Production of (sup148)Gd by 800-MeV Protons on Tungsten	Corzine	R. Karen	Blue Room	Not Available
2002503	Investigation into the Cosmic Ray Sensitivity of High Power Semiconductor Devices for Use in Aerospace and Terrestrial Applications	Coulbeck	Lee	4FP30L-A	Not Available
2002225	Preliminary Search for Amorphous Constituents of Rocks Using PDF Analysis	Darling	Tim	NPDF	Not Available
2002012	Deformation Mechanisms of Titanium as a Function of Temperature	Daymond	Mark	SMARTS	available
2002015	Investigation of Catalysis of E. Coli DHFR and Yeast PGK by Neutron Diffraction	Dealwis	Chris	PCS	Not Available
2002548	Measurement of the 233U(n,2n) Cross Section with gammagamma Coincidences	Devlin	Matthew	4FP60R	Not Available
2002226	Structure of Mixed Valence Perovskites and Ceria-Zirconia Nonopowders	Dmowski	Wojtek	NPDF	Not Available
2002542	Neutron-induced Single-event Upsets and Transients in High-speed Digital Logic Integrated Circuits	Dodd	Paul	4FP30L-A	available
2002068	A Neutron Diffraction Study On (K, Na, H3O) Jarosite Solid Solutions	Drouet	Christophe	HIPPO	Not Available
2002524	High Energy Neutron Health Physics Survey Measurements at the Weapons Neutron Research Facility	Duran	Michael	4FP15L	Not Available
2002163	Proton Dynamics in Very Short Hydrogen Bonds	Eckert	Juergen	FDS	Not Available
2002077	Binding Studies with Immune Protein Fragments	Edmundso	Allen	PCS	available
2002138	Phonons in High-Temperature Superconductors	Egami	Takeshi	PHAROS	available
2002221	Local Structure of Superconducting Cuprates with Stripes	Egami	Takeshi	NPDF	Not Available
2002222	Local Structure of Frustrated Magnet, LiNiO(sub2)	Egami	Takeshi	NPDF	Not Available
2002223	Local Structure of CMR Manganites	Egami	Takeshi	NPDF	Not Available
2002051	High Pressure and Temperature Investigations in the Mn(subx)Fe(sub1-x)S Solid Solution	Ehm	Lars	HIPD	Not Available
2002180	Determination of Residual Stresses in Green Bodies of Steel Powder After High Speed Compaction	Ericsson	Torsten	SMARTS	Not Available
2002559	Test of Big Bang Nucleosynthesis Mode Predictions by Precision Measurement of the (n+p)->(d+gamma) Cross Section	Esch	Ernst	4FP90L	Not Available
2002527	Intermediate Energy Neutron Induced Fission: Fragment Yields & New Isomers	Ethvignot	Thierry	4FP60R	Not Available
2002528	Prompt Fission Neutron Measurements from 235U at WNR Energies	Ethvignot	Thierry	4FP30R	Not Available
2002566	Neutron Soft Error Sensitivity Investigation of SRAM based programmable logic devices with embedded user memory.	Euzent	Bruce	4FP30L-A	Not available
2002146	Coordination Environments That Accommodate Be: The Crictical Role of Ca for Be Occupancy in Crystalline Materials	Evensen	Joseph	HIPPO	Not Available
2002540	Atmospheric Neutron Sensitivity Measurements of Advanced Silicon Sub-micron CMOS Technologies	Fabula	Joseph	4FP30L-A	available
2002561	Study of SOI and Bulk Technologies - Influence of Integration	Ferlet-Cavr	Veronique	4FP30L-A	Not Available
2002091	Texture in U6Nb in High Temperature Beta Phase	Field	Robert	HIPPO	Not Available
2002045	Understanding Exchange Bias Through Control of Uncompensated Moments in Dilute Antiferromagnets	Fitzsimmor	Michael	ASTERIX	available
2002046	How is Frozen Magnetization Correlated with Exchange Bias?	Fitzsimmor	Michael	ASTERIX	available
2002049	Quantifying Spatial Distribution of Magnetization in Spintronic Materials	Fitzsimmor	Michael	ASTERIX	available
2002569	Measurement of (n, xngamma) Cross Sections of Natural Fe	Fotiadis	Nikolaos	4FP60R	Not Available
2002013	Neutron Powder Diffraction Determination of the Laumontite Crystal Structure Under Elevated Temperature and Pressure Conditions	Fridriksson	Thrainn	HIPPO	Not Available
2002543	Neutron Accelerator Soft-error Test of Deep Sub-micron Semiconductor Electron Device	Fujii	Tatsuya	4FP30L-A	available

2002143	Phonons in Ni at Elevated Temperature - Analysis of Coherent Scattering	Fultz	Brent	PHAROS	available
2002549	Investigation of (sup232)Th via the (n,n'gamma) Reaction and Neutron-Induced Fission Studies	Garrett	Paul	4FP60R	available
2002210	Investigation of Carbon Black Flocculation in Rubber Composites	Gerspache	Michel	LQD	Not Available
2002086	Texture in HE-driven Shock-loaded 316 SS and U-6Nb	Gray	George	HIPPO	Not Available
2002087	Texture Development and Phase Transformation in Shock Loaded Zirconium	Gray	George	HIPD	Not Available
2002182	Neutron Reflectivity Studies on the Interface Between Water and Biocompatible, Rigid Organic Monolayer Films	Grunze	Michael	SPEAR	available
2002233	Neutron Reflectivity Studies on the Interface Between Water and Biocompatible, Rigid Organic Monolayer Films	Grunze	Michael	SPEAR	Not Available
2002544	(n,z) Reactions from Threshold to 50 MeV	Haight	Robert	4FP30R	available
2002546	Nuclear Level Densities Studied Through (nxgamma) Reactions at FIGARO	Haight	Robert	4FP30R	available
2002504	Mercury Target Thermal Shock Tests	Haines	John	Blue Room	available
2002129	Electrical Double Layer Formation Near Electrified Surfaces	Hamilton	William	SPEAR	Not Available
2002209	SANS Investigation of Hydride Formation Mechanisms in Uranium Alloys	Hanrahan	Robert	LQD	Not Available
2002509	Accelerated Neutron Testing of Single Event Upsets in Semiconductor Devices	Hareland	Scott	4FP30L-A	Not Available
2002568	Experiments on the Effects of High Energy Neutrons on SRAM Components in HP AlphaServer ES45 Computer Systems Similar to Those Deployed in ASCI-Q Systems in Los Alamos	Harris	Kevin	4FP30L-A	Not Available
2002108	Residual Stress Mapping in Single Crystal S-FAP Boules Used for Laser Amplification	Hill	Michael	SMARTS	available
2002563	Classified Proposal #2002563	Hill	Tony	4FP60R	available
2002014	Magnetization Depth Profiling in Modulation Doped Colossal Magnetoresistive Manganites	Hoffmann	Axel	ASTERIX	available
2002125	Probing the Interphase Structure in the Oxidation of Glucose at a Platinum Electrode	Ingersoll	David	SPEAR	Not Available
2002538	Inclusive (n,xn) Double-Differential Cross Section Measurement (II)	Ishibashi	Kenji	4FP15L	available
2002083	Crystal Structure of RPtSn Compounds (R=Ce,Pr,Nd)	Janousova	Blanka	SCD	Not Available
2002168	Hydrogen Dynamics in the New Hydrogen Storage Material Ti-doped Sodium Aluminium Hydride	Jensen	Craig	FDS	Not Available
2002039	Atomic Structure of CsC(sub60) by the Rietveld and Pair Distribution Function (PDF) Analysis	Jeong	Il-Kyoung	HIPPO	available
2002140	In-Situ Investigation of the Local Phase Transition of Pb(Mg(sub1/3)Nb(sub2/3))O(sub3) Near Burns Temperature Using Neutron Pair Distribution Function (PDF) Analysis	Jeong	Il-Kyoung	HIPPO	available
2002201	In-Situ Investigation of the Local Phase Transition of Pb(Mg(sub1/3)Nb(sub 2/3)O(sub 3) Near Burns Temperature Using Neutron Pair Distribution Function (PDF) Analysis	Jeong	Il-Kyoung	NPDF	available
2002202	Neutron Pair Distribution Function (PDF) Study on the Role of Local Structural Change in the Parraelectric-to-Ferroelectric-to Relaxor Phase Transition of the Sr(sub 1-x)Ca(sub x)Ca(sub x)TiO(sub 3)	Jeong	Il-Kyoung	NPDF	available
2002082	Neutron Diffraction Measurements of Bulk Internal Strains in TiAl-Based Low Symmetry Composite Materials	Kad	Bimal	SMARTS	Not Available
2002115	Probing the Structure of Organosilane Films and Silane/Resin Interphases by X-ray and Neutron Reflection	Kent	Michael	SPEAR	available
2002116	Probing Crosslink Density Gradients in Thin Epoxy Films on Aluminum Using Neutron Reflection	Kent	Michael	SPEAR	available
2002501	Single Event Effects Studies on Commercial Electronic Memories and Field Programmable Gate Arrays	King	Douglas	4FP30L-A	available

2002187	Characterization of Protein/Phospholipid Complexes by SANS	Kirchhoff	Carol	LQD	Not Available
2002514	Improving Reaction Rates for Explosive Nucleosynthesis Studies via (n,a) Cross Section Measurements; Proof-of-Principle Experiment at LANSCE	Koehler	Paul	1FP5	available
2002158	High Pressure Induced Phase Transformations in the Alkaline Earth Dihydrides MgD2, CaD2 and SrD2	Kohlmann	Holger	HIPD	Not Available
2002550	Feasibility Studies for N-D Radiative Capture	Kovash	Michael	4FP15R	Not Available
2002502	Neutron SEU and SEL Testing of Commercial SRAMs and Logic Devices	Kravetz	John	4FP30L-A	available
2002011	Load Sharing in Cemented Carbide Composites	Krawitz	Aaron	SMARTS	available
2002120	Molecular Density and Orientation in Confined Polymer Layers Under Static and Dynamic (flow) Conditions	Kuhl	Tonya	SPEAR	Not Available
2002121	Neutron Reflectometry Studies of Binding and Penetration of Lipid Membranes by Cholera Toxin	Kuhl	Tonya	SPEAR	Not Available
2002213	Crystal Field Levels in (U, Th)O2	Lander	Gerard	PHAROS	Not Available
2002063	Structural Characterisation of Crystals of Alpha-glycine During Anomalous Electrical Behaviour	Langan	Paul	PCS	Not Available
2002167	Neutron Diffraction Studies of the Hydration of Z-DNA Duplex d(CGCGCG)	Langan	Paul	PCS	Not Available
2002193	The Ultra-structural Arrangement of Chitin and Protein in the Pen from a Giant Squid	Langan	Paul	LQD	Not Available
2002165	Hydroxylation of MgO Surfaces	Larese	John	FDS	Not Available
2002179	Determination of Strain Pole Figures From Compressed Steel Samples	Larsson	Cecilia	SMARTS	Not Available
2002565	Single Event Upset in High End Memories SRAM (.13 mu m)	Lauzeral	Olivier	4FP30L-A	available
2002001	Quasielastic Scattering in CeRhin(sub5)	Lawrence	Jon	PHAROS	available
2002230	Order Parameter Measurement of d=3 Random-Field Ising Antiferromagnet Fe(sub0.8)Zn(sub0.2)F(sub2) Thin Films	Lederman	David	ASTERIX	available
2002007	Thickness Dependent Magnetization Reversal Asymmetry in Exchange Biased Bilayers	Leighton	Christophe	ASTERIX	Not Available
2002008	Coercive Mechanisms in NiMn/ferromagnet Bilayers and Epitaxial Superlattices	Leighton	Christophe	ASTERIX	Not Available
2002139	The Structure of Charged Polymer Brushes Created via the Adsorption of Polymeric Surfactants	Li	Feng	SPEAR	Not Available
2002142	The Segment Density Profile and Counterion Cloud of Polyelectrolyte Brushes	Li	Feng	SPEAR	Not Available
2002511	Oxide Film Dielectric Properties: The Influence Proton Irradiation on the Corrosion Kinetics of Structural Materials in LBE Coolant Systems	Lillard	R. Scott	Blue Room	Not Available
2002003	Field Driven Phase Transitions in Monolayers and Bilayers of Amphiphiles at Electrode Surfaces	Lipkowski	Jacek	SPEAR	Not Available
2002204	Local Lattice Distortions Induced by Frustration in ZrCr(sub 2)O(sub 4)	Louca	Despo	NPDF	Not Available
2002235	Structure of Amorphous Metallic Glasses	Louca	Despo	NPDF	Not Available
2002512	Neutron Accelerated Soft Error Rate for Different Memory Technologies	Ma	Manny	4FP30L-A	available
2002118	Deformation Behavior of Superalloys: Micro-strain Measurements, Dislocation Mechanisms, and Modeling [See also 2002164 on HIPPO]	Majumdar	Bhaskar	SMARTS	available
2002164	Deformation Behavior of Superalloys: Micro-strain Measurements, Dislocation Mechanisms, and Modeling [See also 2002118 on SMARTS]	Majumdar	Bhaskar	HIPD	Not Available
2002194	SANS Study of Internal Void Structures in HMX and RDX	Mang	Joseph	LQD	available
2002195	SANS Studies of the Microstructure of HMX-based Composite Energetic Materials	Mang	Joseph	LQD	Not Available
2002123	Experimental Analysis of the Evolution of Radiogenically Produced Helium in Erbium Dihydride Films	Mangan	Michael	HIPPO	available
2002124	Experimental Observation of Hydrogen Diffusion in Scandium Dideuteride Thin Films Using Neutron Reflectometry	Mangan	Michael	SPEAR	available

2002147	Phase Transition in U-6Nb Under Hydrostatic Pressure?	Manley	Michael	HIPPO	Not Available
2002126	Structure Determinations of New Hydrogen Clathrates	Mao	Wendy	HIPPO	available
2002137	Neutron Diffraction of Single-Crystal FeO at High Pressures and Low Temperatures - Investigation of Paramagnetic - Antiferromagnetic Transitions	Mao	Ho-Kwang	SCD	Not Available
2002525	Neutron-Deuteron Elastic Scattering and the Three-Nucleon Force	Matthews	June	4FP15R	Not Available
2002178	Pressure Effects on Block Copolymer Order/Disorder Transition	Mayes	Anne	LQD	Not Available
2002148	Water in Constituents of Yucca Mountain Tuff	McCall	Katherine	HIPD	Not Available
2002519	The Development of a Database of Neutron-induced Gamma-ray Yields for Elements of Interest in General PGNAA Measurements	McGrath	Christophe	4FP90L	Not Available
2002570	Identification of Neutron-induced Light Ion Spallation Products in CsI Using Pulse Shape Discrimination	McLean	Thomas	4FP15L	Not Available
2002042	Deep Inelastic Scattering from Helium Fluid Under Pressure	McQueene	Robert	PHAROS	Not Available
2002031	Internal Strains in Co-deformed Two Phase Compounds	Mecking	Heinrich	HIPPO	available
2002186	Structural Analysis of Nanoarchitectures in Porous and Block Copolymer	Mercer-Sm	Janet	LQD	available
2002522	Response of a High-Energy Neutron Dosimeter [see also 2002541 on FP30L-A]	Miles	Leslie	4FP15L	Not Available
2002541	Response of a High-Energy Neutron Dosimeter [see also 2002522 on FP15L]	Miles	Leslie	4FP30L-A	Not Available
2002097	Critical Experiments for the Assessment of Elastic Moduli in a Multiphase Metallic Alloy Using In Situ Neutron Diffraction	Miller	Matthew	HIPPO	Not Available
2002136	Critical Experiments for the Assessment of Elastic Moduli in a Multiphase Metallic Alloy Using In-Situ Neutron Diffraction	Miller	Matthew	SMARTS	Not Available
2002130	Deformation of Calcium Hydroxide Crystal Lattice in Hydrated Cement Paste	Monteiro	Paulo	SMARTS	Not Available
2002154	Kinetics, Texture, and Decomposition of Ettringite	Monteiro	Paulo	HIPPO	Not Available
2002517	Neutron Spallation Target Experiments in Support of the Advanced Accelerator Applications (AAA) Programs	Morgan	George	Blue Room	Not Available
2002177	Validation of Residual Stress Predictions in Heat Treated Components and Correlation to Distortion Effects	Nash	Philip	SMARTS	Not Available
2002206	Local Structure of Nano Crystalline Clay Particles	Neder	Reinhard	NPDF	Not Available
2002555	Measurement of (sup191)Ir(n,n'gamma), (n,2ngamma), (n,3ngamma), and (n,4ngamma) Cross	Nelson	Ronald	4FP60R	available
2002556	Measurement of Prompt Gamma Rays from Neutron-Induced Fission of Uranium and Other Actinides	Nelson	Ronald	4FP30R	available
2002518	Evaluation of Passive and Active Neutron Personnel Dosimeters	Olsher	Richard	4FP15L	available
2002189	Characterization of Micellar Drug Delivery Systems by Small-Angle Neutron Scattering	Onyuksel	Hayat	LQD	Not Available
2002191	SANS Study of the Structure of Estane	Orler	E. Bruce	LQD	Not Available
2002192	Experiments on the Structure of Polyester Polyurethanes	Orler	E. Bruce	LQD	Not Available
2002111	Structure and Local Ordering of Metal Sites in Zeolites and Nanoporous Materials	Ott	Kevin	HIPPO	Not Available
2002064	Charge States in the Active Site of Orotidine 5'monophosphate Decarboxylase	Pai	Emil	PCS	available
2002010	Probing Depth Dependent Magnetism in Ferromagnet/GaAs Epitaxial Heterostructures	Palmstrom	Chris	ASTERIX	available
2002060	Study of the Atomic Structure of Nanocrystals Using Large-Q Diffraction and RDF Analysis	Palosz	Witold	HIPD	Not Available
2002205	Local Structure of Nano-crystalline (li,D)(sub x)MnO(sub 2) Battery Material from Analysis of PDF Data	Parise	John	NPDF	Not Available
2002207	The Local Structure of "Amorphous" FeS	Parise	John	NPDF	Not Available
2002208	Origin of Ionic Conductivity in Cs(sub 14) (super 6)Li(sub 24)[Si(sub 72) (super 7)Li(sub 18)O(sub 172)]: Exchange between (super 7)Li and (super 6)Li in Channel and Framework Sites, Respectively at High Temperature Using PDF	Parise	John	NPDF	Not Available

2002150	Strain Driven Spin Reorientation Transitions in Co Thin Films	Park	Sungkyun	ASTERIX	available
2002107	Flow-related Microlite Preferred Orientation in Lavas	Pehl	Jenny	HIPPO	available
2002516	Test of Gd Plasma Coatings as a Neutron Absorber for the NPDgamma Experiment	Penttila	Seppo	1FP5	Not Available
2002036	Local Structure of Zeolite Beta	Peral	Immaculad	HIPPO	Not Available
2002228	Local Structure in Semiconductor Alloys	Peterson	Peter	NPDF	Not Available
2002127	Residual Stress Mapping in Two Stainless Steel Pipe Welds Fabricated from Electron Beam Welding	Rangaswa	Partha	SMARTS	Not Available
2002506	Neutron-Induced Failure Tests of IGBT Devices	Reass	William	4FP30L-A	Not Available
2002028	Residual Stresses in Zircaloy-4 Weldments	Ripley	Maurice	SMARTS	available
2002029	Measurements of the Strain Response to Applied Stress in Zircaloy-4	Ripley	Maurice	SMARTS	available
2002172	Structure of Synthesized Non-Linear Optical Films	Robinson	Jeanne	SPEAR	available
2002054	Rare-Earth Substituted PZT	Rodriguez	Mark	HIPPO	available
2002057	In-Situ Neutron Diffraction Study of Sony LI-ion Batteries	Rodriguez	Mark	HIPPO	available
2002539	Neutron Capture on Off-stable Nuclides	Rundberg	Robert	1FP14	Not available
2002135	Neutron Time Distribution and Absolute Neutron Spectrum [see also 2002133 on HIPD and 2002134 on HIPPO]	Russell	Gary	SPEAR	Not Available
2002547	Lujan Center Mark-III Target System Experiments	Russell	Gary	Blue Room	Not Available
2002040	Sound Waves in Highly Viscous Liquids	Russina	Margarita	PHAROS	Not Available
2002109	Morphology of Toughened Anti-Corrosion Films	Schaefer	Dale	SPEAR	available
2002510	Accelerated Tests of the Cosmic Component of Soft Errors in Logical ICs with Embedded DRAM and SRAM Arrays	Schindlbe ck	Guenter	4FP30L-A	available
2002131	Structure and Texture Investigation of Phases Ni(sub 53) Ti(sub 47) and in IrTi	Schmahl	Wolfgang	HIPPO	Not Available
2002152	Primary Creep Behavior of a Precipitation Strengthened Titanium Aluminide	Seo	Dongyi	SMARTS	Not Available
2002122	Texture of Rocks from the Santa Rosa Mylonite Zone	Shomglin	Kome	HIPPO	Not Available
2002505	Cross Section Measurements for Cosmic Ray Studies Using Neutrons	Sisterson	Janet	4FP15R	available
2002114	Structure of Nanoporous Polymer Supported Lipid Bilayers	Smith	Gregory	SPEAR	Not Available
2002212	Pressure Dependence of Structure and Magnetic Structure in Single Crystalline LaSrFe04	Takabatake	Toshiro	SCD	Not Available
2002093	Rubredoxin Crystallography in TOF Neutron Measurement	Tanaka	Ichiro	PCS	available
2002560	Effects of a Pulsed Proton Beam on Liquid Lead-Bismuth Eutectic Target	Tcharnotsk	Valentina	Blue Room	Not Available
2002161	Investigation of Stress-Strain During the Elastic and Plastic Deformation of Marble, Limestone, and Sandstone	Tencate	James	SMARTS	available
2002162	Search for the Atomic-Level/Microscopic Source of "Slow Dynamical" Recovery Processes in Geomaterials	Tencate	James	HIPPO	available
2002092	Texture and Internal Strain Development in Uranium Alloy Samples [see also 2002104 on HIPPO]	Teter	David	SMARTS	available
2002104	Texture and Internal Strain development in Uranium Alloy Samples [see also 2002092 on SMARTS]	Teter	David	HIPPO	Not Available
2002065	Determination of Hydrogens and Bound Water Molecules in Photosynthetic Reaction Center Complex by Neutron Diffraction	Thiyagaraja	Pappanna	PCS	Not Available
2002084	Aging in Uranium Niobium Alloys	Thoma	Dan	SMARTS	available
2002155	Shape Memory Behavior in U-Nb Alloys	Thoma	Dan	SMARTS	available
2002128	Electrosorption of Common Surfactant and Ionic Liquid Molecules from Aqueous Solutions	Tsouris	Costas	SPEAR	available
2002553	Neutron Capture Measurements on (sup147)Pm and (sup151)Sm Using DANCE	Ullmann	John	1FP14	available
2002554	DANCE Development	Ullmann	John	1FP14	available
2002169	Effect of Beam Divergence on Strain Data from SMARTS	Ustundag	Ersan	SMARTS	Not Available
2002173	In-Situ Deformation of Bulk-Metallic Glass-Matrix Composites	Ustundag	Ersan	SMARTS	Not Available

2002056	In Situ Neutron Diffraction Study of Shape-Memory Alloys at Cryogenic Temperatures	Vaidyanath	Rajan	SMARTS	Not Available
2002059	In-Situ Neutron Diffraction Study of the Linear-Superelastic-Effect in Shape-Memory Alloys	Vaidyanath	Rajan	SMARTS	Not Available
2002004	Investigation of Strain in Equal-Channel Angular Pressed (ECAP) Materials	Vogel	Sven	SMARTS	Not Available
2002005	Investigation of Austenite Phase Transformation and Carbon Concentration Changes in Steel in the Intercritical Annealing Process	Vogel	Sven	1FP5	Not Available
2002006	Investigation of Texture in Equal-Channel Angular Pressed (ECAP) Materials	Vogel	Sven	HIPD	Not Available
2002081	Investigation of Pressure Dependence of Nuclear Resonances	Vogel	Sven	1FP5	Not Available
2002567	Neutron Induced Soft Error Rates in Microprocessors	Vrijen	Rutger	1FP4	Not Available
2002551	The Response of Radiochromic Film to High Energy Neutrons	Walker	L. Scott	4FP15L	Not Available
2002055	Polymer Processing in Supercritical CO(sub2): Block Copolymer Phase Ordering and Diffusion and Reaction in Interfaces	Watkins	James	SPEAR	Not Available
2002089	Texture Changes During the alpha-beta Phase Transformation in Quartz	Wenk	Hans-Rud	HIPPO	available
2002521	Development of SEU Cross Sections and Proportional Dose Effects Measurements in an Incrementally Hardened Neutron Beam [see also 2002530 on FP90L]	Wilkins	Richard	4FP30L-A	Not Available
2002523	Development of Comparative Effect Curves Due to Varying Thickness of Intervening Materials	Wilkins	Richard	4FP30L-A	Not Available
2002530	Development of SEU Cross Sections and Proportional Dose Effects Measurements in an Incrementally Hardened Neutron Beam [see also 2002521 on 4FP30L-A]	Wilkins	Richard	4FP90L	Not Available
2002032	Using Inelastic Neutron Scattering for Structural Characterization of Synthetic Binary and Ternary Metal Cyanides	Williams	Darrick	FDS	Not Available
2002033	Using Inelastic Neutron Scattering for Structural Characterization of Synthetic Binary and Ternary Metal Cyanates	Williams	Darrick	FDS	Not Available
2002190	Interactions in Charge-Stabilized Colloidal Dispersions	Wu	Jianzhong	LQD	Not Available
2002066	High-Temperature Neutron Diffraction Studies on NaTixNb1-xO3-0.5x Perovskites	Xu	Hongwu	HIPPO	Not Available
2002170	In-Situ Neutron Single-Crystal Diffraction Study on Methane-Hydrogen Clathrates at High Pressures	Xu	Jian	SCD	available
2002532	Neutron Resonance Spectroscopy (NRS) Measurement of Temperature Rise at a Sliding Interface at high Pressure and Velocities.	Yuan	Vincent	Blue Room	available
2002534	Measurement of Metal Jet Temperatures Using Neutron Resonance Spectroscopy (NRS)	Yuan	Vincent	Blue Room	available
2002535	Sample Characterization for Dynamic Temperature Measurements Using Neutron Resonance Spectroscopy (NRS) on FP5	Yuan	Vincent	1FP5	available
2002037	Study of P-T Diagrams of Si, Ge, SiGe Alloys and Kinetics of Their Reaction with Diamond at High Pressures and Temperatures	Zerda	T. Waldek	HIPD	Not Available
2002016	Thermoelastic Equation of State of b.c.c. Refractory Metal and U-238	Zhao	Yusheng	HIPPO	available
2002017	High Pressure Crystal Chemistry of Hydrous Minerals	Zhao	Yusheng	HIPPO	Not Available
2002019	Development of High P-T Capability for Neutron Powder Diffraction Studies with HIPPO and TAP-98	Zhao	Yusheng	HIPPO	Not Available
2002009	Neutron Brillouin Scattering on a Polymeric Glass Former	Zorn	Reiner	PHAROS	Not Available
2002218	High Resolution, Hi-Q Study of the Structure of Potassium Niobate Tellurite Glass Ceramic	Zwanziger	Joe	NPDF	Not Available

Prop ID	Title	PI Last Name	PI First Name	Instrument	Report Availability
2002001	Quasielastic Scattering in CeRhin(sub5)	Lawrence	Jon	PHAROS	available
2002002	Neutron Reflectivity from Langmuir Monolayers of a Synthetic Electron Transfer Protein	Blasie	J. Kent	SPEAR	available
2002003	Field Driven Phase Transitions in Monolayers and Bilayers of Amphiphiles at Electrode Surfaces	Lipkowski	Jacek	SPEAR	Not Available
2002004	Investigation of Strain in Equal-Channel Angular Pressed (ECAP) Materials	Vogel	Sven	SMARTS	Not Available
2002005	Investigation of Austenite Phase Transformation and Carbon Concentration Changes in Steel in the Intercritical Annealing Process	Vogel	Sven	1FP5	Not Available
2002006	Investigation of Texture in Equal-Channel Angular Pressed (ECAP) Materials	Vogel	Sven	HIPD	Not Available
2002007	Thickness Dependent Magnetization Reversal Asymmetry in Exchange Biased Bilayers	Leighton	Christophe	ASTERIX	Not Available
2002008	Coercive Mechanisms in NiMn/ferromagnet Bilayers and Epitaxial Superlattices	Leighton	Christophe	ASTERIX	Not Available
2002009	Neutron Brillouin Scattering on a Polymeric Glass Former	Zorn	Reiner	PHAROS	Not Available
2002010	Probing Depth Dependent Magnetism in Ferromagnet/GaAs Epitaxial Heterostructures	Palmstrom	Chris	ASTERIX	available
2002011	Load Sharing in Cemented Carbide Composites	Krawitz	Aaron	SMARTS	available
2002012	Deformation Mechanisms of Titanium as a Function of Temperature	Daymond	Mark	SMARTS	available
2002013	Neutron Powder Diffraction Determination of the Laumontite Crystal Structure Under Elevated Temperature and Pressure Conditions	Fridriksson	Thrainn	HIPPO	Not Available
2002014	Magnetization Depth Profiling in Modulation Doped Colossal Magnetoresistive Manganites	Hoffmann	Axel	ASTERIX	available
2002015	Investigation of Catalysis of E. Coli DHFR and Yeast PGK by Neutron Diffraction	Dealwis	Chris	PCS	Not Available
2002016	Thermoelastic Equation of State of b.c.c. Refractory Metal and U-238	Zhao	Yusheng	HIPPO	available
2002017	High Pressure Crystal Chemistry of Hydrous Minerals	Zhao	Yusheng	HIPPO	Not Available
2002019	Development of High P-T Capability for Neutron Powder Diffraction Studies with HIPPO and TAP-98	Zhao	Yusheng	HIPPO	Not Available
2002022	Effect of Texture Randomization Processing on the Deformation Mode Activity in Magnesium Alloys	Agnew	Sean	HIPD	available
2002025	High-Pressure Crystal Chemistry of Clathrates	Bish	David	HIPPO	Not Available
2002028	Residual Stresses in Zircaloy-4 Weldments	Ripley	Maurice	SMARTS	available
2002029	Measurements of the Strain Response to Applied Stress in Zircaloy-4	Ripley	Maurice	SMARTS	available
2002031	Internal Strains in Co-deformed Two Phase Compounds	Mecking	Heinrich	HIPPO	available
2002032	Using Inelastic Neutron Scattering for Structural Characterization of Synthetic Binary and Ternary Metal Cyanides	Williams	Darrick	FDS	Not Available
2002033	Using Inelastic Neutron Scattering for Structural Characterization of Synthetic Binary and Ternary Metal Cyanates	Williams	Darrick	FDS	Not Available
2002036	Local Structure of Zeolite Beta	Peral	Immaculad	HIPPO	Not Available
2002037	Study of P-T Diagrams of Si, Ge, SiGe Alloys and Kinetics of Their Reaction with Diamond at High Pressures and Temperatures	Zerda	T. Waldek	HIPD	Not Available
2002038	Deformation Texture of Plutonium (see also 2002041 on HIPD)	Brown	Donald	HIPPO	Not Available
2002039	Atomic Structure of CsC(sub60) by the Rietveld and Pair Distribution Function (PDF) Analysis	Jeong	Il-Kyoung	HIPPO	available
2002040	Sound Waves in Highly Viscous Liquids	Russina	Margarita	PHAROS	Not Available
2002042	Deep Inelastic Scattering from Helium Fluid Under Pressure	McQueene	Robert	PHAROS	Not Available
2002045	Understanding Exchange Bias Through Control of Uncompensated Moments in Dilute Antiferromagnets	Fitzsimmon	Michael	ASTERIX	available
2002046	How is Frozen Magnetization Correlated with Exchange Bias?	Fitzsimmon	Michael	ASTERIX	available

2002049	Quantifying Spatial Distribution of Magnetization in Spintronic Materials	Fitzsimmon	Michael	ASTERIX	available
2002051	High Pressure and Temperature Investigations in the Mn(subx)Fe(sub1-x)S Solid Solution	Ehm	Lars	HIPD	Not Available
2002052	Phase Separation and Superconductivity in Mg(sub1-x)Al(subx)B(sub2)	Billinge	Simon J.	HIPPO	available
2002053	Average and Local Structure of the Intermediate and High-Temperature Phases of Rb(sub3)D(SeO(sub4))sub2	Billinge	Simon J.	HIPPO	available
2002054	Rare-Earth Substituted PZT	Rodriguez	Mark	HIPPO	available
2002055	Polymer Processing in Supercritical CO(sub2): Block Copolymer Phase Ordering and Diffusion and Reaction in Interfaces	Watkins	James	SPEAR	Not Available
2002056	In Situ Neutron Diffraction Study of Shape-Memory Alloys at Cryogenic Temperatures	Vaidyanath	Rajan	SMARTS	Not Available
2002057	In-Situ Neutron Diffraction Study of Sony LI-ion Batteries	Rodriguez	Mark	HIPPO	available
2002059	In-Situ Neutron Diffraction Study of the Linear-Superelastic-Effect in Shape-Memory Alloys	Vaidyanath	Rajan	SMARTS	Not Available
2002060	Study of the Atomic Structure of Nanocrystals Using Large-Q Diffraction and RDF Analysis	Palosz	Witold	HIPD	Not Available
2002063	Structural Characterisation of Crystals of Alpha-glycine During Anomalous Electrical Behaviour	Langan	Paul	PCS	Not Available
2002064	Charge States in the Active Site of Orotidine 5'monophosphate Decarboxylase	Pai	Emil	PCS	available
2002065	Determination of Hydrogens and Bound Water Molecules in Photosynthetic Reaction Center Complex by Neutron Diffraction	Thiyagaraja	Pappanna	PCS	Not Available
2002066	High-Temperature Neutron Diffraction Studies on NaTixNb1-xO3-0.5x Perovskites	Xu	Hongwu	HIPPO	Not Available
2002067	Comparative Hydrogen Position Studies Using X-rays and Neutrons	Bunick	Gerard	PCS	available
2002068	A Neutron Diffraction Study On (K, Na, H3O) Jarosite Solid Solutions	Drouet	Christophe	HIPPO	Not Available
2002074	Magnetic Structure Determination of the Heavy-Fermion Antiferrmagnet Ce2RhIn8 Using Polarized Neutrons	Bao	Wei	ASTERIX	Not Available
2002077	Binding Studies with Immune Protein Fragments	Edmundso	Allen	PCS	available
2002081	Investigation of Pressure Dependence of Nuclear Resonances	Vogel	Sven	1FP5	Not Available
2002082	Neutron Diffraction Measurements of Bulk Internal Strains in TiAl-Based Low Symmetry Composite Materials	Kad	Bimal	SMARTS	Not Available
2002083	Crystal Structure of RPtSn Compounds (R=Ce,Pr,Nd)	Janousova	Blanka	SCD	Not Available
2002084	Aging in Uranium Niobium Alloys	Thoma	Dan	SMARTS	available
2002085	High Temperature Deformation of Beryllium	Brown	Donald	SMARTS	available
2002086	Texture in HE-driven Shock-loaded 316 SS and U-6Nb	Gray	George	HIPPO	Not Available
2002087	Texture Development and Phase Transformation in Shock Loaded Zirconium	Gray	George	HIPD	Not Available
2002088	Residual Strains in Welded Stainless Steel Parts	Brown	Donald	SMARTS	Not Available
2002089	Texture Changes During the alpha-beta Phase Transformation in Quartz	Wenk	Hans-Rud	HIPPO	available
2002091	Texture in U6Nb in High Temperature Beta Phase	Field	Robert	HIPPO	Not Available
2002092	Texture and Internal Strain Development in Uranium Alloy Samples [see also 2002104 on HIPPO]	Teter	David	SMARTS	available
2002093	Rubredoxin Crystallography in TOF Neutron Measurement	Tanaka	Ichiro	PCS	available
2002094	Microstructural Evolution of Metals During ECAPing	Beyerlein	Irene	HIPPO	Not Available
2002095	Texture Evolution During ECAP'ing of Beryllium	Alexander	David	HIPPO	Not Available
2002096	Texture Evolution in Beryllium as a Function of Deformation [see also 2002102 on HIPD]	Blumenthal	William	HIPPO	Not Available
2002097	Critical Experiments for the Assessment of Elastic Moduli in a Multiphase Metallic Alloy Using In Situ Neutron Diffraction	Miller	Matthew	HIPPO	Not Available

2002098	Investigation of the Nature of Doped Charge Distribution and the Possibility of Local Stripe Correlations in Underdoped La{sub2-x}Sr{subx}CuO{sub4}	Bozin	Emil	HIPPO	Not Available
2002099	Magnetic Coupling in Metal/Native Oxide Multilayers	Beach	Geoffrey	ASTERIX	Not Available
2002100	Investigation of Radiogenically Produced {sup3}He in Erbium Dihydride Systems: Depth Profiling Using Neutron Reflectometry	Browning	James	SPEAR	available
2002103	Texture Evolution During ECAP'ing of Beryllium	Alexander	David	SMARTS	Not Available
2002104	Texture and Internal Strain development in Uranium Alloy Samples [see also 2002092 on SMARTS]	Teter	David	HIPPO	Not Available
2002106	Effect of Texture Randomization Processing on the Deformation Mode Activity in Magnesium Alloys	Agnew	Sean	SMARTS	available
2002107	Flow-related Microlite Preferred Orientation in Lavas	Pehl	Jenny	HIPPO	available
2002108	Residual Stress Mapping in Single Crystal S-FAP Boules Used for Laser Amplification	Hill	Michael	SMARTS	available
2002109	Morphology of Toughened Anti-Corrosion Films	Schaefer	Dale	SPEAR	available
2002111	Structure and Local Ordering of Metal Sites in Zeolites and Nanoporous Materials	Ott	Kevin	HIPPO	Not Available
2002113	Structure of Freely Suspended Lipid Multilayer Films Over Nanoporous Polymer Films	Baker	Shenda	SPEAR	Not Available
2002114	Structure of Nanoporous Polymer Supported Lipid Bilayers	Smith	Gregory	SPEAR	Not Available
2002115	Probing the Structure of Organosilane Films and Silane/Resin Interphases by X-ray and Neutron Reflection	Kent	Michael	SPEAR	available
2002116	Probing Crosslink Density Gradients in Thin Epoxy Films on Aluminum Using Neutron Reflection	Kent	Michael	SPEAR	available
2002118	Deformation Behavior of Superalloys: Micro-strain Measurements, Dislocation Mechanisms, and Modeling [See also 2002164 on HIPPO]	Majumdar	Bhaskar	SMARTS	available
2002120	Molecular Density and Orientation in Confined Polymer Layers Under Static and Dynamic (flow) Conditions	Kuhl	Tonya	SPEAR	Not Available
2002121	Neutron Reflectometry Studies of Binding and Penetration of Lipid Membranes by Cholera Toxin	Kuhl	Tonya	SPEAR	Not Available
2002122	Texture of Rocks from the Santa Rosa Mylonite Zone	Shomglin	Kome	HIPPO	Not Available
2002123	Experimental Analysis of the Evolution of Radiogenically Produced Helium in Erbium Dihydride Films	Mangan	Michael	HIPPO	available
2002124	Experimental Observation of Hydrogen Diffusion in Scandium Dideuteride Thin Films Using Neutron Reflectometry	Mangan	Michael	SPEAR	available
2002125	Probing the Interphase Structure in the Oxidation of Glucose at a Platinum Electrode	Ingersoll	David	SPEAR	Not Available
2002126	Structure Determinations of New Hydrogen Clathrates	Mao	Wendy	HIPPO	available
2002127	Residual Stress Mapping in Two Stainless Steel Pipe Welds Fabricated from Electron Beam Welding	Rangaswa	Partha	SMARTS	Not Available
2002128	Electrosorption of Common Surfactant and Ionic Liquid Molecules from Aqueous Solutions	Tsouris	Costas	SPEAR	available
2002129	Electrical Double Layer Formation Near Electrified Surfaces	Hamilton	William	SPEAR	Not Available
2002130	Deformation of Calcium Hydroxide Crystal Lattice in Hydrated Cement Paste	Monteiro	Paulo	SMARTS	Not Available
2002131	Structure and Texture Investigation of Phases Ni(sub 53) Ti(sub 47) and in IrTi	Schmahl	Wolfgang	HIPPO	Not Available
2002135	Neutron Time Distribution and Absolute Neutron Spectrum [see also 2002133 on HIPD and 2002134 on HIPPO]	Russell	Gary	SPEAR	Not Available
2002136	Critical Experiments for the Assessment of Elastic Moduli in a Multiphase Metallic Alloy Using In-Situ Neutron Diffraction	Miller	Matthew	SMARTS	Not Available
2002137	Neutron Diffraction of Single-Crystal FeO at High Pressures and Low Temperatures - Investigation of Paramagnetic - Antiferromagnetic Transitions	Mao	Ho-Kwang	SCD	Not Available
2002138	Phonons in High-Temperature Superconductors	Egami	Takeshi	PHAROS	available

2002139	The Structure of Charged Polymer Brushes Created via the Adsorption of Polymeric Surfactants	Li	Feng	SPEAR	Not Available
2002140	In-Situ Investigation of the Local Phase Transition of Pb(Mg(sub1/3)Nb(sub2/3))O(sub3) Near Burns Temperature Using Neutron Pair Distribution Function (PDF) Analysis	Jeong	Il-Kyoung	HIPPO	available
2002142	The Segment Density Profile and Counterion Cloud of Polyelectrolyte Brushes	Li	Feng	SPEAR	Not Available
2002143	Phonons in Ni at Elevated Temperature - Analysis of Coherent Scattering	Fultz	Brent	PHAROS	available
2002145	Investigation of Elastic/Plastic Behavior of Pure Uranium	Balzar	Davor	SMARTS	Not Available
2002146	Coordination Environments That Accommodate Be: The Crictical Role of Ca for Be Occupancy in Crystalline Materials	Evensen	Joseph	HIPPO	Not Available
2002147	Phase Transition in U-6Nb Under Hydrostatic Pressure?	Manley	Michael	HIPPO	Not Available
2002148	Water in Constituents of Yucca Mountain Tuff	McCall	Katherine	HIPD	Not Available
2002150	Strain Driven Spin Reorientation Transitions in Co Thin Films	Park	Sungkyun	ASTERIX	available
2002152	Primary Creep Behavior of a Precipitation Strengthened Titanium Aluminide	Seo	Dongyi	SMARTS	Not Available
2002153	Load Partitioning in a Ti-6A1-4V/SiC Composite During Uniaxial Tensile Loading at Elevated Temperature	Choo	Hahn	SMARTS	Not Available
2002154	Kinetics, Texture, and Decomposition of Ettringite	Monteiro	Paulo	HIPPO	Not Available
2002155	Shape Memory Behavior in U-Nb Alloys	Thoma	Dan	SMARTS	available
2002158	High Pressure Induced Phase Transformations in the Alkaline Earth Dihydrides MgD2, CaD2 and SrD2	Kohlmann	Holger	HIPD	Not Available
2002160	Hydrogenation of Acetylene by Metal Catalysts	Chinta	Sivadinara	FDS	Not Available
2002161	Investigation of Stress-Strain During the Elastic and Plastic Deformation of Marble, Limestone, and Sandstone	Tencate	James	SMARTS	available
2002162	Search for the Atomic-Level/Microscopic Source of "Slow Dynamical" Recovery Processes in Geomaterials	Tencate	James	HIPPO	available
2002163	Proton Dynamics in Very Short Hydrogen Bonds	Eckert	Juergen	FDS	Not Available
2002164	Deformation Behavior of Superalloys: Micro-strain Measurements, Dislocation Mechanisms, and Modeling [See also 2002118 on SMARTS]	Majumdar	Bhaskar	HIPD	Not Available
2002165	Hydroxylation of MgO Surfaces	Larese	John	FDS	Not Available
2002167	Neutron Diffraction Studies of the Hydration of Z-DNA Duplex d(CGCGCG)	Langan	Paul	PCS	Not Available
2002168	Hydrogen Dynamics in the New Hydrogen Storage Material Ti-doped Sodium Aluminium Hydride	Jensen	Craig	FDS	Not Available
2002169	Effect of Beam Divergence on Strain Data from SMARTS	Ustundag	Ersan	SMARTS	Not Available
2002170	In-Situ Neutron Single-Crystal Diffraction Study on Methane-Hydrogen Clathrates at High Pressures	Xu	Jian	SCD	available
2002172	Structure of Synthesized Non-Linear Optical Films	Robinson	Jeanne	SPEAR	available
2002173	In-Situ Deformation of Bulk-Metallic Glass-Matrix Composites	Ustundag	Ersan	SMARTS	Not Available
2002177	Validation of Residual Stress Predictions in Heat Treated Components and Correlation to Distortion Effects	Nash	Philip	SMARTS	Not Available
2002178	Pressure Effects on Block Copolymer Order/Disorder Transition	Mayes	Anne	LQD	Not Available
2002179	Determination of Strain Pole Figures From Compressed Steel Samples	Larsson	Cecilia	SMARTS	Not Available
2002180	Determination of Residual Stresses in Green Bodies of Steel Powder After High Speed Compaction	Ericsson	Torsten	SMARTS	Not Available
2002182	Neutron Reflectivity Studies on the Interface Between Water and Biocompatible, Rigid Organic Monolayer Films	Grunze	Michael	SPEAR	available
2002183	Investigation of Radiogenically Produced (sup3)He in Erbium Dihydride Systems: Depth Profiling using Neutron Reflectometry	Browning	James	LQD	available
2002186	Structural Analysis of Nanoarchitectures in Porous and Block Copolymer	Mercer-Sm	Janet	LQD	available

2002187	Characterization of Protein/Phospholipid Complexes by SANS	Kirchhoff	Carol	LQD	Not Available
2002189	Characterization of Micellar Drug Delivery Systems by Small-Angle Neutron Scattering	Onyuksel	Hayat	LQD	Not Available
2002190	Interactions in Charge-Stabilized Colloidal Dispersions	Wu	Jianzhong	LQD	Not Available
2002191	SANS Study of the Structure of Estane	Orler	E. Bruce	LQD	Not Available
2002192	Experiments on the Structure of Polyester Polyurethanes	Orler	E. Bruce	LQD	Not Available
2002193	The Ultra-structural Arrangement of Chitin and Protein in the Pen from a Giant Squid	Langan	Paul	LQD	Not Available
2002194	SANS Study of Internal Void Structures in HMX and RDX	Mang	Joseph	LQD	available
2002195	SANS Studies of the Microstructure of HMX-based Composite Energetic Materials	Mang	Joseph	LQD	Not Available
2002201	In-Situ Investigation of the Local Phase Transition of Pb(Mg(sub1/3)Nb(sub 2/3)O(sub 3) Near Burns Temperature Using Neutron Pair Distribution Function (PDF) Analysis	Jeong	Il-Kyoung	NPDF	available
2002202	Neutron Pair Distribution Function (PDF) Study on the Role of Local Structural Change in the Parraelectric-to-Ferroelectric-to Relaxor Phase Transition of the Sr(sub 1-x)Ca(sub x)Ca(sub x)TiO(sub 3)	Jeong	Il-Kyoung	NPDF	available
2002204	Local Lattice Distortions Induced by Frustration in ZrCr(sub 2)O(sub 4)	Louca	Despo	NPDF	Not Available
2002205	Local Structure of Nano-crystalline (li,D)(sub x)MnO(sub 2) Battery Material from Analysis of PDF Data	Parise	John	NPDF	Not Available
2002206	Local Structure of Nano Crystalline Clay Particles	Neder	Reinhard	NPDF	Not Available
2002207	The Local Structure of "Amorphous" FeS	Parise	John	NPDF	Not Available
2002208	Origin of Ionic Conductivity in Cs(sub 14) (super 6)Li(sub 24)[Si(sub 72) (super 7)Li(sub 18)O(sub 172)]: Exchange between (super 7)Li and (super 6)Li in Channel and Framework Sites, Respectively at High Temperature Using PDF	Parise	John	NPDF	Not Available
2002209	SANS Investigation of Hydride Formation Mechanisms in Uranium Alloys	Hanrahan	Robert	LQD	Not Available
2002210	Investigation of Carbon Black Flocculation in Rubber Composites	Gerspache	Michel	LQD	Not Available
2002211	Search of the Structure and Magnetic Structure of UNi1-xRux and UNi1-xRhxAl Systems	Alsmadi	Abdel	SCD	Not Available
2002212	Pressure Dependence of Structure and Magnetic Structure in Single Crystalline LaSrFe04	Takabatake	Toshiro	SCD	Not Available
2002213	Crystal Field Levels in (U, Th)O2	Lander	Gerard	PHAROS	Not Available
2002215	Phase Separation and Superconductivity in Mg(sub 1-x)A1(sub x)B(sub 2)	Billinge	Simon J.	NPDF	Not Available
2002216	Average and Local Structure of the Intermediate and High-temperature Phases of Rb(sub 3)D(SeO(sub 4))(sub 2)	Billinge	Simon J.	NPDF	Not Available
2002217	High Resolution Atomic Pair Distribution Function Round Robin	Billinge	Simon J.	NPDF	Not Available
2002218	High Resolution, Hi-Q Study of the Structure of Potassium Niobate Tellurite Glass Ceramic	Zwanziger	Joe	NPDF	Not Available
2002221	Local Structure of Superconducting Cuprates with Stripes	Egami	Takeshi	NPDF	Not Available
2002222	Local Structure of Frustrated Magnet, LiNiO(sub2)	Egami	Takeshi	NPDF	Not Available
2002223	Local Structure of CMR Manganites	Egami	Takeshi	NPDF	Not Available
2002225	Preliminary Search for Amorphous Constituents of Rocks Using PDF Analysis	Darling	Tim	NPDF	Not Available
2002226	Structure of Mixed Valence Perovskites and Ceria-Zirconia Nonopowders	Dmowski	Wojtek	NPDF	Not Available
2002228	Local Structure in Semiconductor Alloys	Peterson	Peter	NPDF	Not Available
2002229	Phase Equilibria and Kinetics of Carbon Doixide and Natural Gas Clathrates	Bobev	Svilen	HIPD	Not Available
2002230	Order Parameter Measurement of d=3 Random-Field Ising Antiferromagnet Fe(sub0.8)Zn(sub0.2)F(sub2) Thin Films	Lederman	David	ASTERIX	available

2002233	Neutron Reflectivity Studies on the Interface Between Water and Biocompatible, Rigid Organic Monolayer Films	Grunze	Michael	SPEAR	Not Available
2002235	Structure of Amorphous Metallic Glasses	Louca	Despo	NPDF	Not Available
2002501	Single Event Effects Studies on Commercial Electronic Memories and Field Programmable Gate Arrays	King	Douglas	4FP30L-A	available
2002502	Neutron SEU and SEL Testing of Commercial SRAMs and Logic Devices	Kravetz	John	4FP30L-A	available
2002503	Investigation into the Cosmic Ray Sensitivity of High Power Semiconductor Devices for Use in Aerospace and Terrestrial Applications	Coulbeck	Lee	4FP30L-A	Not Available
2002504	Mercury Target Thermal Shock Tests	Haines	John	Blue Room	available
2002505	Cross Section Measurements for Cosmic Ray Studies Using Neutrons	Sisterson	Janet	4FP15R	available
2002506	Neutron-Induced Failure Tests of IGBT Devices	Reass	William	4FP30L-A	Not Available
2002507	Neutron-Induced Single Event Characterization of 0.8-, 0.35- and 0.18-Micron CMOS Technology Integrated Circuits	Browning	John	4FP30L-A	available
2002509	Accelerated Neutron Testing of Single Event Upsets in Semiconductor Devices	Hareland	Scott	4FP30L-A	Not Available
2002510	Accelerated Tests of the Cosmic Component of Soft Errors in Logical ICs with Embedded DRAM and SRAM Arrays	Schindlbeck	Guenter	4FP30L-A	available
2002511	Oxide Film Dielectric Properties: The Influence Proton Irradiation on the Corrosion Kinetics of Structural Materials in LBE Coolant Systems	Lillard	R. Scott	Blue Room	Not Available
2002512	Neutron Accelerated Soft Error Rate for Different Memory Technologies	Ma	Manny	4FP30L-A	available
2002513	Neutron-Induced Soft Errors in SRAM Devices	Abusaidi	Armin	4FP30L-A	available
2002514	Improving Reaction Rates for Explosive Nucleosynthesis Studies via (n,a) Cross Section Measurements; Proof-of-Principle Experiment at LANSCE	Koehler	Paul	1FP5	available
2002516	Test of Gd Plasma Coatings as a Neutron Absorber for the NPDgamma Experiment	Penttila	Seppo	1FP5	Not Available
2002517	Neutron Spallation Target Experiments in Support of the Advanced Accelerator Applications (AAA) Programs	Morgan	George	Blue Room	Not Available
2002518	Evaluation of Passive and Active Neutron Personnel Dosimeters	Olsher	Richard	4FP15L	available
2002519	The Development of a Database of Neutron-induced Gamma-ray Yields for Elements of Interest in General PGNAA Measurements	McGrath	Christophe	4FP90L	Not Available
2002521	Development of SEU Cross Sections and Proportional Dose Effects Measurements in an Incrementally Hardened Neutron Beam [see also 2002530 on FP90L]	Wilkins	Richard	4FP30L-A	Not Available
2002522	Response of a High-Energy Neutron Dosimeter [see also 2002541 on FP30L-A]	Miles	Leslie	4FP15L	Not Available
2002523	Development of Comparative Effect Curves Due to Varying Thickness of Intervening Materials	Wilkins	Richard	4FP30L-A	Not Available
2002524	High Energy Neutron Health Physics Survey Measurements at the Weapons Neutron Research Facility	Duran	Michael	4FP15L	Not Available
2002525	Neutron-Deuteron Elastic Scattering and the Three-Nucleon Force	Matthews	June	4FP15R	Not Available
2002527	Intermediate Energy Neutron Induced Fission: Fragment Yields & New Isomers	Ethvignot	Thierry	4FP60R	Not Available
2002528	Prompt Fission Neutron Measurements from 235U at WNR Energies	Ethvignot	Thierry	4FP30R	Not Available
2002530	Development of SEU Cross Sections and Proportional Dose Effects Measurements in an Incrementally Hardened Neutron Beam [see also 2002521 on 4FP30L-A]	Wilkins	Richard	4FP90L	Not Available
2002532	Neutron Resonance Spectroscopy (NRS) Measurement of Temperature Rise at a Sliding Interface at high Pressure and Velocities.	Yuan	Vincent	Blue Room	available

2002534	Measurement of Metal Jet Temperatures Using Neutron Resonance Spectroscopy (NRS)	Yuan	Vincent	Blue Room	available
2002535	Sample Characterization for Dynamic Temperature Measurements Using Neutron Resonance Spectroscopy (NRS) on FP5	Yuan	Vincent	1FP5	available
2002538	Inclusive (n,xn) Double-Differential Cross Section Measurement (II)	Ishibashi	Kenji	4FP15L	available
2002539	Neutron Capture on Off-stable Nuclides	Rundberg	Robert	1FP14	Not available
2002540	Atmospheric Neutron Sensitivity Measurements of Advanced Silicon Sub-micron CMOS Technologies	Fabula	Joseph	4FP30L-A	available
2002541	Response of a High-Energy Neutron Dosimeter [see also 2002522 on FP15L]	Miles	Leslie	4FP30L-A	Not Available
2002542	Neutron-induced Single-event Upsets and Transients in High-speed Digital Logic Integrated Circuits	Dodd	Paul	4FP30L-A	available
2002543	Neutron Accelerator Soft-error Test of Deep Sub-micron Semiconductor Electron Device	Fujii	Tatsuya	4FP30L-A	available
2002544	(n,z) Reactions from Threshold to 50 MeV	Haight	Robert	4FP30R	available
2002545	Production of (sup148)Gd by 800-MeV Protons on Tungsten	Corzine	R. Karen	Blue Room	Not Available
2002546	Nuclear Level Densities Studied Through (nxgamma) Reactions at FIGARO	Haight	Robert	4FP30R	available
2002547	Lujan Center Mark-III Target System Experiments	Russell	Gary	Blue Room	Not Available
2002548	Measurement of the 233U(n,2n) Cross Section with gammagamma Coincidences	Devlin	Matthew	4FP60R	Not Available
2002549	Investigation of (sup232)Th via the (n,n'gamma) Reaction and Neutron-Induced Fission Studies	Garrett	Paul	4FP60R	available
2002550	Feasibility Studies for N-D Radiative Capture	Kovash	Michael	4FP15R	Not Available
2002551	The Response of Radiochromic Film to High Energy Neutrons	Walker	L. Scott	4FP15L	Not Available
2002553	Neutron Capture Measurements on (sup147)Pm and (sup151)Sm Using DANCE	Ullmann	John	1FP14	available
2002554	DANCE Development	Ullmann	John	1FP14	available
2002555	Measurement of (sup191)Ir(n,n'gamma), (n,2ngamma), (n,3ngamma), and (n,4ngamma) Cross	Nelson	Ronald	4FP60R	available
2002556	Measurement of Prompt Gamma Rays from Neutron-Induced Fission of Uranium and Other Actinides	Nelson	Ronald	4FP30R	available
2002557	Study of (sup18)O(n,2ngamma) with GEANIE	Becker	John	4FP60R	Not available
2002558	Measurement of the (sup150)Sm(n,2n)(sup149)Sm Cross Section	Cooper	Jeff	4FP60R	available
2002559	Test of Big Bang Nucleosynthesis Mode Predictions by Precision Measurement of the (n+p)->(d+gamma) Cross Section	Esch	Ernst	4FP90L	Not Available
2002560	Effects of a Pulsed Proton Beam on Liquid Lead-Bismuth Eutectic Target	Tcharnotsk	Valentina	Blue Room	Not Available
2002561	Study of SOI and Bulk Technologies - Influence of Integration	Ferlet-Cavr	Veronique	4FP30L-A	Not Available
2002562	Preliminary Study of (sup151)Eu(n,2ngamma) with GEANIE	Becker	John	4FP60R	Not Available
2002563	Classified Proposal #2002563	Hill	Tony	4FP60R	available
2002564	Neutron-Induced Failures in Avionic Systems	Belcastro	Celeste	4FP30L-A	Not available
2002565	Single Event Upset in High End Memories SRAM (.13 mu m)	Lauzeral	Olivier	4FP30L-A	available
2002566	Neutron Soft Error Sensitivity Investigation of SRAM based programmable logic devices with embedded user memory.	Euzent	Bruce	4FP30L-A	Not available
2002567	Neutron Induced Soft Error Rates in Microprocessors	Vrijen	Rutger	1FP4	Not Available
2002568	Experiments on the Effects of High Energy Neutrons on SRAM Components in HP AlphaServer ES45 Computer Systems Similar to Those Deployed in ASCI-Q Systems in Los Alamos	Harris	Kevin	4FP30L-A	Not Available
2002569	Measurement of (n, xngamma) Cross Sections of Natural Fe	Fotiadis	Nikolaos	4FP60R	Not Available
2002570	Identification of Neutron-induced Light Ion Spallation Products in CsI Using Pulse Shape Discrimination	McLean	Thomas	4FP15L	Not Available

Search Instructions

Click the binocular icon in the Acrobat toolbar, this will bring up another window.

In the Find window, type the text you want to find in the Find text box, and click Find Again.

- Text can be a single word, number, a term, or phrase.
- When you click Find Again the Finder will bring up the first page of the word or phrase you typed.

To continue the search through the document for that word or phrase just click on Find Again and it will continue to look for the next time the phrase or word was used.

LANSCE
Los Alamos Neutron Science Center

REPORT ON EXPERIMENT
(Please Type)

Submit all experiment reports to:
LANSCE User Office, MS H831, Los Alamos National Laboratory, Los Alamos, NM 87545

Experiment was carried out at:	**Local Contact**	**Proposal #**	***LANSCE Use Only***
[X] Manuel Lujan Jr. Neutron Scattering Center	Rob McQueeney	**2002001**	**Report Rc'd**
[ ] Weapons Neutron Research Facility	**FP/Instrument Used**		**3/21/03**
[ ] WNR/Blue Room	PHAROS		

Title
Quasielastic Scattering in $CeRhIn_5$

Authors and Affiliations
Jon Lawrence, University of California, Irvine
Andrew Christianson, Colorado State University, NHMFL/LANL
John Sarrao, MST-10, LANL
Rob McQueeney, LANSCE, LANL

Experiment Report

This experiment was the first step in an effort to use PHAROS to better determine the crystal field (CF) splittings and wavefunctions in the new superconductors $CeXIn_5$ (X = Rh, Ir, Co). We have obtained data for $CeRhIn_5$ [PRB 66 (2002) 193102] and $CeIrIn_5$ on the LRMECS spectrometer at IPNS. We used a moderately large initial energy (E_i = 35meV) in those studies to reduce the role of absorption, which is strong in these compounds due to the large number of In, Rh and Ir atoms. We were unable to directly observe the quasielastic (QE) scattering from the ground state doublet, because the QE linewidth is smaller than the elastic resolution on LRMECS for this initial neutron energy. We reasoned that, given the superior resolution on PHAROS, we should be able to utilize a moderately large initial energy to minimize absorption and still resolve the QE scattering.

We measured $CeRhIn_5$, $LaRhIn_5$ and the empty holder at 15K on PHAROS, in each case counting for nearly two days to improve statistics. Measurement of the $LaRhIn_5$ sample is important to help determine the nonmagnetic background sample. Measurement of the empty holder is also particularly important, since it gives rise to a large fraction of the total scattering due to the large absorption in the sample. We employed an initial energy of 48.1meV which also passes neutrons of initial energy 16.6meV; this allowed us to view the scattering both on a broad scale encompassing all the excitations and on a finer scale in the hopes of observing the QE scattering. Data analysis awaits implementation of the appropriate computer software; we intend to adapt the OpenGenie software currently in use at ISIS and IPNS for use on PHAROS, which project should be complete this spring. This will allow for absorption corrections, which are crucial for these compounds.

As a preliminary analysis, we binned a large number of low angle detectors (where magnetic scattering is strongest) and corrected for the k_f/k_i factor and for the time-independent background. We then subtracted the data for $LaRhIn_5$ (scaled by the ratio of the total scattering cross-sections) from the data for $CeRhIn_5$; this procedure is similar to one we used successfully on the LRMECS data to correct for the nonmagnetic background. It also approximately subtracts out the empty holder, and hence crudely corrects for the differences in absorption between the sample-in-holder and the empty holder itself.

Experiment Report *(continued)*

For the E_i = 16.6meV data, we observed no quasielastic scattering over and beyond the empty holder scattering (Fig. 1). This means that the QE linewidth is smaller than instrumental resolution at this E_i. Recent NMR results (Nick Curro, private communication) suggest the QE linewidth is 0.5meV, which would make the QE scattering unobservable in this particular measurement. For the E_i = 48.1meV data, we observed (Fig. 2) a lineshape very comparable to that determined on LRMECS for E_i = 35meV; a strong crystal field excitation can be observed at 7meV, and a weaker broad excitation centered near 23meV (whose amplitude is rather sensitive to the details of the absorption and non-magnetic background corrections). The overall signal-to-noise is also similar to that observed on LRMECS.

Fig. 1

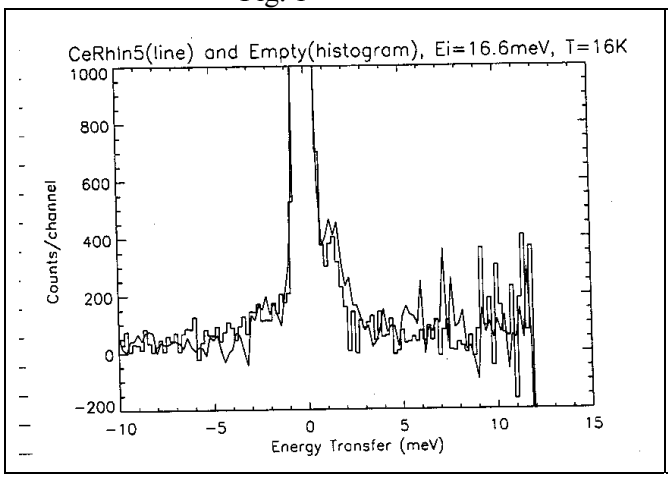

Fig. 2

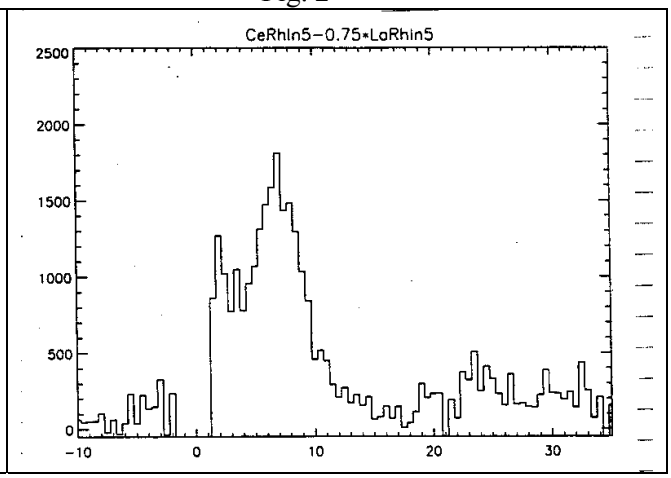

These results indicate that the use of 48.1meV as the initial energy will be quite appropriate for followup studies on $CeIrIn_5$ and $CeCoIn_5$. For the latter compound, NMR (Nick Curro) indicates that the QE linewidth is 1.5meV, which should be resolvable in the E_i = 16.6meV data. Our results from LRMECS for $CeIrIn_5$ also suggest a larger QE linewidth than in $CeRhIn_5$, giving us hope that we also can resolve the QE scattering in that compound. The LRMECS results also suggest that the first excitation in $CeIrIn_5$ occurs at a lower energy (4-5meV) than in CeRhIn5 (7meV); on LRMECS these lower energies lie under the wing of the elastic line, and are not well-resolved. The elastic resolution on PHAROS for 48meV neutrons is sufficiently better than the resolution on LRMECS for 35meV neutrons that we should be able to directly resolve this transition as well.

IMPORTANT! List or attach a list of publications resulting from this experiment (published or in press).

LANSCE
Los Alamos Neutron Science Center

REPORT ON EXPERIMENT
(Please Type)

Submit all experiment reports to:
LANSCE User Office, MS H831, Los Alamos National Laboratory, Los Alamos, NM 87545

Experiment was carried out at:	**Local Contact**	**Proposal #**	***LANSCE Use Only***
[x] Manuel Lujan Jr. Neutron Scattering Center	Dr. Jarek Majewski	**2002002**	**Report Rc'd**
[ ] Weapons Neutron Research Facility	**FP/Instrument Used**		**2/14/03**
[ ] WNR/Blue Room	SPEAR		

Title
Neutron Reflectivity from Langmuir Monolayers of a Synthetic Electron Transfer Protein

Authors and Affiliations
Larry R. Kneller, Center for Neutron Research, NIST, Gaithersburg, MD
Joseph Strzalka and J. Kent Blasie, Department of Chemistry, University of Pennsylvania, Philadelphia, PA

Experiment Report

Introduction

De novo designed peptides show promise as constituents of novel materials. For instance, a family of soluble peptides based on the 4-alpha-helical bundle motif has been developed that can serve as a versatile molecular scaffolding for the arrangement of metallo-porphyrin prosthetic groups whose relative position and orientation would largely determine their electron-transfer properties. Device applications require an oriented ensemble of such molecules, such as the monolayer that can be formed at the air/water interface (and transferred to a solid support) when the peptide is modified by the addition of a hydrophobic group, e.g. a hydrocarbon chain. X-ray and neutron reflectivity are good techniques for studying these monolayers because they apply to non-crystalline structures and can be used at the interface, which may alter the molecules from their structure in solution. Neutron reflectivity becomes particularly attractive when coupled with deuterium labeling. Solid phase synthetic techniques allow us to label the amino acid at any point in the sequence by replacing it with its deuterated analog.

X-ray reflectivity studies demonstrate that the peptide molecules align with their a-helices approximately normal to the plane of the monolayer when high surface pressure is applied. Thus the different amino acids of the peptide are aligned along the direction probed by reflectivity measurements. The challenge for this experiment was to see whether neutron reflectivity could be sensitive enough to permit the location of single deuterated amino acid within the peptide. Because strict isomorphism is required, we thought it better to study monolayers maintained at constant surface pressure at the air/water interface rather than attempt to fabricate identical samples on solid supports. We thought it important to collect data on two different subphases, so that we could use the contrast in scattering length density to help analyze the data. The experiment would also provide some basis for comparison between pulsed sources and monochromatic neutron sources, as a similar experiment was conducted at NIST (Nov 1998).

Methods

We mounted onto the sample stage of SPEAR a Langmuir trough with mechanized barrier motion and a feedback control system for maintaining constant surface pressure.

Experiment Report *(continued)*

We spread monolayers of a mixture of the phospholipid DLPE (dilauryl phosphatidyl ethanolamine, with perdeuterated hydrocarbon chains) and one of a family of deuterium-labeled peptides in a lipid:peptide mole ratio of 2:1, compressed to 35 mN/m and maintained that pressure during data collection, typically 4-6 hours. The single incident angle available and the spectrum of the beam combined to a range of momentum transfer ($q_z=(4\pi/\lambda)\sin\theta$) $0.0156 < q_z < 0.1499$ Å^{-1}.

Samples

To make the peptide for the monolayers, we synthesize a 31 amino acid peptide that is mostly a-helical, except for a flexible loop (3 Glycines) and 1 Cysteine at the N-terminus. The amino group of the Cys is used for coupling a (perdeuterated) C16 hydrocarbon chain while the side chain forms a disulfide bond with the Cys of another peptide unit, forming a dihelix capable of binding two heme groups (by bis-His ligation). Leucines within the sequence are replaced with deuterated D10-Leucine to create a family of singly labeled peptides with labels in positon 9, 14, 21 or 28, as well as the unlabeled peptide with perdeuterated C16 chains but without any D10-Leu.

Results

We were able to collect data on monolayers prepared with each of the labeled peptides and the unlabeled peptide on buffered subphases prepared with 100% or 50% D2O. Within the limited q-range available, the differences between monolayers are subtle and will require careful analysis, currently underway. We intend to apply the model-independent box-refinement method to the data to obtain the gradient of the scattering-length density (SLD) profile of the unlabeled monolayer. Nonlinear fitting of a finite sum of Gaussians in real space to the gradient SLD profile we obtain allows us to integrate the gradient profile analytically and obtain the SLD profile itself, expressed as a finite sum of error functions (as in the traditional "slab-model"). Assuming that the excess SLD due to the label is distributed as a Gaussian in the monolayer SLD profile, we can fit the SLD profiles from the labeled monolayer as a sum of the unmodified SLD profile from the unlabeled monolayer plus the Gaussian whose parameters are found again via nonlinear fitting. This should determine the different label positions. Comparison of the data from the different subphases should provide additional constraints to facilitate interpretation of the results.

IMPORTANT! List or attach a list of publications resulting from this experiment (published or in press).

N/A: Analysis still underway.

LANSCE
Los Alamos Neutron Science Center

REPORT ON EXPERIMENT
(Please Type)

Submit all experiment reports to:
LANSCE User Office, MS H831, Los Alamos National Laboratory, Los Alamos, NM 87545

Experiment was carried out at:	**Local Contact**	**Proposal #**	***LANSCE Use Only***
[X] Manuel Lujan Jr. Neutron Scattering Center	M. Fitzsimmons	**2002010**	**Report Rc'd**
[ ] Weapons Neutron Research Facility	**FP/Instrument Used**		**3/26/03**
[ ] WNR/Blue Room	ASTERIX		

Title

Probing Depth Dependent Magnetism in Ferromagnet/GaAs Epitaxial Heterostructures

Authors and Affiliations
Xuying Dong, Brian Schultz, Chris Leighton, Chris J. Palmstrøm, University of Minnesota
Sungkyun Park, Mike Fitzsimmons, Los Alamos National Laboratory

Experiment Report

The current drive towards utilizing the spin of the electron in electronic devices, rather than just its charge, is leading towards a situation where one wants to combine magnetic and semiconducting components in a single heterostructure.[1] One of the simplest structures would include a metallic ferromagnet / non-magnetic semiconductor interface where spin can be injected from the ferromagnet into the semiconductor. Unfortunately, this has proved to be difficult to achieve with significant efficiency, which is believed to due to spin flip scattering at the interface resulting from interfacial disorder or magnetic dead layer.[2] An enormous obstacle to our understanding is provided by the difficulty involved with probing the magnetic behavior in the ferromagnet, close to the interface.

The proposed work was to investigate the depth dependent magnetization in ferromagnet / GaAs heterostructures to obtain a detailed understanding of the magnetic scattering profile in the ferromagnetic layer. In particular, it accessed whether a magnetic dead layer is present at the interface, as well as determining how the symmetry of the GaAs surface affects the "bulk" properties of the ferromagnetic layer such as its magnetic anisotropy and magnetization reversal mode. Both of these effects are critical to the understanding of the physics of ferromagnetic metal / semiconductor interfaces. Two types of heterostructure samples were studied: FeCo/GaAs (100) and Ni_2MnGe/GaAs (100). These structures were epitaxial systems grown by molecular beam epitaxy that have been comprehensively characterized by *in situ* electron diffraction, and *ex situ* X-ray diffraction, Rutherford backscattering and transmission electron microscopy, providing an in depth picture of the structure and, in particular, the interface structure at the atomic level. [3-6]

The magnetic hysteresis loops obtained from the FeCo/GaAs (100) structures at room temperature with the magnetic field applied along the [011] and $[0\bar{1}1]$ directions are shown in Fig. 1. In bulk bcc FeCo, the crystalline anisotropy would make these two directions equivalent. This is clearly not the case for these epitaxial films. The induced uniaxial anisotropy arises from the 2-fold surface symmetry of GaAs (100), resulting in the [011] direction tbeing the easy axis and the $[0\bar{1}1]$ a hard one.[3,4]

In a Polarized Neutron Reflectometry (PNR) experiment, the intensity of the neutrons reflected from a surface is measured as a function of the momentum transfer that is perpendicular to the surface, $Q=4\pi sin\theta/\lambda$, where θ is the angle of incidence (and reflection) and λ is the neutron wavelength. A scan over a suitable range of Q provides information on the chemical and magnetic depth profile of the film. Figure 2 shows the Q dependence of non spin-flip reflectivities $R^{++}(0^o)$ and $R^{--}(0^o)$ of the film at saturation (H = 1000 Oe: point A on the hysteresis loop in Fig 1.) at room temperature. They yield information on the in-plane magnetization of the sample parallel to the external field direction. The difference of $R^{++}(0^o)$ and $R^{--}(0^o)$ profiles gives an absolute value of the magnetization of the film. There is no significant spin flip signal R^{-+} in this measurement, which indicates that the sample magnetization throughout the film is fully aligned with the external field direction.

Experiment Report *(continued)*

The spin-flip reflectivity, R_s^{-+} (90º), which is related to the in-plane magnetization components perpendicular to the applied field, were measured after the sample was first saturated along the easy axis [011], then the field was brought to zero and then the sample was rotated 90º, finally a guide field of a few Oe, which was too weak to affect the magnetization, was applied to orient the neutron spins for the measurements. The procedure was made possible because for this sample the remnant magnetization is close to the saturated value (point B in Fig. 1). The reflectivities R^{++}(90º) and R^{--}(90º) were also measured, as shown in Fig. 3. Their intensities are exactly the same, implying there is no net magnetic moment along the field direction ($[0\bar{1}1]$). This together with the spin-flip reflectivity R^{-+} confirming that moments are oriented perpendicular to H, i.e. along [011]. Figure 4 shows the reflectivities measured in 60 Oe field after saturation along the hard axis $[0\bar{1}1]$ (point C in Fig. 1). As shown in Fig. 4, R^{++} and R^{--} are not exactly the same but slightly different, indicating a small magnetization component along the applied field axis. This together with the fact that the intensity of spin-flip reflectivity R^{-+} at point C is nearly identical to that at point B implies that the magnetic domains are almost rotated 90º throughout the film, which is in agreement with the MOKE studies.[4] After fitting with the models, the chemical layer thickness (determined using just non-spin-flip neutron data) is 201Å, while the magnetic layer thickness is 197Å (determined using just spin-flip neutron data). These data suggest ~5Å of magnetically dead FeCo, which could exist at either the interface of Al (capping layer)/ FeCo or FeCo/GaAs or both. Further investigations are needed to ascertain whether there are two dead layers (one at each interface) or just one (at the top or the bottom).

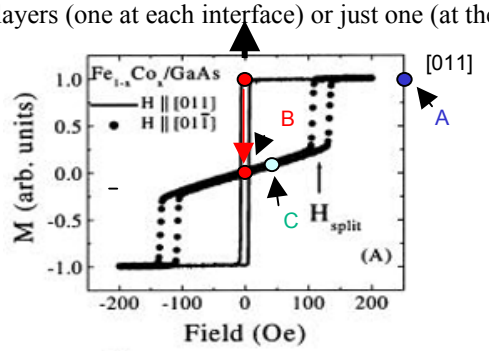

Fig. 1 Room temperature hysteresis loops of bcc-FeCo (100) grown on GaAs (100).

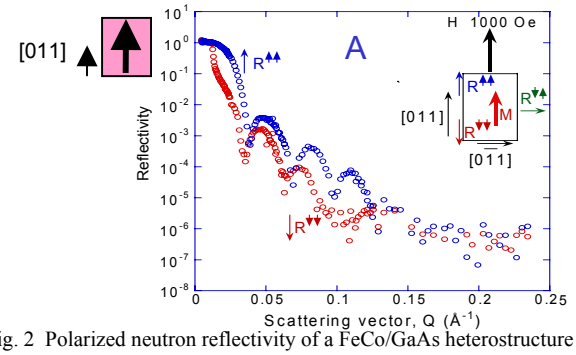

Fig. 2 Polarized neutron reflectivity of a FeCo/GaAs heterostructure in a saturating field of 1000 Oe (point A in figure 1).

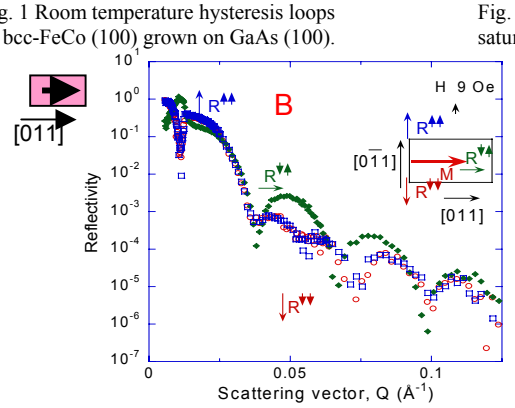

Fig. 3 Polarized neutron reflectivity of a FeCo/GaAs heterostructure in a remnant field (point B in figure 1).

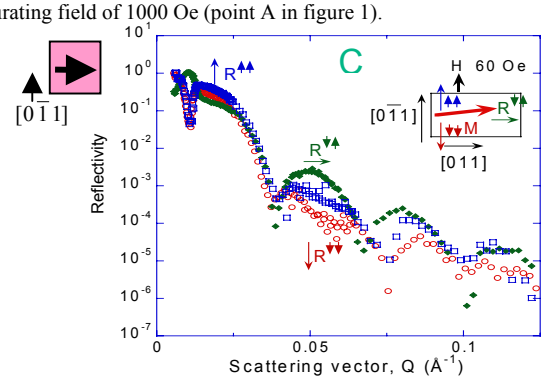

Fig. 4 (a) Polarized neutron reflectivity of a FeCo/GaAs heterostructure in a 60 Oe field along $[0\bar{1}1]$ (point C in figure 1).

The second system we studied is Ni_2MnGe on GaAs (100). This is one of the ferromagnetic Heusler alloys that have been grown and investigated on GaAs by our group.[5,6] These Heusler alloys make very attractive choices for ferromagnet/GaAs structures as they have high Curie temperatures, are well lattice matched to GaAs, and in many cases, have been predicted to be half-metallic from electronic band structure calculations, which offers the possibility of 100% spin-polarized charge currents resulting in distinct advantage over conventional ferromagnets for spin-polarized injectors. However, the polarized neutron reflectivity studies were not completed due to the limited time. Hence, additional neutron beam time is needed in the future to study the magnetic properties of Heusler alloy / GaAs heterostructures in more detail..

[1]S. A. Wolf *et al.*, Science **294**, 1488 (2001).
[2]R. S. Stroud *et al.*, Phys. Rev. Lett. **89**, 166602 (2002).
[3]L. C. Chen *et al.*, J. Vac. Sci. Technol. B **18**, 2057 (2000).
[4]A. F. Isakovic *et al.*, J. Appl. Phys. **89**, 6674 (2001).
[5]J. W. Dong *et al.*, Appl. Phys. Lett. **75**, 1443 (1999).
[6]X. Y. Dong *et al.*, unpublished (2003).

LANSCE
Los Alamos Neutron Science Center

REPORT ON EXPERIMENT
(Please Type)

Submit all experiment reports to:
LANSCE User Office, MS H831, Los Alamos National Laboratory, Los Alamos, NM 87545

Experiment was carried out at:	**Local Contact**	**Proposal #**	***LANSCE Use Only***
[X] Manuel Lujan Jr. Neutron Scattering Center	M. Bourke	**2002011**	**Report Rc'd 3/18/03**
[ ] Weapons Neutron Research Facility	**FP/Instrument Used**		
[ ] WNR/Blue Room	SMARTS		

Title
Load Sharing in Cemented Carbides

Authors and Affiliations
Dr. Aaron Krawitz – Dept of Mech. & Aerospace Engineering
University of Missouri – Columbia
Columbia, MO 65211

Jon W. Paggett – Dept of Mech. & Aerospace Engineering
University of Missouri – Columbia
Columbia, MO 65211

Experiment Report
WC-Ni samples were used with Ni contents of 8, 16, and 31 vol % and WC particle sizes of 2 to 4 μm. The sample microstructures ranged from a continuous WC *skeleton* (8 vol % of Ni) to WC *floating* in Ni (31 vol % of Ni). The samples were cylinders 12 mm in diameter and 28.8 mm in length. The overall composite load (stress) and strain curves were measured with a load cell and an extensometer, respectively, while the WC and Ni phases were simultaneously measured with neutrons. Each sample underwent three load-unload cycles at stress levels of -500, -1,000, and -2,000 MPa successively (i.e., three 0 to -500 MPa to 0 cycles, then three 0 to -1,000 to 0 cycles, and so on).

The first -2,000 MPa cycle for the sample with 31 vol % of Ni (Fig. 1) shows that the composite stress-strain curve shows plasticity at 1,000 MPa. Below this stress, the strains in the Ni and in the composite are the same, as predicted by the shear lag model. The deviation occurs because the diffraction data measures only elastic strain in the Ni whereas the extensometer records total (elastic and plastic) strain. (The Ni phase is elastic to -1,000 MPa because of the previous cycling.) The plastic flow of the Ni phase creates a large hysteresis that narrows on subsequent cycles. The second cycle is shown; the third cycle almost coincides with the second. The decrease in elastic strain accumulation in the Ni phase is taken up by the WC. However, the high Young's modulus (700 GPa) and WC content (69 vol %) lead to an effect too small to be observed. In the transverse direction, the Ni phase yields at which time the strain accumulation rate not only slows down but also reverses back to zero. Apparently the WC is restraining the Ni and creating a compressive elastic reaction stress.[1]

Peak *width* behavior for the 8 vol % Ni sample in the axial direction is shown in Fig. 2, for three crystallographic directions in the Ni: [111], [200], and [311]. The peak widths for each direction are substantially reversible with the applied load. This means they are primarily indicating changes in the *variance* or *distribution* of elastic strain (i.e., the positional strain variation within the Ni regions) during the loading cycle.[2] The fact that they return to their starting values means they are not due to plasticity (dislocations). Furthermore, the plastic strains are too low to cause measurable peak broadening in these experiments. The reversibility also suggests that the thermal residual stress is not decreasing substantially during the loading cycle. The peak width for the (111) planes is strikingly different, and this is not understood at present. WC peak widths show a smaller, reversible increase on loading in the axial direction and little change in the transverse direction.

Experiment Report *(continued)*

Preliminary data was also taken on a WC–16 vol % Co sample. WC–Co is a more commonly used commercial material, but is complicated by a stress-induced phase transformation in the Co from FCC to HCP, faults from the large thermal residual stresses, and by the fact that Co is a poor neutron scatterer. This sample was cyclically loaded to -500 MPa, -1000 MPa, and -2000 MPa (one cycle at each load level, as opposed to the 3 cycles applied to the Ni samples). The data shows that the stress-induced phase transformation is reversible on unload. Fig. 3a shows the Co FCC 111 diffraction peak in the axial direction at zero load. Under increasing applied load, the Co HCP 101 peak appears and its intensity increases until it dominates the FCC 111 peak at -2000 MPa (see Fig. 3b). When unloaded, the HCP 101 peak decreases until it is indistinguishable from the background and only the FCC 111 peak is visible. Previous studies have reported permanent stress induced phase transformations in WC–Co after fatigue cycling[3], but observation of a reversible phase transformation is seen here, we think for the first time.

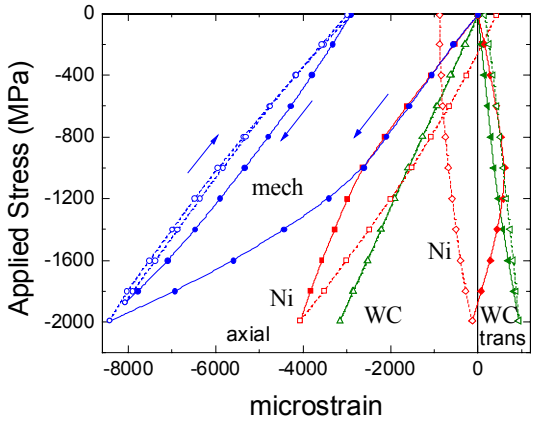

Figure 1. -2000 MPa load cycle for the 31 vol % Ni sample. Solid lines indicate loading, dashed indicate unloading.

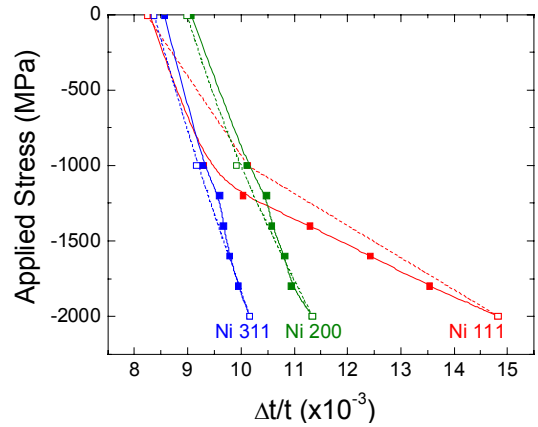

Figure 2. Peak breadth response for the 8 vol % Ni sample in the axial direction. Δt/t is FWHM relative to the TOF for that peak.

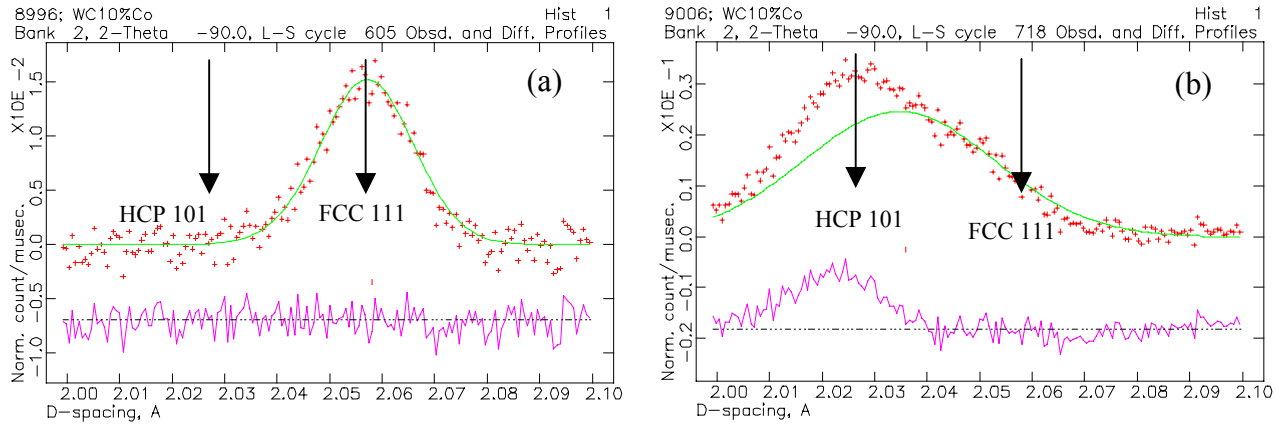

Figure 3. Diffraction data from WC–16 % Co sample at loads of (a) 0 and (b) -2000 MPa in the axial direction. The HCP peak increases with load (above about -1000 MPa) while the FCC peak decreases. FCC 111 peak becomes a shoulder of the HCP 101 peak.

References

1. D.H Carter and M.A.M. Bourke, *Acta Materialia* **48**, 2885-2900 (2002).
2. A.D. Krawitz et al., *Materials Science and Engineering A* **105/106**, 275-281 (1988).
3. C.H. Vasel et al., *Metallurgical Transactions A* **16**, 2309-2317 (1985).

IMPORTANT! List or attach a list of publications resulting from this experiment (published or in press).

LANSCE
Los Alamos Neutron Science Center

REPORT ON EXPERIMENT
(Please Type)

Submit all experiment reports to:
LANSCE User Office, MS H831, Los Alamos National Laboratory, Los Alamos, NM 87545

Experiment was carried out at:	**Local Contact**	**Proposal #**	***LANSCE Use Only***
[x] Manuel Lujan Jr. Neutron Scattering Center	Bjørn Clausen	2002012	**Report Rc'd**
[ ] Weapons Neutron Research Facility	**FP/Instrument Used**		**3/21/03**
[ ] WNR/Blue Room	SMARTS		

Title
Deformation Mechanisms of Titanium as a Function of Temperature

Authors and Affiliations
EC Oliver[1,2]
J Quinta da Fonseca[2]
MR Daymond[1]
PJ Withers [2]

1- ISIS Facility, CCLRC Rutherford Appleton Laboratory, Chilton, Didcot, OX11 0QX, UK
2- Manchester Materials Science Centre, University of Manchester and UMIST, Grosvenor St, Manchester, M1 7HS, UK

Experiment Report

Intergranular stresses in polycrystalline materials are of major concern to the engineer, since they affect material properties such as fatigue resistance, fracture toughness and strength. An important origin of these stresses is mechanical anisotropy on the level of individual grains. This gives rise to the build up of incompatibilities between differently oriented grains during mechanical deformation. While the stresses which develop in face-centred cubic materials are now well characterised, more work is required on lower symmetry materials, in which plastic anisotropy may be greater and the relative activity of different deformation mechanisms is unclear, depending sensitively on factors such as grain size, alloy composition and temperature. In hexagonal close-packed (hcp) materials, deformation parallel to the crystal c-axis is commonly relatively difficult, and may be accommodated either by slip or twinning mechanisms, which have different temperature dependencies. This experiment was carried out to characterise the evolution of intergranular stresses as a function of temperature in titanium, and to assess the temperature dependence of the various deformation modes. Titanium is one of the most technologically important hcp materials, particularly in the aerospace industry.

The alloy tested was IMI 125 commercially pure titanium, which is particularly appropriate for this kind of study because it consists of a single hcp phase, so that the intergranular stresses are not obscured by interphase influences. Moreover, twinning activity is favoured by the relatively large grain size of ≈50μm. Preliminary optical microscopy revealed the formation of deformation twins around indentation pits. The material was in the form of a hot rolled plate with a moderately strong texture, the crystallite c-axis tending to lie parallel to the plate transverse direction. Tensile samples were cut parallel to this direction in order to encourage tensile twinning activity. In situ tensile tests were conducted using the SMARTS stress rig and furnace at room temperature, 190ºC and 380ºC. Count times were approximately 45mins – this demonstrates the excellent capabilities of SMARTS for this type of measurement, since previous internal stress neutron diffraction measurements on titanium have required count times of several hours.

Fig. 1 shows the average elastic strain response to applied stress of three axial grain families, at room temperature and 190ºC. These families correspond to some of the most intense diffraction peaks, and demonstrate the quality of data which can be achieved using SMARTS, even with difficult materials like

Experiment Report *(continued)*

titanium. Interestingly, the trends in the grain family responses are distinctly different to those reported by Daymond and Bonner in IMI 834, which contains a significant Al concentration [1]. This emphasises the sensitivity of deformation mechanisms in titanium to factors such as composition and grain size.

At both temperatures, the slopes of all responses in the elastic regime are very similar. Although titanium exhibits relatively low single crystal elastic anisotropy, self-consistent model calculations predict a greater variation in slopes for an untextured polycrystal. Thus the similarity possibly results from the greater constraint imposed by the alignment of the stiffer crystallite directions along the tensile axis (the c-axis is the stiffest direction).

Upon yielding, redistribution of load between families is evident. Some features of the load responses are similar at both temperatures. In both cases the $\{10\bar{1}1\}$ family is plastically softest while yielding causes the $\{0002\}$ family to bear greater load. A notable feature of the room temperature $\{0002\}$ response is the double inflection above 300MPa, first towards lower and then once more towards greater lattice strain. The double inflection suggests the onset of activity in a new mode, followed by a high rate of work hardening. Since deformation twins are easily observable by optical microscopy in this material, it is likely that the mode in question is tensile twinning, which acts to relieve stress along the $\{0002\}$ normal direction. At 190ºC, an inflection is seen only at a later stage of deformation (in terms of macroscopic plastic strain), suggesting that increasing temperature promotes slip over twinning. The most striking difference between the data acquired at the two temperatures is the behaviour of the $\{10\bar{1}3\}$ family.

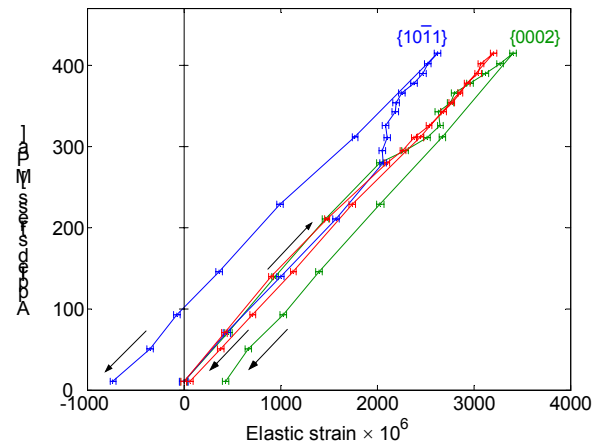

(a) Room temperature

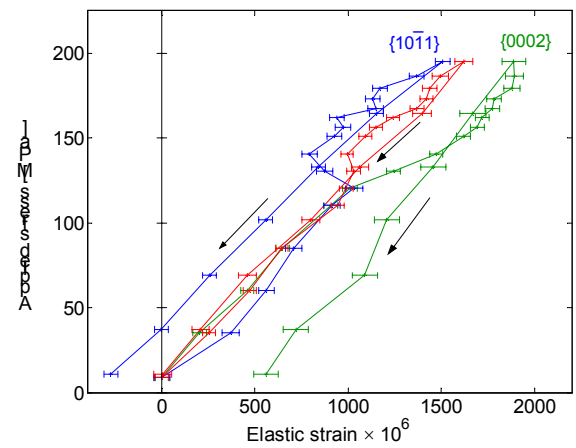

(b) 190ºC

Fig. 1: Axial grain family elastic strains versus applied stress at temperatures of (a) room temperature; (b) 190ºC. Arrows indicate the direction of loading.

At room temperature, the $\{10\bar{1}3\}$ response follows closely the $\{0002\}$ response, although the lack of a double inflection is noteworthy. At 190ºC, however, the response is closer to that of the softer $\{10\bar{1}1\}$ family. Preliminary elastoplastic self-consistent (EPSC) modelling demonstrates that of the available deformation mechanisms, only basal slip can cause this relative softening of the $\{10\bar{1}3\}$ family with respect to both other families. This suggests that the critical resolved shear stress for basal slip varies more rapidly with temperature than that for prismatic and pyramidal slip modes.

This report highlights only a few observations from the excellent dataset acquired. In particular, the variation in peak intensities is also informative, providing evidence of twinning activity. We are presently conducting EPSC modelling for a more quantitative analysis and interpretation.

References: [1] M.R. Daymond, N.W. Bonner, Mat. Sci. Eng. A340 (2002) 272-280.

IMPORTANT! List or attach a list of publications resulting from this experiment (published or in press).

E.C. Oliver, M.R. Daymond, J. Quinta da Fonseca, P. Bate, P.J. Withers, to be submitted to MECA-SENS 2003, Manchester, UK, September 2003

LANSCE
Los Alamos Neutron Science Center

REPORT ON EXPERIMENT
(Please Type)

Submit all experiment reports to:
LANSCE User Office, MS H831, Los Alamos National Laboratory, Los Alamos, NM 87545

Experiment was carried out at:	**Local Contact**	**Proposal #**	***LANSCE Use Only***
[x] Manuel Lujan Jr. Neutron Scattering Center	Mike Fitzsimmons	**2002014**	**Report Rc'd**
[ ] Weapons Neutron Research Facility	**FP/Instrument Used**		**2/12/03**
[ ] WNR/Blue Room	Asterix		

Title
Magnetization Depth Profiling in Modulation Doped Colossal Magnetoresistive Manganites

Authors and Affiliations
Axel Hoffmann, Suzanne te Velthuis; Argonne National Laboratory
Pedro Prieto; Unversidad del Valle, Cali, Colombia

Experiment Report

The Interactions between antiferromagnets and ferromagnets can give rise to exchange bias, which results in an asymmetric shift of the ferromagnetic hysteresis loop. In spite of the technological relevance of this effect, the actual microscopic mechanism is poorly understood. One particularly important, but still unresolved, question is whether the antiferromagnet acquires a net magnetic moment at its interface with the ferromagnet.

Modulation doped Manganite ($La_{1-x}Ca_xMnO_3$) superlattices are a particularly well-suited sample system to study this question with polarized neutron reflectometry (PNR). Due to the chemical similarity between the ferromagnetic and the antiferromagnetic layers (just differing in slightly modified Ca concentration) there is hardly any chemical contrast. This means that in the magnetically ordered state any superlattice Bragg reflections are solely due to the magnetic structure of the sample. Consequently the magnetization depth profile in the modulation doped Manganite superlattices can be determined with very high precision.

In the preformed experiment we tried to answer two questions; first, is in the exchange-biased state the magnetization depth profile different for positive and negative field saturation? Second, does the magnetic depth profile change upon entering the exchange-biased state?

In order to answer the first question, we measured PNR profiles at 10 K and +5 kOe, after either field cooling in –5 and +5 kOe. The resulting PNR profiles are shown in Fig. 1. In both profiles there are clear superlattice peaks observed, which are due to the spatial modulation of the magnetization profile. Overall the profiles for the two different cooling fields look very similar, but there are a few subtle, significant differences. The data for field cooling in –5 kOe [Fig. 1(a)] shows a broa peak underneath the first superlattice peak, which is absent for the data after field cooling in +5 kOe [Fig. 1(b)]. Furthermor there is significantly more splitting between the R^{++} and R^{--}data at the second superlattice peak in Fig. 1(a) compared to Fig. 1(b). While these differences are arguably small, they nevertheless indicate that the magnetization depth profile differs for the two different field-cooling procedures.

For reference we also measured the PNR profile at 110 K and 5 kOe. This temperature is above the blocking temperature of approximately 80 K and thus the sample is in an unbiased state, while it is still ferromagnetic (T_c = 150 K). The main difference between this profile (shown in Fig. 2) and the low temperature data (Fig. 1) is that the spin splitting at the first superlattice Bragg reflection has changed sign. Again, this indicates a modification of the magnetization depth profile upon entering the exchange-biased state.

In order to identify the relevant changes in the magnetization depth profiles further analysis based on model simulations of the data is required. This analysis is currently being performed.

Experiment Report *(continued)*

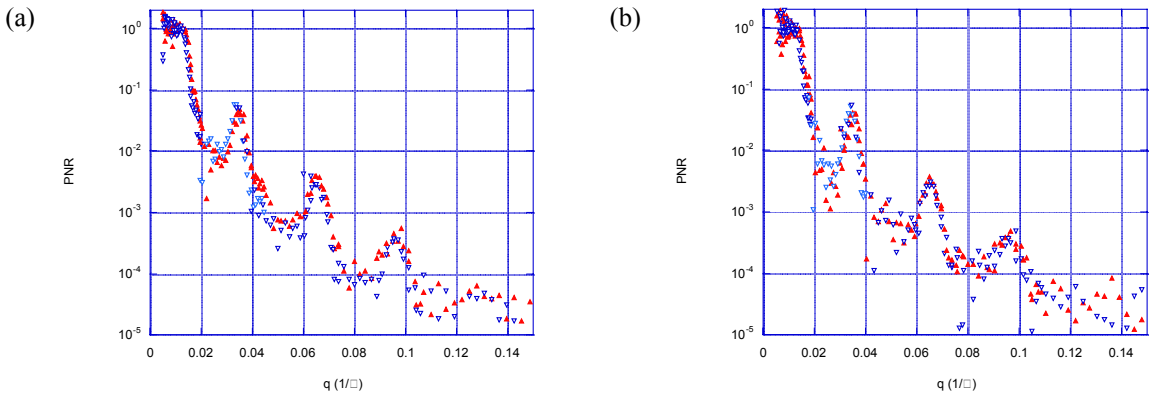

Figure 1. Polarized Neutron Reflectivity measured at 10 K and +5 kOe, after field cooling in (a) –5 kOe and (b) +5 kOe. Shown are R^{++} (solid, red) and R^{--}(open, blue).

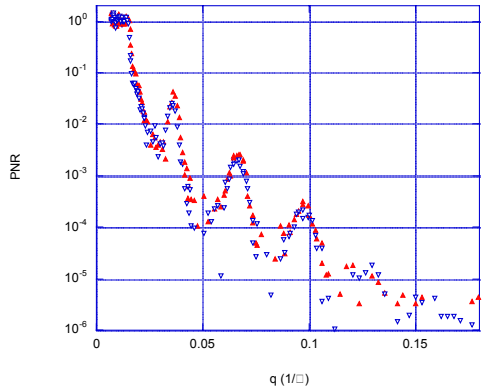

Figure 2: Polarized Neutron Reflectivity measured at 110 K and +5 kOe. Shown are R^{++} (solid, red) and R^{--} (open, blue).

IMPORTANT! List or attach a list of publications resulting from this experiment (published or in press).
None at this point.

LANSCE
Los Alamos Neutron Science Center

REPORT ON EXPERIMENT
(Please Type)

Submit all experiment reports to:
LANSCE User Office, MS H831, Los Alamos National Laboratory, Los Alamos, NM 87545

Experiment was carried out at:	**Local Contact**	**Proposal #**	***LANSCE Use Only***
☑ Manuel Lujan Jr. Neutron Scattering Center	Yusheng Zhao	**2002016**	**Report Rc'd**
☐ Weapons Neutron Research Facility	**FP/Instrument Used**		**3/26/03**
☐ WNR/Blue Room	**HIPPO/TAP-98**		

Title

Thermoelastic Equation of State of Aluminum

Authors and Affiliations

Yusheng Zhao, LANL/LANSCE-12
Duanwei He, LANL/LANSCE-12

Experiment Report

The behavior of aluminum under high pressures and temperatures was investigated by *in situ* time-of-flight neutron-diffraction techniques. Unit-cell dimensions, measured up to P = 6 GPa and T = 900 K , were derived from the refinement results and fitted to a high-temperature third-order Birch-Murnaghan equation of state. All of the previous experimental data involving shock wave, ultrasonic, thermal-expansion measurements were also analyzed and fited to high-temperature Birch/Vinet equation of state and the thermal pressure approach of Mie-Grüneisen EOS, respectively. It was also found that only the (200) peak left in the neutron diffraction pattern when the Al sample was heated to 900 k from 700 k at 4 GPa.

The high *P-T*, *in situ* neutron diffraction experiment was performed at HIPPO with TAP-98. NaCl was used as pressure medium as well as standard. The sample temperature of the high pressure/temperature cell assembly was monitored using a W/5%Re-W/26%Rh thermocouple (C-type, Omega Engineering, Inc.) and was controlled by dc power supply. For *high-P-T* experiments the temperature was stable to within 2 °C over the time period of several hours was constant to within 5 °C in the sample volume. Pressures for the sample were all calculated from the lattice constants of the NaCl pressure calibrant and were estimated to be accurate within $\Delta P = \pm 0.1$ GPa. The time-of-flight neutron-diffraction spectra of the sample were collected by the detector banks at a fixed Bragg angle of $2\theta = \pm 90$ °. To avoid deviatoric stress on the polycrystalline sample, we always preheat the powder sample to 700 K at each incensement in pressure for about 5 min.[1] A particular routine to correct diffraction optical and to determine P-V-T was taken for the data reduction.[2] Fifteen data points of unit-cell volumes collected by *high-P-T* neutron-diffraction technique are shown in Fig. 1.

Experiment Report *(continued)*

Figure 1. Cell volumes of aluminum observed at *high-P-T* conditions are plotted as a function of pressure.

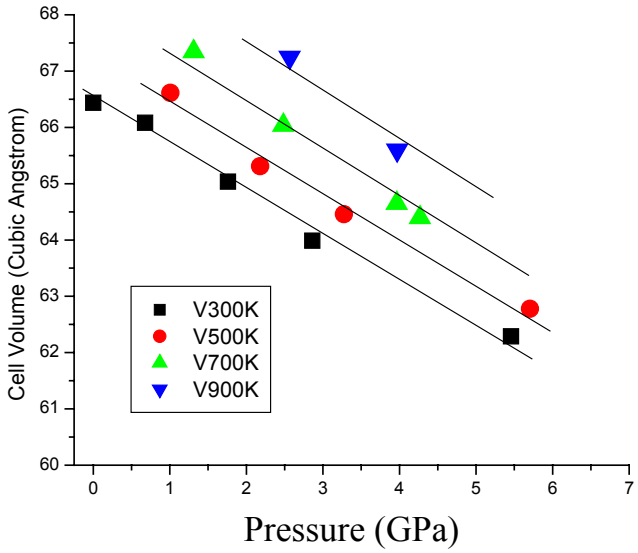

Figure 1

Figure 2. Neutron diffraction of aluminum and NaCl at pressure of 4 GPa and temperature of (a) 700 K; and (b) 900 K. The data was refined using general structure analysis.

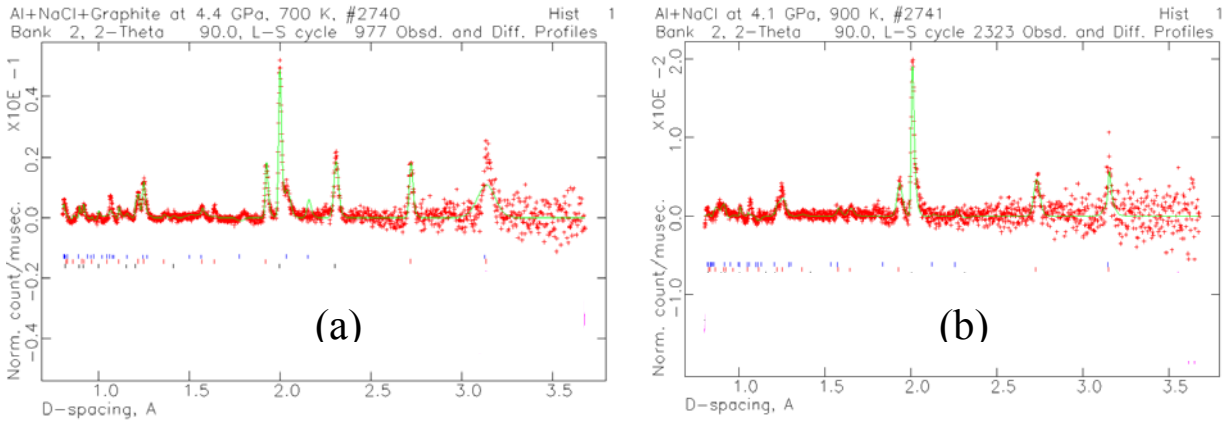

Figure 2

Interestingly, all the diffraction peaks of aluminum disappeared except (200) when the sample was heated to 900 K from 700 K at pressure of 4 GPa (see Fig. 2). Further pressurization and heating of the sample did not change the texture of the aluminum sample.

[1] *Y. Zhao, A. C. Lawson, J. Zhang, B. I. Bennett, and R. B Von Dreele, Phys. Rew. B 62, 8766 (2000)*
[2] *Y. Zhao, R. B. Von Dreele and D. J. Weidner, J. Appl. Cryst. 32, 218 (1999).*

IMPORTANT! List or attach a list of publications resulting from this experiment (published or in press).

LANSCE
Los Alamos Neutron Science Center

REPORT ON EXPERIMENT
(Please Type)

Submit all experiment reports to:
LANSCE User Office, MS H831, Los Alamos National Laboratory, Los Alamos, NM 87545

Experiment was carried out at:	**Local Contact**	**Proposal #**	***LANSCE Use Only***
[X] Manuel Lujan Jr. Neutron Scattering Center	Don Brown	#2002022	**Report Rc'd 2/14/03**
[ ] Weapons Neutron Research Facility	**FP/Instrument Used**		
[ ] WNR/Blue Room	HIPD		

Title
Effect of Texture Randomization Processing on the Deformation Mode Activity in Magnesium Alloys

Authors and Affiliations
Sean R. Agnew, University of Virginia
Donald W. Brown, MST-8, LANL
Thomas M. Holden, consultant

Experiment Report

Texture measurements were performed in HIPD (originally scheduled for HIPPO) in order to support and expand upon the *in-situ* deformation experiments being performed concurrently on SMARTS (see prop. #2002106.)

Previous *in-situ* deformation experiments on magnesium alloy AZ31B performed on NPD (summer 2001) were performed on samples with an essentially axis-symmetric fiber texture, so additional texture measurements outside of that which was possible within NPD, using the GSAS Rietveld analysis program, were not necessary.

This year we were concerned with evaluating reports that Equal Channel Angular Extrusion (ECAE) plus a heat treatment is an effective means to alter the properties of magnesium alloys by essentially randomizing their texture. Experiments were performed on three types of samples:

1. conventionally extruded
2. ECAE processed at 200deg C
3. ECAE processed + annealing at 350deg C for 2 hours

The results obtained showed the conventional extrusion to have the typical fiber texture with (00.2) poles normal to the extrusion axis. The volume fraction of grains with (10.0) and (11.0) poles parallel to the extrusion axis were similar.

In the case of the ECAE material, but the as-processed and the annealed had similar textures. In the future, this information could be incorporated into a study of recrystallization of non-cubic metals. For now, what is significant is that the ECAE processed samples both had very strong textures with peak intensities in the (00.2) pole figures over 13 X random distribution. Even though, previous publications by some Japanese scientists led us to believe this would be a good texture randomization scheme, the overall strength of the texture, characterized by the root mean square value of the orientation distribution function (ODF), was significantly higher in the ECAE processed than in the conventionally extruded.

The results of this study formed the back-bone of a paper explaining the unique mechanical behavior of these materials.

S.R. Agnew, J.A. Horton, T.M. Lillo and D.W. Brown, "Enhanced Ductility in Strongly Textured Magnesium Produced by Equal Channel Angular (ECA) Processing", *submitted to Scripta Mater. (2003)*.

Experiment Report *(continued)*

IMPORTANT! List or attach a list of publications resulting from this experiment (published or in press).

LANSCE
Los Alamos Neutron Science Center

REPORT ON EXPERIMENT
(Please Type)

Submit all experiment reports to:
LANSCE User Office, MS H831, Los Alamos National Laboratory, Los Alamos, NM 87545

Experiment was carried out at:	**Local Contact**	**Proposal #**	***LANSCE Use Only***
[X] Manuel Lujan Jr. Neutron Scattering Center	Dr Don Brown	**2002028**	**Report Rc'd**
[ ] Weapons Neutron Research Facility	**FP/Instrument Used**		**2/12/03**
[ ] WNR/Blue Room	SMARTS		

Title
Residual Stresses in Zircaloy-4 Weldments

Authors and Affiliations
Dr. M. I. Ripley ANSTO, Australia
D. G. Carr ANSTO, Australia
Dr. T. M. Holden LANL, Canada

Experiment Report

The Australian Replacement Research Reactor at Lucas Heights, NSW will have a number of welded Zircaloy-4 components within the core region. It is of great technological importance to measure the texture changes and the residual stresses associated with the welds in order to be able to estimate the lifetime of these components.

There have only been a few reported experiments, by the Chalk River group, on Zircaloy-2 welds and none, to our knowledge, on Zircaloy-4 welds. The reported experiments show that the crystallographic texture departs rapidly from the texture characteristic of rolled plate as the heat affected zone (HAZ) is traversed and changes again in the melt zone. The residual strains are high and different for different reflections, characteristic of the superposition of type-1 and type-2 stresses. An objective of the work will be to determine a suitable reflection to use that reflects the macroscopic stress state of the weld. The advantage of neutron diffraction at a spallation source such as SMARTS is that all reflections, corresponding to the grain orientations allowed by the texture at the location, are obtained. This is very important in the heat-affected zone (HAZ) and melt zone where the texture is different from the base metal.

The experiments were made on butt-welded Zircaloy-4 plate of 8.6 mm thickness prepared by the TIG welding method. Residual stress measurements were made on a locus transverse to the weld in the longitudinal, transverse and normal directions at mid-thickness. Additional measurements were also made near the top and bottom surfaces of the plate in the parent weld, and HAZ regions. Small (2 mm cube) coupons were cut from the parent, weld and HAZ to provide stress-free reference lattice spacings. Due to limited time and some instrument set-up delays a final series of measurements on the stress free reference coupons in the transverse direction could not be made, although this is not expected to affect the outcome.

Progress to date on the analysis of the data is as follows:

- The results of the diffraction scans have been analysed using single peak fitting methods to determine the variation in d-spacings across the weld for 16 diffraction planes.
- Reference d-spacings were measured using 2x2x2mm "stress free" cubes cut from the plate as a function of position across the weld.
- Residual strains have been calculated for the plate transverse, longitudinal and normal directions. The results indicate a tensile strain of up to 2500 microstrain in the weld in the longitudinal direction, and a compressive strain of ~800 microstrain in the longitudinal direction.

Experiment Report *(continued)*

Further work is in progress to complete the analysis:

- Residual stresses will be calculated for each of the 16 diffraction planes studied using plane-specific elastic constants.
- An important objective of the work is to ascertain a macroscopic residual stress state using a suitable diffraction plane. This is the "answer" required by engineers to enable an estimation of the likely behaviour of the zircaloy-4 reactor components
- Possible comparison with results calculated using Rietveld analysis of the TOF spectra.

An extension of the work will be the application of a "stress relieving" heat treatment to the welds and further diffraction studies to determine the effectiveness of the treatment.

IMPORTANT! List or attach a list of publications resulting from this experiment (published or in press).

LANSCE
Los Alamos Neutron Science Center

REPORT ON EXPERIMENT
(Please Type)

Submit all experiment reports to:
LANSCE User Office, MS H831, Los Alamos National Laboratory, Los Alamos, NM 87545

Experiment was carried out at:	**Local Contact**	**Proposal #**	***LANSCE Use Only***
[X] Manuel Lujan Jr. Neutron Scattering Center	Dr Don Brown	**2002029**	**Report Rc'd**
[ ] Weapons Neutron Research Facility	**FP/Instrument Used**		**2/12/03**
[ ] WNR/Blue Room	SMARTS		

Title
Measurements of the Strain Response to Applied Stress in Zircaloy-4

Authors and Affiliations
Dr. M. I. Ripley ANSTO, Australia
D. G. Carr ANSTO, Australia
Dr. T. M. Holden LANL, Canada

Experiment Report

It is of fundamental importance for the understanding of the mechanical properties of materials to determine the operating slip systems and other modes of plastic deformation. Recent measurements on Ziraloy-2 have shown that basal, pyramidal and prismatic slip systems operate under tension and that twinning occurs under compression. Zircaloy-4 has mechanical properties different to those of Zircaloy-2 and had not been investigated. The differences in the slip systems in weld metal and heat-affected zone (HAZ) regions from the parent metal was also of interest for related measurements of the residual stresses around welds.

In this work the strain response to applied stress in coupons cut from rolled Zr-4 plate with the tensile axis parallel and perpendicular to the rolling axis was measured using the stress rig on SMARTS. The particular advantage of spallation source diffraction is that measurements can be made of as many as 20 discrete reflections in Zr alloys covering the whole of the stereographic projection. The measurements were made both in the elastic regime to determine the diffraction elastic constants and in the region beyond the yield point where plastic deformation has occurred and where texture changes and type 2 stresses would have been generated.

The results are being modelled with the aid of the elastic-plastic self-consistent model (EPSC) model in order to find the operating slip systems and check for twinning. The results are also important for the analysis of the stress field associated with welds in Zircaloy-4.

Progress to date is as follows:

- The evolution of *residual* internal lattice strains in Zr-4 under uniaxial tension has been determined for 16 diffraction planes from TOF diffraction measurements of d-spacings.
- The results were analysed using single peak-fit analysis to determine d-spacings, then strains were calculated using the d-spacing at zero load as the reference spacing. This enabled determination of internal (Type II) strains as a arising from during the uniaxial tension test.
- Ziccaloy-4 Weld, HAZ and parent plate tensile samples were studied up to strains of 7% and differences in the evolution of residual strains were observed. These were probably due to texture differences between the samples.
- The EPSC model is being used to model the evolution of strains and to determine probable deformation mechanisms. So far, results seems to compare favourably with previous work.

Experiment Report *(continued)*

- The diffraction elastic constants have also been calculated from the tensile tests and also calculated using EPSC.

The analysis is continuing and further work will include:

- Measurement of texture to confirm trends in results.
- Further characterisation of the strain tensor and yield surface of zircaloy-4 under uniaxial tension.
- Calculation of the evolution of residual internal stresses via Hookes Law
- Determination of the most suitable diffraction plane for macroscopic residual stress measurement in welded plate (ie plane most free of type II stresses)

IMPORTANT! List or attach a list of publications resulting from this experiment (published or in press).

LANSCE
Los Alamos Neutron Science Center

REPORT ON EXPERIMENT
(Please Type)

Submit all experiment reports to:
LANSCE User Office, MS H831, Los Alamos National Laboratory, Los Alamos, NM 87545

Experiment was carried out at:	**Local Contact**	**Proposal #**	***LANSCE Use Only***
[X] Manuel Lujan Jr. Neutron Scattering Center	Dave Bish	**2002031**	**Report Rc'd**
[ ] Weapons Neutron Research Facility	**FP/Instrument Used**		**2/12/03**
[ ] WNR/Blue Room	HIPPO		

Title

Internal Strains in Co-deformed Two Phase Compounds

Authors and Affiliations

H. Mecking, Ch. Hartig, J. Laakmann, O. Meyer

Department of Materials Science and Technology
Technical University Hamburg-Harburg
Eissendorfer Str. 42
21071 Hamburg, Germany

Experiment Report

An experimental program was developed to measure the internal elastic strains in different two-phase compounds (Fe-Cu alloy, Ti α/β , γ/α_2 – TiAl). The measurement is carried out by in-situ neutron diffraction under applied load.

A device for this measurement (CRATES), constructed and built at Technical University Hamburg-Harburg, was inserted into the detector/control facility (HIPPO) at LANSCE.

The goals of the measurement were the following:

1. Test the feasibility of the strain device (CRATES)
2. Measurement of the phase specific elastic strains of 10 different samples:
   6 Fe-Cu specimens, 2 Ti-6Al-4V specimens, 2 TiAl specimens
3. Collection of diffraction spectra from the HIPPO detector array.
4. Comparison of the experimental elastic strains with model calculations
   enabling more insight into the micromechanics of two phase materials.

The measurement was only successful to a minor extent. Because of different technical problems a measurement fulfilling the requirements of the described goals was not possible. The main reasons were the following:

1. The adjustment of a calibration sample and the measured specimens was improper resulting in spectra and calibration data of insufficient quality.

2. The count rate was much lower than expected. Therefore only the measurement of 5 samples (including a calibration specimen) was possible.
3. The beam time was shortened by one day due to a technical shortcoming.
4. A diaphragm for the neutron beam suitable for an accurate measurement of the specimens was not available and had to be assembled during beam time.

Especially the feasibility of a proper adjustment of specimens was not given because of the following reasons: An on-line check of a diffraction spectrum during measurement was not possible; It was not possible to monitor the position of the specimens immediately before and during the measurement. An "almost suitable" position could be found by a trial and error method which resulted in an inaccurate specimen adjustment.

The determination of the phase specific elastic strains by a Rietveld method from the measured spectra was too inaccurate to meet the goals stated above. As an example the development of elastic strains under applied stress in a Fe-Cu alloy with a 50/50Vol.% composition is shown in the following diagram:

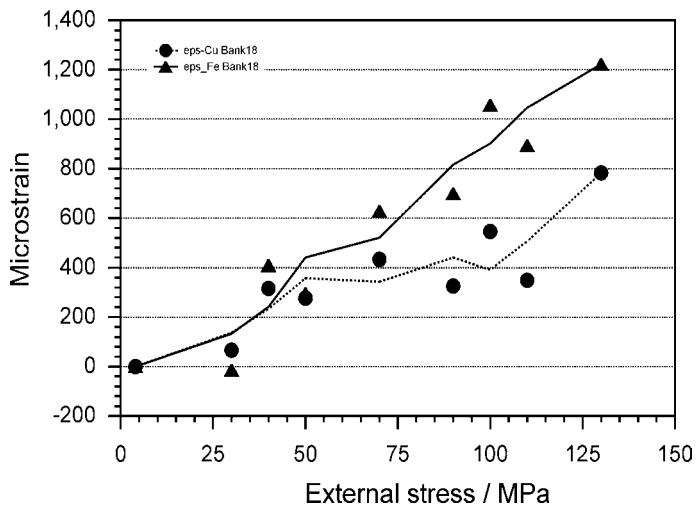

Two fundamental features of the strain development are in accordance with a previous measurement at another neutron facility and with the literature: 1. The strain in Iron (triangles) is distinctly higher than the strain in Copper (circles) after the onset of plastic deformation, 2. Until the onset of plastic deformation the elastic strains are quite similar.

Because of the above stated shortcomings the accuracy of this measurement ($\Delta\varepsilon = 10^{-4}$) is not sufficient for a comparison with model calculations and for publication. But there exists a realistic chance for the achievement of accurate measurements, if the basic requirement of a proper specimen adjustment is fulfilled.

IMPORTANT! List or attach a list of publications resulting from this experiment (published or in press).

LANSCE
Los Alamos Neutron Science Center

REPORT ON EXPERIMENT
(Please Type)

Submit all experiment reports to:
LANSCE User Office, MS H831, Los Alamos National Laboratory, Los Alamos, NM 87545

Experiment was carried out at:	**Local Contact**	**Proposal #**	***LANSCE Use Only***
[x] Manuel Lujan Jr. Neutron Scattering Center	Robert Heffner	**2002039**	**Report Rc'd**
[ ] Weapons Neutron Research Facility	**FP/Instrument Used**		**3/21/03**
[ ] WNR/Blue Room	HIPPO		

Title
Atomic Structure of CsC_{60} by the Rietveld and Pair Distribution Function (PDF) Analysis,

Authors and Affiliations
Il-Kyoung Jeong, Robert H. Heffner, Barbara Simovic, A. C. Lawson, Thomas Proffen, Tim Darling, Los Alamos National Laboratory; Laszlo Forro, Laboratoire de Physique des Solides Semicristallins, Switzerland

Experiment Report]

Polymerized AC_{60} (A=K, Rb, Cs) compounds remain a topic of great interest due to the variety of electronic and magnetic phases found in these polymers [1,2]. For instance, KC_{60} displays 3-dimensional metallic, non-magnetic behavior down to 4 K. On the other hand, CsC_{60} and RbC_{60} exhibit a transition from a quasi-one-dimensional metal to an insulating magnetic state below 40-50 K [2]. Broadly speaking, the nature of the ground state in doped fullerides depends upon a fragile balance between (i) the tendency for the C_{60} molecules to form covalent bonding leading to highly anisotropic structures, (ii) the strong electron-phonon coupling due to some intra-molecular vibrational modes with frequency (0.5eV) close to the electronic bandwidth (0.2eV), and (iii) comparable values of the on-site Coulomb repulsion and the electronic bandwidth, so that all doped fullerides are near a Mott-Hubbard metal-insulator transition [3]. The structure and the electronic properties are therefore intimately related to each other. For example, recent single crystal x-ray diffraction attributed the differences in physical properties of KC_{60} and RbC_{60} (CsC_{60}) to the differences in polymer chain directions in these materials [4].

In order to study the average and local structure of CsC_{60}, we measured powder diffraction patterns of CsC_{60} in the temperature range of $175<T<300$. Figure 1. shows the diffraction patterns of CsC_{60} at 175K, 220K, 260K, and 300K. The preliminary data analysis indicates there are some Aluminum contaminations. We expect that these Al contaminations are from experimental well. For pair distribution function (PDF) analysis, we are working to remove Al contaminations reliably.

Experiment Report *(continued)*

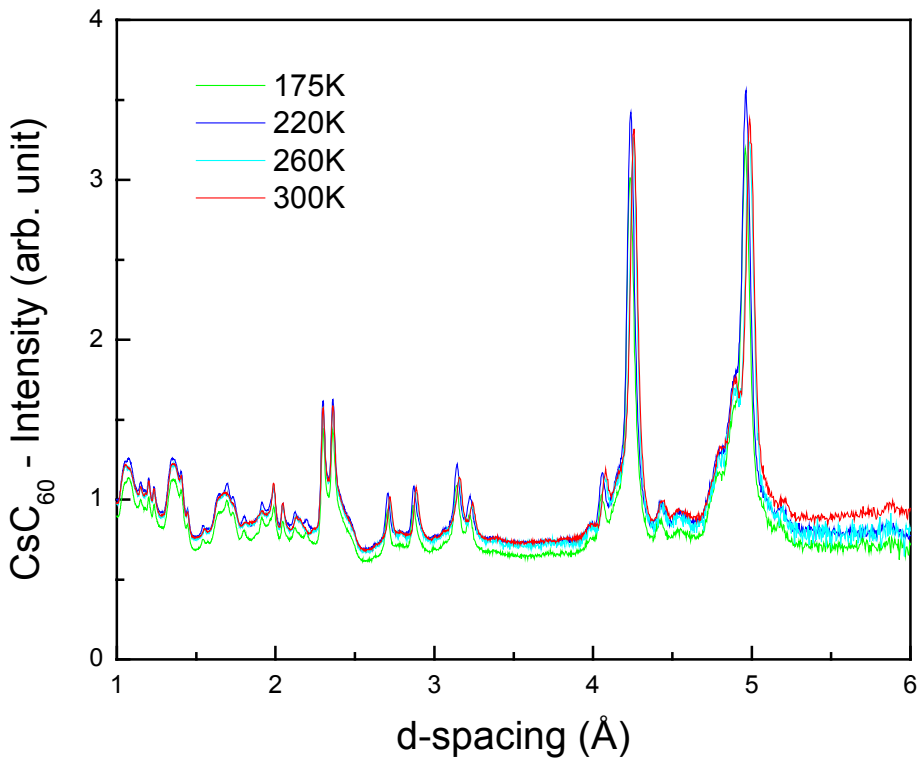

Fig. 1 Diffraction patterns of CsC60 at 175K, 220K, 260K, and 300K.

.

[1] L. Forro et al., Rep. Prog. Phys. 64, 649 (2001)
[2] B. Simovic et al., Phys. Rev. Lett. 82, 2298 (1999)
[3] O. Gunnarson, Rev. Mod. Phys. 69, 575 (1997).
[4] P. Launois et al., Phys. Rev. Lett. 81, 4420 (1998)

IMPORTANT! List or attach a list of publications resulting from this experiment (published or in press).

LANSCE
Los Alamos Neutron Science Center

REPORT ON EXPERIMENT
(Please Type)

Submit all experiment reports to:
LANSCE User Office, MS H831, Los Alamos National Laboratory, Los Alamos, NM 87545

Experiment was carried out at:	**Local Contact**	**Proposal #**	***LANSCE Use Only***
[x] Manuel Lujan Jr. Neutron Scattering Center	m. fitzsimmons	**2002045**	**Report Rc'd**
[ ] Weapons Neutron Research Facility	**FP/Instrument Used**		**3/12/03**
[ ] WNR/Blue Room	ASTERIX		

Title
Understanding Exchange Bias Through Control of Uncompensated Moments in Dilute Antiferromagnets

Authors and Affiliations

M.R. Fitzsimmons et al

Experiment Report

Several theoretical models attribute exchange bias, the shift of the ferromagnetic hysteresis loop away from zero applied field, to pinning of uncompensated moments in the antiferromagnet that occurs during field cooling. The pinned moments ac as if they produced an internal magnetic field that must be overcome (hence the bias) in order to flip the magnetization of a ferromagnetic layer in close proximity to the antiferromagnet. Experimental evidence for pinned moments in the antiferromagnet (or induced magnetization) include a vertical shift of the hysteresis loop away from zero magnetization (not to be confused with exchange bias a horizontal shift), indicating that in a large positive saturating field the sample magnetization is different than when a large negative saturating (with respect to the cooling field direction) is applied. The shift is believed to be produced by uncompensated moments that do not respond to the applied field, i.e., are pinned. Recently, experimental evidence for uncompensated moments was observed at the interface between Co and LaFeO3 with polarized neutron reflectometry (PNR). These results indicated that the pinned moments were concentrated in a 1 nm thick interface layer. In the Co/LaFeO3 experiment, the exchange bias was very small, not even 20 Oe, consequently, the induced magnetization we measured with PNR was also very small. The question arises whether exchange bias is correlated with the concentration of uncompensated moments.

To answer this question, we examined the magnetization profile of a Co/FexZnxFe2 bilayer. Since Zn does not have a magnetic moment, replacement of Fe ions with Zn ions yields uncompensated moments. The concentration of Zn we choose was x=0.2, which is the concentration that yields optimally exchange-biased samples in this system. We examined the time and temperature dependencies of the magnetization profiles in saturation on either side of the hysteresis loop. We show the time dependence of the reflectivity profiles (from which the magnetization profile is obtained), taken at T = 8.5 K (cooling field = 2 kOe) in Figure 1 for applied magnetic fields of + 2 kOe (a) and – 2 kOe (b). These measurements consist of 20 min reflectivity "snapshots" of the sample for different times after reaching base temperature. A curious time dependence of the profiles is evident. Approximately 20 hours after field cooling the reflectivity profiles remain unchanged. Interestingly, the reflectivity profiles taken on opposites sides of the hysteresis loop are different- a possible indication of pinned moments. The reflectivity measurements were repeated for a variety of base temperatures (the temperature to which the sample cooled) Interestingly too, only the measurements at 8.5 and 11 K exhibited time dependence of the reflectivity profiles. Those at and above 16.5 K (Figure 2) remained unchanged after reaching base temperature. We believe this result suggests that for very low temperatures a metastable magnetization condition is achieved that relaxes with time (or with temperature).

Experiment Report *(continued)*

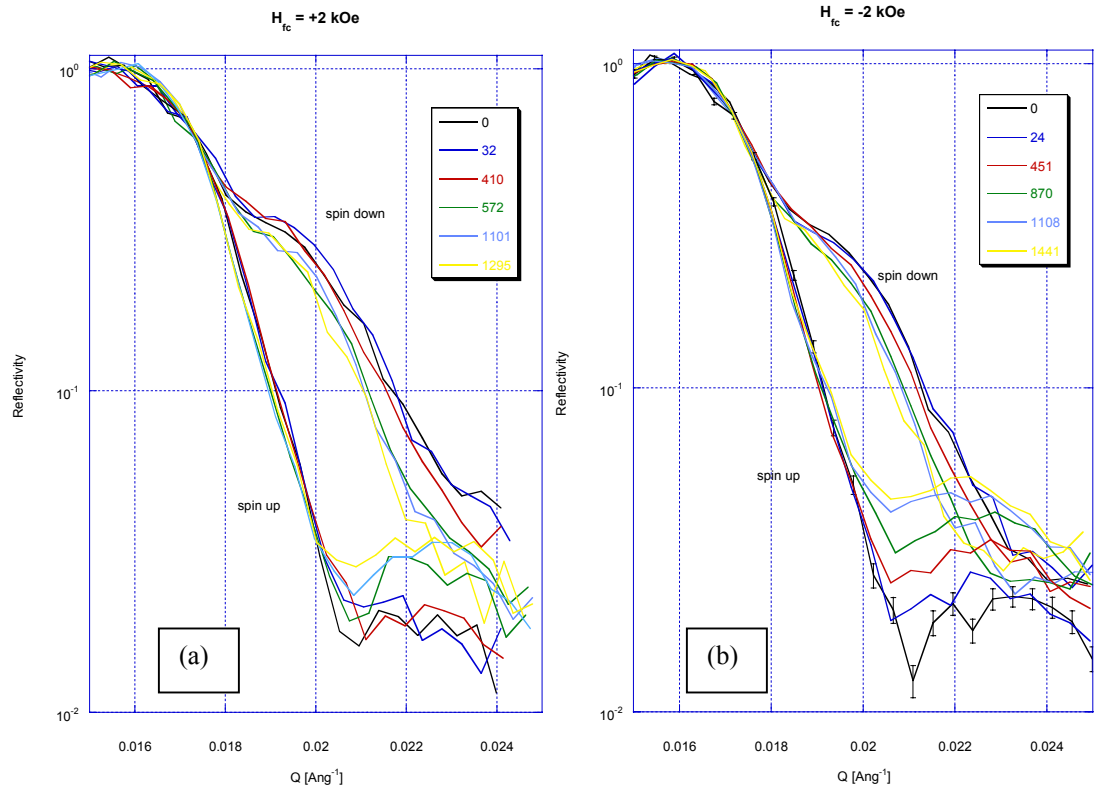

Figure 1 Twenty minute long reflectivity profiles "snapshots" taken at T = 8.5 K for (a) positive and (b) negative saturation. The profiles exhibit time dependence.

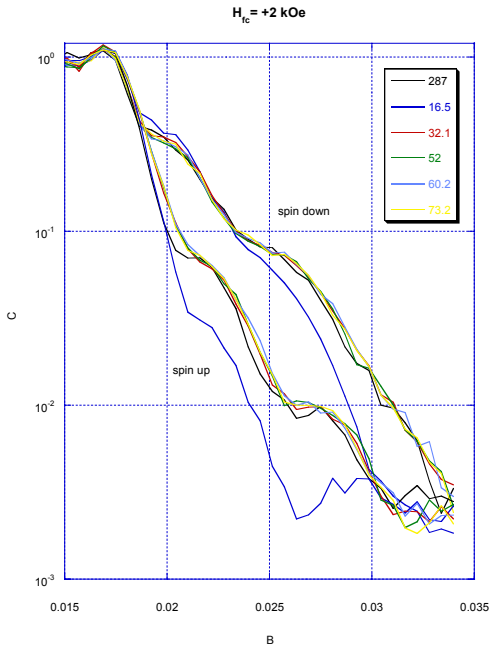

Figure 2 Reflectivity profile snapshots taken at different temperatures immediately after field cooling. For the temperatures shown in the figure, no time dependence was observed. Interestingly, at 16.5 K the reflectivity profiles are different than those at higher temperatures, indicating a difference in the magnetization profile for the exchange coupled bilayer.

IMPORTANT! List or attach a list of publications resulting from this experiment (published or in press).

LANSCE
Los Alamos Neutron Science Center

REPORT ON EXPERIMENT
(Please Type)

Submit all experiment reports to:
LANSCE User Office, MS H831, Los Alamos National Laboratory, Los Alamos, NM 87545

Experiment was carried out at:	**Local Contact**	**Proposal #**	***LANSCE Use Only***
[x] Manuel Lujan Jr. Neutron Scattering Center	m. fitzsimmons	**2002046**	**Report Rc'd**
[ ] Weapons Neutron Research Facility	**FP/Instrument Used**		**3/12/03**
[ ] WNR/Blue Room	ASTERIX		

Title
How is Frozen Magnetization Correlated with Exchange Bias?

Authors and Affiliations

M.R. Fitzsimmons et al

Experiment Report

Several theoretical models attribute exchange bias, the shift of the ferromagnetic hysteresis loop away from zero applied field, to pinning of uncompensated moments in the antiferromagnet that occurs during field cooling. The pinned moments ac as if they produced an internal magnetic field that must be overcome (hence the bias) in order to flip the magnetization of a ferromagnetic layer in close proximity to the antiferromagnet. Experimental evidence for pinned moments in the antiferromagnet (or induced magnetization) include a vertical shift of the hysteresis loop away from zero magnetization (not to be confused with exchange bias a horizontal shift), indicating that in a large positive saturating field the sample magnetization is different than when a large negative saturating (with respect to the cooling field direction) is applied. The shift is believed to be produced by uncompensated moments that do not respond to the applied field, i.e., are pinned. Recently, experimental evidence for uncompensated moments was observed at the interface between Co and LaFeO3 with polarized neutron reflectometry (PNR). These results indicated that the pinned moments were concentrated in a 1 nm thick interface layer. In the Co/LaFeO3 experiment, the exchange bias was very small, not even 20 Oe, consequently, the induced magnetization we measured with PNR was also very small. The question arises whether exchange bias is correlated with the concentration of uncompensated moments.

To answer this question, we examined the magnetization profiles of two samples, a $Co/Fe_{(1-x)}Zn_xFe_2$ bilayer and a $Co/Co_yO_{(1-y)}$. Since Zn and O do not have magnetic moments, replacement of Fe or Co ions with Zn or O ions yields uncompensated moments. The concentration of Zn we choose was x=0.2, which is the concentration that yields optimally exchange-biased samples in this system. We examined the field cooling dependencies of the magnetization profiles in saturation on either sid of the hysteresis loop. Three cooling fields were used, 2 kOe, 350 Oe and 100 Oe that produce exchange biases of +100 Oe, Oe, and –100 Oe, respectively. By examining the magnetization profiles as a function of exchange bias our aim was to identify whether a correlation existed. We show the dependence of the reflectivity profiles (from which the magnetization profile is obtained), taken at T = 16.5 K for the three exchange bias states in Figure 1 for applied magnetic fields of + 2 kOe (a) and – 2 kOe (b). These measurements consist of 20 min reflectivity "snapshots" of the sample for different times after reaching base temperature. Two important conclusions can be made from data in Figure 1. First, the magnetization profiles are different for different exchange bias states, suggesting a difference in the induced magnetization in antiferromagnet (sinc the ferromagnet is always saturated). And second, an asymmetry in the reflectivity profiles is evident in the negative exchange bias state when none is observed in the zero and positive exchange bias states- a difference due to frustration.

Experiment Report *(continued)*

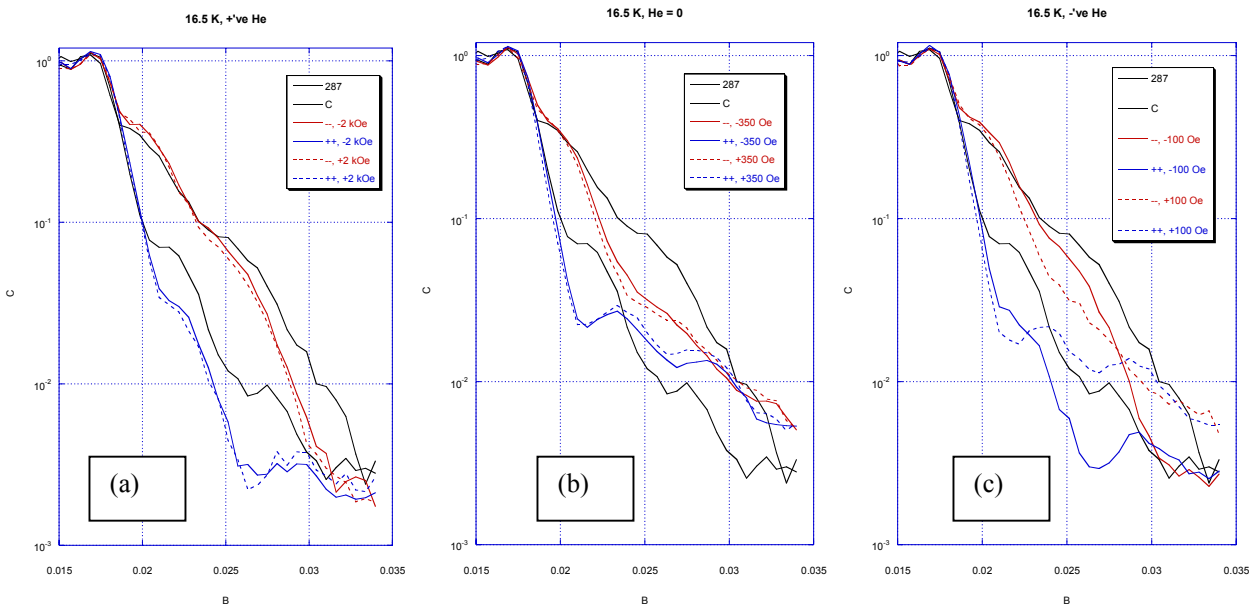

Figure 1 Twenty minute long reflectivity profiles "snapshots" taken at T = 16.5 K for exchange bias of (a) + 100 Oe, (b) 0 Oe, and (c) –100 Oe.

Finally, we performed an experiment to test for frozen magnetization using the Co/CoO bilayer sample (although case (c) in Figure 1 would have been a better choice). The test involve cooling the sample in field to produce the exchange biased state, then rotating the sample about its surface normal by 90 degrees. By measuring the sample reflectivity profiles after rotation in a large field, we had hoped to place scattering from frozen magnetization in the spin flip channel, since frozen magnetization (by definition) must rotate with the sample. The unfrozen magnetization remains in the non-spin-flip channel since the magnetic field is large. We observed some evidence for frozen magnetization, though the evidence is not compelling.

IMPORTANT! List or attach a list of publications resulting from this experiment (published or in press).

LANSCE
Los Alamos Neutron Science Center

REPORT ON EXPERIMENT
(Please Type)

Submit all experiment reports to:
LANSCE User Office, MS H831, Los Alamos National Laboratory, Los Alamos, NM 87545

Experiment was carried out at:	**Local Contact**	**Proposal #**	***LANSCE Use Only***
[x] Manuel Lujan Jr. Neutron Scattering Center	M. Fitzsimmons	**2002049**	**Report Rc'd**
[ ] Weapons Neutron Research Facility	**FP/Instrument Used**		**3/5/03**
[ ] WNR/Blue Room	ASTERIX		

Title
Quantifying Spatial Distribution of Magnetization in Spintronic Materials

Authors and Affiliations
M. Fitzsimmons et al.

Experiment Report

We examined MBE-grown semiconductor trilayers designed specifically to enhance the signature of a magnetic dead-layer a the ferromagnetic/non-magnetic interface. The samples consisted of $Ga_{0.5}Al_{0.5}As$/DMS/ $Ga_{0.5}Al_{0.5}As$/GaAS, where the DMS was either a 40 nm thick layer of $(Ga_{0.97}, Mn_{0.03})As$ or a digital semiconductor consisting of 12 monolayers of GaAs 0.5 monolayer of MnAs repeated to make a 40 nm thick layer. Neutron measurements were taken at 300 K and 10 K. We show these measurements as Fig 1 for the first sample. The magnetic signature of the samples is seen in the splitting betweer the spin-up and down cross-sections in the region of the fringe minima. The difference between the two cross-sections divided by their sum is shown in the upper portion of the figure. The solid curves corresponds to the profiles obtained from model fitted to neutron and X-ray data. The optimized parameters of the model are shown in Figure 2. Presently, our analysi indicates that the magnetic layer thickness is 0.3 nm thinner than the chemical layer thickness- a possible indication of a magnetic dead-layer at the non-magnetic/ferromagnetic interfaces. Additional data taken to larger momentum transfer is needed to confirm this conclusion. Measurements to momentum transfer as large as $Q=2\ nm^{-1}$ should be doable based on the results of this investigation.

Experiment Report *(continued)*

Model reproduces data

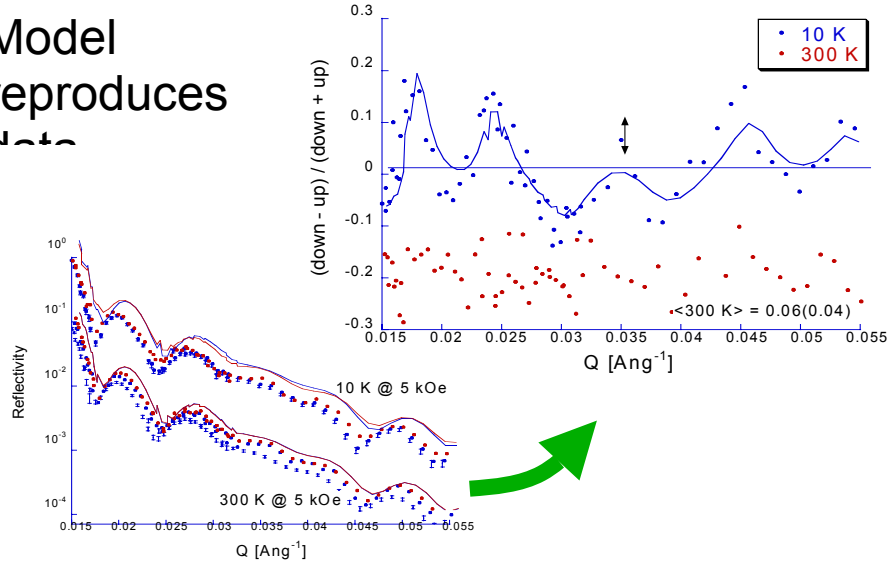

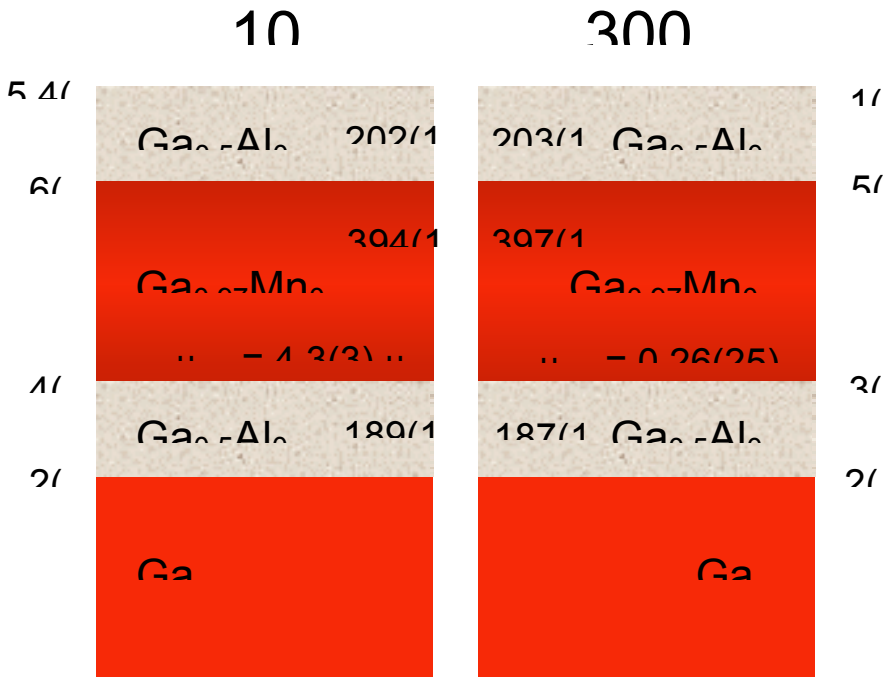

IMPORTANT! **List or attach a list of publications resulting from this experiment (published or in press).**

LANSCE
Los Alamos Neutron Science Center

REPORT ON EXPERIMENT
(Please Type)

Submit all experiment reports to:
LANSCE User Office, MS H831, Los Alamos National Laboratory, Los Alamos, NM 87545

Experiment was carried out at:	**Local Contact**	**Proposal #**	***LANSCE Use Only***
[X] Manuel Lujan Jr. Neutron Scattering Center	Th. Proffen	**2002052**	**Report Rc'd**
[ ] Weapons Neutron Research Facility	**FP/Instrument Used**		**2/3/03**
[ ] WNR/Blue Room	HIPPO		

Title
Phase Separation and Superconductivity in $Mg_{1-x}Al_xB_2$

Authors and Affiliations
Emil Bozin, Michigan State University
Dane Boysen, California Institute of Technology
Antonio Bianconi, U. of Roma "la Sapienza"
Naurang Saini, U. of Roma "la Sapienza"
Simon Billinge, Michigan State University

Experiment Report
MOTIVATION

The recent discovery of superconductivity at 39K in MgB_2 has generated considerable excitement because of the high Tc despite the simplicity of the chemical composition and structure. A large number of metal diborides form, many of which superconduct, however, only MgB_2 seems to have this unusually high Tc. The magnesium diboride is also an important example of a high-Tc superconductor which is non-magnetic, unlike the cuprates, and therefore cannot have a magnetic pairing mechanism. Thus, there can be no magnetic origin for the superconductivity in this case

One of the key aspects of the diborides is to understand why MgB_2 is such a good superconductor whereas its other metallic cousins (AlB_2, TiB_2 etc.) are not. One thing that is known is that in MgB_2 a very flat electronic band in the G-A (*c*-axis) direction lies close to the Fermi-level. This will result in a large density of states close to the Fermi level, but also is expected to give rise to strong electron-phonon coupling. One consequence of this is that the lattice dynamics of the in-plane boron modes (that couple strongly to this band) is expected to be strongly anharmonic, a fact that seems to have been confirmed experimentally and in calculations. Phonon density of states (DOS) measurements have been carried out and qualitative agreement was obtained between the calculated and measured DOS, which was taken to be confirmation of the strong anharmonicity of this mode. However, DOS measurements are a rather imprecise way of measuring this mode, though in the absence of large single crystals, one of the few possibilities. Because the mode of interest is a zone center mode, it can also be studied using Raman scattering. The feature in the Raman is very broad and cannot be unambiguously assigned though is likely to be the E_{2g} mode in question

Detailed studies of the system $Mg_{1-x}Al_xB_2$ have revealed a very interesting evolution of T_c and structure with x. A number of isostructural phase transitions are observed on increasing x resulting in a phase separation into material with different T_c's. A phonon feature corresponding the the E_{2g} mode is evident at around 850 cm^{-1} at x=0.5. The feature softens to around 550 cm^{-1} by x=0; however, it does so by the appearance of a new feature around 750 cm^{-1} that grows up, only to be replaced by the 850 cm^{-1} feature at higher-x. There is clear coexistence of these phases at intermediate x. These observations have been correlated also with broadening in x-ray diffraction lines and T_c in these materials. The different coexisting phases clearly have very different superconducting properties and it will be very important to determine the evolution of these different phases and characterize the structure and dynamics of these inhomogeneous samples as well as possible. Distinct changes are seen in the structure and physical properties around x=0.1 and x=0.66 which may be related to percolation transitions of the intercalant atoms.

Experiment Report *(continued)*
EXPERIMENT

We intended to use a joint real- and reciprocal-space neutron study to do this. We proposed to study a series of samples with x=0, 1/12, 2/12, 3/12, 4/12, 5/12, 6/12, with Rietveld refinement and atomic pair distribution function analysis. Careful multiphase Rietveld fits would help to reveal evidence for macroscopic phase separation. These would be correlated with multiphase fits to the PDFs which would search for evidence of microscopic phase separation. This is a favorable system to study this because the size of the unit cell and the number of structural parameters in each phase is small. Even so, highly constrained two-phase fits might be required. For a limited set of samples we would also carry out a careful temperature dependent study. This would help us to separate the static and dynamic contributions to the disorder.

The nearest neighbor peak in the PDF is well resolved and comes from the in-plane B-B bond. To a good approximation the PDF peak width measures the relative motion of the pair of atoms, projected onto the vector joining them. Because of the nature of the active E_{2g} phonon mode the width of the nearest neighbor B-B PDF peak will be very sensitive to the amplitude of this mode and can therefore be used to extract information about its anharmonicity. It will be very interesting to study this for the 3 distinct modes at around 500, 750 and 850 cm^{-1} that we discussed above. We therefore propose to study the *T*-dependence of the *x*=0 (predominantly 500 cm^{-1} behavior), *x*=4/12 (750 cm^{-1}) and *x*=6/12 (850 cm^{-1}) samples to separate the static and thermal disorder and to look for evidence for anharmonicity in the relative B-B vibrations. We intend to combine these measurements with model potential and first principles calculations that can be used to calculate the PDF including all the lattice dynamics. The model potential calculations do not include electron-phonon coupling effects whereas the ab initio calculations do. The calculations will be carried out in collaboration with S. Massidda at U. Cagliari.

Samples of approx 2 g were made by A. Saccone at U. Genova using pure ^{11}B isotopes. These samples filled the standard sample cans. For reasonable temperature dependence we intended to measure about 12 data sets per sample. We planned to measure 7 samples at low temperature. As in experiment 2002053, performed on the same instrument, extremely high background has been observed, with Bragg scattering coming from the auxiliary equipment (displex in this present experiment). With significant effort and help of the instrument staff during the experiment, the background problem was sorted out using appropriate shielding, and data were collected, however only using the 90° bank. This limited us to measure only two endmember samples, and at limited number of temperatures only. Measurements were carried out on pure MgB_2 sampleat 10K, 50K, 100K, 150K, 200K, 250K and 300K for 2 hours each, and on $Mg_{0.5}Al_{0.5}B_2$ at 10K, 50K and 100K only. The examples of the total scattering function, S(Q), its reduced variant Q(S(Q)-1), and corresponding PDF are shown in the figures below for MgB_2 sample at 10K using 90° bank data only.

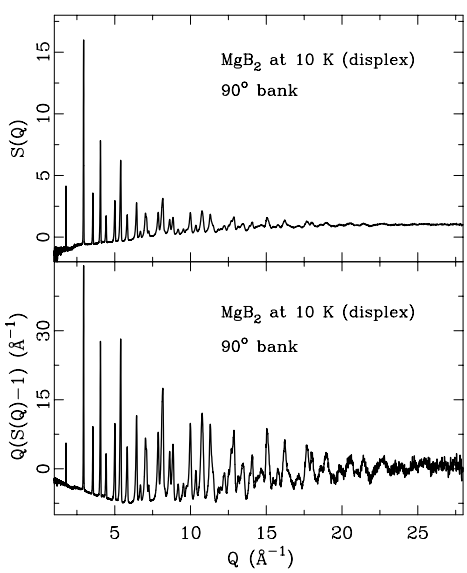

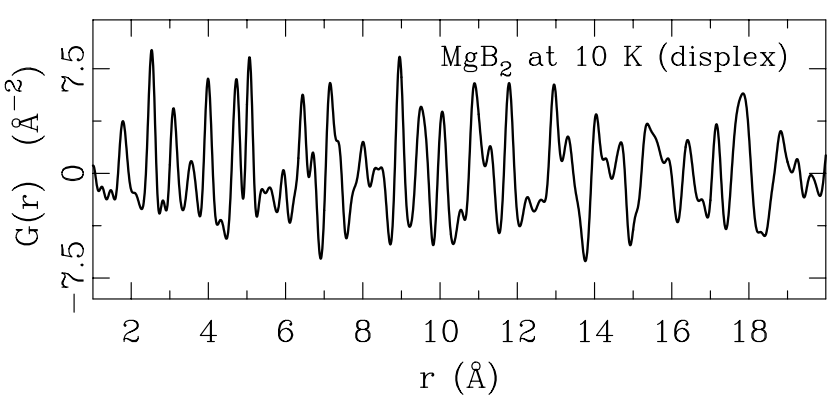

IMPORTANT! List or attach a list of publications resulting from this experiment (published or in press).
Not applicable

LANSCE
Los Alamos Neutron Science Center

REPORT ON EXPERIMENT
(Please Type)

Submit all experiment reports to:
LANSCE User Office, MS H831, Los Alamos National Laboratory, Los Alamos, NM 87545

Experiment was carried out at:	**Local Contact**	**Proposal #**	***LANSCE Use Only***
[x] Manuel Lujan Jr. Neutron Scattering Center	Th. Proffen	**2002053**	**Report Rc'd**
[ ] Weapons Neutron Research Facility	**FP/Instrument Used**		**2/3/03**
[ ] WNR/Blue Room	HIPPO		

Title
Average and Local Structure of the Intermediate and High-Temperature Phases of $Rb_3D(SeO_4)_2$

Authors and Affiliations
Emil Bozin, Michigan State University
Dane Boysen, California Institute of Technology
Sossina Haile, California Institute of Technology
Simon Billinge, Michigan State University

Experiment Report

MOTIVATION

Trirubidium hydrogen biselenate belongs to a family of alkali metal hydrogen sulfate and selenate proton conductors with the general formula $M_3X(AO_4)_2$, where M = NH_4, K, Rb, Cs; X=H, D and A = S, Se. At room temperature most of the $M_3X(AO_4)_2$ crystals are monoclinic with space group *C2/c*. Upon cooling or heating they undergo a number of structural phase transitions which are accompanied by global and/or local changes in the hydrogen bond arrangement. These, in turn, are often accompanied by spectacular changes in physical properties. In particular, upon heating the $M_3X(AO_4)_2$ compounds typically exhibit a change in symmetry from C_{2h6} to $D_{3d\ 5}$ ($C2/c \leftrightarrow R\text{-}3m$). At the phase transition, the protonic conductivity increases by *3-4 orders of magnitude* and, in the high-temperature paraelastic phase, reaches values of $\sigma < 10^{-2}$ Scm^{-1} with an activation energy $E_a < 0.3$ eV. The value of such high conductivity inorganic materials in fuel cell applications has recently been demonstrated.

In the case of $Rb_3H(SeO_4)_2$ careful investigations have revealed that the overall monoclinic to trigonal transformation occurs, in fact, by two-step process:

$$\text{III}(C2/c) \leftarrow 448\text{ K} \rightarrow \text{II}(?) \leftarrow 451\text{ K} \rightarrow \text{I}(R\text{-}3m)$$

The transition at 448 K is second order, in nature, whereas that at 451 K is ferroelastic and appears first order. This behavior is somewhat similar to $(ND_4)_3D(SO_4)_2$ in which an intermediate monoclinic phase with space group *C*2 appears over a 22 K temperature interval between the room-temperature *C*2/*c* and high-temperature *R* -3*m* phases. The intermediate phase of $Rb_3H(SeO_4)_2$, phase II, exists over a very narrow temperature range from 448 K to 451K. Nonetheless, phase II has been detected by acoustic wave measurements and by calorimetric and diffraction methods, and confirmed by optical birefringence experiments. Recent single crystal synchrotron studies suggest phase II has space group C2/m and a cell volume which is half that of the room temperature phase. The main change is likely to be a disordering of H atoms between similar lattice sites, i.e., a proton order-disorder transition.

Experiment Report *(continued)*
EXPERIMENT

We attempted to establish whether the motions of protons (deuterons) may be correlated via a dynamic domain structure; that is, via monoclinic (or other) domains that sweep through the nominally trigonal high temperature structure. Our X-ray studies of phase II and earlier studies of phase I suggest this type of correlated behavior, as opposed to uncorrelated jumps from one hydrogen bond to the next. NMR studies of the trigonal phase similarly indicate correlated proton motion. To address this we wanted to carry out a joint realreciprocal-space analysis using the atomic pair distribution function analysis of the data to complement Rietveld refinements. The samples were made completely deuterated and handled in such a way as to minimize exchange in order to minimize contamination of incoherent scattering from H. At this time is not completely clear how large of an impact the inelasticity corrections (in the total scattering data analysis) will be in this system and we wanted to monitor very carefully the precision with which we can reproduce the low-temperature ordered structure between Rietveld and PDF. Despite these difficulties, the ability to measure deuterogenous samples using wide angle total scattering techniques in the future is a strong additional motivation to attempt these measurements and monitor and attempt to solve these problems. In fact, we were very hopeful that the inelasticity corrections will not limit us in these measurements. In these initial measurements we will confine ourselves to measuring $Rb_3D(SeO_4)_2$ as a function of temperature between room temperature and 500K. Because of data rates on HIPPO we expected that we can get data with sufficient statistics in 15 minutes with 15 minutes per point for temperature equilibration. We planned to take data every 5K from 420K to 480K (12 points), with data steps every 1K in the vicinity of the intermediate phase (around 5 temperature points) once it is located (it may shift in temperature in the deuterated sample). Finally we planned to fill in the temperature series with points every 20K from 300K to 420 (7 points).

Unfortunately, furnace used for the experiment appeared to be inappropriate and was a source of extremely large level of background scattering, making our measurements practically impossible. Despite extensive help of the instrument responsibles we could not solve the problems. Ultimately, we only managed to measure a single dataset of the material at room temperature from a measurement using no auxiliary equipment, which resulted in a single PDF, shown in figure below. Central questions of the proposed experiment have not been addressed at all, and from that point of view the experiment was unfortunately not a successful one.

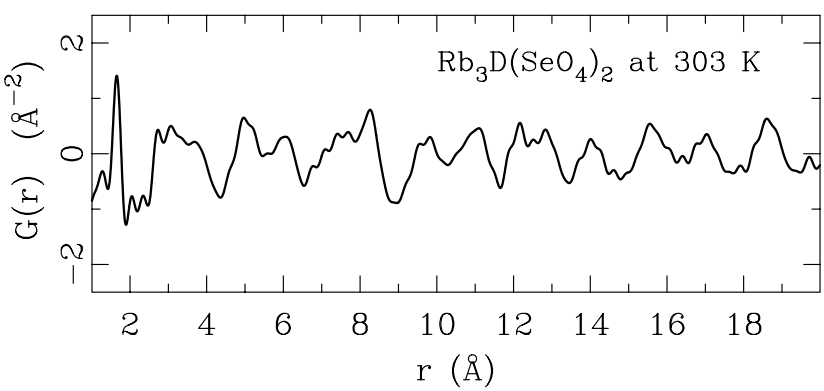

IMPORTANT! List or attach a list of publications resulting from this experiment (published or in press).
Not applicable

LANSCE
Los Alamos Neutron Science Center

REPORT ON EXPERIMENT
(Please Type)

Submit all experiment reports to:
LANSCE User Office, MS H831, Los Alamos National Laboratory, Los Alamos, NM 87545

Experiment was carried out at:	**Local Contact**	**Proposal #**	***LANSCE Use Only***
[x] Manuel Lujan Jr. Neutron Scattering Center	Darrick Williams	2002054	**Report Rc'd**
[ ] Weapons Neutron Research Facility	**FP/Instrument Used**		**1/7/03**
[ ] WNR/Blue Room	HIPPO		

Title Rare-Earth Substituted PZT

Authors and Affiliations

Mark A. Rodriguez, Timothy Boyle, and Bruce Tuttle
Sandia National Laboratories
PO Box 5800, MS1411
Albuquerque, NM 87185

Experiment Report

Our particular interest in this series of lead-zirconium-titanium-oxide (PZT) samples was the location of the 4% rare-earth dopant within the $Pb(Zr_{0.30}Ti_{0.70})O_3$ "PZT 30/70" host phase. It has been speculated that the location of the dopant will have significant impact on the performance of the material.[1] The dopant will either occupy the A site, the B site, or both A and B sites (amphoteric), of the perovskite, depending on the Ln radius. Typically, the larger Ln atoms will substitute on the A site, while the smaller Ln atoms will tend to prefer the B site. We investigated the dopants Ce, Nd, Tb, Y, and Yb in this experiment.

Sample powders were loaded into V canisters and data was collected at room temperature on the HIPPO spectrometer. Three integrated histograms (140°, 90°, 40°) were generated from the three different detector ranges. Additionally, an XRD pattern was collected using a D500 powder diffractometer equipped with Cu Kα radiation and a graphite monochromator. As it turns out, the weighted neutron scattering of the Zr/Ti on the B-site was quite small (-0.25 fm). This made analysis of the B-site via neutron analysis quite difficult. However, addition of the XRD data into the refinements stabilized the B-site atom position, reduced overall errors, and helped bring the refinement to convergence. The use of the neutron data helps considerably in the location and refinement of the oxygen atoms. Hence, data from both techniques are valuable. The dual XRD/neutron Rietveld structure refinements were performed using GSAS; all three of the observed neutron histograms and additional XRD pattern were used in the refinements. Typically the wRp values for the combined refinements were below 6%.

Due to the low dopant level (4%), it was not possible to conclusively determine the location for the RE-dopant as A or B site from the site occupancy. However, significant information concerning the structure was still obtained that yielded valuable insight into the behavior of these perovskite phases. Table 1 shows the refined structural parameters for the five PZT powders. One sees a trend of increased volume for the unit cell as the ionic radius of the dopant decreases. This is consistent with our past observations on thin film samples.[1] The clear exception to this trend is the Ce-doped sample that shows a larger than expected unit cell volume. This is also consistent with past observations that the Ce has oxidized to the (+4) state in the pervoskite structure.[1]

Experiment Report *(continued)*

Using the dz Zr/Ti (or B-site) data one can see that the largest B-site displacements were observed for the Ce, Tb, and Y samples while the Nd and Yb had smaller values. We have speculated that the Nd is an A-site dopant, the Yb is a B-site dopant and the Ce, Tb, and Y are amphoteric dopants.[1] We also observed previously in film samples that the so-called amphoteric doped samples displayed the best performance in terms of remanant polarization.[1] The refinements give credence to this claim, demonstrating the largest dz values for the B-site cation for the Ce, Tb, and Y doped samples. Figure 1 shows a comparison of the observed remanant polarization derived from film samples as compared to B-site cation displacement. There is a clear trend in the data indicating a structural correlation to the observed properties. Therefore, although clear proof of site location/occupancy for the RE-dopant could not be confirmed directly via neutron diffraction, the observed picture based on the XRD/neutron refinements yields a consistent picture to the previous speculation concerning site location of the dopant and indirect evidence of site location based on the relative displacements (from the cubic site) and lattice parameter/volume data.

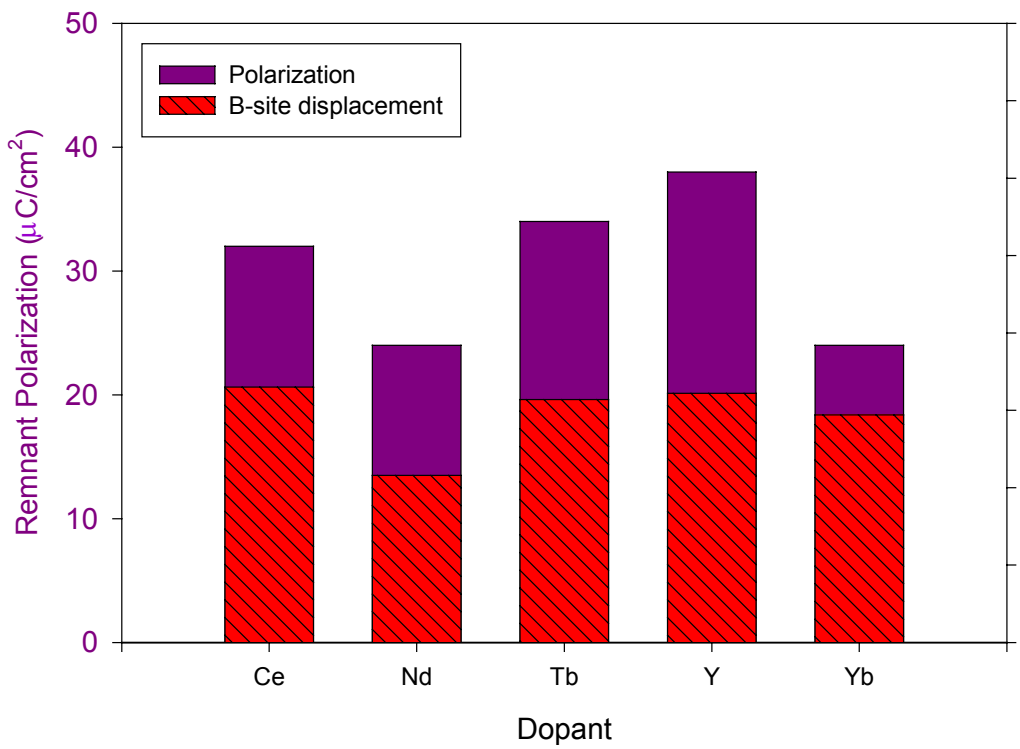

Figure 1. Comparison of refined B-site displacement and observed remanant polarization (film data).

Table 1. Refined Structural parameters for doped PZT 30/70 powders

Sample	*a (Å)*	*c (Å)*	*Vol (Å)*	*dz Pb (Å)*	*dz Ti/Zr (Å)*	*dz O1 (Å)*
Ce-PZT	3.981(1)	4.142(1)	65.65(1)	0.169(1)	0.365(2)	0.585(1)
Nd-PZT	3.992(1)	4.111(1)	65.52(1)	0.145(1)	0.308(3)	0.506(1)
Tb-PZT	3.978(1)	4.150(1)	65.67(1)	0.193(1)	0.357(2)	0.599(2)
Y-PZT	3.986(1)	4.152(1)	65.96(1)	0.197(1)	0.361(2)	0.609(1)
Tb-PZT	3.992(1)	4.137(1)	65.92(1)	0.181(1)	0.347(2)	0.575(1)

Reference:

[1] T.J. Boyle, et. al., *J. Mater. Res.,* **17,** 871-878 (2002).

IMPORTANT! List or attach a list of publications resulting from this experiment (published or in press).

LANSCE
Los Alamos Neutron Science Center

REPORT ON EXPERIMENT
(Please Type)

Submit all experiment reports to:
LANSCE User Office, MS H831, Los Alamos National Laboratory, Los Alamos, NM 87545

Experiment was carried out at:	**Local Contact**	**Proposal #**	***LANSCE Use Only***
[x] Manuel Lujan Jr. Neutron Scattering Center	Darrick Williams	2002057	**Report Rc'd**
[ ] Weapons Neutron Research Facility	**FP/Instrument Used**		**1/7/03**
[ ] WNR/Blue Room	HIPPO		

Title In-Situ Neutron Diffraction Study of Sony Li-ion Batteries

Authors and Affiliations

Mark A. Rodriguez, David Ingersoll, and Daniel H. Doughty
Sandia National Laboratories
PO Box 5800, MS1411
Albuquerque, NM 87185

Experiment Report

In-situ measurements yield the best information about the function of battery cells because the data is collected on actual functioning cells as they undergo charge/discharge. In our first attempt at in-situ neutron diffraction analysis of Li-ion batteries (see proposal 20001008), we succeeded only in observing a change in the uncharged and charged stage of a cell. This pervious experiment, while demonstrated proof-of-principle, did not yield large quantities of information and indicated prohibitively long data collection times (12 hrs/ step) using HIPD. It was our hope that changes in the cell configuration coupled with the new HIPPO spectrometer would improve count rates. These results were realized as discussed below.

In the current experiment, a commercial Li-ion cell (SAEHAN ENERTECH, Inc.) was placed on the HIPPO neutron spectrometer for data collection in the uncharged state. Initial data collection scans indicated useful data could be collected in as short as 15 minutes. This was excellent news as it indicated that in-situ measurements in near real-time were feasible. (Note: this was an improvement of over 40 times in data rates as compared to our previous attempt at data collection on HIPD.) Next, the cell was charged to ~4.1V which represented the full state of charge for the cell. Data was collected in 15-minute increments at seven different states of charge. The entire experiment took five hours to complete; this included equilibration time for the cell. Rietveld structure refinements were performed on observed data to obtain information from the $LiCoO_2$ cathode. A useful range from 1.3 – 1.75 Angstroms contains five reflections from $LiCoO_2$, namely the (113), (110), (108), (107) and (009) along with a single Al (220) reflection from the current collector. By using the Al peak as an internal standard, accurate lattice parameters could be obtained from the refinement of the 140, 90, and 40-degree data banks. Figure 1 shows a plot of lattice parameters for the a- and c-axis as a function of voltage. Here one sees the clear contraction of the $LiCoO_2$ c-axis and expansion of the a-axis upon discharge of the cell (decreasing voltage). This is consistent with other experimental observations.[1] The trends in the data are smooth and the errors (which represent 3σ of the refined values reported from the GSAS output) are small. Additionally, we were successful in obtaining Li occupancy information for the $LiCoO_2$. Although there was strong correlation of the Li site occupancy to the March-Dollase orientation vector, it was possible to refine a site occupancy of Li in $LiCoO_2$ for the various states of charge by first assigning reasonable values to the Li occupancy, based on estimates from the electrochemical data. Then refinement of the preferred orientation, followed by simultaneous refinement of the Li site occupancy converged and resulted in the observed plot in figure 2. Here we see that the refined values track well with the calculated Li content based on electrochemical data.

Experiment Report *(continued)*

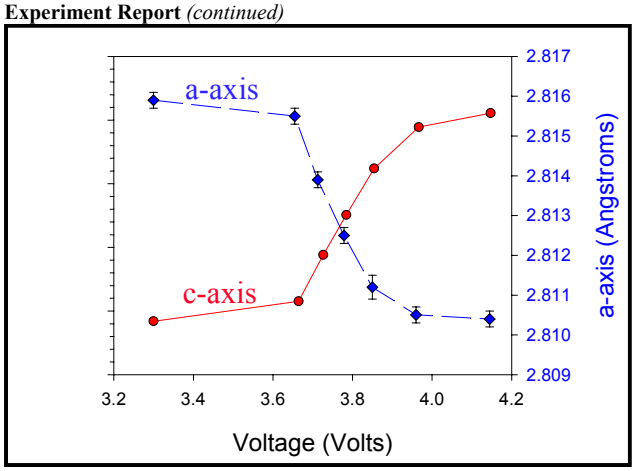

Figure 1. $LiCoO_2$ Lattice parameters as a function of Voltage.

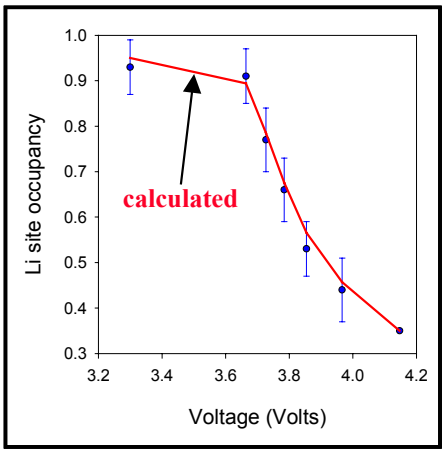

Figure 2. Li site occupancy of $LiCoO_2$.

Finally, in this experiment it was possible to obtain simultaneous structural information regarding the graphite anode as well. A quick plot of the (002) d-spacing as a function of voltage showed evidence of staging of the Li-C alloys during cell discharge (see figure 3). Hence, the anode and cathode of the Li-ion cell can be diagnosed simultaneously in a non-destructive fashion to obtain valuable information about the inner workings of the battery system. This information can be directly correlated to simultaneously collected electrochemical data to obtain a highly detailed picture of cell performance.

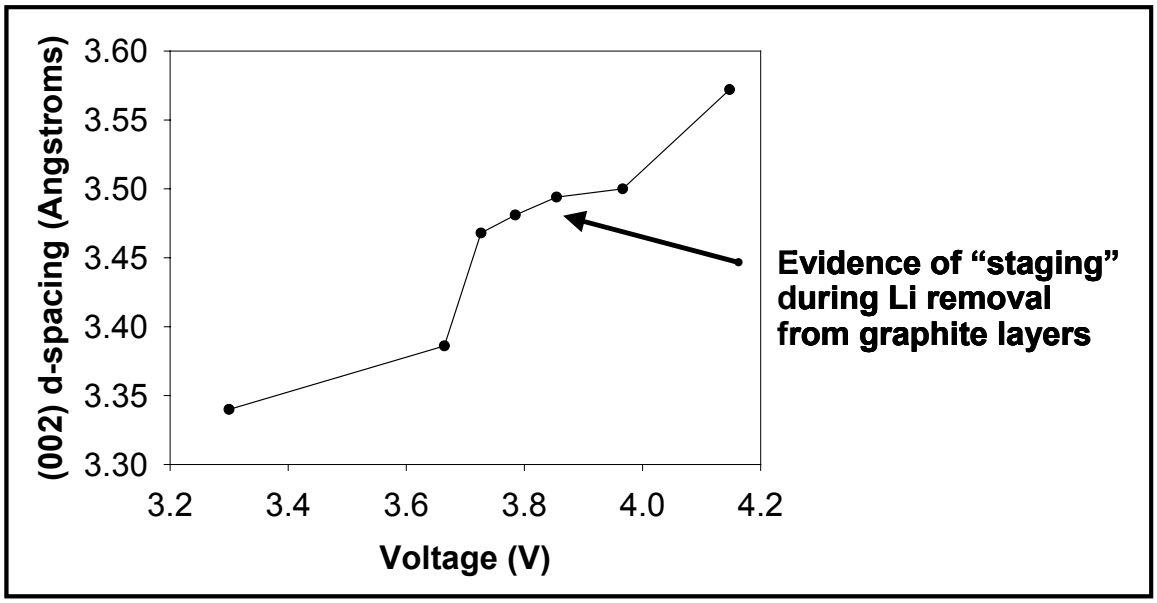

Figure 3. (002) d-spacing for graphite anode during Li-ion cell discharge cycle.

Reference:

[1] M. A. Rodriguez, D. Ingersoll, and D. H. Doughty, *Powder Diffraction.* **18** (2003) in press.

IMPORTANT! List or attach a list of publications resulting from this experiment (published or in press).

LANSCE
Los Alamos Neutron Science Center

REPORT ON EXPERIMENT
(Please Type)

Submit all experiment reports to:
LANSCE User Office, MS H831, Los Alamos National Laboratory, Los Alamos, NM 87545

Experiment was carried out at:	**Local Contact**	**Proposal #**	***LANSCE Use Only***
[X] Manuel Lujan Jr. Neutron Scattering Center	Paul Langan	**2002064**	**Report Rc'd**
[ ] Weapons Neutron Research Facility	**FP/Instrument Used**		**1/29/03**
[ ] WNR/Blue Room	PCS		

Title
Neutron Diffraction Studies on Orotidine Monophosphate Decarboxylase

Authors and Affiliations
Masahiro Fujihashi & Emil F. Pai, University of Toronto; Paul Langan, Los Alamos National Laboratory

Experiment Report

Orotidine monophosphate decarboxylase is the most proficient enzyme known; it accelerates the decarboxylation of OMP by 17 orders of magnitude. Despite major efforts, its exact chemical mechqanism of action is still unknown. Extending our crystallographic studies, we have investigated the possibility of neutron diffraction to determine the charge state of amino acid side chains located in the active site of this enzyme. This information is important for the evaluation of mechanistic proposals and for the general understanding of enzymatic catalysis.

Our experiment was one of the first series of measurements on the new Protein Crystallography Station (PCS) in the Lujan Center. 24 hour data collection revealed that our crystals were most probably ordered well enough to enable neutron diffraction but their size (ca. 0.25 mm^3), although quite respectable, still precluded the collection of statistically significant data. We are now trying to increase the size of our crystals to more than 1 mm^3, which we estimate should provide sufficien scattering volume for successful data collection. In parallel, we are investigating the possibility of full deuteration of the protein as another way to increase the diffraction signal.

LANSCE
Los Alamos Neutron Science Center

REPORT ON EXPERIMENT
(Please Type)

Submit all experiment reports to:
LANSCE User Office, MS H831, Los Alamos National Laboratory, Los Alamos, NM 87545

Experiment was carried out at:	**Local Contact**	**Proposal #**	***LANSCE Use Only***
[x] Manuel Lujan Jr. Neutron Scattering Center	Paul Langan, Benno Schoenborn	2002067	**Report Rc'd**
[ ] Weapons Neutron Research Facility	**FP/Instrument Used**		**2/3/03**
[ ] WNR/Blue Room	PCS (Inst. 15)		

Title
"Comparative Hydrogen Position Studies Using X-rays and Neutrons"

Authors and Affiliations
Gerard J. Bunick, Oak Ridge National Laboratory
B. Leif Hanson, University of Tennessee- Oak Ridge Graduate School of Genome Science and Technology
Jenny P. Glusker, Fox Chase Cancer Institute
Amy Katz, Fox Chase Cancer Institute

Experiment Report

The protein D-xylose isomerase is an enzyme that catalyzes the conversion of D-xylose to D-xylulose and glucose to fructose by hydrogen-atom transfer. The catalytic mechanism of hydrogen-atom transfer is currently believed to involve a metal ion-bound water molecule, a mechanism that is thought to be used by many important proteins involved in human disease.

Neutrons are a unique tool for structural determination of biological materials because light atoms (hydrogen atoms) diffract neutrons as strongly as do the other atoms commonly found in macromolecules (carbon, nitrogen, oxygen, and phosphorus). By contrast, in x-ray diffraction, the hydrogen atoms diffract very weakly. Therefore, these mechanistic details can only be determined by neutron-diffraction techniques.

The primary goal of the experiments on the PCS was to collect neutron-diffraction data on a crystal sample of D-xylose isomerase to compare the structural information obtained by this technique with that derived from x-ray data taken at the Advanced Photon Source (APS) at Argonne National Laboratory. The study is also being done in response to a request by the Department of Energy Office of Biological and Environmental Research to provide clear evidence for neutron diffraction as a tool for macromolecular structure/function research. In a broader perspective, these studies demonstrate that protein crystallography at a spallation neutron source will greatly increase the number of proteins for which hydrogen positions, especially partially mobile hydrogen atoms, can be resolved. PCS is the pioneer instrument of what will be multiple neutron beam lines for macromolecular crystallography at the future Spallation Neutron Source (SNS).

With the end of the 2002 LANSCE run cycle, data collection from the crystal shown in Fig. 1 is now complete. We made diffraction measurements from 23 different crystal orientations to maximize the number of crystal reflections collected. This is one of the best neutron-diffraction data sets ever measured for such a large protein (Fig. 2). More than 56,000 unique reflections were measured to a resolution of 1.5 Å. Our plan is to finish the structure analysis before summer 2003 in order t present our findings at the American Crystallographic Association national meeting as part of a special Transactions Symposium on Neutron Protein Crystallography.

Experiment Report *(continued)*

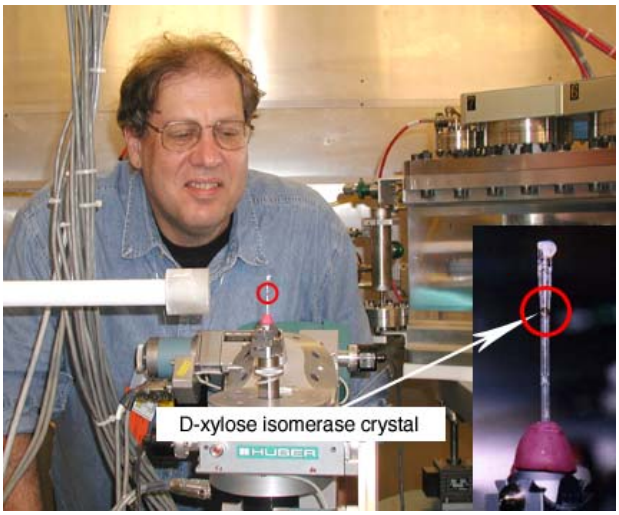

Fig. 1. Leif Hanson , a member of the measurement team, examines the crystal sample of the D-xylose isomerase protein used in the experiments on the PCS at Lujan Center. To right of Leif is the PCS detector array. This sample of D-xylose isomerase is the largest biological molecule ever studied at high resolution using time-of-flight (TOF) neutron diffraction.

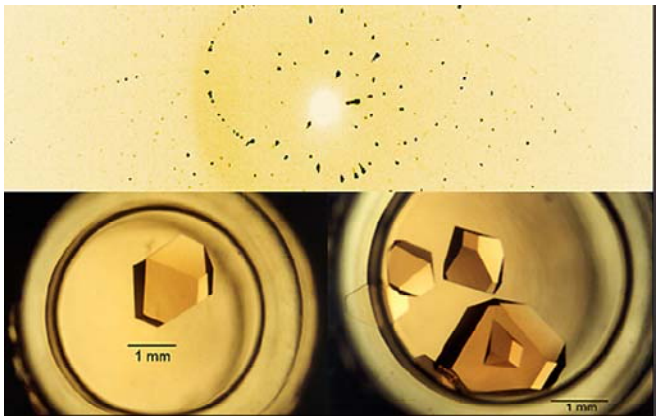

Fig. 2. The top image is the neutron-diffraction data taken on the PCS of one of the D-xylose isomerase protein crystals shown in the bottom right image. This sample was provided by Genencor International, Inc., a worldwide supplier of enzymes and other biochemicals for industrial use. These crystals were grown at Oak Ridge National Laboratory in a counter diffusion cell, which is a National Aeronautics and Space Administration (NASA) device originally developed for microgravity protein crystallization.

IMPORTANT! List or attach a list of publications resulting from this experiment (published or in press).

LALP-02-219 High-Resolution Neutron Diffraction Data Collected on the Protein Crystallography Station at LANSCE Exceed Researchers' Expectations. **http://lansce.lanl.gov/news/features/Xylose.htm**

LANSCE 2002 activity report. Thermal Neutron Protein Crystallography — Enzyme-Mechanism Investigations with D-xylose Isomerase
B.L. Hanson, G.J. Bunick (Oak Ridge National Laboratory), A. Katz, J.P. Glusker (Fox Chase Cancer Center), X. Li, B.P. Schoenborn, P.A. Langan (LANSCE Division)

LANSCE
Los Alamos Neutron Science Center

REPORT ON EXPERIMENT
(Please Type)

Submit all experiment reports to:
LANSCE User Office, MS H831, Los Alamos National Laboratory, Los Alamos, NM 87545

Experiment was carried out at:	**Local Contact**	**Proposal #**	***LANSCE Use Only***
[X] Manuel Lujan Jr. Neutron Scattering Center	Paul Langan	**2002077**	**Report Rc'd**
[ ] Weapons Neutron Research Facility	**FP/Instrument Used**		**2/27/03**
[ ] WNR/Blue Room	PCS		

Title

Binding Studies with Immune Protein Fragments.

Authors and Affiliations

Allen B. Edmundson, Ph.D., Oklahoma Medical Research Foundation
Leif Hanson, Ph.D., Oak Ridge National Laboratory

Experiment Report

Two days of beam time at the Los Alamos Neutron Science Center were assigned to A.B.E. for a trial run on the project. Two immune protein fragments were prepared by batch methods in 1.9 M ammonium sulfate, pH 6.2. One protein, designated a Bence-Jones dimer, was obtained from the urine of a human subject (Mcg) with multiple myeloma (tumors of the bone marrow). The second protein was an engineered molecule consisting of the immunoglobulin light chain from Mcg hybridized into a heterodimer with the corresponding light chain from a second patient (Hud) with multiple myeloma.

The Mcg dimer (Mr of 46,000) crystallized in the trigonal space group $P3_121$, with a = b = 72.3 Å and c = 185.9 Å. This crystal, which measured 1.5 x 0.6 x 0.6 mm (l x w x d), was selected to see if reflections along c could be resolved. Over a two-month period before transfer to Los Alamos, the aqueous crystallization media were replaced with deuterated 2 M ammonium sulfate dissolved in D_2O. The crystal was mounted in a quartz capillary at the Los Alamos site to discourage back hydration with H_2O. In this procedure, nitrogen gas bubbled through D_2O was directed over the area in which the crystal was placed in the capillary.

The capillary was sealed with hot wax and mounted in a goniometer head for removal to the beam line. After exposure to neutrons for approximately eight hours the appearance of the crystal changed dramatically. It had become opaque and seemed to have pieces protruding from its surface. In an X-ray beam, we would have described it as a victim of overheating. Regardless, the crystal was no longer suitable for diffraction.

In the Mcg x Hud hybrid, the crystal measured 2.4 x 0.7 x 0.7 mm. The protein crystallized in the tetragonal space group $P4_12_12$ with unit cell dimensions more favorable for neutron diffraction experiments (a = b = 79.0 Å; c = 124.9 Å). A smaller crystal from the same batch (0.5 x 0.15 x 0.15 mm) was flash cooled and subjected to X-ray analysis in a nitrogen cryostream (100 K). The crystal structure was solved at 1.8 Å resolution. Starting protein phases are available for future interpretation of neutron diffraction data.

Experiment Report *(continued)*

FUTURE PLANS:

We need to develop a hypothesis to explain the destruction of the Mcg crystal. The seals of the capillary appeared to be tight. We are presently assuming that the deleterious effects were attributable to some aberration in the beam. Paul Langan is aware of the problem and collectively we do not know whether a sudden event, like gamma rays, could have destroyed the crystal.

Several years ago, A.B.E. produced a sufficiently large crystal for neutron diffraction of the Sea light chain dimer under microgravity conditions on board the U.S. Space Shuttle (9 day STS-95 Mission in November, 1998). At that time, neutron diffraction was not a priority and A.B.E. carved the crystal into smaller fragments for X-ray work. Now, microgravity appears to be one of the best environments to produce large high quality crystals suitable for neutron diffraction.

In an attempt to duplicate this success, samples of the Sea dimer were placed in a mid-deck locker of the Space Shuttle Columbia in Mission STS-107. Due to the Columbia tragedy, future opportunities for research in space will be limited. While microgravity appears to be one of the best environments to produce high quality crystals sufficiently large for neutron diffraction, we have noted multi-millimeter size crystals in ground-based experiments from time-to-time as part of our routine screening programs. In addition to sperm whale myoglobin, which A.B.E. first crystallized in 1960, at least five antibody fragments have grown to volumes exceeding 3 mm^3 in randomly assorted samples. The advent of powerful neutron diffraction facilities now makes the production of large crystals meaningful and highly worthwhile. In spite of recent impediments, we fully intend to begin anew.

PUBLICATIONS:
An article heavily influenced by our joint effort at Los Alamos is listed below. This article summarizes our aspirations to use neutron diffraction for obtaining protein structures with assigned hydrogen atoms.

Hanson, B.L., Bunick, G.J., Harp, J.M., Edmundson, A.B. (2002). Mcg in 2030: new techniques for atomic position determination of immune complexes. J. Mol. Biol. 15(5):297-305.

IMPORTANT! List or attach a list of publications resulting from this experiment (published or in press).

See Above

LANSCE
Los Alamos Neutron Science Center

REPORT ON EXPERIMENT
(Please Type)

Submit all experiment reports to:
LANSCE User Office, MS H831, Los Alamos National Laboratory, Los Alamos, NM 87545

Experiment was carried out at:	**Local Contact**	**Proposal #**	***LANSCE Use Only***
[x] Manuel Lujan Jr. Neutron Scattering Center	Don Bown	**2002084**	**Report Rc'd**
[ ] Weapons Neutron Research Facility	**FP/Instrument Used**		**4/22/03**
[ ] WNR/Blue Room	2		

Title
Aging in Uranium Niobium Alloys

Authors and Affiliations
Dan Thoma mst-6
Dave teter mst-6
Don Brown mst-8

Experiment Report
Niobium is soluble in uranium in the high temperature bcc phase, but not in the low temperature orthorhombic phase. A metastable U-Nb alloy may be formed by quenching from the high temperature phase, not giving the niobium time to precipitate. U6wt%Nb, which is a critical weapon component, forms a martensitic monoclinic structure following the quench. The purpose of this work was to probe the stability of the monoclinic phase over time. Aging was accelerated by warming to 200C. The U6Nb sample was heated to 200C in the beam and held at that temperature for 18 hours. Diffraction patters were collected every 10 minutes for this period. Figure 1 shows three diffraction patterns, room temperature prior to heating, immediately after reaching 200C, and 18 hours after reaching 200C. The evolution of the diffraction pattern from time=0 to 18 hours is evident. Figure 2 shows the fraction change of the interplanar spacing of the (-111) and (110) peaks as a function of time. The variation of interatomic spacing is due to the continual precipitation of Niobium from solution. Combined with last years measurements of the crystal structure of the U-Nb system as a function of [Nb] we will be able to estimate the niobium content of the solution as a function of time from this data. For instance, the change in lattice paramete observed after 2 hours is consistent with a reduction from U6Nb to U5.2Nb. These results are very important to the enhance surveillance program.

Experiment Report *(continued)*

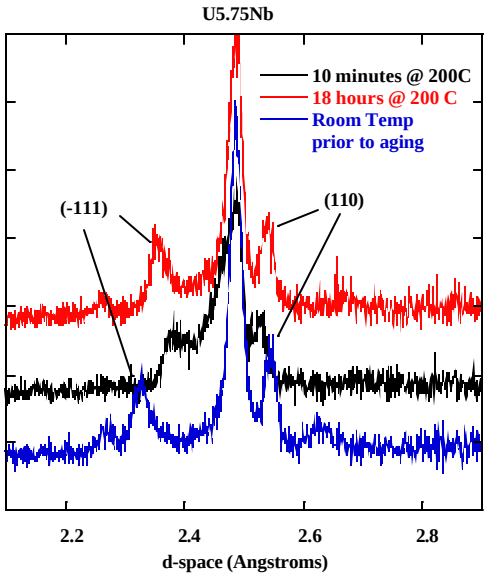

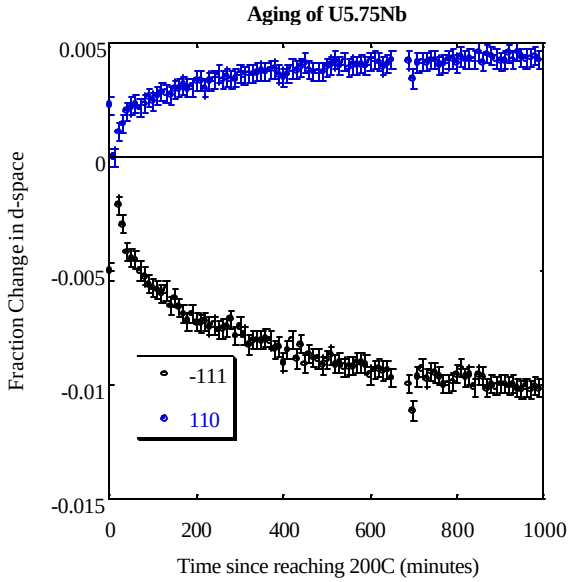

IMPORTANT! List or attach a list of publications resulting from this experiment (published or in press).

LANSCE
Los Alamos Neutron Science Center

REPORT ON EXPERIMENT
(Please Type)

Submit all experiment reports to:
LANSCE User Office, MS H831, Los Alamos National Laboratory, Los Alamos, NM 87545

Experiment was carried out at:	**Local Contact**	**Proposal #**	***LANSCE Use Only***
[x] Manuel Lujan Jr. Neutron Scattering Center	Don Bown	**2002085**	**Report Rc'd**
[ ] Weapons Neutron Research Facility	**FP/Instrument Used**		**4/22/03**
[ ] WNR/Blue Room	2		

Title
High Temperature Deformation of Beryllium

Authors and Affiliations
Don Brown mst-8

Experiment Report
Beryllium is a brittle material at room temperature. This is due to its lack of the necessary independent slip systems at room temperature, where only basal and prismatic slip are active. Above 350C, beryllium gains ductility, presumably due to the activation of pyramidal slip, which completes the yield surface. The purpose of this measurement was to look for the signature of pyramidal slip in the hkl- specific stress strain curves during deformation above 350C. Figure 1 shows the basal tensile stress strain curves at room and high temperature. The reduced deflection of the basal curve is consistent with the activation of pyramidal slip. However, comparison to polycrystalline plasticity models is necessary for interpretation of this data.

Experiment Report *(continued)*

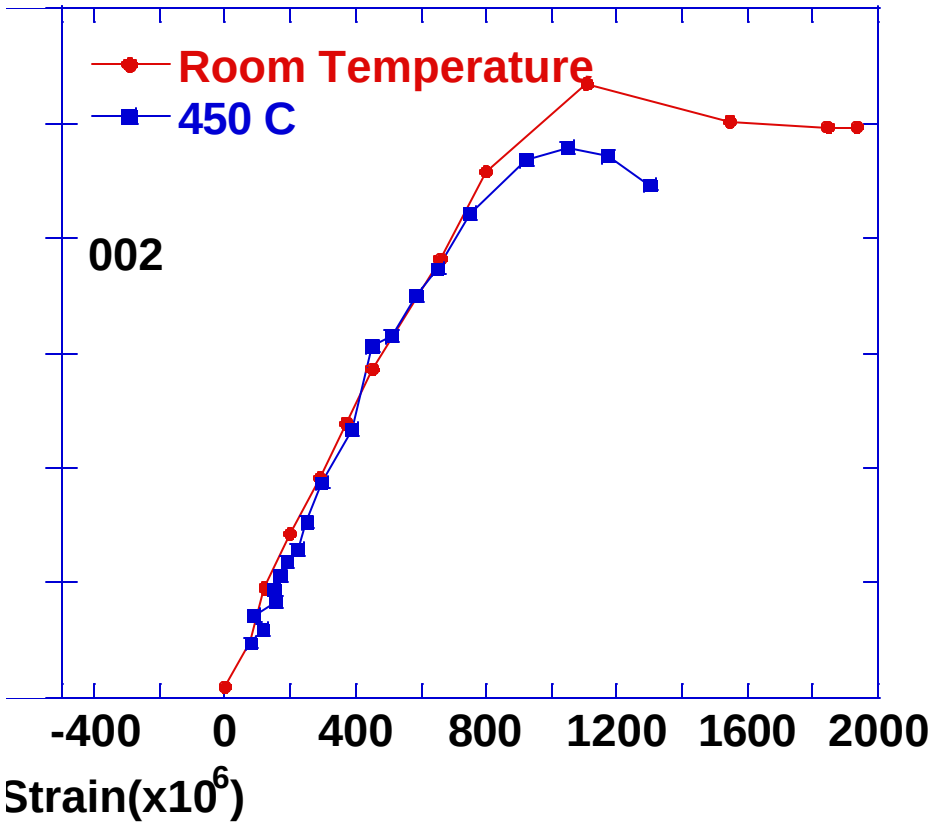

IMPORTANT! List or attach a list of publications resulting from this experiment (published or in press).

LANSCE
Los Alamos Neutron Science Center

REPORT ON EXPERIMENT
(Please Type)

Submit all experiment reports to:
LANSCE User Office, MS H831, Los Alamos National Laboratory, Los Alamos, NM 87545

Experiment was carried out at:	**Local Contact**	**Proposal #**	***LANSCE Use Only***
[X] Manuel Lujan Jr. Neutron Scattering Center	Darrick Williams	**2002089**	**Report Rc'd**
[ ] Weapons Neutron Research Facility	**FP/Instrument Used**		**2/27/03**
[ ] WNR/Blue Room	HIPPO		

Title
Texture Changes During the α–β Phase Transformation in Quartz

Authors and Affiliations
Rudy Wenk, Stephan Grigull, Jenny Pehl, Department of Earth and Planetary Science, University of California, Berkeley CA 94720

Report

Phase transitions in polycrystals have a profound impact on physical properties of materials, in particular, on the anisotropy pattern, which is due to preferred orientation (or texture) of crystals. In general, textures are measured at room temperature, and high-temperature texture is implied by modeling. Time-of-flight neutron diffractometers, such as the High-Pressure-Preferred Orientation (HIPPO) instrument at the Los Alamos Neutron Science Center (LANSCE), have made *in situ* investigations of texture changes during phase transformations possible. We report here on texture changes for the displacive trigonal-hexagonal phase transition of quartz, which occurs at 573ºC (Fig. 1).

The unique features of HIPPO are high count rates, a large array of detectors and a wide range of ancillary instruments for *in situ* low- and high-temperature and -pressure studies. With HIPPO, diffracted neutrons are detected by an array of 50 detector panels with 1,400 ^{3}He detector tubes located at different directions and diffraction angles. Only 30 detectors from the 40º, 90º and 150º banks were used in our experiment because of limitations in resolution that decrease with diffraction angle. Six orientation angles about the vertical axis are possible, resulting in 6 x 30 = 180 orientations. The Rietveld analysis technique could not be used because the diffraction spectra were contaminated by parasitic peaks originating from diffraction by the metal surface of the vacuum furnace. Instead, an automatic intensity-extraction procedure for recording individual diffraction peaks was developed. The 180 corrected intensities at different pole-figure coordinates for four quartz diffraction peaks were then used to calculate the orientation distribution.

From the orientation distribution, individual pole figures for 001 (c-axis), 100 (prism), 101, and 011 were recalculated (Fig. 2 Before the phase transition (Fig. 2 top), we observed a strong texture with a single c-axis maximum — 100 poles are distributed on a great circle with six concentrations at 60º intervals, and 101 and 011 poles each show three slightly asymmetric concentrations related by a 120º rotation about the c-axis. Heating to 625ºC did not change the 001 and 100 patterns, but texture intensities for rhombohedral (101 and 011) poles were distributed over a small circle with six concentrations consistent with hexagonal crystal symmetry (Fig. 2 center). Upon cooling, the texture became trigonal again (Fig. 2 bottom) and was identical with the starting texture — even for minor details. We obtained the same results upon repeating the heating-cooling cycle.

To our knowledge, this is the first *in situ* determination of texture changes during phase transformations by neutron diffractior As such, the experiment opens a new field to investigate texture changes during heating. The 50-minute time period used to record data for one temperature interval allowed us to follow texture changes in real time. The results for quartzite clearly show that the aggregate retains its "shape memory" (i.e., the shape-memory effect refers to a phenomenon whereby a material when mechanically deformed and then heated, returns to its original shape). Quartzite thus emerges as a shape-memory syster similar to those previously observed in metals. When quartz becomes hexagonal upon heating, the orientation distribution als becomes hexagonal. Upon cooling, crystals could choose at random between the two possible trigonal orientation variants. Ye the memory is retained, presumably by elastic strains imposed by neighboring grains, and crystals revert to their initial orientation.

This was one of the first user experiments on HIPPO (in July 2002) and extremely difficult. Most automatic procedures (data acquisition, rotation control, temperature control) did not work and had to be performed manually. Also data corrections had t be done largely empirically. Furthermore a second experiment could not be performed because of a defective furnace. Out of one week of beamtime, we got exactly 12 hours, yet they provided us with some very exciting results and we look forward to continue this experimental series in 2003.

Experiment Report *(continued)*

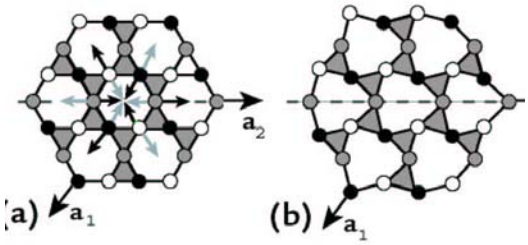

Figure 1. A c-axis projection of the structure of quartz. The SiO_4 tetrahedra are shaded and the oxygen atoms are shown with white, gray, and black circles indicating different z-levels. (a) Hexagonal β–quartz with potential distortions to trigonal α-quartz indicated by black and gray arrows. (b) Trigonal α–quartz representing one orientation variant.

Figure 2. 002, 100, 101, and 011pole figures for quartzite Sci 292 recalculated from the orientation distribution.
Top: 500°C (before heating), Center: 650°C, Bottom: 500°C (after heating). Equal area projection, linear pole density scale in multiples of a random distribution. The scale for the 002 pole figure needs to be multiplied by a factor of 5 relative to the others. Notice that the trigonal low temperature texture becomes hexagonal upon heating and returns to exactly the same pattern
upon cooling.

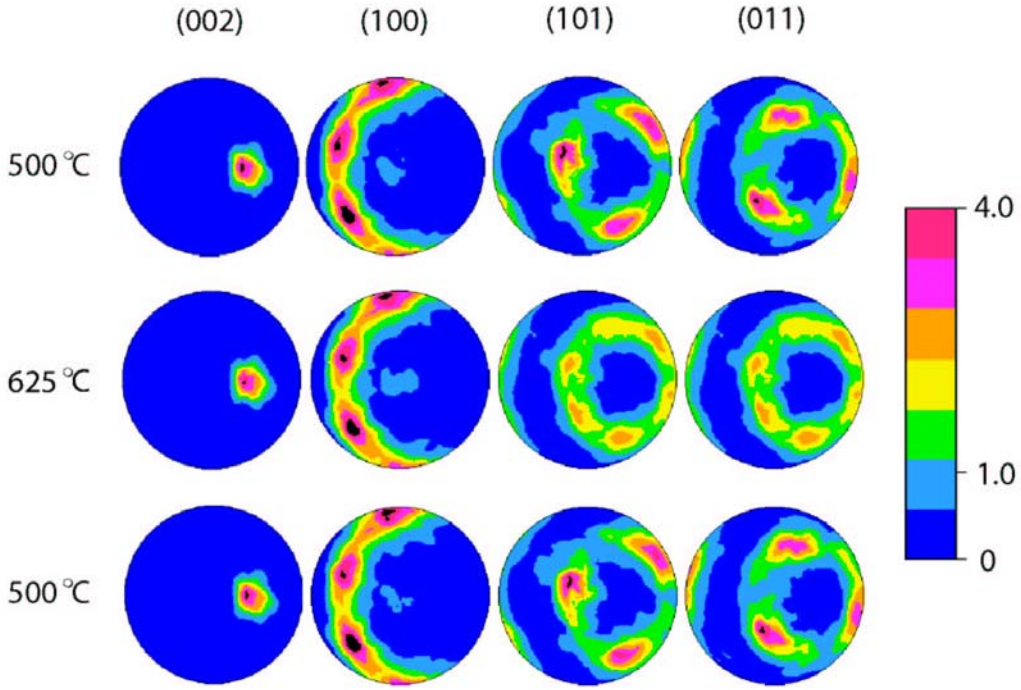

References:

H.-R. Wenk, S. Grigull, J. Pehl , D.J. Williams (2003). Texture Changes During the Quartz α-β Phase Transition Studied by Neutron Diffraction. Research Highlights in LANSCE Activity Report 2002 (in press).
H.-R. Wenk, S. Grigull, J. Pehl, D. Williams (2003). Texture Changes During the Quartz α–β Phase Transition Studied by TOF Neutron Diffraction. Science (in review)

REPORT ON EXPERIMENT
(Please Type)

Submit all experiment reports to:
LANSCE User Office, MS H831, Los Alamos National Laboratory, Los Alamos, NM 87545

Experiment was carried out at:	**Local Contact**	**Proposal #**	***LANSCE Use Only***
[x] Manuel Lujan Jr. Neutron Scattering Center	Don Bown	**2002092**	**Report Rc'd**
[ ] Weapons Neutron Research Facility	**FP/Instrument Used**		**4/22/03**
[ ] WNR/Blue Room	2		

Title
Texture and Internal Strain Development in Uranium Alloy Samples

Authors and Affiliations
Dave teter mst-6
Dan Thoma mst-6
Don Brown mst-8

Experiment Report

In-situ neutron diffraction loading measurements were performed on U-Nb coupons removed from actual parts. Any real discussion of this is classified. Figure 1 shows the evolution of the diffraction pattern with run number. The change in texture with loading which is evident is the expected result, but little more can be presented in this forum.

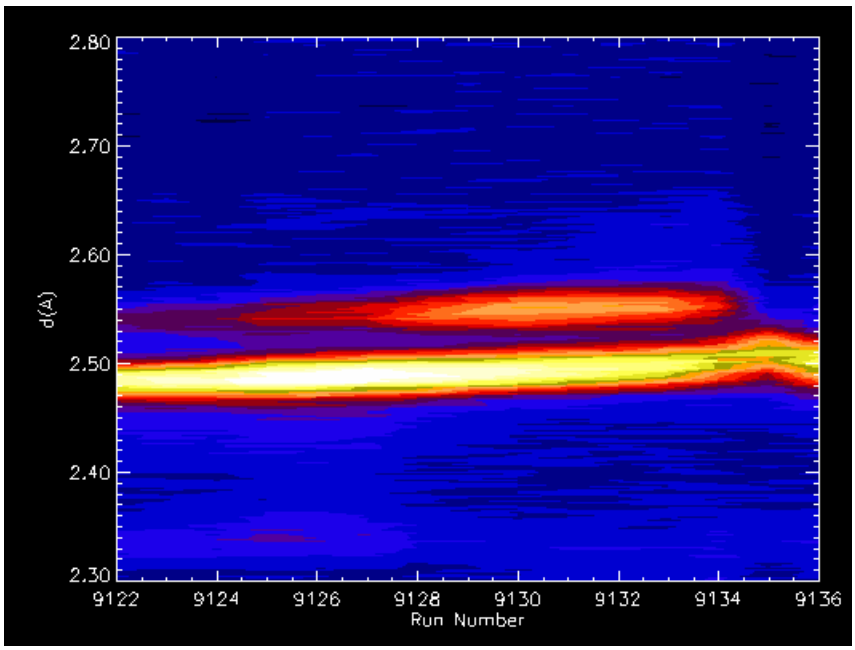

Experiment Report *(continued)*

IMPORTANT! List or attach a list of publications resulting from this experiment (published or in press).

LANSCE
Los Alamos Neutron Science Center

REPORT ON EXPERIMENT
(Please Type)

Submit all experiment reports to:
LANSCE User Office, MS H831, Los Alamos National Laboratory, Los Alamos, NM 87545

Experiment was carried out at:	**Local Contact**	**Proposal #**	***LANSCE Use Only***
[X] Manuel Lujan Jr. Neutron Scattering Center	Paul Langan	**2002093**	**Report Rc'd 3/21/03**
[ ] Weapons Neutron Research Facility	**FP/Instrument Used**		
[ ] WNR/Blue Room	PCS		

Title
Rubredoxin Crystallography in TOF Neutron Measurement

Authors and Affiliations
Ichiro Tanaka, Nobuo Niimura, Japan Atomic Energy Research Institute (JAERI), Japan; Robert Bau, University of South California; Xinmin Li, Paul Langan, Los Alamos National Laboratory

Experiment Report

It is very important in life science to obtain the positional information of hydrogen atoms in biological macromolecules including bound waters because it serves to understand the physiological functions and the protein folding mechanism in biological systems. It is said that neutron is a unique probe to identify hydrogen atoms directly, but it has been difficult to execute real experiments due to the low flux and the low efficiency of detector system. But now the Protein Crystallography Station (PCS) at LANSCE is the virtually unique machine in the world, whcih was well constructed with the most intense neutron flux as a TOF neutron diffractometer for protein crystallography. It is vey interesting to compare the data obtained at two different neutron sources and diffrcatometers with the same sample in order to explore each neutron source possibility for biomacromolecular crystallography.

As a sample Rubredoxin protein was naturally extracted from hyper-thermophile bacteria, purified and the crystal was grown in a phosphate buffer with heavy water up to 6mm^3 with 51kD. The same crystal diffracted up to 1.6 Angstrom under room temperature at BIX-3 at JRR-3M reactor in JAERI. From the data obtained at JRR-3M we can see the various H/D exchange ratios at each amide hydrogen, hydrogen bonds and bound waters' features.

In the experiment Proposal No. 2002093, only small fraction of reflections of the following sample (Rubredoxin) were obtained because of short beam time of two days as a test . Diffraction pattern of Rubredoxin protein was successfully obtained under room temperature at Protein Crystallography Station (PCS). Fig. 1 shows diffraction pattern of wavelength-overlayed image from 0.5 to 3.5 Angstrom. Up to 2.1 Angstrom reflections were observed by naked eyes on the CRT compared with 1.6 Angstrom observed by naked eyes on the CRT in case of BIX-3 and BIX-3M in JAERI. The data processing with d*TREK is under way. The net exposure time was about 20 hours, the camera distance was 70 cm, and ^{3}He 2-dimensional area detector was used.

Experiment Report *(continued)*

Though the result at PCS was a little inferior to one at BIX-3, but 2.1 Angstrom resolution data is good enough to see hydrogens in Fourier maps after collecting all possible reflections because we had an experience to try to analyze rubredoxin raw data at BIX-3 with less resolution around 2 Angstrom. In addition, thanks to the low background due to the long camera distance 70cm, the diffraction spots on the PCS raw data were extremely clear compared to that of BIX-3, 20cm in camera distance. Even at relatively week neutron sources, this nature must contribute to collect higher resolution spots from biological macromolecular crystals which generate high incoherent background inheretly.

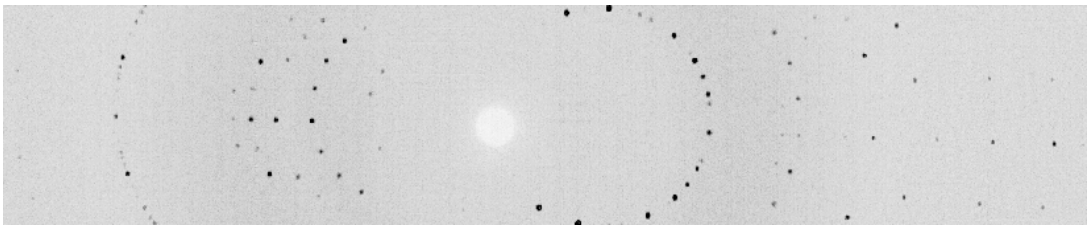

Fig.1; Rubredoxin diffraction pattern at PCS

IMPORTANT! List or attach a list of publications resulting from this experiment (published or in press).

LANSCE
Los Alamos Neutron Science Center

REPORT ON EXPERIMENT
(Please Type)

Submit all experiment reports to:
LANSCE User Office, MS H831, Los Alamos National Laboratory, Los Alamos, NM 87545

Experiment was carried out at:	**Local Contact**	**Proposal #**	***LANSCE Use Only***
[X] Manuel Lujan Jr. Neutron Scattering Center	Jarek Majewski	**2002100**	**Report Rc'd 2/21/03**
[ ] Weapons Neutron Research Facility	**FP/Instrument Used**		
[ ] WNR/Blue Room	SPEAR		

Title
Investigation of Radiogenically Produced ^{3}He in the Erbium Dihydride System: Depth Profiling Using Neutron Reflectometry

Authors and Affiliations
JF Browning Sandia National Laboratories
MA Mangan Sandia National Laboratories
DM Blankenship Sandia National Laboratories
GS Smith Oak National Laboratory
GM Bond New Mexico Institute of Mining and Technology

Experiment Report
This experiment is a continuation of a multiyear experimental program designed to study the evolution of the $ErT_{2-x}{}^3He_x$ metal hydride system as a function of time and helium concentration. In the initial phase of this experiment, seven samples were prepared for analysis on SPEAR at the Lujan Center at LANSCE. The seven samples consisted of 2 molybdenum films (one annealed at 450°C for ~ 2hours to mimic hydriding conditions, the other unannealed), 2 erbium films on molybdenum (one annealed, on unannealed), 2 erbium ditritide films and 1 erbium dideuteride film. The films were prepared at Sandia National Laboratories by physical vapor deposition of 100nm of molybdenum onto a silicon substrate (100) of dimensions 2.54cm x 5.1cm x 1.27cm. A 150nm layer of erbium was then deposited onto the molybdenum layer. Formation of the erbium dihydride layer was accomplished by the subsequent exposure of the erbium layer to a 175torr tritium (deuterium) pressure at a temperature of ~ 450°C. Hydriding of the films was carried out at the Savannah River Technology Center (SRTC) of the Department of Energy's Savannah River Plant. The two-tritiated samples were initially analyzed on SPEAR during the 2001 run cycle and subsequently reanalyzed multiple times during the 2002 run cycle along with the experimental controls listed above. Results showing the observed difference as a function of helium concentration for one of the tritiated samples is presented in the figure below. Efforts are currently underway to analyze data acquired thus far. Further analysis is planned on these samples as well as additional samples sets to extent the range in helium concentration for the 2003 run cycle.

Experiment Report *(continued)*

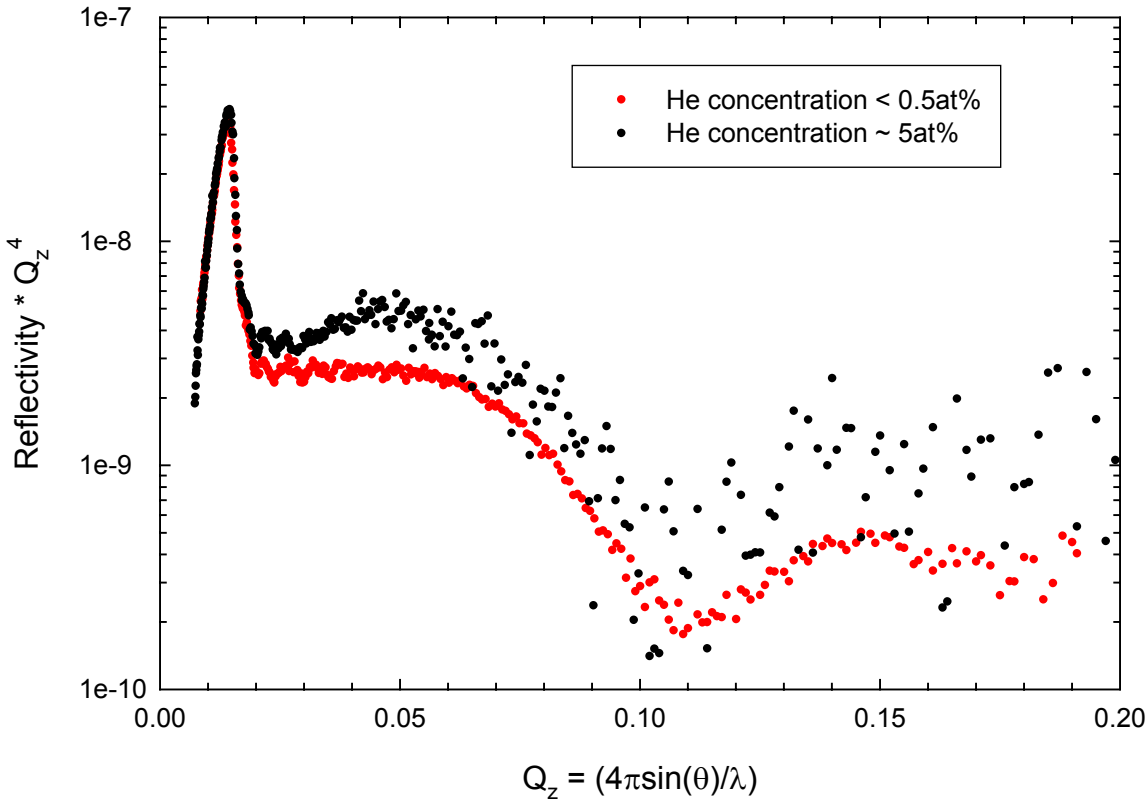

IMPORTANT! List or attach a list of publications resulting from this experiment (published or in press).

LANSCE
Los Alamos Neutron Science Center

REPORT ON EXPERIMENT
(Please Type)

Submit all experiment reports to:
LANSCE User Office, MS H831, Los Alamos National Laboratory, Los Alamos, NM 87545

Experiment was carried out at:	**Local Contact**	**Proposal #**	***LANSCE Use Only***
[X] Manuel Lujan Jr. Neutron Scattering Center	Don Brown	#2002106	**Report Rc'd**
[ ] Weapons Neutron Research Facility	**FP/Instrument Used**		**2/14/03**
[ ] WNR/Blue Room	SMARTS		

Title
Effect of Texture Randomization Processing on the Deformation Mode Activity in Magnesium Alloys

Authors and Affiliations
Sean R. Agnew, University of Virginia
Donald W. Brown, MST-8, LANL
Thomas M. Holden, consultant

Experiment Report

The *in-situ* deformation experiments performed on magnesium alloy AZ31B on SMARTS are similar in character to a set performed on NPD last year (summer 2001). The major distinction was that previous samples were conventionally rolled plate samples having the crystallographic texture characteristic of that process. This year the samples had been processed by a novel technique known as Equal Channel Angular Extrusion (ECAE). The effects of this process are of interest to a number of researchers around the world, including a number at LANL. In the current setting, the ability of this process to enforce a profound grain refinement upon metals was not the primary interest. In fact, the samples were subjected to 8 ECAE passes by route B and then annealed at 350deg C for 2 hours in order to grow the grains back to the size of the original conventionally extruded material. Note a parallel work was being performed to measure the textures of these samples using HIPD (prop. #2002022, originally scheduled for HIPPO).

Previous work has emphasized the importance of a tension/compression asymmetry in wrought magnesium alloys due to mechanical twinning. Therefore, this year the two kinds of samples (conventionally extruded and ECAE + annealed) were tested under both tension and compression type deformation.

In-situ tests were performed under load control. Samples were loaded to a prescribed load and the diffraction patterns collected during a holding period (~0.5 hours each). Samples were loaded to a higher strain than previously attempted because our analysis of last year's work (published in 3 papers listed below) showed the significantly protracted elasto-plastic transition in magnesium, as compared with other metals. Further, scheduled unloads and reloads were performed to gain additional insights into the variations of internal strains with applied stress and strains. In particular the appearance of early onset of reverse plasticity during unloading (Bauschinger effect) was examined. So far, our analysis has not detected a severe Bauschinger effect in any of the magnesium alloys tested.

1. S.R. Agnew, C.N. Tomé, D.W. Brown, T.M. Holden, and S.C. Vogel, "Study of Slip Mechanisms in a Magnesium Alloy by Neutron Diffraction and Modeling", *Scripta Mater (2003) in press.*
2. S.R. Agnew, D.W. Brown, S.C. Vogel, and T.M. Holden, "*In-situ* Measurement of Internal Strain Evolution During Deformation Dominated by Mechanical Twinning," *Mater. Sci. Forum*, 404 (2002) 747-752.
3. C.N. Tomé, S.R. Agnew, W.R. Blumenthal, M.A.M. Bourke, G.C. Kaschner and P. Rangaswamy, "The relation between texture, twinning and mechanical properties in low symmetry aggregates" *Mat. Sci. Forum,* 408-412 (2002) 263-268.

Experiment Report *(continued)*

Due to the details of their textures, the conventionally extruded material exhibited a strong tension/compression asymmetry and we will be able to use the data from this study to further validate models of deformation twinning that we are developing collectively with Carlos N. Tomé (also of MST-8, LANL.) In contrast with the conventionally extruded material, the ECAE+annealed material exhibited essentially no tension/compression asymmetry and there was little signature of twinning in their flow curves or texture evolution (based upon our preliminary analysis of the SMARTS neutron diffraction data.)

We have recently submitted another paper for publication, which explains the reason for the unique behavior of the ECAE+annealed material in terms of its texture. Contrary to the proposal title and concept, the material processed by ECAE+annealing actually proved to have a stronger texture than the original conventionally extruded material. (see also prop. #2002022).

S.R. Agnew, J.A. Horton, T.M. Lillo and D.W. Brown, "Enhanced Ductility in Strongly Textured Magnesium Produced by Equal Channel Angular (ECA) Processing", *submitted to Scripta Mater. (2003)*.

Further analysis of the internal strain data collected during the in-situ diffraction study described here should help to validate this work, or provide unanticipated insights to help broaden and deepen our understanding of the deformation of magnesium, an exceptionally light weight non-cubic structural material.

IMPORTANT! List or attach a list of publications resulting from this experiment (published or in press).

LANSCE
Los Alamos Neutron Science Center

REPORT ON EXPERIMENT
(Please Type)

Submit all experiment reports to:
LANSCE User Office, MS H831, Los Alamos National Laboratory, Los Alamos, NM 87545

Experiment was carried out at:	**Local Contact**	**Proposal #**	***LANSCE Use Only***
[X] Manuel Lujan Jr. Neutron Scattering Center	Darrick Williams	**2002107**	**Report Rc'd**
[ ] Weapons Neutron Research Facility	**FP/Instrument Used**		**3/7/03**
[ ] WNR/Blue Room	HIPPO		

Title
Flow-Related Microlite Preferred Orientation in Lavas

Authors and Affiliations
Jenny Pehl, Michael Manga, Rudy Wenk –Earth and Planetary Science Department, University of California, Berkeley

Experiment Report

This experiment was a test to see if neutron diffraction could be used to measure the orientation of small crystals (approximately 2m x 10m x 10m) in an amorphous matrix. The samples used were volcanic glasses containing pyroxene microlites.

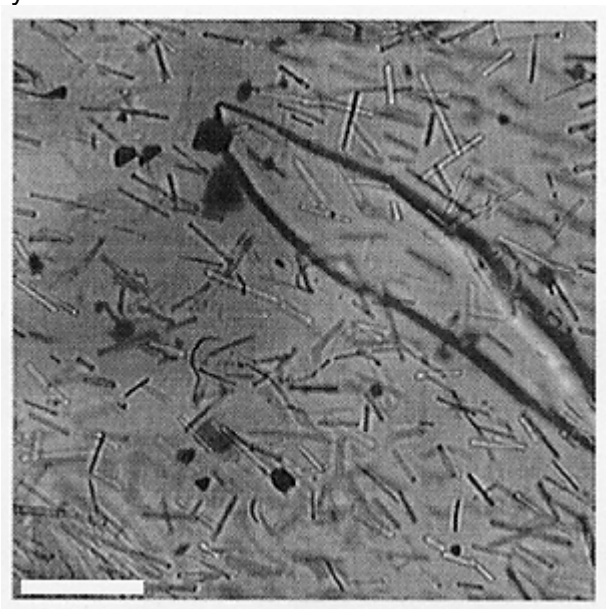

Figure 1. Microlites in obsidian.

Our first experiment was delayed because the HIPPO sample chamber's door was non-operational. After we took data (using one hour to gather each spectra), we found that the peaks in the spectra exactly matched that of an fcc metal. Our conclusion was that the distance to the beam from the top

Experiment Report *(continued)*

of the sample chamber was not correct and that we had centered on the metal ring on the rotating sample stick.

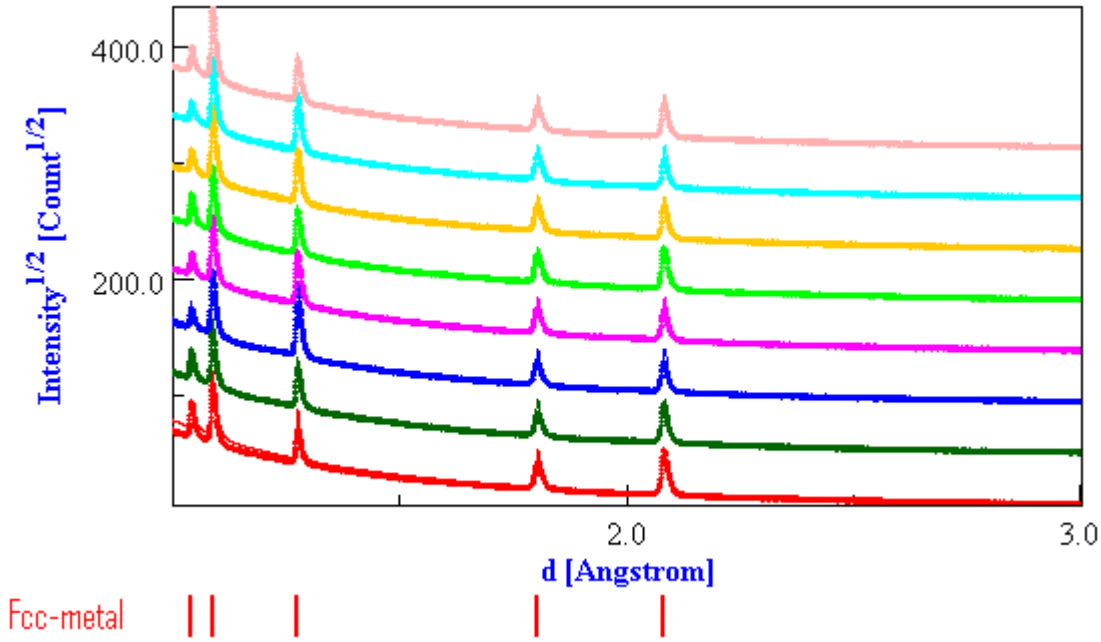

Figure 2. Fcc-metal peaks. Eight panels on 150° detector bank.

During our second day of beamtime in September, we made sure that the sample was in the beam. However, analyzing the spectra showed no peaks that could be used in our software. It seems as though there was not enough crystalline material to scatter neutrons. We may, in the future, try samples with much higher crystallinities. Obsidians, however, typically have crystallinities of around 6% or less.

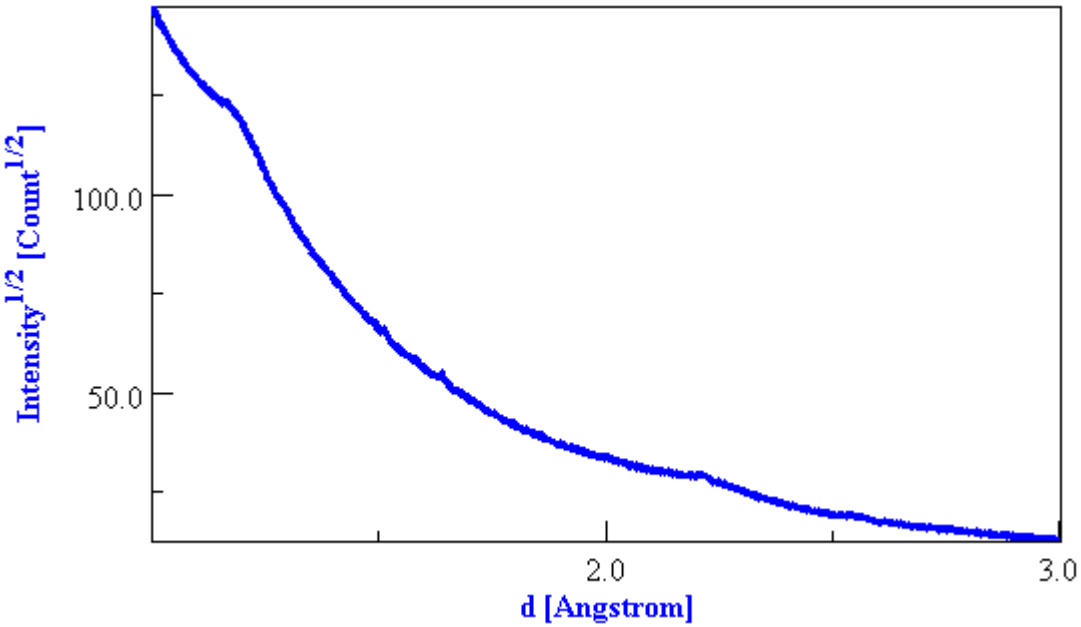

Figure 3. No peaks. Sum of eight panels on 150° bank.

IMPORTANT! List or attach a list of publications resulting from this experiment (published or in press).

none

LANSCE
Los Alamos Neutron Science Center

REPORT ON EXPERIMENT
(Please Type)

Submit all experiment reports to:
LANSCE User Office, MS H831, Los Alamos National Laboratory, Los Alamos, NM 87545

Experiment was carried out at:	**Local Contact**	**Proposal #**	***LANSCE Use Only***
[X] Manuel Lujan Jr. Neutron Scattering Center	Mark Bourke	**2002108**	**Report Rc'd 5/6/03**
[ ] Weapons Neutron Research Facility	**FP/Instrument Used**		
[ ] WNR/Blue Room	SMARTS		

Title

Residual stress mapping in single crystal S-FAP boules used for laser amplification

Authors and Affiliations
Michael R. Hill, University of California, Davis
Michael B. Prime, Los Alamos National Laboratory
Adrian T. DeWald, University of California, Davis
Kathleen Schaffers, Lawrence Livermore National Laboratory

The Laser Science and Technology Program at Lawrence Livermore National Lab has created a new type of apatite crystal called S-FAP (strontium fluoroapatite, $Sr_5(PO_4)_3F$ doped with Yb^{3+}) to serve as a laser amplification medium in second-generation fusion devices. The laser properties of this new crystal are superior to all other types of crystals for high-power lasers. Although LLNL has successfully grown crystal boules of suitable size for a laser amplifier, nearly 75% of crystals fracture during cutting that is required to fabricate amplifier slabs. It is believed that fracture in the crystal boules is driven by internal residual stress that is generated during high-temperature (~1500 K) crystal growth and subsequent cooling. If the residual stress distribution within the crystal were known, an optimal machining process could be designed to help reduce the occurrence of fracture.

An attempt was made to measure the residual strain distribution inside one of these single S-FAP crystal boules (70 mm long and 35 mm in diameter) on the SMARTS instrument at the Manual Lujan Jr. Neutron Scattering Center on August 20-22, 2002. The goals of the experiment were to determine the hoop and axial strain components as a function of radial position, along a single radial line near the center of the crystal, and to check for the assumption of an axially symmetric residual stress state by measuring the hoop and axial components of residual strain on a second radial line perpendicular to the first. Three days of beam time were granted for this experiment and a summary of the actual measurements that were performed during this time follows:

Day 1 (8-20-02) – Experiment set-up, specimen rock test to properly align it with the detectors, sample volume measurement to determine necessary count times, line-scan across the center of the crystal (50 mm from end) with a sampling volume of 3 mm by 3 mm and a count time of 30 minutes with a spacing of 1.5 mm between points (measurement locations at y={-15.0, -13.5, …, 0, 1.5, …, 13.5, 15.0} mm).

Day 2 (8-21-02) – Line-scan across the free end of the crystal (sampling volume of 3 mm by 3 mm and a count time of 10 minutes with a spacing of 1.5 mm between points) to determine the stress free lattice spacing and to check for the presence of crystal nonuniformities in an axially stress free region. A brief data analysis was performed at this stage and it revealed that the count times were not long enough to fully determine the shape of the diffraction peaks so an additional line scan with a sampling volume of 3 mm by 6 mm and a count time of 240 minutes with a spacing of 5 mm between points, y={-15.0, -10.0, -5.0, 0.0} was performed.

Day 3 (8-22-02) – Another round of data analysis from the Day 2 experiments showed that the shape of the diffraction peaks was not well enough defined to give meaningful results. An additional experiment was performed for a sampling volume of 3 mm by 6 mm and a count time of 240 minutes at a single measurement location after a modification to the collimator was made to reduce the scattering of the beam. This experiment did help to improve the shape of the diffraction peak but there was not sufficient beam time left to continue experimenting.

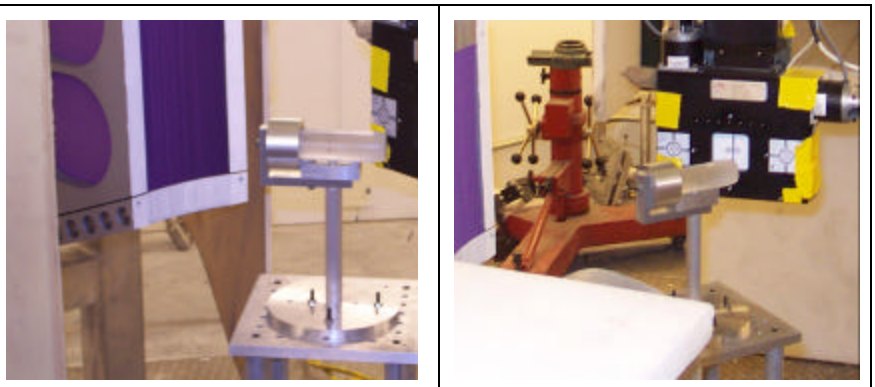

(a) (b)

Figure 1 – Pictures of the S-FAP crystal and its orientation within the SMARTS beam path, the c-axis of the hexagonal crystal is oriented with the long axis of the cylinder and the a-axis is positioned horizontally on the back side of the crystal and it is perpendicular to the c-axis

We are still working to find a successful data reduction method since the typical routines were inconclusive. A data reduction attempt was performed by the scientists at LANSCE but they were unable to determine the distribution of residual strain within the crystal. We were all aware that there was a significant chance that this experiment would not yield any conclusive results. We are not aware of any previous attempts to measure the residual strain within a single crystal using neutron diffraction. The data recorded during the three days of experiments was difficult to reduce because the shape of the diffraction peaks was not very symmetric (Figure 2). The shift in the diffraction peak from the stressed to the stress free state is used to calculate the strain present in the material. A previous residual stress measurement on a similar specimen using the slitting method showed that the magnitude of expected peak residual strain within the crystal is about 400 microstrain which would produce a diffraction peak shift of around 0.0007 (shown as a blue line for reference on Figure 2). Since the size of the expected shift is so small compared to the non-uniformities of the diffraction peak it was difficult to get any sensible results from the experiment.

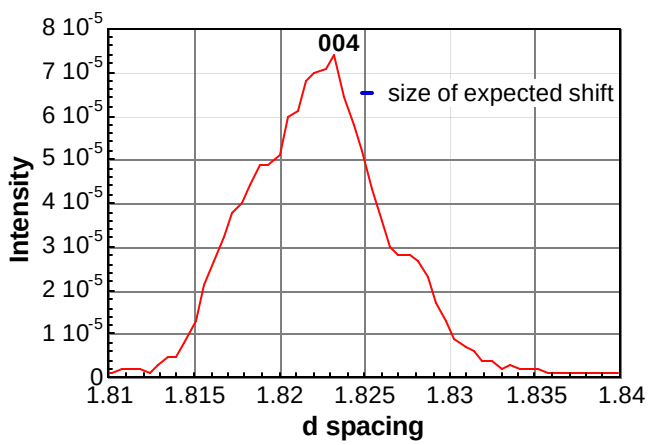

Figure 2 – Example of a typical diffraction peak with the expected magnitude of the shift shown

IMPORTANT! List or attach a list of publications resulting from this experiment (published or in press).

LANSCE
Los Alamos Neutron Science Center

REPORT ON EXPERIMENT
(Please Type)

Submit all experiment reports to:
LANSCE User Office, MS H831, Los Alamos National Laboratory, Los Alamos, NM 87545

Experiment was carried out at:	**Local Contact**	**Proposal #**	***LANSCE Use Only***
[x] Manuel Lujan Jr. Neutron Scattering Center	Al Hurd	**2002109**	**Report Rc'd**
[ ] Weapons Neutron Research Facility	**FP/Instrument Used**		**3/21/03**
[ ] WNR/Blue Room	SPEAR		

Title
Morphology of Toughened Anti-Corrosion Films

Authors and Affiliations
Guirong Pan, University of Cincinnati
Dale W. Schaefer, University of Cincinnati
Mike Kent, Sandia National Lab

Experiment Report

Organofunctional silanes are powerful systems for protecting a wide range of metals against corrosion. Especially, bis-type silanes, with a general formula of $(XO)_3$-Si-$(CH_2)_3$-R-$(CH_2)_3$-Si-$(OX)_3$ were found to perform more efficiently on a wider range of metals in various corrosion tests compared to the well-known mono-silanes of the type $(XO)_3$-Si-$(CH_2)_3$-R.

In order to optimize the silane film and investigate the morphology and degradation of polymer-toughened films, it is important to study bis silane's anti-corrosion mechanism. Dr. Van Ooij's group has done some characterization on the structure of the bis-sulfur and bis-amino silane using FTIR and electrochemical impedance spectroscopy (EIS). They have postulate that for bis-amino silane, there might be a new phase formed between substrate and film after aging in the atmosphere, and further crosslinking reaction might occur in the film upon curing at 100ºC. To elucidate the mechanism by which these films protect metals, use neutron reflectivity to investigate the composition profiles within the silane films after exposure to water and other solvents as well as following hydrothermal conditions.

In this experiment, we examined neutron reflectivity from pure organosilane films, mainly bis-amino silane and bis-sulfur silane film on silicon substrates. We first examined bis-amino silane film in the dry state. Then the films were exposed to D_2O and deuterated-nitrobenzene at room temperature and neutron reflectivity data were collected in this "wet state." Then the samples were redried in a desiccator and a new NR measurement was performed in this redried state.

Figure 1 shows the NR data for bis-amino film in the dry state, exposure to D_2O at room temperature for 14 hours and after following drying in the desiccator for 6 hrs. A large increase in reflectivity is observed after exposure to D_2O. While after drying for 6 hrs, the reflectivity has decreased substantially, almost the same as the as-prepared state.

Experiment Report *(continued)*

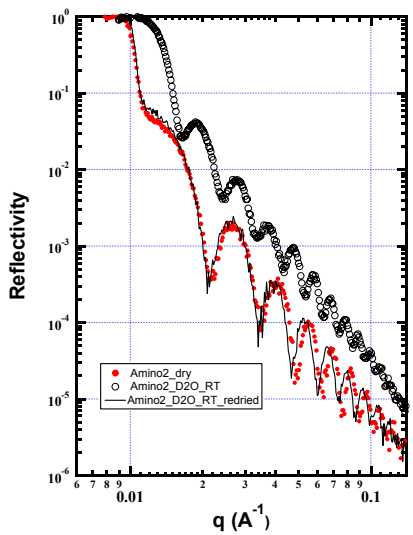

Figure 1: NR data from bis-amino film exposed to D_2O at room temperature for 14 hours

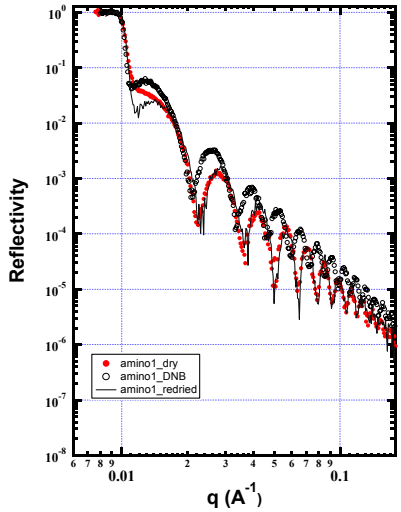

Figure 2: NR data from bis-amino film exposure to d-Nitrobenzene at room temperature

The results show that most of the incorporated D_2O was physically adsorbed, and very little chemical changes have occurred. Figure 1, for example, shows recovery of the original reflectivity profile after swelling in water.

Figure 2 is the NR data for bis-amino film exposure to nitrobenzene. In this case there is an increase in film thickness, but it is clear that bis-amino film swells more in water vapors than in NB vapors. This result indicates that the crosslink density of bis-amino silane film is relatively low and/or also that bis-amino is very hydrophilic.

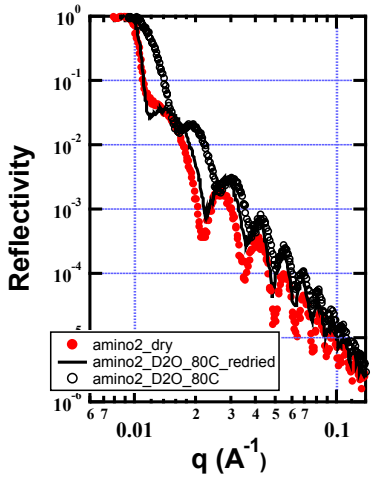

Figure 3: NR data from bis-amino film after exposure to D_2O at 80 ºC for 14 hours

Figure 3: NR data from bis-amino film after exposure to D_2O at 80 ºC for 14 hours. In this case the reflectivity profile is not reversible after drying, whereas the reflectivity was reversible when swelled with D_2O vapors at room temperature. A chemical change occurs upon heating in saturated D_2O at 80 ºC. Presumably unhydrolyzed ethoxysilyl groups remain in the cured film. Only at 80ºC, the hydrolysis and condensation will continue in the presence of water vapor. This process will generate more Si-O-Si linkages in the film and denser film, which coincides with Dr. Van Ooij's results. We plan to continue to do conditioning with this fully hydrolyzed and condensed film in order to separate the roles of hydrophobicity and crosslink density.

IMPORTANT! List or attach a list of publications resulting from this experiment (published or in press).

LANSCE
Los Alamos Neutron Science Center

REPORT ON EXPERIMENT
(Please Type)

Submit all experiment reports to:
LANSCE User Office, MS H831, Los Alamos National Laboratory, Los Alamos, NM 87545

Experiment was carried out at:	**Local Contact**	**Proposal #**	***LANSCE Use Only***
[x] Manuel Lujan Jr. Neutron Scattering Center	Jarek Majewski	**2002115**	**Report Rc'd**
[ ] Weapons Neutron Research Facility	**FP/Instrument Used**		**2/12/03**
[ ] WNR/Blue Room	SPEAR		

Title
Probing the Structure of Organosilane Films and Silane/Resin Interphases by X-ray and Neutron Reflection

Authors and Affiliations
Hyun Yim and Mike Kent, SNL

Experiment Report

In this beamtime allocation, we addressed three questions related to the structure of organosialne/resin interfaces. First we measured the extent of interpenetration of an epoxy resin with a thin ~ 100 Å layer of a common epoxy compatible coupling agent, glicidoxypropyltriethoxysilane (GPS). We spun the GPS film onto a silicon wafer and then measured the reflectivity after curing. Subsequent to that, we spun a ~ 400 Å film of d-epoxy onto the GPS film. The reflectivity was measured for the bilayer both before and after curing the epoxy. Results are shown in Figure 1. The data indicate that the resin penetrates through the entire extent of the GPS film. This result is important as the extent of interpenetration affects mechanical properties and fracture mechanisms.

The second question regards whether the interface structure of such GPS/epoxy bilayer films is a function of the time/temperature conditions of the cure of the epoxy film. In previous work we showed this to be the case for epoxy-epoxy bilayer films [1]. Nominally identical bilayer films were prepared but in the first sample the epoxy was cured at 80C for 1 hr and 120 C for 2hrs, whereas for the second sample the epoxy was cured for 3 weeks at room T and then gradually ramped up to 120 C at a rate of 10 degrees per hour. The results are shown in Figure 2. No significant difference was observed in the reflectivity, indicating that the interface structure of these two films is nearly identical.

The third question regards how water attacks this interface at elevated temperature. In previous work we discovered that H2O degrades a film of GPS alone after roughly 10 days at 80 C 100% rh [2]. In this work we performed the analogous experiment for the epoxy/GPS bilayer. Results are shown in Figure 3. Since the GPS has low SLD and the d-epoxy has high SLD, if H2O is chemically incorporated into the GPS layer due to a chemical reaction such as hydrolysis of Si-O-Si bonds, the contrast with the epoxy layer will be enhanced and the amplitude of the fringes should increase. Up to 13 days of conditioning, no changes were observed in the reflectivity. At 27 days, the reflectivity curve has dropped at the higher q values, although the features remain the same. This result is still being analyzed. One possibility is that the surface of the film has become rougher. This would indicate that the conditioning is beginning to degrade the epoxy film at the air interface. Another possibility is that the interface between the GPS layer and the epoxy layer has become broadened. Further analysis will distinguish between the two models and indicate how water is interacting with this bilayer film.

1. Yim et al, J. Polym. Sci. Part B: Polym. Phys. 2002, 40, 1709.
2. Yim et al, in preparation

Experiment Report *(continued)*

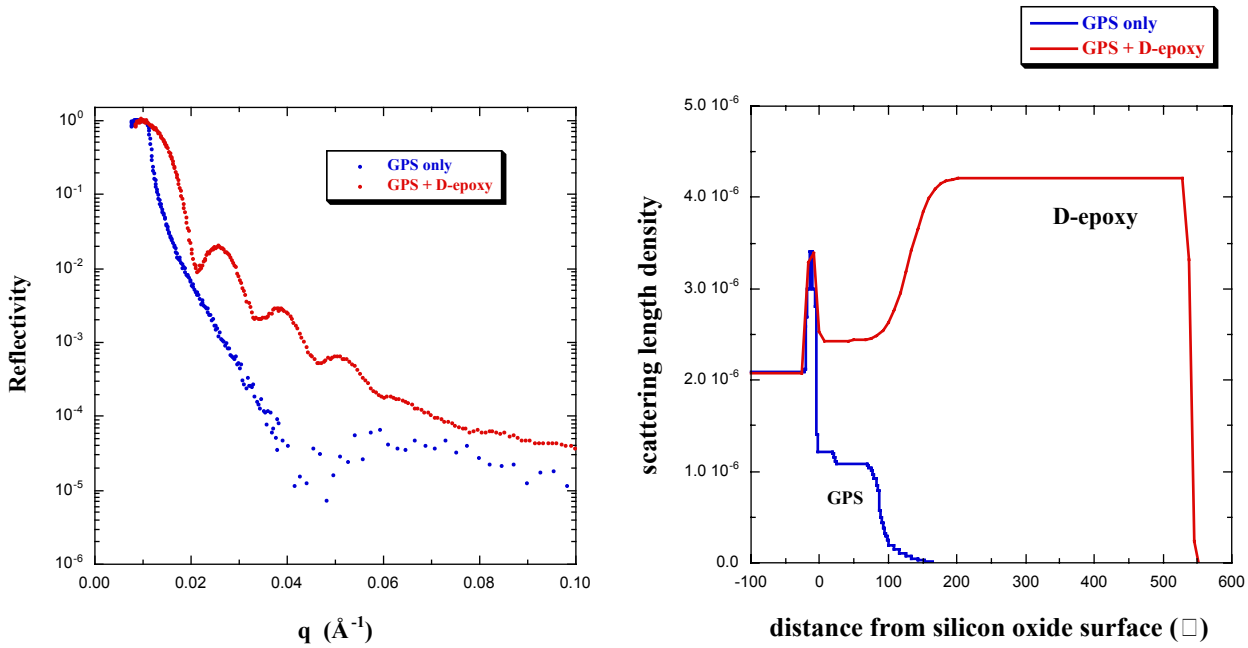

Figure 1. a). Reflectivity data for a GPS film alone and after applying a layer of d-epoxy on top and curing. B) SLD profiles.

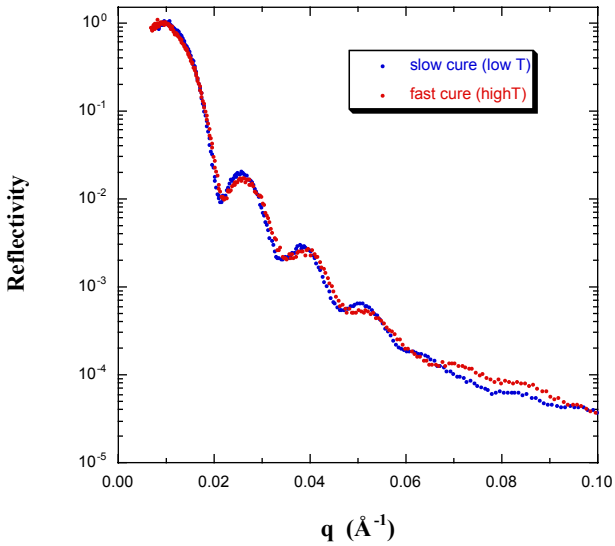

Figure 2. Reflectivity for GPSepoxy biallyers cured at diff T.

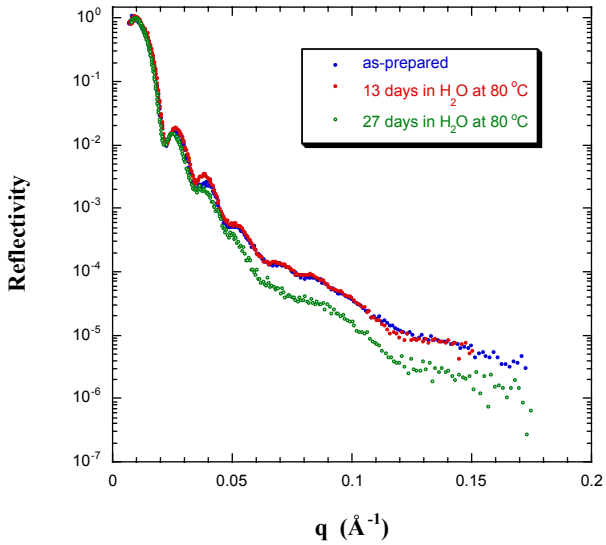

Figure 3. Ref. for GPS/epoxy conditioned in H2O

IMPORTANT! List or attach a list of publications resulting from this experiment (published or in press).

LANSCE
Los Alamos Neutron Science Center

REPORT ON EXPERIMENT
(Please Type)

Submit all experiment reports to:
LANSCE User Office, MS H831, Los Alamos National Laboratory, Los Alamos, NM 87545

Experiment was carried out at:	**Local Contact**	**Proposal #**	***LANSCE Use Only***
[x] Manuel Lujan Jr. Neutron Scattering Center	Jarek Majewski	**2002116**	**Report Rc'd**
[ ] Weapons Neutron Research Facility	**FP/Instrument Used**		**2/12/03**
[ ] WNR/Blue Room	SPEAR		

Title
Probing the Structure of Epoxy Films on Aluminum Coated Wafers by Neutron Reflection

Authors and Affiliations
Hyun Yim and Mike Kent, SNL

Experiment Report

We investigated the interfacial structure between epoxy and aluminum, which can be revealed by combining two techniques, solvent swelling and neutron reflection. This information helps us to understand how the interfacial structure impacts the fracture mechanism and fracture toughness in a glassy adhesive/inorganic solid joint. In previous work, we examined the structure of single layer epoxy films on silicon substrates as a function of composition and cure temperature.[1] The main result was a large degree of swelling near the air surface, indicating a lower crosslink density than in the bulk of the film. However, the gradient in crosslink density near the silicon surface was not observed. For this beamtime experiment, first thin layer of aluminum (200 Å) was sputtered onto a silicon wafer. We spun the epoxy film onto the aluminum coated wafer and then the film was cured at 80 ^{o}C for 1hr and then 120 ^{o}C for 2 hr. We measured neutron reflectivity data for the epoxy film as-prepared and after swelling to equilibrium with deuterated nitrobenzene (d-NB). Results are shown in Figure 1. The results are similar to those obtained for the previous epoxy film on the silicon substrate. No gradient in crosslink density near the aluminum substrate are observed, but a large degree of swelling near the air surface are observed.

1. H. Yim, M. Kent, W. F. McNamara, R. Ivkov, S. Satija, J. Majewski, *Macromolecules* **1999**, *32*, 7932.

Experiment Report *(continued)*

(a) **(b)**

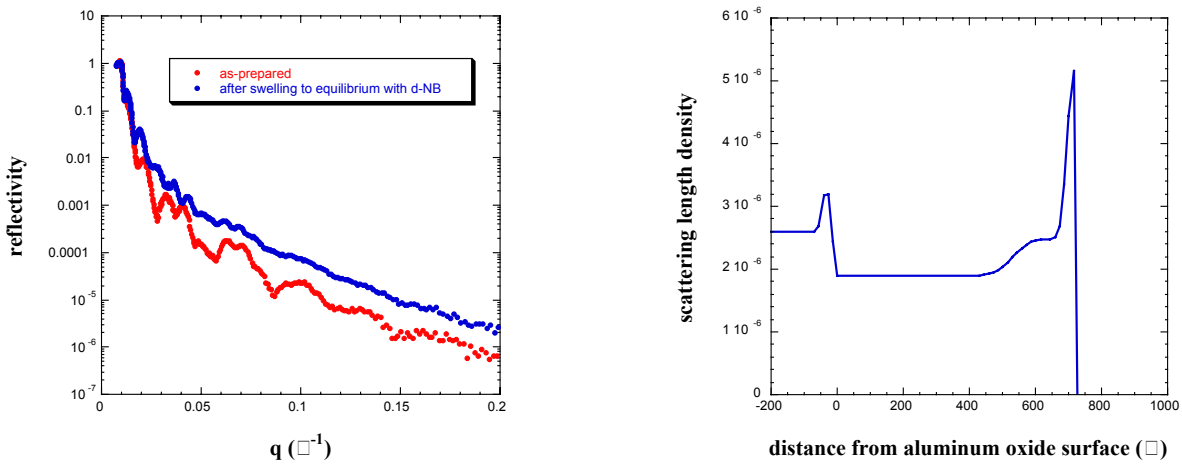

Figure 1. a). Reflectivity data for an epoxy film as-prepared and after swelling to equilibrium with d-NB. b) SLD profile for the epoxy film after swelling to equilibrium with d-NB.

IMPORTANT! List or attach a list of publications resulting from this experiment (published or in press).

LANSCE
Los Alamos Neutron Science Center

REPORT ON EXPERIMENT
(Please Type)

Submit all experiment reports to:
LANSCE User Office, MS H831, Los Alamos National Laboratory, Los Alamos, NM 87545

Experiment was carried out at:	**Local Contacts**	**Proposal #**	***LANSCE Use Only***
[x] Manuel Lujan Jr. Neutron Scattering Center	Don Brown, M. Bourke, P. Rangaswamy	**2002118**	**Report Rc'd**
[ ] Weapons Neutron Research Facility	**FP/Instrument Used**		**2/3/03**
[ ] WNR/Blue Room	SMARTS		

Title
Deformation Behavior of Superalloys: Micro-strain Measurements, Dislocation Mechanisms, and Modeling

Authors and Affiliations
Primary Investigator: Bhaskar S. Majumdar, Associate Professor, Materials Department, New Mexico Tech, Socorro, NM 87801; majumdar@nmt.edu; 505-835-5152
Additional Collaborators: P. Rangaswamy, LANL, D. Brown, MST-8,LANSCE, Mark Bourke, MST-8, LANSCE

Experiment Report

The overall goal of this research is to understand and model the deformation behavior of Ni-base superalloys which contain a high volume fraction (v_f >0.5) of cuboidal γ' precipitates ($Ni_3(Al,Ti)$, $L1_2$ ordered fcc) that are coherently embedded in a γ Ni-alloy-matrix (disordered fcc). These nano-structured materials exhibit unmatched high temperature properties that far exceed (by as much as 10 times) those of the constituents (synergism). Current needs include remaining life assessment of materials in aerospace and nuclear service, and improved high temperature performance through modifications of the bulk alloy and the γ/γ' interface.

The major scientific impact on the Laboratory and DoE is the establishment of a methodology for extracting and modeling diverse microstresses in multi-phase coherent polycrystals, where deformation is influenced by anisotropic elastic constants, and by plastic anisotropy arising both from grain orientation and geometric constraint to dislocation motion. Of particular interest is the probing of high temperature deformation, to understand how the γ' constraint influences deformation in the narrow γ channels, and to evaluate the possible role of γ/γ' interface sliding on creep. In addition, the high temperature creep resistance of these alloys is limited by a phenomenon known as *rafting*, wherein the initially cuboidal particles take on a rectangular shape with time under creep, with the long direction perpendicular to the loading axis. This microstructural instability is greatly detrimental to creep resistance. Recent calculations show that such instability is related to the strain energy component of the free energy (ΔG) difference between the different channels of the γ phase, and is related to the development of a geometrically necessary dislocation structure. Neutron diffraction measurements allow a direct method of measuring the strain energy difference in the different γ channels, and hence is a very promising technique for understanding rafting, as well as to assess the effects of alloy modifications on rafting. Superalloy manufacturers (e.g. Canon Muskegon), engine companies (e.g. Rolls Royce) and the Air Force have expressed significant interest in the work.

Our work has concentrated on a polycrystalline CM 247 LC cast superalloy containing approximately 65 volume percent of γ' phase. In the 2001 run cycle, we had developed a methodology to evaluate individual strains in this coherent two-phase microstructure at room temperature (see publications noted below). Deconvolution schemes were developed to analyze the diffraction patterns using both the single-fit and the Rietveld refinement techniques. Anisotropic elastic constants were evaluated in the individual phases. We were able to detect the onset of dislocation entry into the γ' phase, and relate this stress to calculations based on the anti-phase boundary (APB) energy of the γ' phase, where the latter was measured using TEM techniques at New Mexico Tech (NMT).

Experiment Report *(continued)*

In the 2002 run cycle we have conducted creep tests on the alloy at 900 C and 850 C in the SMARTS diffractometer. Creep experiments were conducted at a number of applied stress levels, and time-of-flight data were binned at 15 minute intervals. A higher beam current than the previous year helped us to reduce the counting time, and thereby it provided better time-resolved data on the evolution of elastic microstrains. This improvement was particularly useful during the tertiary stage of creep, and in the last few minutes prior to failure of samples. Understanding of material behavior is lacking in these regimes, and our preliminary analyses have provided important new insights.

We would also like to make a few comments regarding the test and data acquisition techniques. Compared to our previous run cycle, we observed that the tests were greatly automated using script files, and these in turn helped us to conduct the experiments more efficiently with less manual fatigue. Indeed, there have been significant improvements in the SMARTS facility, and we thank Mark Bourke and his group for making the system both user-friendly and efficient. The vacuum furnace malfunctioned during one of the experiments, but the fast and efficient solution to the problem by the LANSCE researchers is truly noteworthy. The worked round the clock to put the system in order and helped us conduct the experiments within the allocated beam time.

The high temperature experiments were successful, and we are currently in the process of analyzing the data, and develop plasticity models to explain the microstrain response. We provide some initial results in the rest of this report.

Figure 1 shows the misfit as a function of temperature. Data from other investigations are also included for reference. The results show fairly large negative misfit at 900 C, and this effect is anticipated to have adverse effect on the creep resistance. We have since correlated the trend of misfit data with calculations based on the Eshelby model, utilizing available data on the thermal expansion of the individual phases.

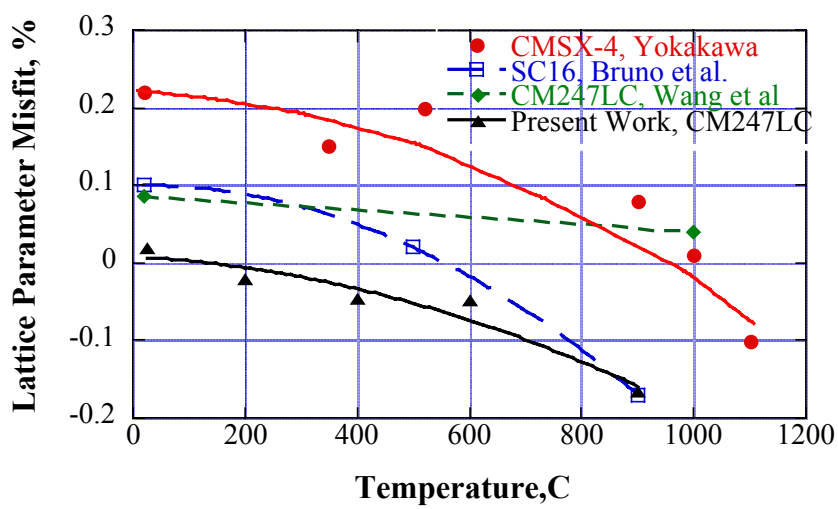

Figure 1. Misfit strain, $\delta = \frac{2(a_{\gamma'} - a_{\gamma})}{(a_{\gamma'} + a_{\gamma})}$, measured as a function of temperature in superalloys with a high volume fraction of γ' phase.

Figure 2 illustrates the change in elastic microstrains (in the loading direction) in the γ and γ' phases, for grains with [001] axis aligned along the loading axis of the specimen. The specimen was tested in creep at 900 C at an applied stress of 425 MPa. Figure 2 shows a number of important trends. The intergranular strains increased monotonically with time. This behavior is likely a result of higher creep resistance in this orientation, compared with grains that have [011] direction oriented along the loading direction. Because of strain compatibility requirement, these latter grains with low creep resistance must necessary transfer load to a more creep resistant grain. Coinciding with the intergranular strain trend is the increase of elastic microstrain in the [001] oriented γ' phase (size ~ 400 nm). Since much of the deformation in this grain is localized in the narrow γ channels (~ 100 nm width), an increase in γ' stress must occur through a constraint effect.

Note also that the rate of increase of elastic microstrain in the γ' phase reduces, and ultimately levels off at times approaching failure time.

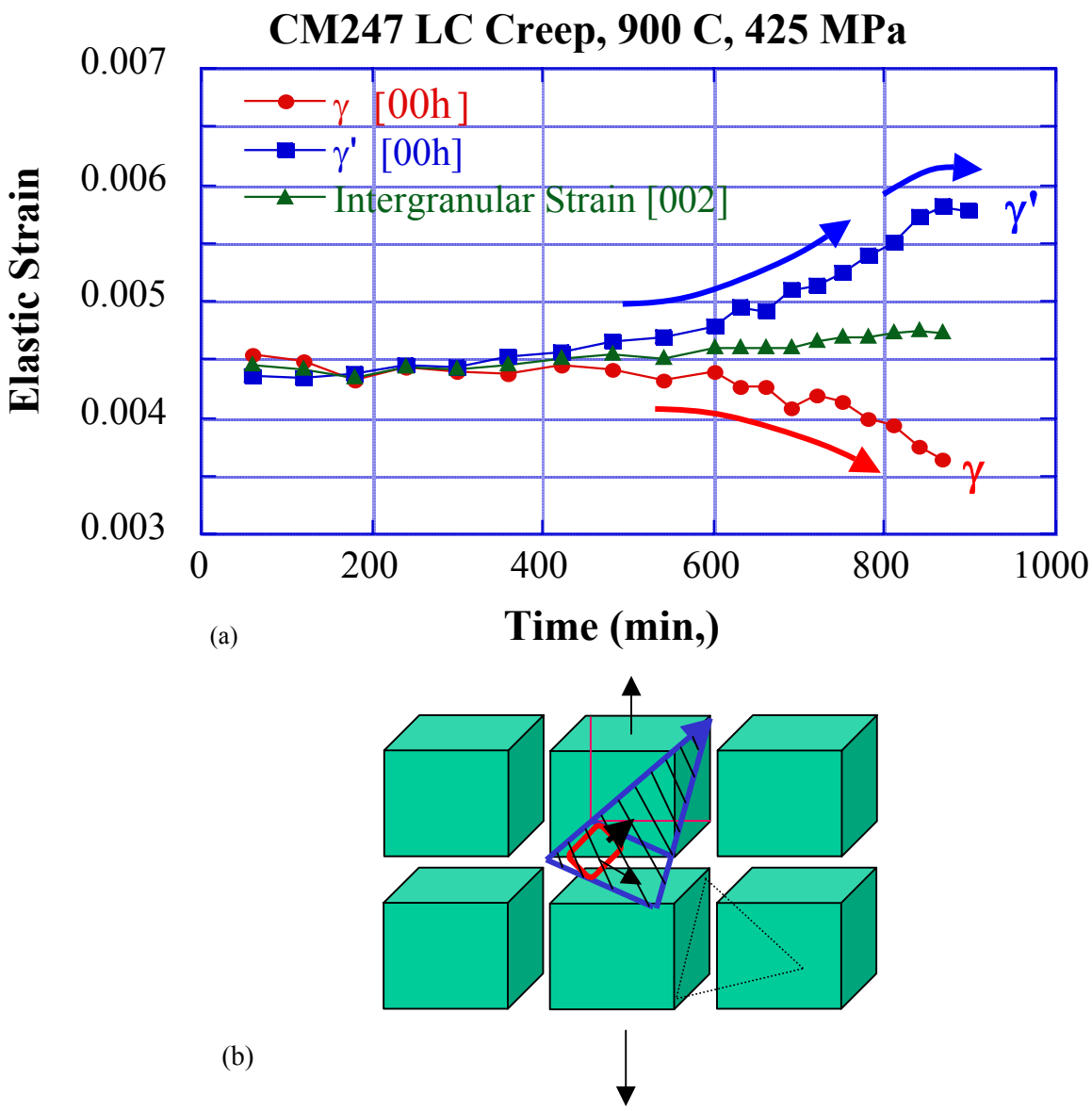

Figure 2. (a) Evolution of elastic strain in the coherent γ and γ' phases in a [001] oriented grain of superalloy CM 247 LC, creep tested at 900 C. (b) Schematic showing geometry of the γ' precipitates in the [001] grains.

While we do not have additional evidence yet about dislocation structures (TEM specimens are being prepared), we suspect that the leveling off in the γ' elastic strain is likely a result of dislocations entering into the γ' phase. In other words, when the stress in the γ' phase reaches a critical value (CRSS), it will be possible for the γ dislocations to enter the γ' phase. The dislocation entry will also mark a critical point in the specimen history, because then dislocations can rapidly pass through the large γ' particles and lead to fast accumulation of creep strain, and ultimately specimen failure. This may be a possible reason why the plateau region in the γ' phase (see Figure 2) was short lived. We will try to confirm this behavior in future proposed experiments.

The third important observation about Figure 2 is with regard to the evolution of elastic microstrain in the narrow γ channels. Since γ' precipitates exhibit increasing strain response, it may be conjectured that at least the

horizontal γ channels (see Figure 3 for definition of the channel) must experience larger stress. Therefore, the only possible explanation for the decreasing overall trend in the γ phase must be a fairly large reduction in stress in the γ channels parallel to the loading axis (vertical channels). Finite element analysis do not appear to explain in this trend. We believe that the significant reduction in the vertical γ channels must arise from a network of dislocations that accumulate on the vertical γ/γ' interfaces. These geometrically necessary dislocations will lead to a higher elastic strain energy in the vertical channels compared to the horizontal channels, and impact the rafting behavior. To our knowledge, this work represents the first direct measurement of elastic microstrains in the two γ channels, and is anticipated to significantly help in understanding and quantifying rafting in superalloys.

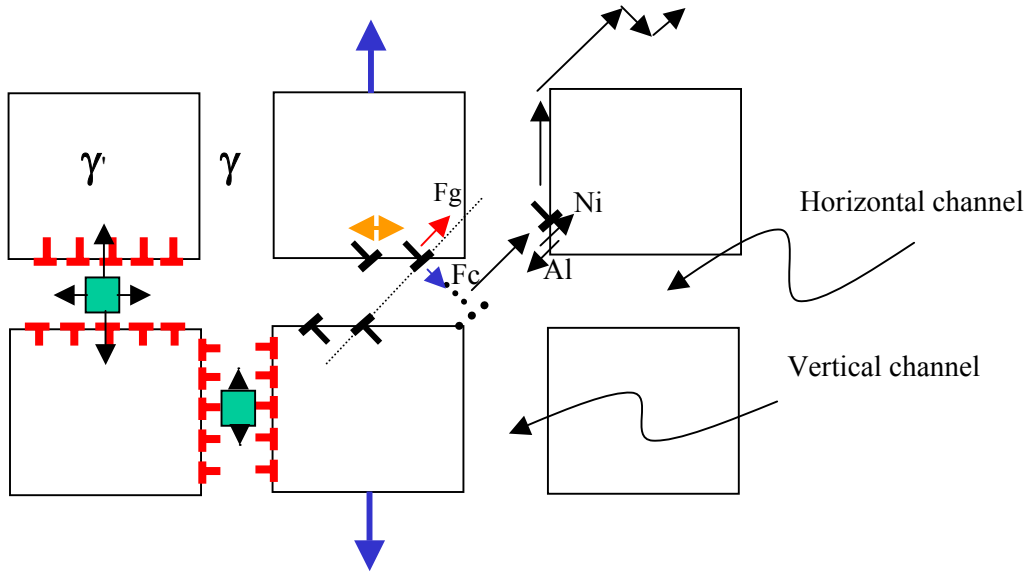

Figure 3. Schematic illustrating the build up of interface dislocations in the [001] oriented grain with time. The dislocations in the horizontal channels reduce the original misfit strain, whereas those in the vertical channel increase the misfit strain.

PUBLICATIONS:

Manuscripts published:

1. S. Ma, P. Rangaswamy, and B.S. Majumdar, "Microstress Evolution During In-Situ Loading Of A Superalloy Containing High Volume Fraction of γ' Phase", Scripta Materialia, Vol. 48, No.5, pp.525-530 (2003)
2. H. Choo, B.S. Majumdar, P. Rangaswamy, and M.A.M. Bourke,"Effect of reinforcement particle fracture on load partitioning in an Al-SiC Composite", Proc. of Denver X-ray Conference, (May 2002)
3. S. Ma, P. Rangaswamy, D. Brown, and B.S. Majumdar, "Microstresses And Plasticity Mechanisms In High-Volume Fraction Superalloys", in Modeling the Performance of Engineering Structural Materials", Eds. T.S. Srivatsan, M. Leseur, and E. Taleff, TMS Publication, Warrendale, PA (Oct. 2002), p. 357-370

Presentations:

1. The following poster won the best graduate paper at the Annual RioGrande Conference in Albuquerque (October 2002) S. Ma et al.," Microstress Evolution in a Polycrystalline Superalloy Containing a High Volume fraction of γ' Phase"
2. S. Ma, D. Brown, B. Clausen, M. Bourke, and B.S. Majumdar, "Microstrain Evolution During Creep Of A Polycrystalline Superalloy", to be presented at the 2003 Spring TMS Meeting, San Diego, Mar 2-6, (2003)

The following manuscripts are in different stages of preparation:

1. S. Ma, P. Rangaswamy, M. Daymond, and B.S. Majumdar,"Measurement and Modeling of Microstresses in CM 247 LC Polycrystalline Superalloy Containing High Volume fraction of Gamma-prime Phase", to be submitted to Metall. Trans., (Mar. 2003)
2. B.S. Majumdar, H. Choo, and P. Rangaswamy,"Particle fracture and the sequence of damage in an Al-SiC composite, based on neutron diffraction measurements", to be submitted to Acta Materalia (Apr. 2003)

LANSCE
Los Alamos Neutron Science Center

REPORT ON EXPERIMENT
(Please Type)

Submit all experiment reports to:
LANSCE User Office, MS H831, Los Alamos National Laboratory, Los Alamos, NM 87545

Experiment was carried out at:	**Local Contact**	**Proposal #**	***LANSCE Use Only***
[x] Manuel Lujan Jr. Neutron Scattering Center	Sven Vogel	2002123	**Report Rc'd**
[ ] Weapons Neutron Research Facility	**FP/Instrument Used**		**3/18/03**
[ ] WNR/Blue Room	HIPPO		

Title
Experimental Analysis of the Evolution of Radiogenically Produced Helium in Erbium Dihydride Films

Authors and Affiliations
M. A. Mangan, Sandia National Laboratories
J. F. Browning, Sandia National Laboratories

Experiment Report

The effective use of tritide materials requires an understanding of dynamical environment surrounding the radioactive decay of tritium. One aspect of this problem involves the change of material characteristics due to the formation, migration and release of radiogenically formed helium within the material. Some applications, the release rate of helium plays a critical role in the engineering of the product or application. Questions that may play an important role in the development of an understanding of these issues are: Does the site that the tritium atom occupies in the lattice, play an important role in the evolution of the resulting helium? Once helium is formed, what are the primary physical attributes that determine where, how fast, and how large bubble are formed? With answers to this family of questions, it may be possible to engineer tritide materials with optimized characteristics during the manufacturing processes, by altering processing parameters and hydriding conditions. An improved understanding of these systems may provide important benefits to the current nuclear weapons program.

Traditionally, thin films investigations have not used neutron diffraction techniques, primarily due to the lack of substantial target volume coupled with the low neutron scattering cross sections of many materials. However, several attributes of neutron diffraction show promise in exploring thin films hydrides. Those include the ability of neutron scattering to detect and differentiate the various hydrogen isotopes, the non destructive nature of the technique allowing for multiple observation of one sample set, among others.

In anticipation of using the various attributed in a long term study of thin film hydrides, we have attempted to begin by using dideuteride thin films in the HIPPO instrument. This was our first attempt using the instrument, and as such, we were not entirely successful. While the anticipated lattice parameters and texture data of the erbium dihydride films were not measured, a better understanding of the needs of future experiments was gained. In the following, the experimental procedure we followed is summarized. Most importantly, changes to our experiment, for future experiments, are listed.

The experimental procedure involved manufacturing of four thin film sample sets followed by the interrogation of the samples using neutron diffraction. The thin film sample sets were manufactured at Sandia National Laboratories. Each of the samples consisted of a silicon substrate with a molybdenum layer. Three of the sample sets had an additional erbium layer on the molybdenum. Two of those sample sets were hydrided forming am erbium dihydride thin film. Each of the four sample sets was put into a vanadium sample holder. A sample set consisted of 6 films oriented such that film's surface was perpendicular to the axis of the neutron beam.

Experiment Report *(continued)*

The samples were then put in the HIPPO instrument. Each sample set was in the beam for approximately 15 minutes with a current of ~100 microamps and rotated through 8 angles; zero, 45, 67.5, 90, 112.5, 135 and 157.5 degrees with respect to the beam direction.

The data collected was then analyzed by two researchers; Sven Vogel, of LANSCE, and Mark Rodriguez, of SNL. Both independently reached the conclusion that no portion of the data resulted, definitively, from the diffraction of neutrons off of the erbium dihydride portion of the samples. There was an overwhelming signal due to the substrate, which likely masked th weak diffraction signal resulting from the hydride film.

Due to the result of this experiment, thought has been put into corrections for future experiments. The most promising alterations are the following.

- Increase the sample volume – this must be done by (1) using more samples and (2) increasing the thin film volume to substrate volume, possible by coating both sides of the substrate with the thin film of interest and reducing the thickness of the substrate as much as possible.
- Increase the beam time
- Use an amorphous substrate, such as molybdenum.

In addition, it is probably unlikely that this experiment can be conducted using the mutiplexer used for powder diffraction experiments due to the additional geometrical constraints it places on the samples and sample holders.

IMPORTANT! List or attach a list of publications resulting from this experiment (published or in press).

LANSCE
Los Alamos Neutron Science Center

REPORT ON EXPERIMENT
(Please Type)

Submit all experiment reports to:
LANSCE User Office, MS H831, Los Alamos National Laboratory, Los Alamos, NM 87545

Experiment was carried out at:	**Local Contact**	**Proposal #**	***LANSCE Use Only***
[x] Manuel Lujan Jr. Neutron Scattering Center	Jaroslaw Majewski	2002124	**Report Rc'd**
[ ] Weapons Neutron Research Facility	**FP/Instrument Used**		**3/21/03**
[ ] WNR/Blue Room	SPEAR		

Title
Experimental Observation of Hydrogen Diffusion in Scandium Dideuteride Thin Films Using Neutron Reflectometry

Authors and Affiliations

M. A. Mangan, Sandia National Laboratories
J. F. Browning, Sandia National Laboratories
R. J. Welberry, Sandia National Laboratories

Experiment Report

Thin film hydrides are used in components of nuclear weapons and play an important role in the operation and reliability of the stockpile. As part of the manufacturing process of thin film hydride based components, it is desirable to have a through understanding of the behavior of hydride materials under conditions encountered during the manufacturing process. This plays an important role in insuring the integrity and quality of the end product.

The purpose of this experiment is to illuminate the effectiveness of neutron scattering in studying changes in film characteristics under various

- manufacturing
- processing
- and storage conditions.

The data obtained in this neutron reflectivity experiment contains atomic compositional information as a function of depth. The experimental procedure has been contrived to revel the isotopic exchange between gaseous hydrogen and scandium dideuteride thin films, specifically:

- total change in the isotopic composition, and
- change in composition as a function of film depth.

The results of this experiment will be used in the evaluation of this technique for use in further studies. Future studies would look for correlations between changes in the film characteristics (due to variations in manufacturing, processing and storage steps) with respect to performance of the materials. The aim of this work is to find improvements in the manufacturing process that improved quality, increase manufacturing yield, and lower manufacturing costs.

In this experiment, scandium dideuteride films exposed to a hydrogen environment for various exposure times. The resulting samples are analyzed by neutron reflectivity. The resulting data, shown in figure 1, illustrates the observed changes that are likely due to isotopic exchange followed by diffusion through the film.

Experiment Report *(continued)*

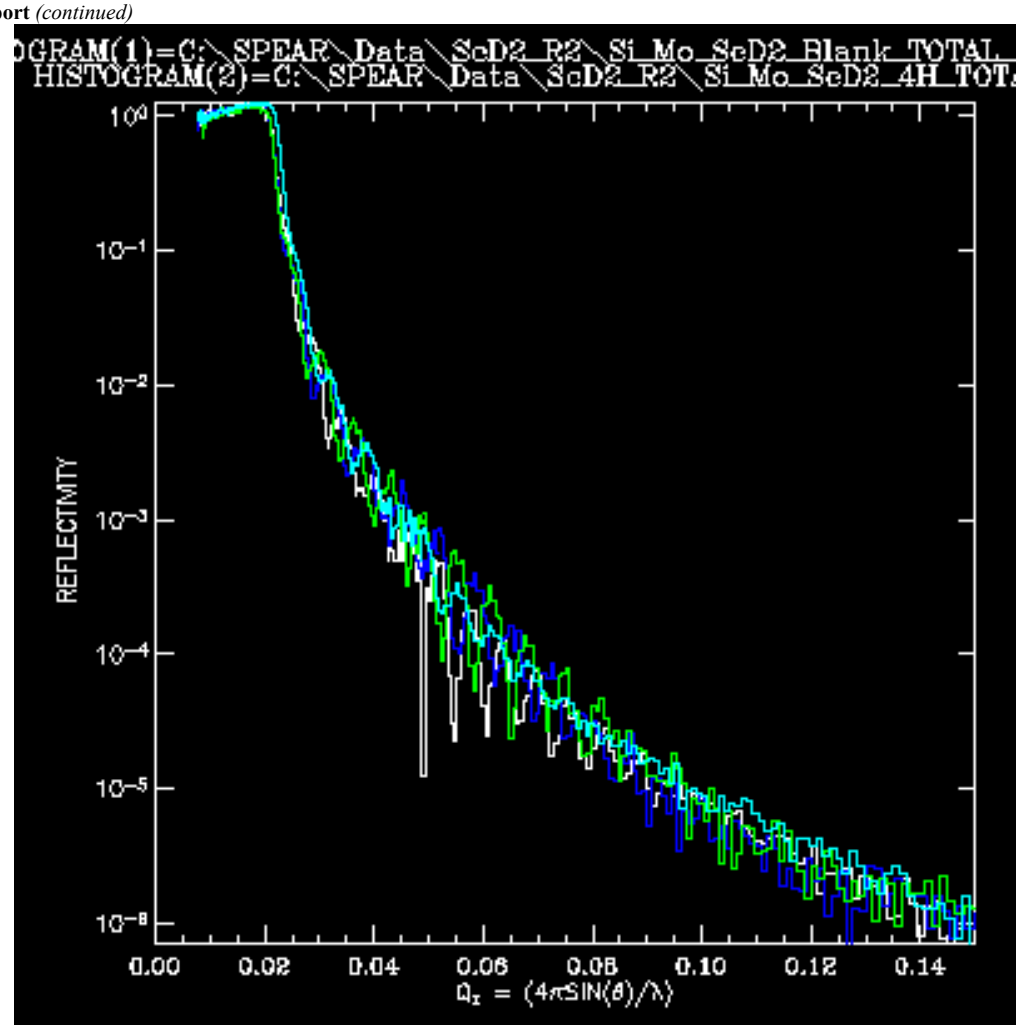

Figure 1: Results of neutron reflectivity on scandium dideuteride thin films with various exposure time to a hydrogen enviroment: (white) no exposure, (blue) 4-hour exposure, (light blue) 16-hour exposure, and (green) 24-hour exposure.

The conditions used in this experiment do not reflect probable conditions. These conditions were chosen to explore the applicability of this technique for future studies.

In this study, we have investigated the effects on the isotopic exchange between gaseous hydrogen and scandium dideuteride thin films using neutron reflectometry. Using this technique, the isotopic composition is measures as a function of the depth in the film. Our preliminary results look promising although further analysis of this data is required.

IMPORTANT! List or attach a list of publications resulting from this experiment (published or in press).
This work will be presented at the THERMEC'2003 conference in Madrid, Spain in July of 2003 and has been submitted for publication as a part of the published conference proceedings (Materials Science Forum by Trans Tech Publishers.)

LANSCE
Los Alamos Neutron Science Center

REPORT ON EXPERIMENT
(Please Type)

Submit all experiment reports to:
LANSCE User Office, MS H831, Los Alamos National Laboratory, Los Alamos, NM 87545

Experiment was carried out at:	**Local Contact**	**Proposal #**	***LANSCE Use Only***
[x] Manuel Lujan Jr. Neutron Scattering Center	Y. Zhao	**2002126**	**Report Rc'd**
[ ] Weapons Neutron Research Facility	**FP/Instrument Used**		**3/17/03**
[ ] WNR/Blue Room	SCD		

Title

Neutron Diffraction of Single-Crystal FeO at High Pressures and Low Temperatures – Investigation of Paramagnetic- Antiferromagnetic Transitions

Authors and Affiliations

H. K. Mao, R. J. Hemley and J. Xu
Geophysical Laboratory, Carnegie Institution of Washington,
5251 Broad Branch Road, Washington, DC 20015, USA

Experiment Report

The neutron diffraction performed on a single crystal of FeO (in the volume of 1mm^3) was mad in the SCD beam station in Los Alamos Neutron Science Center.

Measurement was done in a collimated neutron beam (5mm in diameter) at fixed ω- (0°) and κ-angle (45°), but various ϕ-angles (0, 40, 80, 120, 160, 200 and 240 degree, respectively). Exposure tim was used as 1.5-2.5 hours for each ϕ-angle listed above.

Actually, it was the first time to run such a large single FeO crystal by neutron diffraction ever; w expected to see a number of new phenomena.

First at all, a twin was shown in each histogram in neutron diffraction patterns. It was a little surprise because it has not been found in the previous X-ray diffraction test.

At room temperature, the normal simple cubic lattice was observed with its lattice constant as 4.3068A as examined by X-ray diffraction, but the super lattice was found in the 311, 331 (Fig. 1 and 2) directions, but eliminated at its (111) direction (222, 444,… diffraction without 111, 333,…diffraction) a low temperatures (<195K). The anti-parallel magnetic arrangement at (111) direction provided the best understanding (Shull et al., 1951; Li, 1955; Roth, 1958). The Neel temperature of such a sample is observed below than 195K in comparison with the 198K in literatures. However, the prelimarily calculation shows that the popular magnetic structure of FeO is not agree with our new experimental data The single crystal was crashed after a couple of cooling/heating processes, therefore, in the future in repeating such an experiment, we should start the cooling process after the completion of refinement for the structure at room temperature and do refinement in the first cooling.

Same process has been done on a single crystal 75FeO-25MgO. This crystal has much large size (more than 60mm^3). Different with FeO sample, the super lattice has been found at room temperature. Such a super lattice is not the anti-magnetic ordering as observed in FeO at low temperatures. It is actually the ordering of different atomic ions

Experiment Report *(continued)*

(Mg, Fe^{+++} and Fe^{++}). At low temperatures, the picture of the anti-magnetic ordering is overlapped on the original image, and it makes difficult to determine whether the anti-magnetic ordering appears or not? We have taken our effort to solve such a problem. The progress makes us believe that the anti-ferromagnetic ordering is existed in this crystal based on the intensity analysis. The primarily conclusion is that the Neel temperature of such a sample could be dropped to between 120-160K. We are preparing to continue our search in this sample and 78FeO-22MgO, and other crystals with various compositions.

Such new phenomena give us confidence to continue our collaboration with LANSCE in this research area.

The research environment in Lujan center, LANSCE, Los Alamos National Laboratory is very good. However, the current situation of the SCD station is actually not comparable with such the first grade of research Institution in the world. The facilities are more than 20 years old; the system in SCD is very tight and difficult to align. Its vacuum system is leaking badly and, therefore, cooling system are unstable and need constant refilling of He gas because of serious leaking, its low-temperature environment could not keep constantly, it is actually the reason that our FeO single crystal has broken because of several cooling-warming circles.

More importantly, no beam line scientist works in this line. Many times, we could not receive necessary support in time when the system appeared problems. The only workable scientist, Mr. A. Alsmadi went to a conference without notice to Dr. Y. Zhao, and went back to his University during our experiment period.

In addition, the software has actually a serious problem in the SCD beam station. The collected data could not be easily process to find peaks, index and integration, and finally, **it is no way to perform refinement**. If such a situation could not be changed in near future, a question mark will be given to the existence of this SCD beam station in comparison with a number of challengers (ISIS, IPNS, and in the future, SNS).

References:

Li, Y. Y., *Phys. Rev.*, **100**, 627, 1955.
Roth, W,L., *Phys. Rev.*, **110**, 1333, 1958.
Shull, C.G., W.A.Strauser, and E.O.Wollan, *Phys. Rev.*, **83**, 333, 1951.

IMPORTANT! List or attach a list of publications resulting from this experiment (published or in press).

LANSCE
Los Alamos Neutron Science Center

REPORT ON EXPERIMENT
(Please Type)

Submit all experiment reports to:
LANSCE User Office, MS H831, Los Alamos National Laboratory, Los Alamos, NM 87545

Experiment was carried out at:	**Local Contact**	**Proposal #**	***LANSCE Use Only***
[X] Manuel Lujan Jr. Neutron Scattering Center	G.S. Smith	**2002128**	**Report Rc'd**
[ ] Weapons Neutron Research Facility	**FP/Instrument Used**	**(20011061**	
[ ] WNR/Blue Room	**SPEAR**	**CONT)**	

Title

Electrosorption of Common Surfactant and Ionic Liquid Molecules from Aqueous Solutions

Authors and Affiliations

Costas Tsouris, William A. Hamilton - Oak Ridge National Laboratory
and K.-L. Yang - Georgia Tech

Experiment Report

Electrostatically induced sorption or electrosorption of charged species such as ions, surfactants, polyelectrolytes, and proteins by charged surfaces has been recently investigated because of important applications in separations, aqueous cleaning, sensors, and environmental processes (Farmer et al., 1996; Yang et al, 2001). Electrostatic attraction between these species and a charged surface causes a change in the chemical potential and thus a different concentration at the surface than in the bulk. In the case of surfactant molecules, surface charge may cause a change in the surface aggregate structure. Surface micelle formation should also be favored over bulk micelle formation. The surface charge is determined by surface groups, salt concentration, and pH; therefore, these parameters are expected to affect the surfactant concentration at the surface, as well as the structure of the aggregates. Additional parameters that affect interfacial and bulk behavior of surfactant molecules are the temperature, surfactant concentration, and type of surfactant molecules, including charge and length of alkyl chains. Effects of these parameters on surfactant adsorption and aggregate structure formation in the absence of an electric field have been investigated by Liu and Ducker (1999). The question here is whether electrosorption can be used to control the micellar structure on the surface from spherical to cylindrical to bilayers. As the maximum surface coverage of the surfactant increases from 0.60 for spherical micelles, 0.70 for cylindrical aggregates, and close to 1.00 for bilayers (Schulz et al., 2001), electrosorption may lead to enhanced electrochemical and interfacial phenomena.

To investigate electrosorption of surfactant ions at a charged surface, we used neutron reflectivity with a metal-coated quartz crystal. Initial neutron reflectivity measurements in air were used to characterize the electrode surface made of a chromium coating of approximately 60 Å on a quartz crystal and then gold coating of approximately 90 Å on the top of chromium. Experiments with CTAB in D_2O were conducted at various values of applied potential ranging between –0.9V and +0.9V. (See experimental report 20011061). At a positive surface potential of about 0.45V, the cationic CTAB layer apparently began to be driven from the surface, while being unaffected by negative voltages of the same order or positive voltages of 0.3V. However, increasing the voltage further had no appreciable effect on the supposedly remnant adsorbed surfactant layer, up to metallic

Experiment Report *(continued)*

film's destruction at +0.9V. Cyclic voltammetry measurements characterizing CTAB adsorption versus voltage behavior for gold powders suggested that at about +0.4V the surfactant should have been totally driven from the surface. Of course, these results may be reconciled if the fixed remnant layer was not adsorbed surfactant. The most probable scenario is that the thinness of the gold film allowed chromium ions to migrate to the surface creating a layer of chromium oxide at the surface.

In our second series of measurements, a Cr/Au film from this same series was characterized against pure D_2O solution. The inferred scattering length density data were essentially consistent with that observed using the previous film for the CTAB solution at +0.45V (See Figure) – tending to confirm the oxide layer hypothesis. In the intervening period, we also fabricated metallic films with a gold layer ~150Å and using the minimal amount of chromium ~20-30Å judged necessary to promote gold adhesion to the quartz surface. In D_20 characterization runs, no "remnant" layer was observed at the surface of these films. In low voltage (-0.1V, 0V, and +0.1V) fits of CTAB solution runs were consistent with a full thickness of 28Å bilayer of CTAB absorbed at the surface at close to 100% coverage. However, these films failed at a voltage of +0.2V during these runs either due to weak adhesion or possibly stability problems with power supply.

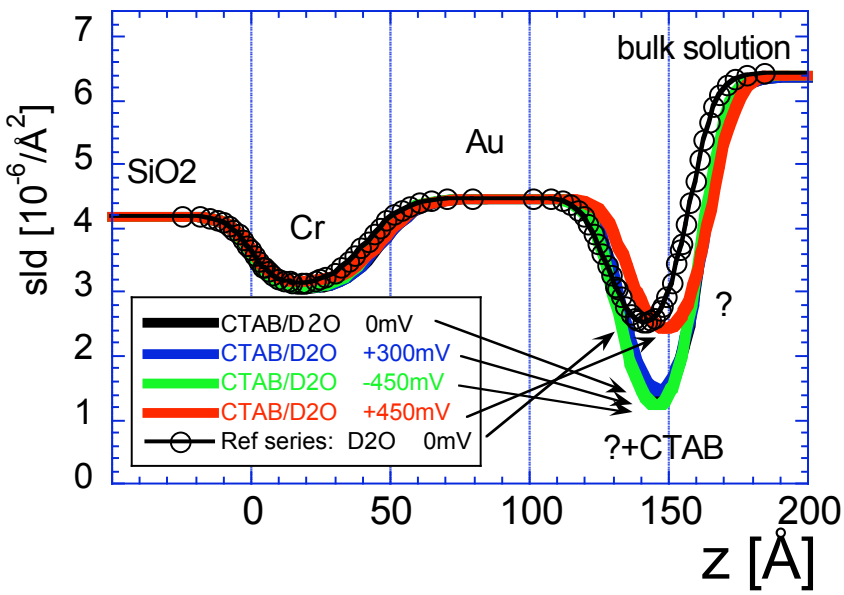

Figure: Sld variation of with absorbed CTAB with voltage

References

Liu, J.F., and W.A. Ducker, "Surface-Induced Phase Behavior of Alkyltrimethylammonium Bromide Surfactants Adsorbed to Mica, Silica, and Graphite," *J. Phys. Chem. B*, **103**, 8558 (1999).

Farmer, J.C., D.V. Fix, G.V. Mack, R.W. Pekala, J.F. Poco, "Capacitive Deionization of NaCL and $NaNO_3$ Solutions with Carbon Aerogel Electrodes," *J. Electrochem. Soc*. **143**, 159 (1996).

Schulz, J.C., G.G. Warr, P.D. Butler, and W.A. Hamilton, "Adsorbed Layer Structure of Cationic Surfactants on Quartz," *Physical Review E*., **63**, 041604 (2001).

Yang, K.-L., T.-Y. Ying, S. Yiacoumi, C. Tsouris, and E. S. Vittoratos, "Electrosorption of Ions from Aqueous Solutions by Carbon Aerogel: An Electrical Double-Layer Model," *Langmuir*, **17**, 1961 (2001).

IMPORTANT! List or attach a list of publications resulting from this experiment (published or in press).

LANSCE
Los Alamos Neutron Science Center

REPORT ON EXPERIMENT
(Please Type)

Submit all experiment reports to:
LANSCE User Office, MS H831, Los Alamos National Laboratory, Los Alamos, NM 87545

Experiment was carried out at:	**Local Contact**	**Proposal #**	***LANSCE Use Only***
[x] Manuel Lujan Jr. Neutron Scattering Center	Rob McQueeney	2002138	**Report Rc'd**
[ ] Weapons Neutron Research Facility	**FP/Instrument Used**		**3/21/03**
[ ] WNR/Blue Room	Pharos		

Title
Phonons in High-Temperature Superconductors

Authors and Affiliations
Takeshi Egami, Jae-Ho Chung, University of Pennsylvania; Robert McQueeney, Los Alamos National Laboratory

Experiment Report

The understanding of the phonon dispersions in cuprates has a vital importance in elucidating the role of electron-phonon coupling in the high T_C mechanism. Although there have been extensive studies, the experimental picture of the phonon dispersion is still not complete. The neutron time-of-flight spectroscopy has recently proven to be useful for studying the phonon dispersions in layered compounds in a relatively short measurement time [1]. In the present study, we used the Pharos spectrometer to observe a single crystal phonon dispersion of $YBa_2Cu_3O_{6.15}$, as well as phonon density of states of several different LSCO compounds. All the data included in this report are taken at 15K.

The single crystal measurement of insulating YBCO was performed with a flux-grown crystal of ~ 30 gram for roughly 72 hours. The sample was oriented in such a way that c-axis is parallel to the incident beam and one of principal in-plane axes lying within the horizontal plane. In this geometry, one can primarily observe the phonons with in-plane momentum transfer, and the ratio between in-plane and out-of-plane polarizations change for different detector angles. The obtained spectrum successfully revealed, after proper corrections, the dispersions of several phonon modes. The 2-dimensional intensity on (*h*, E) plane, corrected with standard procedure, is shown in Figure 1 for the detectors lower than 90º. The detectors higher than 90º also produced a similar spectrum, supposedly better highlighting the modes with *c*-axis polarization. The details of the dispersion are currently under the investigation.

The phonon density of states was also measured with the Pharos spectrometer for the powder samples of $La_{1.85}Sr_{0.15}CuO_4$ and $La_{1.475}Nd_{0.4}Sr_{0.125}CuO_4$. The amount of powder samples used were roughly 60gram, and 12 ~18 hours of measurement produced data with excellent statistics. While the incident energy was chosen to be 120 meV, there was a fortuitous second harmonics transmission providing higher-resolution picture of low energy spectrum. By combining two spectra simultaneously obtained, we could build a complete phonon density of states as shown in Figure 2.

This work proved that the Pharos is extremely useful for the high-resolution measurement of the phonon density of states in HTSC cuprates. It was also found that single crystal phonon dispersion is also observable as long as enough measurement time is allowed, which is not prohibitive considering the importance of the subject.

Reference

1. T. Egami *et al*., Physica B 316-317 (2002) 62; J.-H. Chung *et al*., Phys. Rev. B 67 (2003) 14517

Experiment Report *(continued)*

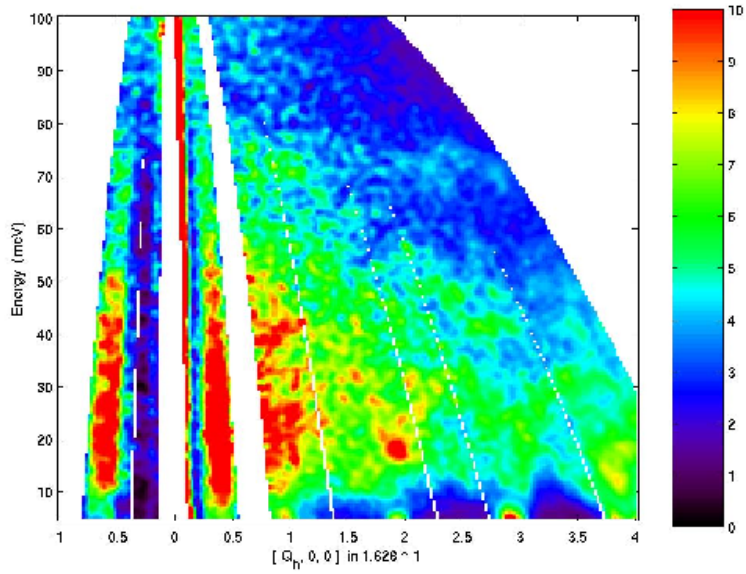

Figure 1. The phonon intensity of $YBa_2Cu_3O_{6.15}$ single crystal measured with the Pharos spectrometer is plotted as a function of *h* and energy transfer. The intensity is integrated over *l* and sliced for $-0.1 < k < 0.1$. Only the detectors below 90º are included.

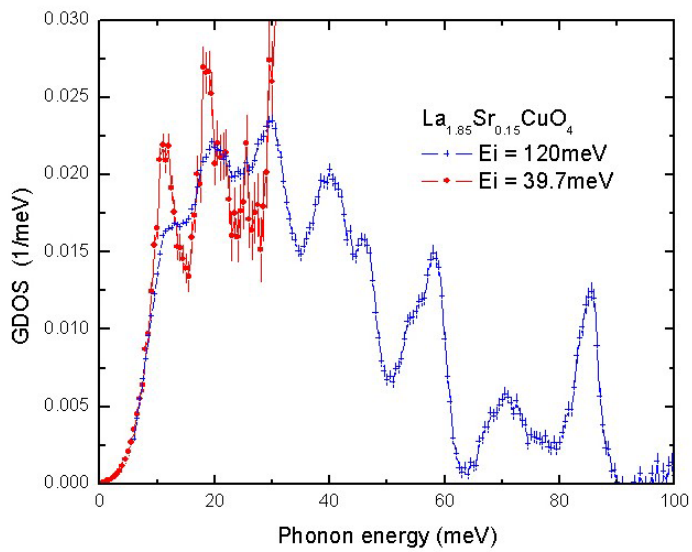

Figure 2. Phonon density of states of $La_{1.85}Sr_{0.15}CuO_4$ measured by the Pharos spectrometer. Blue and red profiles are spectra from different incident transmissions simultaneously obtained.

IMPORTANT! List or attach a list of publications resulting from this experiment (published or in press).

LANSCE
Los Alamos Neutron Science Center

REPORT ON EXPERIMENT
(Please Type)

Submit all experiment reports to:
LANSCE User Office, MS H831, Los Alamos National Laboratory, Los Alamos, NM 87545

Experiment was carried out at:	**Local Contact**	**Proposal #**	***LANSCE Use Only***
[x] Manuel Lujan Jr. Neutron Scattering Center	Sven Vogel	**2002140**	**Report Rc'd**
[ ] Weapons Neutron Research Facility	**FP/Instrument Used**		**3/21/03**
[ ] WNR/Blue Room	HIPPO		

Title
In-situ Investigation of the Local Phase Transition of $Pb(Mg_{1/3}Nb_{2/3})O_3$ Near Burns Temperature Using Neutron Pair Distribution Function (PDF) Analysis

Authors and Affiliations
Il-Kyoung Jeong, Robert H. Heffner, Thomas Proffen, Tim Darling, Los Alamos National Laboratory;
T. Egami, University of Pennsylvania

Experiment Report]

In relaxor ferroelectrics $Pb(Mg_{1/3}Nb_{2/3})O_3$, the inverse susceptibility is known to deviate strongly from the Curie-Weiss behavior over a wide temperature range above permittivity maximum temperature, T_M. Burns *et al.* explained this deviation as an indication of the local phase transition which starts above T_M [1]. The change in the slope of optical index near Burns' temperature (T_B), higher than T_M by a few hundred degrees, supported this explanation. Below T_B, it was suggested that very small regions with local, randomly oriented, and non-reversible polarization grow from a cubic non-polar matrix [2].

The average structure of PMN is a nearly ideal perovskite and Pb is not off-centered, but the neutron PDF clearly shows that Pb is strongly off-centered with respect to the oxygen cage. Recent x-ray absorption analysis supports this observation that the local polarization of Nb is small, and thus the bulk of polarization is carried by Pb [3].

In order to understand the atomistic nature of Burns temperature and local distortion due to the onset of the of Pb displacement, we measured pair distribution function (PDF) of PMN in the temperature range between 300K and 750K. However, as shown in Fig. 1 the 'corrected' temperature is much lower than the apparent temperature reading and the discrepancy increases with increasing temperature.

Figure 2. shows PDFs of PMN at 300K, 350K, 480K, 520K. The peak around 2.5Å which is due to Pb off-center displacement persists up to 520K. We plan to study how this peak evolves near and above Burns temperature (T_B ~345 ^oC) when the 'real' furnace is available.

Experiment Report *(continued)*

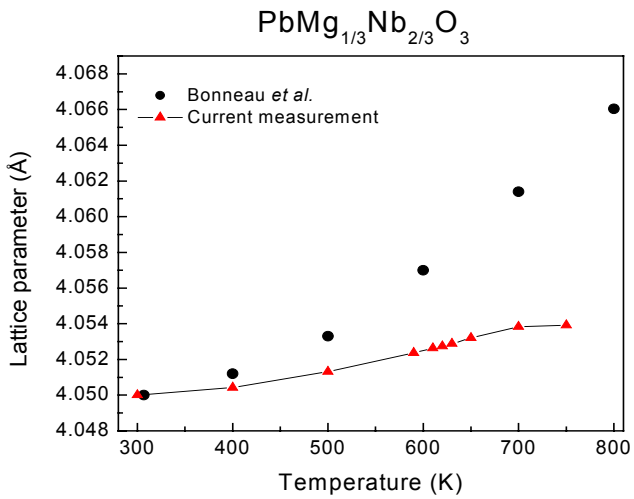

Fig. 1 Comparison of PMN lattice parameters by Bonneau *et al.* [4] and current measurements. It is quite clear that the 'corrected' cryofurnace temperature is much lower than the apparent temperature reading.

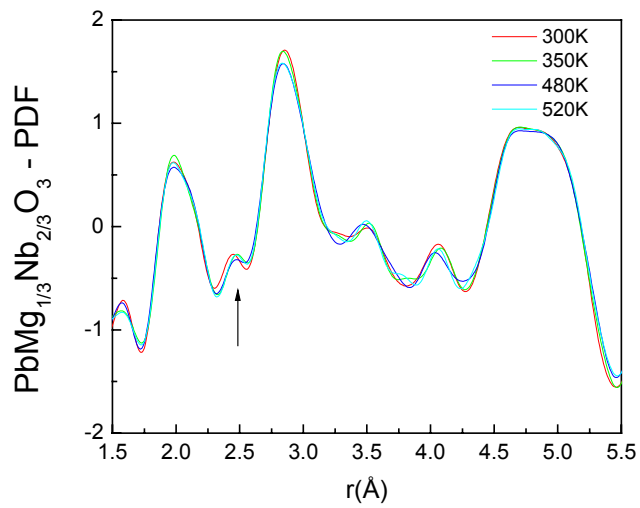

Fig. 2 PDFs of PMN at 300K, 350K, 480K, 520K. The peak around 2.5Å which is due to Pb off-center displacement persists up to 520K. Q_{max}=24 $Å^{-1}$.

References:

[1] G. Burns and F. H. Dacol, *Sold State Commun*., 48, 853 (1983).
[2] G. Burns and F. H. Dacol, *Phys. Rev. B* 28, 2527 (1983).
[3] T. Egami, E. Mamontov, W. Dmowski, T. Gog, C. Venkataraman, P. W. Rehrig and L. E. Cross, *AIP Conf. Proc.*, in press
[4] P. Bonneau *et al.,* J. Solid State Chem 91, 350 (1991).
[5] Wakimoto *et al.,* Phys. Rev. B 65, 172106 (2002).

IMPORTANT! List or attach a list of publications resulting from this experiment (published or in press).

LANSCE
Los Alamos Neutron Science Center

REPORT ON EXPERIMENT
(Please Type)

Submit all experiment reports to:
LANSCE User Office, MS H831, Los Alamos National Laboratory, Los Alamos, NM 87545

Experiment was carried out at:	**Local Contact**	**Proposal #**	***LANSCE Use Only***
[X] Manuel Lujan Jr. Neutron Scattering Center	Rob McQueeney	**2002143**	**Report Rc'd**
[ ] Weapons Neutron Research Facility	**FP/Instrument Used**		**2/7/03**
[ ] WNR/Blue Room	Pharos		

Title
Phonons in Ni at Elevated Temperature - Analysis of Coherent Scattering

Authors and Affiliations
Brent Fultz, Tim Kelley, Tabitha Swan-Wood, Olivier Delaire, Max Kresch
Mail 138-78
California Institute of Technology
Pasadena, CA 91125

We knew that it would be challenging to complete the experiment for which we were awarded beamtime, number 3 below, so we prepared samples for two other experiments, numbers 1 and 2.

1. Experimental Report: Vibrational entropy change upon delithiation of Li_xCoO_2. Pharos, 9/26 – 10/3, 2002.

Purpose:
The effects of delithiation on the occupation of phonon modes and the vibrational entropy of Li_xCoO_2 will be explored in the analysis of this experiment.

Sample Preparation:
Samples were prepared by chemically charging (delithiating) $LiCoO_2$ powders, which were provided by Enax Inc. Chemically prepared samples are preferred over electrochemically delithiated materials because spectral artifacts from binders and conductive diluents can be eliminated. In this study, an aqueous solution of potassium persulfate ($K_2S_2O_8$) was used as an oxidant. The Li concentration was altered by mixing powders of $LiCoO_2$ into different amounts of the oxidizing solution, and samples were agitated for ~ 24 hours at 60 C. The delithiated powders were filtered and rinsed several times in water to remove all of the $K_2S_2O_8$. To remove the residual water the samples were dried in air at 60 C for 24 hours and stored in an Ar atmosphere. The delithiated samples were characterized using x-ray diffraction. Annular Al sample cans were prepared to hold the samples in vacuum.

Experiment:
Inelastic neutron scattering spectra were measured on PHAROS at room temperature.

Li_xCoO_2	E_i = 147 meV	E_i = 192 meV	E_i = 243 meV
x = 1.0	X		X
x = 0.8			X
x = 0.6	X	X	X
x = 0.5			X

Table 1: Table of samples and incident energies, X indicates data was measured.

Analysis and Preliminary Results:
The data have been refined by the following procedure: normalized for incident flux, remove a time-independent background, corrected for the absorption of the sample, corrected for the detector efficiency, an empty can (or background) has been removed from the data, rebinned into energy transfer from time-of-flight. The data was then summed into angle ranges of approx. 10 degrees per bank. Each angle bank was then treated to extract a phonon density of states via a correction for: thermal occupancy, Debye Waller factor, subtraction of the elastic peak, and a crude multi-phonon subtraction (a more sophisticated multi-phonon correction will be performed later, along with a full analysis of all the collected data, as now we have completed only x=1 and 0.6 for E_i=147).

The density of states show that the occupation of modes, shift slightly with delithiation. Also there is a peak in the x=0.6 data that maybe consistent with water modes. Fig. 1 shows the DOS obtained from two of the samples.

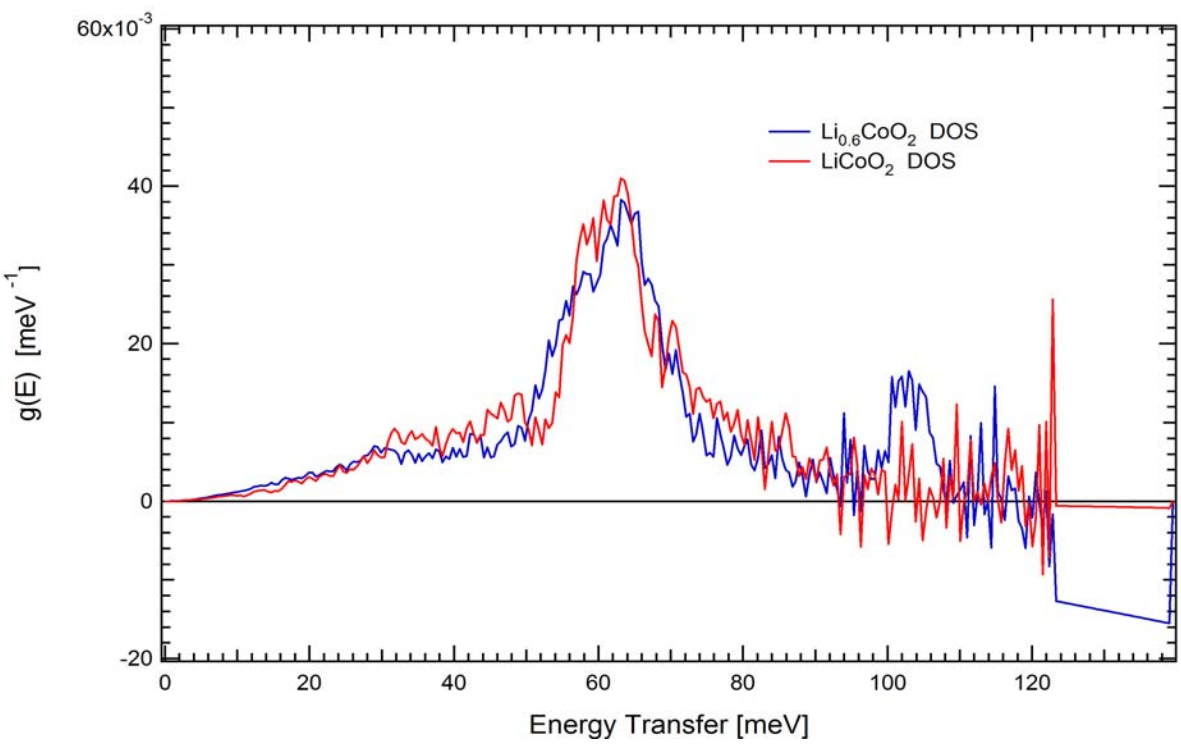

Fig. 1 Neutron-weighted phonon DOS for $LiCoO_2$ and $Li_{0.6}CoO_2$.

This experiment was a success. The instrument scientist provided all the materials and data analysis tools necessary to complete our experiments. The data obtained from PHAROS is exceptional. Publication of this work is anticipated upon completion of the analysis of the data.

2. Experimental report: Vibrational entropy change upon martensitic phase transformation in a Fe – 29% Ni sample. Pharos, 9/26 – 10/3, 2002.

The goal of this experiment was to investigate the influence on the phonon density of states and vibrational entropy of a martensitic phase transition at low temperature in a Fe – Ni alloy.
The alloy Fe – 29% Ni is known to undergo a martensitic phase transition from its high temperature γ phase (FCC) to its lower temperature α‘ phase (BCT) when cooled below 240 K [1]. This transformation is irreversible unless the material is heated back to 650 K. Using the displex refrigerator on the Pharos instrument, we measured inelastic neutron scattering spectra from this material at different temperatures across the range of the martensitic phase transition.

The sample was prepared by arc-melting under inert argon atmosphere and was then cold-rolled to the desired thickness to produce a 10% scatterer. The stresses associated with cold work were relieved by annealing the material in vacuum, at 950 C for an hour. Strips of the material obtained were mounted vertically on two aluminum discs in a cylindrical fashion. The sample was mounted directly onto the Pharos displex, without need for any additional sample holder, thus minimizing background counts in our measurement.

The neutron scattering function S(Q, E) for this sample was measured at the following temperatures: 300 K, 235 K, 210 K, 80 K. In addition, after each low temperature run, we acquired data after the sample was brought back to room temperature in order to examine thermal occupancy effects. A measurement of the scattering from the aluminum mounting discs was also carried at room temperature, to allow for subsequent background subtraction. The incident energy was fixed at 60 meV for all measurements.
The experiment was a success. All the runs went well and we acquired a full set of data. The data obtained is of high quality and shows indication of a sizable effect of the phase transition on the scattering function and phonon density of states. The background counts level observed in the collected data was very low, thanks to the low background inherent to PHAROS and the absence of any intrusive sample holder. A publication detailing our results is expected soon.

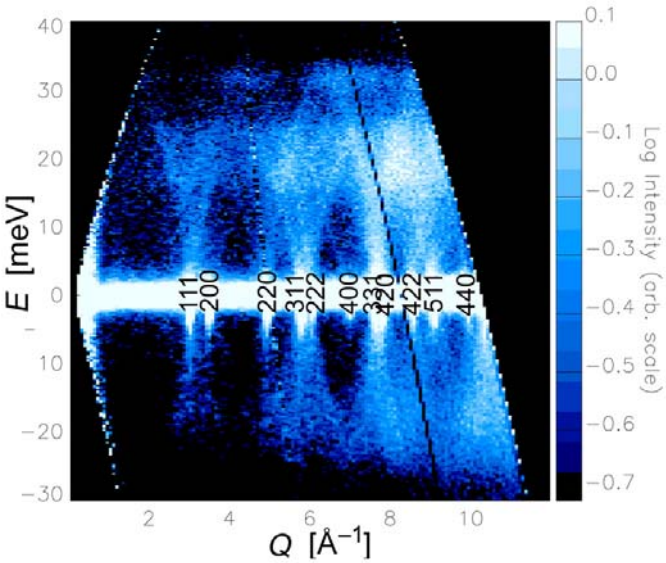

Fig. 2 S(Q, E) data from fcc Fe – 29% Ni at room temperature. The acquisition time was over 8 hours.

References:

[1] L. Kaufman and M. Cohen, Trans. AIME, 206, 1393 (1956).

3. Experimental report: Anhamonicity of fcc Ni at elevated temperature. Pharos, 9/26 – 10/3, 2002.

This was the experiment for which we were awarded beamtime. It was the most important of the three that we actually worked on during our allocated beamtime, but it was not completed for reasons described below. We knew this experiment would be a challenge for Pharos, since the high temperature furnace had not been used before on this instrument.

The sample was a rolled sheet of polycrystalline nickel metal, shaped into a cylinder and mounted in the ILL furnace built by AS Scientific, Abbingdon, UK. This furnace was kindly provided to Pharos by the HIPPO team. An adapter ring was fabricated for this furnace to match the sample height of Pharos, and some plumbing and electrical feedthrough modifications were also made. These were nearly complete when we arrived, although not by the first weekend. During the time for furnace preparation we ran two other experiments, described in the first part of this experimental report.

The measurements on nickel metal were successful to a point. We acquired data at room temperature and at two elevated temperatures. Unfortunately, as we were within a few degrees of the highest temperature, the sample touched the heating element of the furnace, formed a nickel-niobium alloy, and melted. The furnace was shut down and could no longer heat.

Although we see clear dispersions from nickel metal at all temperatures, an a probable phonon lifetime broadening at the highest temperatures, we need to have a background measured from an empty furnace at these same temperatures. We did acquire a room temperature background, but the elevated temperature data were not possible because the furnace was no longer operational. Unfortunately, a new heating element for the furnace was not available before the end of the run cycle. We hope that Pharos

will be in the same configuration during the next run cycle so that we can acquire the required furnace background at two elevated temperatures and complete the experiment.

LANSCE
Los Alamos Neutron Science Center

REPORT ON EXPERIMENT
(Please Type)

Submit all experiment reports to:
LANSCE User Office, MS H831, Los Alamos National Laboratory, Los Alamos, NM 87545

Experiment was carried out at:	**Local Contact**	**Proposal #**	***LANSCE Use Only***
[x] Manuel Lujan Jr. Neutron Scattering Center	Sungkyun Park	2002150	**Report Rc'd**
[ ] Weapons Neutron Research Facility	**FP/Instrument Used**		**3/12/03**
[ ] WNR/Blue Room	FP11/Asterix		

Title: Strain Driven Spin Reorientation Transitions in Co Thin Films

Authors and Affiliations
Sungkyun Park, Michael R. Fitzsimmons and Marilyn E. Hawley, Los Alamos National Laboratory
Sukmock Lee, Inha University, Korea
Charles M. Falco, The University of Arizona, Tucson, AZ

Experiment Report

The goal of the proposed experiment is to determine whether the SRT is triggered by the magnitude of interfacial strain. To investigate this issue, we have grown Au/Co/Au/Cu(111) samples whose interface strain between Co and under Au layer can be varied for different Au underlayer thickness under ambient conditions and are thoroughly characterized by X-ray diffraction, magnetic optical Kerr measurements and Brillouin light scattering measurements.

Figure 1 shows the spinwave frequency shift as a function of the external field from Brillouin light scattering experiments. The data from sample (a) shows the magnetization is out-of-plane due the (as we believe) larger interfacial strain between Au underlayer and Co. On the other hand the magnetization of the sample (b) is in-plane. The magnetic properties of these two samples completely difference even though their magnetic layer thickness is the same. However those measurements only reflect the average magnetic profile of the sample.
In order to understand more specific magnetic profile (depth profile) of the sample, we performed polarized neutron reflectrometry (PNR) experiments at LANSCE (FP11, Asterix). PNR obtains an average of the magnetization over a lateral length scale (typically on the order of microns) that is much smaller than most magnetic domains; therefore, using PNR we can determine a value (rms deviation) for the in-plane component of the sample even as the sample magnetization breaks up into domains.

Figure 2 shows the PNR profile of the sample (a) as function of the external field strength. It clearly shows the at the in-plane magnetization of the sample reduced as decreased the field strength. This indicates that the magnetization of the sample becomes either out-of-plane or 90 degree rotation (in the sample plane) in the absence of the external field.
If the magnetization is rotates in the plane, this will give spin flip scattering from the PNR measurements. The preliminary analysis indicates that we do see this spin flip scattering when the external field is very low (~ 30 Oe) but it is significantly week. Therefore, the majority of the moments are pointing out of plane. However the rotation mechanism of the magnetic moments might not be simple which requires further investigation. The current efforts to analyze data are based on the uniform magnetization through the Co film. However, the interface contribution of the film is not negligible since we do see different magnetic property between sample (a) and (b). This suggests that the non uniform magnetic profile through the Co film should be examined.

Experiment Report *(continued)*

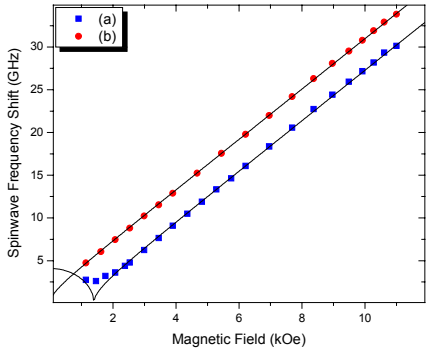

Figure1. The Spinwave frequency as a function of the external field strength. (a) Si(111)/Cu 4 nm/Au 2 ML/Co 8 ML/Au 3.5 nm sample (b) Si(111)/Cu 4 nm/Au 6 ML/Co 8 ML/Au 3.5 nm simple. The solid lines indicate the fitted data.

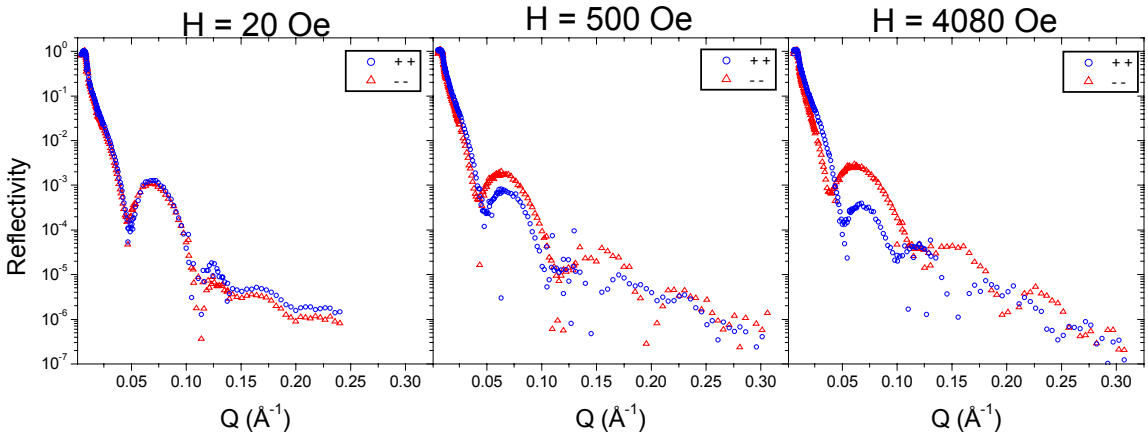

Figure 2. The polarized neutron reflectivity of the Si(111)/Cu 4 nm/Au 6 ML/Co 8 ML/Au 3.5 nm sample with various external field strength.

IMPORTANT! List or attach a list of publications resulting from this experiment (published or in press).

Strain driven spin reorientation transition of ultra thin Co films; **S. Park**, M. Fitzsimmons, M. Hawley, S. Lee, J. Shaw and C. M. Falco, Material Research Society Annual Meeting (Boston, MA Dec. 2 ~ 6, 2002)

Influence of interfacial strain on spin reorientation in ultra-thin Co films; **S. Park**, M. Fitzsimmons, M. Hawley, S. Lee, J. Shaw, C.M. Falco, 47th Annual Conference on Magnetism and Magnetic Materials (Tampa, FL Nov. 11 ~ 15, 2002)

LANSCE
Los Alamos Neutron Science Center

REPORT ON EXPERIMENT
(Please Type)

Submit all experiment reports to:
LANSCE User Office, MS H831, Los Alamos National Laboratory, Los Alamos, NM 87545

Experiment was carried out at:	**Local Contact**	**Proposal #**	***LANSCE Use Only***
[x] Manuel Lujan Jr. Neutron Scattering Center	Don Bown	**2002155**	**Report Rc'd**
[ ] Weapons Neutron Research Facility	**FP/Instrument Used**		**4/22/03**
[ ] WNR/Blue Room	2		

Title
Shape Memory Behavior in U-Nb Alloys

Authors and Affiliations
Dan Thoma mst-6
Dave teter mst-6
Don Brown mst-8

Experiment Report

Uranium niobium alloys are known to exhibit the shape memory effect (SME). Several years ago, we performed a study on U6Nb, which has a monoclinic structure, on NPD that showed that the shape memory behavior was attributable to deformation twinning, a processes that may be reversed by heating. U7Nb is also known to exhibit SME, but it has a body centered tetragonal structure, and thus, may utilize a different mechanism to achieve SME. Figure 1 shows diffraction patterns from U7Nb before and after loading to 450 MPa. Clearly, a new crystallographic phase is present. Subsequent analysis has determined the new phase to be the monoclinic structure associated with U6Nb, but with slight different lattice parameters. This is the first report of stress induced phase transformation is in single phase U-Nb alloys.

The evolution of the diffraction pattern is shown in figure 2. The phase transformation initiates at roughly 200 MPa and continues to our maximum stress measurement at 450 MPa. It appears that some reversion to the bct phase occurs during unloading. Rietveld analysis indicates that roughly 65% of the material is in the monoclinic phase after unloading, although we do not have sufficient data to make this more than an estimate.

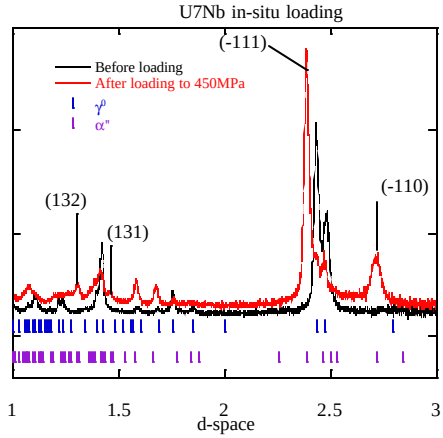

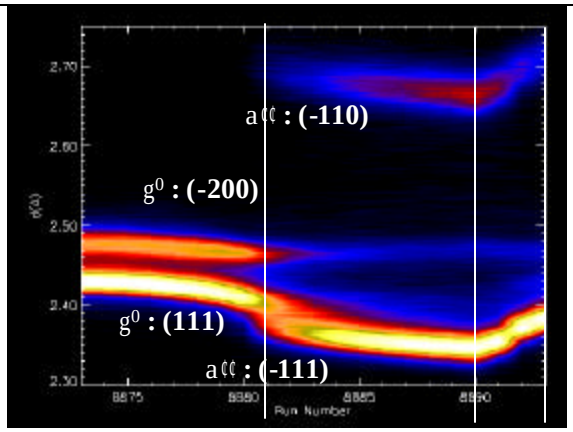

200MPa 450MPa Unloaded

Experiment Report *(continued)*

IMPORTANT! List or attach a list of publications resulting from this experiment (published or in press).

LANSCE
Los Alamos Neutron Science Center

REPORT ON EXPERIMENT
(Please Type)

Submit all experiment reports to:
LANSCE User Office, MS H831, Los Alamos National Laboratory, Los Alamos, NM 87545

Experiment was carried out at:	**Local Contact**	**Proposal #**	***LANSCE Use Only***
[X] Manuel Lujan Jr. Neutron Scattering Center	Mark Bourke	2002161	**Report Rc'd**
[ ] Weapons Neutron Research Facility	**FP/Instrument Used**		**3/18/03**
[ ] WNR/Blue Room	FP2/SMARTS		

Title
Investigation of Stress-Strain During the Elastic and Plastic Deformation of Marble, Limestone, and Sandstone

Authors and Affiliations
J. A. TenCate LANL EES-11,
T. W. Darling LANL MST-10,
S. C. Vogel LANL LANSCE-12,
B. Clausen LANL LANSCE-12
M. Bourke LANL MST-8

Experiment Report

The large scale elastic (or inelastic) response of rocks to stress, and the time scales over which such behaviors persist, is of great interest to the community studying seismic events such as earthquake aftershocks or nuclear explosion shocks. On a smaller scale, rocks are complex aggregate materials and their responses may shed light on other complex materials studied by the solid state physics community.

It has been observed that most rocks display hysteretic behavior under quasistatic loading conditions, with "memories" of the load history ranging from minutes to months. This "memory" seems also to be linked to nonlinear, hysteretic behavior observed using high frequency elastic modulus measurements.

Models using hysteretic switching elements can qualitatively reproduce some of this behavior, but there is currently no suggested atomic, micro- or meso- structure in real rocks corresponding to these elements.

Our experiments will use the load frame of the SMARTS beamline to observe the atomic plane strains in the crystalline components of marble and sandstones to attempt to determine which components of the rock are responsible for the hysteretic behavior.

Several samples of marble and sandstones were made by coring cylindrical samples 13.4mm diameter and 26.0mm long. Care was taken to produce parallel ends. The samples were mounted between the faces of the load frame pistons and a strain-gauge extensometer was attached to the sample with rubber bands. Our intent was to measure the cyclic response to loading but to determine the upper yield point we compressed one sample of each material to fracture (figure on right: marble sample fracture at ~ 55Mpa)

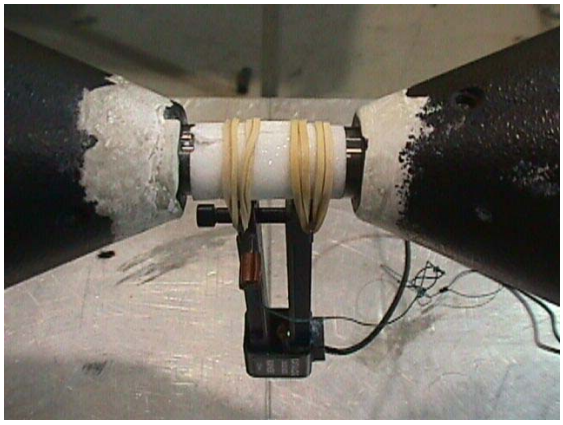

We acquired diffraction data on samples of marble and Berea and Fontainebleau sandstone mounted at 45° to the incident beam, using 20 minute count times at constant stress, while accumulating macro strain data from the extensometer, the piston position LVDT, and also from a laser interferometer

Experiment Report *(continued)*

which we set up with special end platens. A portion of the experiment protocol is shown to the right. Ideally we would have changed stress smoothly but the count time introduces the steps. The three strain measuring techniques produced more scatter than we expected. The extensometer is the trusted measurement on SMARTS, but we are still working to resolve the discrepancies.

Below we show a macro stress-strain curve showing the initial conditioning and repeatable hysteretic loops for marble Neutron data was acquired during the loops.

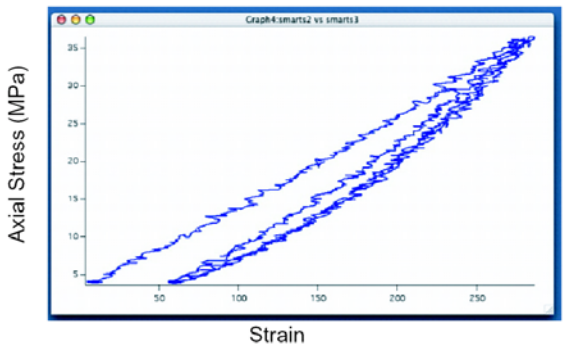

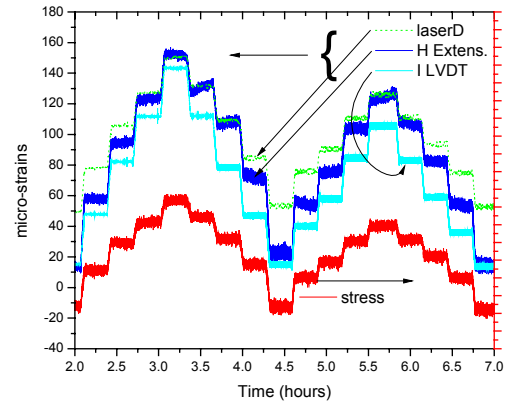

We show below the neutron measured strains for the marble sample, (calcite is trigonal) with both a and c lattice parameters, parallel and perpendicular to the stress. Both sets of planes show hysteresis and the difference in the elastic moduli is apparent.

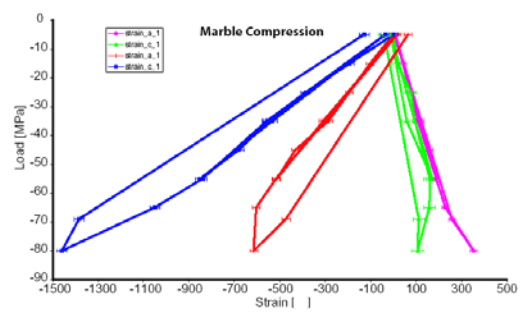

Below, and below right, we show the same kind of data for the Fontainebleau sandstone. While the macro curve shows the expected behavior, the lattice parameters of the quartz grains show no hysteretic behavior and the average strain in the grains seems to be about an order of magnitude lower than the apparent macroscopic strain. We attribute these differences to the fact that the sandstone is porous and the strain state of the grains is determined by essentially point contacts, in contrast to a polycrystal with complete grain boundaries. Analysis of this data is continuing.

We hope to continue this program on SMARTS in the next run cycle where we will use the samples not covered in this run, and use improved strain resolution .

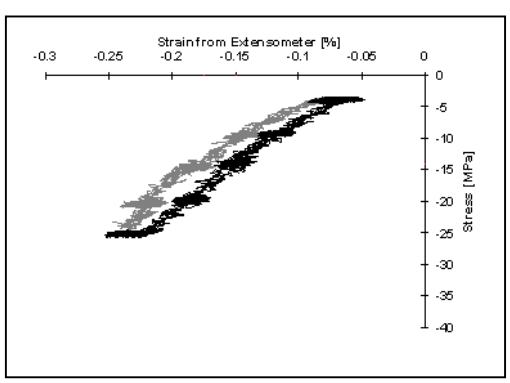

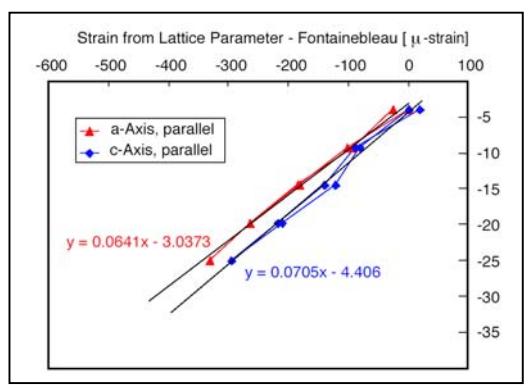

IMPORTANT! List or attach a list of publications resulting from this experiment (published or in press).

This data has been presented at several conferences: 1) Invited talk: IWNEM7 Italy Aug. '02, LAUR-02-3902 2)AGU Fall mtg.San Fransisco Dec. '02: invited poster, 3)TMS annual meeting, San Diego Mar. '03 contributed talk LAUR02-3902-, 4)NICEST workshop Mar. '03 contributed poster, LAUR-03-1711

LANSCE
Los Alamos Neutron Science Center

REPORT ON EXPERIMENT
(Please Type)

Submit all experiment reports to:
LANSCE User Office, MS H831, Los Alamos National Laboratory, Los Alamos, NM 87545

Experiment was carried out at:	**Local Contact**	**Proposal #**	***LANSCE Use Only***
[X] Manuel Lujan Jr. Neutron Scattering Center	Sven Vogel	2002162	**Report Rc'd**
[ ] Weapons Neutron Research Facility	**FP/Instrument Used**		**3/18/03**
[ ] WNR/Blue Room	FP4/HIPPO		

Title
Search for the Atomic-Level/Microscopic Source of "Slow Dynamical" Recovery Processes in Geomaterials

Authors and Affiliations
T. W. Darling LANL MST-10,
J. A. TenCate LANL EES-11,
S. C. Vogel LANL LANSCE-12,

Experiment Report

The elastic moduli or sound speeds in a material are extremely sensitive to the state of the material, but provide no details of properties on scales less than the wavelength of sound. Observations of new memory and recovery effects in rocks ("slow dynamics") by acoustic methods provide no insight to the underlying microscopic origins.
Our intent in this set of experiments is to use the high count rate capability of the new HIPPO beamline to perform measurements where we follow the behavior of the lattice parameters of a sandstone rock as rapid temperature changes are made. We intend to do this in real time and make simultaneous measurements of the acoustic response of the sample.
We have constructed a "candlestick" type holder for cylindrical samples of Berea and Fontainebleau sandstone (chosen due t the large amount of acoustic data we have) which uses a heater for temperature changes has and temperature and acoustic resonance monitoring of the sample. The figure at right shows the insert with flange and vacuum port. Below, the sample with its heater base and differential thermocouple. Piezoelectric transducers at the top and bottom of the sample provide acoustic resonance monitoring.

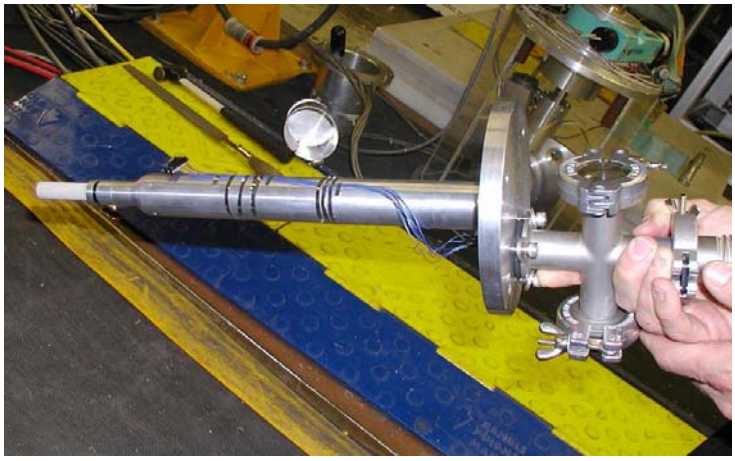

Experiment Report *(continued)*

Because these samples are porous and sensitive to humidity levels we made counts of 5 minute duration continuously as we pumped out the chamber to monitor the effect of pressure (lack of it) on the temperature and lattice of the quartz grains, and also for all the temperature varying runs. We made tests to determine how quickly we could make runs with sufficient statistics, and found that a *10 second* run could provide usable data, see figure left below. Right below is a 60s run.

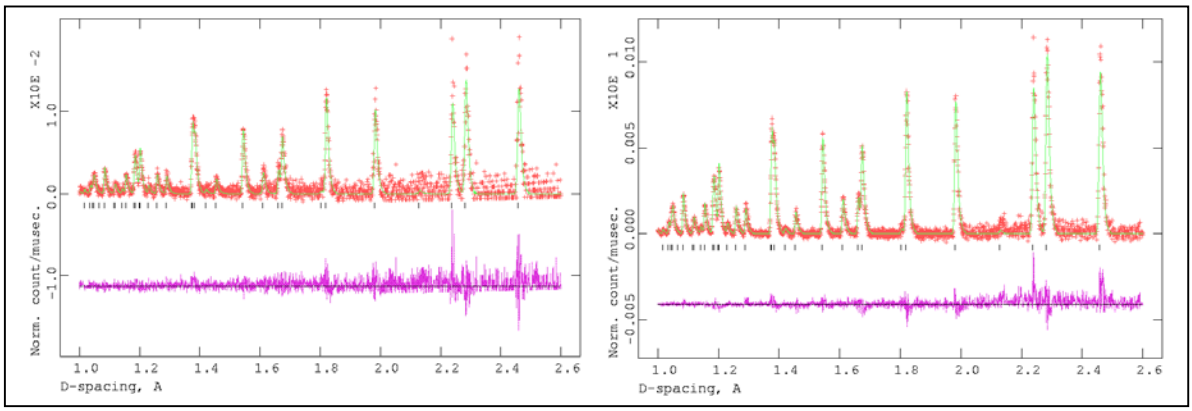

We performed 3 measurements during the runtime, of which only one (Fontainebleau #2) had the full simultaneous data set of neutron, thermal and acoustic data. The thermal and acoustic data were recorded by a labview program on a separate acquisition system.

The near right figure shows temperatures (red near heater, blue for free end of sample) and the resonance behavior (black). At far right the same temperatures and the corresponding a-axis lattice parameter for the quartz grains. The "spike" at 50hrs is the change from atmosphere to vacuum in the well chamber. The removal of water from the stone leads to strains in the grains. We note that, although the temperature becomes constant, the acoustic behavior is still changing significantly with a long time constant, and that the behavior of the strain in the quartz grains seems to be following the temperature variation rather than the acoustic properties. We deduce (up to the obvious scatter apparent in the data) that the acoustic effects that we see are not due to the strains evolved in the bulk of the quartz grains by temperature variations. We believe these are the first measurements at LANSCE to simultaneously measure neutron, acoustic and thermal properties.

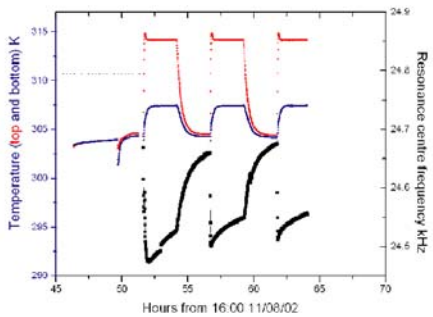

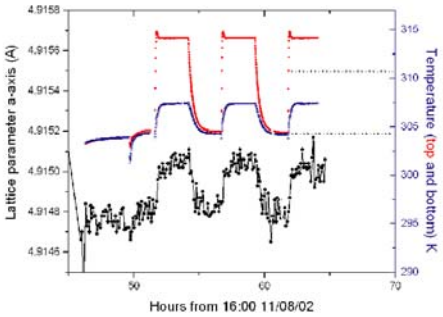

We see two major problems with our setup: the large temperature difference between the ends of the sample provides a gradient that we do not want and a significant reduction in the temperature changes we are able to induce, and the time constant difference between heating and cooling seriously complicates our determination of acoustic and strain time constants. We believe we have improved our holder with active cooling and distributed heating and intend to revisit this experiment to achieve publishable certainty with our deductions and expand our range of measured samples. We (JT, TD) particularly appreciate the efforts of the instrument scientist (Sven Vogel) toward making this complex experiment successful and look forward to continuing this collaboration next run cycle.

IMPORTANT! List or attach a list of publications resulting from this experiment (published or in press).

AGU Fall mtg.San Fransisco Dec. '02: invited poster, TMS annual meeting, San Diego Mar. '03 contributed talk LAUR02-3902-, JINS NICEST workshop Mar. '03 contributed poster, LAUR-03-1711

LANSCE
Los Alamos Neutron Science Center

REPORT ON EXPERIMENT
(Please Type)

Submit all experiment reports to:
LANSCE User Office, MS H831, Los Alamos National Laboratory, Los Alamos, NM 87545

Experiment was carried out at:	**Local Contact**	**Proposal #**	***LANSCE Use Only***
[X] Manuel Lujan Jr. Neutron Scattering Center	Yusheng Zhao	**2002170**	**Report Rc'd**
[ ] Weapons Neutron Research Facility	**FP/Instrument Used**		**3/24/03**
[ ] WNR/Blue Room	SCD		

Title
In-Situ Neutron Single-Crystal Diffraction Study on Methane-Hydrogen Clathrates at High Pressures

Authors and Affiliations
Jian Xu, Carneigie Institution of Washington
Ho-Kwang Mao, Carneigie Institution of Washington
Russell Hemley, Carneigie Institution of Washington

Experiment Report

The neutron diffraction is a sole research tool to understanding the hydrogen bond in detail, it is very useful tool to tackle high-profile scientific problems. However, the sample size required in the neutron diffraction technique was always an obstacle for high-pressure scientists because in a long period of time, the DAC high-pressure technique could handle only th sub-mm sample size.The use of large size diamond anvil and the appearance of the moissanite anvil changed such a situation (Xu and Mao, 2000), until now, we have been working in this area for three years. In Los Alamos, we have been able to manage our research on the single crystal methane hydrate, especially, its sII phase.This crystal has been grown in a 2.8-mm moissanite anvil cell with its volume of 2.4-mm3. Both In-situ Raman measurements and X-ray diffraction measurements confirmed the crystal is sII methane hydrate, its cubic structure with the lattice constant of 17.22 A was found. This compare with 17.1A found previously (Chou et al., 2000). In LANSCE, we have observed a series diffraction peaks (with its differen orders of overtone) from this crystal as shown in Fig. 1. However, we faced three problems right now.The first -- and I believe the most serious -- problem is the software used in the SCD. It was wrote in VAX/VMS system and with extremely slow computer power for data processing. It almost lost all of its functions except the data acquisition when we used the k=45o configuration, many data collected cannot be processed al all for this setting. If such a problem could not be solved, we can only set the k back to 60o and lose the best setting angle for our high-pressure cell. It will strongly influent our further progress in the research on this crystal. More seriously, even Dr. Allen Larson, the program writer, does not know why it happens?

Experiment Report (continued) Second, there are problems with beam line support (both in software and in hardware). The well-aligned neutron beam in 2001 was far away from its original position. Although we have been able to obtain the help from Mr. Abedel Alsmadi and Dr. Yusheng Zhao, Dr. Zhao was very busy in other matters and Mr. Alsmadi seems to need more training. Third, we faced the intensity correction from our high-pressure panoramic-type moissanite anvil cell (Mao et al., 2001). The absorption from the gasket, anvils and cell body makes complicate for further data process (Fig. 2). This problem different with the two listed above is solvable from our effort. In the experimental runs, we designed a special experiment: the determination of the diffraction pattern when a single crystal of Pd has been loaded in the cell.A single crystal Pd (1.4-mm in diameter and 0.7-1.0-mm in thickness) has been loaded in the sample hole of a moissanite anvil cell. I comparison the diffraction intensities of various possible diffractions from this crystal with the same diffractions from a sam crystal without the cell, we can estimate the absorption of the cell on various directions.We prepare to collect all of the diffractions in future experimental runs, and a rough absorption pattern will be given after our data processing.References:Chou, I.-M. et al., Proc. Nat. Acad. Sci., 97, 13,484, 2000.Chou, I.-M. et al., J. Phys. Chem., A, 105, 4664, 2002.Mao, H. K. et al., Science, 292, 914, 2001.Xu, J. and H. K. Mao, Science, 290, 783, 2000.

Captions:
Figure 1. The diffraction observed from a sII single crystal of methane hydrate in the SCD station, LANCSE, Los Alamos Laboratory. This figure shows the observed overtone in (620) direction.
Figure 2. The different absorption can be experienced when the diffraction beam passed through different parts: the gasket (beam 1); the gasket-support ring (beam 2); the anvil-support ring (3) and the anvil-support ring-cell body (beam 4), respectively.

Experiment Report *(continued)*

IMPORTANT! List or attach a list of publications resulting from this experiment (published or in press).

LANSCE
Los Alamos Neutron Science Center

REPORT ON EXPERIMENT
(Please Type)

Submit all experiment reports to:
LANSCE User Office, MS H831, Los Alamos National Laboratory, Los Alamos, NM 87545

Experiment was carried out at:	**Local Contact**	**Proposal #**	***LANSCE Use Only***
[X] Manuel Lujan Jr. Neutron Scattering Center	Jarek Majewski	**2002172**	**Report Rc'd**
[ ] Weapons Neutron Research Facility	**FP/Instrument Used**		**2/6/03**
[ ] WNR/Blue Room	SPEAR		

Title
Structure of Synthesized Non-Linear Optical Films

Authors and Affiliations
Jeanne Robinson, Hsing-Lin Wang, Jarek Majewski, Joanna Casson, Erik Watkins; Los Alamos National Laboratory

Experiment Report

When light is transmitted through non-linear optical materials its frequency is changed. By exploiting this property, non-linear optical films can be created for use as second harmonic generators. A variety of such films containing optically active AZO molecules were synthesized. Using neutron reflectometry, we examined the structure of these layered, non-linear optica films. The following samples were prepared and measured:

AZO-C18/d-Stearic acid Bilayers:
An octadeclytrichlorosilane (OTS) layer was attached to quartz substrates to provide a hydrophobic surface. Then, using the Langmuir Blodgett technique, alternating layers of deuterated stearic acid and AZO-C18 molecules were deposited. Each pa of stearic acid and AZO-C18 layers was designated as one bilayer. One, two and four bilayer samples were measured.

AZO-C18 and Lauric Acid/d-Stearic acid Bilayers:
Samples were prepared in the same way that the AZO-C18/d-Stearic acid bilayers were prepared using alternating layers of deuterated stearic acid and a mixture of lauric acid and AZO-C18. One, two and four bilayer samples were measured.

PEI/PAZO/PVP Trilayers:
Trilayer samples were prepared on both quartz and silicon substrates and by both spinning and Langmuir Blodgett depositio techniques. The following trilayer samples were measured:

- One, two, and three trilayer samples spun on silicon and measured in air
- One, two, and three trilayer samples Langmuir deposited on silicon and measured in air
- One, two, and three trilayer samples spun on quartz and measured in air
- One, two, and three trilayer samples spun on quartz and measured in D_2O saturated air

Box models have been used to fit the data for the AZO-C18/d-stearic acid bilayers and the AZO-C18 and Lauric Acid/d-stearic acid bilayers reflectivity measurements.

Experiment Report *(continued)*

In **Figure 1** the measured reflectivity of three different bilayer samples is compared to the reflectivity of the models we developed. The data is plotted as Q_z vs $R*Q_z^4$ to better demonstrate the closeness of the fit. The profiles of these three models are presented in **Figure 2**. The first dip represents the OTS layer. Subsequent dips represent the lower scattering AZO-C18 layers while the peaks represent strongly scattering d-stearic acid layers. Several interesting conclusions can be drawn from these profiles:

- Scattering length density of deuterated peaks decreases as the bilayer number increases
  - Indicates sparsely packed layers
- Decreasing order within layers as the bilayer number increases
  - Indicates intermixing of molecules between adjacent layers
- Model corresponds to the observed decrease in the SHG signal with increasing bilayer number

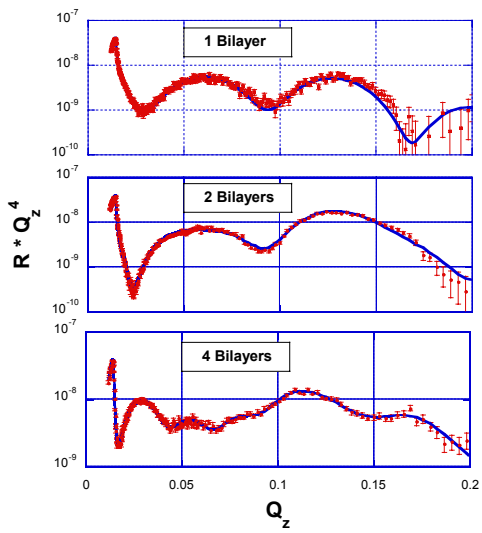

Fig. 1:AZO-C-18/d-Stearic Acid Bilayer Reflectivities

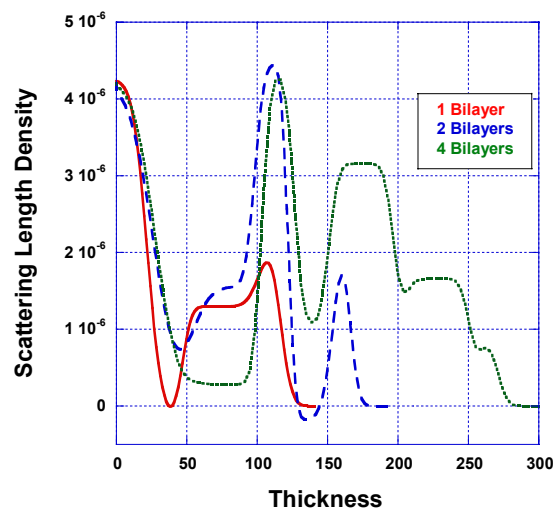

Fig.2 AZO-C18/d-Stearic Acid Bilayer Profiles

The analysis of the AZO-C18 and Lauric Acid/d-Stearic acid bilayer data showed similar features with a greater level of disorder than the samples without lauric acid.

The trilayer samples have not yet been analyzed but should provide comparable information about the structure of the film and information about the structural differences resulting from different deposition techniques.

IMPORTANT! List or attach a list of publications resulting from this experiment (published or in press).

LANSCE
Los Alamos Neutron Science Center

REPORT ON EXPERIMENT
(Please Type)

Submit all experiment reports to:
LANSCE User Office, MS H831, Los Alamos National Laboratory, Los Alamos, NM 87545

Experiment was carried out at:	**Local Contact**	**Proposal #**	***LANSCE Use Only***
[x] Manuel Lujan Jr. Neutron Scattering Center	Dr. Jarek Majewski	**2002182**	**Report Rc'd**
[ ] Weapons Neutron Research Facility	**FP/Instrument Used**	Sept. 27-Oct. 4, 02	**3/20/03**
[ ] WNR/Blue Room	SPEAR		

Title
Temperature Dependent Interaction of Protein with Biocompatible Organic Monolayers Studied by Neutron Reflectivity

Authors and Affiliations
Dirk Schwendel, Dr. Reiner Dahint, and Prof. Dr. Michael Grunze
Angewandte Physikalische Chemie
University of Heidelberg
Im Neuenheimer Feld 253
D-69120 Heidelberg
Germany

Experiment Report

Neutron reflectivity measurements on protein resistant self assembled monolayers (SAM) of methoxy tri(ethylene glycol) terminated undecylthiolate (EG3-OMe) on Au confirmed an unexpectedly extended (~ 4 nm) water layer with a noticeably reduced density (85 - 90% of bulk water) at the interface between bulk water and the organic film which has already been observed in previous room temperature experiments.[1] In view of the fact that solvent/surface interactions have been suspected to render materials inert towards protein adsorption, this interfacial water layer could be considered as the physical cause that EG3-OMe repels proteins. Based on this assumption, we would expect changes in the interfacial water structure at lower temperatures, since EG3-OMe on Au loses its protein resistant properties below ~ 12 °C.[2] However, no significant differences could be observed for EG3-OMe in contact with D_2O at 25, 17, 12, and 5 °C (see Figure 1). Thus, no direct correlation exists between the observed density-reduced water layer at the interface and the protein resistant film characteristics.

In addition, temperature dependent neutron reflectivity measurements were performed to investigate the interaction between EG3-OMe and proteins in solution at 25, 17, 5 °C. In contrast to previous studies, which focused on the characterization of adsorbed protein layers, neutron reflectivity has now been used to study repulsive forces experienced by native proteins in their natural environment. For this purpose, a 15 wt.-% protein solution was prepared from bovine serum albumin (BSA) in D_2O.

Figure 2a shows the neutron reflectivity of an EG3-OMe sample when exposed to a 15 wt-% BSA solution in D_2O at 25 and 5 °C. A box model fit based on the Parratt algorithm yields a significantly protein depleted zone next to the SAM with an extension of about 13 nm (Fig. 2a, green line). It is followed by a second, approximately 38 nm thick layer, which has a SLD of about 92% with respect to bulk D_2O corresponding to a 11.4 wt-% BSA solution. A third, semi-infinite box represents the 15 wt-% BSA bulk phase. The calculated model assuming a homogeneous BSA distribution between the SAM and the bulk phase (red line) does not show satisfying correlation with the experimental data. Actually, the assumption of a protein depleted layer improves the χ^2 deviation by a factor of 2.6. The corresponding real space profile shows the protein depletion zone (Fig. 2b).

Experiment Report *(continued)*

At 5 °C the reflectivity data substantially differ from the profile at 25 °C (Fig. 2a, blue circles). A depletion layer cannot be observed at these conditions. The fit (Fig. 2b, blue line) yields an extremely rough interface between the SAM and the protein bulk phase as displayed by the real space profile (Fig. 2b, blue line). The high roughness can be attributed to an adsorbed protein layer, which has already been observed in former *ex situ* infrared studies at these temperatures.[2]

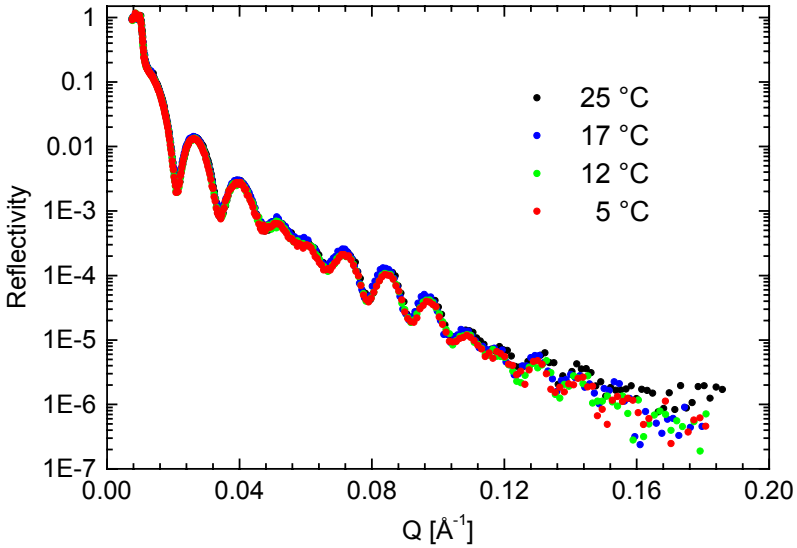

Fig. 1: Neutron reflectivity profile of EG3-OMe on Au in contact with D_2O at four different temperatures.

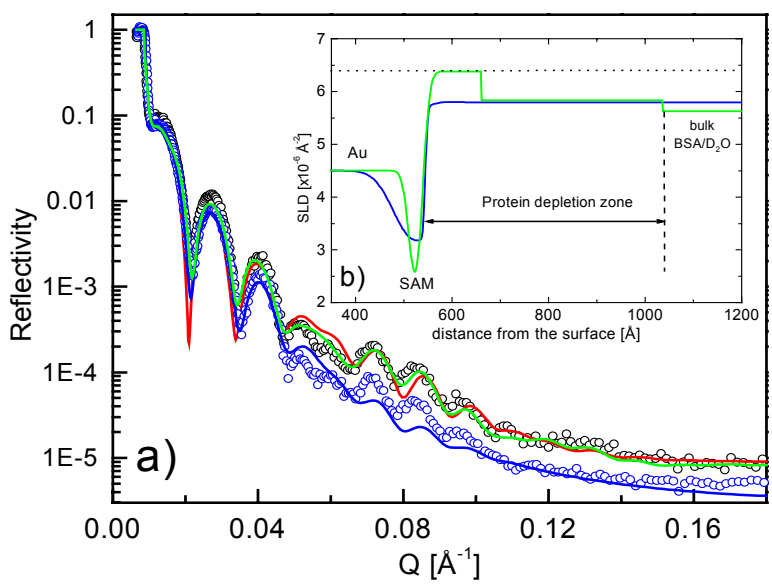

Fig. 2: Neutron reflectivity profile of EG3-OMe on Au in contact with a 15 wt-% BSA solution in D_2O at 25 °C (black circles) and 5 °C (blue circles). The green line refers to a model assuming a protein depleted zone of about 50 nm. This depletion zone is displayed by the green line in the real space profile (Fig. 2b). The red line refers to a model assuming a homogenous protein distribution. The best fit to the reflectivity data at 5 °C is represented by the blue line. Its real space profile is represented by the blue line in Fig. 2b.

References:

[1] D. Schwendel, T. Hayashi, R. Steitz, F. Schreiber, R. Dahint, A. Pertsin, M. Grunze, *Langmuir*, **2003**, *19*, 2284-2293.
[2] D. Schwendel, R. Dahint, S. Herrwerth, M. Schloerholz, W. Eck, M. Grunze, *Langmuir*, **2001**, *17*, 5717-5720.

A publication of these results is currently in preparation.

LANSCE
Los Alamos Neutron Science Center

REPORT ON EXPERIMENT
(Please Type)

Submit all experiment reports to:
LANSCE User Office, MS H831, Los Alamos National Laboratory, Los Alamos, NM 87545

Experiment was carried out at:	**Local Contact**	**Proposal #**	***LANSCE Use Only***
[X] Manuel Lujan Jr. Neutron Scattering Center	Rex Hjelm	**2002183**	**Report Rc'd 3/18/03**
[ ] Weapons Neutron Research Facility	**FP/Instrument Used**		
[ ] WNR/Blue Room	LQD		

Title

Investigation of Radiogenically Produced ^{3}He in Erbium Dihydride Systems: Bubble Formation and Coarsening Mechanism.

Authors and Affiliations

JF Browning Sandia National Laboratories
MA Mangan Sandia National Laboratories
DM Blankenship Sandia National Laboratories
GS Smith Oak National Laboratory
GM Bond New Mexico Institute of Mining and Technology

Experiment Report

This experiment is a continuation of a multiyear experimental program designed to study the evolution of the $ErT_{2-x}{}^3He_x$ metal hydride system as a function of time and helium concentration. In the initial phase of this experiment, three sample sets were prepared for analysis on LQD (2001 run cycle exp # 20011072) at the Lujan Center at LANSCE. The films were prepared at Sandia National Laboratories by physical vapor deposition of 100nm of molybdenum onto a silicon substrate (100) of dimensions 1.25cm x 1.25cm x 0.076cm. A 500nm layer of erbium was then deposited onto the molybdenum layer. Formation of the erbium dihydride layer was accomplished by the subsequent exposure of the erbium layer to a 175torr tritium pressure at a temperature of ~ 450°C. Hydriding of the films was carried out at the Savannah River Technology Center (SRTC) of the Department of Energy's Savannah River Plant. Results showing the observed difference as a function of helium concentration for one of the tritiated samples are presented in the first two figures below. The initial measurement from a sample containing a very low concentration of helium is also presented. An evident symmetry apparent in each of the Q maps is suggestive of an ordering or periodicity associated with helium formation within the hydride. Efforts are currently underway to analyze data acquired thus far. Further analysis is planned on these samples as well as additional samples sets to extent the range in helium concentration for the 2003 run cycle.

Experiment Report *(continued)*

Q_y

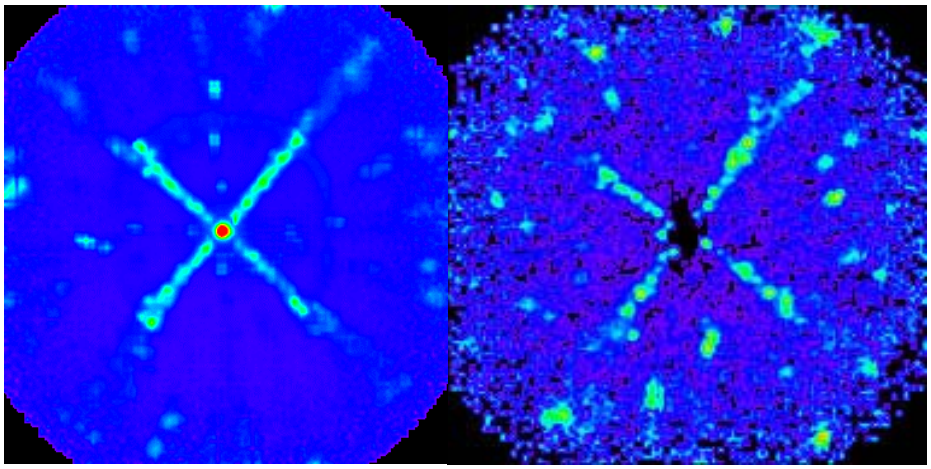

Q_x

$ErT_{2-x}{}^{3}He_x$ sample for x ~ 1% for the initial measurement and x ~ 3.5% for second measurement.

Q_y

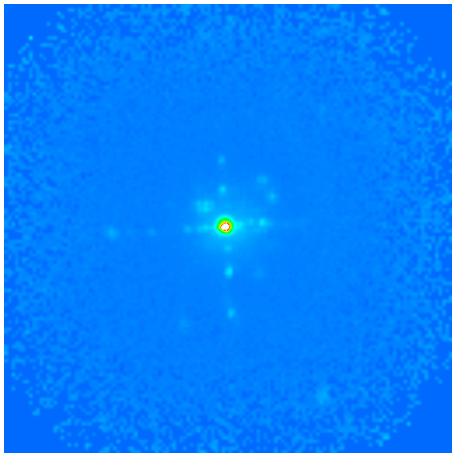

Q_x

$ErT_{2-x}{}^{3}He_x$ sample for x << 1%

IMPORTANT! List or attach a list of publications resulting from this experiment (published or in press).

LANSCE
Los Alamos Neutron Science Center

REPORT ON EXPERIMENT
(Please Type)

Submit all experiment reports to:
LANSCE User Office, MS H831, Los Alamos National Laboratory, Los Alamos, NM 87545

Experiment was carried out at:	**Local Contact**	**Proposal #**	***LANSCE Use Only***
[X] Manuel Lujan Jr. Neutron Scattering Center	R. Hjelm	**2002-186**	**Report Rc'd**
[ ] Weapons Neutron Research Facility	**FP/Instrument Used**		**3/21/03**
[ ] WNR/Blue Room	LQD		

Title Structural Analysis of Nanoarchitectures in Porous and Block Copolymer Systems

Authors and Affiliations
Janet Mercer-Smith, LANL mercer-smith_janet@lanl.gov
Rex P. Hjelm, LANL hjelm@lanl.gov
Mark Smith, LANL msmith@lanl.gov
Greg Long, LANL glong@lanl.gov

Experiment Report

The instrument time during the last experimental run was applied to the investigation of two distinct sample types: side chain grafted copolymers, comprised of a polycaprolactam (nylon-6) chain with deuterated polystyrene side chains; and silica particles with specific nanometer scale porosity, having alkyl species.

The copolymer samples were prepared as cast films on quartz windows. Our investigation was focused on determining the radius of gyration of these molecules. The copolymer pair (polycaprolactam/polystyrene) phase separate to form a structure that is comprised of a polystyrene shell surrounding a polycaprolactam core. Key factors in this study are the relative molecular weights of the main chain versus the grafted arms, and the frequency of the grafted arms along the main chain. The samples employed in our investigation were predicted to form cylindrical structures at their equilibrium state.

Samples where the main (polycaprolactam) chain was ~5000 mwt and the side (polystyrene) chain molecular weight was ~ 10000, with a graft frequency of 1 arm per ~70 main chain atoms were measured. The samples demonstrated very good scattering behavior with the utilization of deuterated styrene. It was determined that the radius of the cylindrical structures is ~130A.

These results have led to the synthesis of new samples of varying main chain/arm length ratios and various graft frequencies for further study.

The designed porosity silica samples were investigated in a two phase approach. Our first measurements were performed on particles of 30, 100 and 300A with and without a C(10) alkyl surface. These measurements were performed in DMSO solvent (71% deuterated for contrast matching) to determine the structural features of the particles. As readily seen in the figures below, the C10 modification shows strong scattering peaks associated with the sample porosity. The larger pore size shifts the scattering peak to lower Q values.

Experiment Report *(continued)*

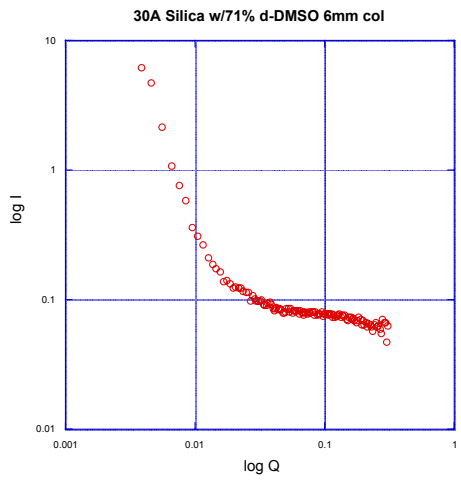

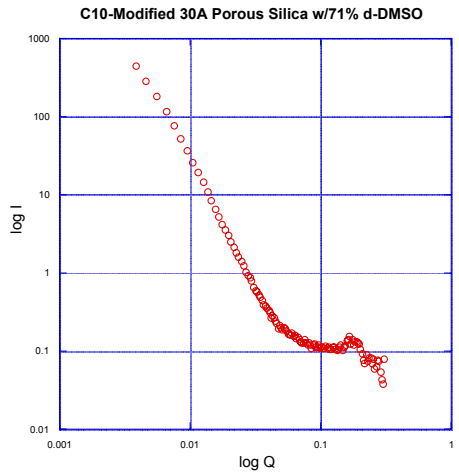

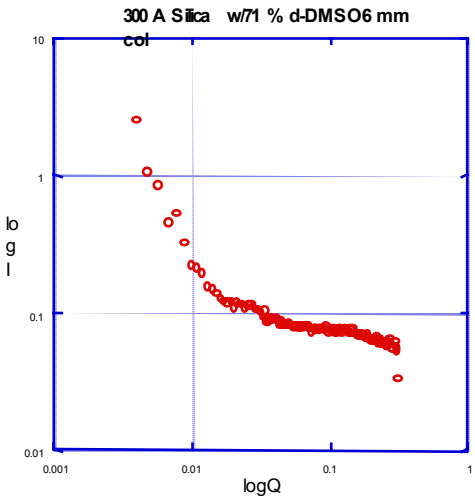

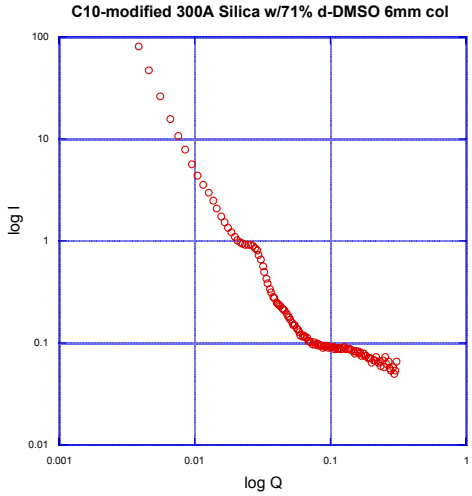

The second phase was a series of measurements with 300A pore, silica particles in four acetone solvent mixtures (0%, 32%, 67% and 100% deuterated). This series was performed to decouple the particle size scattering effects form the porosity scattering. While the data is not entirely clear on the specific structural contributions, preliminary findings are encouraging. The measurements were hampered by the high vapor pressure of the acetone, therefore we are evaluating a different cuvette design and/or the use of an alternative solvent for future studies.

IMPORTANT! List or attach a list of publications resulting from this experiment (published or in press).

Manuscript in preparation

LANSCE
Los Alamos Neutron Science Center

REPORT ON EXPERIMENT
(Please Type)

Submit all experiment reports to:
LANSCE User Office, MS H831, Los Alamos National Laboratory, Los Alamos, NM 87545

Experiment was carried out at:	**Local Contact**	**Proposal #**	***LANSCE Use Only***
[x] Manuel Lujan Jr. Neutron Scattering Center	Rex P. Hjelm	**2002194**	**Report Rc'd**
[ ] Weapons Neutron Research Facility	**FP/Instrument Used**		**4/8/03**
[ ] WNR/Blue Room	FP-10/LQD		

Title

SANS Study of Internal Void Structures in HMX and RDX

Authors and Affiliations

Joseph T. Mang, DX-2, LANL
Rex P. Hjelm, L-12, LANL

Experiment Report

Introduction

We have used the small angle neutron scattering (SANS) technique in conjunction with the method of contrast variation[1] to characterize the microstructure of the high explosives, HMX and RDX. Such information is essential for understanding the influence of microstructure on the behavior of high explosive (HE) materials. The current work is part of an international collaboration (Data Exchange Agreement 7304), with Dr. Lionel Borne of the French-German Research Institute of Saint-Louis (ISL), to correlate particle characteristics of HMX and RDX with shock sensitivity. We have received various preparations of HMX and RDX, for which Borne has published shock sensitivity trends.[2,3,4,5] The different preparations of HMX and RDX reflect differences in *total* internal void volume ("apparent density") as measured by Borne using his unique "float-sink" method[5], and surface defects as observed qualitatively by Borne using electron microscopy. The contrast variation technique, in conjunction with SANS, can isolate scattering contributions that originate from surfaces and internal voids; thus providing the necessary, quantitative, information on particle surface structure and internal void size distribution. Measured parameters, such as surface area and mean internal void size will be correlated with the shock sensitivity data.

During the 2002 run cycle we performed SANS and contrast variation measurements on five of the twenty-two high explosives samples we proposed to study. An abbreviated schedule and instrument difficulties on LQD prevented us from completing the entire matrix of measurements.

Experimental

SANS and contrast variation measurements were performed on five different HMX and RDX powders. The HE powders were dispersed in H2O/D2O containing different percentages of the two components in order to vary the scattering length density contrast. Five to six different contrasts were measured for each sample.

Results

Our results are very encouraging and demonstrate the power and utility of this technique. Figure 1 displays the SANS data obtained on the sample labeled HMX-4. As seen in the figure, as the amount of D_2O was increased, significant changes in the measured lineshapes was found. As the contrast was varied, a distinct feature emerged, centered at Q ~ 0.01 $Å^{-1}$. This feature corresponds to an internal void population in the HMX crystals of ~ 100 Å in size. Similar results were obtained for the other four powders studied. We are currently completing the contrast variation analysis, which will allow a more accurate assessment of surface area and internal void structures.

Experiment Report *(continued)*

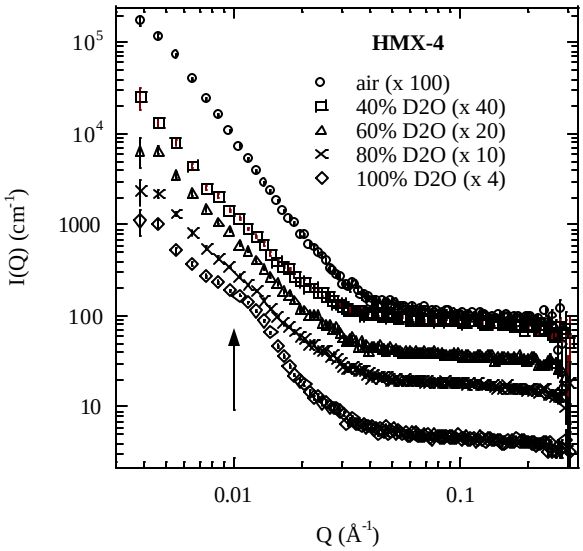

Figure 1: SANS and contrast variation measurements of an HMX sample reveal internal void structures.

Summary

We have performed SANS and contrast variation measurements on five different powders of HMX and RDX. The powders have different "apparent densities" and hence internal void volumes and different surface features. Our results reveal the presence of internal void populations. Upon completion of our analysis, these results will be correlated with the known "apparent density" of the powders and their shock sensitivity, allowing a more direct measure of the effect of microstructure on the shock sensitivity of HMX and RDX.

References

[1]Joseph T. Mang, Cary B. Skidmore, Rex P. Hjelm *et al*., "Application of Small Angle Neutron Scattering to the Study of Porosity in Energetic Materials," Journal of Materials Research **15** (5), 1199-1208 (2000).

[2]Lionel Borne, "Influence of Intragranular Cavities of RDX Particle Batches on the Sensitivity of Cast Wax Bonded Explosives," Tenth International Detonation Symposium, Boston, Massachusetts, July 12 - 16, 1993, 286 - 293.

[3]Lionel Borne, "Microstructure effect on the shock sensitivity of cast plastic bonded explosives," Europyro 95, Tours, France, June 5-9, 1995, 125-131.

[4]Lionel Borne, "Explosive Crystal Microstructure and Shock-Sensitivity of Cast Formulations," Eleventh International Detonation Symposium, Snowmass Village, Colorado, August 31 - September 4, 1998.

[5]Lionel Borne, Jean-Claude Patedoye, and Christian Spyckerelle, "Quantitative Characterization of Internal Defects in RDX Crystals," Propellants, Explosives, Pyrotechnics **24** (4), 255-259 (1999).

IMPORTANT! List or attach a list of publications resulting from this experiment (published or in press).

REPORT ON EXPERIMENT
(Please Type)

Submit all experiment reports to:
LANSCE User Office, MS H831, Los Alamos National Laboratory, Los Alamos, NM 87545

Experiment was carried out at:	**Local Contact**	**Proposal #**	***LANSCE Use Only***
[x] Manuel Lujan Jr. Neutron Scattering Center	Thomas Proffen	**2002201**	**Report Rc'd**
[ ] Weapons Neutron Research Facility	**FP/Instrument Used**		**3/21/03**
[ ] WNR/Blue Room	NPDF		

Title
In-situ Investigation of the Local Phase Transition of $Pb(Mg_{1/3}Nb_{2/3})O_3$ Near Burns Temperature Using Neutron Pair Distribution Function (PDF) Analysis

Authors and Affiliations
Il-Kyoung Jeong, Robert H. Heffner, Thomas Proffen, Tim Darling, Los Alamos National Laboratory;
T. Egami, University of Pennsylvania

Experiment Report]

In relaxor ferroelectrics $Pb(Mg_{1/3}Nb_{2/3})O_3$, the inverse susceptibility is known to deviate strongly from the Curie-Weiss behavior over a wide temperature range above permittivity maximum temperature, T_M. Burns *et al.* explained this deviation as an indication of the local phase transition which starts above T_M [1]. The change in the slope of optical index near Burns' temperature (T_B), higher than T_M by a few hundred degrees, supported this explanation. Below T_B, it was suggested that very small regions with local, randomly oriented, and non-reversible polarization grow from a cubic non-polar matrix [2].

The average structure of PMN is a nearly ideal perovskite and Pb is not off-centered, but the neutron PDF clearly shows that Pb is strongly off-centered with respect to the oxygen cage. Recent x-ray absorption analysis supports this observation that the local polarization of Nb is small, and thus the bulk of polarization is carried by Pb [13].

In order to understand the atomistic nature of Burns temperature and local distortion due to the onset of the of Pb displacement, we measured pair distribution function (PDF) of PMN at 20K, 300K, 500K, 600K, and 700K. However, as shown in Fig. 1 we found out from the lattice parameter of standard Si as a function of temperature, the corrected cryofurnace high temperature were 300K, 410K, 510K, 575K, respectively. These results indicate that for

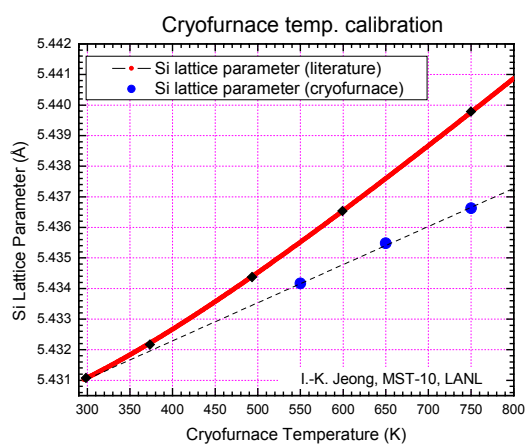

Fig. 1 Cryofurnace temperature calibration using powder diffraction of standard Si.

Experiment Report *(continued)*

large volume powder sample the cryofurnace temperature reading is unreliable and need correction.

Figure 1. shows PDFs of PMN at 300K, 440K, 510K, 575K. As temperature increases PDF peaks become broader but the shoulder around 2.55Å which is due to Pb off-center displacement persists up to 575K. We plan to study how this shoulder evolves near and above Burns temperature (T_B ~345 ^oC) when the 'real' furnace available.

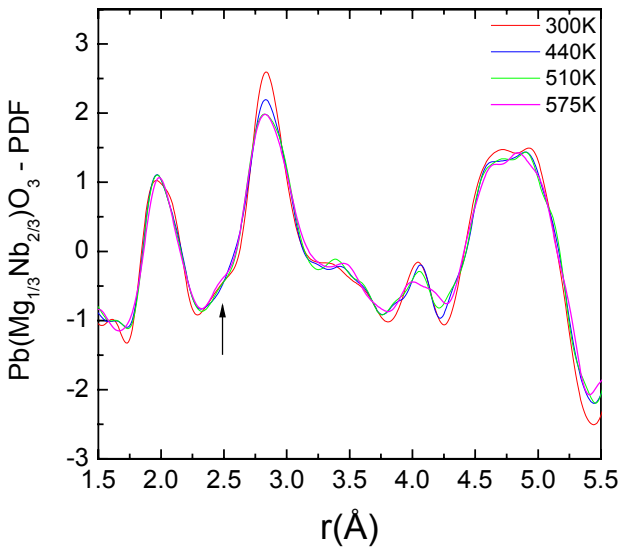

Fig. 1 PDFs of PMN at 300K, 440K, 510K, 575K. The shoulder around 2.5Å which is due to Pb off-center displacement persists up to 575K.

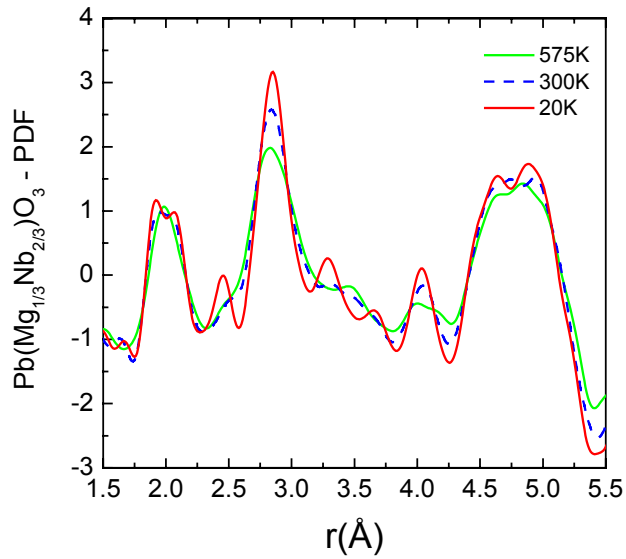

Fig. 2. PDFs of PMN at 20K, 300K, 575K. The 20K PDF clearly shows splitting of (Mg,Nb)-O bond, indicating polarization of Nb. And Pb-O peaks at 2.5Å is well separated.

Figure 2. shows the comparison of PDFs of PMN at 20K, 300K, and 575K. The 20K PDF clearly shows splitting of (Mg, Nb)-O peak, indicating the rhombohedral symmetry of local polar region. In addition, the Pb-O peaks at 2.5 Å and 3.25 Å are quite well separated. It is quite clear that these Pb-O peaks at 2.5 and 3.25 Å are not a temperature effect since PDFs at 575K and 300K show little difference. We expect these peaks are related to the local ferroelectric transition inferred from the soft-mode behavior below 220K [4].

References:

[1] G. Burns and F. H. Dacol, *Sold State Commun.*, 48, 853 (1983).
[2] G. Burns and F. H. Dacol, *Phys. Rev. B* 28, 2527 (1983).
[3] T. Egami, E. Mamontov, W. Dmowski, T. Gog, C. Venkataraman, P. W. Rehrig and L. E. Cross, *AIP Conf. Proc.*, in press.
[4] Wakimoto *et al.,* Phys. Rev. B 65, 172106 (2002).

IMPORTANT! List or attach a list of publications resulting from this experiment (published or in press).

LANSCE
Los Alamos Neutron Science Center

REPORT ON EXPERIMENT
(Please Type)

Submit all experiment reports to:
LANSCE User Office, MS H831, Los Alamos National Laboratory, Los Alamos, NM 87545

Experiment was carried out at:	**Local Contact**	**Proposal #**	***LANSCE Use Only***
[x] Manuel Lujan Jr. Neutron Scattering Center	Thomas Proffen	**2002202**	**Report Rc'd**
[ ] Weapons Neutron Research Facility	**FP/Instrument Used**		**3/21/03**
[ ] WNR/Blue Room	NPDF		

Title
Neutron Pair Distribution Function (PDF) Study on the Role of Local Structural Change in the Paraelectric-to-Ferroelectric-to-Relaxor Phase Transition of the $Sr_{1-x}Ca_xTiO_3$

Authors and Affiliations
Il-Kyoung Jeong, Robert H. Heffner, Thomas Proffen, Tim Darling, Los Alamos National Laboratory

Experiment Report]

$SrTiO_3$ is a quantum paraelectrics, polarizable material which does not undergo ferroelectric transitions at finite temperature, presumably due to quantum fluctuations [1]. Ferroelectricity can be induced in this system by the introducing substitutional impurities into the lattice. For example, Bednorz and Müller observed a crossover from an XY quantum ferroelectric state to a 'diffusive' state in $Sr_{1-x}Ca_xTiO_3$ [1]. Since then, it has been established that these doped systems remain paraelectric when the impurity concentration x is low, undergoing a paraelectric-to-ferroelectric transition when $x > x_c$. With increasing x the Curie temperature T_C is $\propto (x-x_c)^{1/2}$. When $x > x_r > x_c$ the system can exhibit 'relaxor' behavior, where the permittivity peak broadens and the temperature of the peak maximum is frequency dependent, much as in the analogous magnetic spin glass systems.

In order to study the role of structure in paraelectric-to-ferroelectric-to-relaxor transitions as a function of Ca concentration in $Sr_{1-x}Ca_xTiO_3$ we measured powder diffraction patterns and corresponding pair distribution functions (PDF) of $Sr_{1-x}Ca_xTiO_3$. Due to the beam time loss caused by beam down and extra measurements for the cryofurnace calibrations we only managed to collect data for x=0, 0.011 at 20K and 80K. Figure 1. shows diffraction patterns of $Sr_{1-x}Ca_xTiO_3$ (x=0, 0.011) at 20K and 80K. It seems that the temperature and concentration effects are small. This is same for the corresponding PDFs. Since we measured data only for two concentrations at two different temperatures, it is not clear yet how the structure is involved in the phase transitions. Therefore, we plan to collect some more data for wider ranges of concentration and temperatures.

Experiment Report *(continued)*

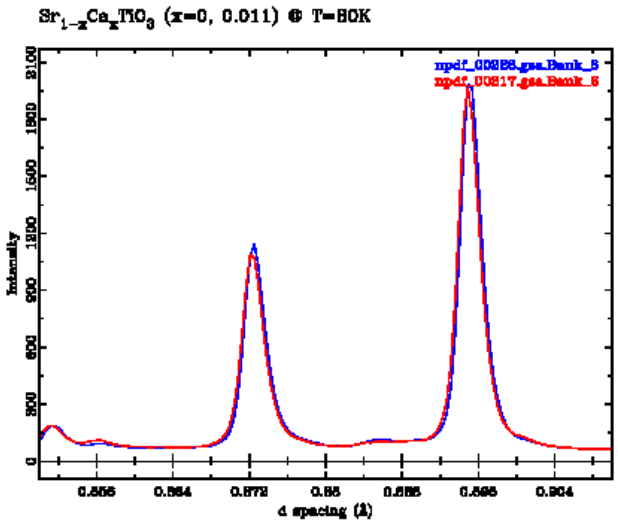

Fig. 1 Comparison of powder diffraction patterns of $SrTiO_3$ (228) and $Sr_{1-x}Ti_xO_3$ (217, x=0.011) at 80 K.

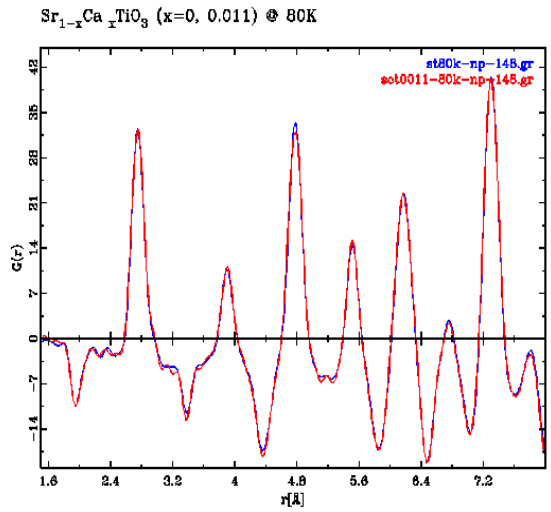

Fig. 2 PDF of $SrTiO_3$ and $Sr_{1-x}Ti_xO_3$ (x=0.011) at 80 K.

IMPORTANT! List or attach a list of publications resulting from this experiment (published or in press).

LANSCE
Los Alamos Neutron Science Center

REPORT ON EXPERIMENT
(Please Type)

Submit all experiment reports to:
LANSCE User Office, MS H831, Los Alamos National Laboratory, Los Alamos, NM 87545

Experiment was carried out at:	**Local Contact**	**Proposal #**	***LANSCE Use Only***
[x] Manuel Lujan Jr. Neutron Scattering Center	m. fitzsimmons	**2002230**	**Report Rc'd**
[ ] Weapons Neutron Research Facility	**FP/Instrument Used**		
[ ] WNR/Blue Room	11		

Title
Order Parameter Measurement of d=3 Random-Field Ising Antiferromagnet Fe(sub0.8)Zn(sub0.2)F(sub2) Thin Films

Authors and Affiliations
D. Lederman (WVU)
D. Belanger (UCSC)

Scientists Perform First Neutron-Scattering Experiment Using the 11-T Superconducting Magnet at the Lujan Neutron Scattering Center

D. Lederman (West Virginia University), D. Belanger, L.J. Shelton, F. Ye (University of California at Santa Cruz), M.R. Fitzsimmons, S. Park (LANSCE Division)
LALP-03-028

During the 2002 run cycle at the Los Alamos Neutron Science Center, scientists successfully completed the first neutron-scattering experiment using the 11-T Oxford superconducting magnet on the Asterix spectrometer — an instrument designed for studies of magnetic materials. As a consequence of a special October 2002 call for proposals for experiments requiring high-magnetic fields, an experiment involving the order-parameter measurement of a three-dimensional, random-field Ising model, as realized in a dilute antiferromagnet, was selected. The intent of the experiment was to measure how the sublattice magnetization of the dilute antiferromagnet changes with temperature near the phase transformation. Magnetic ordering in this system results within the formulism of the Ising model when the magnetic moments align themselves in one of two anti-parallel directions.

Our experiment was noteworthy for several reasons. First, neutron beams in bulk single crystals have often confounded order-parameter measurements of these systems with neutron scattering. To overcome this problem, the researchers used a 1-cm- by 1-cm- by 250-nm-thick $Fe_xZn_{1-x}F_2$ (where $x > 0.754$) single crystal as their sample. Because the sample was so thin, extinction of the neutron beam was minimized. Secondly, a 10-T (or more) magnetic field was needed to cause a crossover to the critical behavior (i.e., the behavior of magnetic spin near a phase transition as predicted by theory and computer models and measured experimentally) observed in the random-field Ising model. Thirdly, precise and accurate control of the thermal environment to better than 5 mK was needed in the 63.8-K thermal transition region. With this experiment, we demonstrated the capability of Asterix to obtain high-quality data from exceedingly small samples at high fields under extremely stable thermal conditions.

Achieving Thermal Stability in an Unstable Temperature Region

Our most challenging technical problem was to obtain thermal stability in a temperature region where the Oxford cryostat is most unstable. Near 60 K, the measured temperature stability of the Oxford cryostat is on the order of 50 mK when better than 5 mK is needed. We solved this problem by connecting a spare calibrated carbon-glass thermometer (i.e., with the fiber axis parallel to the field axis of the magnet) at the sample location to a Lakeshore temperature controller. We then used the Lakeshore controller to regulate the sample temperature with a second heater wired to the sample stage (Fig. 1). With this arrangement we could change the temperature of the sample in a completely monotonic fashion. During subsequent neutron measurements, which typically lasted between 30 and 120 minutes, we measured the sample temperature to acquire a thermal distribution. The standard deviation of the distribution was typically less than 0.3 mK — much less than the 5-mK requirement.

During the two-week experimental run, we used Asterix to measure the intensity of the (100) Bragg reflection from the antiferromagnetic order in the $Fe_xZn_{1-x}F_2$ crystal sample. Because the d-spacing of the (100) Bragg reflection is large, we used ~ 6-Å neutrons to measure this reflection with the Asterix spectrometer in the unpolarized mode. This setup minimized background scattering from the aluminum in the magnet cryostat (Fig. 2), the variable temperature insert, and the sample holder. To further reduce background scattering, we inserted borated polyethylene neutron shields between the magnet and the two-dimensional, position-sensitive-detector (PSD) array (Fig. 2). The stepper-motor-controlled goniometer and sample stick allowed us to align the sample within about one minute after it was inserted in the magnet. (Prealignment of the sample with a Laue camera was not performed.)

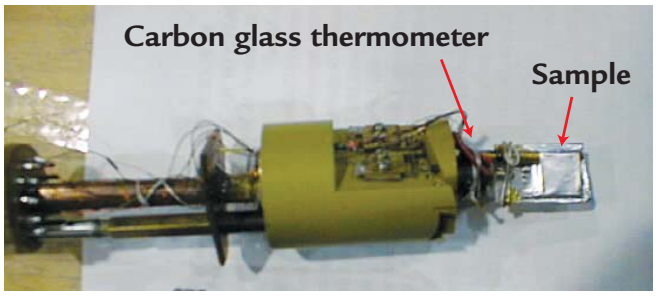

Fig. 1. View of the end of the sample stick for the 11-T Oxford superconducting magnet. The gold-colored object is a stepper-motor-controlled goniometer used to quickly align the sample. To achieve 0.3-mK thermal stability, we attached a carbon-glass thermometer and heater wire to the sample holder and used a Lakeshore temperature controller to control them.

Fig. 2. View of the 11-T Oxford superconducting magnet during the neutron-scattering measurement. To the right of the magnet is the Asterix two-dimensional PSD array. Between the magnet and the detector, we installed borated polyethylene shields, which helped reduced the neutron background by one order of magnitude.

Fig. 3 shows an image of the intensity of neutron scattering as a function of scattering angle (i.e., in the equatorial plane of the magnet) and wavelength taken with a magnetic field of 10.000 ± 0.001 T and a sample temperature of 50.0000 ± 0.00003 K in 30 minutes (i.e., with a 120-µA target current). The arrow points to the (100) Bragg reflection that resulted from antiferromagnetic ordering in the sample. The mass of the sample material contributing to this reflection is about 100 µg (its volume is about 0.025 mm^3). The intensity of the reflection is plotted in Fig. 4 as a function of temperature for two of the six measurement conditions investigated. The first measurement is of the sample after it was cooled in a zero magnetic field and then warmed up through the transition (in zero field). The second measurement is of the sample after as it was warmed up in a 10-T magnetic field after first being cooled in a zero magnetic field.

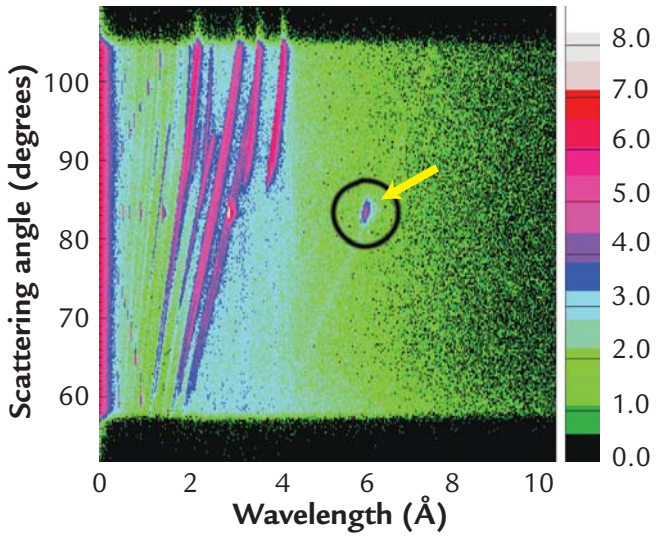

Fig. 3. An intensity image of neutron-scattering data plotted versus scattering angle and wavelength. The arrow points to the (100) Bragg reflection that resulted from antiferromagnetic ordering in the sample.

Conclusion

We have succeeded in obtaining data that provides insight into critical behavior predicted by the random-field Ising model. We have also demonstrated that Asterix can obtain wide-angle diffraction data from a single-crystal, thin-film sample in a timely manner; can obtain measurements from a sample in the presence of high magnetic fields; and can maintain an extremely stable thermal environment. Interestingly as well is the juxtaposition of the roles for magnetic scattering using x-rays and neutrons. Extinction of the neutron beam would confound order-parameter measurements for some bulk single crystals, whereas the problem was successfully studied with neutron scattering using a thin-film single crystal. Magnetic scattering of x-rays was successful at solving a similar problem using a bulk single crystal.[1] However, this technique failed in a thin-film-crystal study because the

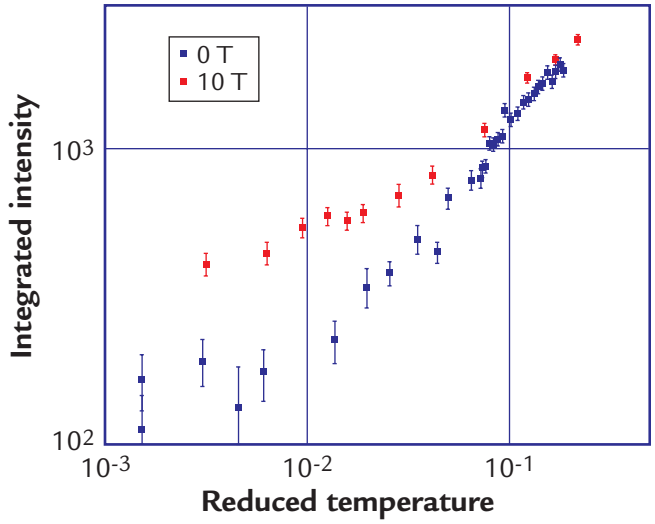

Fig. 4. The intensity of the (100) Bragg reflection from $Fe_xZn_{1-x}F_2$ after the sample was cooled in a zero magnetic field. The intensity was then measured as the sample was warmed up through the Néel transition in a zero magnetic field (●) and in a 10-T magnetic field (■). The latter condition is one that promotes detection of critical behavior in the random-field Ising model.

charge scattering from the forbidden Bragg reflection from the surface of the non-magnetically ordered MgF_2 single-crystal substrate (on which the $Fe_xZn_{1-x}F_2$ crystal is grown) is superimposed on and overwhelms the x-ray measurement of the (100) Bragg reflection from antiferromagnetic order in $Fe_xZn_{1-x}F_2$.

Acknowledgements

The magnet and construction of Asterix were supported by Laboratory-Directed Research and Development funding.

References

1. F. Ye, L. Zhou, S. Larochelle, L. Lu, D.P. Belanger, M. Greven, and D. Lederman, "Order Parameter Criticality of the d = 3 Random-Field Ising Antiferromagnet $Fe_{0.85}Zn_{0.15}F_2$," *Physical Review Letters* **8915** (15), 7202 (2002).

LANSCE
Los Alamos Neutron Science Center

REPORT ON EXPERIMENT
Single Event Effects Studies on Commercial Electronic Memories and Field Programmable Gate Arrays

Submit all experiment reports to:
LANSCE User Office, MS H831, Los Alamos National Laboratory, Los Alamos, NM 87545

Experiment was carried out at:	**Local Contact**	**Proposal #**	*LANSCE Use Only*
☐ Manuel Lujan Jr. Neutron Scattering Center	B. Takala	**2002501**	**Report Rc'd**
☒ Weapons Neutron Research Facility	**FP/Instrument Used**		**2/12/03**
☐ WNR/Blue Room	4FP30L-A		

Title

Single Event Effects Studies on Commercial Electronic Memories and Field Programmable Gate Arrays

Authors and Affiliations

Dr. D.B.S. King, BAE SYSTEMS, Warton, England

Dr. T. Granlund, SAAB Avionics, Linkoping, Sweden

Experiment Report

Two main experiments were performed in the ICE House, the first to determine the single event upset rate of commercial memory and the second to study a field programmable gate array.

SAAB and BAE SYSTEMS collaborated to test a range of static random access memories. BAE SYSTEMS provided two test sets and tested the following devices.

The projected times between upsets for the devices tested were calculated for an altitude of 9.1 km on a high latitude transatlantic flight at 55 degrees north and are given in hours.

The main test set was used to test the following 3.3V devices.

Cypress CY7C1009V33-25VC (128 KB) devices upset between 9,090 and 46,600 hours.
Mitsubishi M5M5V408BFP-85HI (512 KB) devices upset between 1,660 and 2,620 hours.
Cypress CY62128VL-70SC (128 KB) devices upset between 29.7 and 27,400 hours.
Cypress CY7C1399V-15VC (32 KB) devices upset between 22,300 and 28,860 hours.

The prototype test set was used to test the following 5V devices.

Cypress CY7C109B-15VC (128 KB) devices upset between 7,060 and 63,800 hours.
Cypress CY7C109B-12VC (128 KB) devices upset between 21,200 and 33,500 hours.
Hitachi HM628512BLP-7 (512 KB) devices catastrophically failed. Three out of four devices tested burnt out. The failure mode is single-event-burnout. One device survived with an upset rate of 5,780 hours. Prior to catastrophic failure a device upset rate of 5.7 hours was determined.
Hitachi HM628512CLP-7 (512 KB) devices upset between 3,590 and 90,440 hours.
Sony CXK581020SP-35 (128 KB) devices upset between 110,000 and 240,000 hours.
These highly resilient Sony parts were manufactured approximately 12 years ago. They are now obsolete.

BAE SYSTEMS tested a static random access memory based field programmable gate array alternately configured t run a traditional and a fault tolerant processor architecture. The results of testing the FPGA with two comparative architectures is given below. Overall, the traditional architecture failed 8 out of 17,811 tests. Overall, the tolerant architecture failed 2 out of 17,812 tests. More test data would be required to see the expected trend in failure rate versus operating frequency. It would be wise to test more samples in order to determine sensitivity within a batch.

Experiment Report (contd)

BAE SYSTEMS performed an additional study by placing an active pixel sensor at the back of the beam-line to view "tracks" caused by secondary particles. Many interactions were captured. The sensor degraded gracefully over a couple of days exposure.

BAE SYSTEMS will issue three full technical internal reports and lodge a copy of each with LANSCE. The report reference numbers are:-

a) Cosmic Radiation Testing of Commercial Static Random Access Memories, BAE-WEL-RP-GEN-100730, Issue 1 December 2002.
b) Cosmic Radiation Testing of a Tolerant Processor Architecture, BAE-WEL-RP-GEN-100729, Issue 1, December 2002.
c) High Energy Neutron Radiation Testing of a Silicon Active Pixel Sensor, BAE-WEL-RP-GEN-100751, Issue 1, January 2003.

Most errors were single bit or double bit errors – these can be designed around using error detection and correction logic and voting mechanisms. Single event burnout occurs to sensitive devices – even with good power supply design. The use of commercial devices in a high cosmic radiation environment in safety involved systems implies the need to screen them on a batch basis to exclude devices with a burnout and latch-up propensity. Further work is required to show the effect of system architecture on system upset rates; for example different data coding techniques and different frequency of operation.

SAAB tested 24 different SRAM's in their own test set, which may test up to 8 devices at a time. From each of the 24 SRAM's there were 4 to 8 individual samples. The SRAM's were of different process technologies (PT), supply voltage, size and manufacturer s. The PT ranged from 0.16 to 0.25 µm. The sample supply voltage was 1.8, 2.5 or 3.3V The 0.25 µm SRAM's using 3.3V power supply yield low single event upset rate (SER) comparable to the Cypress CY7C109B-12VC(5V), Hitachi HM628512BLP-7(5V) and CY7C1009V33-25VC(3.3V) of 0.25, 0.35 and 0.42 µm PT, respectively, measured by BAE SYSTEMS. However, and most importantly, the 0.18 and 0.16 µm PT showed a large increase in SER, indicating a change in trend. SER was greatest for 0.16 µm PT. If this trend continues the electronic industry may encounter problems when going to smaller PT's especially for bulk SRAM's. This exponential trend for SER predicts SER for 0.1 µm PT to almost 1E-9 errors per bit and hour at 10 km altitude, corresponding to flux of 2 neutrons per cm^2 and second. Moreover, the voltage dependence was surprisingly weak for the 0.16 µm PT compared to larger PT's.
This test at WNR will hopefully be presented at NSREC conference in July 2003, both orally and in paper form.

LANSCE
Los Alamos Neutron Science Center

REPORT ON EXPERIMENT
(Please Type)

Submit all experiment reports to:
LANSCE User Office, MS H831, Los Alamos National Laboratory, Los Alamos, NM 87545

Experiment was carried out at:	**Local Contact**	**Proposal #**	***LANSCE Use Only***
☐ Manuel Lujan Jr. Neutron Scattering Center	B. Takala	2002502	**Report Rc'd**
☐ Weapons Neutron Research Facility	**FP/Instrument Used**		**3/21/03**
☐ WNR/Blue Room	4FP30L		

Title
Neutron SEU and SEL Testing of Commercial SRAMs and Logic Devices

Authors and Affiliations
Keith Forbes, Vincent O'Sullivan, Rodney Kadura, Stephen Wong, Motorola, Semiconductor Products Sector

Experiment Report

Introduction

Cosmic-ray induced soft-error rates (SER) are an increasing concern for microelectronic memory devices. As the size of embedded memories increase, bit cell capacitances decrease and supply voltage decrease, susceptibility to SER becomes increasingly important. The purpose of these experiments was to obtain neutron SER on a variety of products and test vehicles to characterize SER trends for changing semiconductor process technology. A major advantage of the WNR Facility is that the energy spectrum of neutrons is tuned to that for terrestrial neutrons substantially simplifying accurate extrapolations to operating conditions. All accelerated SER measured were extrapolated to NYC conditions according to JEDS89.

Experiments were performed on devices with 150, 130, 90 and 60 nm nominal poly lengths. Both real products and test vehicles were used. This allows us to characterize SER for customer applications and also gain early learning for products manufactured with future process technologies.

Diagnostic boards were mounted upright and perpendicular to the neutron beam. Multiple devices are tested at one time by stacking test boards in the path of the beam.

MPC8245 Testing

Tests were performed on single MPC8245 devices. This data will be correlated with system-level SER tests in a sub-system that use this device to better understand how customer applications affect SER performance.

The MPC8245 devices were tested in a SandPoint X3 test system at nominal voltage. Memory arrays in this device were tested separately and are plotted in Figure 1. Arrays 1 and 2 contained more than 130kbits of memory; arrays 3, 4 and 5 contained just over 13kbits of memory. Thus statistically significant analysis of arrays 3, 4 and 5 is limited due to the comparatively lower number of hits. A test pattern dependence is evident in this data suggesting asymmetry in the device design. Also so memory arrays have increased SER susceptibility. This data provides useful information to correlate device design to SER performance.

MPC8202 Testing

Four MSC8202 devices from four separate process lots were tested. A MSC8102ADS diagnostic board served as the test hardware. Failing bits were monitored at regular intervals during the test and the test was completed after a minimum of 250 single event upsets (SEU) was observed.

Experiment Report *(continued)*

The SER observed for the MSC8202 device is shown in Figure 2. No significant variations were observed with changing test patterns or between devices from different lots. The voltage dependence of this device was also characterized; increased SER susceptibility at 1.4V (200mV below nominal) demonstrates the operation limits of this device.

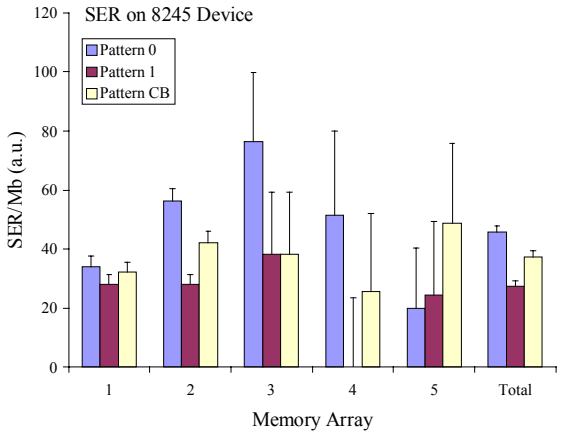

Figure 1: SER Measured on different memory arrays on the same device.

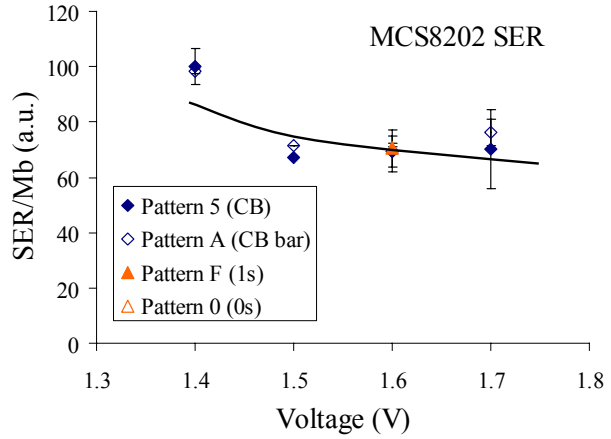

Figure 2: SER measured as a function of supply voltage on a 1.6V nominal device.

TDSRAM Testing

A 4Mbit test vehicle was used to characterize SER sensitivity for various different processes. The TDSRAM setup uses two parallel test boards. Devices are mounted so that up to eight devices (4 per board) are exposed to the 80cm diameter beam at one time.

Seven different transistors were tested; some transistors were tested with different bit cell layout. The various transistors and bit cells can be scaled according to the stored charge for the memory node. In figure 3, the results from the different transistors are plotted together in this manner. There is some decrease in SER susceptibility observed in transistors 2 and 3 compared to transistors 1, 4, and 5. Differences in the process used for these transistors appear to explain these effects.

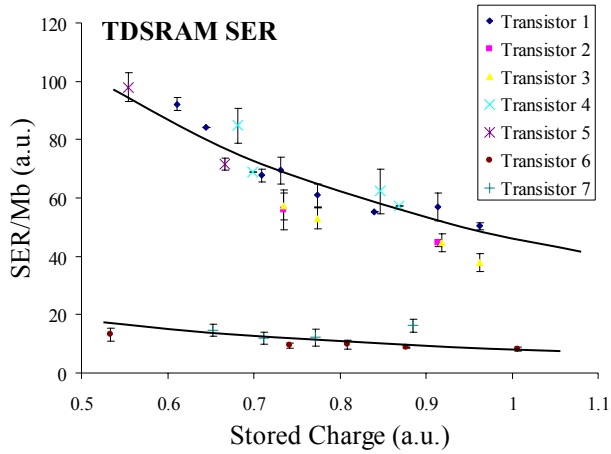

Figure 3: SER for various transistors on the same 4Mb test vehicle.

The decreased SER susceptibility for transistors 6 and 7 is more striking. These transistors provide the first look at silicon on insulator (SOI) technology, suggesting improved SER for SOI products.

These TDSRAM results provide a clear overview of many process effects. This will information will be used to calibrate models and improve device design for future products.

Conclusions.

These tests characterized the SER of various shipping and future products. Trends in for test pattern dependence, memory array, voltage and process technology where studied. This information will be used to develop models for SER predictions as well as to provide customer characterization of product SER performance.

IMPORTANT! List or attach a list of publications resulting from this experiment (published or in press).

Publication in process: P. Roche, K. Forbes, V. O'Sullivan, G. Gasiot and V. Ferlet, Comparison of Soft Error Rate for SRAMs in Commercial SOI and Bulk below the 130nm Technology Node to be presented at the 2003 IEEE Nuclear and Space Radiation Effects Conference.

LANSCE
Los Alamos Neutron Science Center

REPORT ON EXPERIMENT
(Please Type)

Submit all experiment reports to:
LANSCE User Office, MS H831, Los Alamos National Laboratory, Los Alamos, NM 87545

Experiment was carried out at:	**Local Contact**	**Proposal #**	***LANSCE Use Only***
☐ Manuel Lujan Jr. Neutron Scattering Center	S. Wender/B. Takala	**2002504**	**Report Rc'd**
☐ Weapons Neutron Research Facility	**FP/Instrument Used**		**1/29/03**
☒ WNR/Blue Room	Blue Room		

Title

Mercury Target Thermal Shock Tests

Authors and Affiliations
John Haines, John Hunn, Bernie Riemer, Chin Chi Tsai
Oak Ridge National Laboratory

Experiment Report

Based on results of previous WNR tests studying cavitation erosion in mercury targets, the SNS team defined a process and deadline for making a final decision on whether to maintain mercury as the reference target material. To support this critical decision, 21 targets were tested in the June 2003 WNR tests, including variations in target material, geometry, power level, use of gas injection to mitigate the damage, and number of beam pulses (one test ran for 1,000 pulses, which represents an order of magnitude increase over the nominal 100 pulses). Highly polished plates that formed portions of the target container were used as the primary test specimens to measure the degree of pitting damage.

Pre-test SEM examinations were performed on all of the polished plates. A 5 x 5 array of micro-indentation marks were applied on each plate to serve as fiducial marks for pre- and post-test images. These marks were centered on the plates and spaced on an orthogonal grid with a spacing of 5 mm. Images with magnifications of 100x and 400x were recorded at each mark.

The WNR tests were successfully conducted and the irradiated targets were returned to ORNL for mercury decontamination followed by post-test SEM examinations. Pitting damage was determined using image processing software. The pitting was characterized primarily using two parameters. The first was simply the fraction of area that was damaged. Data are quoted for the worst SEM image found on a specific plate. The second is the mean depth of erosion (MDE) for the SEM image with the worst damage. The MDE was calculated by determining the area of each individual pit on an SEM image, calculating an equivalent radius, and assuming that the pit has a conical shape with a depth equal to its radius. Based on a limited amount of profilometry measurements, this assumption likely overestimates the pit depth by as much as an order of magnitude.

Experiment Report *(continued)*

Results for six of the targets are summarized in Table 1. These data were taken from the front plate of six of the targets that had a rectangular cross-section. The equivalent power level, as scaled from the peak energy density within the target, is shown in this table to facilitate comparisons.

The strong dependence on energy density (power level) is quite remarkable. Reducing the equivalent power level from 2.5 MW to 1.1 MW reduces the mean depth of erosion by more than an order of magnitude. Data for the lowest power level (0.4 MW equivalent) are unreliable since the number of pits in the worst SEM frame is too small to be statistically significant. Increasing the number of beam pulses by an order of magnitude has little effect on the damage, thus indicating a weak dependence on this parameter, consistent with the classical cavitation data in the so-called incubation regime.

Injecting a layer of gas along the front plate also reduced the erosion by more than an order of magnitude. Based on pre-test videos, the gas layer was imperfect, covering the beam interaction region of the plate about 80 % of the time. Improvements in this concept could lead to further reductions in the cavitation damage. Additional tests, not shown in Table 1, with tall, thin targets showed that injection of bubbles reduced the erosion by about a factor of four compared to an equivalent target without bubbles. The bubble injection concept can likely be greatly improved as the first operation of the bubble injection system in this configuration occurred moments before the in-beam test.

The results for the target plate treated with the Kolsterising process showed essentially no pitting damage for the 100-pulse test. This process involves diffusion of carbon in the near surface material thereby insuring that the treatment is graded, i.e. no sudden changes in properties such as those typically encountered with hard coatings. The primary uncertainty in utilizing this treatment is whether or not it maintains its properties after significant irradiation.

The results obtained from this test campaign along with a series of off-line tests formed the basis for deciding to maintain mercury as the baseline target material for SNS.

Table 1. Summary of pitting damage on the front plate of rectangular shaped targets tests at the WNR facility.

Target	Equivalent SNS Power Level (MW)	Fraction of Area with Pits (%)	Mean Depth of Erosion (nm)
TL - High Power	2.5	4.6	132
TM - Medium Power	1.1	0.3	12
TH - Low Power	0.4	0.2	4
KILO - 1,000 Pulse	2.9	3.6	101
BL - Bubble Layer	2.7	0.3	8
K - Kolsterized	3.1	0.03	0.1

All targets, except KILO, exposed to 100 WNR beam pulses

All plates except the Nitronic 60 plate were constructed from 316 type stainless steel

IMPORTANT! List or attach a list of publications resulting from this experiment (published or in press).

Haines, J. R., et al., "Overview of the R&D Program for the Spallation Neutron Source Target," 11th International Conference on Nuclear Engineering, Tokyo, Japan, April 2003, ICONE11-36570.

LANSCE
Los Alamos Neutron Science Center

REPORT ON EXPERIMENT
(Please Type)

Submit all experiment reports to:
LANSCE User Office, MS H831, Los Alamos National Laboratory, Los Alamos, NM 87545

Experiment was carried out at:	**Local Contact**	**Proposal #**	***LANSCE Use Only***
☐ Manuel Lujan Jr. Neutron Scattering Center	John Ullmann	2002505	**Report Rc'd**
☒ Weapons Neutron Research Facility	**FP/Instrument Used**		**12/2/2002**
☐ WNR/Blue Room	4FP15R		

Title
Cross Section Measurements for Cosmic Ray Studies Using Neutrons

Authors and Affiliations
Janet Sisterson, Northeast Proton Therapy Center, Massachusetts General Hospital.
John Ullmann, LANSCE, Los Alamos National Laboratory

Experiment Report
We were scheduled 11 days of beam time in 4FP15R from July 21 to July 31 2002. Two separate irradiations were made.

Aim of the Experiment

The primary goal was to measure average spallation cross sections for reactions initiated by neutrons in Mg, SiO_2 for oxygen) and Ca targets using a white neutron beam with an energy range of ~0.1 – 750 MeV. Mg, O and Ca are elements found in both meteorites and the lunar surface. These cross sections are needed to understand the interactions of cosmic rays with extraterrestrial materials. We made two runs. The first run was quite short and SiO_2 targets were irradiated. The second run used the majority of the allocated beam time and metallic Mg, and $CaCO_3$ targets were irradiated. Al, Cu, Ni and Au monitor foils were included in the target stacks.

The primary cross sections that we want to measure are Mg(n,x)Ne, Mg(n,x)^{14}C, Mg(n,x)^{22}Na and Ca(n,x)Ar. No cross section measurements have been reported for these neutron-induced reactions. SiO_2 was irradiated to measure the cross section O(n,x)^{14}C. The ^{14}C produced in the targets will be measured using Accelerator Mass Spectrometry (AMS) by Dr A. J. T. Jull at the University of Arizona. In 1998 we had irradiated SiO_2 targets to measure this cross section but unfortunately the target 'exploded' during the AMS measurement and no ^{14}C was collected. A new AMS line has been built and the targets irradiated in 2002 will be analyzed using the new AMS line. The yield of neon and argon isotopes will be measured by Dr. Marc Caffee, who was formerly at the Lawrence Livermore National Laboratory.

A secondary aim of these experiments is to identify reactions to use as monitor reactions in future experiments in this beam line. In this run we used the uranium fission chamber to directly monitor the neutron fluence. This will give us a calibration for these monitor reactions, which could be used in later runs in 4FP15R in the same irradiation position under conditions when the uranium fission chamber could not be used. We will compare our measurements of cross sections induced in Cu monitor foils and those measured using quasi-monoenergetic neutron beams at iThemba LABS, Somerset West, South Africa to published cross sections [1]. Preliminary measurements for these cross sections made at iThemba LABS differ by about a factor of two from these published cross sections.

Experimental conditions: Targets: The Mg target was made up of three 50 x 50 mm, 3 mm thick metallic plates. $CaCO_3$ is a white powder. Targets were made by packing the powder into an aluminum weighing dish covering it with aluminum foil and then sealing the package with masking tape. Each target weighed 17-20g, which meant that the effective target density was ~1g/cm^3. The target diameter was 41 mm at the base (the downstream surface) and 44 mm at the top, the upstream surface. The $CaCO_3$ target was placed behind the Mg target stack. In the other irradiation, three 50 x 50 mm, 1mm thick SiO_2 targets were irradiated plus monitor foils.

Experiment Report *(continued)*

The 15 mm diameter monitor foils of Ni (0.1 cm thick), Al (0.1 cm thick), Cu (0.1 cm thick), and Au (0.025 cm thick) were attached to the downstream surface. The entire target stack was wrapped in carefully in aluminum foil, Additional aluminum foil and masking tape were used to 'square-off' the package to make it easier to hold in the target holder.

Beam line: This was the second time that we had used 4FP15R for our irradiation. To get a beam big enough to entirely cover the targets, a collimator made up of ~2.5 feet of donuts with a 2-inch diameter hole were placed just downstream of the X and Y jaws. To reduce the number of low energy neutrons, 2 inches of polyethylene were placed well upstream in flight path 15R. The neutron dose outside downstream of the target was initially high. To reduce this to acceptable levels, the beam pipe downstream of the target was removed.

Irradiation set-up: The existing equipment in place in the irradiation position in 4FP15R constrained the location of our target holder to a position about 2 meters downstream of the fission chamber. Image plates were used to center the target holder with the beam and to center the target stack in the beam. This location is about 10 m upstream of our previous irradiation position in 4FP15L so that the penumbra of the beam is much larger in this irradiation position.

Irradiation: The proton beam current on the tungsten target was ~3 - 4 microA throughout the irradiations. There were several significant periods of no beam and on the whole the beam was relatively unstable. The target stack was designed to keep the neutron attenuation through the target stack generally <10% with the possible exception of energies < 1 MeV.

The WNR beam operation logs were used to record all periods of no beam > ~15 minutes. This information is used to determine an 'actual' beam on time for the target irradiation, and appropriate corrections made for all the short-lived radionuclides produced. The actual periods of beam on were 31.22 hours for the SiO_2 target irradiation and 158.6 hours for the $Mg/CaCO_3$ target irradiation.

Experimental results:

Fluence calculations: These are still in progress.

Yield of short-lived radionuclides: Short-lived radionuclides are measured in the monitor foils using non-destructive gamma-ray spectroscopy both at LANSCE and at the Northeast Proton Therapy Center (NPTC), Massachusetts General Hospital. We cannot measure the cross section for the reactions, $Ca(n,x)^{22}Na$ because of the large production of ^{22}Na in the aluminum holder.

Several different counting conditions are used at both LANSCE and NPTC. Counting periods ranged from a few hours to several days. If possible each foil is measured at least twice. The isotopes identified include: ^{7}Be, $^{22,24}Na$, $^{46,48}Sc$, ^{48}V, ^{51}Cr, $^{52,54}Mn$, $^{56,57,58,60}Co$, and $^{56,57}Ni$. A third measurement is made on the Ni and Cu foils after ~1 month to separate the contributions from $^{48}Sc/^{48}V$, $^{56}Ni/^{58}Co$ and $^{48}Sc/^{56}Co$. Corrections are made for the finite size of the foils and the foil thickness. These corrections are dependent on the counting configuration.

Yield of long-lived radionuclides: The targets will be sent for analysis in the near future.

References: [1] E. J. Kim et al., (1999) J. Nucl. Sci. Tech. 36, 29-40.

Publications:

There are no new publications at this time. A presentation will be made at the 34th Lunar and Planetary Science meeting to be held in March 2003.

IMPORTANT! List or attach a list of publications resulting from this experiment (published or in press).

LANSCE
Los Alamos Neutron Science Center

REPORT ON EXPERIMENT
(Please Type)

Submit all experiment reports to:
LANSCE User Office, MS H831, Los Alamos National Laboratory, Los Alamos, NM 87545

Experiment was carried out at:	**Local Contact**	**Proposal #**	***LANSCE Use Only***
☐ Manuel Lujan Jr. Neutron Scattering Center	Steve Wender	2002507	**Report Rc'd**
☒ Weapons Neutron Research Facility	**FP/Instrument Used**		**11/14/2002**
☐ WNR/Blue Room	FP30L		

Title
NEUTRON-INDUCED SINGLE EVENT CHARACTERIZATION OF 0.8-, 0.35- AND 0.18-MICRON CMOS TECHNOLOGY INTEGRATED CIRCUITS

Authors and Affiliations
John Browning, Phil Federico; Sandia National Laboratories
Mike Tucker; Alpha Sciences Inc.

Experiment Report

This report describes the accelerated single event rate (ASER) testing of six CMOS SRAM device types, and summarizes the results of these tests. The tests were designed and executed to comply with the requirements and procedures for soft-error rate testing of the JEDEC Standard, "*Measurement and Reporting of Alpha Particles and Terrestrial Cosmic Ray-Induced Soft Errors in Semiconductor Devices*," JESD89, dated August 2001.

A variety of device technologies were tested, spanning a range of feature sizes from 0.8 to 0.12 microns (Figure 1), and the per bit upset cross section was measured for each device under test (DUT) across the operating voltage range for each device (Figure 2). A minimum of two parts per wafer lot was tested. The tester used was the JD Instruments Algorithmic/Test Vector (ATV) portable tester, which was cabled to a motherboard with sockets to fit up to twelve DUT test cards. A test card specifically for each DUT was designed, with the capability of fitting up to six devices on one test card. Each test card was monitored individually. Test conditions included static and dynamic operations, as well as monitoring the power supply current for latchup.

In Figure 2 it can be seen that the per bit upset cross section decreases with decreasing feature size down to about 0.2 microns, as would be expected as the ramcell areas are decreasing with decreasing feature size. However, at about 0.2 microns feature size the per bit upset cross section stops decreasing and then begins to increase with decreasing feature size.

Statistically, the word error count and the bit error count would be expected to be the same for a small number of upsets (one upset per several thousand bits). For the DUT with feature sizes of 0.8 and 0.35 microns, the word error counts and bit error counts were almost identical. However, as can be seen Figure 3, for the DUT with features sizes of 0.12, 0.15, and 0.18 microns (all biases) and 0.25 microns (biases of 2 volts or less), the bit error count was greater than the word error count, suggesting that multiple bits were upset from single neutron interactions.

Using the measured per bit upset cross sections, the soft error rate (New York City baseline) for terrestrial cosmic ray-induced upsets has been estimated for the six CMOS SRAM part types. Figure 4 is a graphical representation of the results in terms of FIT (failures per billion device-hours). From Figure 4 it can be seen that the overall device reliability is significantly impacted by the presence of multiple bit upsets.

Experiment Report (continued)

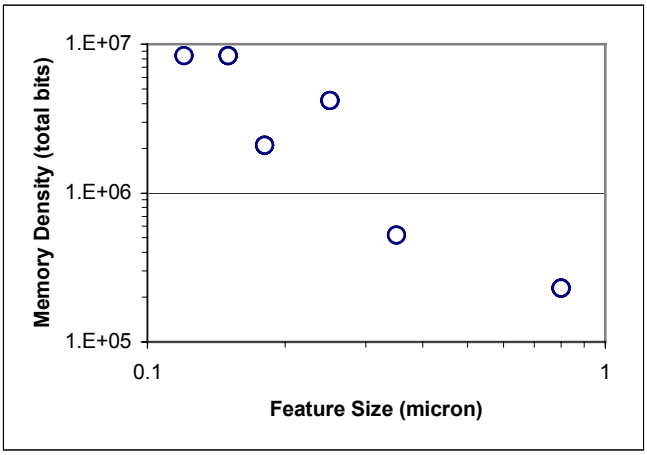

Figure 1. Summary of DUT Characteristics.

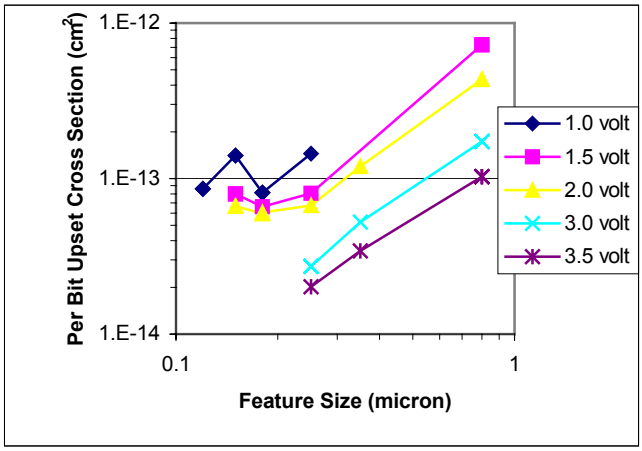

Figure 2. DUT Upset Susceptibility

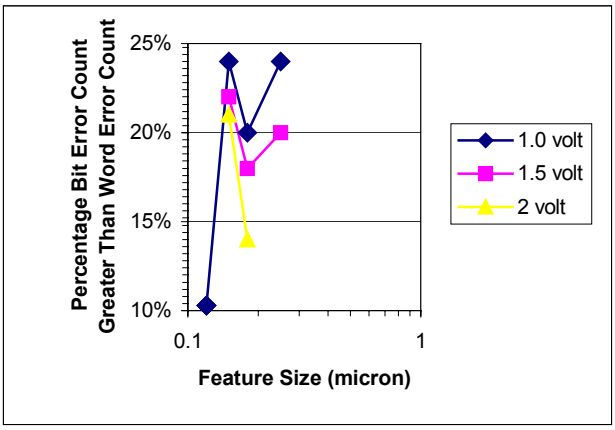

Figure 3. Evidence of Multiple Bit Upsets.

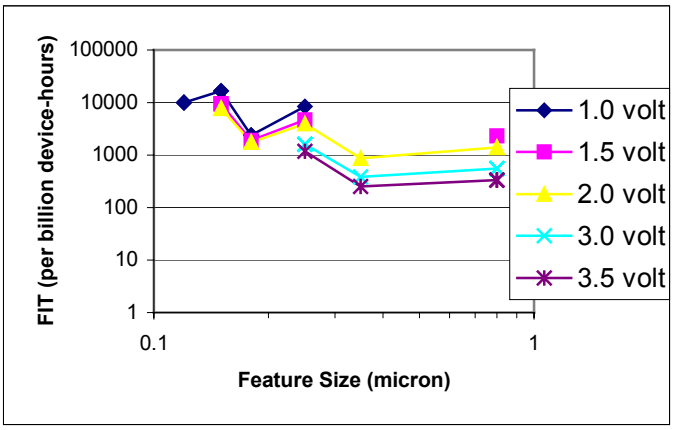

Figure 4. Summary of Device Reliability.

IMPORTANT! List or attach a list of publications resulting from this experiment (published or in press).

Never stop thinking

Customer Information

Soft Errors of SDRAMs

Creation

Status:	Version C
Date / Version:	21.10.2002
Author:	Günter Schindlbeck
Approver:	Hans-Peter Klein

Contact

Department:	MP QM
Address:	Balanstrasse 73 81541 München, Germany guenter.schindlbeck@infineon.com

Summary / Keywords

- Soft Error Rate
- Single Event Upset
- Alpha Particle Test
- Neutron Beam Test
- Cosmic Radiation
- Accelerated Soft Error Test
- System Soft Error Test

Content

1 DEFINITION OF SOFT ERRORS 3
2 SOURCES OF SOFT ERRORS 3
3 NOMENCLATURE 3
4 SOFT ERROR TESTS 4
4.1 Accelerated Tests 4
4.1.1 ASER Tests 4
4.1.2 NSER + TSER Tests 4
4.2 System Test 4
5 CONCEPT FOR LOW SOFT ERROR RATE 5
6 SOFT ERROR MODEL 6
6.1 Relative Comparison of the Susceptibility of Components to Ionizing Radiation 6
6.2 Overall SER test 6
6.3 Evaluation of the SER 6
7 ACTUAL RESULTS 6
7.1 SSER Test with 64M S20 SDRAMs 6
7.2 SSER Test with 256M S17 SDRAMs 6
7.3 SSER Test with 256M S14 SDRAMs 7
7.4 SER Calculated from ASER Tests 7
7.5 SER Calculated from NSER Tests 7
7.6 Complete Soft Error Situation 8
8 EFFECTS ON THE SER 9
8.1 Comparison of Design Steps Via ASER Tests 9
8.2 Effect of Cycle Time on ASER and NSER Results 11
8.3 Effect of the Alpha Source 11
8.4 Effect of Elevation 12
9 HISTORY OF ASER VALUES OF DRAMS 13
10 REFERENCES 13

This work has benefited from the use of the Los Alamos Neutron Science Center at the Los Alamos National Laboratory. This facility is funded by the US Department of Energy under Contract W-7405-ENG-36.

1 Definition of Soft Errors

Soft errors are non-destructive disturbances of information in integrated circuits induced by ionizing radiation. In order to highlight the difference from “Total Dose Defects” (TDD), the term “Single Event Upset” (SEU) is also used. Most TDDs are soft errors. Sometimes latch-up, gate rupture, etc. also occur as single-event defects, but usually they are several orders of magnitude less frequent than soft errors.

Soft errors are temporary, not permanent malfunctions. They do not affect the long-term reliability of devices.

2 Sources of Soft Errors

Soft errors are produced by radiation with a sufficiently high ionization rate. In terrestrial applications there are three main sources of soft errors. One source is alpha particles from traces of uranium and thorium with their daughter products, which are present in most IC materials. Two other sources are high-energy neutrons from cosmic radiation and thermal neutrons from cosmic radiation and terrestrial sources.

3 Nomenclature

SER	Soft error rate in the field (for operational conditions of components in systems)
ASER	Proportion of the SER from alpha particles (tested in accelerated tests with alpha sources)
NSER	Proportion of the SER from cosmic radiation (tested in accelerated tests with high-energy neutrons)
PSER	Proportion of the SER from cosmic radiation (tested in accelerated tests with high-energy protons)
TSER	Proportion of the SER from thermal neutrons (from cosmic radiation and terrestrial sources, tested in accelerated tests with thermal neutrons)
SSER	Result of non-accelerated tests with components where all possible sources of soft errors are active (usually called “system soft error rate”)

4 Soft Error Tests

4.1 Accelerated Tests

Accelerated tests are performed at a greatly increased flux of ionizing radiation. This enables rates and signatures of soft errors to be evaluated and the effects of test conditions and radiation parameters assessed in reasonable time.

4.1.1 ASER Tests

We test the ASER using a Radium-226 alpha source. In accelerated tests, devices are irradiated during dynamic operation. For tests with alpha particles, it must be ensured that the particles are not shielded from the active regions of the DUT (device under test). This is necessary because of the relatively short range of alpha particles in matter (typically about 25 micrometers in silicon for a particle energy of 5 MeV). During measurements the alpha source is therefore placed directly on top of an open device. If devices use special packaging technologies such as “lead on chip”, the dies have to be mounted in lidless ceramic packages for tests.

4.1.2 NSER + TSER Tests

We perform combined NSER +TSER tests with the WNR neutron beam at the Los Alamos National Laboratory.

Tests are performed at the minimum specified Vcc voltage level at room temperature.

Various data patterns and cycle times are used, but standard conditions are logical checkerboard plus inverted logical checkerboard and the minimum possible cycle time.

A WORM (“Write Once, Read Many”) test pattern is used to ensure that no “escapes” can occur during testing and all soft errors are detected.

4.2 System Test

In system tests, all sources of soft errors are active (alpha particles from IC materials, high-energy neutrons and thermal neutrons from cosmic radiation). The devices under test are operated under well-defined conditions. Several thousand devices have to be operated in parallel for several weeks (e.g. 5 million device hours). The result simulates the soft errors which occur during dynamic operation of devices in the field.

Special test patterns and test routines have to be used to ensure that all soft errors are detected and that system errors can be separated from soft errors due to ionizing radiation.

Usually logical checkerboard and inverted logical checkerboard are used for tests. For Vcc, the minimum specified voltage level is applied. Ambient temperature in the test chamber is 70°C. The cycle time (activate + write/read + precharge) is 300 ns. The test pattern is WORM.

5 Concept for Low Soft Error Rate

Infineon uses special techniques to reduce the susceptibility of its SDRAMs to ionizing radiation.

One reason for the low SER of our devices is the concept of the storage cell. We use “trench cells with internal charge”, which are extremely resistant to ionizing radiation.

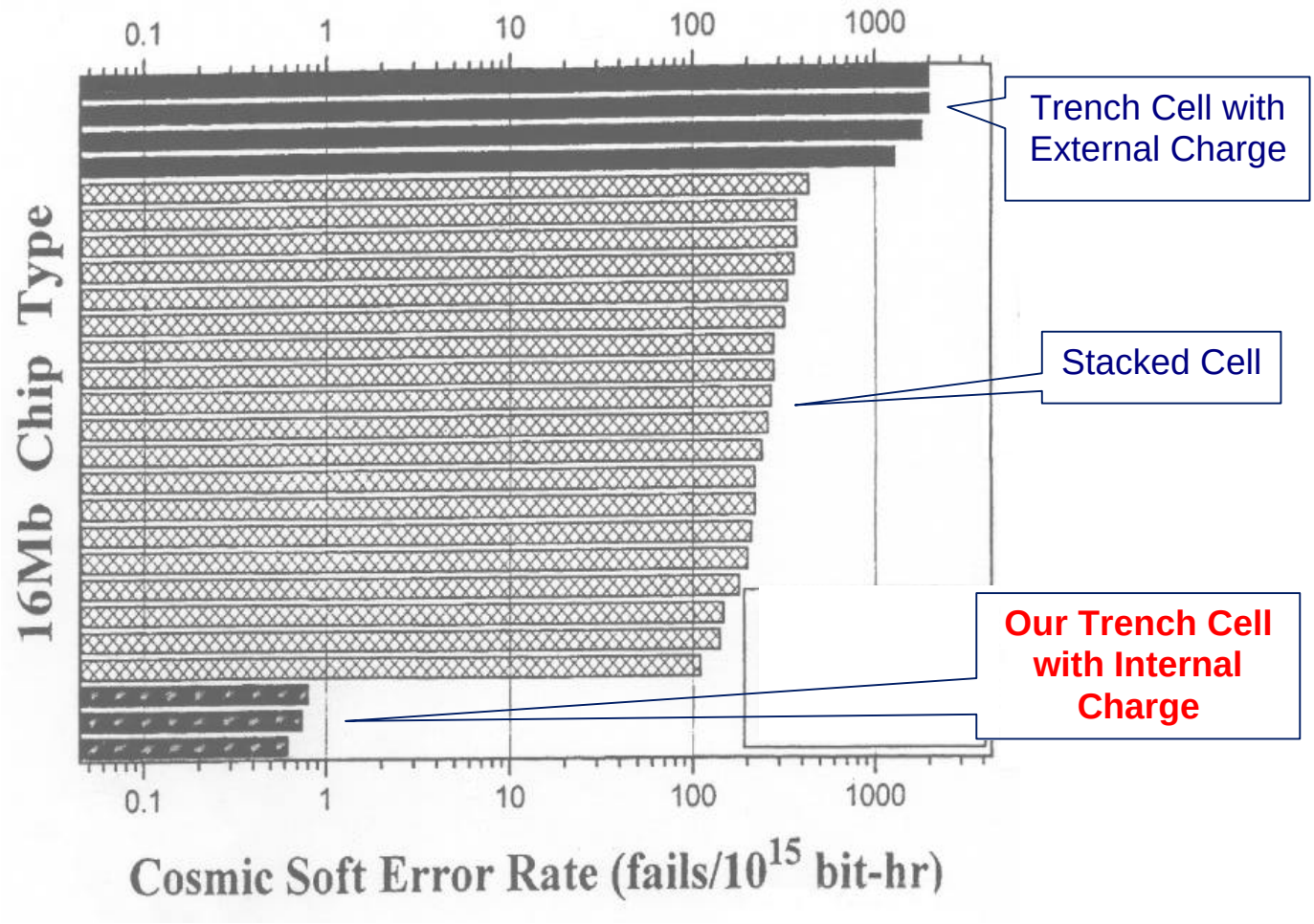

(Results from J.F. Ziegler et al, IBM, 1998) /2/

A second method of reducing the SER is employed in the layers of the silicon substrate.
A positively charged “buried n-well” is located below the negatively charged “deep p-well”.
Ionizing radiation generates electron-hole pairs. Electrons from this charge are collected by the

buried n-well so that they do not affect the charge in active areas near the surface of the semiconductor.

6 Soft Error Model

6.1 Relative Comparison of the Susceptibility of Components to Ionizing Radiation

We compare our components after all major changes in design or process with their predecessors using ASER tests.

6.2 Overall SER test

SSER tests are used to ensure a sufficiently low SER of our components from all possible sources of soft errors.

6.3 Evaluation of the SER

To calculate the actual value of the SER, we perform ASER tests and neutron beam tests (NSER + TSER).

7 Actual Results

7.1 SSER Test with 64M S20 SDRAMs

In a test on 3823 devices from 5 lots over 7.42 million device hours, no soft error was detected. We were therefore able to demonstrate a

SER < 125 FIT (60% C.L.).

Test conditions were 300 ns cycles for complete write/read operations, ambient temperature of 70°C, supply voltage level of 3.0 V, physical checkerboard and inverted checkerboard for data pattern, and WORM test pattern (Write Once, Read Many).

7.2 SSER Test with 256M S17 SDRAMs

7012 components from 5 lots were tested in two SSER tests up to a total of 14.14 million device hours. No soft error was detected during these two runs. This corresponds to a

SER < 65 FIT (60% C.L.).

Test conditions were also 300 ns for complete write/read operations (activate, write/read, precharge), ambient temperature of 70°C, Vcc = 3.0 V, physical checkerboard and inverted

checkerboard data pattern, and WORM test pattern. The tests were performed in Malacca/Malaysia (longitude = 103° east, latitude = 2° north, elevation = 0 = sea level).

7.3 SSER Test with 256M S14 SDRAMs

2512 components from 1 lot were tested. In 8 million device hours, no soft error could be detected. This corresponds to a

SER < 115 FIT (60% C.L.).

With one exception, test conditions were the same as for 256M S17. Instead of a physical checkerboard data pattern, a logical checkerboard was used.

7.4 SER Calculated from ASER Tests

For 150 ns cycle time (complete read/write operation), Vcc = 3.0 V, logical checkerboard data pattern, room temperature, 60% C.L.

256M SDRAM Design Step	**S17**	**S14**
Calculated SER	**< 0.2 FIT**	**< 0.02 FIT**

7.5 SER Calculated from NSER Tests

For the New York location , sea level, PC 133 timing with 75 ns for complete write/read operations (7.5 ns clock cycle), Vcc = 3.0 V, logical checkerboard data pattern, room temperature, 60% C.L.

256M SDRAM Design Step	**S17**	**S14**
Calculated SER	**< 17 FIT**	**< 11 FIT**

7.6 Complete Soft Error Situation

For comparison purposes, all SER values were standardized to the value of the cosmic radiation at **New York** City and a cycle time of **75 ns** for a complete write/read operation (7.5 ns clock cycle; 60% C.L.). Vcc = 3.0V and data pattern is logical checkerboard.

SSER (system test) only came down to a SER somewhere below 500 or 900 FIT for the worst-case condition. The gap between the minimum achievable value from SSER tests and the real SER values could only be bridged using accelerated tests (ASER and NSER). The results proved that the SER of our 256M SDRAMs is dominated by cosmic radiation, not by alpha particles.

256M SDRAM Design Step	**S17**	**S14**
from SSER (70°C)	**< 491 FIT**	**< 868 FIT**
from ASER (20°C)	**£ 0.4 FIT**	**£ 0.04 FIT**
from NSER (20°C)	**£ 16.2 FIT**	**£ 10.2 FIT**
Total SER	**£ 17 FIT**	**£ 11 FIT**

8 Effects on the SER

8.1 Comparison of Design Steps Via ASER Tests

The comparison showed that all subsequent design steps (64M S19, 128M S19/S17, 256M S17) are significantly less susceptible to ionizing radiation than the 64M S20.

This is mainly due to the optimized geometry of the sense amplifiers.

“Box and whisker” plot of ASER results for different design steps of SDRAMs.

Test conditions:	Complete write/read cycle	150 ns
	Data pattern	Phys. checkerboard + inverted ph. ch.
	Vcc	3.0 V
	Ambient temperature	20°C
	Test pattern	WORM (Write Once, Read Many)

Comparison of ASER values of 3 design steps of the 256M S14 component generation show the enhancement of the S14 DD2 and the SD14 (double data rate) compared with the previous step S14 DD1 (caused by design improvements).

Test conditions as before but logical checkerboard instead of physical checkerboard for data pattern.

8.2 Effect of Cycle Time on ASER and NSER Results

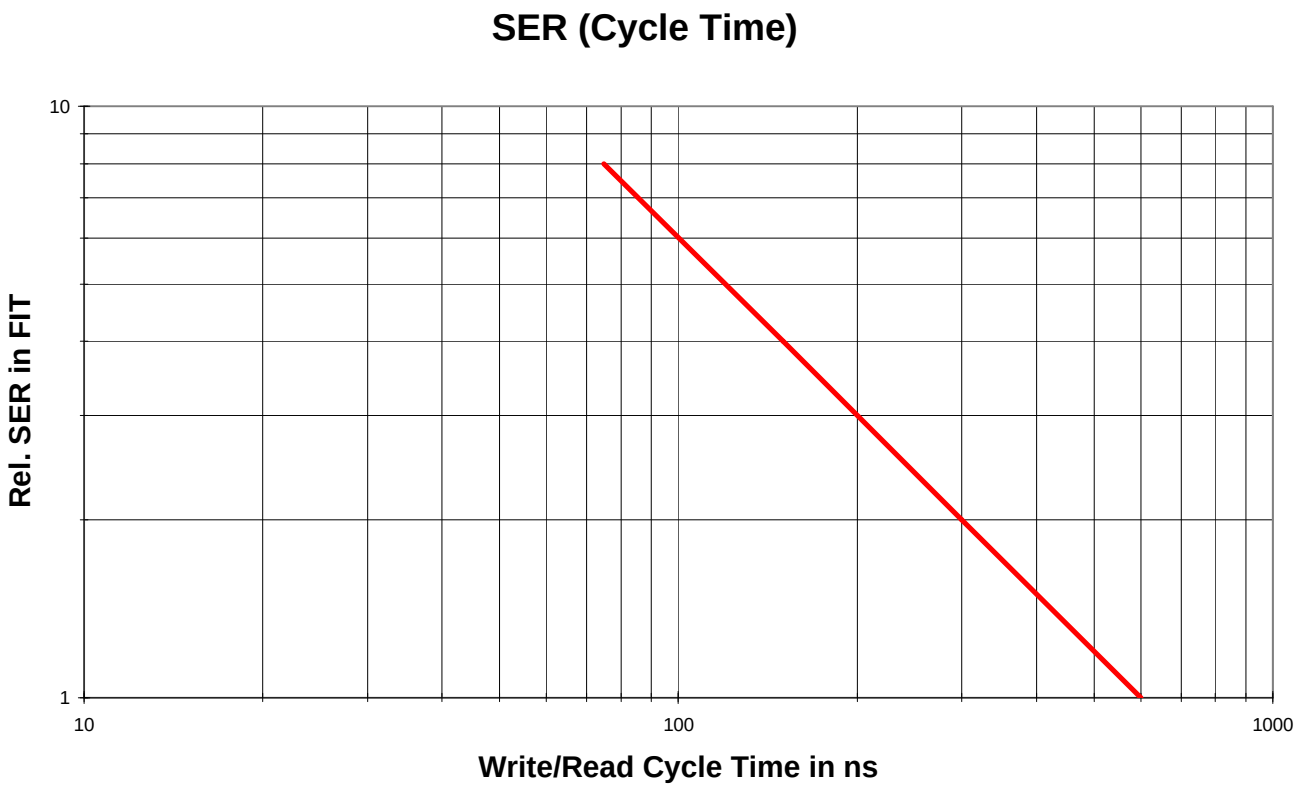

The strong dependence of ASER and NSER values on cycle times indicates that bit line / sense amplifier hits are chiefly responsible for soft errors. Cell hits and hits in peripheral circuits are of minor influence.

8.3 Effect of the Alpha Source

Tests showed that our Ra-226 source produces ASER values which are slightly over 300 times higher than natural Th-232. This helps us keep the duration of ASER tests in the order of hours rather than weeks.

8.4 Effect of Elevation

The neutron flux from cosmic radiation increases with elevation. The proportion of the SER from cosmic radiation is proportional to this neutron flux.

Shown here is the relative neutron flux from sea level to an elevation of 5000 m above sea level, calculated using the “IBM method” /1/.

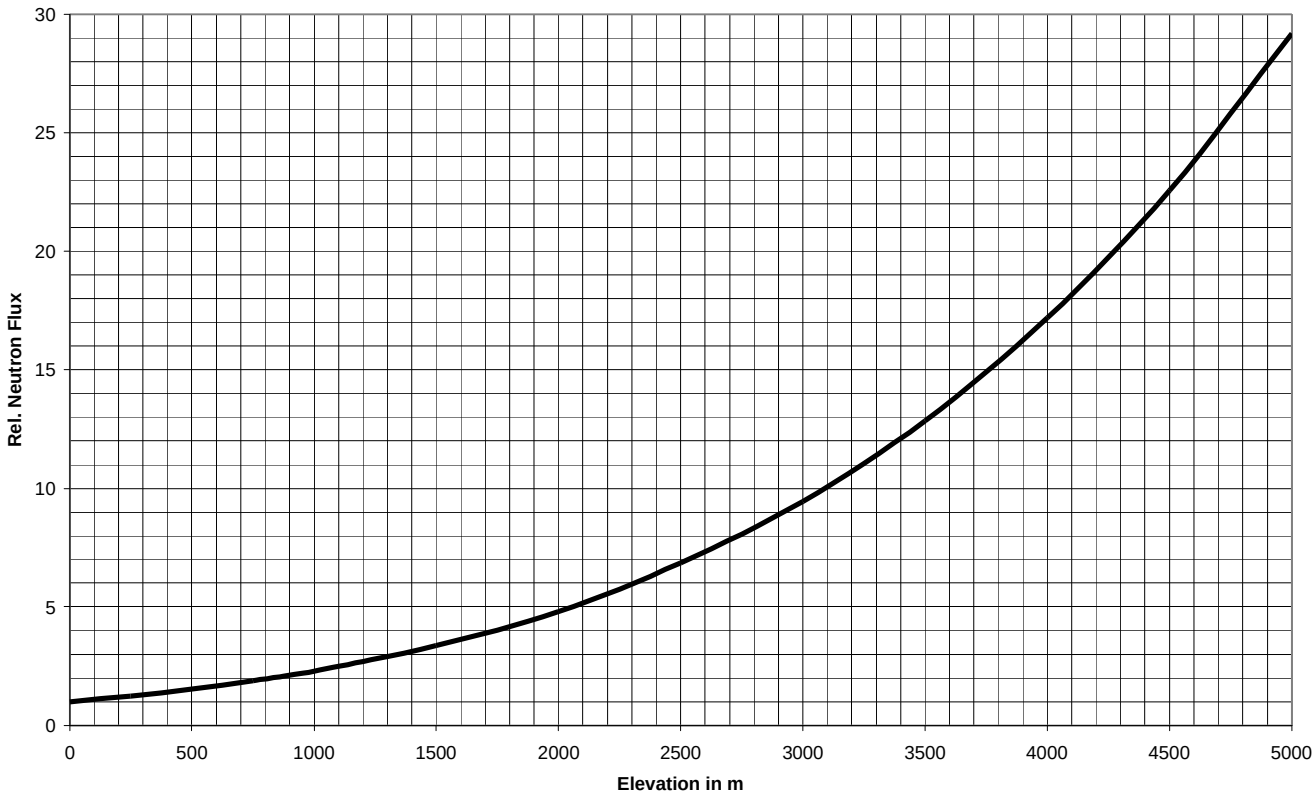

9 History of ASER Values of DRAMs

The ASER per Mb dropped about 8 orders of magnitude in 7 steps from 16M to 256M DRAM. The main reason for this improvement is the ever-decreasing area of the storage cells with a nearly constant storage capacity of about 30 fF. The remaining improvement was due to improved designs and processes.

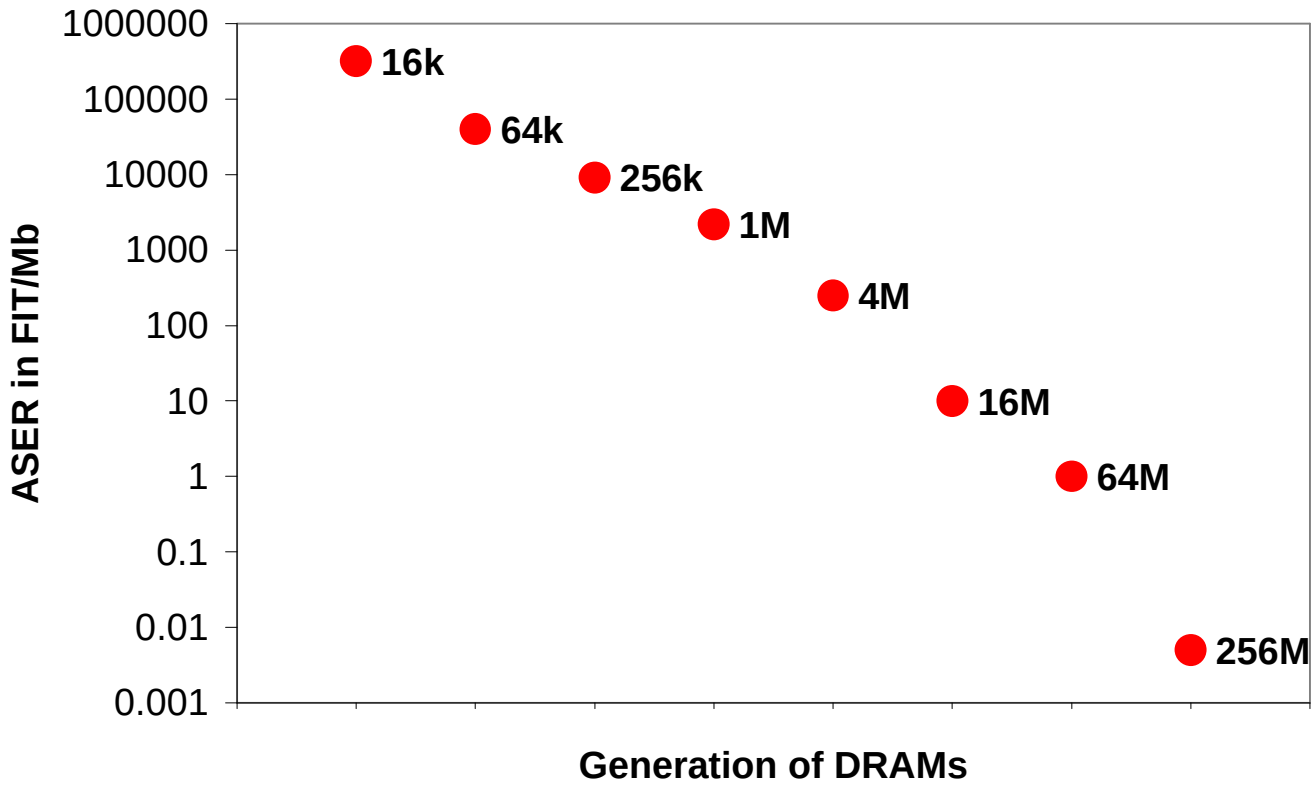

10 References

/1/ JEDEC Standard JESD 89, August 2001

/2/ James F. Ziegler et al, IBM, “Cosmic Ray Soft Error Rates of 16Mb DRAM Memory Chips”, IEEE Journal of Solid State Circuits, Vol.33, No.2, Feb. 1998

LANSCE
Los Alamos Neutron Science Center

REPORT ON EXPERIMENT
(Please Type)

Submit all experiment reports to:
LANSCE User Office, MS H831, Los Alamos National Laboratory, Los Alamos, NM 87545

Experiment was carried out at:	**Local Contact**	**Proposal #**	***LANSCE Use Only***
☐ Manuel Lujan Jr. Neutron Scattering Center	Takala	**2002512**	**Report Rc'd**
☒ Weapons Neutron Research Facility	**FP/Instrument Used**		**2/14/03**
☐ WNR/Blue Room	4FP30L		

Title

Neutron Accelerated Soft Error Rate for Different Memory Technologies

Authors and Affiliations

Manny Ma, Robert Cross, Eric Nelson, Jay Wilcox, Scott Lindley, Steve Bodily, Lindia Wiseman
Micron Technology, Inc.

Experiment Report

Soft errors in CMOS memories are non-recurring spontaneous changes in logic state of memory cell tha do no permanent damage to the device. Neutrons of sufficient energy can cause CMOS memory soft errors through the generation and collection of excess charge in the electrically active regions of the silicon substrate as a result of n-Si interaction. Atmospheric neutrons have been shown to cause soft errors in memory devices in field operation. These errors can cause a host of problems resulting in incalculable loss of productivity and revenue. In order to mitigate this problem, the phenomenon must be characterized as thoroughly as possible. Soft error studies under field operating conditions, also known as system level testing, require many millions of device hours of monitoring in order to generate a statistically valid number of events for analysis. Testing under accelerated conditions using a high flu neutron source with an appropriate energy distribution allows for rapid characterization and feedback that, in turn, results in more timely and cost effective technological solutions.

In this experiment, various CMOS memories and discrete device structures were exposed to the beam in order to determine the following:

- Baseline soft error rates (SER) for DRAM and SRAM memories
- Variation in SER as a function of operating conditions such as Vcc and cycle time
- Variation in SER as a function of process technology
- Correlation between system level and accelerated testing
- Post irradiation effect on transistor and capacitor test structures

Experiment Report *(continued)*

In beam SER tests were successful, as errors were observed and response varied as a function of multiple variables. The relationship between input variables and SER response require further analysis. Post irradiation analysis of transistors and capacitors do not show parametric or performance shifts. In the case of discrete structures, in beam analysis may shed more light on this issue. This evaluation has set the stage for further analysis in order to make improvements in SER performance of CMOS memories. These are:

- Effects of improved transistor processes
- Effects of circuit modifications
- Orientation effects
- Test methodology

IMPORTANT! List or attach a list of publications resulting from this experiment (published or in press).

LANSCE
Los Alamos Neutron Science Center

REPORT ON EXPERIMENT
(Please Type)

Submit all experiment reports to:
LANSCE User Office, MS H831, Los Alamos National Laboratory, Los Alamos, NM 87545

Experiment was carried out at:	**Local Contact**	**Proposal #**	***LANSCE Use Only***
☐ Manuel Lujan Jr. Neutron Scattering Center	Bruce Takala	**2002513**	**Report Rc'd**
☒ Weapons Neutron Research Facility	**FP/Instrument Used**		**2/3/03**
☐ WNR/Blue Room	4FP30L-A		

Title

Neutron-Induced Soft Errors in SRAM devices

Authors and Affiliations

Hajime Kobayashi, Hideki Usuki; Sony Corporation
Jun Kase; Sony Electronics Inc.

Experiment Report

High energy neutron-induced soft error will be a main cause of soft errors near future. Especially, since critical charge of SRAM decreases with downsizing, the soft error problem of SRAM becomes more serious compared with DRAM or flash memories. It is important to evaluate the relationship between SER and process rules not only to obtain the SER of the latest device but also to predict SER of future devices. As one of effective measures, we hope ECC (Error Correction Code) works well. However, it is reported that high energy neutrons induce more multi-bit errors compared with thermal neutrons or alphaparticles because they produce larger electrical charge in smaller area. Since a simple ECC does not work effectively against multi-bit errors, we have to investigate the feature of multi-bit errors.

The goals of the experiments were to:

- Evaluate the relationship between SER and process rules.
- Obtain the dependence on Vdd.
- Measure SER with different neutron energy spectra.
- Evaluate multi-bit error rate.

The experiment was a success.
- Relationship between SER and process rule was obtained. As we concerned, SER/device increased with downsizing of devices.
- Vdd dependence was obtained. It is useful to estimate SER of future devices.
- SERs with different neutron energy spectra were obtained. Differential cross section of soft error is being analyzed.

Experiment Report *(continued)*

- Multi-bit error rate was obtained. Adjacent cells upset with some probability. However, since physically adjacent cells are not in the same word, the probability of the multi-bit event was very small. It means that a simple ECC such as mirroring or Hamming code is effective to reduce SER even induced by high energy neutrons.
- Beam quality was excellent. Few thermal neutrons were contained in the beam.

Acknowledgement
We would like to thank B. Takala, John O'Donnel, A. Bridge and S. Wender for their kind support and helpful discussion.

IMPORTANT! List or attach a list of publications resulting from this experiment (published or in press).

LANSCE
Los Alamos Neutron Science Center

REPORT ON EXPERIMENT
(Please Type)

Submit all experiment reports to:
LANSCE User Office, MS H831, Los Alamos National Laboratory, Los Alamos, NM 87545

Experiment was carried out at:	**Local Contact**	**Proposal #**	*LANSCE Use Only*
[X] Manuel Lujan Jr. Neutron Scattering Center	John Ullmann	**2002514**	**Report Rc'd**
[ ] Weapons Neutron Research Facility	**FP/Instrument Used**		**2/18/03**
[ ] WNR/Blue Room	IFP5		

Title: Improving Reaction Rates for Explosive Nucleosynthesis Studies via (n,α) Cross Section Measurements; Proof-of-Principle Experiment at LANSCE.

Authors and Affiliations: P. Koehler, Oak Ridge National Laboratory; J. Ullmann, W. Trela, V. Yuan, and R. Haight, LANL.

Experiment Report

This was a proof-of-principle experiment to demonstrate that an in-beam ionization chamber could detect low-energy alpha particles to relatively high neutron energies. The main challenge is that the intense "flash" of high-energies particles at the start of each neutron pulse can overload the detector electronics for hundreds of microseconds, effectively limiting the range of measurements to low neutron energies. The main solution was to employ a compensated ion chamber as the detector. We have made this detector work in the intense γ flash of the neutron beam at the Oak Ridge Electron Linear Accelerator (ORELA) facility, but experiments at the Lujan Center presents a greater challenge because of the much higher energy particles (800 MeV protons versus 150 MeV electrons) used to produce the neutron beam and the higher peak intensity. On the other hand, the much larger flux of low energy neutrons at the Lujan Center should allow measurements in the thermal to few tens of keV neutron energy range to be made much more quickly or with smaller samples.

After some effort, the detector was made to work at counting rates approximately ten times larger than attainable at ORELA. The experiment revealed that small modifications to the detector electronics should lead to even better performance. The experiments also revealed that it probably would be advantageous to use a longer (~30 m) flight path than was available.

Below are two sample spectra from the ^{95}Mo(n,α) reaction taken with a flight path length of 11 m and a collimator of 0.75" diameter over a total beam time of 12 hours at a proton beam current of 100 μA. Despite the short time of the run (typical ORELA experiments last for about 4 weeks), several resonances to energies as high as 16 keV are readily visible.

Experiment Report *(continued)*

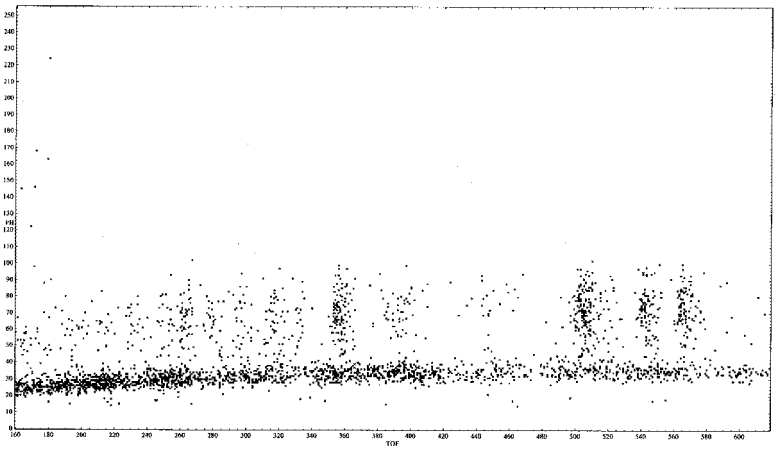

Figure 1. Pulse height versus time of flight (horizontal) spectrum from a measurement with a ^{95}Mo sample. The data were taken over a 12-hour period when the proton beam intensity was 100 μA. Several resonances in the ^{95}Mo(n,α) reaction are visible as the vertical bands at specific times of flight.

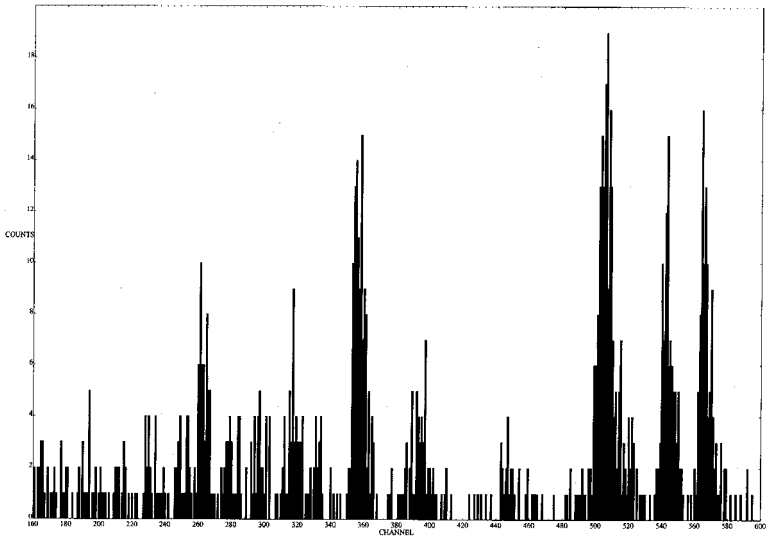

Figure 2. Time of flight spectrum generated from Fig. 1 by projecting over pulse heights corresponding to the ^{95}Mo(n,α) reaction.

As a proof-of-principle experiment, no publications are expected. However, the results were very encouraging, and follow-on experiments in nuclear astrophysics and basic nuclear physics are being planned.

IMPORTANT! List or attach a list of publications resulting from this experiment (published or in press).

LANSCE
Los Alamos Neutron Science Center

REPORT ON EXPERIMENT
(Please Type)

Submit all experiment reports to:
LANSCE User Office, MS H831, Los Alamos National Laboratory, Los Alamos, NM 87545

Experiment was carried out at:	**Local Contact**	**Proposal #**	*LANSCE Use Only*
☐ Manuel Lujan Jr. Neutron Scattering Center	John Ullmann	2002518	**Report Rc'd 11/15/02**
☒ Weapons Neutron Research Facility	**FP/Instrument Used**		
☐ WNR/Blue Room	4FP15L		

Title
Evaluation of Passive and Active Neutron Personnel Dosimeters

Authors and Affiliations

Main Investigator: Richard H. Olsher, Group HSR-4, LANL
Co-Investigators: Thomas McLean, Leonard Romero, Rich McKeever, Group HSR-4, LANL

Experiment Report

During the week of July 22, 2002 several types of active and passive neutron personnel dosimeters were irradiated at WNR, flight path 15L, 90-meter shed, to determine their response in a high-energy neutron field. Dosimeters tested included a new design being marketed by Fuji Electric, which incorporates dual neutron sensors, BTI bubble detectors, Aloka neutron dosimeters, and Track Etch dosimeters.

The primary purpose of the experiment was to determine the dose response of the dosimeters under test and to establish their suitability for personnel monitoring in high-energy neutron fields. The dose rate in the 90-meter shed was reduced by the addition of filters (4" copper plus 4" polyethylene) to approximately 2 rem/h. The collimation was adjusted to give a 4" x 4" rectangular beam. All of the irradiations were performed with the dosimeters mounted on an acrylic phantom to simulate the albedo effect of the human body.

One of the surprising findings was the large over response of the Fuji Electric EPD. This effect appears to be due to charge particle contamination of the neutron beam and charged particle production in the case of the EPD. The PIN silicon diode, which is used as a detector in the fast neutron channel, normally counts proton recoils from a polyethylene radiator mounted in front of the diode. However, the diode is almost 100% efficient for high-energy charged particles in the beam, which far exceeds the fast neutron sensitivity of the EPD. Monte Carlo simulations using the LANL MCNPX code have shown that charged particle contamination on FP15L was on the order of 0.5% of the neutron fluence rate.

Data analysis is still in progress and a paper is being planned for calendar year 2003.

Experiment Report *(continued)*

IMPORTANT! List or attach a list of publications resulting from this experiment (published or in press).

LANSCE
Los Alamos Neutron Science Center

REPORT ON EXPERIMENT
(Please Type)

Submit all experiment reports to:
LANSCE User Office, MS H831, Los Alamos National Laboratory, Los Alamos, NM 87545

Experiment was carried out at:	**Local Contact**	**Proposal #**	***LANSCE Use Only***
☐ Manuel Lujan Jr. Neutron Scattering Center	Vincent Yuan	**2002532**	**Report Rc'd**
☐ Weapons Neutron Research Facility	**FP/Instrument Used**		**3/21/03**
☒ WNR/Blue Room	WNR TGT 2 FP120L		

Title
Neutron Resonance Spectroscopy (NRS) Measurement of Temperature Rise at a Sliding Interface at High Pressures and Velocities

Authors and Affiliations
V. Yuan (P-23, LANL), J. Hammerberg (X-7, LANL), J. D. Bowman (P-23, LANL), D. J. Funk (DX-2, LANL), G. L. Morgan (P-23, LANL), R. Pelak (DX-3, LANL), C. E. Ragan (X-5, LANL)

Experiment Report
J. Hammerberg (X-7, LANL), J. D. Bowman (P-23, LANL), D. J. Funk (DX-2, LANL), G. L. Morgan (P-23, LANL), R. Pelak (DX-3, LANL), C. E. Ragan (X-5, LANL), V. Yuan (P-23, LANL)

During FY02 we accomplished the following tasks for fielding the NRS experiment.

1. Redesigned the Forest Flyer to accommodate a thicker flyer (Al) to increase the duration of the steady-state shock. This work was accomplished by D.Funk (DX-2), R.Pelak (DX-3), and K. Rainey (DX-3).
2. Several configurations of the Forest Flyer were tested using the new design. 15mm and 18 mm thick Al flyers were fired successfully with a plane-wave lens and multipoint initiator. The optimal configuration consisted of an 18 mm flyer, plane-wave initiated. This configuration will be used for both NRS and Prad experiments in FY03.
3. Sapphire (Al_2O_3) central target material for the NRS friction experiment has been obtained. Construction of the target is under way for a proof test at a DX site prior to finalizing the design for and NRS Blue Room shot.
4. J. Hammerberg (X-7) has completed simulations for hydro evolution of the Cu/ Al2O3 target with depleted uranium (DU) and Ta foils.
5. C.Ragan (X-5) and V.Yuan (P-23) carried out neutron resonance absorption measurements on LANSCE flight path 5 using DU and Ta foils in order to confirm compatibility of the resonances in a single NRS friction experiment.
6. The DU/Ta measurements in (5) above confirmed previous calculations of the neutron absorption by C.Ragan (X-5

These accomplishments have laid the foundation for a full-up NRS friction experiment in the Blue Room during the FY03 run cycle.

IMPORTANT! List or attach a list of publications resulting from this experiment (published or in press).

LANSCE
Los Alamos Neutron Science Center

REPORT ON EXPERIMENT
(Please Type)

Submit all experiment reports to:
LANSCE User Office, MS H831, Los Alamos National Laboratory, Los Alamos, NM 87545

Experiment was carried out at:	**Local Contact**	**Proposal #**	***LANSCE Use Only***
☐ Manuel Lujan Jr. Neutron Scattering Center	Vincent Yuan	**2002534**	**Report Rc'd**
☐ Weapons Neutron Research Facility	**FP/Instrument Used**		**3/13/03**
☒ WNR/Blue Room	WNR TGT 2 FP120L		

Title
Measurement of Metal Jet Temperatures Using Neutron Resonance Spectroscopy

Authors and Affiliations
R.A. Pelak (DX-3, LANL), L. Hull (DX-3, LANL), J. D. Bowman (P-23, LANL), M. Burkett (X-4, LANL),G. L. Morgan(P-23, LANL), C. E. Ragan (X-5, LANL), V. Yuan (P-23, LANL)

Experiment Report

The shape of a metal sample driven by high explosives is strongly influenced by the temperature dependent flow stress. The temperatures of such a metal sample is dependent on the total accumulated strain which is, in turn, governed by the flow stress. Thus temperature is both a parameter that determines the behavior of the system as well as a dependent variable that can used to validate models.

Few techniques exist for the measurement of bulk temperatures of metals in dynamic situations. One of these is Neutron Resonance Spectroscopy where the Doppler modification of an epithermal neutron scattering resonance is used to deduce a temperature. This technique has been under development at LANSCE for several years and has been successfully applied to a silver sheet jet. We have now performed a series of four similar shots to study another material of great interest, copper. A cross section of the apparatus used to produce the jet is shown in Fig. 1. To insure that the smallest jet dimensions are larger than the copper grain size, specially prepared copper with grains smaller than 25 microns was used. Proton radiographs were taken of identical assemblies previously; from them, it was determined that an opportune time to perform NRS measurements was 80.5 microseconds following the firing of the capacitive discharge unit. Each of the four shots were conducted under nominally identical conditions to study shot-to-shot variations in NRS measurements. If the variations are sufficiently small, the spectra may be combined to obtain a higher resolution temperature measurement.

Experiment Report *(continued)*

The shapes of two copper resonances (230 eV and 579 eV) were successfully obtained from all four measurements. All four were indicative of elevated copper temperatures. Analysis of these results, combined with characterization measurements performed in the Blue Room and along Flight Path 5, is currently underway. Some small but significant differences between the four neutron spectra were observed. We intend to attempt to correlate these differences with similarly small variations in jet performance as seen in the damage done to armor used to stop the jet.

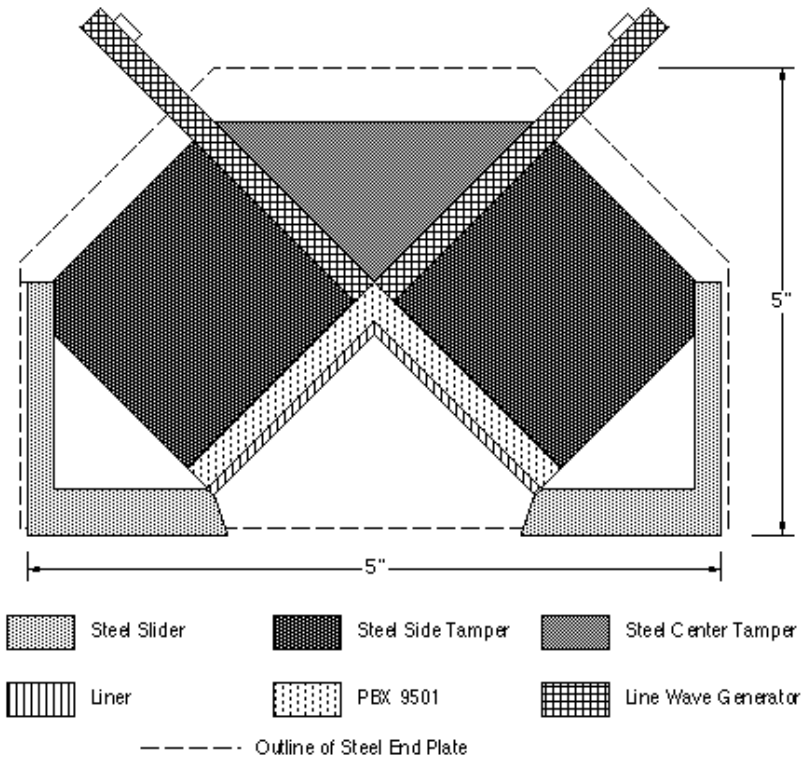

Figure 1: Cross section of copper sheet jet assembly

IMPORTANT! List or attach a list of publications resulting from this experiment (published or in press).

LANSCE
Los Alamos Neutron Science Center

REPORT ON EXPERIMENT
(Please Type)

Submit all experiment reports to:
LANSCE User Office, MS H831, Los Alamos National Laboratory, Los Alamos, NM 87545

Experiment was carried out at:	**Local Contact**	**Proposal #**	***LANSCE Use Only***
[X] Manuel Lujan Jr. Neutron Scattering Center	Vincent Yuan	**2002535**	**Report Rc'd**
[ ] Weapons Neutron Research Facility	**FP/Instrument Used**		**3/20/03**
[ ] WNR/Blue Room	FP5		

Title
Sample Characterization for Dynamic Temperature Measurements using Neutron Resonance Spectroscopy (NRS) on FP5

Authors and Affiliations
V.Yuan (P-23, LANL), C. E. Ragan (X-5, LANL), J. D. Bowman (P-23, LANL), D. J. Funk (DX-2, LANL), L. Hull (DX-3 LANL), G. L. Morgan (P-23, LANL), R. Pelak (DX-3, LANL)

Experiment Report

Flight Path 5 was important to NRS during the 2002 run cycle for conducting experiments to characterize samples used in our Blue Room dynamic shots and for other static experiments conducted in the Blue Room and in FP5. During the 2002 run cycle, NRS conducted over 600 one-hour long runs on FP5 that:

1. **Determined the dead time of our 55-phototube detector array and its associated electronics. Dead time studies were performed both by reducing the beam current (only very limited beam time was available for this) and by inserting flux absorbers such as Pb.**
2. **Measured the moderator parameters for the moderator/reflector used onFP5. These determinations were performed using samples such as U and W which possess well known resonance parameters. Both thick and thin samples were utilized.**
3. **Determined the interference and overlap of neighboring resonances when the samples of dynamic interest are combined with other samples used for reference purposes. The combinations studied include Cu + U, Cu + Th, W + Ag, and W+U.**
4. **Measured resonance parameters of materials used in dynamic shots. The samples, where possible, were studied in more than one thickness in order to vary resonance depth. The include:**
   - **Ag (used to provide the broadened resonance for study in Ag jet shots and as a reference for background determination in other shots).**
   - **W, Mo (used in 182W/Mo experiments to determine the temperature behind the shock front in metals**
   - **W (used in 186W/HE experiments to determine the temperature behind the burn front in high explosives (HE))**
   - **Cu (used for copper jet shots)**
   - **Cd (used in some runs as a neutron absorber which reduces wrap-around by low-energy neutrons.**
   - **In (used to determine backgrounds for other samples)**
5. Identify and quantify amounts of trace residuals in FP5 beam line.
6. Identify and quantify impurities found in the containment vessel windows used for dynamic experiments in the Blue Room.

LANSCE
Los Alamos Neutron Science Center

REPORT ON EXPERIMENT
(Please Type)

Submit all experiment reports to:
LANSCE User Office, MS H831, Los Alamos National Laboratory, Los Alamos, NM 87545

Experiment was carried out at:	**Local Contact**	**Proposal #**	***LANSCE Use Only***
☐ Manuel Lujan Jr. Neutron Scattering Center	Robert C. Haight	**2002538**	**Report Rc'd**
☒ Weapons Neutron Research Facility	**FP/Instrument Used**		**3/20/03**
☐ WNR/Blue Room	4FP15L		

Title
Inclusive (n,xn) Double-Differential Cross Section Measurement (II)

Authors and Affiliations
Kenji Ishibashi, Nobuhiro Shigyo, Yosuke Iwamoto, Daiki Satoh, Satoshi Kunieda, Kyushu University, Fukuoka, Japan
Robert C. Haight, LANSCE-3, Los Alamos National Laboratory, Los Alamos, NM, USA

Experiment Report

The recoil proton method was tested for measuring the continuous-energy neutron-incident (n, xn) reaction cross section. The flight-path length between the target and each recoil proton detectors was about 50 cm. The detection angles were 15, 30 and 90 degrees. Phoswich-type scintillators were used as the recoil proton detectors to discriminate the full-energy deposition events in the scintillator from the partial-energy deposition ones. The detectors consist of NaI(Tl) scintillators surrounded by plastic scintillators. Two sizes of large and small detectors were tested, which were 36 and 5 cm in length, respectively. Polyethylene disks were used as the radiator. The thickness of radiators for the large- and small- size phoswich detectors were 20 and 4 mm, respectively. To subtract the influence from carbon in the radiator, we also made measurement by the use of dummy carbon disks. The target was an iron disk 4 cm thick and 5 cm in diameter. To eliminate the charged particle events coming from the iron target, plastic scintillators were set between the target and the radiators. Since partial energy deposition events might take place by high-energy recoil protons fully-penetrating the phoswich scintillator, they were redundantly checked by a plastic scintillator set behind the phoswich detector. In addition to the charge signal of the scintillators, the flight time data between the accelerator signal and the phoswich detectors were also taken to obtain the incident neutron energy. In order to increase effective detection efficiency of emitted neutron below 100 MeV, we used the NE213 liquid organic scintillators instead of the recoil proton method. The emitted neutron energy was obtained by unfolding the light output data of liquid organic scintillator. The dimension of each liquid organic scintillator was 125 mm thick and 125 mm long. The detection angles were 15, 30, 60, 90, 120 and 150 degrees. The flight path between sample and each scintillator was about 50 cm.

The goals of this experiment were as follows;

- To study the feasibility of the measurement.
- To compare the recoil proton method and using the liquid organic scintillator for emitted neutron detection.
- To measure the continuous energy (n, xn) reaction cross sections for the iron and the lead sample.

In a current analysis we found that

- Pulse-shape discrimination of the events in the NaI region from ones in the plastic scintillator was clear for the phoswich detectors.

Experiment Report *(continued)*

- Event rate by fully-penetraiting protons (above 400 MeV) was rather low for the large size detectors.
- The energy calibrations of the large size phoswich detectors were difficult, where the standard gamma ray sources such as ^{60}Co or Pu-Be were used.
- Pulse-shape discrimination of the neutron and gamma-ray events in the liquid organic scintillators were good.

Our further analysis will include;

- Correction of the detection efficiency of the phoswich detectors for proton incidence.
- Subtraction of carbon effects in the polyethylene radiator.
- Unfolding the light output of the liquid organic scintillators to obtain the energy of emitted neutron.
- Deduction of the (n, xn) cross sections after all correction.
- Comparison between the experimental cross section and the calculated values by computer codes such as the preequilibrium, the intranuclear-cascade-evaporation, and the quantum-molecular-dynamics models

IMPORTANT! List or attach a list of publications resulting from this experiment (published or in press).

None for this potion of work done on experiment 2002538

LANSCE
Los Alamos Neutron Science Center

REPORT ON EXPERIMENT
(Please Type)

Submit all experiment reports to:
LANSCE User Office, MS H831, Los Alamos National Laboratory, Los Alamos, NM 87545

Experiment was carried out at:	**Local Contact**	**Proposal #**	***LANSCE Use Only***
☐ Manuel Lujan Jr. Neutron Scattering Center	Bruce Takala	**2002540**	**Report Rc'd**
☒ Weapons Neutron Research Facility	**FP/Instrument Used**		**10/29/02**
☐ WNR/Blue Room	FP30L-A		

Title
Atmospheric Neutron Sensitivity Measurements of Advanced Silicon Sub-Micron CMOS Technologies

Authors and Affiliations
Joseph J Fabula
Xilinx Corporation

Experiment Report
Our neutron experiments, which were performed over a 48 hour period, evaluated the effects of accelerated exposure to a neutron flux which approximated the energy spectrum of the neutrons seen in the atmosphere (Hess spectrum). During this 48 hour period we experienced better than 98% beam availability and the experiment was successfully completed.

The experiment utilized the 30L beam line at the LANSCE facility, and the data taken was compared with data taken previously at this facility on earlier versions of our products, and with data taken by other researchers in reactor neutron sources. It is necessary to periodically evaluate such data to maintain the accuracy of our neutron modeling efforts. The reactor data had been previously published. All data taken at the LANSCE facility remains proprietary to Xilinx Corporation and cannot be disclosed externally without the written consent of Xilinx Corporation and/or its representatives.

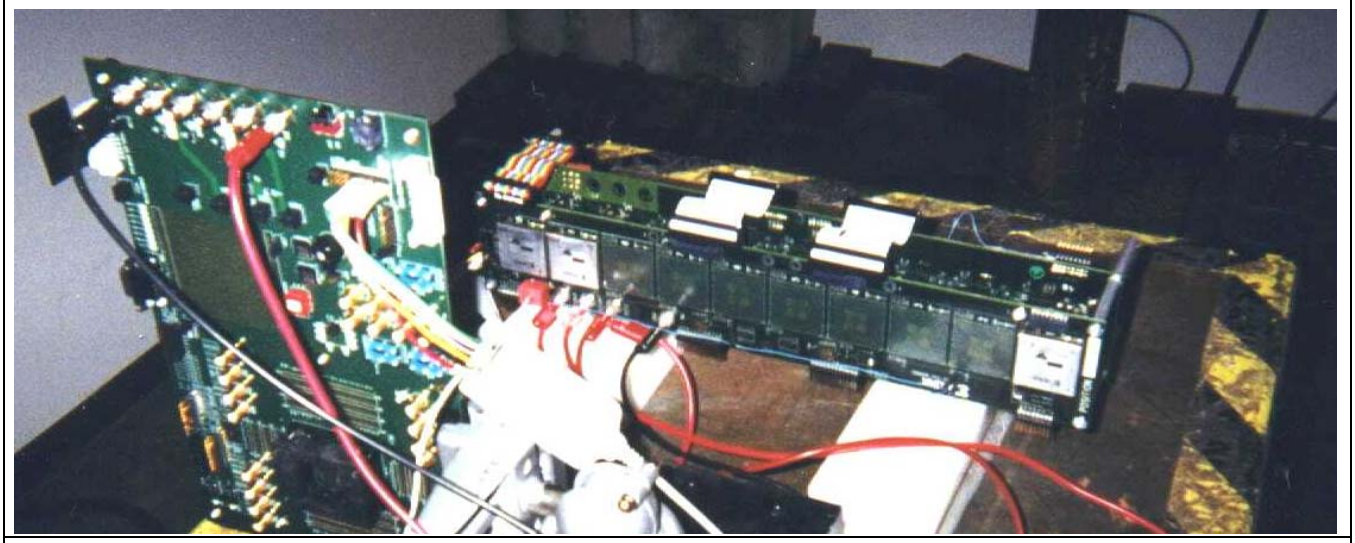

IMPORTANT! List or attach a list of publications resulting from this experiment (published or in press).

none

LANSCE
Los Alamos Neutron Science Center

REPORT ON EXPERIMENT
(Please Type)

Submit all experiment reports to:
LANSCE User Office, MS H831, Los Alamos National Laboratory, Los Alamos, NM 87545

Experiment was carried out at:	**Local Contact**	**Proposal #**	***LANSCE Use Only***
☐ Manuel Lujan Jr. Neutron Scattering Center	Bruce Takala	2002542	**Report Rc'd**
☒ Weapons Neutron Research Facility	**FP/Instrument Used**		**2/13/03**
☐ WNR/Blue Room	FP30L		

Title

Neutron-Induced Single-Event Upsets and Transients in High-Speed Digital Logic Integrated Circuits

Authors and Affiliations

Paul Dodd, Marty Shaneyfelt, Gerald Hash, Jim Schwank; Sandia National Laboratories

Experiment Report

In our previous experiment in 8/2002, we demonstrated the existence of neutron-induced latchup in high-density SRAMs, and found significant neutron-induced latchup rates (NLR) in 4-Mbit SRAMs. During this test, we performed latchup testing on two other 4-Mbit SRAMs. These SRAMs were new revisions of an SRAM that we had previously tested at WNR that did not show a latchup sensitivity. Although we have not yet performed a detailed construction analysis of the revised SRAMs, it is our understanding that the revised SRAMs are a shrunk version of the original parts using a 0.18-µm technology (*vs.* the original parts' 0.25-µm technology).

In previous testing, these 4-Mbit SRAMs showed no latchup susceptibility, and in fact had a very low SER (<20 FIT/Mbit at minimum rated voltage). However, when a new die revision of the very same SRAM was released it was found to be sensitive to heavy-ion induced latchup. Since this part had previously been an excellent choice for high-reliability applications, we decided to retest the revised SRAM (both 3.3-V and 5-V versions) to determine if it would be sensitive to neutron-induced latchup. The results are displayed in Figure 1. At room temperature and maximum rated voltage (3.6 V), the NLR is about 100 FIT/Mbit, five times the previous SRAM's *error* rate. Under worst-case conditions (maximum voltage and maximum temperature of 85ºC), the NLR doubles to ~200 FIT/Mbit. Increasing the temperature still further increases the latchup rate, and also lowers the voltage required to trigger latchup. Similar characteristics were observed for the 5-V version of this vendor's 4-Mbit SRAM, with a room-temperature NLR of 100 FIT/Mbit at 5.5 V.

Of some concern is the fact that what one might have presumed from the part number was a relatively minor change to the Vendor B SRAM design and/or process technology resulted in such a drastic change in the SRAM cosmic-ray reliability. This indicates the importance of continuous testing for terrestrial cosmic ray reliability by either the IC vendor or the system integrator to assure continued reliability in the face of process or design changes. Interestingly, these SRAMs use a 4T polysilicon resistor load cell design. One would expect the NMOS memory array in a polysilicon resistor-load four-transistor SRAM to be latchup immune because it wouldn't contain any classical CMOS latchup paths. However, the supporting logic circuitry is full CMOS and can exhibit latchup, as amply demonstrated by Figure 1.

Experiment Report *(continued)*

As part of our continuing study of the impact of technology trends on SER, we characterized the SER in advanced 1.2-V, 0.13-µm SRAMs, as well as 0.35-µm SRAMs fabricated in a non-SEU-hardened version of Sandia's own 3.3-V silicon-on-insulator (SOI) technology (SRAMs from our SEU-hardened technology showed no neutron upset sensitivity). The results of these tests are shown in Figure 2, where the new data are plotted along with all of our past SRAM SER data from WNR testing. For reference, an uncorrected SER of 1000/Mbit would lead to 1 error every three weeks in a 256-Mbyte computer system. From this figure, it is clear that low-voltage SRAMs exhibit unacceptably high SER without error correction, and that different IC technologies can have SER varying by two orders of magnitude at a given voltage.

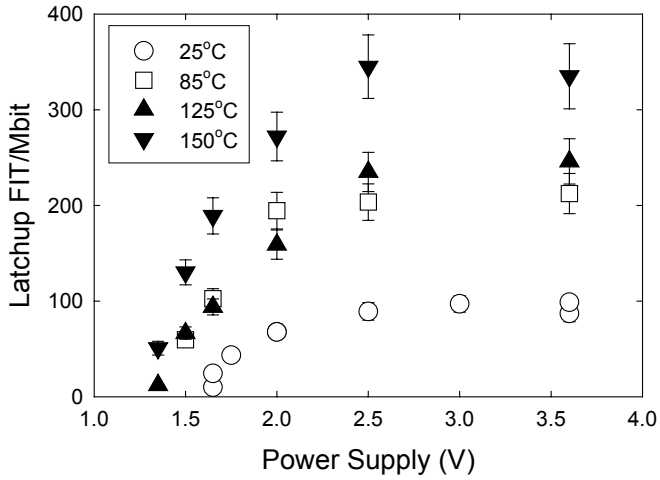

Figure 1. Neutron-induced latchup rate in 3.3-V 4T CMOS commercial 4-Mbit SRAMs as a function of power supply voltage and operating temperature.

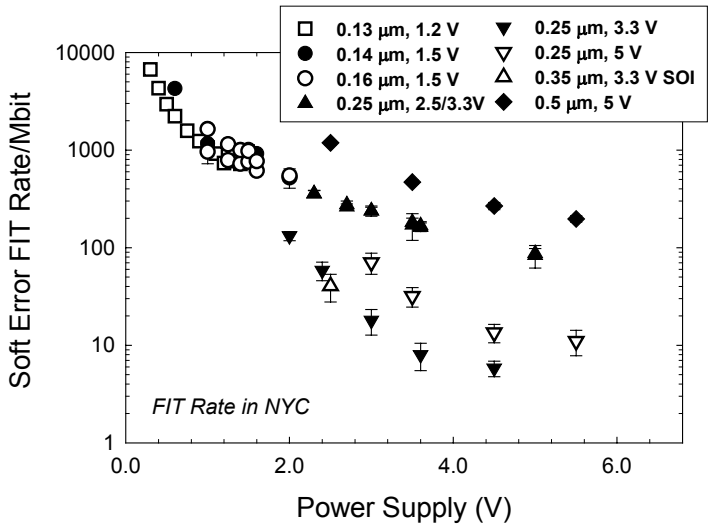

Figure 2. Soft error failure rate as a function of power supply voltage for SRAMs manufactured in several different technologies by several vendors.

IMPORTANT! List or attach a list of publications resulting from this experiment (published or in press).

1. P. E. Dodd, M. R. Shaneyfelt, J. R. Schwank, and G. L. Hash, "Neutron-induced soft errors, latchup, and comparison of SER test methods for SRAM technologies," *IEDM Tech. Digest.,* pp. 333-336, 2002.
2. P. E. Dodd, M. R. Shaneyfelt, J. R. Schwank, and G. L. Hash, "Neutron-induced latchup in SRAMs at ground level," *Proc. IRPS 2003¸ in press.*

LANSCE
Los Alamos Neutron Science Center

REPORT ON EXPERIMENT
(Please Type)

Submit all experiment reports to:
LANSCE User Office, MS H831, Los Alamos National Laboratory, Los Alamos, NM 87545

Experiment was carried out at:	**Local Contact**	**Proposal #**	***LANSCE Use Only***
☐ Manuel Lujan Jr. Neutron Scattering Center	Bruce Takala	2002542	**Report Rc'd**
☒ Weapons Neutron Research Facility	**FP/Instrument Used**		**2/13/03**
☐ WNR/Blue Room	FP30L		

Title

Neutron-Induced Single-Event Upsets and Transients in High-Speed Digital Logic Integrated Circuits

Authors and Affiliations

Paul Dodd, Marty Shaneyfelt, Gerald Hash, Jim Schwank; Sandia National Laboratories

Experiment Report

Latchup due to energetic particle strikes is well documented in the space radiation effects literature. The mechanism for single-event latchup (SEL) is the same as for classical electrical latchup, except that charge generation by a particle strike provides the trigger that initiates latchup. Given the similarity between proton and neutron reaction cross sections for particle energies greater than 50 MeV, the inevitable existence of neutron-induced latchup has been recognized. Surprisingly, there have been no documented reports of neutron-induced latchup in terrestrial systems. In this experiment we demonstrated the existence of neutron-induced latchup in high-density SRAMs, and found significant neutron-induced latchup rates (NLR). These IC failure rates could lead to very poor system reliability in systems with large amounts of memory, and can't be circumvented using error correction. We also characterized latchup FIT rates as a function of operating voltage and temperature.

The SRAMs were powered using a computer-controlled power supply and were allowed to power-up into their preferred state. The threshold current for latchup detection was set based on each IC's static current (typically on the order of a few mA). The beam shutter was opened and current monitoring began. Each time that the IC static current increased above the threshold current, a counter was incremented and power was automatically removed from the device for 0.5 seconds before being reapplied. In order to obtain accurate latchup rates, it is important to ensure that the time between latchups is long compared to the dead time introduced by the reset process. The temperature of the devices was controlled using resistive strip heaters.

The SRAMs tested included 2 different part types from 2 vendors. These SRAMs had been the subject of previous WNR soft error test campaigns, and were known to exhibit high current states that we suspected were latchups. The NLR of one of the 4-Mbit SRAMs is presented in Figure 1. At the maximum rated voltage (3.6 V) and room temperature, the latchup FIT rate is 336 FIT/Mbit. At this FIT rate, a 256-Mbyte system using these SRAMs could experience 0.0165 latchups/day, or about 1 latchup every 60 days. Even worse, at this part's maximum permitted operating temperature of 85ºC, the NLR rises to 566 FIT/Mbit at 3.6 V, or nearly one latchup per month in a 256-Mbyte system! These SRAMs exhibited latchup even at 1.5 V, and indeed at 85ºC the latchup rate is still more than 100 FIT/Mbit.

Experiment Report *(continued)*

It is clear from the data that neutron-induced latchup in advanced SRAMs not only exists, but poses a significant reliability risk for some technologies. The NLR measured for this SRAM are expected to result in significant failure rates in fielded systems. These latchups can't be circumvented using error correction. We recommend that any SER characterization campaign should include explicit tests to monitor neutron-induced latchup.

SER testing can also be performed using monoenergetic protons (above 50 MeV proton and neutron reaction cross-sections in silicon are similar). To confirm the accuracy of this method, we tested the same set of SRAMs at the TRIUMF Proton Irradiation Facility in Vancouver, Canada using proton beams with energies of 8, 20, 50, and 100 MeV. Calculating the terrestrial SER from mono-energetic proton exposures is slightly more involved than for the WNR source because it is necessary to convolve the differential neutron energy spectrum with the experimental data to determine the full-spectrum SER. The calculated SER from proton exposures is compared to the WNR continuous neutron SER in Table 1. For the ICs tested here, SER calculated from either broad-spectrum neutron or monoenergetic proton tests agree to within experimental uncertainty, validating the use of either source per the JEDEC specification.

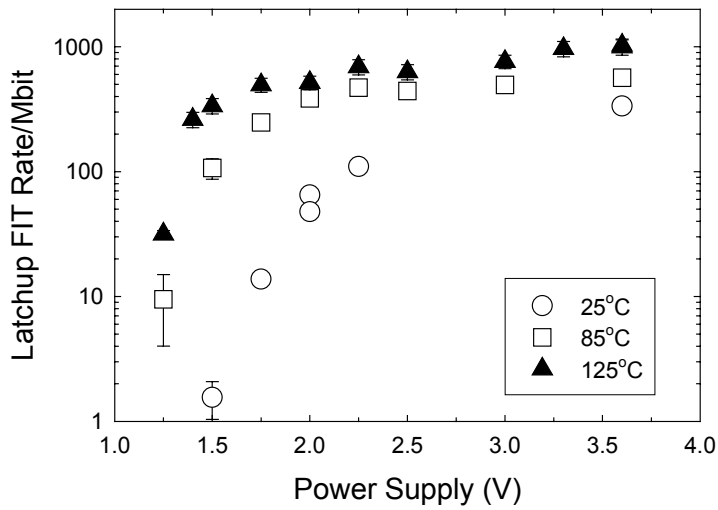

Figure 1. Neutron-induced latchup rate in 3.3-V 6T CMOS commercial SRAMs as a function of power supply voltage and operating temperature.

Table 1. Comparison of measured neutron and proton SER in commercial SRAMs.

Part B.	*Vendor A*	*Vendor A*	*Vendor A*	*Vendor A*	*Vendor B*	*Vendor B*	*Vendor C*	*Vendor C*
Test V_{DD} (V)	3.0/2.3	3.0/1.4	1.4	1.4	4.5	3.0	4.5	1.5
Neutron FIT/Mbit	239 ± 20/ 359 ± 29	381 ± 69/ 995 ± 82	1016 ± 81	747 ± 46	13.5 ± 3	18 ± 5	267 ± 23	1399 ± 11
Proton FIT/Mbit	Not tested	352 ± 24/ 707 ± 69	954 ± 82	784 ± 80	17.3 ± 4	27 ± 8	233 ± 16	1330 ± 49

IMPORTANT! List or attach a list of publications resulting from this experiment (published or in press).

1. P. E. Dodd, M. R. Shaneyfelt, J. R. Schwank, and G. L. Hash, "Neutron-induced soft errors, latchup, and comparison of SER test methods for SRAM technologies," *IEDM Tech. Digest.,* pp. 333-336, 2002.
2. P. E. Dodd, M. R. Shaneyfelt, J. R. Schwank, and G. L. Hash, "Neutron-induced latchup in SRAMs at ground level," *Proc. IRPS 2003¸ in press.*

LANSCE
Los Alamos Neutron Science Center

REPORT ON EXPERIMENT
(Please Type)

Submit all experiment reports to:
LANSCE User Office, MS H831, Los Alamos National Laboratory, Los Alamos, NM 87545

Experiment was carried out at:	**Local Contact**	**Proposal #**	***LANSCE Use Only***
☐ Manuel Lujan Jr. Neutron Scattering Center	Bruce Takala	2002543	**Report Rc'd**
☒ Weapons Neutron Research Facility	**FP/Instrument Used**		**1/10/03**
☐ WNR/Blue Room	Target 4, Flight Path 30L		

Title
Neutron Accelerated Soft-Error Test of Deep Sub-Micron Semiconductor Electron Device.

Authors and Affiliations
Tatsuya Fujii, Ryosuke Fujio, NEC Electronics America Inc.;
Koichi Kumagai, Hideyuki Nakamura, Takashi Yamada, NEC Electronics Corp.;
Masami Hane, Yukiya Kawakami, NEC Corp.

Experiment Report

1. Introduction:

Neutron-induced single event upset (SEU) becomes a serious problem for reliability of semiconductor memory devices in deep sub-micron (DSM) technology due to more number of memory cells in a chip and lower supplied voltage.

Joint Electron Device Engineering Council (JEDEC) established the standard, JESD89, defining how to measure soft-errors in semiconductor devices, in August 2001. It recommends WNR in LANSCE as a facility for experiments.

We had estimated the neutron-induced soft-error rate (SER) using modified Burst Generation Rate (BGR) method [1] and in-house soft-error simulator. We intended to correlate the theoretical approaches with measurement of real SEUs in DSM devices by this experiment, and utilize the result to improve the simulator.

2. Experiment purposes:

1) Estimate neutron-induced SER for single-port and dual-port static random access memory (SRAM) macros embedded in logic devices of 0.15um technology through an accelerated test at WNR. The estimated data are mainly utilized for designing electronic instruments with our chips in our North American customers.
2) Improve soft error simulator's accuracy by correlation with experimental results.
3) Estimate neutron-induced SER of the future semiconductor devices, such as 0.13um and beyond.

3. Experimental apparatus:

Fig. 1 shows the experimental apparatus for neutron-accelerated test. Fig. 2 is the photograph of the motherboard and the daughter boards. There are two sockets for sample chips on each daughter test board. The motherboard holds up to eight daughter boards vertically on it. Desirable neutron beam is from 8cm to 10cm in diameter.

The test controller unit is placed inside the shielding wall and power units are set above the shielding wall. Operators control the test system by notebook PC. Software programs in PC allow operators to control test modes and parameters such as supplied voltage, read/write timing, test sequence and so on. It can record failure bit counts and failure bit maps.

Experiment Report *(continued)*

4. Samples:

Two kinds of test chips are used in this experiment. The one has single-port embedded SRAM macros. The other has dual- port ones. They are manufactured at in-house fabrication line by 0.15um technology.

5. Test parameters:

We evaluated SER's dependency upon the following parameters:

1) Retention voltage: Nominal +/– tolerance for normal operation and even lower voltages only for data retention. These data are helpful especially in improving soft-error simulator.
2) Beam direction: From the front to the back in Fig. 2 (from device's top to bottom. We called "head.") and opposite ("tail").
3) Test pattern: Data pattern used in write operation including checker board, its complement, all 0, all 1, row stripe and column stripe patterns.
4) Process deviation: The samples are also prepared with intentional deviation (threshold voltage and gate length of transistors) in process of fabrication. The experiment is useful for estimating the range between best / worst cases of SER.
5) Energy spectrum: The experiment with or without 8-inch absorber shows the influence of lower-energy neutron.

6. Summary

We are analyzing the data from the experiment, and correlating it with the simulator.

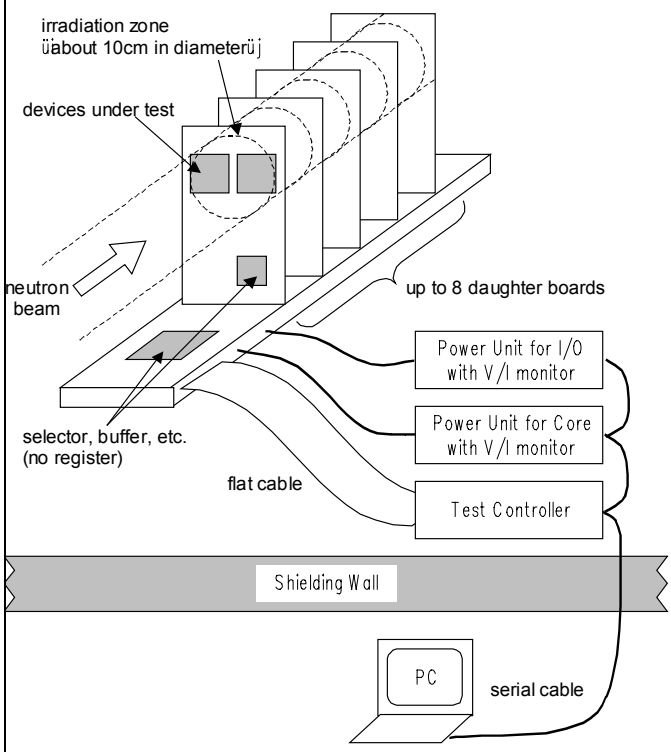

Fig. 1 The experimental apparatus

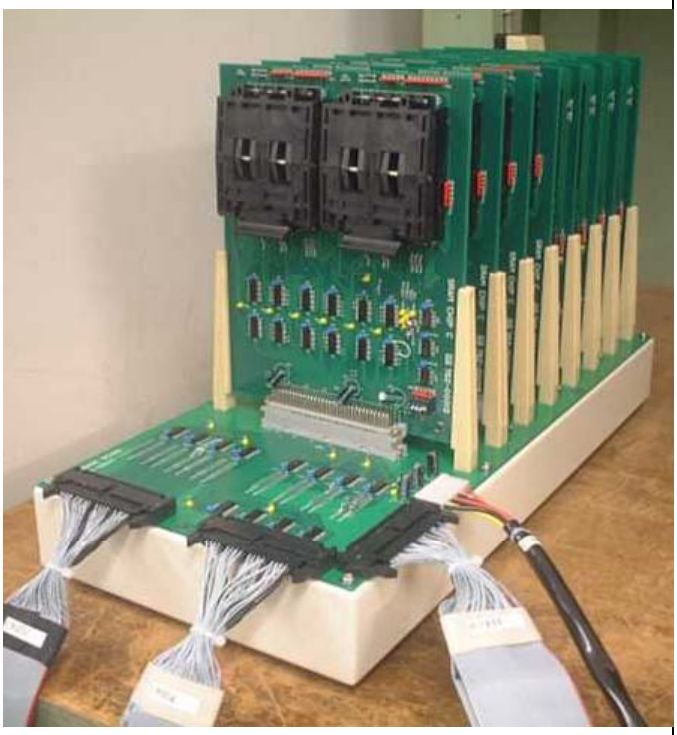

Fig. 2 The mother board and daughter boards

Reference: [1] Y. Tosaka, et al., IEEE EDL Vol. 20, pp.89-pp.91 (1999)

IMPORTANT! List or attach a list of publications resulting from this experiment (published or in press).

None for this experiment

LANSCE
Los Alamos Neutron Science Center

REPORT ON EXPERIMENT
(Please Type)

Submit all experiment reports to:
LANSCE User Office, MS H831, Los Alamos National Laboratory, Los Alamos, NM 87545

Experiment was carried out at:	**Local Contact**	**Proposal #**	***LANSCE Use Only***
☐ Manuel Lujan Jr. Neutron Scattering Center	R. C. Haight	**2002544**	**Report Rc'd**
☒ Weapons Neutron Research Facility	**FP/Instrument Used**		**2/19/03**
☐ WNR/Blue Room	30R-A		

Title
(n,z) Reactions from Threshold to 50 MeV

Authors and Affiliations
Robert C. Haight, LANSCE-3
Steven M. Grimes, Ohio University
Dimitri Rochman, LANSCE-3
Jacquelyne K. Gallegos, LANSCE-3

Experiment Report

During the 2002 run cycle at the LANSCE, we began measurements of the cross sections for hydrogen and helium production in neutron-induced reactions from threshold to 100 MeV on structural materials important to the Advanced Fuel Cycle Initiative (AFCI) program at Los Alamos National Laboratory. Our approach is to directly measure hydrogen and helium isotopes as they are emitted in nuclear reactions such as (n,xp), (n,xd), and (n,xα). The data include not only the gas-production cross sections corresponding to the emission of these hydrogen and helium isotopes but also the angular distributions and energy spectra of the emitted particles. These benchmark data further serve as tests of nuclear-reaction model calculations. Materials under study include iron, chromium, and the two principal isotopes of nickel (^{58}Ni and ^{60}Ni).

Hydrogen and helium are known to contribute significantly to radiation damage and alteration of the mechanical properties of materials subjected to neutron irradiation. At present, there are few data for such important elements as iron, chromium, nickel, and molybdenum. New evaluations that extend to higher neutron energies[1] are based to a great extent on nuclear model calculations. The data in these new evaluations, especially for the structural materials, invite tests and validation. We have therefore begun a program to measure these cross sections on the elemental constituents of structural materials. This work is a continuation of our measurements made up to 60 MeV on other materials such as silicon[2] and cobalt.[3]

Our method is to detect protons, α-particles, and other isotopes of hydrogen and helium emitted in reactions induced by neutrons at the WNR spallation-neutron source at LANSCE. Schematically, our measurement approach is shown in Fig. 1, where the correspondence of these microscopic measurements is made to the realm of structural materials. Protons, deuterons, tritons, ^{3}He and α -particles are emitted in reactions of neutrons with the constituent elements of the material. In a thick sample (i.e., more than a few millimeters thick), most of these light charged particles stop in the material itself, although a few with high enough energy will exit the component and stop in neighboring materials. For our experiments, we select thin foils of the material of interest so that all of the light charged particles can escape with little energy loss. We are thereby able to measure not only the gas-production cross sections corresponding to hydrogen and helium isotopes but also the energies of the emitted particles and their angular distributions. These latter two quantities do not affect the hydrogen and helium production, but they are important for validating nuclear model calculations because they serve as further constraints on the models. With improved models, we will have greater confidence in calculations of gas-

Experiment Report *(continued)*

production cross sections for materials that are difficult to study in the laboratory. The reaction chamber and collimation for the neutron beam, target position, and array of detectors that identify charged particles and their energies are shown in Fig. 2.

Our present work is based on developmental experiments in late 2001 to commission the detector station, shielding, detectors, and the data-acquisition system. We used an iron sample in this experimental run and concentrated on proton emission at several angles. Detection of protons from the sample was challenging because protons are easily produced by neutron interactions with shielding materials. A measure of the quality of data is the signal-to-background ratio, which we found to be 6:1 in the forward angles and 3.5:1 at 90° at an incident-neutron energy E_n = 100 MeV. At lower neutron energies, the signal-to-background ratio was significantly better.

This year we began taking production data on iron, chromium and two isotopically enriched nickel isotopes (^{58}Ni and ^{60}Ni) in July 2002. Preliminary analysis of the data shows that the signal-to-background ratios are significantly higher with the upgraded collimation and shielding.

References:
1. M.B. Chadwick et al., *Nuclear Science and Engineering* **13**, 293 (1999).
2. F.B. Bateman et al., *Physical Review C* **60**, 064609-1 (1999).
3. S.M. Grimes et al., *Nuclear Science and Engineering* **124**, 271 (1996).

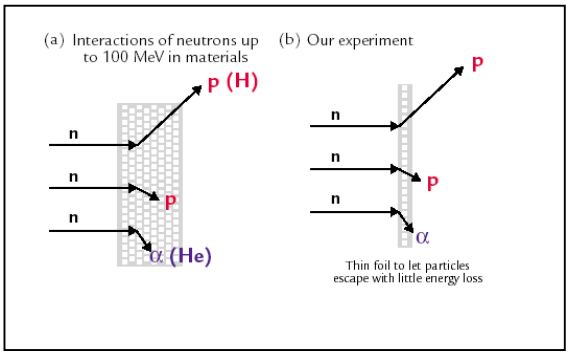

Fig. 1. Gas production by neutrons in materials. (a) Charged particles stop in the material or neighboring materials, depending on the range. Protons have millimeter to centimeter ranges. They capture an electron when they stop in the material and become hydrogen. Alpha particles have millimeter ranges. They capture two electrons when they stop and become helium. (b) We detect outgoing charged particles and measure their energy and angular distributions. Then hydrogen and helium production can be calculated with confidence.

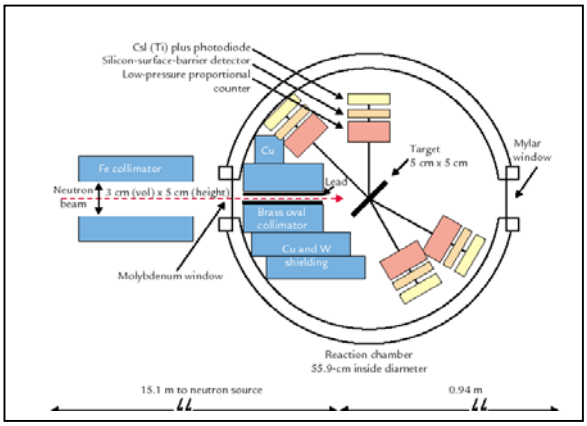

Fig. 2. Layout of apparatus for measuring neutron-induced hydrogen and helium production showing collimation for the neutron beam, target position, and array of detectors that identify charged particles and their energies.

IMPORTANT! List or attach a list of publications resulting from this experiment (published or in press).

1. R. C. Haight, "GAS PRODUCTION CROSS-SECTION MEASUREMENTS AT LANSCE: FY2002 REPORT" LA-UR-02-7445 (2002)

LANSCE
Los Alamos Neutron Science Center

REPORT ON EXPERIMENT
(Please Type)

Submit all experiment reports to:
LANSCE User Office, MS H831, Los Alamos National Laboratory, Los Alamos, NM 87545

Experiment was carried out at:	**Local Contact**	**Proposal #**	***LANSCE Use Only***
☐ Manuel Lujan Jr. Neutron Scattering Center	R. C. Haight	**2002546**	**Report Rc'd**
☒ Weapons Neutron Research Facility	**FP/Instrument Used**		**2/19/03**
☐ WNR/Blue Room	30R-B		

Title
Nuclear Level Densities Studied through (n,xgamma) Reactions at FIGARO

Authors and Affiliations
Robert C. Haight, LANSCE-3
Dimitri Rochman, LANSCE-3
John M. O'Donnell, LANSCE-3
Matthew Devlin, LANSCE-3
Jacquelyne K. Gallegos, LANSCE-3

Experiment Report

Neutron emission from reactions induced by fast neutrons is a subject of much interest due to the fundamental nature of the interactions, free from the complications of the Coulomb interaction, and due to the many applications in defense, nuclear energy, waste transmutation, accelerator shielding, medical therapy, and geological studies. Nevertheless, the experimental database for these processes is very meager due to the difficulty of measuring them. At the Los Alamos Neutron Science Center, we are developing the FIGARO array (Fast neutron-Induced GAmma-Ray Observer) for carrying out these measurements with the pulsed spallation, "white" neutron source at WNR/LANSCE.

The FIGARO array (Fig.1) consists of gamma-ray and neutron detectors arranged around the sample, which is placed 22 meters from the pulsed source of fast neutrons at WNR. Both high-resolution high purity germanium detectors (HPGe) as well as very fast BaF_2 detectors are used to detect the gamma rays. The detected gamma-ray gives several important pieces of information: it indicates that a reaction has taken place; it identifies the residual nucleus and therefore the type of reaction by the characteristic energy; it stops the "clock" that had been started by the spallation source for measuring the time of flight and therefore the energy of the incident neutron; and it starts the "clock" for measuring the time of flight and therefore the energy of the emitted neutron between the sample and one of the array of the neutron detectors, which are liquid scintillators that can differentiate neutrons from gamma rays.

To test the capabilities of gamma-ray-neutron coincidences, we studied samples of carbon, silicon, and iron in this running cycle of LANSCE. Each of these elements has a dominant isotope and a strongly populated first excited state, which decays to the ground state with an easily detected gamma ray. An example of the data is shown in Fig. 2, where the energy imparted to the nucleus, the "excitation energy", is plotted against the incident neutron energy up to 13 MeV.

We are analyzing the data to deduce the level density as a function of excitation in these nuclides. Our goal is to use a HPGe detector with excellent gamma-ray resolution so that level densities in many isotopes of the same element can be deduced from a single experiment that uses one sample of the natural element with the natural abundance of the isotopes. The work this year therefore was to develop the techniques of data acquisition and analysis in preparation for expanding the array of neutron detectors to at least 20 in 2003 and approximately 50 in 2004.

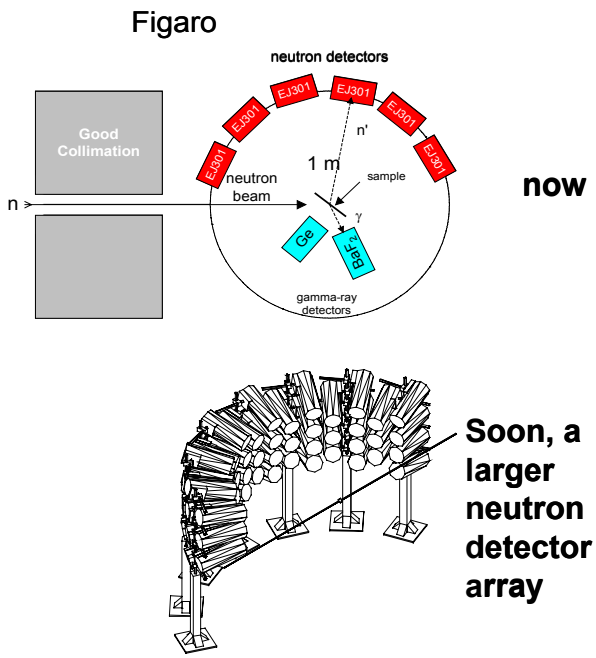

Experiment Report *(continued)*

Figure 1 – FIGARO detector array showing Ge and BaF2 gamma-ray detectors and the present and future array of neutron detectors. The energy of neutrons emitted from the sample is determined by time of flight over a 1-meter flight path.

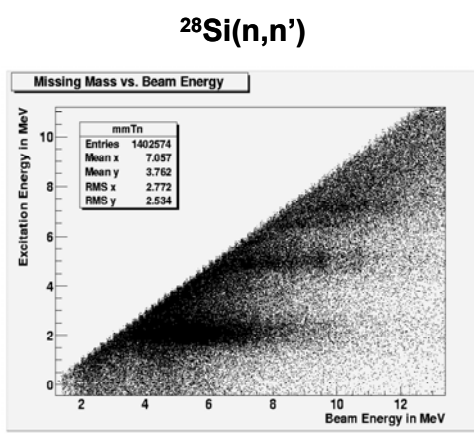

Figure 2 -- Neutron emission from inelastic neutron scattering on ^{28}Si as a function of incident neutron energy from threshold to 13 MeV. The excitation energy of the ^{28}Si nucleus is given as "missing mass" and distinct regions for exciting the first, second, third and higher lying states are clearly seen.

IMPORTANT! List or attach a list of publications resulting from this experiment (published or in press).
See attached list.

Publications in press:

R. C. Haight, D. Rochman, J. M. O'Donnell and M. Devlin, "New Approaches To Nuclear Level Densities Through Particle Emission Measurements", Proc. Int. Conf. Accelerator Applications in Research and Industry, Denton TX, Nov. 12-16, 2002 (invited).

R. C. Haight, J. M. O'Donnell, L. Zanini, M. Devlin, and D. Rochman, "FIGARO: Measuring neutron emission spectra with a white neutron source," Proc. Eleventh International Symposium on Capture Gamma-Ray Spectroscopy and Related Topics, Pruhonice, Czech Republic, September 2-6, 2002 (invited).

LANSCE
Los Alamos Neutron Science Center

REPORT ON EXPERIMENT
(Please Type)

Submit all experiment reports to:
LANSCE User Office, MS H831, Los Alamos National Laboratory, Los Alamos, NM 87545

Experiment was carried out at:	**Local Contact**	**Proposal #**	***LANSCE Use Only***
☐ Manuel Lujan Jr. Neutron Scattering Center	R. Nelson	**2002549**	**Report Rc'd**
☐ Weapons Neutron Research Facility	**FP/Instrument Used**		**4/9/03**
☒ WNR/Blue Room	60R/GEANIE		

Title
Investigation of ^{232}Th via the (n,n′γ) reaction and neutron induced fission studies

Authors and Affiliations
P.E. Garrett, W. Younes, J.A. Becker, L.A. Bernstein, J. Cooper, L. Ahle (LLNL)
R.O. Nelson, N. Fotiades, M. Devlin (LANL)

Experiment Report
An experiment to measure the γ rays produced following bombardment of ^{232}Th foils was conducted at LANSCE using the WNR spallation neutron source and the GEANIE spectrometer located on the 60R flight path. One purpose of the experiment was to measure the γ rays from the (n,n′) channel, or ^{232}Th, in order to build a better level scheme. There are a number of nuclear structure issues in ^{232}Th, and the (n,n′γ) reaction is an ideal tool in which to investigate them. The other purpose of the experiment was to measure fission γ rays in an effort to determine the yield of fission products, using the same method as was successfully applied in the case of ^{235}U. The experiment ran in August/Sept. of 2002 for a total of 20 days, and we encountered no experimental difficulties during the course of the experiment. The raw data have been successfully transported to LLNL, and are awaiting analysis.

Experiment Report *(continued)*

LANSCE
Los Alamos Neutron Science Center

REPORT ON EXPERIMENT
(Please Type)

Submit all experiment reports to:
LANSCE User Office, MS H831, Los Alamos National Laboratory, Los Alamos, NM 87545

Experiment was carried out at:	**Local Contact**	**Proposal #**	***LANSCE Use Only***
[X] Manuel Lujan Jr. Neutron Scattering Center	John Ullmann	**2002553**	**Report Rc'd**
[ ] Weapons Neutron Research Facility	**FP/Instrument Used**		**3/28/03**
[ ] WNR/Blue Room	FP-14/DANCE		

Title
Neutron Capture Measurements on ^{147}Pm and ^{151}Sm using DANCE

Authors and Affiliations
John Ullmann, John O'Donnell, Rene Reifarth, Robert Haight, LANSCE-3, Los Alamos National Laboratory.
Robert Rundberg, Todd Bredeweg, Dave Vieira, Jerry Wilhelmy, C-INC, Los Alamos National Laboratory.
Jan Wouters, IM-8, Los Alamos National Laboratory.

Experiment Report

Although progress was made on this experiment, several events worked against successful completion, and only 1 day of beam was taken on the ^{151}Sm target. As noted in the experiment report for DANCE development, Experiment 554, several factors, including late delivery of the DANCE BaF_2 crystals, delayed development and calibration, and the partial DANCE array was not ready for data taking until nearly the end of the beam time. In addition, although the ^{147}Pm material was produced by an irradiation at the ILL in the summer of 2002, new licensing and shipping restrictions delayed the shipping of the material to Los Alamos from France, and in fact it has not been yet been received.

The figure (next page) shows the neutron spectrum in the resonance region for a 0.5 mg/cm^2 ^{151}Sm target. This spectrum has been gated to exclude alpha-particle decay, and to include only summed gamma energies (Esum) greater than 3.30 MeV. The resonances in ^{151}Sm are clearly identified, and contaminant resonances from the even-even Sm isotopes ^{150,152}Sm are also evident. Analysis of this data has only begun, and detector efficiencies and backgrounds are being investigated. As anticipated, the scattered neutron background at energies above 1 keV is large, and unless the background can be reduced, high statistics data will be required for a good background subtraction. We expect to be able to improve the quality of the data during the next DANCE development period.

.

Experiment Report *(continued)*

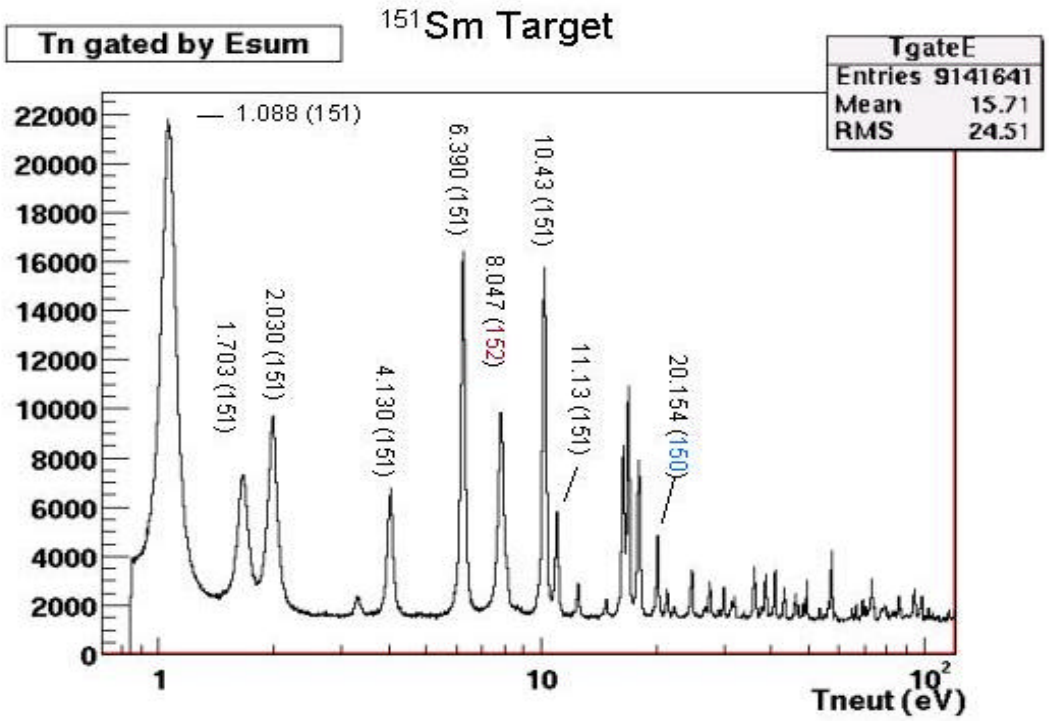

Neutron energy spectrum in the resonance region for ^{151}Sm neutron capture. The y-axis shows counts.

IMPORTANT! List or attach a list of publications resulting from this experiment (published or in press).

REPORT ON EXPERIMENT
(Please Type)

Submit all experiment reports to:
LANSCE User Office, MS H831, Los Alamos National Laboratory, Los Alamos, NM 87545

Experiment was carried out at:	**Local Contact**	**Proposal #**	***LANSCE Use Only***
[X] Manuel Lujan Jr. Neutron Scattering Center	John Ullmann	**2002554**	**Report Rc'd**
[ ] Weapons Neutron Research Facility	**FP/Instrument Used**		**3/31/03**
[ ] WNR/Blue Room	FP-14/DANCE		

Title
DANCE Development

Authors and Affiliations
John Ullmann, Robert Haight, John O'Donnell, Rene Reifarth, , LANSCE-3, Los Alamos National Laboratory.
Robert Rundberg, Todd Bredeweg, Dave Vieira, Jerry Wilhelmy, C-INC, Los Alamos National Laboratory.
Jan Wouters, IM-8, Los Alamos National Laboratory.
Uwe Greife, Colordao School of Mines.

Experiment Report

The DANCE development proposal requested time for detector assembly and alignment, data acquisition development and debugging, and calibration and background studies. The delivery of BaF_2 crystals for the detector was slower than anticipated, but 146 crystals were received, assembled, mounted, and aligned in the ball by mid November. Data acquisition and trigger electronics were assembled and tested, and the full system was working for debugging by mid December. Prior to that, a week of beam was used to test the "continuous mode" data acquisition. For this, the trigger was simply the beam To signal, and the entire beam spill, out to 600 μsec, was digitized (at 10 ns/channel) and analyzed.

Data acquisition was done with 159 8-bit fast transient digitizers organized into 14 Compact PCI crates. Each PCI crate also had a 500 MHz analysis computer. The 14 distributed computers were networked to a "head node" computer. The distributed front end computers analyzed the waveforms for pulse area and timing, and this had to be accomplished in the 50 ms between PSR beam spills. Two waveforms were taken for each crystal, one with high gain and one with low gain. The waveform was sampled in 2 ns increments out to 1 μsec. A sample set of waveforms is shown in the adjacent figure, the fast component of BaF_2 is obvious in the low-gain waveform.

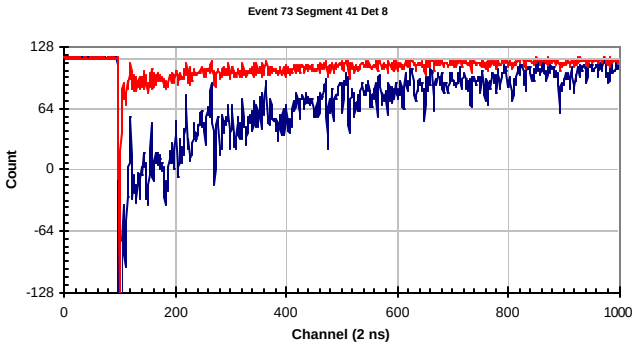

Algorithms for waveform analysis were developed and tested, and methods of handshaking between the distributed computers and the head node were also developed. Several problems were encountered, the most serious of which was a firmware error in about one-third of the digitizers that required them to be used in a slower mode. This error will be corrected in all the digitizers, resulting in a faster data acquisition. The network handshaking seemed to contribute a large deadtime to the system, so we are designing an alternate control system that will remove the handshaking from the ethernet used for data transfer. An average of 230 events per To were recorded with a 20 mg/cm^2 Au target.

Experiment Report *(continued)*

An important feature of DANCE is that it is a calorimeter; it measures the full energy of the gamma-ray cascade following neutron capture. This is illustrated in the adjacent figure, which is the summed energy of a ^{60}Co calibration source. The sum peak is obvious. This spectrum was taken with only 140 active crystals, and the resulting inefficiency allows the individual gamma peaks to also be seen. This figure was made using a linear energy calibration; it has since been determined that a quadratic calibration should be used.

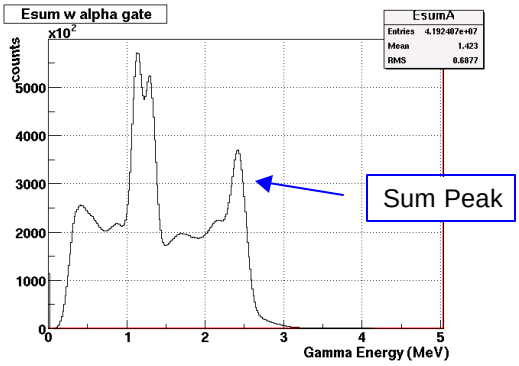

The next figure shows the sum-energy spectrum taken with a 3 mg/cm^2 Au target, gated by neutron energies from 100 to 1000 eV. The Au peak at 6.51 MeV is obvious, but the figure illustrates three problems to be addressed in the 2003 development. First, the resolution of the Au peak is poorer than anticipated, this may be due to the single-detector threshold energy of roughly 400 keV, so that low-energy gammas in the cascade were not accepted. Next, the number of events due to scattered neutrons is larger than anticipated in the simulations. The peaks at 4.72 MeV, 6.9 MeV, and 8.62 MeV are due to capture on the isotopes of Ba in the BaF_2. We are studying the origin of this background, and ways to reduce it. Finally, there is a large gamma peak at 2.2 MeV, presumably from capture on hydrogen in the cave shielding. While we can gate this background out, that will reduce the efficiency of the detector, and we are studying this background as well.

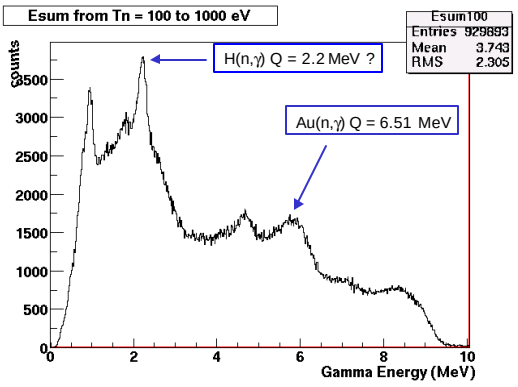

The last figure shows the energy spectrum from a 3 mg/cm^2 Au target along with the background from n empty target frame. Both spectra were gated by multiplicity=2 and Esum = 3.5 to 7.0 MeV to minimize scattered-neutron background, and a ^{6}LiH shield was installed for these runs. The resonance region is obvious, and can be easily analyzed. However, in the continuum region, 1 to 100 keV, the background count rate is of the same order as the data. Background subtraction can be accomplished with good-statistics runs, but we are investigating ways to reduce the background. It should be noted that a background from sample-scattered neutrons was anticipated in simulations, and that the "cluster multiplicity" software test that was designed to reduce this background has not yet been applied.

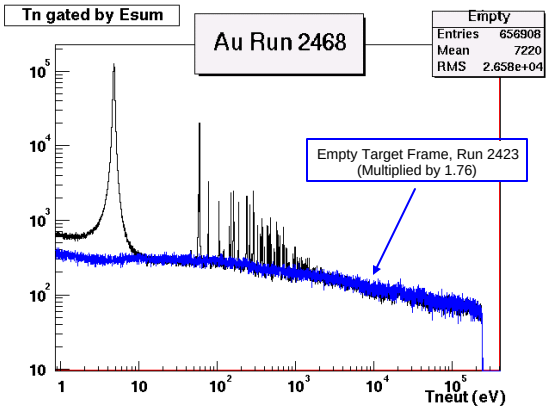

During the last run cycle, targets of Au, Fe, Pb, and C were run to calibrate study the behavior of the detector. Targets of ^{234,235,236,238}U, and ^{151}Sm were ran for physics data. The resonance region of these targets are being analyzed and will be compared to existing data, where it exists.

IMPORTANT! List or attach a list of publications resulting from this experiment (published or in press).

LANSCE
Los Alamos Neutron Science Center

REPORT ON EXPERIMENT
(Please Type)

Submit all experiment reports to:
LANSCE User Office, MS H831, Los Alamos National Laboratory, Los Alamos, NM 87545

Experiment was carried out at:	**Local Contact**	**Proposal #**	***LANSCE Use Only***
☐ Manuel Lujan Jr. Neutron Scattering Center	Ron Nelson	**2002555**	**Report Rc'd**
☒ Weapons Neutron Research Facility	**FP/Instrument Used**		**4/8/03**
☐ WNR/Blue Room	4FP60R/GEANIE		

Title

Measurement of ^{191}Ir(n,n'g), (n,2ng), (n,3ng), and (n,4ng) Cross Sections

Authors and Affiliations
R. Nelson, N. Fotiades, and M. Devlin (LANSCE-3, LANL)
T. Ethvignot (CEA/Bruyeres-le-Chatel, France)
J.A. Becker, P.E. Garrett, W. Younes, L.A. Bernstein (N-Division, LLNL)

Experiment Report

Ir has been used as a radiochemical detector of neutron fluence. To properly interpret such data a good knowledge of reaction probabilities (cross sections) as a function of the incident neutron energy is necessary. These measurements address the need for such cross section data. In particular, the present measurements help determine the probability of populating isomeric states in the Ir nuclei, even in cases where the use of radiochemical techniques is not feasible.

Experiments on ^{191}Ir(n,xγ) were carried out from October 19 – November 3, 2002 using GEANIE. The GEANIE spectrometer, configured with both LEPS and coaxial Ge detectors was used to detect gamma-rays from the product nuclei. The sample was 2 grams of highly (98.23%) enriched ^{191}Ir. A total of 12 days of beam time were used with 80% of maximum availability.
The measurement of ^{191}Ir(n,nxγ) was performed mostly in γ-γ coincidence mode at 1.8 μs beam pulse spacing in order to corroborate and supplement the only existing gamma-ray spectroscopic data for ^{190}Ir of Garrett *et al*.(1) About two days of beam time were used to acquire singles gamma-ray data from which preliminary cross sections can be obtained. For (n,n'γ) measurements "frame overlap" is a problem in this data set. That is, we observe the sum of cross sections for faster and slower neutrons due to the overlap of lower-energy neutrons from a preceding beam pulse with higher-energy neutrons from the following proton beam pulse.

Experiment Report *(continued)*

For (n,2n), (n,3n) and (n,4n) reactions frame overlap is not a problem due to the higher reaction thresholds. In particular, this data set will enable us to study the levels and gamma rays in ^{190}Ir via the (n,2nγ) reaction using γ-γ coincidence data. The goal is to measure the population of long-lived states in the Ir products by observing the gamma-rays that feed the isomeric levels and ground states in the reactions ^{191}Ir (n,2n)^{190}Ir, ^{191}Ir (n,3n)^{189}Ir, and ^{191}Ir (n,4n)^{188}Ir.

Preliminary excitation functions have been generated from the ^{191}Ir(n,xγ) data. Further analysis of these data is continuing. Previous results from ^{193}Ir(n,xnγ) studies have demonstrated that we can observe significant gamma-rays in product nuclei from ^{193}Ir through ^{187}Ir. Analysis of the γ-γ data will allow us to check the γ-ray and energy level assignments of Garrett, *et al*., and aid in determining reaction channel and isomer population cross sections from additional γ-ray singles data. This analysis is now beginning.

References

(1) P.E. Garrett, *et al*., Nucl. Phys. A **611** 68 (1996); P.E. Garrett, *et al*., Nucl. Phys. A **662**, 235 (2000).

IMPORTANT! List or attach a list of publications resulting from this experiment (published or in press).

List of Recent Publications and Reports

W. Younes, H. C. Britt, J. A. Becker, L. A. Bernstein, P. E. Garrett, C. A. McGrath, D. P. McNabb, R. 0. Nelson, M. Devlin, and N. Fotiades, "Preliminary Report on the Population of the ^{235}U $T_{1/2}$ = 25-minute Isomer by the (n,n'γ) Reaction", LLNL Report UCRL-ID-15 1071 (2002).

R.O. Nelson, M. Devlin, N. Fotiades, A. Michaudon, J.A. Becker, J. Cooper, P.E. Garrett, and W. Younes (LLNL), "Improving Radiochemical Diagnostics: Studying Iridium and Europium with GEANIE", Los Alamos Publication, LALP-02-242 and LLNL Report UCRL-ID-151058 (2002).

T. Ethvignot, Th. Granier, L. Giot, P. Casoli, and R.O. Nelson, "A Fission-Fragment-Sensitive Target for X-Ray Spectroscopy in Neutron-Induced Fission", Nucl. Instrum. Meth. **A490**, 559 (2002), LA-UR-02-2234.

E. Tavukcu, L.A. Bernstein, K. Hauschild, J.A. Becker, P.E. Garrett, C.A. McGrath, D.P. McNabb, W. Younes, R.O. Nelson, G.D. Johns, G.E. Mitchell, and J.A. Cizewski, "States in ^{196}Pt observed with the (n,n'γ) reaction", Phys. Rev. C **65,** 064309 (2002).

L.A. Bernstein, J.A. Becker, P.E. Garrett, W. Younes, D.P. McNabb, D.E. Archer, C.A. McGrath, H. Chen, W.E. Ormand, M.A. Stoyer, R.O. Nelson, M.B. Chadwick, G.D. Johns, W.S. Wilburn, M. Devlin, D.M. Drake and P.G. Young, "The ^{239}Pu(n,2n) cross section deduced using a combination of experiment and theory", Phys. Rev. C **65**, 021601(R) (2002).

R.O. Nelson and A. Michaudon, "High-Resolution Cross-Section Measurements for Production of the 0.478-MeV Gamma Ray from the ^{9}Be(n,xγ)^{7}Li Reaction for Neutron Energies Between 12 and 200 MeV with Insight into the ^{10}Be Level Scheme", Nucl. Sci. and Eng. **140**, 1 (2002), LA-UR-01-3552.

T. Ethvignot, T. Granier, P. Casoli, R. O. Nelson, R. C. Haight, M. Devlin, R. Drosg, N. Fotiades, J. M. O'Donnell, W. Younes, P. E. Garrett, and J. A. Becker, "Experimental Studies of Prompt Neutron and Photon Emission in Intermediate Energy Neutron-Induced Fission", Third International Conference on Fission and Properties of Neutron-Rich Nuclei, Sanibel Island, Florida, November 3-8, 2002. LA-UR-03-0478.

R.O. Nelson, T. Ethvignot, T. Granier, P. Casoli, N. Fotiades, M. Devlin, G.D. Johns, W. Younes, P.E. Garrett, J.A. Becker and L.A. Bernstein, "Fast Neutron-Induced Fission Studied by Gamma-Spectroscopy", 11th International Symposium on Capture Gamma-Ray Spectroscopy and Related Topics, Pruhonice (Prague) Czech Republic, 2-6 September, 2002, LA-UR-02-6252. In press World Scientific.

M. B. Chadwick, P. Talou, R. O. Nelson, N. Fotiades, J. A. Becker, L. A. Bernstein, and D. McNabb, Nuclear Modeling of (n,xγ) reactions and determination of partial cross sections", 11th International Symposium on Capture Gamma-Ray Spectroscopy and Related Topics, Pruhonice (Prague) Czech Republic, 2-6 September, 2002, LA-UR-03. In press World Scientific.

LANSCE
Los Alamos Neutron Science Center

REPORT ON EXPERIMENT
(Please Type)

Submit all experiment reports to:
LANSCE User Office, MS H831, Los Alamos National Laboratory, Los Alamos, NM 87545

Experiment was carried out at:	**Local Contact**	**Proposal #**	***LANSCE Use Only***
☐ Manuel Lujan Jr. Neutron Scattering Center	Ron Nelson	**2002556**	**Report Rc'd**
☒ Weapons Neutron Research Facility	**FP/Instrument Used**		**4/8/03**
☐ WNR/Blue Room	4FP30R/FIGARO		

Title

Measurement of Prompt Gamma Rays from Neutron-Induced Fission of Uranium and Other Actinides

Authors and Affiliations
R.O. Nelson, R.C. Haight, N. Fotiades, M. Devlin, and J.M. O'Donnell (LANSCE-3, LANL)
T. Ethvignot and T. Granier (CEA/Bruyeres-le-Chatel, France)

Experiment Report

Knowledge of the partitioning of energy release in fission among neutrons, gamma rays and the kinetic energy of the fragments is important, both for a detailed understanding of the fission process and to better understand fissioning systems. However, there have been very few measurements of the fission gamma-ray spectrum that had good efficiency at high-gamma-ray energies and that were performed over a wide range of incident neutron energies. This experiment was a first attempt to improve the fission gamma-ray data set by using the wide neutron energy range available at the WNR facility and large gamma-ray detectors with good high-energy efficiency. The technique depends upon having special fission chambers with many thin foils. The deposits of fissioning material must be thin so that the fragments can escape and be detected, and there must be many of them so that a suitable count rate is achieved in the available neutron flux. The gamma-ray detectors must be located relatively far (~1 m) from the fission chamber so that time-of-flight can be used to separate gamma rays from the fission neutrons.

Combined experiments on ^{235}U(n,f) measuring gamma-ray and neutron spectra were carried out from Nov. 15 – Dec. 24, 2002 using the FIGARO flight path. Two suitable gamma-ray detectors were available. One was a 10-cm diameter by 15-cm long BGO crystal and the other was a wedge-shaped BaF_2 crystal that is a spare for the DANCE array. The BaF_2 crystal is 15-cm long. The fission chamber contained 350 mg of highly enriched ^{235}U in a multi-foil configuration. A total of 28 days of beam time were used with 72% of maximum availability.

Experiment Report *(continued)*

Data were acquired for ^{235}U. These data will provide preliminary results and a benchmark for planning improvements in this type of measurement. This experiment ran simultaneously with #2002528 to measure the fission neutron spectra. The measurement was performed at 3.6 μs beam pulse spacing to reduce the effects of frame overlap. Due to delays in shipping the fission chambers from France, very little useful data were acquired with the ^{238}U fission chamber.

In order to be able to normalize the data to the gamma-ray spectrum of ^{252}Cf spontaneous fission, ~3 weeks of data using a Cf fission chamber were acquired after the beam time. In addition, data were taken with a number of gamma-ray sources to provide efficiency calibrations up to 6.13 MeV.

Because these data were taken with a new acquisition system, new analysis codes are being developed to analyze them.

IMPORTANT! List or attach a list of publications resulting from this experiment (published or in press).

LANSCE
Los Alamos Neutron Science Center

REPORT ON EXPERIMENT
(Please Type)

Submit all experiment reports to:
LANSCE User Office, MS H831, Los Alamos National Laboratory, Los Alamos, NM 87545

Experiment was carried out at:	**Local Contact**	**Proposal #**	***LANSCE Use Only***
☐ Manuel Lujan Jr. Neutron Scattering Center	Ron Nelson	2002558	**Report Rc'd**
☒ Weapons Neutron Research Facility	**FP/Instrument Used**		**2/20/03**
☐ WNR/Blue Room	4FP60R GEANIE		

Title
Measurement of the ^{150}Sm(n,2n)^{149}Sm Cross Section

Authors and Affiliations
J.R. Cooper LLNL
P.E. Garrett LLNL
L.A. Bernstein LLNL
W. Younes LLNL
J.A. Becker LLNL
M. Devlin LANL
N. Fotiades LANL
R.O. Nelson LANL

Experiment Report

The ^{150}Sm(n,2n)^{149}Sm cross sections as a function of neutron energy is important for rad-chem diagnostics. The (n,2n) reaction was studied in [1], but there is a systematic difference between model cross sections and experiment [2]. Partial gamma ray cross sections will be measured using the high purity germanium detector array, GEANIE located on WNR/60R.

The experiment was performed 9/27/2002 through 10/4/2002. An additional two days of data was taken at a later period to provide a total of 10 out of 10 days of the requested beam time. During this period, however, the beam current was bout 20% less than anticipated. A 8.7 g samarium oxide target was placed in the GEANIE target position perpendicular to the neutron beam. Approximately $5*10^7$ gamma singles were collected in the coaxial germanium detectors for neutron time of flights corresponding to 1 to 20 MeV neutrons. Approximately $3*10^7$ gamma singles were collected in the planar germanium detectors overt the same energy range.

The data is currently being analyzed using the xgam software package developed by Walid Younes at LLNL. The planar spectrum has been analyzed and preliminary ^{150}Sm(n,n'γ)^{150}Sm and ^{150}Sm(n,2nγ)^{149}Sm partial gamma ray cross sections have been determined. Currently, the coaxial spectrum is being fitted and the results will be checked for consistency with the planar results.

The codes GNASH and STAPRE will then be used to deduce the total reaction cross sections from the partial cross sections. The resulting (n,2n) data will be compared to previous results which were made using a different technique involving a large GD-Loaded liquid scintillator. In addition, the (n,n') cross section will be measured and compared to model predictions and the data will be searched for (n,p) and (n,α) cross sections. However, the (n,p) and (n,α) cross sections are small (<10 mb at 14MeV).

The experimental results will be combined with calculations using the codes GNASH and STAPRE to deduce the total reaction cross sections from the partial cross sections. The resulting (n,2n) data will be compared to previous results which were made using a different technique involving a large GD-Loaded liquid scintillator.

[1] J. Frehaut, A. Bertin, R. Bois, J. Jary, Symposium on Neutron Cross Sections from 10-50 MeV, Upton, L.I. (USA), May 12-14, 1980.
[2] R.D. Hoffman, Lawrence Livermore National Laboratory, private communication.

IMPORTANT! List or attach a list of publications resulting from this experiment (published or in press).

LANSCE
Los Alamos Neutron Science Center

REPORT ON EXPERIMENT
(Please Type)

Submit all experiment reports to:
LANSCE User Office, MS H831, Los Alamos National Laboratory, Los Alamos, NM 87545

Experiment was carried out at:	**Local Contact**	**Proposal #**	***LANSCE Use Only***
☐ Manuel Lujan Jr. Neutron Scattering Center	Ron Nelson	**2002563**	**Report Rc'd**
☒ Weapons Neutron Research Facility	**FP/Instrument Used**		
☐ WNR/Blue Room	4FP60R/GEANIE		

Title
Measurement of (n,xgamma) Cross Section of ^{11}B

Authors and Affiliations
Tony Hill, LLNL
Ron Nelson, LANL
Walid Younes, LLNL
Dennis McNabb, LLNL
John Becker, LLNL
Paul Garrett, LLNL
Matt Devlin, LANL
R.C. Haight, LANL
S.A. Wender, LANL
Nick Fotiades, LANL

Data was successfully taken at GEANIE using a boron 11 target. The data has been transported to LLNL. The process of sorting the data for analysis has begun. The data will be analyzed to produce (n,Xgamma) cross sections as a function of incident neutron energy and published in the open literature.

IMPORTANT! List or attach a list of publications resulting from this experiment (published or in press).

LANSCE
Los Alamos Neutron Science Center

REPORT ON EXPERIMENT
(Please Type)

Submit all experiment reports to:
LANSCE User Office, MS H831, Los Alamos National Laboratory, Los Alamos, NM 87545

Experiment was carried out at:	**Local Contact**	**Proposal #**	***LANSCE Use Only***
☐ Manuel Lujan Jr. Neutron Scattering Center	B.Takala	2002565	**Report Rc'd**
☐ Weapons Neutron Research Facility	**FP/Instrument Used**		**2/25/03**
☒ WNR/Blue Room	Target 4		

Title
"Single Event Upset in High End Memories SRAM (.13µm)"

Authors and Affiliations
Remi Gaillard, Marcos Olmos, Olivier Lauzeral
iRoC Technologies Corp.

Experiment Report

VDSM (Very Deep Sub Micron) technologies are becoming sensitive to Soft Errors to a point that system integrators have to take a careful look at the reliability issue created. Memories, especially SRAM and DRAM, are more prone to creating soft errors than other electronic components. The need of accurate assessment of this threat has become a real concern for reliability engineers, not only for severe environment applications like aerospace, but also for networking, high end computing and other ground applications. So far, the only way to accurately measure the risk is through testing, either system testing where a batch of hundreds of devices is tested in the normal environment for a period of time long enough to have a statically significant number of errors (several months) or through accelerated soft error rate testing (ASER). This test is described in a JEDEC standard: JESD89.

ASER is twofold to comply with the existence of the two main contributors of soft errors: alpha particles and cosmic rays. Alpha particles testing is done using regular alpha particles sources (Am241 or Th232). Cosmic ray testing is performed using high-energy neutron beam.

LANSCE offers a full spectrum high-energy neutrons beam, which spectrum is very close to the natural spectrum of cosmic rays induced particles.

The scope of the experiment was to test different types of stand-alone memories and logic embedded memories for the SER effect. 9 PCBs carrying a total of 30 DUT (devices under test) were stacked in front of the beam (see picture). Every single DUT was independently controlled by the tester and run a different test pattern. Test patterns are combinations of write and read cycles, at different speeds, under different conditions of temperature and voltage in order to study the sensitivity of the tested technologies to various parameters. The test lasted 50 hours, with very little off time for tune up and configuration changes.
In order to reach a good accuracy in the SER result, a statistically significant number of soft errors were detected: 300 to 1000 were the typical numbers. In the measurement accuracy, other factors also come into consideration: accuracy of neutron counting in the fission chamber and uniformity of neutron flux between the front and the back PCB (a decay of 26% between front an 9th board has been measured). The results analysis differentiates single-cell and multiple-cell upset due to single neutron hit. Furthermore, the analysis shows new phenomena of particular interest such as multi-bit upset at blocks of addresses.

This test not only showed the feasibility of testing a large number of devices at the same time in the Ice House at LANSCE, but also confirmed the sensitivity of VDSM memories to cosmic rays for both CMOS and SOI technologies. Accuracy achieved in measuring the SER (Soft Error Rate) depends on the number of error generated and spanned from 6% to 15%.

Experiment Report *(continued)*

Overview of the test set-up:

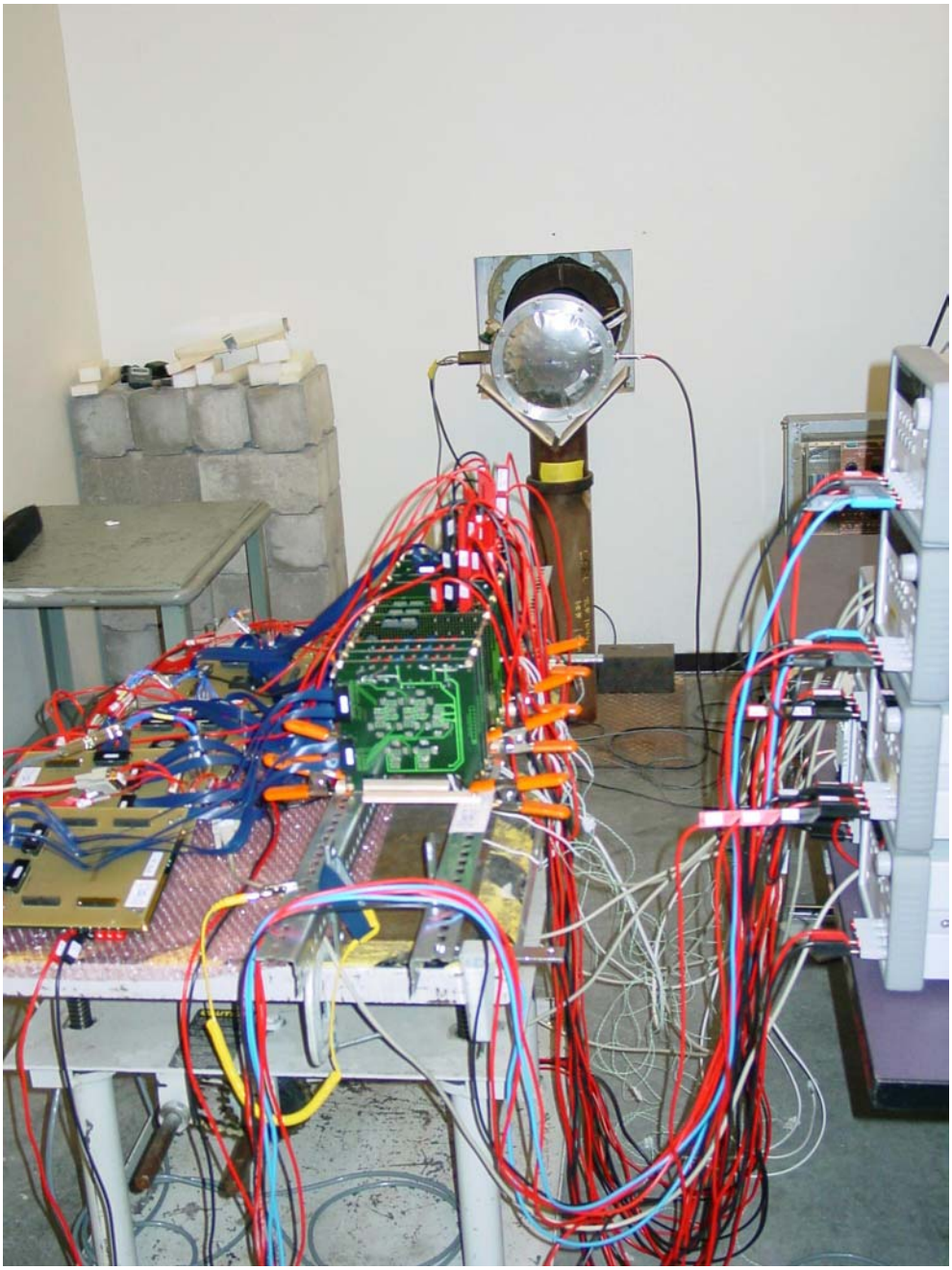

IMPORTANT! List or attach a list of publications resulting from this experiment (published or in press).
There will be no public disclosure of the results, since this test has been performed on behalf of private companies.